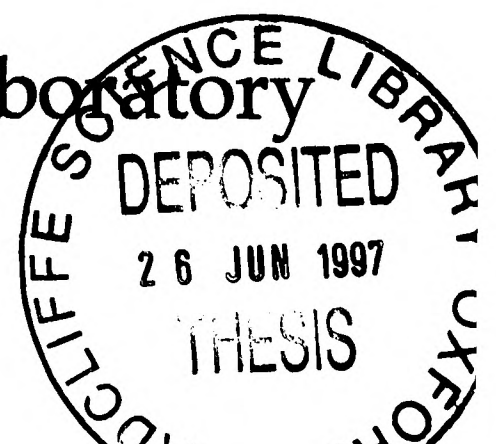


# SHORT WAVELENGTH LASERS AND THEIR APPLICATIONS

ADAM WHYBREW

A thesis submitted for the degree of Doctor  
of Philosophy at the University of Oxford

Jesus College & Clarendon Laboratory  
Trinity term 1996





# Abstract

---

## Short wavelength lasers and their applications

Adam Whybrew, Jesus College

*A thesis submitted for the degree of Doctor of Philosophy  
Oxford University  
Trinity Term 1996*

Most of this thesis describes experiments conducted in order to generate soft x-rays of energy  $>67$  eV from a laser-generated plasma, in order to pump the Xe III Auger laser at 109 nm.

In attempts to obtain the optimal sub-nanosecond laser pulses for amplification in a very simple KrF (248 nm) laser a compact KrF oscillator was used to obtain 1 mJ pulses of FWHM duration 2 ns, and plasma-truncated reflection of a focused KrF beam from metal targets gave 1.8 ns pulses. Longer pulses were obtained by truncated stimulated Brillouin scattering (TRUBS), and by plasma-truncated spatial-filtering.

Experiments were conducted to pump the Xe III laser using the leading edge of a 20 ns KrF laser pulse. An off-axis spherical mirror produced a 3 cm line plasma on a tantalum target. A poor conversion efficiency to soft x-rays was observed. Unexpectedly poor KrF beam quality was shown to have been a potential cause, a fault in the detection system having been ruled out. A repeat experiment was started, employing tighter focusing and better KrF beam quality.

A 7 ps KrF laser system was also investigated for the generation of the necessary plasmas. No 109 nm lasing was observed, and a low conversion efficiency into soft x-rays was measured. The short duration of the KrF pulse was suspected as the cause, and some attempts were made to compensate for this by means of preformed plasmas.

Over the course of the work, several aspects of KrF laser technology were improved, including: the characterisation of a novel, safe, solid-state source of fluorine ( $F_2$ ); the quantitative characterisation of nitrogen dioxide ( $NO_2$ ) as a variable attenuator for KrF radiation; and the manufacture of uniform, transparent, electrodes led to the laser system having the highest single pulse energy (2.55 J) of any UV-preionised, discharge-excited, conventional-aperture KrF laser.

Finally, separate work led to the development and absolute characterisation of a laser-plasma source of tunable VUV/EUV/XUV radiation (30 nm to 200 nm; 6 eV to 41 eV), as well as a sodium salicylate scintillator-based detection system. After optimisation of the target material, laser focusing, and micro-channel-plate (MCP) focusing of the plasma emission, an output of between  $10^6$  and  $10^7$  photons per shot in a 4 nm bandwidth could be delivered on target.



# Acknowledgements

---

I owe a great deal to the people listed below, and it is not possible to do justice to them here. It is a genuine pleasure to thank:

**Colin Webb**, my supervisor, for never failing to make time to help me, with his real wealth of experience and ingenuity.

**Tony Andrews**, for always being available to give me vital lessons in laser building, electronics, optics, and plumbing, as well as rescuing my pot plants from an arid doom.

**Julian Fletcher**, my predecessor, for teaching me how to use the laser he made, and then how to repair it.

**David Coutts**, for showing me what a post-doc is for. His often unsolicited but invariably welcome day-to-day interest in what I was doing was a real boon.

**Constantin Cristescu**, for his enthusiasm and charm, and for his perspiring jobs.

**Deborah Swarts**, for dropping an electrode, leading to the KrF laser becoming a world-beater.

**George Matthews**, for patiently teaching me everything I know about making things, and saving me from injury as necessary.

**Chris Goodwin** for making optical coatings and lending me a spin-coating kit.

**Bill Silfvast, Ian Ross, Henry Kapteyn, Adrian Baughan, Sean McGrady** and **Andrew Kearsley** for helpful discussions many of which led to work reported here.

**Edmond Turcu** for his infectious enthusiasm, for arriving early for a meeting, and for encouraging me to use his laser system, and fighting to make sure I could.

**Ric Allott** and **Nicola Lisi** for their help, enthusiasm, and calm confidence at RAL.

**David Hepburn-Scott**, for teaching me to write physics - if you find any wit in this thesis, you have him to thank.

**Adrian Haxell, Geoff Hogan, Simon Hooker**, and other past and present members of the laser group, including **Heather Booth** for being herself, **Julian Cashmore** for becoming himself, **Daniel Kapitan** for providing so much vicarious pleasure, **Laure Montandon-Varoda** for being a *rigole-brosse*, and **William Wadsworth** for being very reasonable. All of them good-naturedly lifted large pieces of steel, and provided numerous discussions, both useful and salacious, and made life in the lab a pleasure.

**My family and my friends, Tig, Tony, Ruth, Matt, James, Jim, Mona, Mette** and especially the last of the few, **William Osborn** and **Ursula Wielgosz** who variously kept me happy, sane, intrigued and inspired.

**SERC/EPSRC, Jesus College**, and **my parents** for letting me eat.

**Liz West** for proof-reading this thesis, and most of all, for putting up with me.



# Abbreviations

---

AR	Anti-reflection
ASE	Amplified spontaneous emission
cw	continuous wave
emf	electro-motive force
FWHM	Full-width at half-maximum
HeNe	Helium-Neon (laser)
IR	infrared
KF	Klein flange
LGP	Laser generated plasma
MCP	Microchannel plate
PET	Polyethylene terephthalate (“polyester”)
PMMA	Polymethylmethacrylate, also known by the brand names of Perspex and Plexiglas
PMT	Photomultiplier tube
PTFE	Polytetrafluoroethylene
PVDF	Polyvinylidene fluoride
RGH	rare-gas halide
RIO	Radiation induced opacity
SBS	Stimulated Brillouin scattering
SFUR	Self-filtering unstable resonator
SI	<i>systeme internationale</i> (MKS-based system of units)
SXR	Soft X-ray
TRUBS	Truncated stimulated Brillouin scattering
UV	ultraviolet
VPD	Vacuum photodiode
VUV	Vacuum ultraviolet
XUV	Extreme ultraviolet
Z	Atomic number



# Contents

---

<b>1. Introduction</b>	<b>1</b>
<b>1.1 Short wavelength lasers</b>	<b>1</b>
1.1.1 A fundamental problem	1
<b>1.2 Discharge excitation</b>	<b>3</b>
1.2.1 The KrF laser	3
1.2.2 Other excimer lasers	5
1.2.3 The molecular fluorine laser	6
1.2.4 A new generation of discharge-excited lasers	6
1.2.5 Laser-excited short wavelength lasers	7
1.2.6 Nonlinear techniques	7
<b>1.3 Plasma-pumped lasers</b>	<b>9</b>
1.3.1 Recombination and collisionally pumped lasers	10
1.3.1.1 Collisional excitation	10
1.3.1.2 Recombination pumping	12
1.3.1.3 Summary	13
<b>1.4 Photopumped schemes</b>	<b>13</b>
1.4.1 Resonance excitation	13
<b>1.5 Photoionisation lasers</b>	<b>14</b>
1.5.1.1 Photoelectron pumped lasers	14
1.5.2 Photoexcited lasers	15
1.5.2.1 Use of an Auger-metastable upper laser level	16
1.5.2.2 Use of an Auger-stable upper laser level	16
1.5.2.3 Use of Auger decay to obtain a population inversion	17
<b>1.6 Aim of project</b>	<b>19</b>
<b>1.7 Layout of thesis</b>	<b>21</b>
 <b>2. The Xe III laser, and laser-generated plasmas</b>	 <b>22</b>
<b>2.1 The Xe III laser</b>	<b>22</b>
2.1.1 Introduction	22
2.1.1.1 Principle of operation	22
<b>2.2 Review of Xe III lasers reported in the literature</b>	<b>24</b>
2.2.1 Systems with a gain channel	25
2.2.2 Travelling-wave geometry	26
2.2.2.1 Choice of target material	28
2.2.2.2 Prepulsing	28
2.2.2.3 Ion beam pumping	28
2.2.3 Summary	28
<b>2.3 Laser-generated plasmas</b>	<b>30</b>
2.3.1 Introduction	30



2.3.2 Zones in the plasma .....	30
2.3.3 Energy deposition.....	32
2.3.3.1 Inverse bremsstrahlung.....	32
2.3.3.2 Resonant absorption.....	33
2.3.4 Energy transport.....	33
2.3.5 Emission mechanisms .....	34
2.3.5.1 Bound-bound transitions .....	34
2.3.5.2 Free-bound transitions.....	34
2.3.5.3 Free-free transitions.....	34
2.3.6 Emission properties .....	34
2.3.6.1 Blackbody radiation.....	34
2.3.6.2 Temporal properties of output.....	34
2.3.7 Experimental considerations .....	35
2.3.7.1 Laser wavelength .....	35
2.3.7.2 Target material.....	36
2.3.8 Black body radiation.....	37
2.3.9 Plasma conversion efficiency.....	39
2.3.9.....	39
2.3.9.....	39
<b>2.4 Model for Xe III pumping .....</b>	<b>40</b>
2.4.1.1 Plasma emission .....	40
2.4.1.2 Bleaching of the absorption .....	41
2.4.2 Quenching .....	42
2.4.2.1 Electron density.....	42
2.4.2.2 Two-body quenching.....	43
2.4.2.3 Three-body quenching.....	45
2.4.2.4 Collisions with neutral xenon.....	45
2.4.2.5 Stark broadening.....	46
2.4.2.6 Conclusions about long-timescale pumping.....	47
 <b>3. Approaches to pulse shortening, and a compact oscillator</b>	 <b>48</b>
<b>3.1 Short pulses from KrF .....</b>	<b>48</b>
3.1.1 Introduction.....	48
3.1.1.1 Rationale.....	48
3.1.1.2 Suitability of KrF for short-pulse amplification.....	48
3.1.1.3 Dye system front ends .....	48
3.1.1.4 Saturable absorbers .....	49
3.1.1.5 Related systems.....	49
3.1.1.6 Electro-optic switching.....	50
3.1.1.7 Modelocking.....	50
3.1.1.8 Systems without feedback .....	52
3.1.1.9 Conclusions.....	52
<b>3.2 Compact oscillators.....</b>	<b>52</b>
3.2.1 Experimental arrangement for small oscillator .....	54
3.2.1.1 Laser module.....	54
3.2.1.2 Electrical driver circuit .....	55



3.2.1.3 Detection system .....	56
3.2.1.4 Experimental results .....	56
<b>4. Plasmas for pulse-truncation</b>	<b>58</b>
4.1 Introduction.....	58
4.2 Truncated Brillouin Scattering (TRUBS) .....	58
4.2.1 Stimulated Brillouin scattering (SBS).....	58
4.2.1.1 Description of the phenomenon .....	58
4.2.1.2 Frequency-shift of SBS radiation .....	58
4.2.1.3 Phase-conjugation .....	59
4.2.1.4 Application of SBS to pulse-shortening .....	60
4.2.2 Truncated Brillouin Scattering (TRUBS) .....	61
4.2.2.1 Overview .....	61
4.2.2.2 A specific experimental arrangement.....	62
4.2.3 Initial experimental investigation.....	64
4.2.3.1 Experimental arrangement .....	64
4.2.3.2 Experimental results and interpretation .....	65
4.2.4 Further TRUBS experiments.....	67
4.2.5 Conclusions about TRUBS .....	68
4.3 Plasma-truncated reflection.....	68
4.3.1 Rationale for experiments .....	68
4.3.2 Preliminary investigations: a copper target .....	69
4.3.3 Experimental variations.....	70
4.3.3.1 Target materials .....	70
4.3.3.2 Optical arrangement .....	70
4.3.3.3 Finding the focus.....	71
4.3.4 Experimental results .....	71
4.3.5 Discussion .....	73
4.3.5.1 Evolution of divergence.....	73
4.3.5.2 Cause of initial truncation.....	73
4.3.5.3 Cause of spatial structure in reflected beam .....	74
4.3.5.4 Comparison with previous reports in the literature...	75
4.4 Plasma-truncated spatial filtering.....	75
4.4.1 Beam quality considerations.....	75
4.4.2 Experimental arrangement .....	76
4.4.3 Discussion .....	77
4.5 Conclusions about short pulses.....	77
4.5.1.1 Arrangements for amplification of 4 ns pulses in KrF amplifier module .....	79
4.5.1.2 Gain-recovery time and upper-state lifetime.....	79
4.5.1.3 Extraction techniques .....	80
4.5.1.4 Implications for further work.....	82
<b>5. KrF laser technology</b>	<b>84</b>
5.1 Existing KrF laser system.....	84
5.1.1 Introduction.....	84
5.1.2 Discharge laser modules .....	84



5.1.2.1 Master oscillator.....	85
5.1.2.2 Amplifier module.....	85
5.1.2.3 Gas system.....	86
5.1.3 Electrical driver circuit.....	87
5.1.4 Injection seeded cavity.....	89
<b>5.2 Modifications to the KrF laser system .....</b>	<b>92</b>
5.2.1 Electrical changes.....	92
5.2.1.1 Simplified geometry for external driver circuit .....	92
5.2.1.2 Mechanised electrode winding .....	93
5.2.2 Minor modifications.....	94
<b>5.3 A safe solid-state fluorine source.....</b>	<b>94</b>
5.3.1.1 Introduction .....	94
5.3.1.2 The fluorine source.....	95
5.3.1.3 Installation of fluorine source .....	95
5.3.2 Characterisation of the source.....	96
5.3.2.1 Pulse energy & gas lifetime.....	96
5.3.2.2 Explanation of gas-lifetime results .....	98
5.3.2.3 Gas purity considerations .....	99
5.3.2.4 Conclusions about pulse-energy.....	100
5.3.2.5 Temporal profiles .....	101
<b>5.4 Nitrogen dioxide: a variable attenuator for KrF laser radiation .....</b>	<b>102</b>
5.4.1 Introduction.....	102
5.4.2 Physical chemistry of the $\text{NO}_2 \rightleftharpoons \text{N}_2\text{O}_4$ equilibrium.....	102
5.4.3 Absorption measurements.....	104
5.4.4 Photobleaching .....	105
5.4.4.1 Experimental observations.....	105
5.4.4.2 Explanation for photobleaching .....	106
<b>5.5 Summary .....</b>	<b>107</b>
 <b>6. A first attempt at the Xe III laser .....</b>	 <b>109</b>
6.1 Introduction.....	109
6.2 Focusing geometries.....	109
6.2.1 Introduction.....	109
6.2.2 Focal intensity required.....	109
<b>6.3 Normal incidence focusing geometries .....</b>	<b>111</b>
6.3.1 Random phase plates .....	111
6.3.2 Control of KrF beam-divergence.....	111
6.3.3 Cylindrical lenses & mirrors .....	112
6.3.3.1 Cylindrical lenses.....	112
6.3.3.2 Cylindrical mirror .....	114
6.3.3.3 Reducing beam size to reduce aberrations.....	114
6.3.4 Off-axis spherical mirrors.....	115
6.3.4.1 Mirror & lens scheme .....	115
6.3.4.2 Single mirror scheme.....	115
6.3.5 Travelling-wave geometry .....	117
6.3.5.1 Cylindrical mirror systems .....	117



6.3.5.2 Off-axis spherical mirror systems .....	118
<b>6.4 Conclusions.....</b>	<b>119</b>
<b>6.5 Focusing through a window .....</b>	<b>119</b>
<b>6.6 Experimental arrangement.....</b>	<b>122</b>
6.6.1 Focusing system .....	122
6.6.2 Target chamber.....	122
6.6.3 Target winder .....	123
6.6.4 Alignment.....	124
6.6.5 Overview.....	125
6.6.6 Yaw .....	126
6.6.6.1 Overview of yaw alignment .....	126
6.6.6.2 How a pentaprism works.....	127
6.6.6.2 .....	127
6.6.6.3 Geometrical spreading of KrF beam.....	129
6.6.6.4 Overall yaw accuracy .....	129
6.6.7 Pitch.....	129
6.6.8 Roll .....	130
6.6.8.....	130
6.6.9 Depth .....	130
6.6.9.....	130
6.6.9.1 Crude geometric estimation.....	130
6.6.9.1 .....	130
6.6.9.2 Line etching .....	131
6.6.9.2 .....	131
6.6.9.2 .....	131
<b>6.7 Detection of soft x-rays.....</b>	<b>131</b>
<b>6.8 Sodium salicylate as a scintillator.....</b>	<b>132</b>
<b>6.9 Other SXR detectors.....</b>	<b>132</b>
6.9.1.1 Photographic film.....	132
6.9.1.2 Photoelectric effect based detectors.....	132
6.9.1.3 Silicon PIN photodiodes.....	133
<b>6.10 SXR filters .....</b>	<b>133</b>
<b>6.11 Manufacture and use of scintillators .....</b>	<b>134</b>
6.11.1 Spray coating technique.....	134
<b>6.12 Quantum efficiency of sodium salicylate.....</b>	<b>134</b>
<b>6.13 Experiments to detect SXRs .....</b>	<b>135</b>
6.13.1 Experimental arrangement .....	135
<b>6.14 Results.....</b>	<b>136</b>
<b>6.15 Repercussions .....</b>	<b>137</b>

<b>7. Experimental repercussions: beam cleaning and spot foci</b>	<b>138</b>
7.1 Introduction.....	138
7.2 Beam quality.....	138
7.3 Soft x-rays from a plasma spot.....	141



7.3.1 Introduction.....	141
7.3.2 Filter breakage.....	141
7.3.3 Direct coating of Sodium Salicylate .....	142
7.3.3.1 Theory .....	142
7.3.3.2 First attempt.....	142
7.3.3.3 Spin coating .....	143
7.3.3.4 Characterisation of spun coatings .....	144
7.3.4 Use of helium to reduce debris.....	145
7.3.4.1 Results .....	146
<b>7.4 Search for 109 nm fluorescence pumped by spot-plasma emission .....</b>	<b>149</b>
7.4.1 VUV monochromator.....	149
7.4.2 Experimental results .....	150
<b>7.5 Tighter line focusing arrangement .....</b>	<b>152</b>
<b>7.6 Effect of spot size on conversion efficiency .....</b>	<b>154</b>
<b>7.7 Conclusions.....</b>	<b>156</b>
<b>7.8 Summary .....</b>	<b>157</b>
 <b>8. Picosecond pumping .....</b>	 <b>158</b>
<b>8.1 Introduction.....</b>	<b>158</b>
8.1.1 Rationale .....	158
8.1.2 Picosecond laser system.....	159
<b>8.2 Experimental arrangement.....</b>	<b>159</b>
8.2.1 Line focus geometry .....	159
8.2.2 Alignment.....	160
8.2.2.1 Roll.....	161
8.2.2.2 Yaw .....	162
8.2.2.3 Pitch.....	163
8.2.2.4 Depth.....	163
<b>8.3 Search for soft x-rays .....</b>	<b>165</b>
<b>8.4 Search for 109 nm emission .....</b>	<b>167</b>
8.4.1 Experimental arrangement .....	167
8.4.2 A first attempt .....	168
8.4.3 Plasma shadowing .....	169
8.4.4 A second attempt.....	171
8.4.4.1 109 nm mirror alignment .....	171
8.4.4.2 LiF diffuser .....	171
8.4.4.3 Double knife-edge plasma shadowing .....	171
8.4.4.4 Experimental results: still no 109 nm action.....	172
8.4.5 Preheating .....	174
8.4.5.1 Double pulses.....	175
8.4.5.2 Pulse trains.....	175
8.4.5.3 Picosecond prepulse .....	175
<b>8.5 Discussion .....</b>	<b>177</b>
8.5.1 Vacuum quality .....	177
8.5.2 Upper limit on SXR conversion efficiency.....	177
8.5.3 LiF windows.....	178



8.5.4 Upper limit on laser pulse energy .....	181
8.5.5 Conclusions .....	182
8.5.6 Suggestions for further work .....	183
<b>9. Photons for biologists: a laser-plasma source for the VUV</b>	<b>184</b>
9.1 Introduction .....	184
9.1.1 Picosecond KrF laser system .....	185
9.2 Investigations of the source .....	185
9.2.1 Experimental arrangement .....	185
9.2.1.1 Pellicle .....	187
9.2.1.2 Vacuum quality .....	187
9.2.2 Possible harmonic generation .....	188
9.2.3 Microchannel plate focusing .....	189
9.2.4 Target material .....	191
9.2.5 Defocusing .....	192
9.2.6 A whiff of neon .....	195
9.3 Photon detectors .....	196
9.3.1 Sodium salicylate & photomultiplier .....	196
9.3.1.1 Geometrical collection efficiency .....	196
9.3.1.2 Spectral response of sodium salicylate .....	198
9.3.1.3 Absolute quantum efficiency vs. number of photons collected .....	199
9.3.1.4 Total internal reflection .....	200
9.3.1.5 Radiation damage .....	201
9.3.1.6 Photomultiplier efficiency and gain .....	201
9.3.1.7 Electrical detection circuit .....	202
9.3.2 Overall detection efficiency .....	202
9.3.3 Calibrated diode .....	202
9.4 Conclusions .....	203
<b>10. Conclusion</b>	<b>205</b>
10.1 Discussion and suggestions for further work .....	205
10.1.1 Nanosecond pumping of the Xe III laser .....	205
10.1.2 Pulse-shortening .....	205
10.1.3 Picosecond pumping of the Xe III laser .....	205
10.1.4 Laser-plasma VUV/XUV source .....	206
10.1.5 Ultraviolet laser technology .....	206
10.2 Summary .....	207
<b>11. References</b>	<b>209</b>



# 1. Introduction

---

## 1.1 Short wavelength lasers

### 1.1.1 A fundamental problem

In their proposal for extending maser action to optical frequencies, Schawlow & Townes [1958] concluded “*The prospect is favourable for masers which produce oscillations in the infrared or optical regions. However, operation of this type of device at frequencies which are still very much higher seems difficult*”. Almost exactly two years later, the “optical maser”, or laser, was demonstrated, operating at 694.3 nm [Maiman 1960]. The next major milestones in the development of lasing at shorter wavelengths were the development of the nitrogen laser at 337 nm [Heard 1963], and then the molecular hydrogen lasers at ~160 nm [Hodgson 1970, Waynant *et al.* 1970] and 116 nm [Waynant 1972, Hodgson & Dreyfus 1972]. The prediction of Schawlow & Townes [1958] proved extremely accurate, however, because it took another twelve years to achieve lasing at a shorter wavelength than that of the hydrogen laser [Matthews *et al.* 1985, Suckewer *et al.* 1985].

There is a fundamental reason, first elucidated by Schawlow & Townes [1958], why it has been so difficult to achieve short wavelength lasing. The problem is that the power required to sustain a population inversion against spontaneous decay rises very sharply with the laser transition frequency. Einstein [1917] used a thermodynamic argument to show that the *spontaneous* decay rate,  $A_{21}$  for any optical transition, is related to the *stimulated* emission rate coefficient,  $B_{21}$ , according to

$$A_{21} = \frac{8\pi h \nu^3}{c^3} B_{21} \quad (1.1),$$

for a nondispersive medium of unit refractive index, where  $h$  is Planck’s constant,  $\nu$  is the frequency of the optical transition, and  $c$  is the vacuum speed of light. From this, the small-signal gain coefficient,  $\alpha(\nu)$ , for a laser transition may be written\* in terms of the *spontaneous* decay rate

$$\alpha(\nu) = A_{21} \frac{c^2}{8\pi \nu_0^2} g(\nu) N^* \quad (1.2),$$

where  $\nu_0$  is the central frequency of the laser transition, and  $g(\nu)$  is the lineshape function, normalised such that

$$\int_0^\infty g(\nu) d\nu = 1 \quad (1.3).$$

In expression (1.2), the variable  $N^*$  is the inversion density, given by

---

\* See any general textbook on lasers, for example [Verdeyen 1981].



$$N^* = N_2 - \frac{g_2}{g_1} N_1 \quad (1.4),$$

where  $N_1$ ,  $N_2$ ,  $g_1$ , and  $g_2$  are the lower and upper laser level population densities and degeneracies, respectively.

This allows us to express the instantaneous power per unit volume,  $P$ , lost to spontaneous decay in the laser medium, as

$$P = (h\nu)(A_{21}N_2) \geq h\nu A_{21}N^* \quad (1.5),$$

since  $(h\nu)$  is the photon energy, and  $(A_{21}N_2)$  is the spontaneous decay rate per unit volume. The justification for the inequality in (1.5) comes from expression (1.4) which shows that the inversion density cannot exceed the upper laser level population density.

In order to sustain the population inversion against spontaneous decay, we must provide a power of at least  $P$ . Furthermore, combining (1.2) and (1.5), we find that if we wish to achieve a given line-centre small signal gain coefficient  $\alpha(\nu_0)$ , we must supply a power  $P_{\text{pump}}$ , such that

$$P_{\text{pump}} > \alpha(\nu_0) \frac{8\pi}{c^2} h\nu_0^3 \frac{1}{g(\nu_0)} \quad (1.6).$$

Whatever the main line broadening mechanism, we may write

$$g(\nu_0) \approx \frac{1}{\Delta\nu} \quad (1.7),$$

where  $\Delta\nu$  is the FWHM linewidth. For Doppler broadening, for example, this is given by

$$\Delta\nu = \nu_0 \left( \frac{8k_B T \ln 2}{Mc^2} \right)^{1/2} \quad (1.8),$$

where  $M$  is the mass of the emitting species,  $T$  is the temperature, and  $k_B$  is Boltzmann's constant. Combining (1.6), (1.7), and (1.8), we find that the power needed to sustain a given gain coefficient against spontaneous decay, is proportional to the fourth power of the laser frequency.

If we assume a Doppler broadened laser transition at 100 nm, in room temperature xenon gas, and require a gain of  $1 \text{ cm}^{-1}$  (typical for a short wavelength laser), then (1.6), (1.7), and (1.8) indicate that we require a pumping power density of at least  $1.6 \text{ kW cm}^{-3}$ . This assumes perfect efficiency - in fact, 1% would be extremely impressive for a short wavelength laser. Thus, we can expect to need a pumping power density of hundreds of kilowatts per cubic centimetre in order to achieve lasing at 100 nm. There are only very few technologies capable of meeting these specifications. These include thermonuclear explosions (clearly of very limited application), electrical discharges in the laser medium, electron (or ion) beams, and other lasers. Here we review how the last three of these have been used to achieve short wavelength lasing.

For this review, we shall consider short wavelength lasers to be those operating at 250 nm and below. Technologically, the wavelength range between  $\sim 190 \text{ nm}$  and  $105 \text{ nm}$  is very important. It is known as the vacuum ultraviolet (VUV). This is because air strongly absorbs light in this wavelength range, mainly on account of the Schumann-Runge absorption bands of molecular oxygen. Thus, evacuated (or transparent gas) systems are needed. The 105 nm lower wavelength of the VUV region is determined



by the transmission cut-off of the widest bandgap window material known, namely lithium fluoride (LiF). Thus, there are no window materials available for wavelengths below 105 nm, so differential pumping techniques are required to contain any laser medium, while allowing the light produced to escape from it.

Other reviews of the techniques reported here have been given by Key [1985] on recombination and for collisionally excited plasma lasers; Keane *et al.* [1989] (and others - see §1.3.1) on soft x-ray lasers within laser-generated plasmas and their applications; Kapteyn *et al.* [1992] on recombination, collision, and photopumped lasers; Hooker & Webb [1994] on the generation of coherent VUV radiation; Tsakiris [1996] on recent developments in high harmonic generation; and Rocca [1996] on recent developments in sub-100 nm lasers, especially capillary discharge excitation.

## 1.2 Discharge excitation

One way to achieve high powers is to store electrical charge in capacitors, and discharge them. This can take the form of a discharge through a laser medium, or one can generate an electron beam, which is introduced to the laser medium through a thin solid wall. Technologically, these are very important techniques, since they enable the pumping of the rare-gas halide excimer lasers, as well as the molecular fluorine and hydrogen lasers. We shall consider one such laser system in detail, the krypton-fluoride (KrF) laser, since lasers of this type have been used extensively for the work described in this thesis.

### 1.2.1 The KrF laser

The KrF laser is one a family of rare-gas halide (RGH) *excited-dimer* (excimer) lasers, which all operate on the same principle. The first report of such a laser (XeBr at 282 nm) was made by Searles & Hart [1975]. A month later, Ewing & Brau [1975] reported lasing using XeCl (308 nm) and KrF (249 nm). Since then several other RGH systems have been made to lase, including ArF (193 nm), ArCl (175 nm), KrCl (223 nm), and XeF (351 nm) [Webb 1983].

Put simply, the principle of operation is that a laser transition occurs between a bound excited state, and an unbound (or very weakly bound in the case of XeF) ground state of a molecule. The fact that the ground state is unbound means that it is impossible to populate it, because any molecules in it dissociate after a time of approximately one vibrational period, which is of order 0.1 ps. Thus, any population in the upper state, of natural lifetime 7 ns for KrF [Eden *et al.* 1978], corresponds to a population inversion. Fig. 1.1 shows the molecular energy curves for KrF.



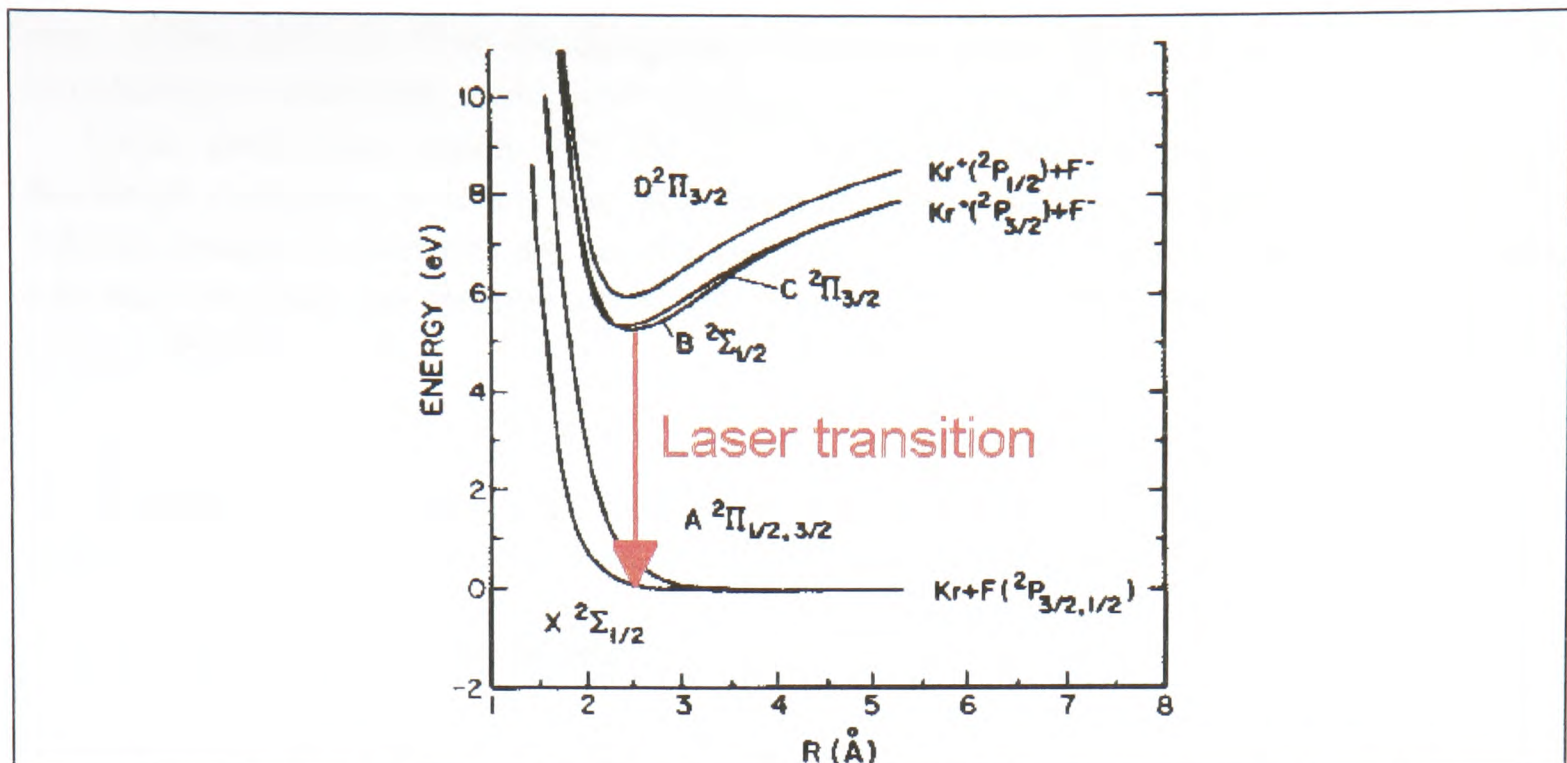


**Figure 1.1.** Molecular potential energy curves for KrF laser system. Diagram is adapted from Webb [1983], and is based on calculations made by Hay & Dunning [1977].

The upper laser level  $\text{KrF}^*$  (excimer) state may be generated by the reaction



which is known as the neutral channel or metastable channel, or by an alternative reaction



which is known as the ion channel. A third body is required for the ion channel reaction in order to carry away excess momentum and energy, stabilising the excimer. Although this is shown as helium in reaction (1.10), other buffer gases may also be used - and indeed neon gives better lasing, but is much more expensive. Yoshida *et al.* [1994] have recently deduced that for a (particular) discharge-excited KrF laser, the ion channel dominated when neon was used as the buffer gas. On the other hand, when the buffer gas was helium, they deduced the ion channels and neutral channels contributed equally to the excimer formation. This contrasts with kinetic studies of the XeCl laser in which Kearsley [1980] deduced that the ion channel dominated when helium was used as the buffer gas.

All commercial excimer lasers, as well as the home-built device described in chapter 5, employ discharge excitation. In this case the precursors to the excimer molecule are generated by energy transfer from the free electrons in the discharge, according to the reactions



and



This electron-attachment reaction (1.12) has a very important consequence for the discharge-excitation of KrF lasers. This is known as the halogen-donor depletion instability and was first proposed by Coutts & Webb [1986] with regard to the XeCl laser system. Suppose that in some localised region in the discharge there is a higher than ambient electron density. This causes reaction (1.12) to proceed faster (per fluorine molecule) and so the fluorine density must become lower than elsewhere. This, in turn, leads to a faster growth in the electron density, since fewer fluorine molecules remain to



remove free electrons from the discharge. This is a positive feedback loop, and gives rise to discharge instabilities, as do other mechanisms described in §5.3.2.2.

These instabilities mean that for wide aperture, long pulse-duration KrF lasers, discharge excitation is unsuitable and electron beam pumping is used instead. In this scheme, beams of electrons are accelerated, *in vacuo*, to 0.2-1 MeV from cold cathodes, and enter the laser gas through a thin foil. Energy deposition occurs by ionisation, such as [Shaw 1991]



A technological disadvantage with electron beam pumping is the dangerous x-ray emission generated by the impact of very high energy electrons on the beam-transmitting metal foil.

## 1.2.2 Other excimer lasers

The requirement for an excimer laser scheme is an unbound lower laser level, and a bound upper level, and the RGH lasers are not the only possible way to achieve this. Indeed, lasing has been achieved from the rare-gas excimers,  $\text{Xe}_2^*$ ,  $\text{Kr}_2^*$ , and  $\text{Ar}_2^*$ , at wavelengths near 170 nm, 146 nm, and 125 nm respectively. These wavelengths are all shorter than the shortest-wavelength RGH laser, the ArCl laser at 175 nm. The first report of a rare-gas excimer laser was made by Basov *et al.* [1970]. They used a 1 MeV electron beam to excite liquid xenon, which was found to lase at 171.5 nm, 178.5 nm and 181.5 nm. The advantage of using a liquid target over a gas is that it does not require containment, and so there are no losses to the electron beam in foil walls. Furthermore, a high density of rare gas is desirable, since the excimer is created by a three-body process.

Edwards *et al.* [1979] have demonstrated an  $\text{Xe}_2^*$  excimer system at 172 nm, capable of operation at 0.5 Hz, giving up to 25 mJ per pulse. The maximum output energy was limited by the damage threshold of the cavity optics. Kurosawa *et al.* [1991] have tackled the problem of damage to the optical elements, and used a silicon carbide rear mirror which was not found to damage, and an  $\text{MgF}_2$  output coupler, which had to be moved to expose a fresh region between each laser shot. This allowed Kurosawa *et al.* [1991] to obtain the current state-of-the-art performance from the  $\text{Ar}_2^*$  excimer laser system. This is a pulse energy of 80 mJ, in a pulse of 5 ns duration at 125 nm.

All rare gas excimer lasers reported to date have required electron beam pumping in order to achieve the very high excitation power density needed for lasing. Expressions (1.6) and (1.7) indicate that the power requirement can be relaxed if the linewidth of the laser transition can be reduced. This can be achieved by supersonic cooling of a discharge, by expansion through a nozzle. The idea is that the cooling results in only the lowest lying rotational and vibrational levels of the upper electronic levels being populated. The technique has been investigated by Efthimiopoulos *et al.* [1989], who claimed it allowed them to achieve lasing from a discharge-excited (rather than electron-beam excited)  $\text{Ar}_2^*$  excimer laser. However, Hooker & Webb [1994] have questioned whether this could be possible as described by Efthimiopoulos *et al.* [1989].

Other excimer schemes are possible if the excimer has a net charge. These are known as ionic excimer systems. They are alkali halide ions  $(\text{AX})^+$ , rare gas halide ions  $(\text{RgX})^+$ , and rare gas alkali ions  $(\text{ARg})^+$ . These are isoelectronic with the rare gas halide (e.g. KrF), interhalogen (e.g. molecular fluorine laser), and rare gas excimer (e.g.  $\text{Ar}_2^*$ ) neutral laser schemes respectively. Myriad potential laser transitions have been calculated for ionic excimers, ranging in wavelength from 64 nm to 190 nm. Fluorescence has been observed



on many of these transitions, excited by heavy-particle ion beams, soft X-rays, and electron beams (see, for example, Kubodera *et al.* [1992] or Wang *et al.* [1995]). However, gain has been demonstrated on only one system, namely the  $\text{Cs}^{2+}\text{F}^-$  alkali halide ionic excimer, which is isoelectronic with  $\text{XeF}$  [Tóth *et al.* 1993]. Excitation was achieved by means of soft x-rays (SXR) from a laser-generated plasma (LGP). We return to this in §1.5.1.1.

### 1.2.3 The molecular fluorine laser

At 157.8 nm, the molecular fluorine laser has the shortest wavelength of any commercially-available laser. Although the system can usually be made to operate in the same apparatus as RGH excimer lasers (by a suitable change of optics and laser gas, which must be very pure), it differs from these systems in that the lower level is bound. This means that the radiation is narrowband (on two or three lines, depending on the pumping conditions) with a linewidth (on each line) of  $\sim 0.1\text{-}0.3\text{ cm}^{-1}$  [Hooker & Webb 1994].

The excitation kinetics favour operation at high pressures of helium buffer gas. The current state-of-the-art for a discharge excited system has been reported by Hooker *et al.* [1992a]. They obtained 237 mJ pulse energies from a double-ended (*i.e.* output taken from both ends) fluorine laser, operating with 11 bar (absolute) of helium buffer gas. For single-ended operation, the maximum output energy was 176 mJ.

### 1.2.4 A new generation of discharge-excited lasers

Until recently, the shortest-wavelength laser which could be excited by an electrical discharge through the laser medium was the molecular hydrogen laser at 116 nm [Waynant 1972]. However, during the course of the (unrelated) work described in this thesis, a new generation of short-wavelength discharge-excited lasers has started to emerge. The technique, which involves a capillary discharge, was proposed for recombination pumped lasers by Rocca *et al.* [1988], and collisionally pumped lasers by Rocca *et al.* [1993a]. Recombination and collisionally excited lasers are discussed in §1.3.1. Early experimental work showed fluorescence on several proposed laser transitions [Rocca *et al.* 1993b, 1993c]. The breakthrough was reported by Rocca *et al.* [1994]. They obtained a gain-length product of 7.2 from collisionally excited neon-like  $\text{Ar}^{8+}$ , at a wavelength of 46.9 nm. More recently, Rocca *et al.* [1995], have reported nearly saturated output from the same laser system, with a gain-length product of 14, obtained from a 15 cm long discharge. Less spectacular gain-length products have also been reported recently, for similar discharge schemes, used to pump recombination lasers. Table 1.1 gives a summary of the reports of gain from short wavelength, discharge-excited systems.



Reference	Lasing species	$\lambda$ nm	Pumping type	Discharge type	Gain length product
Glenzer & Kunze 1994	O <sup>5+</sup>	52.0	recombination	Gas-liner pinch	4.5
Rocca <i>et al.</i> 1994	Ar <sup>8+</sup>	46.9	collisional	capillary	7.2
Shin <i>et al.</i> 1994	C <sup>5+</sup>	18.2	recombination	capillary	3.9
Wagner <i>et al.</i> 1996	O <sup>5+</sup>	52.0	recombination	z-pinch	2.5
		49.8			2.2
Rocca <i>et al.</i> 1995	Ar <sup>8+</sup>	46.9	collisional	capillary	14

**Table 1.1.** Discharge excited VUV lasers reported to have shown appreciable gain.

We shall concentrate on the Rocca *et al.* [1994, 1995] capillary laser scheme, since this has shown by far the most gain. A discharge is formed along the walls of a long (~15 cm) narrow (4 mm) capillary tube. As the current increases, the magnetic field generated compresses the plasma, until it reaches a diameter of ~300  $\mu\text{m}$ . During this process, the discharge plasma becomes increasingly ionised, eventually reaching the Ar<sup>8+</sup> ionisation stage. Near the end of the compression the plasma reaches the electron temperature and densities necessary for gain in the neon-like argon ions. The properties of the capillary discharge excitation system which make it suitable for pumping the Ar<sup>8+</sup> laser system are that it generates a highly-ionised, hot, dense, and, crucially, uniform plasma. One of the main technological hurdles to be overcome with the scheme is how to achieve the very low inductance, high voltage (700 kV) discharge circuits needed.

1.2.5 Laser-excited short wavelength lasers

As well as discharges, another technique capable of generating the power densities required to pump short wavelength lasers is the use of another laser. By using temporal and spatial compression (*i.e.* extracting energy in short pulses, and focusing them) the required power can be obtained from less powerful technologies (*e.g.* electrical discharges).

The simplest way of achieving this is to use a short wavelength laser as a flashlamp to excite a longer wavelength laser. For example the molecular fluorine laser has been used to pump lasing on several lines between 163 nm and 589 nm in nitric oxide gas [Hooker *et al.* 1992b, Haxell *et al.* 1993]. For this scheme the absorption spectrum of nitric oxide must be shifted to coincide with the wavelength of the fluorine laser. Hooker *et al.* [1992] used the Zeeman effect to achieve this by subjecting the nitric oxide to a magnetic field.

The use of a laser medium with broadband absorption at the fluorine laser wavelength avoids the problem of tuning the absorption. Cashmore [1995] has recently investigated two such laser media - the rare earth doped fluoride crystals LaF<sub>3</sub>:Nd<sup>3+</sup> and LiYF<sub>4</sub>:Nd<sup>3+</sup>. Despite an earlier report of lasing at 172 nm from one of these, Cashmore [1995] has shown that VUV lasing is impossible in both of these laser media, on account of excited state absorption.

1.2.6 Nonlinear techniques

The two schemes discussed above, which are both linear processes, give rise to (or were intended to give rise to) laser radiation at wavelengths longer than that of the pumping



laser. On the other hand, there are several nonlinear techniques by which radiation having a shorter wavelength than a pumping laser may be obtained. An extensive review of these techniques is given by Hooker & Webb [1994]. For the sake of brevity, we shall do little more than list these techniques here.

There have been tens of reports of four wave mixing in metal vapours or noble gases. Noble gas systems have recently been reviewed by Wellegehausen *et al.* [1996]. Taken together, four wave mixing systems (in metal vapours and noble gases) have been used to obtain tunable radiation of wavelengths between  $\sim 90$  nm and  $\sim 220$  nm, at efficiencies ranging from  $10^{-2}$  to  $10^{-10}$ . For example, Hillbig & Wallenstein [1983] obtained tunable VUV radiation over the range 155 nm to 220 nm by four wave mixing in xenon. A two photon resonance for UV radiation at frequency  $\omega_{UV}$  was used to enhance the conversion efficiency, which was 0.05%-0.2%. A dye laser, at a tunable visible frequency,  $\omega_{dye}$  was mixed with the UV radiation, such that the output frequency was  $\omega_{out} = 2\omega_{UV} - \omega_{dye}$ .

Stimulated anti-Stokes Raman scattering provides a way of generating short wavelength coherent radiation. Experimentally, the technique is very straightforward - pump laser radiation at frequency  $\omega_p$  is focused into a cell containing a gas (often  $H_2$ ). This generates a first Stokes wave at a (lower) frequency  $\omega_{s1} = \omega_p - \Delta\omega$ , where  $\Delta\omega$  is the frequency difference between the ground state and an excited state in the Raman medium. The process is stimulated, and so amplification occurs. The first Stokes wave can become sufficiently intense to generate a second Stokes wave at angular frequency  $\omega_{s2} = \omega_{s1} - \Delta\omega$ . The process can repeat to increasingly high Stokes orders, and a set of emission lines, separated by a constant energy difference are observed.

Output at shorter wavelengths than the pumping radiation is also observed, on account of an anti-Stokes process. This is a four-wave mixing process, the first order anti-Stokes frequency being given by  $\omega_{AS1} = 2\omega_p - \omega_{s1}$ . This process also extends to high orders, the  $N^{th}$  order frequency being given by  $\omega_{ASN} = \omega_p + \omega_{AS(N-1)} - \omega_{s1}$ . The result is a set of spectral lines at progressively shorter wavelengths and decreasing intensity.

As an example, Wada *et al.* [1992] have observed 10 orders of anti-Stokes radiation from a hydrogen medium, pumped by a KrF laser of peak power 150 MW. The first order output at 226 nm had a power of 10 MW, whereas the tenth order power was 10 kW.

The conversion efficiency of anti-Stokes Raman schemes may be improved by cooling the Raman medium, thus increasing the population of ground state [Wallmeier & Zacharias 1988]. Efficiency improvements can also be achieved by the application of radiation at other frequencies (first Stokes, or 2<sup>nd</sup> harmonic of pump), as well as the pump radiation [Wallmeier & Zacharias 1988, Schulz-von der Gathen *et al.* 1990].

If a population inversion can be created in a Raman medium, an Anti-Stokes Raman laser may be possible. The inversion may be created by photodissociation of a parent molecule, which preferentially populates a metastable level in one of the products. We consider two typical reports of the technique. High photon efficiencies ( $\sim 40\%$ ) are possible, as reported by White & Henderson [1983], for frequency up-conversion of a molecular fluorine laser (157 nm  $\rightarrow$  149 nm) in inverted atomic bromine. This gave an output energy of 100  $\mu$ J. By using a higher pulse-energy (but longer-wavelength) ArF laser at 193 nm for frequency conversion, Ludewigt *et al.* [1987] have obtained higher-energy 350  $\mu$ J pulses at 146 nm from inverted selenium.

High harmonic generation, or high-order frequency mixing, may be used to generate very short wavelength radiation. The shortest wavelength generated in this way to date is 6.7 nm [Preston *et al.* 1996]. This was achieved by focusing 250 mJ of KrF laser



radiation, in a 380 fs FWHM pulse, to an intensity of  $4 \times 10^{17} \text{ W cm}^{-2}$  in helium gas jets. The conversion efficiency for the highest harmonics (the 37<sup>th</sup> was the highest observed) was  $\sim 10^{-12}$ . Ionisation of the noble gas medium occurs, with two effects. Firstly, it improves the conversion efficiencies into the higher order harmonics. Preston *et al.* [1996] deduced that  $\text{He}^+$  ions were responsible for almost all of the nonlinear response for the  $\sim 15^{\text{th}}$  harmonic and higher. Secondly, however, the generation of a plasma (owing to ionisation) in the nonlinear medium means that the technique cannot be scaled to much shorter wavelengths, since the plasma destroys the phase-matching needed for efficient nonlinear conversion at shorter wavelengths [Tsakiris 1996].

This problem can be avoided by harmonic generation at a plasma-vacuum interface, using a laser-generated plasma. The most promising results from this technique have been reported recently by Norreys *et al.* [1996]. They focused 2.5 ps pulses containing 20 J of 1053 nm radiation to an intensity of  $10^{19} \text{ W cm}^{-2}$  onto CH targets. They observed harmonics up to the 75<sup>th</sup> at 14.0 nm, which showed an estimated conversion efficiency of  $\sim 10^{-6}$ . Emission was into a much broader region than the focal cone of the incident laser.

The experiments reported by Norreys *et al.* [1996] and Preston *et al.* [1996] both required state-of-the-art ultra-high-power lasers at national facilities. This limits the application of their research in other fields, since time at these facilities is extremely expensive, and the repetition rates are low. On the other hand, Wellegehausen *et al.* [1996] have recently reported more modest systems which are more suited to applications. These systems employ only commercially-available pumping laser modules, albeit in complicated ultra-short-pulse optical arrangements. The key to their approach has been to achieve very high focused intensities by generating very short pumping laser pulses (a few hundred femtoseconds) which need not be of very high energy (tens of millijoules). The significance of the high intensities ( $> 10^{13} \text{ W cm}^{-2}$ ) is that nonlinear processes become very important as the optical electric field generated ceases to be a small perturbation to the atomic electric field.

Wellegehausen *et al.* [1996] used high-power KrF (248 nm), ArF (193 nm), and Ti:sapphire ( $\sim 800$  nm, tunable) lasers for four wave mixing in xenon. They generated tunable VUV output near 146 nm, 157 nm, and 193 nm. They also achieved fixed-frequency harmonic generation in noble gases. They obtained, for example,  $\sim 30$  nJ in the third harmonic (83 nm), and  $\sim 8$  nJ in the fifth harmonic (50 nm) from 25 mJ KrF pulses of duration 400 fs. High-order frequency mixing of fixed-frequency Ti:sapphire radiation with lower power tunable visible radiation was also achieved, at wavelengths down to 37 nm in argon. At this wavelength each output photon corresponded to 20 Ti:sapphire photons mixed with one visible photon. However, no absolute efficiencies were measured for this process.

## 1.3 Plasma-pumped lasers

Another technology capable of achieving a very high power density is the laser-generated plasma (LGP). The idea is that a laser is focused to a small volume, usually onto a solid (or liquid) target. Ablated material is ionised and heated by absorption of the laser radiation. Laser-generated plasmas are discussed in more detail in §2.3.



### 1.3.1 Recombination and collisionally pumped lasers

The use of LGPs is the longest-established technology for achieving lasing at wavelengths shorter than that of the molecular hydrogen laser (116 nm). The use of the technique was pioneered simultaneously by Matthews *et al.* [1985] at the Lawrence Livermore Research Laboratory, and Suckewer *et al.* [1985] at the Princeton Plasma Physics Laboratory. These two groups used different approaches to generate gain. These were collisional excitation and recombination respectively. Reviews of the experimental work on these schemes have been given by Key [1985], Matthews & Rosen [1988], Keane *et al.* [1989], Suckewer & Skinner [1990], Kapteyn *et al.* [1992], and Rocca [1996]. The method of populating the upper laser level depends whether it is collisional or recombination pumping which is used. But in both cases transitions from the upper laser level to the ground state are forbidden (for the most common schemes). On the other hand, there is fast decay to the ground state from the lower laser level. Thus, a population inversion may be generated. This is illustrated in Fig. 1.2.

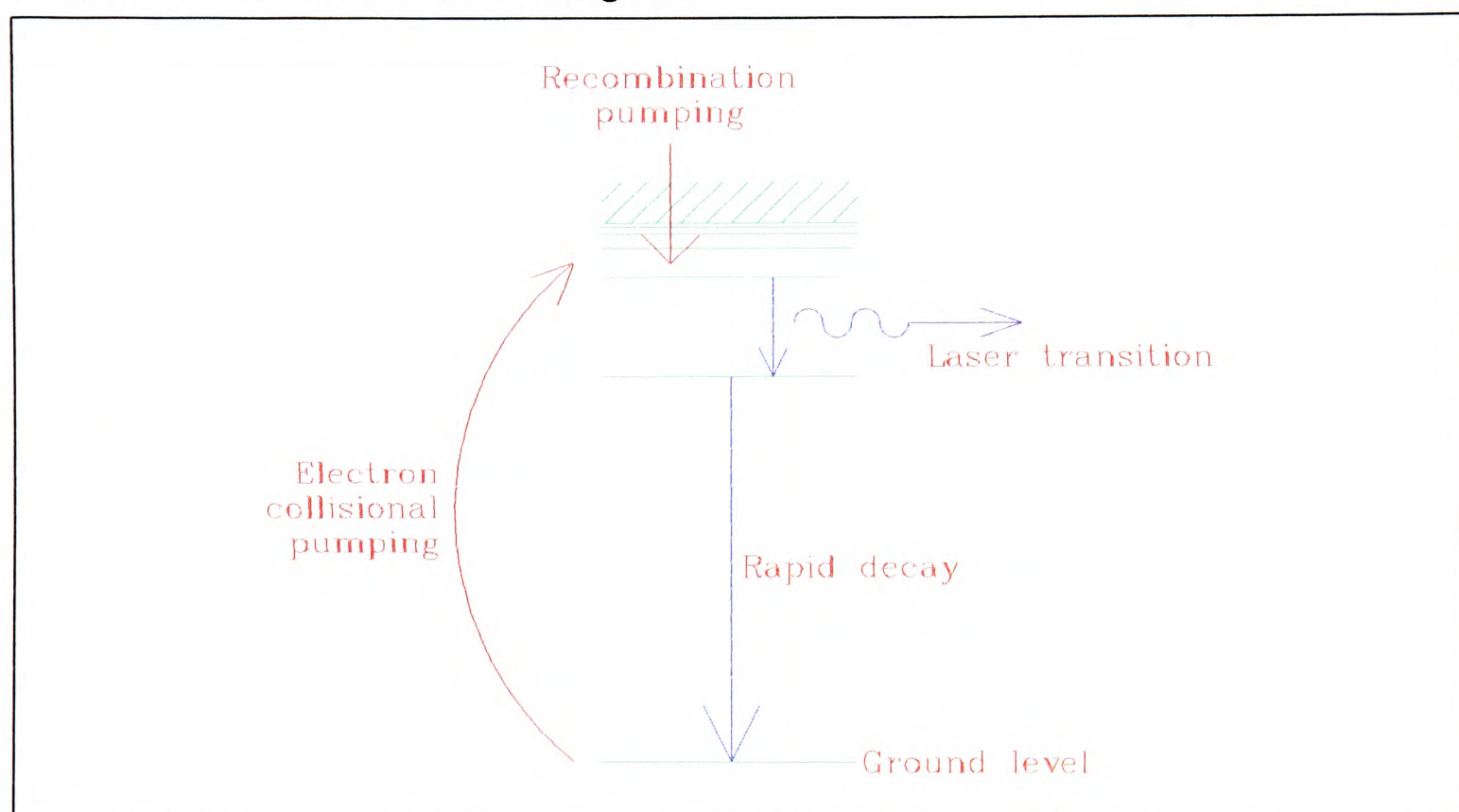


**Figure 1.2.** Schematic of electron collision and electron recombination soft x-ray laser excitation schemes. Only one type of pumping (collision or recombination) is present for any given scheme.

#### 1.3.1.1 Collisional excitation

For the collisional excitation scheme the upper laser level is populated by electron collisions with ground state ions. This was the approach taken by Matthews *et al.* [1985], who focused 500 J of second harmonic Nd:YAG laser radiation to a 200  $\mu\text{m}$  x 22 mm line on a 75 nm thick selenium foil, deposited onto a 150 nm polymer film substrate. The laser intensity was  $5 \times 10^{13} \text{ W cm}^{-2}$ , and this generated a plasma which underwent an explosive expansion. This exploding foil technique was proposed by Rosen *et al.* [1985], and produces a uniform electron density in the plasma, which prevents refraction of the laser radiation out of the gain region. The thin target also ensures that the ion density in the plasma is too low to cause significant absorption of the emitted radiation. In this way, Matthews *et al.* [1985] obtained a gain-length product of 6.5, at 20.6 nm and 21.0 nm, on transitions in neon-like  $\text{Se}^{24+}$ .



The neon-like collisional excitation scheme has been applied to many other isoelectronic ionic species (*e.g.* Lee *et al.* [1987]; see Kapteyn *et al.* [1992] and Basu *et al.* [1993] for further references). As well as neon-like schemes, nickel-like collisional schemes have also been observed. Both neon-like and nickel-like ions have a closed shell electronic structure in the ground state, and the nickel-like lasers work in the same way as the neon-like lasers. The first such scheme to be demonstrated was reported by MacGowan *et al.* [1987], and isoelectronic scaling of the technique to  $\text{Au}^{51+}$  has allowed gain at a wavelength of 3.56 nm [MacGowan *et al.* 1992].

Basu *et al.* [1993] have investigated low-energy pumping of the Ni-like ion  $\text{Nb}^{13+}$ . They achieved a gain-length product of  $\sim 3$  at 20.4 nm using only 720 mJ of 1064 nm laser radiation, in an 80 ps pulse. This was, for a while, the most efficient pumping (in terms of gain-length product per joule of pump energy) of any collisionally excited soft x-ray laser scheme.

However, recent developments look very promising for reducing the pumping requirements of collisionally pumped lasers. One of these, the use of capillary discharges, has already been described in §1.2.4. The other promising technique was proposed by Lemoff *et al.* [1994], following ideas mooted by Burnett & Corkum [1989], and has now been demonstrated experimentally by Lemoff *et al.* [1995, 1996]. Key features of the technique are:

- A gas “target” is used. This comprised 5 torr\* to 12 torr of xenon for the experiments reported by Lemoff *et al.* [1995, 1996].
- A circularly-polarised, low-energy (70 mJ), but ultrashort (40 fs) laser pulse at 800 nm is focused longitudinally to an intensity of  $3 \times 10^{16} \text{ W cm}^{-2}$ . This gives rise to tunnelling ionisation.
- The ionisation is extremely selective. The tunnelling rate from neutral Xe I to eight-times ionised Xe IX is  $1.5 \times 10^{17} \text{ s}^{-1}$ . The rate of removal of a further electron, to give Xe X, is more than eleven orders of magnitude slower. The reason for this is that Xe IX is isoelectronic with palladium (which is the equivalent of nickel in the following period of the periodic table), and this has a closed-shell electronic structure. Thus, the energy barrier for the removal of a further electron is large, and tunnelling is strongly suppressed.
- The electrons removed have sufficient energy to allow collisional pumping of the ions. This feature stems from the use of circularly polarised light, and it represents conservation of angular momentum.

In this way, Lemoff *et al.* [1996] observed a gain-length product of 11 at 41.8 nm. The length of the gain region was limited to  $\sim 1$  cm by the focusing arrangement. This technique represents a very exciting advance in the technology of short wavelength lasers. The system operates at 10 Hz, and has shown the highest gain to date of any “tabletop” laser system operating at less than 90 nm. The limit on the scaling of the technique to longer gain regions is expected to be that the plasma refracts the laser light generated out of the gain region (a common problem for lasers generated within plasmas). Work is currently in progress to create plasma waveguides to avoid this problem [Milchberg *et al.* 1996]. These use axicon focusing optics to achieve long, thin optical foci known as Bessel-beams. [Durnin 1987, Laycock & Whybrew 1990, Laycock & Webster 1992]. These foci, in a gas, generate a plasma, which expands. This gives rise to a low density in

---

\* 1 torr is the pressure associated with a column of 1 mm of mercury in the Earth’s gravitational field. In SI units 1 torr is 133.3 Pa.



the centre of the plasma, corresponding to a low refractive index. The plasma then shows properties very similar to an optical fibre, and amplified light need not be guided out of the gain region.

### 1.3.1.2 Recombination pumping

The other short-wavelength laser scheme which was first reported in 1985, employed recombination pumping [Suckewer *et al.* 1985]. This scheme works by the generation of a highly-ionised (often fully ionised) plasma. In the system reported by Suckewer *et al.* [1985], this plasma was obtained from a solid carbon target irradiated by 500 J of CO<sub>2</sub> laser radiation at 10.6  $\mu\text{m}$ , focused to  $5 \times 10^{12} \text{ W cm}^{-2}$  in a 75 ns pulse. The ions in the plasma undergo three-body recombination according to the reaction



Provided the plasma is sufficiently cool, this process can generate a population inversion. Recombination occurs into the upper levels of the hydrogen-like (*i.e.* single electron) ion. These upper levels are collisionally quenched in a cascade process to lower levels. In general, the rate of collisional quenching is greatest for closely spaced energy levels. On the other hand, radiative decay is fastest for widely spaced energy levels. Thus, a population inversion may be generated between an  $n=3$  and an  $n=2$  level, owing to rapid (spontaneous decay) depopulation of the  $n=2$  level to the  $n=1$  ground state, coupled with population of the  $n=3$  level by electron collisional quenching from higher levels. For the C<sup>5+</sup> Balmer- $\alpha$  transition excited by Suckewer *et al.* [1985] this process gives rise to gain at 18.2 nm.

Isoelectronic schemes in other ions have also been demonstrated, *e.g.* by Kato *et al.* [1990], who observed gain at 5.42 nm from hydrogenic sodium ions. Lithium-like schemes are also possible, and operate in a similar way to the hydrogenic schemes, with inversions generated on  $n=5$  and  $n=4$  to  $n=3$  levels. For example, Hara *et al.* [1989] have observed gain at 10.6 nm in lithium-like aluminium ions. Other H-like and Li-like schemes have been reviewed by Kapteyn *et al.* [1992].

Dense, cool plasmas are required for recombination lasers. High electron densities are required to ensure fast three-body recombination of the plasma - the rate for the process scales with the square of the electron density. A low temperature plasma is required, since this enhances the rates of both three-body recombination, and electron collisional quenching. On the other hand, the generation of short wavelengths requires the use of highly-ionised plasmas, in order to take advantage of the  $Z^2$  scaling of the energy levels in hydrogenic ions. But the production of highly ionised states requires a plasma which is initially hot. This means that rapid cooling of the plasma is required.

Several techniques have been used to achieve this rapid cooling. Suckewer *et al.* [1985] used a technique proposed by Suckewer & Fishman [1980] which was to confine magnetically a plasma expanding from a spot, so that it formed a column. The plasma cooled by radiation, while still at a high density. Other cooling schemes have also been used. These are considered below.

- Adiabatic expansion of a plasma formed by the total ablation of a fine (7  $\mu\text{m}$ ) carbon fibre has been reported by Chenais-Popovics *et al.* [1987]. The scheme uses fast plasma generation (70 ps laser pulse), followed by expansion and lasing over  $\sim 2$  ns.
- Cooling by heat conduction into a cold solid has been achieved by using thicker fibre targets (which are not fully ablated by the laser) or by introducing a knife blade into the plasma region. For example, Kim *et al.* [1989] found that the use of a knife-blade



technique increased, by about an order of magnitude, the small-signal gain of an 18.2 nm collisional laser scheme in  $C^{5+}$ .

- An alternative is not to cool the plasma at all, but to generate a cool, highly-ionised plasma some other way. This approach has been taken by Nagata *et al.* [1993]. They used a 20 ns duration KrF laser focused to only  $10^9 \text{ W cm}^{-2}$  to generate a singly ionised Li plasma. This plasma was then subjected to a 500 fs KrF laser pulse of only 50 mJ energy but focused to  $10^{17} \text{ W cm}^{-2}$ . This was sufficient to remove *all* the remaining electrons, by optical field ionisation. Recombination of the free electrons generated in this way can give rise to a population inversion with respect to the ground state. This is because the ground state has no initial population, on account of the *complete* ionisation of the plasma [Eder *et al.* 1992]. Thus, Nagata *et al.* [1993] were able to generate a population inversion on a Lyman- $\alpha$  transition of the hydrogen-like ion. A small signal gain of  $20 \text{ cm}^{-1}$  was deduced for the 13.5 nm laser line, although the maximum gain-length product observed was only 4, since the focal region of the sub-picosecond pulse was only 2 mm long.

### 1.3.1.3 Summary

Collisionally-pumped and recombination lasers are now well-established techniques for generating short wavelength lasers. For example, applications of such lasers have been reported by MacGowan *et al.* [1992].

Pumping requirements have relaxed significantly since the first demonstrations of the schemes, which used two of the largest lasers in the world at the time [Matthews *et al.* 1985, Suckewer *et al.* 1985]. The lowest energy “conventional” pumping systems, involving LGPs obtained by irradiating solid targets, have been reported by Hara *et al.* [1989] (6 J; 5 ns; 1053 nm pump for Li-like  $Al^{10+}$  at 10.6 nm), Skinner *et al.* [1990] (6 J; 3 ns; 1053 nm pump for H-like  $C^{5+}$  at 18.2 nm) for collisional schemes, and by Basu *et al.* [1993] ( $\leq 1$  J; 80 ps; 1053 nm pump for Ni-like  $Nb^{13+}$  at 20.4 nm) for collisional excitation. Some current work on these “conventional” schemes is concentrating on the use of nanosecond prepulses followed by picosecond pumping pulses to reduce the energy pumping requirements of the neon-like titanium collisional laser scheme. The nanosecond pulses achieve the required ionisation state; then the picosecond pulses heat the electrons, and a transient population inversion may be created with low pump energies [Präg *et al.* 1996, Rocca 1996].

During the course of the work described in this thesis, the development of solid-state, ultrashort-pulse “tabletop” laser systems have led to the development of optical field ionisation pumping schemes using much lower laser energies [Nagata *et al.* 1993, Lemoff *et al.* 1995, 1996]. In parallel with this has been the development of viable discharge excitation schemes for collisional pumping of short wavelength laser schemes [Rocca *et al.* 1995].

## 1.4 Photopumped schemes

### 1.4.1 Resonance excitation

Laser-generated plasmas can emit strong incoherent radiation in the x-ray region of the spectrum. This radiation can be used as a source of high-power pumping for laser systems. One might expect that this radiation could be used to achieve direct pumping to



the highest level of a three- or four-level laser system. The problem with the technique is that laser-generated plasmas are, in general, broadband emitters, whereas the transitions which must be pumped are sharp atomic (or ionic) resonances. Thus, resonant photopumping can only be efficient if there are electronic transitions in the LGP which happen to have the same wavelength as a resonance in the atom or ion system to be pumped. Several such coincidences have been identified, and the subject is still under investigation; but, as yet, no lasers have been pumped resonantly by laser-generated plasmas [Kapteyn *et al.* 1992, Nilsen 1992, Nilsen *et al.* 1992, Ilcisin *et al.* 1994]. For a while it was thought that one such system has been discovered accidentally [Boehly *et al.* 1990]. However, recent work has suggested that resonant photopumping was unlikely to have been the cause of the effects observed [Nilsen *et al.* 1994].

## 1.5 Photoionisation lasers

### 1.5.1.1 Photoelectron pumped lasers

The problem of tuning the absorption of a laser system with the emission from an LGP can be avoided if a broad-band excitation technique is used. Photoionisation is just such a technique; excess photon energy can be removed in the kinetic energy of the emitted electron. A review of photoionisation pumped lasers has been given by Barty *et al.* [1990].

Once photoionisation has been achieved, the photoelectrons produced may either be a nuisance to the lasing in some ionic system, or they may be instrumental in the operation of the laser. For most photoionisation pumped systems the former is true, but there have been a few systems for which the latter is the case. We consider these first.

In an attempt to pump the Cs III Auger laser at 63.8 nm (§1.5.2.3), Barty *et al.* [1988, 1992] observed saturated lasing at 96.9 nm. This was attributed to a transition in neutral Cs I, which was excited by electron collisions from the ground state. Another unique feature of the system is that the energy of the upper laser level is above the ionisation threshold, *i.e.* the upper laser level is in the continuum. This means the upper level has a lifetime against ionisation of 60 ps. On the other hand, the spontaneous decay lifetime of the upper laser level is 43 ns. This means that spontaneous decay is negligible, and so the laser must be operated in a very high-gain arrangement, to make the stimulated emission rate faster than the autoionisation rate. This required short-pulse (20ps), travelling wave excitation (§2.2.2).

Another photoelectron-pumped scheme has been reported by Benerofe *et al.* [1991]. In this case the laser system was the molecular hydrogen laser. Soft x-ray (~25 eV) photons from an LGP were used to photoionise ambient hydrogen gas. These electrons then pumped the molecular hydrogen laser, which had been excited in a travelling-wave electric discharge by Waynant [1972], and excited by an electron beam by Hodgson & Dreyfus [1972]. In such a laser the ground electronic (X) state molecular hydrogen is excited to the B (for Lyman band emission around 160 nm) or C (for Werner band emission at 116 nm and 123 nm) states. This excitation occurs by electron collisions. Gain is obtained by stimulated emission to upper vibrational levels of the X state.

Benerofe *et al.* [1991] obtained a gain of  $0.8 \text{ cm}^{-1}$  from room temperature hydrogen on the Lyman 116 nm line. This was an order of magnitude greater than had been obtained by Hodgson & Dreyfus [1972] using electron-beam pumping. One of the reasons for this was that the electron flux generated by the LGP was equivalent to a current density of



$10^6 \text{ A cm}^{-2}$ , whereas the electron-beam current density used by Hodgson & Dreyfus [1972] was only  $10^4 \text{ A cm}^{-2}$ . Thus, the pumping was more intense for the LGP scheme. Furthermore, Benerofe *et al.* [1991] showed that the LGP did not heat the hydrogen gas, which would have reduced the gain, both on account of increased Doppler broadening, and by making thermally accessible higher vibrational levels of the ground state. On the other hand, both electron beam excitation and discharge excitation can be expected to heat the laser gas.

The neutral caesium laser and the molecular hydrogen laser are both *collisionally* pumped. A hydrogen-like *recombination* pumped laser scheme in  $\text{C}^{5+}$  has been proposed by Pakula [1991]. In this scheme, x-ray emission from a titanium LGP is used to completely photoionise *ambient* C vapour. Subsequent recombination could then give laser action on exactly the same 18.2 nm Balmer- $\alpha$  transition of the hydrogenic ion as was pumped *within* an LGP by Suckewer *et al.* [1995].

### 1.5.2 Photoexcited lasers

By making a suitable choice of laser medium, however, it is possible to dispense with the need for photoelectrons to pump a laser system. Instead, electronic processes in the photo-ions can be used to give rise to a population inversion. The first proposal for such a scheme was made by Duguay and Rentzepis [1967]. In their scheme, sodium vapour is irradiated by photons of energy greater than 38 eV for which the ionisation cross section for ejecting a 2p electron is more than 100 times greater than that for an outer 3s electron. Thus, a population inversion is produced in a single step in the ions generated. For the case of sodium, this suggests laser action at 37.2 nm.

In fact, all atoms show similar behaviour in their photoionisation cross sections, *i.e.* inner-shell photoionisation dominates at sufficient photon energies (see §2.1.1.1). Thus, the choice of sodium for a photoionisation scheme may appear somewhat arbitrary. The reason for the choice is that Auger decay will, in general, limit the lifetime of the upper laser level. In general, if an ion has an inner-shell vacancy, an outer-shell electron will relax into it. Excess energy may be carried off by a photon. Alternatively, the excess energy may be carried off by another outer-shell electron (Auger decay), provided the ion energy exceeds its ionisation threshold.

The rate of radiative decay for systems of equal oscillator strength increases with the cube of the transition energy. On the other hand, Auger decay rates are comparatively insensitive to the transition energy, and are typically 1-10 fs [Kapteyn 1992]. Thus, Auger decay can make it impossible to achieve a significant population in the upper laser level.

For the sodium scheme proposed by Duguay and Rentzepis [1967], the outer 3s shell contains only a single electron, and Auger decay is impossible. Duguay and Rentzepis [1967] also proposed a photoionisation laser scheme for copper. In this scheme, Auger decay is avoided by having the population inversion span such a large energy gap (8 keV) that radiative decay is faster than Auger decay. Experimental realisation of this system has never been attempted on account of the huge pumping power density which would be necessary to sustain a population inversion against spontaneous decay (at least  $100 \text{ PW cm}^{-3}$ ).

However, the sodium system proposed by Duguay and Rentzepis [1967], with its more modest pumping requirements, likewise has never been realised. The problem is that collisions between photoionised electrons and neutral Na atoms can cause ionisation, stripping the 3s electron, and producing ions in the lower laser state, depleting the population inversion. A way around this problem is to pump the system so fast that there



is insufficient time for electron ionisation. The advent of femtosecond table-top laser systems had made this an increasingly attractive proposition, and the technique has recently been considered for direct generation of a population inversion in Ne II in order to generate lasing at 849 eV [Murnane *et al.* 1991, Kapteyn 1992].

The problem of Auger decay rapidly depleting upper-level population can be avoided in several ways, which are summarised below.

#### *1.5.2.1 Use of an Auger-metastable upper laser level*

Auger decay may be avoided by pumping to a state which is metastable (on account of selection rules) against Auger decay (see, for example, Harris *et al.* [1984] for further discussion of the relevant selection rules). For example, this technique has been proposed in works by Weigold & Piper [1990] and Weigold [1991] for a lasing scheme at 24.7 nm in Mg II. The scheme involves inner-shell (2p) photoionisation of an excited state of the neutral atom. Population in the relevant excited state of Mg I is achieved by resonant pumping at 285 nm, by means of another laser. The resonant pumping followed by inner-shell photoionisation generates an excited Mg II ion, with a lifetime against further ionisation of 1 ns, compared to a radiative lifetime of 250 ps.

#### *1.5.2.2 Use of an Auger-stable upper laser level*

An obvious solution to the problem of Auger decay is to pump to a state which is energetically stable against further ionisation. This was the approach suggested by Duguay & Rentzepis [1967] for the sodium photoionisation laser. It was also used for the first successful demonstration of a photoionisation pumped laser [Silfvast *et al.* 1983]. This was a laser in Cd II at 441.6 nm and 325.0 nm. Excitation was achieved by broad-band inner-shell photoionisation of neutral Cd I vapour. This populated the upper laser level directly. The same scheme has since been developed by other workers [Hube *et al.* 1988a, Tambay & Thareja 1993].

The price to be paid for using an upper laser level which is stable (with respect to Auger decay) is that the laser wavelength is longer than can be obtained from an unstable scheme, since the transition energy cannot exceed the ionisation energy of the ion. Within this restriction, the use of ions of a higher charge allows shorter wavelengths to be attained. Thus, Lacy *et al.* [1989] have obtained gain at 185 nm in In III. This system is isoelectronic to Cd II, and employs inner-shell photoionisation of  $\text{In}^+$  ions, rather than the neutral atoms which are ionised in the Cd scheme.

Many other similar photoionisation lasers have also been proposed or demonstrated. All of the systems which have been demonstrated, and some of the proposals are listed in table 1.2. Many of these employ resonant pumping, by means of a dye laser, as well as broadband SXR photoionisation. The resonant pumping can be used to generate an excited state suitable for photoionisation directly to upper laser level, (e.g. [Hube *et al.* 1988b]). Alternatively, in an anti-Stokes Raman scheme, resonant pumping is used to transfer population from a metastable (storage) level obtained by photoionisation, into the upper laser level (e.g. [Tünnermann *et al.* 1991]).

“Shake-up” lasers form a further sub-class of photoionisation lasers [Harris & Caro 1986, Weigold *et al.* 1993, Derzhavin & Noraev 1991]. In these systems, the removal of an electron by photoionisation is accompanied by the excitation of another electron. For example, in the Ar II system reported by Weigold *et al.* [1993] and Derzhavin & Noraev [1991], one of the six ground state 3p electrons is removed, and another of them is



excited to a 4p configuration. The laser transition, at 476 nm, occurs as this excited electron relaxes to a 4s configuration.

Finally, we note that photoionisation of a *molecule* has been used to pump a laser, namely the  $\text{Cs}^{2+}\text{F}^-$  ionic excimer laser, at 185 nm [Tóth *et al.* 1993]. Indeed, this has been the only successful demonstration of gain from an ionic excimer system.

### 1.5.2.3 Use of Auger decay to obtain a population inversion

Rather than avoiding Auger decay, laser systems can be devised which take advantage of the process in order to generate a population inversion. Early proposals involved using rapid Auger decay from a lower laser level to ensure a population inversion. However, these require very fast pumping, on account of electron collisions, and rapid Auger depopulation of the upper laser level, and have not yet been experimentally realised (see Kapteyn [1992] for a review).

A successful approach, however, has been to create a population in Auger-stable product states of a primary Auger decay. The idea was first proposed by McGuire [1975]. He proposed a system in which  $\text{Na}^+$  ions are photoionised, and decay selectively to various  $\text{Na}^{2+}$  configurations and terms. Decay to one such level is precluded by selection rules, and thus several population inversions ending on this level may be generated. Unfortunately, the scheme requires pumping by photons of energy  $>850$  eV, yet only gives lasing at  $\sim 25$  eV, and it has never been tested.

Instead of using schemes in which Auger decay to some states is *impossible*, one may use schemes in which the Auger decay populates some states *preferentially*, in order to generate a population inversion. A similar technique was demonstrated by Bokor *et al.* [1982] to give a visible laser in  $\text{Ba}^+$ . In this laser scheme the inversion was created by preferential autoionisation (one electron ejected from an atom with two excited electrons) rather than by preferential Auger decay (a total of two electrons removed from an excited atom).

The first Auger system was proposed by Mendelsohn & Harris [1985], and demonstrated by Walker *et al.* [1987]. An inner-shell 3p electron is removed from neutral Zn (in vapour form), by photons having an energy of 96 eV or more. The resulting Zn II state undergoes super Coster-Kronig decay to several levels of Zn III, of which three were found to be inverted with respect to two lower laser levels, giving gain on three transitions at  $\sim 130$  nm. Super Coster-Kronig decay is a special case of Auger decay in which the relaxing electron, emitted electron, and initial hole all have the same principal quantum number. This gives rise to a large radial wavefunction overlap, and hence dominates the Auger decay.

A disadvantage with the Zn III system is that the excitation requires the removal of a 3p electron, which has a much lower cross-section than that for removal of a 3d electron. Thus, most of the photoionisation is wasted, and generates unwanted photoelectrons which quench the gain. A different Auger scheme was proposed by Walker *et al.* [1986] which does not suffer from this disadvantage. The technique involves removing a 4d electron from neutral Cs. Selective Auger decay into Cs III levels generates a population inversion corresponding to gain at 63.8 nm. Attempts to pump the Cs III laser have not been successful; this has been ascribed to absorption of the laser radiation by ambient neutral Cs, and population of the lower laser level (the ion ground state) by electron collisional quenching [Barty *et al.* 1990].

Much the most successful Auger laser, however, has been the Xe III system, at 109 nm. This was first demonstrated by [Kapteyn *et al.* 1986a]. Since then there have



continuous improvements to the system; the most recent developments have been reported by Yamakoshi *et al.* [1996]. The system is described in much more detail in chapter 2. Briefly, the operating principle is the same as the other Auger lasers, *i.e.* photoionisation is followed by Auger decay which populates some states selectively, giving rise to a population inversion.

Table 1.2 summarises some of the properties of all the photoionisation and photoelectron lasers which have been demonstrated, and selected schemes which have been proposed but never realised (shown in *italics*).

<i>Lasant</i>	<i>Laser wave-length (nm)</i>	<i>Time constraints</i>	<i>Plasma generating laser</i>	<i>References</i>	<i>Comments</i>
<b>Single-stage photoionisation pumped laser schemes</b>					
Cd II	441.6 & 325.0	Quenched by photoelectrons; not self-terminating	Various, see individual references	Silfvast <i>et al.</i> 1983, Hube <i>et al.</i> 1988a, Tambay & Thareja 1993	Commercially available HeCd lasers operate on these transitions
In III	185	Quenched by photoelectrons; not self-terminating	Nd:YAG, 50 mJ, 100 ps, spot focus on Ta	Lacey <i>et al.</i> 1989	In <sup>+</sup> ions generated by ablation of liquid In target by 67 mJ of 532 nm light, 400 ns before photopumping. Isoelectronic to Cd II laser above.
Zn II	747.8		Nd:YAG, 300 mJ, 10 ns, spot focus on W	Lundberg <i>et al.</i> 1984	Analogous to Cd II
Ar II	476.5	CW pumping possible on this transition	1053 nm, 5J, 100 ps, 10 cm line focus on threaded Ta	Weigold <i>et al.</i> 1993	Commercial argon ion lasers operate on this transition. Shake-up scheme.
Ne II	335.2 & 332.4	Tens of nanoseconds	CO <sub>2</sub> , 0.4 J, 100 ns, 4 spot foci on Ta	Derzhavin & Noraev 1991	Authors also report gain on Ar II transitions at 476.5, 454.5, and 427.8 nm, with same geometry. Shake-up scheme
(CsF) <sup>+</sup>	185	Not self-terminating, but synchronous pumping used to mitigate short upper state lifetime	Nd:YAG, 225 mJ, 100 ps, 6 cm travelling wave focus on stainless steel	Tóth <i>et al.</i> 1993	Ionic excimer scheme
Li II	165.3	<i>not detailed; electron quenched</i>	<i>Nd:YAG, 6J, 1 ns, 3 spot foci</i>	<i>Harris &amp; Caro 1986</i>	<i>Transition at 113.2 nm can also be reached by exciting at 359 nm as well</i>
Na II	37.2	<i>fs Auger decay of upper laser level; electron quenching</i>		<i>Duguay &amp; Rentzepis 1967</i>	<i>Upper laser level not energetically stable against Auger decay</i>
Mg II	24.7	<i>250 ps upper laser level lifetime; electron quenching</i>	<i>1064 nm, 10 J, 200 ps, 3 cm travelling wave focus on Ta</i>	<i>Weigold &amp; Piper 1990</i>	<i>Upper laser level not energetically stable against Auger decay, but radiative decay rate is faster</i>
<b>Two-stage photoionisation pumped laser schemes (photoionisation and resonant pumping)</b>					
Hg II	165	Self terminates; upper state lifetime 1.8 ns	308 nm, 200 mJ, 20 ns, 2 spot foci on W	Tünnermann <i>et al.</i> 1991	399 nm, 15 mJ, 15 ns, dye laser provides population transfer
Rb II	678 - 993	Varies according to transition; some 100 ns	Nd:YAG, 300 mJ, 10 ns	Tünnermann <i>et al.</i> 1993	780 nm or 419-478 nm, 10 ns, dye laser provides population transfer. Analogous to Cs II and K II.
Sr II	155 - 457			Tünnermann <i>et al.</i> 1993	193 nm radiation to give Sr II, then SXR and 207-542 nm pumping. Isoelectronic to Rb II above.
Cs II	672-715 or 800 & 698	Electron quenched, ~ 4 ns	Nd:YAG, 600 mJ, 8 ns, 3 spot foci on W	Hube <i>et al.</i> 1989	487-535 nm or 1266-1404 nm dye laser radiation for population transfer. Analogous to K II, Sr II, & Rb II.
K II	612 - 660	Lower laser state metastable ( $\Rightarrow$ self termination), K II pulse ~ 3 ns	Nd:YAG, 400 mJ, 6 ns, 3 spot foci on W	Hube <i>et al.</i> 1988b	767 or 770 nm, 12 mJ, 6 ns, dye laser provides excitation before SXR photoionisation. Analogous to Cs II, Sr II, and Rb II.



<i>Lasant</i>	<i>Laser wave-length (nm)</i>	<i>Time constraints</i>	<i>Plasma generating laser</i>	<i>Reference</i>	<i>Comments</i>
<b>Photoelectron pumped laser schemes</b>					
Cs I	96.9	60 ps Auger lifetime of upper laser state. Self terminates.	Nd:YAG & Nd:glass, 3 J, 10 ps, 17 cm travelling wave focus on Fe	Barty <i>et al.</i> 1988, 1992	1.5 $\mu$ J output energy measured
H <sub>2</sub>	116.1 123.0 149.5 160.3	600 ps lifetime of upper laser level for Werner band. Not self-terminating	1064 nm, 580 mJ, 200 ps, 27 cm travelling wave focus on Fe	Benerofe <i>et al.</i> 1991	Can also be discharge or e-beam excited
C VI	18.2	<i>Tens of nanoseconds</i>	<i>Frequency doubled Nd focused to <math>10^{12}</math> W cm<sup>-2</sup> line on Ti in C gas</i>	<i>Pakula 1991</i>	<i>Recombination laser</i>
<b>Auger systems</b>					
Xe III	108.9	Self terminates; upper state lifetime 4.75 ns	See table 2.1	See table 2.1	
Kr III	90.7	Self terminates; upper state lifetime 2.0 ns	Nd:glass, 38-50 J, 0.5 ns, 9 cm line focus on Ta	Kapteyn & Falcone 1988	Equivalent to Xe III system
Zn III	127.0, 130.6, 131.9	Electron quenched	1064 nm, 5 J, 300 ps, 28 mm line focus on Ta	Walker <i>et al.</i> 1987	Super Coster-Kronig system proposed by Mendelsohn & Harris [1985]
Cs III	63.8	<i>Self terminates; upper state lifetime 0.4 ns</i>	<i>532 nm, 1 J, 100 ps, proposal</i>	<i>Walker et al. 1986</i>	<i>Attempts to pump with 100 ps pulses have been unsuccessful [Barty et al. 1990]. Analogous scheme in Rb III at 49 nm also proposed</i>

**Table 1.2.** All the photoelectron and photoionisation schemes employing soft x-rays from laser-generated plasmas for pumping reported in the literature, and selected proposals. Schemes shown in italics have not been realised experimentally.

## 1.6 Aim of project

The Xe III laser is currently being investigated in Canada, the USA, and Japan. The reason for its popularity is that it combines:

- **a short wavelength of technological importance** - from table 1.2 it is clear that at 108.9 nm, the Xe III laser system has one of the shortest wavelengths of any successful photopumped laser system. The wavelength is technologically important because it is just longer than the cut-off of LiF, and thus there is a window material available. Furthermore, the photon energy is 30% greater than that of the shortest wavelength commercially-available laser, the molecular fluorine laser at 157 nm.
- **modest pumping requirements** - for example, at the time of starting the work described in this thesis, it had already been shown that the laser intensity required to generate a plasma suitable for pumping the Xe III system was only  $3 \times 10^{10}$  W cm<sup>-2</sup> [Sher *et al.* 1991]. This intensity is about 100 times less than typical intensities which had been used to pump collisional or recombination schemes [Kapteyn *et al.* 1992].
- **experimental simplicity** - compared to the other photopumped laser systems the Xe III laser requires no population transfer laser, and the laser medium is a gas at room temperature, removing the need for laser pre-ablation or heat-pipes which have been essential for metal-based photopumped systems.

The aim of the project described in most of this thesis was to pump the Xe III laser system, using a KrF laser system, which had been developed by Cotton [1990] and



Fletcher [1993]. The laser is described in detail in chapter 5, but table 1.3 summarises some of its beam properties, as it was at the start of the work described in this thesis. Figure 1.3 shows a photograph of the laser (in its form at the end of the work described here).

Wavelength	248 nm*
Energy per pulse	2.22 J with new gas fill
Pulse length (FWHM)	~20 ns
Beam Dimensions	3 cm x 3 cm square
Divergence	30 $\mu$ rad
Repetition rate	>10 shots per minute

Table 1.3. Selected beam properties of 2J KrF laser available for work described in this thesis.

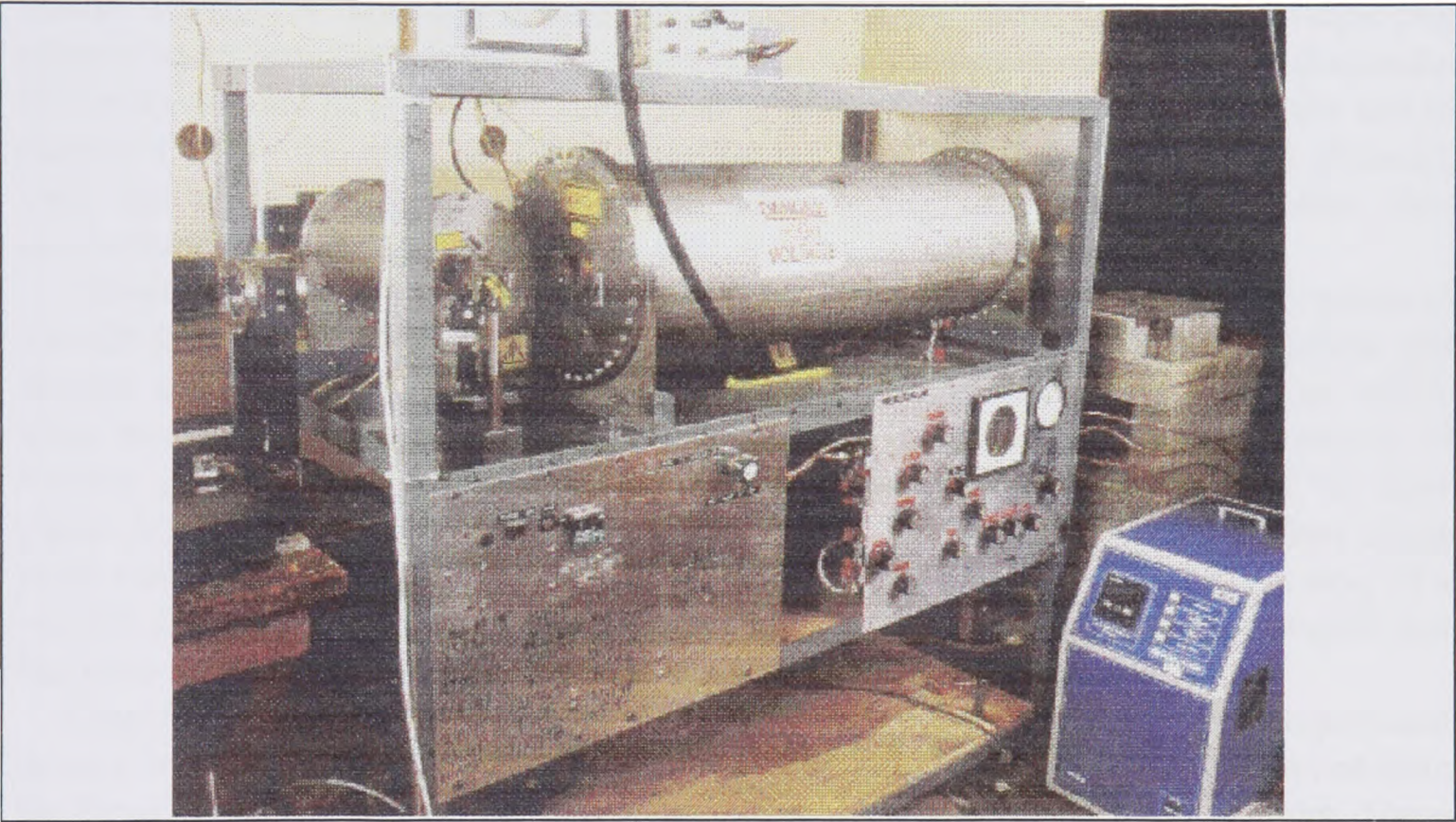


Figure 1.3. KrF laser system used in most of the work described in this thesis.

The laser was built for soft x-ray (SXR) contact microscopy and was used to generate laser plasmas emitting soft x-rays in the “water window”, specifically 280 - 530 eV. The significance of the water window is that light in this range is transmitted by water, but absorbed by carbon, hence the application to (biological) microscopy. These x-rays were used to make contact prints of biological samples, which were read by electron or atomic-force microscopy. In this way a resolution of 100 nm was obtained, in images of live, hydrated samples. Whereas x-ray microscopy was already fairly well-established at national facilities, the idea of the earlier project was to produce a *transportable* laser system. For this reason, the laser was mounted to a frame sufficiently small to fit through a standard sized door. Furthermore, the design of the pumping laser was to be sufficiently simple to allow any laboratory with workshop facilities to make a copy of the system.

\* On account of the comparatively broad laser transition, the wavelength of the KrF laser is quoted in the literature variously as 248 nm and 249 nm. See Kearsley [1980] for a spectrum.



The aim of the project described in this thesis was to see whether this particularly simple KrF laser could be used to pump an Xe III laser at 109 nm. The emphasis was on experimental simplicity - it was already established that complex laser systems could pump the Xe III laser - the idea here was to employ only very simple techniques, so that the system could be copied easily.

## 1.7 Layout of thesis

This thesis is laid out in approximately the order that the work was conducted. First of all, in chapter 2 laser generated-plasmas and the Xe III laser are described in more detail, and some calculations are given of parameters relevant to the pumping of the system. Pulse shortening of the KrF laser pulse was desirable, and chapter 3 reviews how this may be achieved, and describes experimental work using a compact oscillator carried out for this reason. Chapter 4 describes different approaches to the same problem, all employing plasmas to achieve pulse shortening. Short pulses were obtained and a detailed discussion of factors relevant to the amplification of short pulses in KrF lasers is given at the end of chapter 4. From this discussion it is clear that the short pulses which had been obtained, were not sufficiently short for it to be worth trying to amplify them, rather than concentrating on making shorter pulses still.

Instead, an attempt was made to pump the Xe III laser without any pulse-shortening of the KrF laser. The KrF laser system developed by Fletcher [1993] was reassembled, and chapter 5 describes this, and details some other aspects of KrF laser technology which were investigated. These were the installation of a novel, safe, solid-state source of fluorine gas, and an improvement to the manufacturing technique of one of the laser electrodes. Together, these improvements led to the laser system having the highest single pulse energy of any laser of its type. Also discussed in chapter 5 is the calibration of a variable attenuation system for KrF lasers, which was already in use around the world, but had been incompletely and incorrectly characterised in the literature.

Chapter 6 discusses how tight line foci may be achieved, and describes an experiment using a line focus intended to pump the Xe III laser system. No SXR's were observed from the focus, however, and several other experiments were conducted to find out why. These experiments are detailed in chapter 7, and involved the characterisation of the beam quality of the KrF laser, and the use of a spot focus to generate SXR's to test the detection system, and produce fluorescence at 109 nm from Xe III ions. Finally, an experiment was assembled for a further attempt at pumping the Xe III laser system, this time using a tighter line-focusing arrangement of the KrF beam. Unfortunately there was insufficient time to complete this investigation, on account of a higher priority being given to some promising experiments employing a picosecond laser system. These experiments are described in chapters 8 and 9.

Chapter 8 describes attempts to pump the Xe III laser system using a much higher power, short-pulse KrF laser system, at the Rutherford Appleton Laboratory (RAL). Chapter 9 describes further work carried out at RAL, for a related, but distinct goal. This was to make and characterise a continuously tunable incoherent source of radiation from 30 nm to 250 nm, using a laser-generated plasma.

Finally, chapter 10 summarises the work conducted, discusses the results, and gives some pointers to further work.



## 2. The Xe III laser, and laser-generated plasmas

### 2.1 The Xe III laser

#### 2.1.1 Introduction

In this chapter we introduce the Xe III laser, and indicate how it may be pumped by means of an LGP. First of all, a brief summary of the principle of operation of the laser will be given, then we shall consider the reports of lasing from the system. After this, we shall consider how LGPs work, and consider in detail how one may be used to pump the Xe III system.

##### 2.1.1.1 Principle of operation

Neutral xenon (Xe I), has atomic number  $Z=54$ , and ground state electronic configuration  $[\text{Kr}]4d^{10}5s^25p^6 \ ^1S_0$ . Berkowitz [1979] has collated experimental measurements of photoionisation cross-sections for the neutral atom for ejection of an electron from the various shells. His results are shown in Fig. 2.1. From this we may see that for photons of energy greater than the threshold of 67.55 eV, the cross section for ejection of a 4d electron is significantly greater than those for the 5s and 5p electrons. This enhancement is much greater than one would expect simply from statistics (*i.e.* the fact that there are ten 4d electrons, but only two 5s electrons, and six 5p electrons).

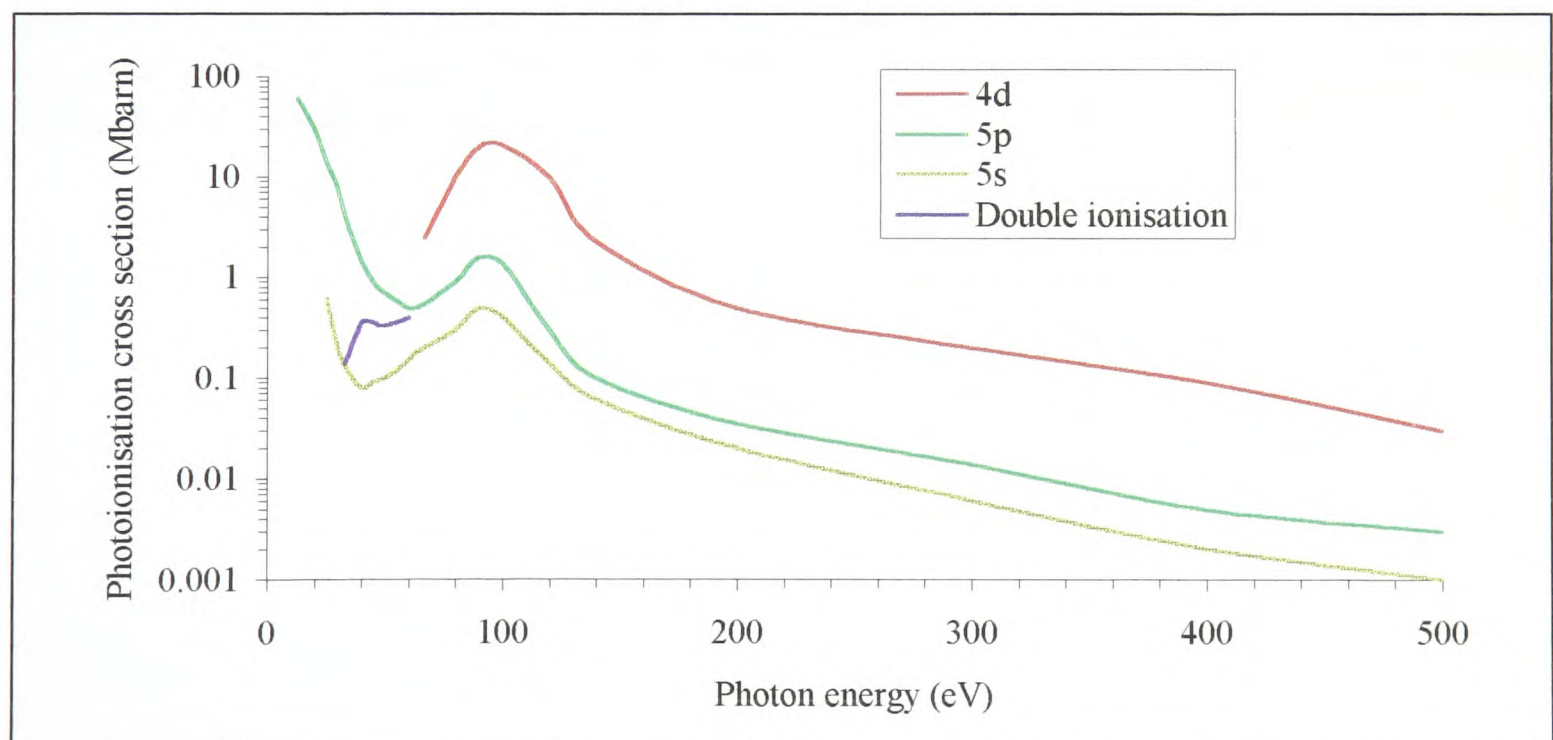


**Figure 2.1.** Photoionisation cross sections for ejecting various electrons of the neutral Xe atom, as a function of photon energy [Berkowitz 1979].

There is nothing special about xenon giving it this property. In general, specific photoionisation cross-sections peak near the threshold energy and decay at higher energies. Time-dependent perturbation theory indicates why this is so. The reason is that



the (radial) wavefunctions of the bound and free electrons show strong overlap when they have comparable energy.

Ejection of a 4d electron forms an Xe II ion, with configuration  $[\text{Kr}]4d^9 5s^2 5p^6 \ ^2D_{3/2,5/2}$ . This rapidly suffers Auger decay to various configurations and terms. There is some (21%) double Auger decay, to Xe IV states, but the majority (79%) decays into various configurations and terms of Xe III [Kapteyn 1989]. Two are significant in the lasing system - a  $[\text{Kr}]4d^{10} 5s^0 5p^6 \ ^1S_0$  upper state and a lower  $[\text{Kr}]4d^{10} 5s^1 5p^5 \ ^1P_1^o$  state. In fact, these spectroscopic descriptions are somewhat inaccurate, since the LS coupling approximation is not valid. For example, Persson *et al.* [1988] have calculated that the  $5s^1 5p^5 \ ^1P_1$  contribution to the lower level wavefunction is only 28%.

The branching ratios into the upper and lower laser levels are very similar. Kapteyn [1989] deduced from Auger spectra that they were 4.5% and 5.5% respectively. The lower level has a degeneracy of 3 ( $m_J = -1, 0, 1$ ), whereas the upper level is nondegenerate. This difference in degeneracy can potentially give rise to a population inversion, since the inversion density,  $N^*$ , in a laser system, is given by

$$N^* = N_u - \frac{g_u}{g_l} N_l \quad (2.1)$$

where  $N_u$ ,  $N_l$ ,  $g_u$ , and  $g_l$ , are the upper and lower laser level populations and degeneracies respectively.

This means that for any given density,  $N_{\text{XeII}^*}$ , of Xe II ions in the  $[\text{Kr}]4d^9 5s^2 5p^6 \ ^2D_{3/2,5/2}$  states which may be produced, an inversion density  $N^* = f \cdot N_{\text{XeII}^*}$  is generated, where

$$f = 0.79 \left( 0.045 - \frac{1}{3} 0.055 \right) = 2.1\% \quad (2.2).$$

Provided the upper level population is produced in a sufficiently short timescale, and provided there are no other mechanisms feeding the lower laser level, a population inversion can be produced. Thus, laser gain at 108.9 nm ensues. A schematic of the whole excitation and decay process is found in Fig. 2.2.



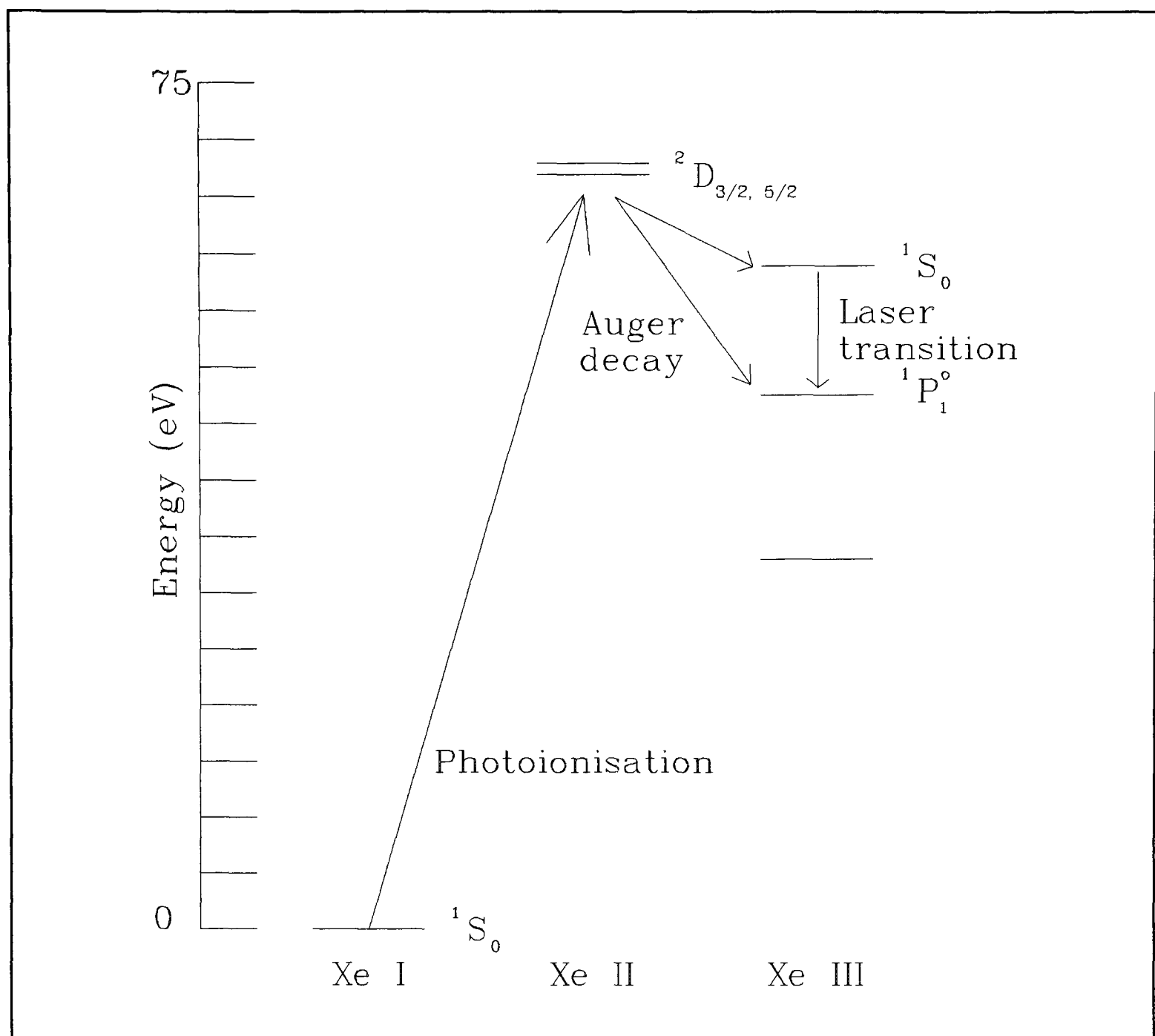


**Figure 2.2.** Schematic of Xe III laser scheme

An analogous scheme is found in the lighter Kr ( $Z=36$ ), but because the atom is smaller and the electrons more tightly bound to the nucleus, the pumping photon energy required is 200 eV. Unfortunately, the Kr III laser wavelength, which is 90.7 nm, is only 15% less than the Xe III equivalent. Not only is this rather a poor return on the requirement to double the quantum energy of the pumping radiation, but also there are no window materials available for 90.7 nm radiation. This means that differential pumping must be used. For these reasons, there has only been limited experimental effort expended on the Kr III system [Kapteyn 1988, Falcone & Kapteyn 1988].

## 2.2 Review of Xe III lasers reported in the literature

In this section we shall give a historical review of all the reports of lasing action in Xe III which have appeared in the literature. A comprehensive table (2.1) of the parameters of the various schemes is given in §2.2.3.



### 2.2.1 Systems with a gain channel

The first reported work on the Xe III laser system was the measurement of the Auger decay branching ratios, upper and lower laser level lifetimes, and (neutral atom) collisional quenching rates [Kapteyn *et al.* 1986b, Kapteyn 1986]. This work suggested that Xe III might work as an Auger laser, and successful operation of the scheme was soon reported by Kapteyn, Lee and Falcone [Kapteyn *et al.* 1986a]. The pumping geometry they used for this experiment is illustrated in Fig. 2.3.

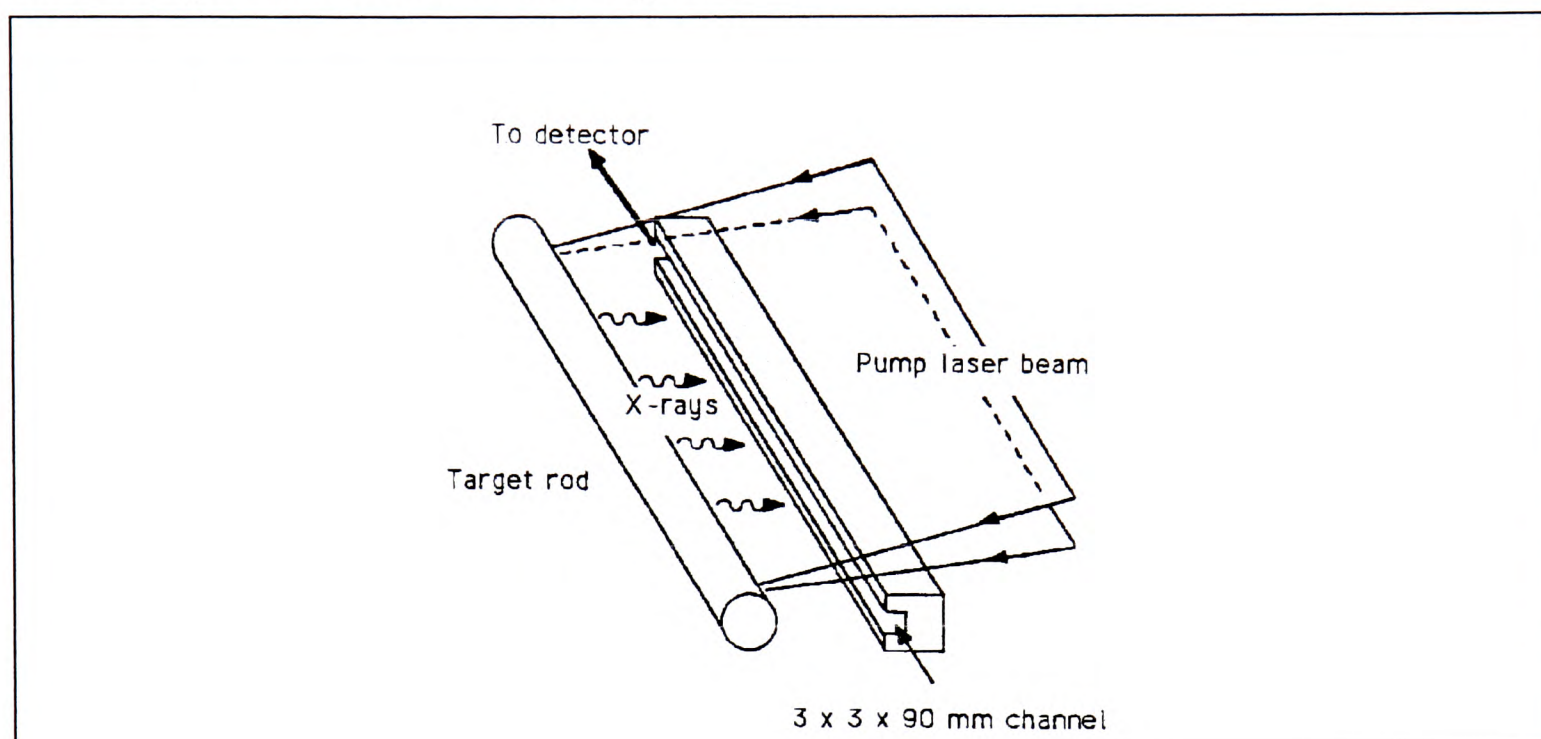


**Figure 2.3.** Pumping geometry used for first demonstrations of the Xe III laser. Diagram is taken from Falcone & Kapteyn [1988].

A 55 J pulse, of duration 1 ns, from a Nd:YAG laser\* was brought to a focus in a line 9 cm long on a solid tantalum target. The resulting intensity of  $10^{12} \text{ W cm}^{-2}$  was sufficient to generate the SXR required to pump the Xe III laser system. The target arrangement was placed in a chamber containing 1 torr of xenon gas. A 3 mm x 3 mm x 90 mm channel faced the plasma, at a distance of 20 mm from it. The channel defined a long, narrow region which was viewed by a wavelength-sensitive detection system. A gain coefficient of  $0.4 \text{ cm}^{-1}$  was observed for the 108.9 nm output. This geometry illustrates a universal feature of Xe III laser systems, which is invariably missed by the casual browser, and is emphasised here.

**The lasing at 109 nm takes place in ambient xenon gas, well outside the laser-generated plasma (LGP). The LGP is used as an x-ray flashlamp.**

As will become clear, the Xe III scheme reported by Kapteyn *et al.* [1986a], showed very low gain compared to subsequent systems. The reason for this was that ASE travelling radially from the plasma towards the lasing channel clamped the gain available. Kapteyn [1988] gives a model for this. Kapteyn *et al.* [1986a] found that the problem could be eased by the use of a 150 nm parylene filter placed over the open side of the gain channel. This is discussed further in §2.4.2.5.

---

\* Every Xe III laser system reported in the literature to date has employed a Nd:YAG or Nd:glass laser used at its fundamental wavelength (1064 nm or 1053 nm) to generate the pumping plasma.



The next developments were the application of the geometry shown in Fig. 2.3 to the pumping of the Kr III laser system [Falcone & Kapteyn 1988, Kapteyn & Falcone 1988]. Meanwhile, for the Xe III system, the use of a 10% reflectivity LiF mirror was found to enhance the 109 nm output fourfold [Kapteyn & Falcone 1988].

The use of a channel as far as 20 mm from the LGP was in order to make the system operate in a region of low electron density, because it was feared that the electrons would quench the inversion (§2.4.2). In fact, this fear was unfounded, and the next stage in the evolution of the Xe III system was to use an observation channel much nearer the LGP. This approach was adopted by Yin *et al.* [1987]. They used a plasma 3 cm long, and a gain channel 2 mm away from it. In this way, they achieved similar total gain-length products to those which had been obtained by Kapteyn *et al.* [1986a], but with almost 100 times less energy in the pumping laser beam.

### 2.2.2 Travelling-wave geometry

The next major breakthrough in the evolution of the Xe III laser was the invention of the travelling-wave geometry [Sher *et al.* 1987]. This has subsequently been used in several other plasma-pumped laser schemes [Benerofe *et al.* 1991, Barty *et al.* 1992, Weigold *et al.* 1993]. The technique is illustrated in Fig. 2.4.

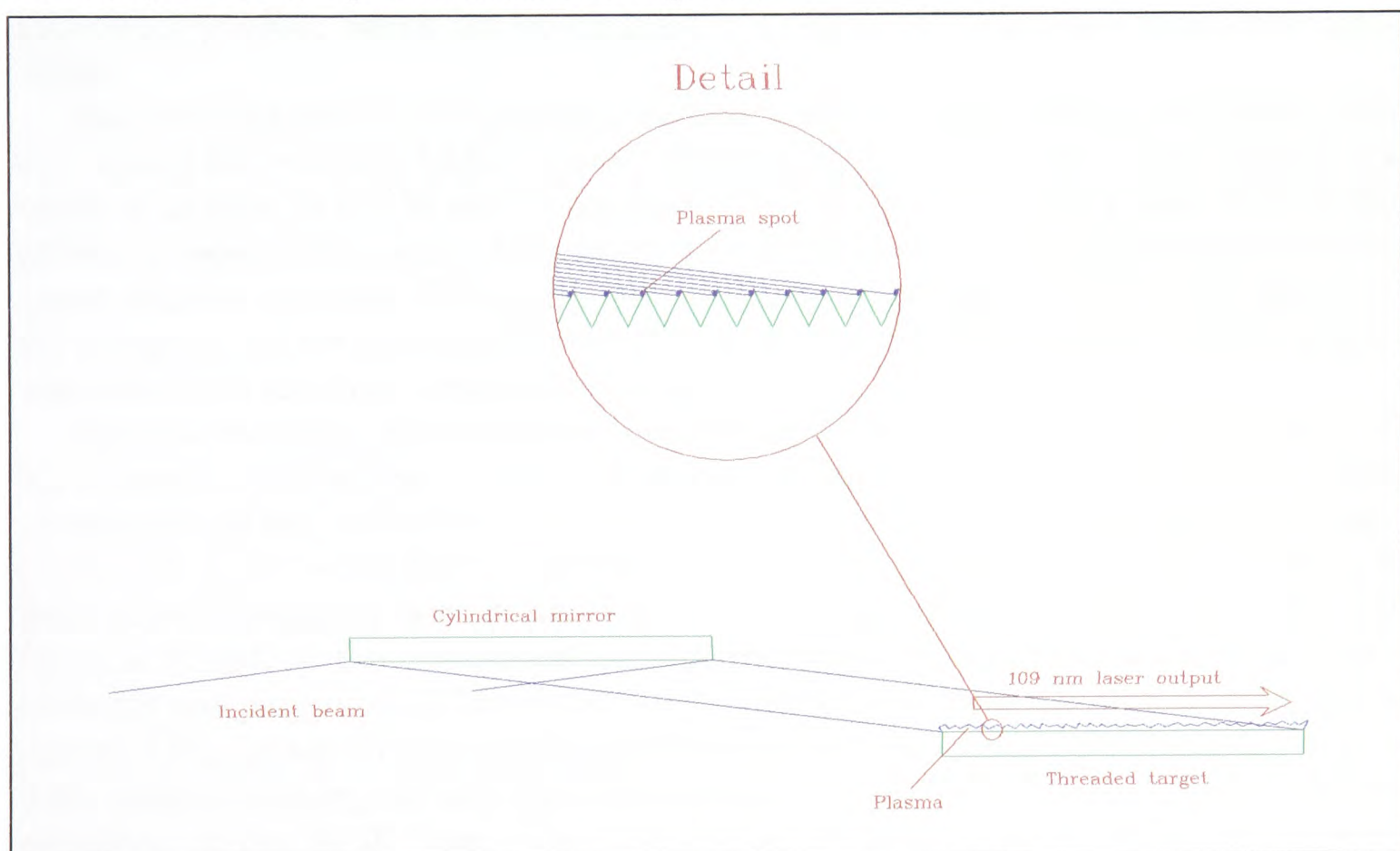


**Figure 2.4.** Travelling wave geometry invented by Sher *et al.* [1987]. Scheme shown uses a mirror for focusing, but early implementations used cylindrical lenses [Sher *et al.* 1987, Sher *et al.* 1991, Sher & Benerofe 1991].

The scheme works by focusing a beam at oblique incidence on a threaded target. This gives rise to a line of microscopic spot foci at the thread tips. There are two main features of the scheme which make it very attractive. The first is that the light arrives at one end of the target before the other. If the angle of incidence on the target is  $\theta_i$  from the normal, then the leading edge of the plasma sweeps along the target at a speed of  $c / \sin \theta_i$ . For typical angles of incidence, this is only 1% to 10% faster than the speed of light. Thus, it is



possible to use a total gain length having a transit time much longer than the duration of the output pulse, and still achieve efficient energy extraction from the scheme.

The second advantage associated with the travelling-wave geometry, compared to conventional line-focus techniques, is that the former splits up the plasma into smaller spots. These are spread over a distance much longer than the total aggregate length of the microscopic plasma spots. This is quantified in §6.3.5.

A subtle, but crucial, consequence of using a long gain region, comes from the fact that *provided a sufficiently hot laser-plasma can be generated, the gain of an Xe III laser system is almost independent of the intensity of the plasma emission*. The argument for why this is the case was first proposed by Sher *et al.* [1991], and runs as follows. Near one of the plasma spots, the emission fluence decays with distance. This is illustrated (for a line focus) in §2.4.1.1. A high pumping fluence gives rise to a high inversion density, but also to a high density of electrons, which limit the gain (for reasons discussed in §2.4.2). This means there is an optimum fluence of pump energy giving rise to a maximum gain coefficient. If the energy of the pumping plasma is reduced, and provided the relative shape of the emission spectrum does not change appreciably, the region of maximum gain moves in towards the plasma, but does not change in magnitude.

Thus, for efficient extraction of the 109 nm radiation, the energy of the pumping laser must be spread over as long a line as possible. This will maximise the total longitudinal gain-length product, which can be expected to scale linearly with the length of the gain region.

There are two limits to the process. The first is that the plasma must be sufficiently hot to generate the pumping SXR's required. Empirically, it is found that a laser intensity on target of at least  $3 \times 10^{10} \text{ W cm}^{-2}$  is required\* [Sher *et al.* 1991]. The second limit to the process is found if the region of maximum gain moves so near to the plasma spot that it is nearer than the next spot. This means that the system is sensitive to the spot-like nature of the pumping, and the gain-length product does not rise as fast as linearly with the length. This effect was observed empirically by Sher *et al.* [1991].

Since its invention, the travelling-wave geometry has been used in all the reports of Xe III lasers. The first report of its use, with a 9 cm gain region, was also the first report of saturation of the Xe III laser [Sher *et al.* 1987]. By extending the gain region to 25 cm, Sher *et al.* [1991] were able to saturate the Xe III laser, using only 500 mJ of energy in their infrared pumping laser beam. The repetition rate of high pulse-energy Nd:YAG lasers is limited by the requirement to cool the laser rod. The use of this low energy (500 mJ) pumping allowed Sher *et al.* [1991] to operate the Xe III laser at a repetition rate of 2 Hz, giving 109 nm output pulses of energy 1  $\mu\text{J}$ . Similar performance, from a 6 Hz tabletop system, has also been reported by Clement *et al.* [1994]. They achieved saturation of the Xe III laser using only 250 mJ of laser pumping energy. In another similar system Kubodera *et al.* [1995] have reported (near) saturation of the Xe III laser using 400 mJ of pumping laser energy. They also claim (but see §2.4.2.2) to have devised a model of their system.

The other two main areas of research into the Xe III laser system have related to the choice of target material, and the use of prepulses to improve the efficiency of the laser-generated plasmas. These are considered in the following two sections.

---

\* This limit is only valid for 1064 nm pumping with pump pulse of duration a few hundred picoseconds.



### 2.2.2.1 Choice of target material

Ablation of the target used for the laser-generated plasma means that, periodically, a new region of target surface must be exposed. Furthermore, debris from the target tends to coat the optical surfaces of the target chamber. An elegant solution to both of these problems has been reported by Yamakoshi *et al.* [1993]. They used a target wetted with (liquid) mercury. Clearly, this solves the problem of having to replenish the target surface. The scheme was also made self-cleaning, by water cooling the mercury reservoir, forcing splattered mercury droplets to vaporise from the other (warmer) surfaces and condense in the cooled mercury pool.

Yamakoshi *et al.* [1993] compared the results obtained from the mercury ( $Z=80$ ) target to those obtained when a gold ( $Z=79$ ) target was used. Slightly better results were obtained with the gold target. Another study of target materials has been made by Dennis *et al.* [1995]. We return to this in §2.3.7.2.

### 2.2.2.2 Prepulsing

The other two reports of lasing action from Xe III have concentrated on the use of prepulses to enhance the laser plasma conversion efficiency [Sher & Benerofe 1991, Yamakoshi *et al.* 1996]. For pumping laser durations of less than  $\sim 100$  ps, this technique is found to be very helpful. We return to this in §8.4.5.

### 2.2.2.3 Ion beam pumping

Finally, we note that Andreev & Ryzhov [1992] have proposed that it might be possible to pump the Xe III laser using the bremsstrahlung radiation of a beam of multicharged ions in neutral Xe I. No experimental work on this has been reported.

## 2.2.3 Summary

Table 2.1 gives a summary of some of the key features of Xe III lasers reported in the literature.



Reference	Pumping laser		Laser-generated plasma					Geometry		Gas	Output				
	$E_p$ mJ	$\tau_p$ ps	Target (Z)	$l_p$ cm	$w_p$ $\mu\text{m}$	$I_p$ $\text{W cm}^{-2}$	$\theta_i$ $^\circ$	$d$ $\mu\text{m}$	$P_{xe}$ torr	$\alpha_g$ $\text{cm}^{-1}$	$E_{109}$ $\mu\text{J}$	$\tau_{109}$ ps	Sat.?	$\eta$	
Normal incidence systems with gain channel															
Kapteyn <i>et al.</i> 1986	55 000	1 000	Ta (73)	9	50	$1 \times 10^{12}$			1	0.4		600	no		
Yin <i>et al.</i> 1987	10 000	600	Ta (73)	2.8	100	$5 \times 10^{11}$			2.5	2.36			no		
Travelling-wave systems															
Sher <i>et al.</i> 1987	3 500	300	Stainless*	9	200	$2 \times 10^{11}$	68	526	4	4.4	20	50	yes	$6 \times 10^{-6}$	
Sher <i>et al.</i> 1991	500	500	Stainless*	25	150	$3 \times 10^{10}$	82.5	318	15	1.6	1	250	yes	$2 \times 10^{-6}$	
Sher & Benerofe '91	75	80†	Au (79)	4.2	100	$1.7 \times 10^{11}$	82.5	318	15	1.7			no		
Yamakoshi <i>et al.</i> '93	1 000	400	Hg (80)	12	60	$1.4 \times 10^{11}$	82.5	320	10	1.4	0.1		yes	$1 \times 10^{-7}$	
Clement <i>et al.</i> 1994	250	100	Stainless*	20	75	$1 \times 10^{11}$	83	330	14	1.2	1		yes	$4 \times 10^{-6}$	
Kubodera <i>et al.</i> '95	400	100	Stainless*	17	250	$5 \times 10^{10}$	83	330	20	1.0	0.8		just		
Dennis <i>et al.</i> 1995	260	200	Au (79)	20	75	$1 \times 10^{11}$	83	330	10	1.65	1.3		yes	$5 \times 10^{-6}$	
Yamakoshi <i>et al.</i> '96	140	32‡	Hg (80)	19	140	$1.3 \times 10^{11}$	82.5	320	15	2.4			yes		

**Table 2.1.** Xe III laser systems reported in the literature. Where parameters listed have been optimised by the experimenters, the set which gave the best results have been quoted here. Quantities listed:  $E_p$ ,  $\tau_p$  pumping laser energy and duration;  $l_p$ ,  $w_p$ ,  $I_p$  plasma length, width, and (microscopic) intensity;  $\theta_i$ ,  $d$ , angle of incidence and target thread pitch for travelling-wave geometry;  $E_{109}$ ,  $\tau_{109}$ , Xe III laser pulse energy and duration; Sat.?, whether or not saturated;  $\eta$  overall conversion efficiency infrared→109 nm. Colour codes:

Not applicable	Not measured
----------------	--------------

\* Stainless steel (Z=28 & 26).

† 20% prepulses applied 1.6 ns earlier to area twice as wide as main plasma pulse.

‡ 300% prepulses applied 1-3 ns earlier



## 2.3 Laser-generated plasmas

### 2.3.1 Introduction

All the Xe III laser systems created to date have been pumped by SXR from laser-generated plasmas. In this section we give an introduction to laser-generated plasmas. Some further aspects of their operation are also discussed in later chapters (in §7.6 and §8.4.5). Much of this introduction is based on reviews by Max [1982], O'Neill [1988], Bakos [1990], Michette & Buckley [1993], Cotton [1990], Fletcher [1993] and Sigel [1989]. These sources will be used without specific credits.

### 2.3.2 Zones in the plasma

Laser-generated plasmas have myriad applications. They may be used to generate, for example: particles (§7.3.4), pressure waves (for inertial confinement fusion), mirrors, absorbers (§4.3), coherent radiation (§1.3.1), and incoherent radiation. It is the last of these which will be the subject of this section.

Even for the production of incoherent radiation, LGPs are used under a very wide variety of conditions. The common feature is that a laser beam is focused on to a solid (or sometimes liquid mercury) target. The intensity at the focus varies enormously, depending on the application. For the experimental work described in this thesis, intensities spanning seven orders of magnitude were used. Laser systems at national facilities can give about another further five orders of magnitude more intensity. This discussion, however, will be restricted to the intensities needed for Xe III laser pumping. These are in the range  $2 \times 10^{10}$  to  $10^{12}$  W cm<sup>-2</sup>. These are very much at the low end of focal intensities for LGPs which have been widely studied and reported in the literature [Spitzer *et al.* 1996].

The high intensity laser beam at the focus both vaporises and ionises atoms from the target material. This gives rise to a plasma, which absorbs the laser radiation, giving rise to further heating and ionisation. Radiative processes within the very hot ( $10^5$ - $10^6$  K) plasma which ensues, give rise to the plasma emission.

The key to understanding the processes in the laser-generated plasma is to divide it into two zones, which show quite distinct behaviour. These are labelled the conversion layer and the reemission zone [Fabbro *et al.* 1985, Sigel 1989], and are illustrated in Fig. 2.5.



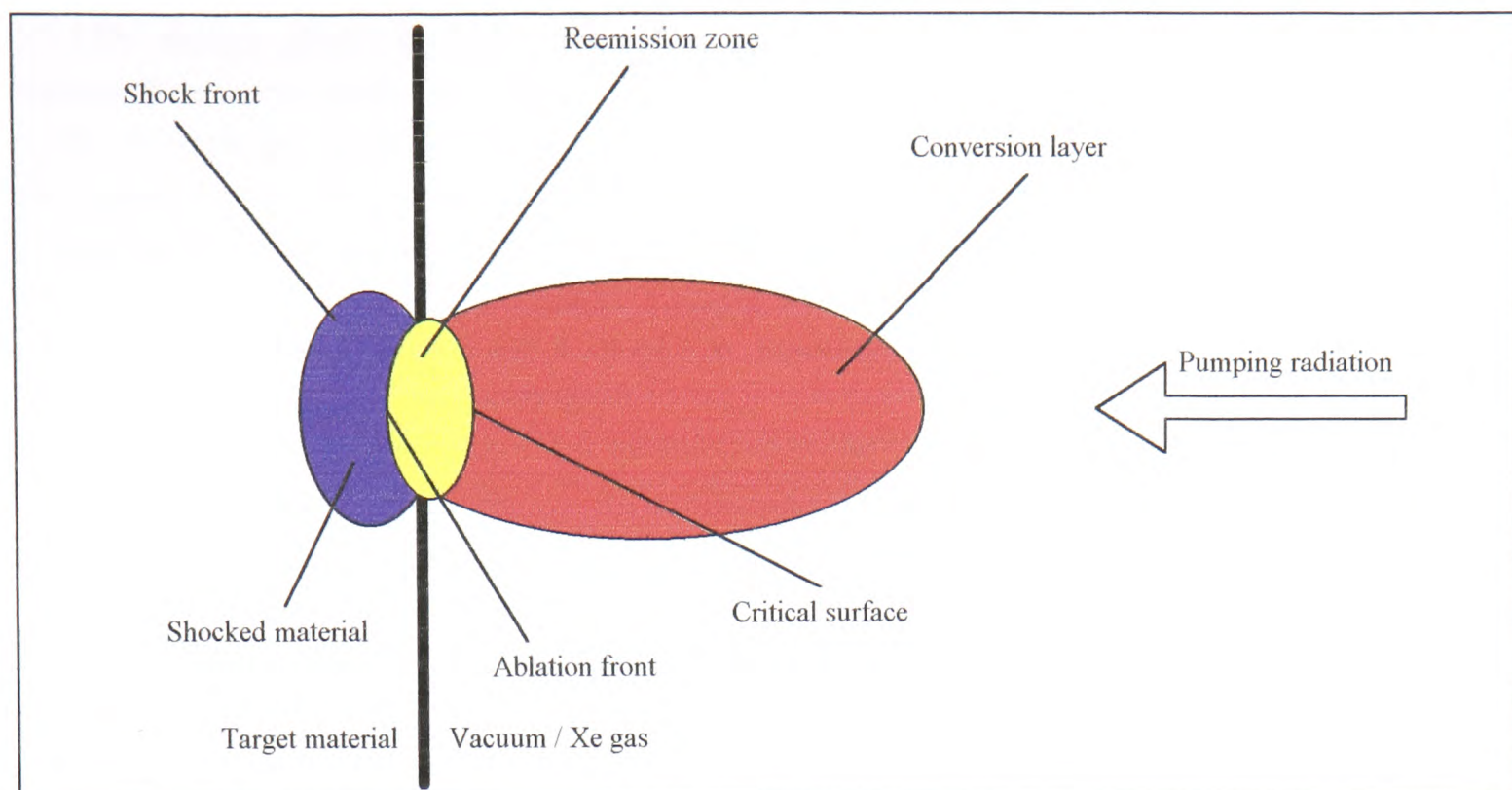


**Figure 2.5.** Schematic of a laser-generated plasma. Relative sizes of layers are arbitrary. After Fletcher [1993].

The vital difference between these two regions is the free electron density,  $n_e$ , in them. A plasma cannot be penetrated by light of a frequency lower than a critical, plasma (angular) frequency,  $\omega_p$ , given by

$$\omega_p = \left( \frac{e^2 n_e}{\epsilon_0 m_e} \right)^{\frac{1}{2}} \quad (2.3),$$

where  $e$  is the elementary charge, and  $m_e$  is the electron mass. This is because the response (to the oscillating electric field of the incident radiation) of the free electrons in a plasma gives rise to a purely imaginary refractive index for light of a frequency below the plasma frequency. Thus, in the same way as the conduction electrons in a metal reflect visible radiation, so the free electrons in a plasma reflect radiation of a frequency below the plasma frequency.

This means that for laser light of a given frequency,  $\omega_{las}$ , there is a critical electron density,  $n_c$ , above which the plasma will not transmit, given by

$$n_c = \frac{\omega_{las}^2 m_e \epsilon_0}{e^2} = 1.8 \times 10^{22} \text{ cm}^{-3} \quad (2.4)$$

for KrF laser radiation.

The conversion layer\* has an electron density lower than the critical density, whereas in the reemission zone the electron density is greater than the critical density. Thus, the laser energy cannot penetrate the reemission zone, and so can only be deposited in the conversion layer. This means the conversion layer is the hottest part of the plasma. For long wavelength laser radiation the critical electron density is small, and so the conversion layer is small. This means the laser energy is deposited into a small region, and so gives rise to hotter plasmas than are produced by short wavelength lasers. This has been repeatedly confirmed experimentally, for example by Chaker *et al.* [1988].

---

\* The conversion layer is also referred to in the literature as the coronal region, although it may not be well modelled by coronal equilibrium.



The names given to the regions indicate their role in the plasma process. The conversion layer serves to absorb the incident laser energy, and hence convert it into high-temperature thermal energy. Some of this thermal energy is transported to the reemission zone, by the mechanisms discussed in the following sections. In the reemission zone this thermal energy is emitted as thermal x-rays. The conversion layer is optically thin to these x-rays, and so these escape the plasma (or are reabsorbed within the reemission zone), and form the bulk of the radiative output of the plasma. The rest of the emission is from the conversion layer.

The laser plasma also generates an intense pressure wave. This gives rise to a shocked region in the target material. This is illustrated in Fig. 2.5, and is significant in the production of debris from the plasma. This is considered further in §7.3.4.

### 2.3.3 Energy deposition

In the following sections we shall consider how the laser energy is deposited in the plasma, how it is transported within it, and how it is emitted. For the comparatively short laser wavelength, low temperature, low focal-intensity plasmas considered here, the two most important absorption processes are inverse bremsstrahlung, and resonant absorption.

#### 2.3.3.1 Inverse bremsstrahlung

The main mechanism for energy deposition into the plasma is inverse bremsstrahlung, or collisional absorption. The forward process, bremsstrahlung, is the phenomenon of a fast-moving electron decelerating in the electric field near a nucleus. The reverse process, inverse bremsstrahlung occurs when an electron gains energy by absorbing a photon during a collision with an ion or atom. Initially, the inverse bremsstrahlung will be by electron-atom collisions, but electron-ion collisions will begin to dominate as the plasma forms.

The absorption coefficient of radiation of angular frequency,  $\omega$ , for inverse bremsstrahlung,  $\alpha_{ib}$ , scales as [Hughes 1980]

$$\alpha_{ib} \propto \frac{n_e N_i Z_i^2}{\omega^2 T_e^{3/2}} \quad (2.5),$$

where  $n_e$ , and  $N_i$  are the electron and ion densities respectively, and  $Z_i$  is the ion charge (*not* the atomic number of the target element). The number density scaling in expression (2.5) suggests that the inverse bremsstrahlung absorption is most where the number density is high, *i.e.* near the critical density. Noting that  $n_e = Z_i N_i$  and applying (2.3), we find that the maximum inverse bremsstrahlung absorption scales as

$$\alpha_{ib}^{\max} \propto \frac{\omega^2 Z_i}{T_e^{3/2}} \quad (2.6).$$

This means that we expect inverse bremsstrahlung to be most important for low temperature plasmas, pumped by short wavelength radiation. This is exactly the situation for the plasmas described in this thesis for pumping the Xe III laser.

It should be pointed out that we have only considered linear inverse bremsstrahlung here. Nonlinear inverse bremsstrahlung occurs when the electron velocity is not thermal, but determined by its response to the oscillating electrical field of the incident laser pulse.



This only becomes relevant at much higher focal intensities ( $10^{15} \text{ W cm}^{-2}$ ) than used here ( $10^{11} \text{ W cm}^{-2}$ ).

### 2.3.3.2 Resonant absorption

The other important absorption mechanism for low intensity LGPs is resonant absorption. This is the excitation of plasmons, at the critical surface. Plasmons are (undriven) collective oscillations of the electrons in a plasma. The restoring force required is provided by the electric field of the (almost) stationary ions. It is easily shown that the frequency of such oscillations is the same as the (electron-density dependent) plasma transmission cut-off frequency given by expression (2.3). Thus, we may expect that optical radiation of a given frequency may excite these oscillations near the critical surface.

If a ray is incident on the plasma at a slight angle,  $\theta_i$ , to the density gradient, it will be refracted so much that it is reflected, with the turning point at an electron density,  $n_e$ , very close to the critical density,  $n_c$ , given by

$$n_e = n_c \cos^2 \theta_i \quad (2.7).$$

If the polarisation of the incident radiation is such that, at the turning point, its electric field is perpendicular to the critical surface, then the electric field is directed along the density gradient. The oscillations are longitudinal, and so (for light of the correct polarisation) some of the waves generated travel towards the critical surface, where the natural frequency of plasma oscillations is exactly the driving frequency. Thus, there is resonant excitation of plasma oscillations. Resonant absorption is maximised for small but finite angles of incidence of light on the critical surface. However, plasma instabilities, density perturbations, and roughness of the target surface ensure that such angles are found even when no special efforts are made to achieve them. The process is independent of the plasma temperature, laser wavelength, and intensity, and so is most important where inverse bremsstrahlung is insufficient to cause complete absorption. This is the long laser wavelength, high plasma temperature regime, and so resonant absorption (as well as the many nonlinear processes also possible in the conversion layer [Bakos 1990]) will not dominate the absorption for the plasmas considered here.

### 2.3.4 Energy transport

Heat is transported around the plasma by several mechanisms. Heat is transferred within the conversion layer, and from the conversion layer to the reemission zone, by electronic heat conduction. This process ensures the temperature in the conversion layer is fairly uniform, provided short wavelength lasers are used to generate the plasma. The significance of short wavelength generating lasers in this is that these give rise to energy deposition into a large conversion layer, and so sharp temperature gradients are avoided. For long wavelength lasers, electron heat transport may be insufficient to eliminate these sharp temperature gradients, and this can cause convective cooling of the conversion layer, thus reducing the overall conversion efficiency of the plasma.

Another mechanism for heat transport is radiation. Radiation from the conversion layer can heat the reemission zone, as well as transporting energy within both regions. The process is particularly important for target materials of high atomic number, since these have many absorbing and emitting transmissions available.



## 2.3.5 Emission mechanisms

There are several mechanisms by which LGPs emit radiation. The most important ones for the laser intensities considered here may be categorised as bound-bound, free-bound, and free-free transitions.

### 2.3.5.1 *Bound-bound transitions*

Optical transitions within ions in the LGP give rise to line emission. The electron undergoing the transition is bound both before and after the process, and so these are known as bound-bound transitions. The effect of these processes depend on the target material. For targets of low atomic number, there are few transitions, and it is possible to achieve a conversion efficiency as high as 1% into a single spectral line. For targets of higher atomic number, many more lines are observed. For M, N, & O shell emission\* complete overlap occurs, owing to fine structure broadening, and band emission is observed. The transition from line to continuum emission for plasmas of elements of increasing atomic numbers may be seen clearly in LGP emission spectra given by Bridges *et al.* [1986].

### 2.3.5.2 *Free-bound transitions*

The recombination of an electron with an ion can give rise to radiative emission, with the excess kinetic energy of the electron carried off by a photon. The excess kinetic energy may also be carried away by another electron in a three body recombination process, and this competes with radiative recombination. Free-bound transitions give rise to continuum radiation, since there is a continuous spread of energies available to the incident electron.

### 2.3.5.3 *Free-free transitions*

“Forwards” bremsstrahlung, is the radiative deceleration of an electron in the coulomb field of a nucleus. It is important in hotter, more highly ionised plasmas than those considered here.

## 2.3.6 Emission properties

### 2.3.6.1 *Blackbody radiation*

If an emission region is optically thick to its own radiation, absorption of radiation before it escapes the region modifies the emission spectrum, and the region will radiate as a black body. This condition pertains in the denser parts of the reemission zone. The presence of many optical transitions in ions may also make a high atomic number plasma optically thick in the conversion layer as well. Blackbody radiation is considered in more detail in §2.3.8.

### 2.3.6.2 *Temporal properties of output*

The temporal properties of plasma emission have not been studied in detail for the laser intensities considered here. In general, laser plasmas produced by nanosecond duration (as

---

\* See §2.3.7.2 for a definition.



opposed to picosecond or femtosecond) lasers may emit for the same [Spitzer *et al.* 1996], a longer [Morsell *et al.* 1992], or a shorter [Davis *et al.* 1988] time than the pumping laser radiation, and the temporal profile depends on the emission wavelength [Bijkerk 1993]. Which of the regimes is found depends on the plasma conditions. Unless significant heating is required, the leading edge (first few nanoseconds) of the emission is generally found to follow the leading edge of the laser pulse.

For the application here, it is only the leading edge of the emission which is of interest, since any Xe III lasing will be finished after this time. No detailed attempt has been made to predict the temporal and spectral dependence of the emission on the leading edge of the laser pulse. It should be pointed out, however, that these properties are essential to whether or not the experiment described in chapter 6 could be expected to work. It was hoped that the emission in the SXR region suitable for pumping the Xe III laser would only occur a few nanoseconds into the laser pulse, due to the plasma temperature rising to reach the threshold for such emission. A similar effect was observed by Bijkerk [1993], using rather higher laser intensities of  $4 \times 10^{12} \text{ W cm}^{-2}$ . It should be pointed out that the hydrodynamic expansion effect described in §7.6, may have made this a vain hope.

## 2.3.7 Experimental considerations

In choosing how to generate a LGP having the emission properties required, several factors are important. We shall consider these here.

### 2.3.7.1 Laser wavelength

As illustrated in the discussion above, the laser wavelength is a very important consideration in the generation of LGPs. All the LGPs described in this thesis were made using KrF laser radiation at 248 nm. On the other hand, all the Xe III schemes reported in the literature to date have used infrared (1064 nm or 1053 nm) laser radiation. Laser plasmas generated by short wavelength lasers are cooler but more efficient than their long wavelength counterparts. This means the emission peaks at longer wavelengths, but is greater, in total, than that found for long wavelength pumping.

This has been found empirically over a wide range of experimental conditions. For example, such effects have been found at focal intensities much greater than used here for Xe III pumping, of  $\sim 3 \times 10^{14} \text{ W cm}^{-2}$  [Kodama *et al.* 1986]. For conditions more like those used here, Bridges *et al.* [1986] have found similar effects. The results most directly applicable here, however, have been reported by Chaker *et al.* [1988] and Toubhans *et al.* [1989]. The experimental results presented in the two works are very similar, and we shall concentrate on those presented by Chaker *et al.* [1988]. They found that with a copper ( $Z=29$ ) target, a constant conversion efficiency of  $\sim 8\%$  into 100-750 eV radiation was observed for a 1064 nm laser pump, at target intensities between  $2 \times 10^{10} \text{ W cm}^{-2}$  and  $10^{13} \text{ W cm}^{-2}$ . On the other hand, the equivalent efficiency was  $\sim 35\%$  for pumping with the laser frequency-quadrupled to a wavelength of 266 nm. They found similar results with gold ( $Z=79$ ) targets, but did not extend their measurements to such low intensities. Clearly, this indicates a higher efficiency for the UV laser plasma generation. The threshold laser intensity to generate plasma emission in the 750-2000 eV range was  $\sim 10^{12} \text{ W cm}^{-2}$  for 1064 nm pumping, whereas it was  $\sim 2.5$  times greater for 266 nm pumping. Thus, we may deduce a cooler plasma for the shorter wavelength pumping.

On the other hand, for lower laser intensities, contradictory results have been reported by Wellegehausen *et al.* [1989]. They found that in the spectral region from 20 to 62 eV,



the conversion efficiency fell as the laser wavelength was reduced, for a tungsten target, with a laser intensity of  $6 \times 10^9 \text{ W cm}^{-2}$ . There was also a shift of the peak of the emission spectrum to longer wavelengths, as the laser wavelength was reduced. The plasma temperature,  $T_{\text{plas}}$ , was found to vary more slowly with the laser wavelength,  $\lambda$ , than predicted by scaling laws derived from analytic plasma models. The scaling was found empirically to be  $T_{\text{plas}} \propto \lambda^{0.1}$ , whereas analytic models typically predict the exponent to be 0.5-1 [Sigel *et al.* 1990, Wellegehausen *et al.* 1989].

### 2.3.7.2 Target material

The atomic number of the target material is a very important parameter for LGP emission. If one only considers a limited wavelength range, the conversion efficiency of LGPs is found to vary strongly with the atomic number of the target [Popil *et al.* 1987, Kauffman *et al.* 1993, Spitzer *et al.* 1993, Spitzer *et al.* 1996]. The reason for this is that the x-ray emission lines of a given element form bands, according to the principal quantum number of the lower level of the electronic transition concerned. These are denoted L, M, N, O, *etc.* shell emission, for principal quantum numbers of 1, 2, 3, 4, *etc.* The photon energies corresponding to a particular shell increase with atomic number, but decrease with the principal quantum number. Thus, as the atomic number of the target is changed, the bands “sweep through” the spectral region of interest. In general, there is also an increase in conversion efficiency with increasing atomic number. This is because there are many electronic transitions possible for the many electrons in the high-Z ions. This gives rise to a high density of states which undergo radiative decay. Thus, radiative emission competes favourably with nonradiative processes.

The experimental studies of the Z-dependence of SXR emission most relevant to pumping the Xe III laser have been made by Kauffman *et al.* [1993], Spitzer *et al.* [1996], Wellegehausen *et al.* [1989], Yamakoshi *et al.* [1993] and Dennis *et al.* [1995].

Dennis *et al.* [1995] investigated the performance the Xe III laser system as the target material was changed. They compared cadmium ( $Z=48$ ), zinc ( $Z=30$ ), gold ( $Z=79$ ), and copper ( $Z=29$ ) targets, to stainless steel ( $Z=26$  &  $28$ ). The reasoning behind these choices was (presumably) that stainless steel, zinc and copper are M shell emitters in the relevant SXR region, whereas cadmium is an N shell emitter, and gold is an O shell emitter. They found gold to give the best small signal gain improvement (25%) over stainless steel, but cadmium to give the maximum output energy improvement (112%). Despite considering it to be a good candidate for investigation, they were unable to investigate tantalum ( $Z=73$ ), since its hardness meant they could not make uniform coatings of it on their threaded target. It should also be pointed out that the pumping conditions were not identical between these experiments, and so we cannot use them, for example, directly to compare gold with cadmium.

Yamakoshi *et al.* [1993] compared gold ( $Z=79$ ) and mercury ( $Z=80$ ) targets. At low pump laser intensities ( $< 6 \times 10^{10} \text{ W cm}^{-2}$ ), at which saturation did not limit the apparent small signal gain, gold targets gave rise to higher gains. For all pumping conditions, the 109 nm output was greater with a gold target than with a mercury target.

The general trend of increasing conversion efficiency with increasing atomic number was confirmed by Wellegehausen *et al.* [1989], for conversion into the 20 eV to 62 eV spectral region, using low intensity ( $6 \times 10^9 \text{ W cm}^{-2}$ ) laser radiation of 355 nm wavelength.

The most comprehensive work on conversion efficiencies into SXRs at  $\sim 100$  eV has been reported recently by Spitzer *et al.* [1996], although the same experiments had been summarised earlier by Kauffman *et al.* [1993]. They used 1064 nm radiation, and 532 nm



radiation, focused to  $2 \times 10^{11} \text{ W cm}^{-2}$ , for various target materials. They measured conversion efficiencies into a 4 eV bandwidth centred at 95 eV\*. They also made more broadband (50 eV to 110 eV) measurements, but did not describe the results in detail. For the narrowband measurements, they found the conversion efficiency showed three peaks, at iron ( $Z=26$ , M shell), tin ( $Z=50$ , N shell + strong narrowband spectral feature at detection wavelength), and gold ( $Z=79$ , O shell). No significant differences were found for the different pumping laser wavelengths, for a given target material. For broadband conversion, the peak N shell and O shell elements gave similar efficiencies, which were both greater than the M shell peak. This is in qualitative agreement with the results of Dennis *et al.* [1995].

All the experiments described in this thesis were conducted with a tantalum target ( $Z=73$ , O shell). Superficially, the data presented by Spitzer *et al.* [1996] and Dennis *et al.* [1995] suggest that tin ( $Z=50$ ), or cadmium ( $Z=48$ ) might have been equally good, whereas gold ( $Z=79$ ), or lead ( $Z=82$ ) might have been slightly better. However, the use of an O shell emitter (like Ta) rather than an N shell emitter (Sn or Cd), is probably safer for a first attempt since it will be less reliant on the specific ionisation stages created in the plasma. The ionisation stages created are a function of the pumping laser wavelength. Furthermore, for low power pumping, as used here, a plasma cooler than optimal is to be expected. Thus, we require an element with many transitions at lower energies than 100 eV. This suggests the use of an element of slightly lower atomic number (*e.g.* Ta,  $Z=73$ ) than is optimal (*e.g.* Au,  $Z=79$ , or Pb,  $Z=82$ ) for 100 eV photon generation. Furthermore, gold is much more expensive than tantalum, and lead can be expected to give problems with debris [Dennis *et al.* 1995].

### 2.3.8 Black body radiation

Wellegehausen *et al.* [1989] have shown that the time-integrated emission spectra of some laser plasmas they generated could be well approximated by a black body distribution. Furthermore, the plasmas considered in this thesis (chapter 6) were created under very similar conditions to those considered by Wellegehausen *et al.* [1989]. Their conditions were: short wavelength (355 nm) generating laser, 8 ns duration, low intensity ( $2 \times 10^{10} \text{ W cm}^{-2}$ ) laser pulses.

In this case, we may approximate the plasma emission as a black body radiator, of temperature,  $T_{\text{plas}}$ . It is important to realise that this does not mean that the plasma is a black-body radiator. It simply means that the time-integrated emission spectrum is well fitted by a black-body curve. Thus, we do not need to consider the area of the source nor any time dependent cooling effects; both of these would be important in treating the emission of a true black-body. In this section we shall consider the optimum temperature for a black body with regard to pumping the Xe III laser.

We consider the overlap of the black body spectrum with the photoionisation cross spectrum of Xe. The proportion,  $n(E_p, T_{\text{plas}})dE_p$  of the black body photons having their energies in the range  $E_p \rightarrow E_p + dE_p$  is given by

---

\* This is an uncharacteristically well studied region of the SXR spectrum. This is because it is technologically significant for projection lithography, since Mo/Si multilayer mirrors can give 60%-70% reflectivity in this region. This high reflectivity is crucial, since projection lithography systems typically use  $\sim 7$  reflective surfaces in series [Richardson *et al.* 1993].



$$n(E_p, T_{plas})dE_p = \frac{0.416}{(k_B T_{plas})^3} \frac{E_p^2}{\exp\left(\frac{E_p}{k_B T_{plas}}\right) - 1} dE_p \quad (2.8)$$

which is normalised such that

$$\int_0^\infty n(E_p, T_{plas})dE_p = 1 \quad (2.9).$$

The extent to which the plasma radiation spectrum overlaps the photoionisation spectrum of neutral Xe may be quantified. Simplistically, we might calculate an overlap integral (as a function of the plasma temperature) of the form

$$\int_0^\infty n(E_p, T_{plas}) \cdot \sigma^{4d}(E_p) \cdot dE \quad (2.10).$$

However, this does not represent a “fair” comparison between plasmas of different temperatures. The reason for this is that the total number of photons emitted by a black body depends on the plasma temperature, for a given total emitted energy. This is relevant because it is found empirically that the broad-band energy conversion efficiency,  $\zeta$ , of a laser-generated plasma varies very slowly over a broad range of plasma conditions [Chaker *et al.* 1988]. Thus, expression (2.10) cannot be used to compare plasmas of different temperatures obtained from a laser of fixed pumping energy. Different plasma temperatures can be achieved by adjusting the focal intensity of the laser spot [Wellegehausen *et al.* 1989].

However, the overlap integral (2.10) may be weighted to allow for a constant total emission energy (rather than constant total number of photons). The energy emitted from a black-body scales as  $T_{plas}^4$  whereas the total number of photons emitted scales as  $T_{plas}^3$ . In this case we expect the total number of photons,  $N_{phot}$  emitted by the plasma to scale as

$$N_{phot} \propto \frac{1}{T_{plas}} \quad (2.11).$$

Thus, we may calculate a weighted photoionisation cross section,  $\sigma_w^{4d}(T_{plas})$ , given by

$$\sigma_w^{4d}(T_{plas}) = \frac{1}{T_{plas}} \int_0^\infty n(E_p, T_{plas}) \cdot \sigma^{4d}(E_p) \cdot dE \quad (2.12)$$

where  $\sigma^{4d}(E_p)$  is the cross section for photoionisation of a 4d electron. The  $(1/T_{plas})$  scaling factor in (2.12) comes from (2.11), and means that the weighted cross section does not have the dimensions of area.

Photoionisation of a 4d electron is the first stage to achieving the Xe III inversion, but is not the only possibility. At photon energies lower than 67 eV (the 4d ionisation threshold), photoionisation of a 5p electron dominates, with double ionisation and 5s ionisation also observed (§2.1.1.1). The severity of these competing processes was quantified by calculating their corresponding total weighted photoionisation cross section,  $\sigma_w^{other}(T_{plas})$ , in the same way. The results obtained are shown in Fig. 2.6.



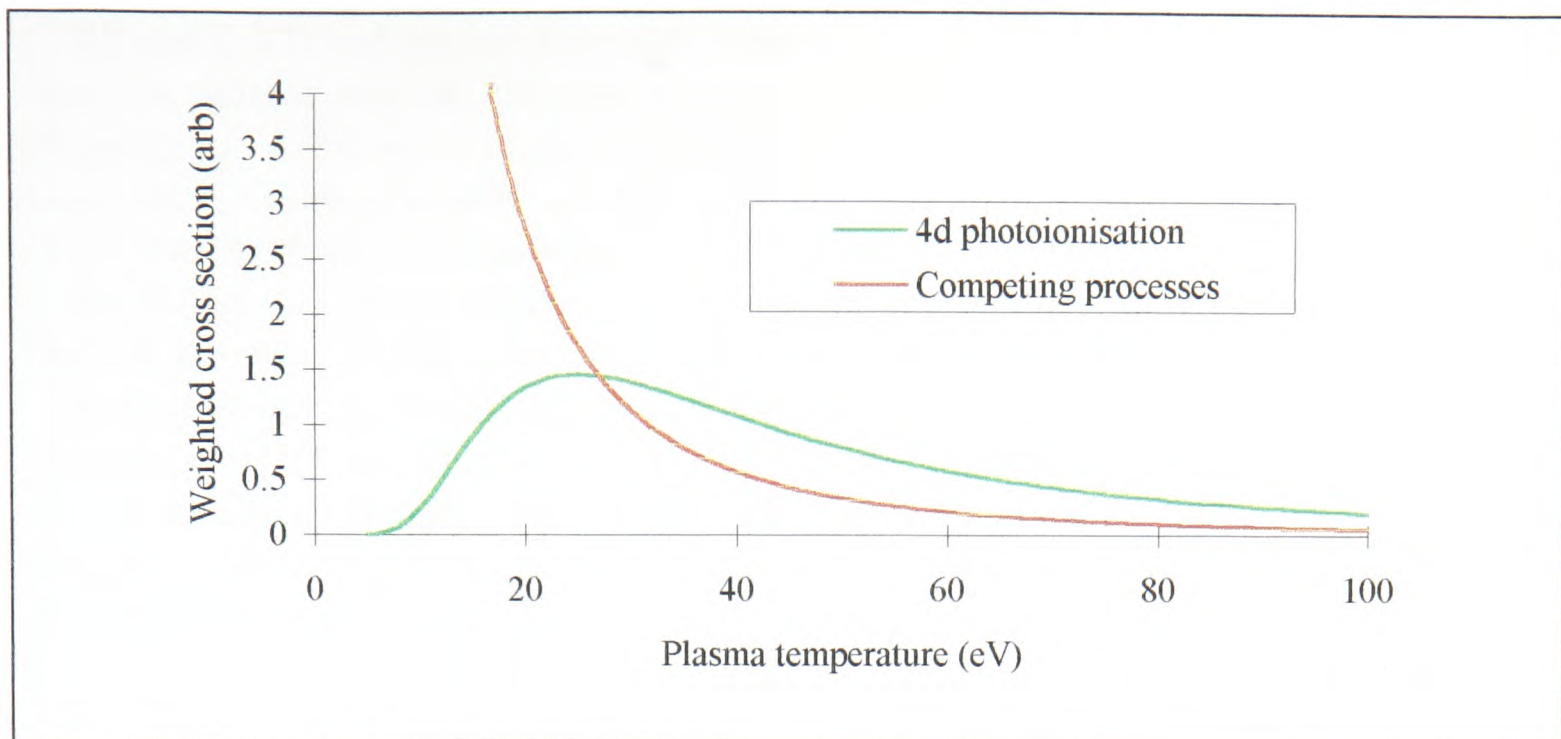


**Figure 2.6.** Effective cross sections for 4d photoionisation and competing processes.

Two conclusions may be drawn:

- The optimum blackbody temperature for 4d photoionisation is 25 eV. For this plasma temperature, however, 55% of the absorption will give rise to unwanted Xe ions.
- A hotter blackbody (40 eV or so) could be more suitable for pumping the Xe III laser system, since it will cause less unwanted photoionisation.

We return to these results in §2.4.2.5.

### 2.3.9 Plasma conversion efficiency

The blackbody model also allows us to estimate the x-ray conversion efficiency we might expect from a laser-generated plasma. In particular, we shall estimate an efficiency for the nanosecond laser system used to produce LGPs in chapters 6 and 7. The most similar LGP scheme (in terms of pulse length, laser wavelength, focal intensity, and target material) from the literature has been reported by Powers & Shields [1994]. Indeed, as will be shown in §7.3.4.1, similar (relative) results were obtained using the KrF laser system described in this thesis.

Powers & Shields [1994] measured the absolute conversion efficiency of 5 ns duration 308 nm (XeCl) radiation LGPs, as a function of focal intensity, for a copper ( $Z=29$ ) target. They obtained similar results with gold ( $Z=79$ ) and tin ( $Z=50$ ) targets. The spectral region of the plasma radiation which was detected was centred at 92.5 eV, with a FWHM of 6.2 eV.

Assuming 100% conversion efficiency to blackbody radiation, we may predict the maximum conversion efficiency Powers & Shields [1994] could have observed. We require a slightly different formulation of the blackbody spectrum to that given by (2.8). This is given by  $u(E_p, T_{plas})$ , defined such that  $u(E_p, T_{plas})dE_p$  represents the proportion of the *energy* of blackbody emission (rather than the proportion of the *photons*) to be found in photons of energy range  $E_p \rightarrow E_p + dE_p$ . This is given by

$$u(E_p, T_{plas}) = \frac{15}{(\pi k_B T_{plas})^4} \frac{E_p^3}{\exp\left(\frac{E_p}{k_B T_{plas}}\right) - 1} \quad (2.13).$$



We use (2.13) and assume a triangular sensitivity profile (in the energy domain) for the detection system used by Powers & Shields [1994]. This suggests a peak conversion efficiency of 4.9% at a plasma temperature of 23.6 eV. Powers & Shields [1994] measured a maximum conversion efficiency (into the spectral region of interest) of 1.6%, which was observed for a laser intensity of  $10^{11} \text{ W cm}^{-2}$ . This suggests a value of 33% for  $\zeta$ , the overall conversion efficiency. This may be pessimistic - the shorter wavelength of the KrF laser should make it more efficient.

It is important to realise that there are significant uncertainties in this figure. Powers & Shields [1994] do not report what precautions they took to eliminate angular effects, nor how well calibrated their detection system was. Any failings on either count could introduce significant errors. A further source of error is present if the plasma emission does not have a black-body spectrum; there was no investigation of this. Nevertheless, this figure is in agreement with conversion efficiencies deduced under similar conditions, for a copper target, by Chaker *et al.* [1988].

It is also instructive to compare this deduced conversion efficiency of 33% with the efficiencies quoted in the literature for SXR conversion by the plasmas which have pumped Xe III systems. These are 5% (IR→all plasma emission) [Yin *et al.* 1987], and 2% (IR→plasma emission in range suitable for 4d photoionisation) [Sher *et al.* 1987]. Clearly, this suggests that the use of short wavelength laser for LGP production, may give rise to a major improvement to the overall conversion efficiency of Xe III laser systems.

## 2.4 Model for Xe III pumping

As can be seen from table (2.1), all of the reports of Xe III lasing have used laser pulses of duration 1 ns or less. There are two quite different reasons for this. The first is that a short pulse gives a high intensity on target, and this is needed to generate a laser plasma sufficiently hot to emit the 67-100 eV photons required to pump the Xe III laser. The second reason is that the Xe III laser self-terminates, and so any pumping must be at least as fast as the upper-state lifetime of 4.75 ns, or it will be wasted\*. In this section we shall consider whether it is the upper-state lifetime which actually limits the longest pulse which may be used, or whether some other factor is important.

We shall develop a very simple model for the pumping of the Xe III system. The parameters chosen for the pumping laser are suitable for the experimental schemes described in chapters 6 and 7. The model is designed to give us an insight into how an Xe III laser is pumped, and a feel for the magnitudes of physical quantities relevant to the scheme. We take a similar approach to one adopted by Silfvast [1982] for modelling the gain in the photoionisation pumped Cd II laser which he then went on to demonstrate [Silfvast *et al.* 1983].

### 2.4.1.1 Plasma emission

In order to approximate the plasma emission we make the following assumptions:

- The plasma emission has a blackbody spectrum, given by (2.13).
- The total conversion efficiency of the plasma,  $\zeta$ , is 33% (§2.3.9).
- The emission follows the leading edge of the KrF laser pulse.

---

\* This is not quite true. If the pumping rises exponentially it can defeat the self-termination. Obviously, this is not a practical solution.



- The laser is focused to a line, at an *energy-line-density*,  $E_0$ , of  $57 \text{ mJ cm}^{-1}$ . This corresponds to the 170 mJ of energy which may be obtained from the KrF laser described in chapter 5, in the first 4.75 ns of its output, spread over a 3 cm line-focus. The significance of the 4.75 ns is that it is the natural upper-state lifetime of the Xe III laser; any pumping after this time must be wasted.
- We neglect end effects, and assume isotropic emission into a wedge of half apex angle,  $\theta_c$ , of  $65^\circ$ . This is somewhat arbitrary, but for a lambertian source (having area but no volume, giving a cosine variation of angular emission)  $\sim 80\%$  of the energy is emitted into a wedge of this size.

A section of the geometry assumed is given in Fig. 2.7.

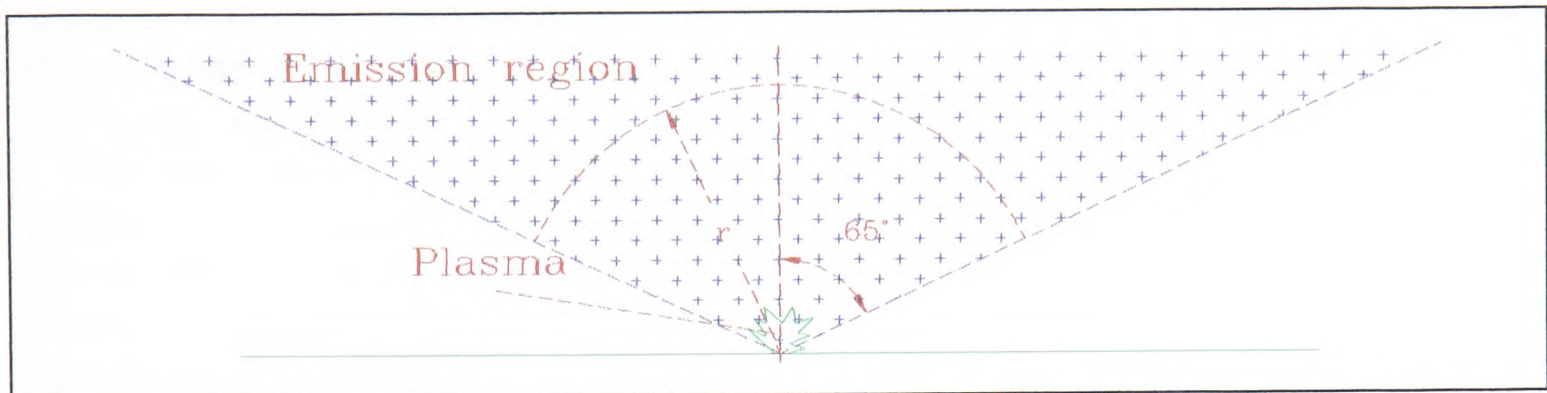


**Figure 2.7.** Geometry assumed for plasma emission.

Provided the absorption is not bleached (a vital assumption which is justified in §2.4.1.2), and considering for the moment only the emission in the energy range  $E_p \rightarrow E_p + dE_p$ , we may write down the fluence (energy per unit area, per unit photon energy) at a radius,  $r$ , from the plasma, given by

$$F(r, E_p) = \zeta E_0 u(E_p, T_{plas}) \frac{\exp(-N_{Xe} \sigma^{total}(E_p) r)}{2r\theta_c} \quad (2.14),$$

where  $\sigma^{total}(E_p) = \sigma^{4d}(E_p) + \sigma^{other}(E_p)$  is the total photoionisation cross section of Xe, and  $N_{Xe}$  is the number density of neutral Xe atoms.

#### 2.4.1.2 Bleaching of the absorption

The fact that the absorption does not bleach is the most important conclusion of the model. First we shall show that this is the case, and then we shall consider the consequences.

Gower *et al.* [1982] have modelled the passage of a pulse of light of arbitrary temporal profile through an absorbing medium. The absorbing medium modelled is such that once an absorption event has occurred, the absorbing atom (or molecule) is no longer available for further absorption. This is exactly the case for the photoionisation of xenon modelled here\*. Gower *et al.* [1982] found that bleaching occurs at a given point in the absorbing medium when the time-integrated intensity (*i.e.* the fluence) of the pulse passing that point exceeds a bleaching fluence given by

$$F_{bleach} = \frac{h\nu}{\sigma_{abs}} \quad (2.15),$$

---

\* In fact this is slightly misleading. Xenon ions as well as neutral atoms may absorb the plasma radiation. However, this further reduces the scope for bleaching.



where  $h\nu$  is the photon energy, and  $\sigma_{abs}$  is the absorption cross-section. If we assume that all the plasma emission is at  $\sim 100$  eV, the peak of the photoionisation cross-section, we may use (2.15) to calculate a bleaching fluence of  $0.7 \text{ J cm}^{-2}$ .

The bleaching-free absorption model embodied in expression (2.14) predicts a fluence exceeding the bleaching fluence over a distance of  $\sim 100 \mu\text{m}$  from the line focus (again assuming the emission is all at 100 eV, and considering the situation at the end of 4.75 ns). For a typical xenon pressure of 10 torr, this distance is more than an order of magnitude smaller than the absorption length for the 100 eV emission. As far as the bleaching goes, this is a worst-case model, *i.e.* the broadband nature of the emission and absorption means there is less scope for bleaching. Furthermore, the Xe III lasing may be complete well before 4.75 ns into the laser pulse, in which case the energy supplied by the plasma is effectively lower than assumed, corresponding to a shorter length over which the absorption is bleached.

The fact that the bleaching length is much shorter than the absorption length has two important consequences. The first is that in assuming the absorption is not bleached, we do not underestimate the fluence of radiation able to escape the bleached region, so that (2.14) is valid (for  $r > 100 \mu\text{m}$ ). The other implication of this calculation is that the  $1/r$  (geometric) dependence of the fluence decay is much more important than the exponential (absorption) decay. This means that the region surrounding the plasma samples fluences of plasma-emission which vary from being sufficient to bleach the absorption to at least an order of magnitude lower, all within the absorption length for the SXR radiation.

If a spot focus is used, a similar conclusion may be drawn. This observation is essential to the validity of the argument of Sher *et al.* [1991] (§2.2.2), that the gain of Xe III lasers is independent of the plasma emission fluence, provided a sufficiently hot plasma is generated.

## 2.4.2 Quenching

### 2.4.2.1 Electron density

Some of the work described in this thesis relates to pumping the Xe III laser system by using long KrF laser pulses. The self-termination of the laser system means any pumping will be wasted if it is provided after about one upper-level lifetime. This means that the net upper-state lifetime (allowing for quenching processes) is an important consideration in the comparison of a nanosecond timescale system with the shorter systems which have been used previously.

First of all, it should be pointed out that the duration of the 109 nm laser pulses obtained from the Xe III laser system is not a direct measure of the upper-state lifetime. This is because stimulated emission can be expected to deplete the population inversion very quickly when a threshold inversion is reached. Thus, it may be possible to pump the system slowly ( $\sim 2$  ns), but extract the stored energy quickly (in a few hundred picoseconds).

Suppose we wish to achieve a small-signal gain coefficient,  $\alpha$ , of  $1.6 \text{ cm}^{-1}$ , which is typical for an Xe III laser system (see table 2.1), and is assumed in §6.2.2. In order to calculate the inversion density required, we must know the line-centre gain cross-section,  $\sigma_g$ . From expression (1.2) we see that this may be calculated from the natural lifetime of the upper laser level against decay to the lower laser level, and the line-width of the laser transition. Assuming only Doppler broadening, we find  $\sigma_g = 3 \times 10^{-13} \text{ cm}^2$  for room



temperature xenon [Kapteyn *et al.* 1986a]. Thus, we find the inversion density required is given by

$$N^* = \frac{\alpha}{\sigma_g} = 5 \times 10^{12} \text{ cm}^{-3} \quad (2.16).$$

To put this in to context, the number density of atoms in 1 torr of xenon gas at room temperature is  $3 \times 10^{16} \text{ cm}^{-3}$ .

From the discussion in §2.1.1.1, the precursor to this inversion is a population of Xe II ions in the  $[\text{Kr}]4d^9 5s^2 5p^6 \ ^2D_{3/2,5/2}$  states. This population must be greater than the inversion density by a factor  $1/f = 48$ . For each Xe II ion in the  $[\text{Kr}]4d^9 5s^2 5p^6 \ ^2D_{3/2,5/2}$  states we must also create 1 photoelectron and 1.21 Auger electrons, *i.e.* a total of 2.21 electrons. From §2.3.8, we see the lowest plasma temperature we may use to pump the Xe III system efficiently is  $\sim 25 \text{ eV}$ . For each 4d photoionisation, at this plasma temperature, we can also expect  $\sim 1$  other photoionisation (Fig. 2.6). Combining all these factors, we expect an electron density greater than the inversion density by a factor of at least  $(1+1+1.21) \times 48 = 154$ . Secondary ionisation by the faster photoelectrons may enhance this a little. Overall, this means that in order to create the inversion density required, we must also generate an electron density,  $n_e$ , of at least  $\sim 8 \times 10^{14} \text{ cm}^{-3}$ .

#### 2.4.2.2 Two-body quenching

These electrons will lead to quenching of the upper laser level. First we consider two-body quenching processes. In order to calculate the severity of the problem we must know a rate coefficient for the reaction  $\text{Xe}_{\text{upper}}^{2+} + e^- \rightarrow \text{Xe}_{\text{other}}^{2+} + e^-$  which represents electron collisional de-excitation, and for the reaction  $\text{Xe}_{\text{upper}}^{2+} + e^- \rightarrow \text{Xe}^{3+} + 2e^-$  which represents electron collisional ionisation\*.

First we consider electron collisional de-excitation. In general, the rate of this will depend on the electron energy distribution, although Green & Webb [1975] have shown that the electron temperature dependence of the process is not strong for the range of electron energies (compared to the energy of the de-excitation transition) likely to present here. The only measurement in the literature for this rate constant has been given by Kubodera *et al.* [1995]. They deduced the rate constant,  $K_e$ , to be  $5 \times 10^{-8} \text{ cm}^3 \text{ s}^{-1}$ , by fitting a theoretical model of an Xe III laser system to empirical results.

For de-excitation from the lower laser level, they deduced a rate constant fifty times lower, so that the process does not actually enhance the inversion density, by clearing the lower laser level. Taking the rate coefficient to be  $5 \times 10^{-8} \text{ cm}^3 \text{ s}^{-1}$ , and the electron density to be  $8 \times 10^{14} \text{ cm}^{-3}$ , we find a lifetime of the upper laser level against electron collisional de-excitation of 25 ns, some five times longer than the natural lifetime. This suggests that electron collisional de-excitation will not significantly reduce the lifetime of the upper laser level.

Unfortunately, there is considerable doubt about the figure of  $5 \times 10^{-8} \text{ cm}^3 \text{ s}^{-1}$  for the electron collisional de-excitation rate constant, deduced by Kubodera *et al.* [1995]. The

---

\* Two body quenching by (radiative) recombination is also possible, but the rate will be much lower than that for non-radiative collisional quenching. An estimate for the rate coefficient of the former process (for hydrogenic ions) may be made following Hutchinson [1987] as  $\sim 5 \times 10^{-13} \text{ cm}^3 \text{ s}^{-1}$  for the conditions here. This is five orders of magnitude lower than the value deduced by Kubodera *et al.* [1995] for collisional quenching.



reason for this is that their model is riddled with oversights and inaccuracies, including that it:

- neglects the Auger electrons in calculating the electron density;
- considers three-body electron recombination (§2.4.2.3) to limit the electron density, but not the ion density (the limiting of the ion density in this way serves to limit the degree of reduction of the electron density made possible by three-body electron recombination);
- neglects electron collisional ionisation;
- does not allow for electron quenching from the upper laser level to the lower level; and
- neglects Stark broadening (§2.4.2.5).

Thus, the conclusion, based on the rate coefficient deduced empirically by Kubodera *et al.* [1995], that electron collisional de-excitation will not limit the gain lifetime, may not be justified. The coefficient they deduced was five times more than their initial guess, based on a semi-empirical model quoted by Bates *et al.* [1962], and this might appear a better first estimate of the de-excitation rate. However, this gives a rate coefficient some three orders of magnitude lower than some which have been measured experimentally by Green & Webb [1975] for some singly charged ions, under similar conditions. The doubly charged Xe III ions could be expected to show greater electron collisional de-excitation rates.

Electron collisional ionisation is also possible as a quenching mechanism. A semi-empirical model given by Hutchinson [1987] suggests that the lifetime against this process of an Xe III ion in the upper laser level is of the order of 10 ns. From this, we would expect the process to give rise to moderate quenching (~30% reduction in upper-state lifetime).

However, there is also some experimental evidence that electron-collisional quenching (whether by de-excitation or by ionisation) may be much more severe than indicated here so far. This emerged during the course of the work described in this thesis, when a report appeared which suggested that nanosecond pumping may be far from optimal for xenon pressures of 5 torr or greater [Clement *et al.* 1994]. This report describes a pump-probe experiment in which a 3 cm long gain region was pumped, and then, after a variable delay, the output from a 12 cm region was passed through the 3 cm region, as a probe beam. Thus, the gain of the 3 cm region could be measured as a function of the time after its creation. What Clement *et al.* [1994] found was that the gain lifetime was ~300 ps for a xenon pressure of 5 torr, which was the lowest xenon pressure their experiment allowed. Stimulated emission in the 3 cm region may have depressed this lifetime. Furthermore, the technique only measures the gain in the part of the probed region corresponding to the (spatial) region of maximum brightness of the probe beam. The spatial distribution of the brightness in the probe beam will have been a very strong function of the spatial distribution of the small signal gain coefficient, since the system was not saturated. Thus, the experiment measured the lifetime of the gain, in the region of maximum gain. There might still have been a region of slightly lower gain, with a much longer lifetime.

Nevertheless, these results suggest that quenching of some sort may limit the upper-state lifetime of Xe III laser systems, at least for xenon pressures greater than 5 torr, and nanosecond duration pumping may be largely wasted in this regime. As we shall see from the discussion which follows, electron quenching is the most likely culprit, since three-body recombination and collisions with neutral atoms are not fast enough to reduce the lifetime this much.



### 2.4.2.3 Three-body quenching

Another possible quenching process due to the electrons, is three-body recombination, *i.e.* the process



The rate (number of recombinations per unit volume per unit time),  $\Gamma_3$ , for the process is given by

$$\Gamma_3 = \gamma_{3\text{III}} N_{\text{XeIII}} n_e^2 \quad (0.18),$$

where  $N_{\text{XeIII}}$  is the total number density of Xe III ions, and  $\gamma_{3\text{III}}$  is a rate constant. Xe ions with other charges may undergo equivalent processes, and there are equivalent rate constants for these processes. Hasted [1972] gives an expression for  $\gamma_3$  for bare nuclei of charge  $Z$  (and independent of their atomic mass). Although Xe III is evidently not a bare nucleus, our justification for this estimate comes from the observation that for singly charged ions the rate coefficient does not depend strongly on the species [Hasted 1972]. This suggests

$$\gamma_{3\text{III}} = Z^{1.25} \gamma_3^0 \left( \frac{T_e^0}{T_e} \right)^{3.625} \quad (2.19),$$

where  $\gamma_3^0 = 7 \times 10^{-21} \text{ cm}^6 \text{ s}^{-1}$ , and  $T_e^0$  is 250 K. In order to use expression (2.19) we must estimate an electron temperature. The photoelectrons will have an energy spectrum determined by energy of the photons giving rise to them, and the threshold for the relevant ionisation processes (e.g. removal of a 4d electron). Thus, a reasonable estimate for the photoelectron temperature is about 33 eV, since this is the difference between the 4d threshold (67 eV) and the optimum photon energy for 4d photoionisation (100 eV). The Auger electron energy spectrum will depend on the Xe III states produced, e.g. for the upper laser state 8 eV electrons will be generated.

There will be cooling of the electrons by inelastic collisions with the ions, which will excite optical transitions in them. A typical threshold for an optical transition is  $\sim 1$  eV, and so we shall use this as a lower estimate for the effective electron temperature, which will give us an upper estimate for the three body recombination coefficient. This gives  $\gamma_{3\text{III}} = 1.5 \times 10^{-26} \text{ cm}^6 \text{ s}^{-1}$ . At the electron density calculated above, this gives a lifetime against three-body recombination of 100  $\mu\text{s}$ . Thus, there is no danger of three-body recombination giving rise to quenching of the upper laser level.

### 2.4.2.4 Collisions with neutral xenon

So far, we have only considered effects due to the *electrons* in the lasing region. Quenching by collisions with *neutral atoms* are also possible. The quenching coefficients for the upper laser and lower laser levels, have been measured to be  $2.8 \times 10^7 \text{ torr}^{-1} \text{ s}^{-1}$  and  $2.3 \times 10^7 \text{ torr}^{-1} \text{ s}^{-1}$  respectively [Kapteyn *et al.* 1986b, Kapteyn *et al.* 1987]. Although these are rather similar, the greater degeneracy of the lower laser level means that quenching of the lower laser level does not significantly help the inversion density. Thus, we may estimate the lifetime of the inversion against collisional quenching by neutral xenon atoms. This becomes equal to the natural lifetime at a xenon pressure of 7.5 torr. Thus, we can see that the  $\sim 300$  ps gain lifetime measured at 5 torr by Clement *et al.* [1994] is much



shorter than the 7 ns collisional lifetime. Thus, electron quenching seems the most likely cause of the low gain lifetime measured by Clement *et al.* [1994].

#### 2.4.2.5 Stark broadening

Stark broadening may be an essential consideration in the operation of the Xe III laser system. Typical Stark widths are on the order of 0.1 Å at electron densities of  $10^{17} \text{ cm}^{-3}$ , for electron temperatures similar magnitudes to those described in §2.4.2.3 [Gigosos *et al.* 1994, Purić *et al.* 1991, Konjević & Pittmann 1987]. Stark widths for non-hydrogenic transitions vary linearly with electron density, and so we might expect a Stark broadening of the Xe III laser transition on the order of 0.001 Å for the electron density calculated above. This is about the same as the Doppler width. Thus, Stark broadening may be the dominant line-broadening process in Xe III lasers.

Indeed, Stark broadening makes an elegant explanation for the fact that there has been only a narrow range of small-signal gain coefficients for Xe III lasers reported in the literature (see table 2.1). A similar observation is that the small signal gain observed by Yamakoshi *et al.* [1996] was found to saturate as the pumping energy was increased. These observations can be explained by noting that (in a system pumped sufficiently fast for electron quenching not to matter) the electron density scales linearly with the inversion density. Since the Stark width scales linearly with the electron density, the line-centre gain cross-section will be inversely proportional to the electron density. Thus, the overall gain coefficient, which is the product of the inversion density and the line-centre gain cross-section, will be independent of the inversion density. Thus, the maximum gain coefficient available from an Xe III system is fixed. It should be pointed out, however, that the small signal gain of  $4.4 \text{ cm}^{-1}$  obtained by Sher *et al.* [1987] is about twice what anyone else has ever observed. If Stark broadening is what limits the gain, this anomalously high gain could be explained by a very hot plasma giving rise to a low photoelectron density. Nevertheless, it seems unlikely that this would be sufficient to double the gain, since it could not halve the photoelectron density. This suggests there may be some gain-limiting due to quenching processes as well as Stark broadening.

A further piece of evidence for Stark broadening having been important in Xe III laser systems used in the literature is found in the two experiments which have employed isotopically-enriched xenon [Kapteyn *et al.* 1986a, Yin *et al.* 1987]. Naturally occurring xenon is an isotopic mixture of largest components 27%  $^{132}\text{Xe}$ , 26%  $^{129}\text{Xe}$ , 21%  $^{131}\text{Xe}$ , 10%  $^{134}\text{Xe}$ , 9%  $^{136}\text{Xe}$ , and 4%  $^{130}\text{Xe}$  [Ellis 1984]. The hyperfine structure and isotope shifts of the different species smear the purely electronic levels, and hence reduce the line-centre gain. Kapteyn *et al.* [1986a] comment that calculations of the severity of the problem are difficult since the hyperfine splitting is comparable to the Doppler linewidth, but could be expected to reduce the gain by a factor of 2-3 for normal xenon\*. A simple, but very expensive†, way around the problem is to use a single isotope of Xe, and choose one with no net ground state nuclear spin (and so no hyperfine splitting), such as  $^{136}\text{Xe}$ .

---

\* This means that, assuming naturally-occurring xenon is used, the inversion density calculated in §2.4.2.1 is an underestimate, and likewise the electron density. This makes the magnitudes of the Stark broadening and electron quenching rate even more critical in the consideration of long timescale pumping of the Xe III laser.

† 80% to 90%  $^{136}\text{Xe}$  costs about £8000  $\text{dm}^{-3}$  from Isotec Inc., of Dayton, Ohio, USA. This compares to £10  $\text{dm}^{-3}$  for normal Xe.



Kapteyn *et al.* [1986a] found their macroscopic gain doubled when they used 84%  $^{136}\text{Xe}$ , but only when they shielded their observed gain region from both ASE and low energy photons (giving rise to unwanted outer-shell photoionisation) by means of a 150 nm parylene filter. The use of either enriched xenon alone, or the filter alone, did not increase the gain. It is difficult to draw conclusions from this because the effect of the filter is complicated - it will have reduced the pumping flux by 40%, reduced the ASE, and reduced the electron density in their gain channel. Nevertheless, the observation that the gain increased only when the electron density was reduced is consistent with Stark broadening having been a limiting factor.

Yin *et al.* [1987] report a less dramatic improvement of the macroscopic gain, with only a 10% gain improvement in switching to enriched  $^{136}\text{Xe}$ . They comment that this was observed consistently, including under low gain conditions, for which ASE limiting was not a problem. This suggests that Stark broadening was the dominant line-broadening mechanism in their laser system.

#### 2.4.2.6 Conclusions about long-timescale pumping

It is not possible to draw firm conclusions about how long-timescale pumping of the Xe III laser system would affect the gain. This is because the relative importance of Stark broadening with respect to electron quenching is not known. From the discussion above, however, it appears that both effects are important in limiting the gain of Xe III systems. Indeed, this was the conclusion drawn by Yamakoshi *et al.* [1996].

If Stark broadening has been an important factor limiting the gain of Xe III laser systems, then we may expect that long timescale pumping might be possible, since the gain will be fixed by the broadening, for a wide range of electron densities. Thus, at sufficient distance from the plasma, there may be an electron density at which collisional quenching is slow, compared with the natural upper state lifetime. Thus, we would expect lasing in this region. Although faster pumping would allow a greater volume to lase, it would not greatly increase the longitudinal small-signal gain coefficient.

On the other hand, the results of Clement *et al.* [1994] are less promising, although not completely damning, with regard to slow pumping of the Xe III laser. The only sure way to find out is to try, and chapters 6 and 7 are devoted to just this.



# 3. Approaches to pulse shortening, and a compact oscillator

---

## 3.1 Short pulses from KrF

### 3.1.1 Introduction

#### 3.1.1.1 *Rationale*

The self-terminating nature of the Xe III laser scheme, as discussed in the preceding chapter, implies that most of the energy in the  $\sim 20$  ns pulse from the KrF laser described in §5 would be wasted. For this reason, attempts were made to reduce the pulse-duration from the KrF laser system. The aim was to generate short (sub-nanosecond) pulses, and amplify them in the KrF amplifier module.

#### 3.1.1.2 *Suitability of KrF for short-pulse amplification*

The fact that the ground state of the KrF laser transition is unbound, gives rise to significant ( $200\text{ cm}^{-1}$ ) homogenous broadening of the gain [Shaw 1991]. This means KrF can be used (and has been used) to amplify pulses as short as 45 fs [Szatmári 1994] and 60 fs [Szatmári & Schäfer 1988]. In KrF systems with the highest possible brightness, at beam powers in the several-terawatt range, direct amplification of single short pulses becomes less desirable (although not impossible [Endoh *et al.* 1989]), because of nonlinear effects in anything put in the beam path. This problem may be avoided by chirped pulse amplification [Lister *et al.* 1994] or by windowless Raman beam recombination [Divall *et al.* 1996].

#### 3.1.1.3 *Dye system front ends*

All the systems described in the last paragraph rely on complex and expensive dye-laser front-ends, to generate short pulses for amplification. Similarly complex systems have also been used in more modest KrF laser systems, to generate pulses having durations from tens to hundreds of picoseconds [Schwarzenbach *et al.* 1986, Szatmári *et al.* 1987, Luk *et al.* 1989, Steyer *et al.* 1990]. Another dye-excimer hybrid system, which generates 7 ps pulses, is described in more detail in §8.1.2. Such systems are necessarily complex because they operate at several wavelengths, and require frequency-conversion, accurate synchronisation of laser systems, several dye laser modules, saturable absorbers, and in many cases, one or two Nd:YAG lasers.

Because of the complexity of using dye-laser hybrid systems, there has been considerable effort expended in devising all-excimer short pulse systems. Although these systems have not yet shown the femtosecond performance which can be achieved from dye-excimer hybrids, pulse durations in the range of nanoseconds to tens of picoseconds have been obtained. These systems will be reviewed in the following sections, and experimental investigations into some of them will be described in this, and the following chapter. First of all, we shall review some of the basic tools available to us, which have been found useful for pulse-shortening of excimer lasers - particularly KrF lasers.



### 3.1.1.4 Saturable absorbers

Saturable absorbers are well established tools in laser physics. Hercher [1967] gives a theoretical treatment of their operation. Their uses include: suppression of ASE, Q-switching, pulse shaping, degenerate four wave mixing, and modelocking. Applications of saturable absorbers to excimer laser systems have been rather limited by lack of suitable materials. For example, Caro & Gower [1981] report phase conjugation of KrF laser pulses by degenerate four-wave mixing. They used a selection of dyes as saturable absorbers, but found strong evidence that thermal effects rather than saturable absorption were responsible for establishing the dynamic hologram required to observe phase conjugation (see §4.2.1.3 for a description of phase conjugation).

Several substances have been investigated for use as saturable absorbers for KrF laser radiation. Clearly, it is desirable to find an absorber with low absorption when saturated. Another desirable property is rapid (nanosecond) absorption recovery, if the absorber is to be used again during the laser pulse (*e.g.* in a modelocking scheme). For KrF radiation there is no perfect saturable absorber, but the most promising candidates are acridine dye and ozone gas.

Acridine ( $C_{13}H_9N$ ) dye (dissolved in methanol) was proposed and characterised as a saturable absorber for KrF by Nishoika *et al.* [1989]. They found a small-signal (unsaturated) absorption cross-section of  $6.8 \times 10^{-16} \text{ cm}^2$ , with the saturated absorption cross-section 6.25 times smaller. The performance is limited by the absorption recovery having a slow component (115 ns), as well as fast one (400 ps). Nevertheless, the use of acridine has been proposed and numerically modelled in a short-pulse generation system requiring absorption recovery [Badziak & Jablonski 1993].

Ozone gas has been proposed for use as a saturable absorber for KrF laser radiation by Bigio & Thomas [1986]. It shows negligible nonsaturable absorption, since it works by the photodissociation reaction



and the photodissociation products have negligible absorption at the KrF wavelength. Photodissociation of alkali-halide vapours (*e.g.* CsI at  $\sim 1000 \text{ K}$ ) also gives lower nonsaturable absorption than acridine, but is inconvenient since it requires the use of an oven cell [Kaplan & Gibson 1986]. Ozone has a small-signal absorption cross-section of  $1.2 \times 10^{-17} \text{ cm}^2$  [Bigio & Thomas 1986]. This is about half that of acridine, and so requires higher fluences for saturation. Nevertheless, it is possible to saturate the absorption of ozone at fluences below the damage thresholds of typical window materials [Bigio & Thomas 1986]. The absorption-recovery time has not been measured, though operation in a buffer of atmospheric pressure oxygen might allow sufficiently fast recombination for the use of ozone in a modelocked system.

### 3.1.1.5 Related systems

A Raman cell may also be used in a similar way to a saturable absorber. This has been reported by Tünnermann *et al.* [1990], who used depletion of a KrF Raman pumping beam to obtain 3.5 ns pulses (at the KrF wavelength) from the leading edge of 25 ns input pulses. It must be emphasised that this technique is fundamentally different from the Raman beam recombination technique described in §4.5.1.3. In the former scheme the Stokes pulse is rejected, whereas in the latter it forms the output of the system.



A scheme which is the converse of saturable absorption has been reported by Cotton *et al.* [1989]. This “*radiation induced opacity*” (RIO) technique involves focusing a KrF beam into a cell containing, for example, 0.1% benzene in cyclohexane. For a fluence of  $2 \text{ J cm}^{-2}$  (limited by the need to avoid damage to the cell windows) the tail could be removed from pulses of duration 23 ns. This gave 3 ns output pulses. A mechanism suggested by Cotton *et al.* [1989] is the generation of scattering centres in the liquid. These are formed during the laser pulse, and disperse from the irradiated region before the next pulse arrives.

Saturable absorbers may be used in several ways to achieve pulse-shortening. Even on its own, a saturable absorber [*e.g.* Christov *et al.* 1984] or a RIO medium [Cotton *et al.* 1989] can give pulse-shortening. In general, however, saturable absorbers have been used in combination with other techniques, including further amplification of shortened pulses. We consider these in §3.1.1.7ff.

### 3.1.1.6 *Electro-optic switching*

Another common feature of many pulse-shortening systems is the use of a Pockels cell as an electro-optic switch. The main technological hurdle to be overcome in using such a scheme is the achievement of fast, high-voltage switching of the cell - typical requirements are a few kilovolts to be switched in a nanosecond or less. Several approaches have been taken:

- By means of a fast switch (krytron) and reflection from the end of a transmission line acting as a voltage-doubler, Jaroszynski & King [1983] sliced single 400 ps pulses from a 12 ns duration ArF pulse, using a KD\*P Pockels cell.
- If full transmission of the Pockels cell is not needed, a potential lower than the half-wave voltage may be used, relaxing the requirements on the switching circuit. This approach allowed Reksten *et al.* [1981] to use an all solid-state switching system, with a Pockels cell used for active modelocking of an XeCl laser. Pulses of duration 300 ps were obtained.
- Fast switching to the half-wave voltage of a Pockels cell may be achieved by overdriving the Pockels cell. In other words, the cell is switched to several times the half-wave voltage, and the optical transmission switches on and off repeatedly in the process. Curry *et al.* [1989] have used this approach, combined with a gap in a strip transmission-line to achieve fast switching. Dielectric breakdown occurs at the gap in the strip line, and this sharpens the rise of the voltage pulse seen by the Pockels cell. In this way, Curry *et al.* [1989] were able to slice a train of pulses of individual duration  $\sim 100 \text{ ps}$  from a 10 ns KrF pulse.

### 3.1.1.7 *Modelocking*

An obvious pulse-shortening technique which takes advantage of saturable absorption or electro-optic switching is modelocking. This is a well established tool for the generation of short pulses from both homogeneously, and inhomogeneously-broadened lasers.



Unfortunately, the gain in excimer lasers does not last long enough for steady-state modelocking to develop\*. Thus, simply inserting a saturable absorber (passive modelocking), or an amplitude or phase modulator (active modelocking) into an excimer laser cavity, cannot be expected to give very short pulses. Prediction of the evolution of the pulse widths is difficult, since the gain varies significantly over the timescale of the laser pulse, and may have a very significant effect on the pulse-shape if saturation occurs. In general, a numerical model must be used in order to predict the performance of such excimer systems [Badziak & Jablonski 1993, Di Lazzaro *et al.* 1995].

Nevertheless, empirical attempts at straightforward modelocking (*i.e.* employing only a single modelocking element) have generated subnanosecond pulses from excimer systems. The shortest pulses (120 ps) have been obtained by active modelocking of an XeCl system [Shay *et al.* 1988]. For this system, a comparatively long-duration discharge module (80-120 ns, compared to ~50 ns for the KrF amplifier module available for the current project) allowed up to 28 round-trips of the gain medium. Not all these round-trips were needed - individual pulses lasting only 7% longer than the shortest obtained had developed after only eight round-trips.

Longer pulses (~300 ps) have also been reported from actively-modelocked XeCl systems, where fewer (five) round-trips have been available [Reksten *et al.* 1981], and also where eight or more round-trips have been available [Reksten *et al.* 1981, Wisoff & Young 1984].

Other excimer media have been used in straightforward modelocked systems, including XeF (<2 ns pulses, active modelocking, four round-trips) [Christensen *et al.* 1976], and KrF (<2 ns pulses, passive modelocking, three round-trips) [Efthimiopoulos *et al.* 1979].

If a long-duration gain module is not available, short pulses may still be obtained from excimer systems, using combinations of active and passive modelocking elements. This approach has been used to obtain 300 ps pulses from an XeCl laser [Watanabe *et al.* 1983]. For KrF systems, Badziak & Jablonski [1993] have proposed and modelled a scheme employing both a Pockels cell and a saturable absorber. The Pockels cell is normally (optically) closed, but is opened once every cavity round-trip time. The first opening gives rise to a seed pulse, which is subsequently re-amplified. Its duration can be reduced well below the switching time of the Pockels cell, mainly owing to saturation in the gain medium. A saturable absorber is also used in the cavity to prevent ASE from reducing the gain available to the short pulse, as well as providing extra pulse-shortening. Badziak & Jablonski [1993] have concluded from their model that pulses shorter than 100 ps could be obtained from such a system with only fairly modest requirements on the Pockels cell switching time (~1 ns), although a gain duration of 50 ns is required.

A similar technique to modelocking is self-injection-locking. This involves allowing lasing action to build up within a cavity, and then dumping all but a short time-slice of it from the cavity. The short pulse obtained in this way is repeatedly amplified, and then extracted from the system. The technique differs from modelocking in that the optical

---

\* Excimer lasers have negligible lower-state population, and so one might expect CW operation to be possible. This is not the case in practice; the longest excimer laser pulses are only a few hundred nanoseconds. The reason for this is discussed in §1.1.1, and is that the pumping power density required to sustain an excimer population inversion against spontaneous decay is at least 100 kW cm<sup>-2</sup>. Clearly then, we must expect short timescale pumping, both to prevent the laser vessel melting or exploding, and because the technologies capable of providing this power density are necessarily pulsed for similar technological reasons.



switching element is only switched twice (however many round-trips are used for amplification) - once to create a short pulse, and then once again to extract it. This technique has recently been applied to an excimer (XeCl) laser for the first time, by Di Lazzaro *et al.* [1995]. The shortest pulses they obtained had FWHM duration 1.8 ns. The pulse-duration was found to *lengthen* with increasing the number of round-trips before extraction. This was because of the combined effects of gain-saturation and recovery, discussed in §4.5.

#### 3.1.1.8 Systems without feedback

Modelocked systems employ feedback of shortened laser pulses into the laser module which generated them. Other schemes have been used to amplify short pulses in separate laser modules.

One of the most attractive schemes (for the current application) has been reported by Curry *et al.* [1989]. As described in §3.1.1.6, they obtained a train of short (<100 ps) pulses, sliced from a KrF beam by an overdriven Pockels cell. After double-pass amplification in a further KrF laser module, the first pulse in the train dominated (by a factor of ~5) over all the others, owing to gain-depletion. This required the whole pulse-train to be shorter than the gain-recovery time (§4.5.1.2). Further pulse-shortening and total elimination of the satellite pulses was obtained by focusing the beam in a xenon cell. The plasma formed at the focus scattered all but the first part of the first pulse, giving rise to 30 ps output pulses.

#### 3.1.1.9 Conclusions

As well as the pulse-shortening schemes already described, it is not difficult to envisage schemes employing combinations of saturable absorbers, RIO, and electro-optic switching which might be expected to generate pulses of duration on the order of 100 ps. No such schemes were investigated, however. This was not for any fundamental reason, but because other schemes, especially TRUBS (§4.2), appeared to be more straightforward experimentally. We now consider these schemes.

## 3.2 Compact oscillators

Takahashi *et al.* [1984] have pointed out that “*the most primitive approach to produce short pulses in a laser is to shorten the pumping duration itself*”. Starting from this approach, several groups have reported short pulses (~1 ns FWHM) obtained from compact excimer oscillators. These reports include Takahashi *et al.* [1984], Yamada *et al.* [1988], Rácz *et al.* [1992], and Xia & Ballik [1993]. The exact mechanism behind this is quite subtle, and is complicated by the fact that the pump duration, cold cavity lifetime, gain recovery time, and laser pulse length are all of comparable magnitude [Rácz *et al.* 1992]. Here we shall consider the general principles involved. Table 3.1 summarises the some of experimental parameters of these short-pulse systems, as well as the system investigated here (§3.2.1). In every case the cavity used has been a plane-plane arrangement, consisting of a high-reflectivity (~100%) rear mirror, and uncoated silica flat (8% reflectivity) output coupler.



Reference	Gain medium	Fluorescence FWHM duration (ns)	Laser pulse FWHM duration (ns)	Gain region dimensions (mm)	Cavity length (mm)
Takahashi <i>et al.</i> 1984	XeCl	7	1	1 x 3 x 60	80
Yamada <i>et al.</i> 1988	XeCl & KrF	6 (XeCl)	1 (XeCl & KrF)	1.5 x 3.2 x 100	240
Rácz <i>et al.</i> 1992	XeCl	3	0.7	2 x 4.5 x 90	
Xia & Ballik 1993	XeCl	~8	0.8	2 x 5 x 100	200
This work	KrF		2	~3.5 x 6 x 75	190

**Table 3.1.** Selected experimental parameters (where measured) of short-pulse compact excimer systems reported in the literature.

From table 3.1 it is clear that the laser output is significantly shorter than the fluorescence duration. The reason for this is that the short gain region, combined with the use of a lossy cavity, ensures that the laser only reaches threshold at, or soon after, the time in the pumping when the gain is at its peak. Gain depletion caused by the intense laser pulse may then serve to terminate the output. This is not straightforward relaxation oscillation, however, because the gain storage time is short (~1 ns). Takahashi *et al.* [1984] give a discussion and model for this.

Thus, the gain depletion does not, alone, prevent further lasing. Instead, the decay of the gain precludes further lasing, owing to the pumping being past its peak. This process is not always effective, and the gain can recover sufficiently to give some further amplification of the tail of the short pulse. This can be expected to give pulses having a sharp rise, a short FWHM, but a long tail. Indeed, exactly these features were observed by Takahashi *et al.* [1984], Yamada *et al.* [1988], and Xia & Ballik [1992]. For example, Yamada *et al.* [1988] illustrate XeCl pulses having a FWHM duration of 1 ns, but a 10%-to-10% (of peak power) total duration of 5 ns.

It is clear from table 3.1 that not only have the gain volumes used been short, but they have also had a small\* cross-section. This is no coincidence, and we consider, qualitatively, why it is the case. The production of laser pulses shorter than the fluorescence of the laser module relies on the gain changing rapidly near its (temporal) peak. Clearly, the faster the pumping can be achieved, the faster this gain switching will occur. Thus, a short total pumping time is desirable. Discharge excitation of excimer lasers (as used in all the lasers described in table 3.1) works by discharging a capacitance,  $C_p$ , through a suitable laser gas mixture. The limit on the speed of the pumping is the stray inductance,  $L_i$ , of the discharge loop, giving an associated time constant  $\tau_p = (L_i C_p)^{1/2}$  [Kearsley 1980, Ford *et al.* 1986]. Pumping a small gain region allows a smaller capacitance,  $C_p$ , to be used for a given energy-deposition into the discharge. Furthermore, a compact discharge loop gives rise to a lower stray inductance,  $L_i$ , of the discharge loop.

\* Compare the few square millimetre cross-sections reported in table 3.1 with the few square centimetre cross-sections used in the other KrF laser modules described in this thesis.



Thus, a discharge-excited excimer laser of small cross-section can be made faster than a larger one.

### 3.2.1 Experimental arrangement for small oscillator

The compact-oscillator technique for short-pulse generation was investigated, using a laser module which had been made in the Laser Group at the Clarendon Laboratory for a different experiment. As we shall see, the system was not ultimately used, and so only a brief summary of the work will be given here.

#### 3.2.1.1 Laser module

A cross-section of the laser module is given in Fig. 3.1. A total of six 0.5 nF peaking capacitors were used, in two rows of three. Two high-voltage, high pressure, feed-throughs were used, separated by 75 mm. The gain-region electrode spacing was 6 mm. The dimensions of the gain region given in table 3.1 were estimated by inspecting the burn pattern on the electrodes\*.

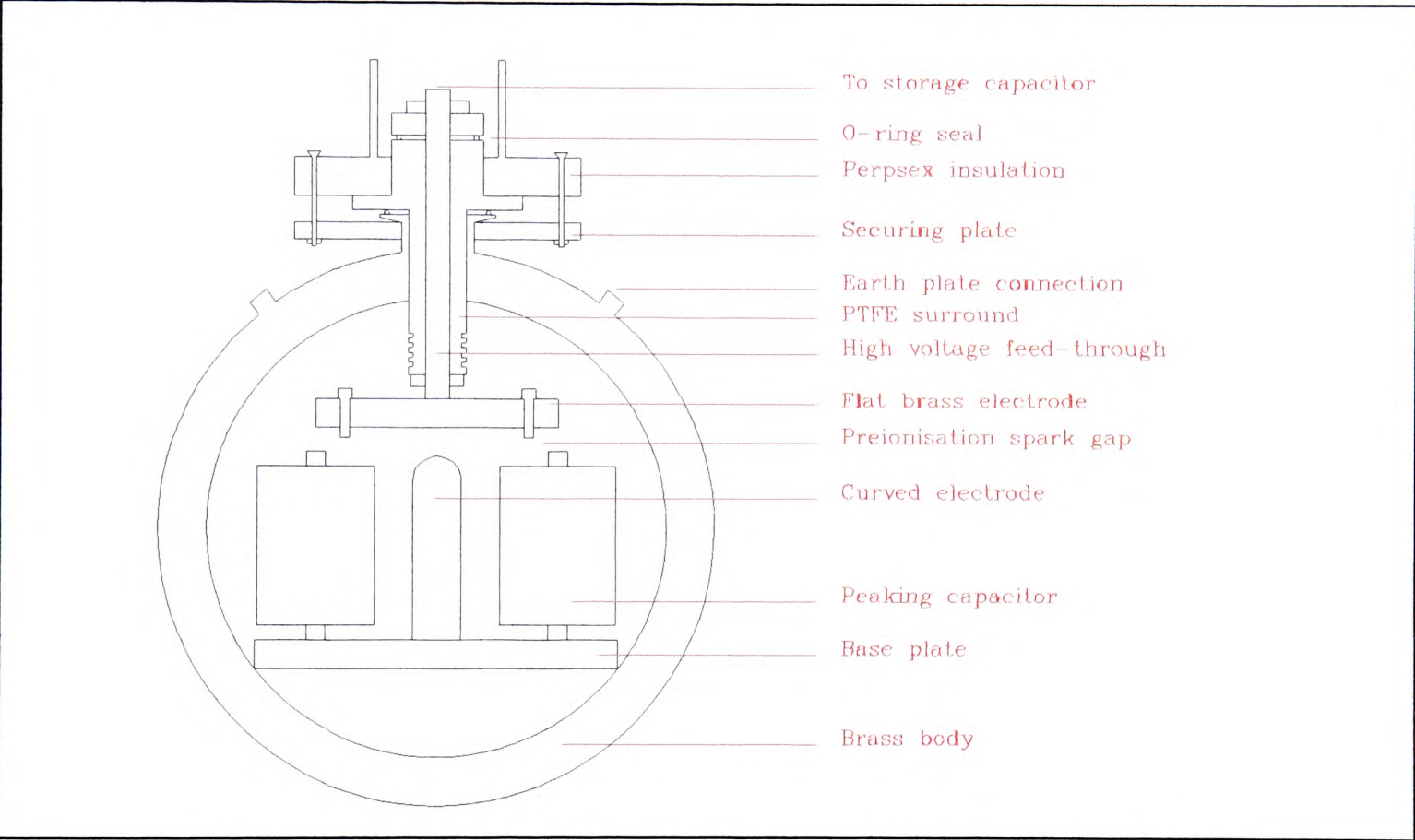


**Figure 3.1.** Section of small oscillator investigated for short pulse generation. For clarity PTFE supports separating the flat brass electrode and the base plate have been omitted. Discharge region is to scale.

Intimate electrical contact between the base of the curved electrode support and the brass walls of the laser tube was made by a piece of spring steel screwed to the base of the plate, which protruded and was bent to the shape of the walls. This steel was sufficiently stiff to push the electrode structure of the oscillator hard against the vacuum feed-throughs, providing good electrical contact there, too.

\* The burn pattern on the curved electrode was ~2 mm wide, and 75 mm long (corresponding exactly to the distance between the high-voltage feed-throughs), with the central third very faint. On the flat electrode the burn pattern was easily visible along all of its 75 mm length, and varied between 4.5 mm wide at one end, 3 mm in the centre and 3.5 mm at the other end.



The laser cavity was 19 cm long, and consisted of a flat aluminised rear mirror (reflectivity  $\sim 88\%$  at 249 nm) used as one window, and an uncoated quartz flat (reflectivity  $\sim 8\%$ ) used as the other window. These were mounted between thick O-rings to allow them to be aligned.

### 3.2.1.2 Electrical driver circuit

The high voltage electric circuit used to drive the small oscillator is functionally the same as that used by Cotton [1990], Fletcher [1993] and first described by Kearsley *et al.* [1979]. A circuit diagram is given in Fig. 3.2. The diagram is slightly simplified, because only one preionisation spark gap and one peaking capacitor are shown. In fact, there are six of each, but this does not affect a simple analysis of the circuit (provided the total peaking capacitance is considered).

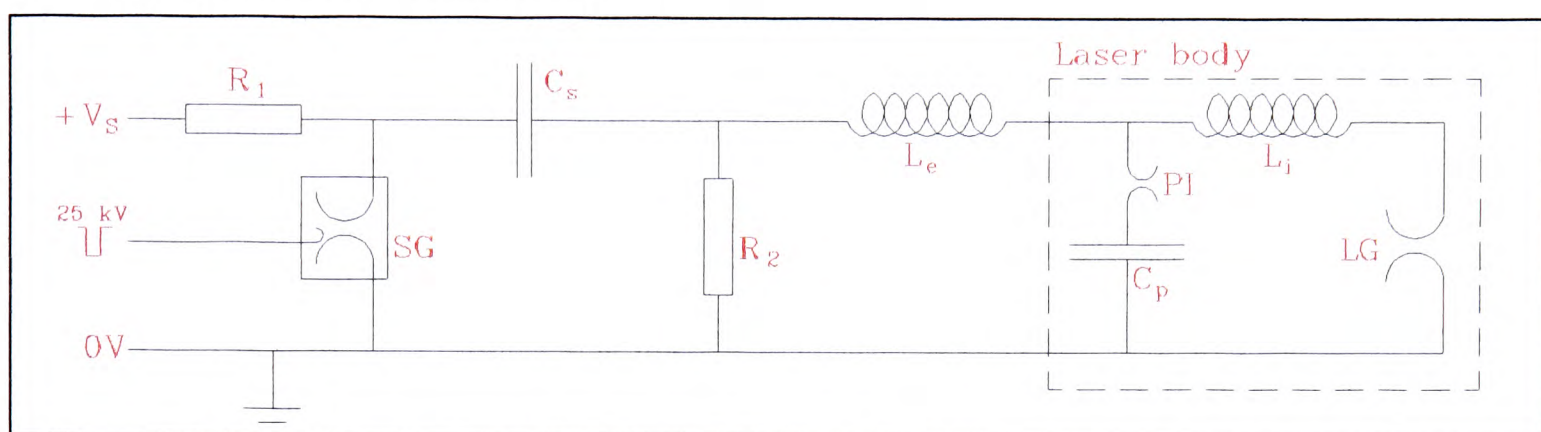


**Figure 3.2.** Schematic of high-voltage transfer circuit used to drive small oscillator. Abbreviations are: SG; spark gap, PI; preionisation spark gap, LG; laser gap. Charging resistances:  $R_1=1\text{ M}\Omega$ ,  $R_2=25.7\text{ k}\Omega$ .

The circuit employs a simple charge-transfer arrangement. An analysis of its operation is given by Kearsley [1980], and Fletcher [1993]. For the sake of brevity, this analysis will not be repeated here, although there is some discussion of the important properties of the system in §3.2.1.2.

The peaking capacitance,  $C_p$  was fixed at 3 nF by the capacitors already mounted in the oscillator. Various storage capacitors,  $C_s$ , were tested. The capacitances used were 105 nF, 15 nF, 10 nF, and 7.5 nF. During this investigation a gas mix of 5.1 mbar  $\text{F}_2$ , 120 mbar Kr, and He to a total pressure of 4 bar was used\*.

A storage capacitance,  $C_s$ , of 10 nF was selected as optimal. This was a compromise. On the one hand, a smaller charging capacitance gave very low energy output, whereas on the other hand, when larger capacitances were used, hard arcs (filaments) were observed in the gain medium, owing to the excessive pumping power density. Hard arcs are undesirable for two reasons. Firstly, they reduce the energy available to the glow discharge, which is what generates excimers efficiently. Secondly, they can absorb the laser radiation. These effects caused a central dark streak to appear in the laser output, corresponding to a hard arc observed between the electrodes. This was eliminated when the inductance of the external circuit,  $L_e$ , was reduced. This was achieved by replacing a wire delivering the current from the storage capacitor by a parallel-plate arrangement. The reason this helped is probably that it led to a faster rising voltage-pulse over the laser gap (§5.2.1.1).

\* Subsequent investigations showed this to be a very poor mix.



### 3.2.1.3 Detection system

Pulse energies were measured by a pyroelectric detector (GenTec ED100). Temporal profiles were measured using a fast (100 ps risetime) ITL S-20 vacuum photodiode (VPD). This was connected to a 500 MHz storage oscilloscope (Hewlett Packard model HP54111D with channel interleaving). The overall speed of the detection system was limited by the oscilloscope, having a 0.7 ns risetime. All the FWHM durations and risetimes presented here have been corrected for the instrument response\*, but there has been no deconvolution of the temporal profiles presented. This detection system was used for all the temporal profiles reported in this thesis. Attenuation of the beam intensity was required to prevent damage to the VPD. This was achieved by placing a diffusing screen a few centimetres in front of the VPD, or by means of the absorbing NO<sub>2</sub> cell described in §5.4.

### 3.2.1.4 Experimental results

The laser was passivated†, and its performance investigated. An Oxford Lasers GP2000 was used for cryogenic purification of the gas mixture, and to circulate the laser gas. A second laser (the discharge module used for the experiments described in §4.2.2) was also connected into the gas system, and this gave a ballast gas volume. The gas lifetime was found to be 2500 shots (half-life)‡. No data presented here was taken after more than 450 shots had been fired with a particular gas fill.

The system was investigated with the operating parameters which had been found by Fletcher [1993] to be optimal for the KrF amplifier which was to be used for amplification of short pulses. Specifically, these were a 60 kV charging potential, and a gas mix of 5.1 mbar F<sub>2</sub>, 120 mbar Kr, and the remainder He to a total pressure of 4 bar absolute. Under these conditions, the compact oscillator gave pulses of FWHM duration 3.0 ns, and 67 µJ energy. These operating parameters would be much the easiest to use for an oscillator-amplifier configuration, since a common gas system and spark gap could be used for both the oscillator and amplifier.

These conditions were not, however, optimal for the generation of short pulses. A brief optimisation of the gas-mix and charging-potential was undertaken. The 107 variations tested encompassed seven pressures of F<sub>2</sub>, between 4.8 mbar and 20.1 mbar; six Kr pressures between 25 mbar and 128 mbar; total pressures of 3 bar and 4 bar absolute; and charging voltages of 30 kV, 40 kV, 50 kV, and 60 kV.

---

\* Correction is based on  $T_m^2 = T_c^2 + T_i^2$ , where  $T_m$  is a measured time,  $T_c$  is the true, or corrected time, and  $T_i$  is the instrument response time, taken as 0.7 ns for 10% to 90% risetimes, and 1.2 ns for FWHM durations.

† Passivation of fluorine systems is required to ensure that all the exposed reactive surfaces are coated with a protective fluoride layer, and so do not reduce the amount of fluorine in the gas mixture. The recipe for this process was 24 hours vacuum pumping, followed by circulation of F<sub>2</sub> of at least double the working partial pressure, in a helium buffer. After at least 30 minutes the gas was refreshed and the process repeated. After this, a few sessions of firing of the laser were needed before optimum output was obtained.

‡ The other discharge module was fired at the same time as the compact oscillator being investigated here. This can be expected to have reduced the gas lifetime, *i.e.* it would have been greater than 2500 shots if this laser had not also been fired.



The shortest pulses obtained had mean FWHM duration 2.0 ns. The operating conditions for this were 11.5 mbar F<sub>2</sub>, 48 mbar Kr, 3 bar total pressure, and a charging potential of 30 kV. These pulses had an energy 17 times greater than those obtained using the optimum parameters for the amplifier. 40% more energy still could be obtained under different operating conditions. All these results are summarised in table 3.2.

	Charging potential (kV)	F <sub>2</sub> pressure (mbar)	Kr pressure (mbar)	Total pressure (bar)	FWHM duration (ns)	Energy (μJ)
<b>Optimum for amplifier</b>	60	5.1	120	4	3.0	67
<b>Shortest FWHM</b>	30	11.5	48	3	2.0	1160
<b>Greatest energy</b>	50	15.5	85	4	2.5	1640

*Table 3.2. Results of optimisation of operating parameters of compact oscillator.*

No further attempts were made to obtain short pulses from the compact oscillator. At the time, the reason for this was that the TRUBS technique (described in §4.2) appeared to be a more promising solution to the problem of making short pulses.

Several improvements might be expected to have given shorter pulses. One of these is the reduction of the peaking capacitance. As well as reducing the time constant  $(L_i C_p)^{1/2}$ , this would mean that greater charging potentials could be used, for a given energy deposition into the discharge. This is desirable, in order to allow efficient short-pulse operation of the compact oscillator, at the amplifier charging voltage of 60 kV. Further reduction in the peaking capacitance would be possible by using a different discharge circuit, for example an L-C inversion arrangement (*e.g.* see [Ford *et al.* 1986]). This effectively doubles the voltage seen by the peaking capacitor, allowing the use of a smaller capacitor.

It should be pointed out, however, that even if the pumping could be made very fast, the shortest pulses which can be expected from such a system are at least as long as the cold-cavity decay time. This is because even if the gain switches off instantly, it takes this long to extract the optical energy which has built up in the cavity. This means that the shortest pulses which could be obtained by such a technique are many hundreds of picoseconds. Indeed, the shortest pulses which have been obtained from compact excimer lasers, are 670 ps FWHM [Rácz *et al.* 1992]. As we shall see in §4.5, rather shorter pulses (~100 ps) are needed to provide a significant improvement in the intensity of KrF radiation which can be obtained on target. Thus, the compact-oscillator technique is unsuitable for the application here.



## 4. Plasmas for pulse-truncation

---

### 4.1 Introduction

The compact oscillator described in §3.2.1 generates intrinsically short pulses. Another way to produce short pulses is to truncate the output of a long-pulse laser. This chapter describes several diverse techniques which were investigated, with the aim of producing shortened pulses. They share a common feature, however, which is that a laser-generated plasma was used.

### 4.2 Truncated Brillouin Scattering (TRUBS)

The technique known as truncated Brillouin scattering (TRUBS) has recently been the subject of much research on the pulse shortening of excimer lasers. A brief review of this research is given here, and then a summary of experimental investigations of the technique, undertaken for this work.

#### 4.2.1 Stimulated Brillouin scattering (SBS)

##### *4.2.1.1 Description of the phenomenon*

Brillouin scattering is the scattering of light in a medium by the presence of sound waves. These give rise to variations in the density, and hence the refractive index, of the medium. This generates a dynamic diffraction grating, which scatters light.

Stimulated Brillouin Scattering (SBS) is an extension of this phenomenon. For SBS no external source of sound waves is required. The process is initiated by thermal phonons. These scatter an intense generating light wave (a little) in all directions. Some of the scatter is in the reverse direction to the incident wave. SBS occurs when the net electric field generated in this way gives rise to electrostriction, which generates more phonons of the correct wavelength to give further scattering. Provided a threshold intensity in the incident beam is exceeded, there is gain associated with the process, and this is greatest in the reverse direction.

##### *4.2.1.2 Frequency-shift of SBS radiation*

A quantum picture of the process gives a useful insight. This is illustrated in Fig. 4.1, which shows dispersion curves for photons and phonons (assumed nondispersive) for a particular direction in an SBS medium.



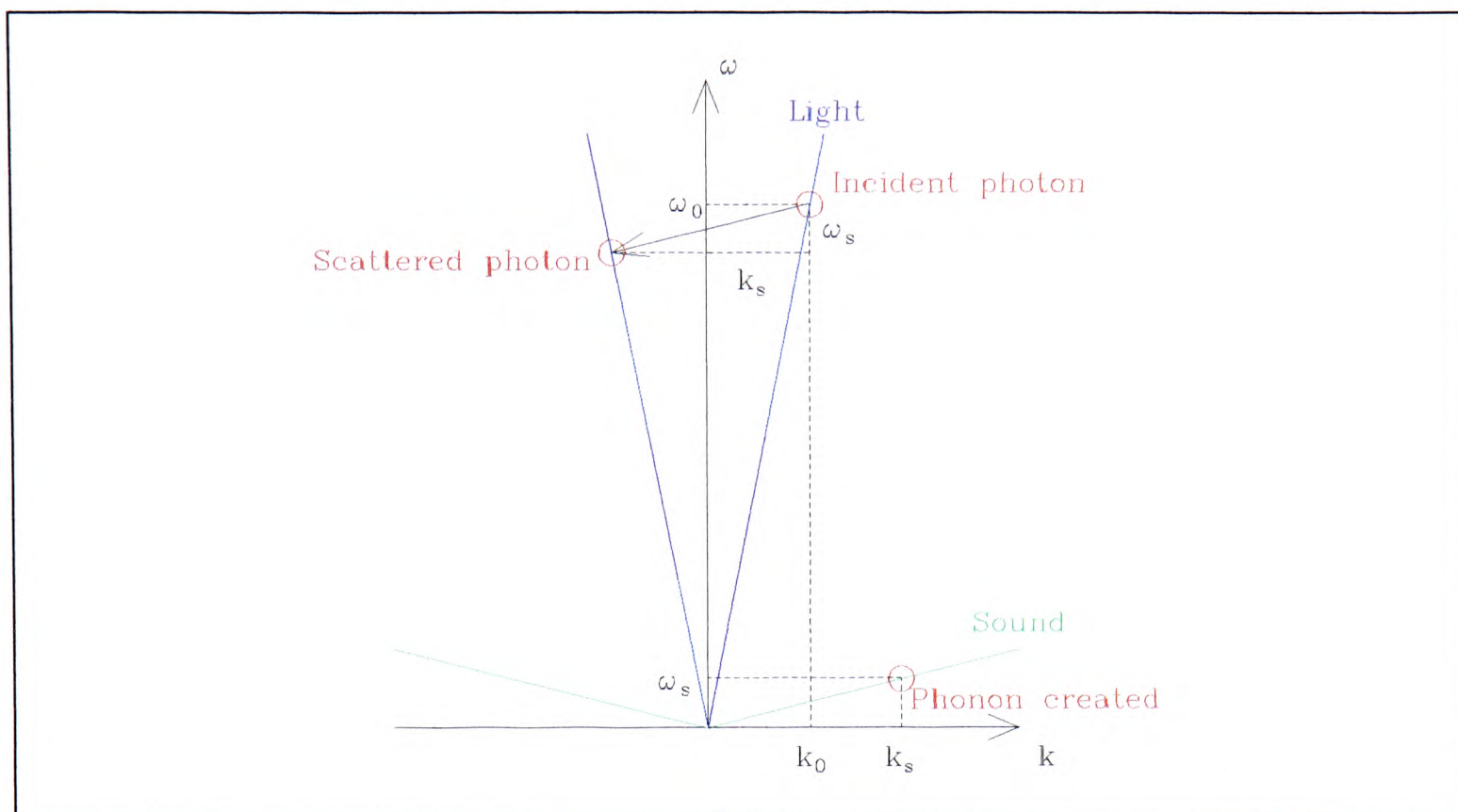


**Figure 4.1.** Schematic of quantum processes involved in SBS. Idealised dispersion curves for light and sound are shown, as are the incident and scattered photons and the phonon created in the process. The gradients are exaggerated for clarity.

The process shown in Fig. 4.1 conserves energy and momentum. We create a phonon of wavenumber  $k_s$  and frequency  $\omega_s$ , and in the process annihilate a photon of wavenumber  $k_0$  and frequency  $\omega_0$ , replacing it by one with wavenumber  $(k_0 - k_s) \approx (-k_0)$  and frequency  $(\omega_0 - \omega_s)$ . Thus, it is clear that there is a frequency-shift in the scattered wave. From Fig. 4.1 we may write down the magnitude of this shift,  $\omega_s$ , for the backscattered radiation in a medium of refractive index,  $n$ , as

$$\omega_s = 2\omega_0 \frac{nv_s}{c} \quad (4.1),$$

where  $v_s$  is the speed of sound in the medium, and  $(c/n)$  the local speed of light.

It was the presence of this frequency shift which provided the first evidence for SBS having been observed. This was reported by Chiao *et al.* [1964]. They describe effects observed when the beam from a ruby laser was focused to an intensity of  $10^{12} \text{ W cm}^{-2}$  in crystals of quartz and sapphire. They found slightly red-shifted backscattered radiation. The magnitude of the frequency shifts, for incidence along various crystallographic axes, was accurately predicted by the SBS model.

#### 4.2.1.3 Phase-conjugation

Brillouin mirrors not only differ from conventional mirrors by virtue of their nonlinearity; they also have a special phase property. This was first observed by Zel'dovich *et al.* [1972]. The Brillouin-scattered beam is a phase-conjugate, or time-reversed copy of the incident beam. This means that the reflected wavefronts exactly coincide with the incident wavefronts, whatever their shape. The overlap of the incident and reflected wavefronts provides an elegant (but somewhat simplified) explanation for why SBS reflections are phase-conjugated. This is that the maximum electric field is generated in regions of constructive interference between the incident and reflected waves. The electrostrictive pressure depends on the square of the electric field [Chiao *et al.* 1964]. Thus, efficient



generation of pressure waves will be associated with high electric field. This means the greatest positive feedback (on which SBS relies) will be generated for phase-conjugate reflections.

Phase-conjugation has many applications. For example, Gower [1982] describes its application to automatic target alignment for LGPs, and Davis [1987] has investigated its application to excimer laser lithography. It should also be pointed out here that SBS is not the only method of achieving phase-conjugation - for a review see Pepper [1982].

#### 4.2.1.4 Application of SBS to pulse-shortening

SBS has also been applied to pulse-shortening. The first (deliberate) use of SBS for this application was reported by Hon [1980]. Some extensions to his technique were reported by Damzen & Hutchinson [1983]. The mechanism for the pulse-shortening in these reports will not be given here, since the techniques employed were more complicated than has subsequently been found to be necessary. In particular, they required single-longitudinal-mode lasers, and tapered-waveguide SBS interaction regions as long as the (spatial) length of the incident laser pulses.

The simplest techniques which have been used to make SBS mirrors for excimer lasers (KrF, XeCl & XeF), have involved taking laser pulses of durations of order 10 ns, and focusing them into liquid (often hexane or a light alcohol) or high-pressure gas (*e.g.* SF<sub>6</sub> at 20 bar) cells [Gower 1982, Gower & Caro 1982, Slatkline *et al.* 1982, Alcock *et al.* 1987, Kurnit & Thomas 1989, Filippo & Perrone 1992, Filippo & Perrone 1993, Nassisi & Pecoraro 1993]. The mechanisms for pulse-shortening vary slightly between these reports, and we shall not look at them in detail, except to make the following general comments:

- Pulse-shortening of the SBS radiation with respect to the pumping pulse is a universal feature of the reports of SBS listed in the last paragraph. Truncation of both the leading-edge and trailing-edge of the incident pulse is observed.
- Truncation of the leading edge has the effect of sharpening the risetime of the SBS pulse with respect to the incident pulse. It is easily explained [Huo *et al.* 1985] by considering that SBS is a nonlinear process, and the reflectivity increases with increasing incident intensity (up to a limit [Gower 1982, Filippo & Perrone 1993]). Clearly, the intensity rises at the start of the incident pulse, and the associated increase in reflectivity gives rise to a sharpening of the risetime of the reflected pulse.
- By attenuating the incident radiation, it is possible to ensure that the SBS threshold is not reached until several nanoseconds into the pulse [Kurnit & Thomas 1989, Filippo & Perrone 1992]. A similar effect can be achieved by adjusting the position of the focus of the incident beam within a liquid sample [Nassisi & Pecoraro 1993]. This works by bringing the focus near the surface, which limits the length of the SBS gain region, and so the threshold intensity is increased.
- Truncation of the trailing edge of the SBS pulse with respect to the incident pulse is also found, for the same reason as the truncation of the leading edge, namely the nonlinear reflectivity of SBS mirrors. This can be seen clearly in the work of Kurnit & Thomas [1989], for example. Short (a few nanosecond) SBS pulses can be obtained by attenuating the incident pulses so that they are above threshold for only a short time. This is at the cost of low SBS reflectivity [Filippo & Perrone 1992].
- Further pulse-shortening is possible by amplifying SBS reflections, if gain-saturation occurs. By injecting the pulse into an amplifier at the end of its gain time-window, gain recovery can be avoided, at the cost of low extraction energy. The shortest pulses



obtained by SBS were produced in this way, and were of duration  $\sim 1$  ns [Kurnit & Thomas 1989].

## 4.2.2 Truncated Brillouin Scattering (TRUBS)

### 4.2.2.1 Overview

A simple extension of the SBS technique allows sub-nanosecond pulses to be obtained. Instead of focusing radiation into the bulk of an SBS medium, the focus is made at the surface. A breakdown spark is observed at the surface, and reflected pulses lasting tens to hundreds of picoseconds are obtained, depending on how near the focus is to the surface. This experimental technique is known (probably incorrectly, as we shall see) as truncated Brillouin scattering (TRUBS).

The first demonstration of the technique was made by Bourne & Alcock [1984]. They achieved 200 ps TRUBS pulses by focusing XeCl (308 nm) radiation into ethylene glycol. The incident pulses were of diffraction-limited divergence, 10 mJ energy, 10 ns duration, and line-narrowed to  $0.0003 \text{ cm}^{-1}$ . They also obtained similar results with 450 nm incident radiation.

Over the following few years, several other reports of TRUBS appeared, for pulses from line-narrowed lasers. These were: 584 nm dye lasers [Huo *et al.* 1985], XeCl lasers [Alcock *et al.* 1987], and KrF lasers [McIntyre *et al.* 1987]. The first report of TRUBS action from a laser without line-narrowing was made by Kurnit & Thomas [1989], who applied the technique to a free-running ( $30 \text{ cm}^{-1}$  linewidth) KrF laser system. Since then other non-line-narrowed lasers have also been used to generate TRUBS pulses. These are XeCl [Filippo & Perrone 1992], and ArF (and KrF) [Alimpiev *et al.* 1993a, Alimpiev *et al.* 1993b].

The exact mechanism giving rise to the experimental results is not well understood. Bourne & Alcock [1984] proposed that it was reflection due to SBS, terminating when a plasma was formed. The mechanism they proposed for the termination was *phase-disruption* of the incident beam by the plasma. On the other hand, Huo *et al.* [1985] attributed the truncation to *absorption* in the plasma.

But, more recently, Alimpiev *et al.* [1993a, 1993b] have questioned whether, in fact, it is SBS which gives rise to the reflection observed in the TRUBS process. The gist of their argument is that the fact that SBS can be observed from a TRUBS experimental arrangement (by focusing beneath the liquid surface), does not necessarily mean that SBS is responsible for the reflections. Furthermore, there is reason to believe that SBS cannot be responsible. They cite several pieces of evidence for this. The first is that the relaxation time for an SBS phonon in hexane (their TRUBS medium) is a few hundred picoseconds, whereas the shortest TRUBS pulses they observed had 10 ps risetimes, and 40 ps duration. As other authors had already commented [Huo *et al.* 1985], this does not preclude SBS, but it does mean it cannot be efficient\*. Another piece of evidence cited by Alimpiev *et al.* [1993a, 1993b] is the experimental observation that, as the laser-beam focus is brought nearer the surface of the TRUBS medium, and a plasma spark is observed, “the reflected pulse becomes shorter, while the intensity of the scattered light

---

\* This can be explained in the following way: when a lightly-damped harmonic oscillator is driven at its resonant frequency, the time taken to reach its full response is comparable to the natural decay time of the (undriven) system. Thus, if it is on a timescale of tens of picoseconds, any SBS occurs in the transient regime.



*increases by two orders of magnitude.*” This observation is not consistent with a transient process (*i.e.* SBS) being responsible for the reflection. It should be pointed out that this only precludes SBS from being present in the case of very short ( $\ll 500$  ps) TRUBS pulses. For example, the shortest pulses observed by Filippo & Perrone [1992] were of duration 300 ps.

Alimpiev *et al.* [1993a, 1993b] go on to suggest (tentatively) a possible mechanism for the short pulses observed. This is that a dynamic grating is formed in the plasma, by the interference of incident light and scattered light. The scattering process proposed is stimulated thermal scattering, caused by nonlinear absorption. The scattering is enhanced by a large value of  $\partial\epsilon/\partial T$  (corresponding to a large change of refractive index with temperature) associated with a phase transition at the surface of the TRUBS medium. The grating is taken to be responsible for the reflection. It is destroyed when the intensity in the grating minima becomes sufficient to generate free charges there too, and a uniform plasma is formed.

#### 4.2.2.2 A specific experimental arrangement

Despite the uncertainty about the exact mechanism of the technique, the experimental results appeared very promising. In particular, the extraction of sub-nanosecond pulses from an all-excimer laser system, was very attractive for the application here. To illustrate the simplicity of the technique, we shall consider in detail one of the experimental arrangements which has been reported to give good results, from a KrF laser system. This is due to Alimpiev *et al.* [1993b].

The experimental arrangement they used is illustrated in Fig. 4.2. Two stages of TRUBS truncation were used; here we shall concentrate on the first one. Referring to Fig. 4.2, the cavity for discharge module D1 comprises a 70% reflective meniscus mirror M1, having a 260 mm radius-of-curvature; a pinhole, P; and a TRUBS mirror system (L1 and C1). The discharge module output is quoted as 100 mJ for KrF, with a 20 ns pulse duration (presumably when used with a plane-plane cavity).

The meniscus mirror and pinhole appear to have been chosen to form part of a self-filtering unstable resonator (SFUR) cavity [Gobbi & Reali 1984], although Alimpiev *et al.* [1993b] do not go into sufficient detail to allow us to be sure of this. SFURs are used to extract low-divergence light from lasers, (at the expense of extraction efficiency) early in the laser pulse. For example, an SFUR has been shown to generate diffraction-limited output after less than two round-trips of an amplifier [Luches *et al.* 1989]. If the arrangement is an SFUR, then the pinhole must be placed in the focal plane of the mirror M1, and have a diameter given by  $\sqrt{1.22R\lambda}$ , where  $R$  is the radius-of-curvature of the mirror, and  $\lambda$  the laser wavelength. Alimpiev *et al.* [1993b] state that this is how the pinhole size was calculated (280  $\mu\text{m}$  for their system), but do not say where it was positioned.



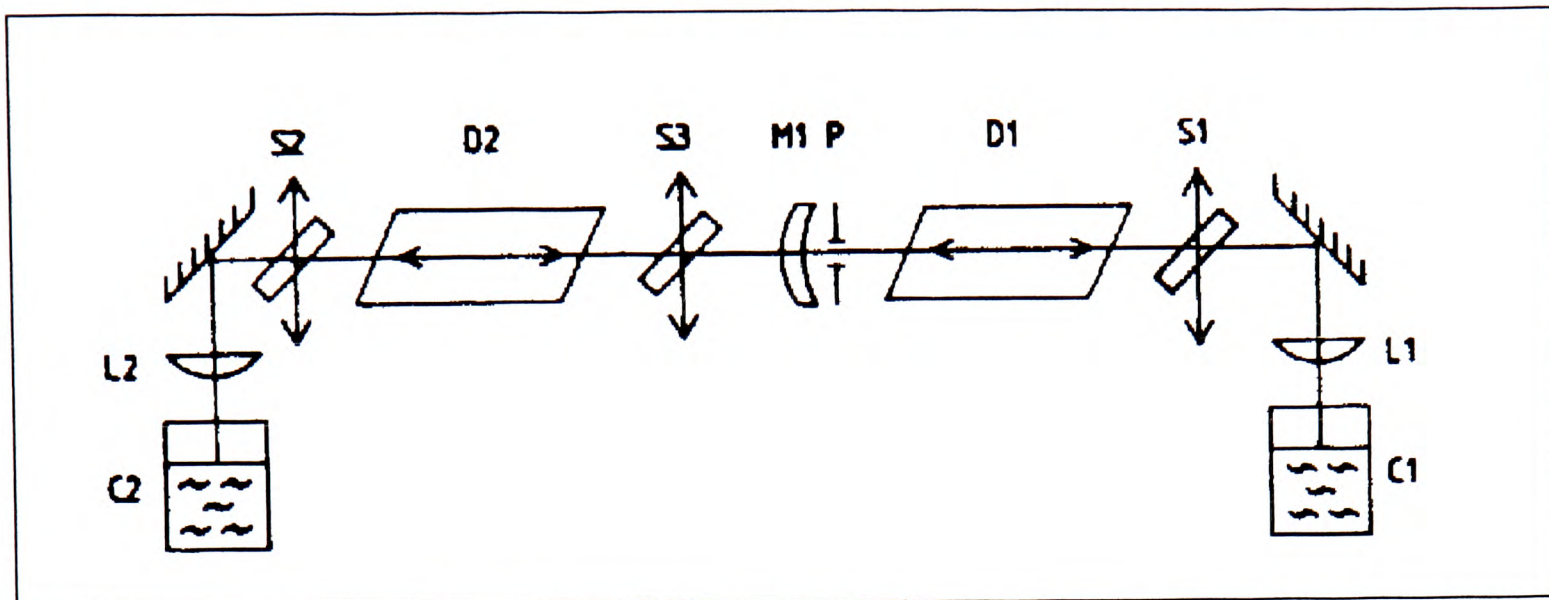


**Figure 4.2.** Experimental arrangement used by Alimpiev *et al.* [1993b] for their demonstration of TRUBS (reproduced from that work). D1 & D2: excimer discharge modules; M1: meniscus mirror; P: pinhole; S1, S2, & S3: beamsplitters; L1 & L2: focusing lenses; C1 & C2 covered TRUBS cells.

Lens L1, of focal-length 50 mm, was used to focus light from the discharge module onto the surface of the first TRUBS cell, C1, containing *n*-hexane. This was covered with a 1 mm thick quartz window (presumably to prevent fires). Alimpiev *et al.* [1993b] state that breakdown on the hexane surface, was caused by 8 mJ single-pass ASE being focused on to the target cell. If this is true, it makes the meniscus mirror pointless (except after the second TRUBS amplification stage). Furthermore, the focus produced by this high-divergence light would be too smeared for them to have observed the effects they describe.

We shall quantify this. After this single stage of TRUBS shortening (after amplification of TRUBS radiation in D1, but not yet D2) Alimpiev *et al.* [1993b] found they could generate pulses of duration down to 150-200 ps, provided the laser focus was on the hexane surface. On the other hand, the pulse duration rose to 4 ns if the focus was 2 mm below the hexane surface and no breakdown spark was observed. The pulse duration was also 4 ns if the focus was above the liquid surface (in which case breakdown was still observed). The gain region used by Alimpiev *et al.* [1993b] had dimensions of 1 cm x 2.2 cm x 60 cm. This suggests the divergence of their beam at the start of the laser pulse, assuming it was single-pass ASE, was approximately 17 mrad x 37 mrad. Using expression (6.3), this implies a depth-of-focus of ~6 mm for the  $f=5$  cm focusing lens, used at an (estimated) aperture of  $f/2.5$ . The fact that Alimpiev *et al.* [1993b] found qualitatively different TRUBS behaviour when the focus was moved by only 2 mm suggests that it cannot have been the single-pass ASE causing the effects observed. In this case, the low divergence double-pass output of the SFUR half-cavity seems a much more likely cause of the breakdown.

The 150-200 ps pulses obtained after the first TRUBS process had an energy of 100  $\mu$ J. Further shortening, to 40 ps, was obtained after the second TRUBS process, in cell C2 of Fig. 4.2. Alimpiev *et al.* [1993b] also commented that they obtained similar (but less stable) output when they used water, ethanol, and ethylene glycol as the TRUBS medium.



### 4.2.3 Initial experimental investigation

The TRUBS experiment described in this section was designed and performed in close collaboration with Professor Constantin Cristescu, who was visiting the Clarendon Laboratory from the Polytechnic University of Bucharest, Romania.

#### 4.2.3.1 Experimental arrangement

An experimental arrangement was devised for investigating the TRUBS technique. This was loosely based on that of Alimpiev *et al.* [1993a, 1993b], and is shown in Fig. 4.3. KrF radiation was provided by the laser module used as a master oscillator by Cotton [1990] and Fletcher [1993], described in §5.1.2.1. This was used with a 15 nF storage capacitor charged to a potential of 57 kV. The gas mix was 7.8 mbar F<sub>2</sub>, 68 mbar Kr, and the balance He to give a total pressure of 4 bar absolute. This gas mix had been described by Cotton [1990] to be approximately\* optimal for this particular laser module, giving rise to a ~120 mJ pulse energy with a plane-plane cavity.

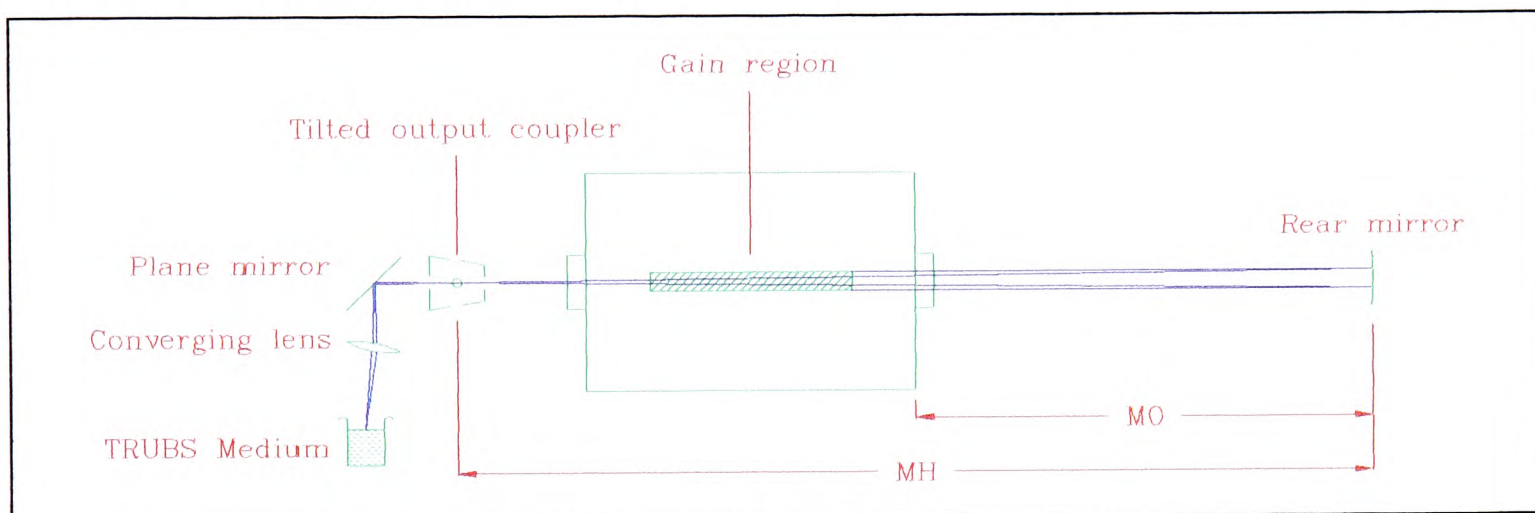


**Figure 4.3.** Schematic of experimental arrangement used to investigate the TRUBS technique. View is side elevation. Output coupler was tilted at 45°, i.e. sending light directly out of the page and to diagnostics. Plane mirror was high reflectivity dielectric and converging lens focal-length was 5 cm.

ASE from the gain region travelled to a converging rear mirror, a distance  $MO$  from the laser casing. Mirrors of focal-lengths 50 cm, 68 cm, and 1 m were investigated\*. The converging, reflected light passed through the gain region again, and reached a focus in a 3 mm hole drilled through a high reflectivity output coupler. Light diverging from this focus was reflected by a plane mirror down into a 5 cm focal-length lens. The path distance between focus and lens was ~10 cm and so light passing the lens was focused ~10 cm beneath it, on or near the surface of the TRUBS medium. Unless otherwise stated, this was distilled water or deionised water for all the experiments described here.

Radiation backscattered from the TRUBS medium then retraced the path described, i.e. it diverged to the lens, was brought to a focus in the hole in the output coupler, diverged through the gain medium, was reflected by the rear mirror to form a parallel

\* Pressures given here have been corrected for the inaccuracy of the pressure gauge described in §5.3.2.1. It is not known whether Cotton [1990] used the same gauge. If he did, the gas mix was exactly optimal; if not, it contained 15% too little of both F<sub>2</sub> and Kr.

\* No sufficiently large ~50 cm focal-length mirror was available and so one was synthesised by placing a 2m focal-length converging lens next to a 1m focal-length converging mirror.



beam, passed through the gain region again, and was then coupled out of the system by the output coupler. The detection system was the same as that used for the other time-dependent measurements, and is described in §3.2.1.3.

#### 4.2.3.2 *Experimental results and interpretation*

The experimental investigation of TRUBS turned out to be deceptively difficult. In particular, it was extremely difficult to prevent the system lasing from spurious reflections, despite considerable effort being expended to prevent this. Fresnel reflection from the surfaces of the focusing lens could be prevented from reaching the gain medium by tilting the lens. This process was tested by checking that the system would not lase when the TRUBS medium was completely removed\*. On the other hand, Fresnel reflections from the surface of the TRUBS medium may have been able to reach the gain medium. This is suspected because the system could be made to lase when a sheet of PMMA was put in place of the TRUBS medium, although a long pulse (16 ns FWHM) with a slow rise (4.5 ns) was observed in this case.

With the benefit of hindsight, it is clear that the experimental investigation of this TRUBS system was neither as thorough nor systematic as it could have been. In particular, many adjustments to the experimental technique were investigated, with a view to making it generate short pulses, rather than in order to undertake a systematic study of the physical processes involved. These variations included the use of an uncoated silica flat in place of the holed output coupler, translating the output coupler so that only half of it was in the beam, the use of cyclohexane† and aqueous NaCl as TRUBS media, placing the output coupler closer to the rear mirror than the focal plane of this mirror, and adjusting the position of the gain medium within the optical cavity. Since these variations were unsuccessful at generating sub-nanosecond pulses, and not entirely systematic, we shall not discuss them in detail. Only a general summary of the experimental results will be given here.

A breakdown spark could be achieved on the surface of the TRUBS medium, although not for every cavity arrangement investigated. Despite the presence of breakdown, no pulses of duration anywhere approaching the 1.2 ns resolution limit of the detection system were obtained. The shortest pulses observed had FWHM duration ~5 ns.

There was some evidence that SBS was observed because 1.5 ns pulse risetimes were observed. This is significantly shorter than the risetime observed, both when the laser module had a plane-plane cavity (2.2 ns, see Fig. 4.7), and when it was used in the TRUBS arrangement but with a PMMA sheet used in place of the TRUBS medium (4.5 ns).

There was also evidence that the presence of a plasma gave rise to pulse-shortening. This is illustrated in Fig. 4.3, which shows temporal profiles observed when the position of the TRUBS medium surface was adjusted both to give, and to preclude, a breakdown spark.

---

\* This rather obvious check was not devised until several of the experiments on the system had been undertaken. In particular, the profiles illustrated in Fig. 4.4 were taken without this check having been made. Although it is possible that these results may have been contaminated by Fresnel reflection from the lens, the specific results obtained suggest they were not.

† This was subsequently found to be contaminated by an unknown contaminant, which gave an absorption of  $\sim 0.3 \text{ cm}^{-1}$  at the KrF laser wavelength.



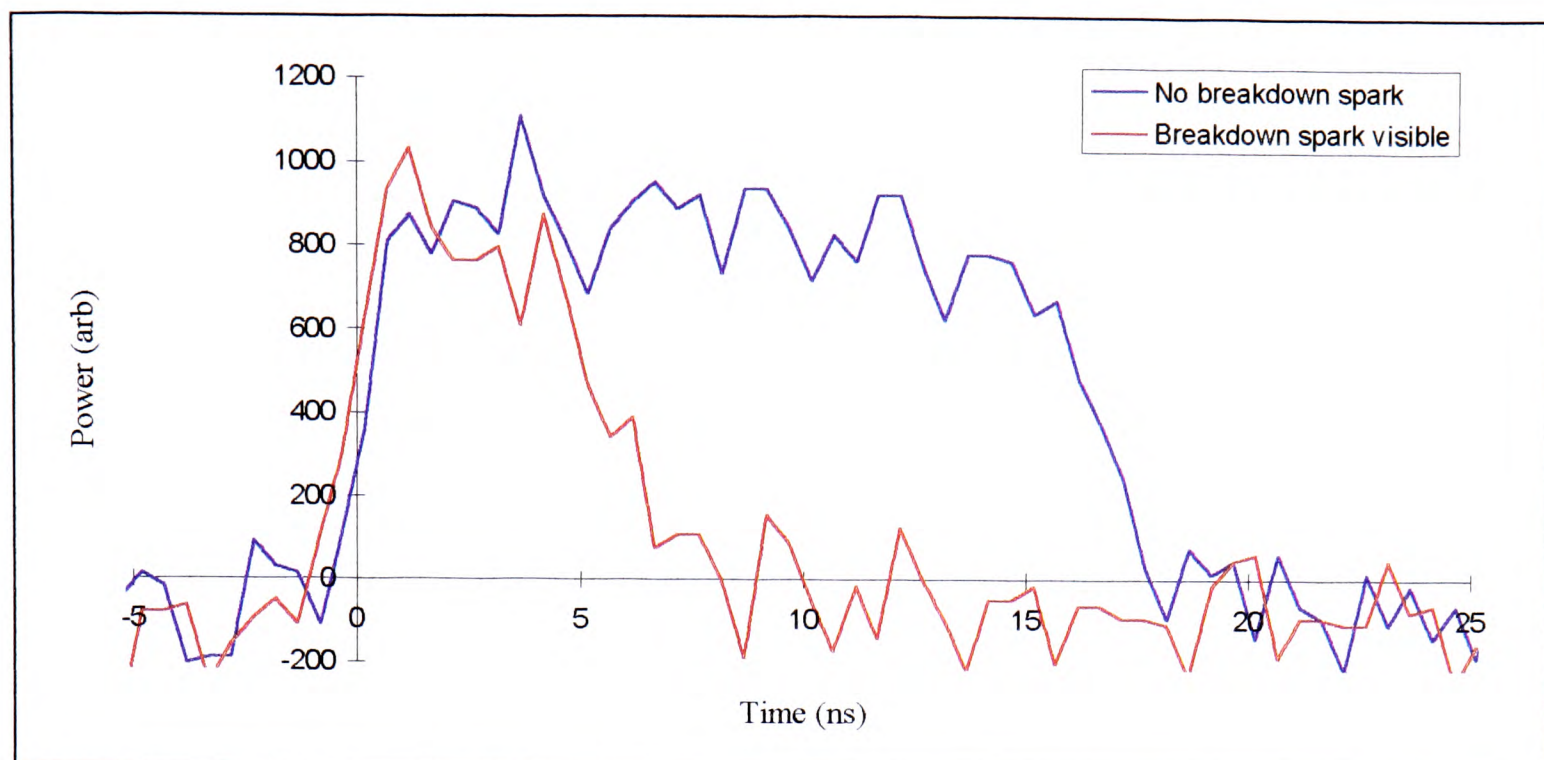


**Figure 4.4.** Temporal profile of (amplified) TRUBS reflections from distilled water, when its position was adjusted either to give, or to preclude, a visible surface breakdown spark. Experimental parameters (referring to Fig. 4.3) are  $MO=10$  cm,  $MH=50$  cm, with rear mirror focal-length 50 cm. Relative timing of pulses is arbitrary.

However, the presence of a plasma spark did not ensure a short pulse. Nor was the presence of a visible plasma spark required to observe pulse-shortening. This suggests that SBS may have been observed.

No pulses shorter than the cavity round-trip time were observed. To illustrate this: the shortest pulses from a 50 cm long cavity were of duration 5.1 ns FWHM (1.6 times the round-trip time), and the shortest pulses obtained from a 1 m cavity were 8.1 ns (1.2 times the round-trip time).

One of the possible explanations of the results obtained, is as follows. SBS (or possibly merely Fresnel) reflections were present, and these could be terminated by the formation of a plasma. However, the double-pass output of the oscillator alone was insufficient to cause breakdown, and so amplification of the reflected pulses was needed before a focal intensity could be achieved which was sufficient to generate a truncating plasma.

We may also consider why no pulses could be obtained which were anything like as short as those observed by Alimpiev *et al.* [1993a, 1993b], despite the use of a similar experimental arrangement. We assume the light causing the breakdown in the TRUBS experiments reported by Alimpiev *et al.* [1993b], was double-pass ASE (as proposed in §4.2.2.2). The divergence of this double-pass radiation is given approximately by the ratio  $a/f$ , where  $a$  is the pinhole radius, and  $f$  the focal-length of the rear mirror [Gobbi & Reali 1984]. This ratio was similar for the experiments described here, and those described by Alimpiev *et al.* [1993b]. This means that the initial divergences will have been similar for the beam incident on the TRUBS medium for the experiments described here, and for the beam used in the experiments described by Alimpiev *et al.* [1993b].

However, Alimpiev *et al.* [1993b] may have generated a significantly greater focal intensity than was obtained here. This is because of the position of their aperture in relation to the gain region. In their experimental arrangement, all the light which was fed back into the gain region after its first pass, subsequently formed the double-pass output. For the experimental arrangement used here, however, most of the light fed back into the gain region will not have formed the output. This will have depleted the gain available to that portion of the returning light which did form the output.



Without measurements (or more detailed modelling) of the intensity of the double-pass light, it is not possible to be sure that there was such a difference in intensity. However, if there was, it would explain a lot. In particular, it would explain why amplification of backscattered pulses was found to be necessary here before a reflection-truncating plasma could be formed, whereas this was not the case for the experiments described by Alimpiev *et al.* [1993b]. Furthermore, the fact that surface breakdown could not always be achieved in the experiments described here, also points to a lower intensity being present. In contrast, Alimpiev *et al.* [1993b] commented that their laser intensity “*was quite enough for initiation of optical breakdown*”.

#### 4.2.4 Further TRUBS experiments

After the experimental arrangement described in §4.2.3.1 failed to deliver sub-nanosecond pulses, a new experiment was devised. This was a simplification of the previous experiment, designed to give a greater insight into the TRUBS process. The simplifications were to replace the pinhole and converging-mirror cavity by a plane-plane arrangement, and to observe any TRUBS signal before feeding it back into the gain region. The experimental arrangement is shown in Fig. 4.5. The output from the laser was passed through a  $\sim 30\%$  transmitting beamsplitter (BS in Fig. 4.5), and was then incident on the TRUBS system. TRUBS reflections returned to the beamsplitter and were directed to the detection system.

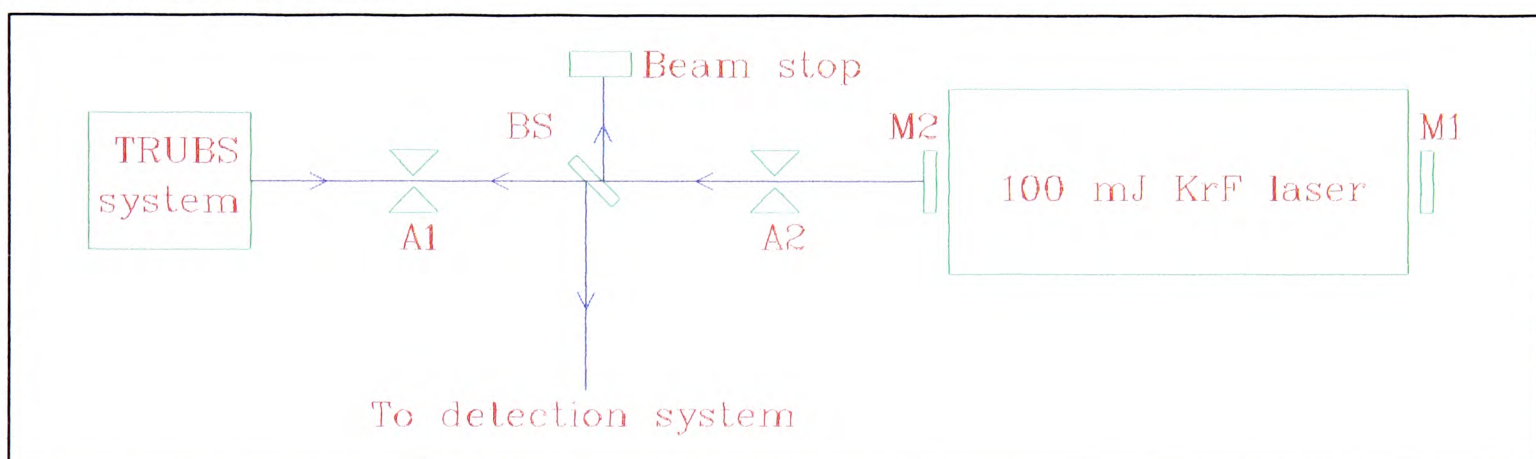


**Figure 4.5.** Schematic plan of simple TRUBS experiment. Symbols are: M1 100% plane mirror; M2 uncoated silica flat (8% reflectivity); A1, A2 were apertures used to prevent back-reflections and did not vignette beam; BS, beamsplitter.

The laser was operated with a different gas mix, for these (and all subsequent pulse-shortening) experiments. This was the mix which Fletcher [1993] had found to be optimal for the 2J KrF amplifier module. The recipe was 5.1 mbar  $F_2$ , 119 mbar Kr and the remainder He to 4 bar absolute. This gave 100 mJ pulses, of FWHM duration 15 ns. A temporal profile obtained from the laser alone is given (amongst others) in Fig. 4.7.

The tilt of the optics was adjusted such that all the Fresnel reflections from the TRUBS system could be observed on the rear (TRUBS system) side of the aperture A1 of Fig. 4.5. The TRUBS systems investigated were similar to those described in §4.2.3.1, except that an 18 cm focal-length focusing lens was used.

Several non-flammable liquids were investigated as TRUBS media. These were distilled water, a solution of 10% industrial ethanol in water, and industrial purity 1,1,1 trichloroethane. In his work on radiation induced opacity, Cotton [1990] used a solution of benzene in methanol. He suspected backscatter to be the cause of the opacity of the solution, and so a solution of 1% benzene in methanol was investigated as a TRUBS medium. In order to prevent fires, this was held in a stoppered cuvette.



A fluorescent (white paper) screen was used to observe any backscattered radiation heading towards the detection system. None was observed. We shall not consider why this was the case. The reason for this is that the apparent simplification of using a plane-plane cavity, was, in fact, a significant complication. This is because it will have given rise to light of initially very high divergence. This divergence fell sharply over the course of the laser pulse, as is discussed in §4.3.5.1.

## 4.2.5 Conclusions about TRUBS

With no spectacular pulse-shortening having been observed, no further significant investigation of TRUBS was undertaken. With the benefit of hindsight, this may have been a mistake. In particular, a more thorough investigation of the initial experimental arrangement, perhaps modified to make it more like that reported by Alimpiev *et al.* [1993a, 1993b], might have been fruitful.

## 4.3 Plasma-truncated reflection

### 4.3.1 Rationale for experiments

Two observations from the investigation of TRUBS prompted a different approach to pulse shortening. Firstly, it was found to be very difficult to avoid contaminating any backscattered radiation with conventional reflections from the horizontal surface of the TRUBS medium; a similar system which took advantage of this conventional reflection would be desirable. Secondly, there was evidence that plasma formation could truncate a reflection.

The experimental arrangement investigated in the light of these observations was broadly similar to that used to investigate TRUBS (see Fig. 4.5). The experimental arrangement is shown schematically in Fig. 4.6. The detection system used was as described in §3.2.1.3.

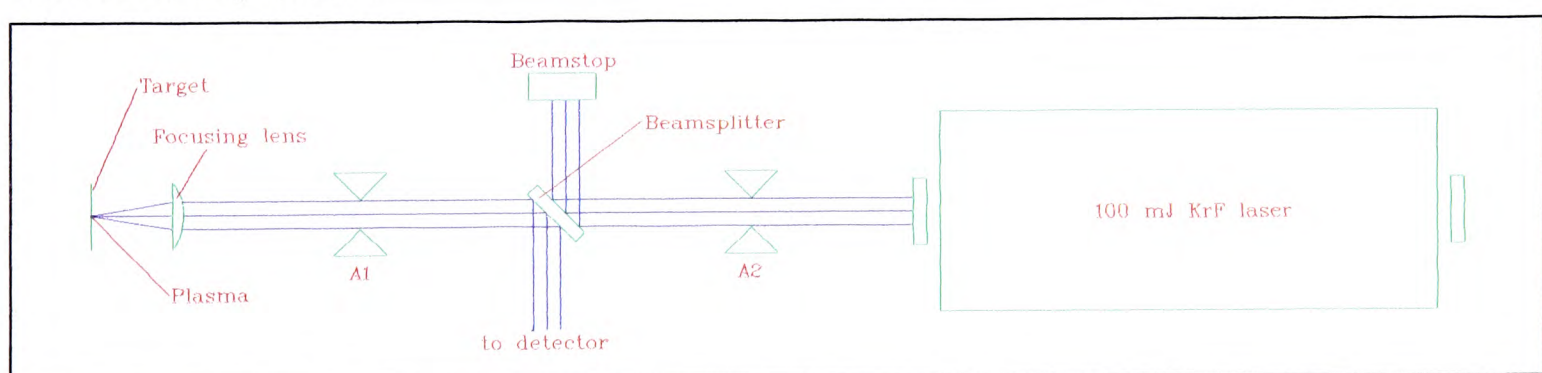


**Figure 4.6.** Schematic section of experimental arrangement used to investigate plasma-truncated reflection from metal surfaces. A1 and A2 are apertures the size of the incident beam (i.e. they do not vignette the beam).

Light was focused onto the surface of a metal target and reflected back to the lens, which re-collimated it. Provided there was sufficient intensity at the focus, however, a plasma was formed. The idea was that, if this occurred fast enough, further reflection could be prevented by plasma absorption or scatter. Metal target ribbons were held in a holder which allowed a fresh region of target to be exposed without translating or tilting the plane of the target surface.



### 4.3.2 Preliminary investigations: a copper target

A plano-convex lens, of focal-length 6.8 cm, was used to focus light from the laser onto a copper foil target. The surface of the copper was cleaned with an organic solvent, but some surface contamination was still visible.

A quick, preliminary investigation was made. A 70:30 (reflection:transmission) beamsplitter was used, and visible breakdown on the copper surface was easy to obtain, with the  $\sim 30$  mJ incident energy. This occurred over a range of separations between the focusing lens and target surface spanning 15 mm. A simple geometrical calculation based on the beam size (25 mm x 12 mm) at the lens suggests this corresponds to a threshold fluence of  $\sim 1$  J cm $^{-2}$ , corresponding in turn to a threshold power of  $\sim 6 \times 10^7$  W cm $^{-2}$ . This is a threshold for an observable plasma spark, under normal laboratory lighting conditions, and so is somewhat subjective.

Spatial filtering of the output was necessary to observe pulse-shortening. No pulse-shortening was observed when the detection system collected (by means of a focusing lens) all the light heading towards it. However, pulse-shortening was observed when the light detected was restricted to that passing through a 4 mm aperture placed 1.55 m from the focusing lens. From the length of the pulses obtained, it was clear that the mechanism of the shortening was the truncation of the trailing edge of the pulse. These observations are illustrated in Fig. 4.7.

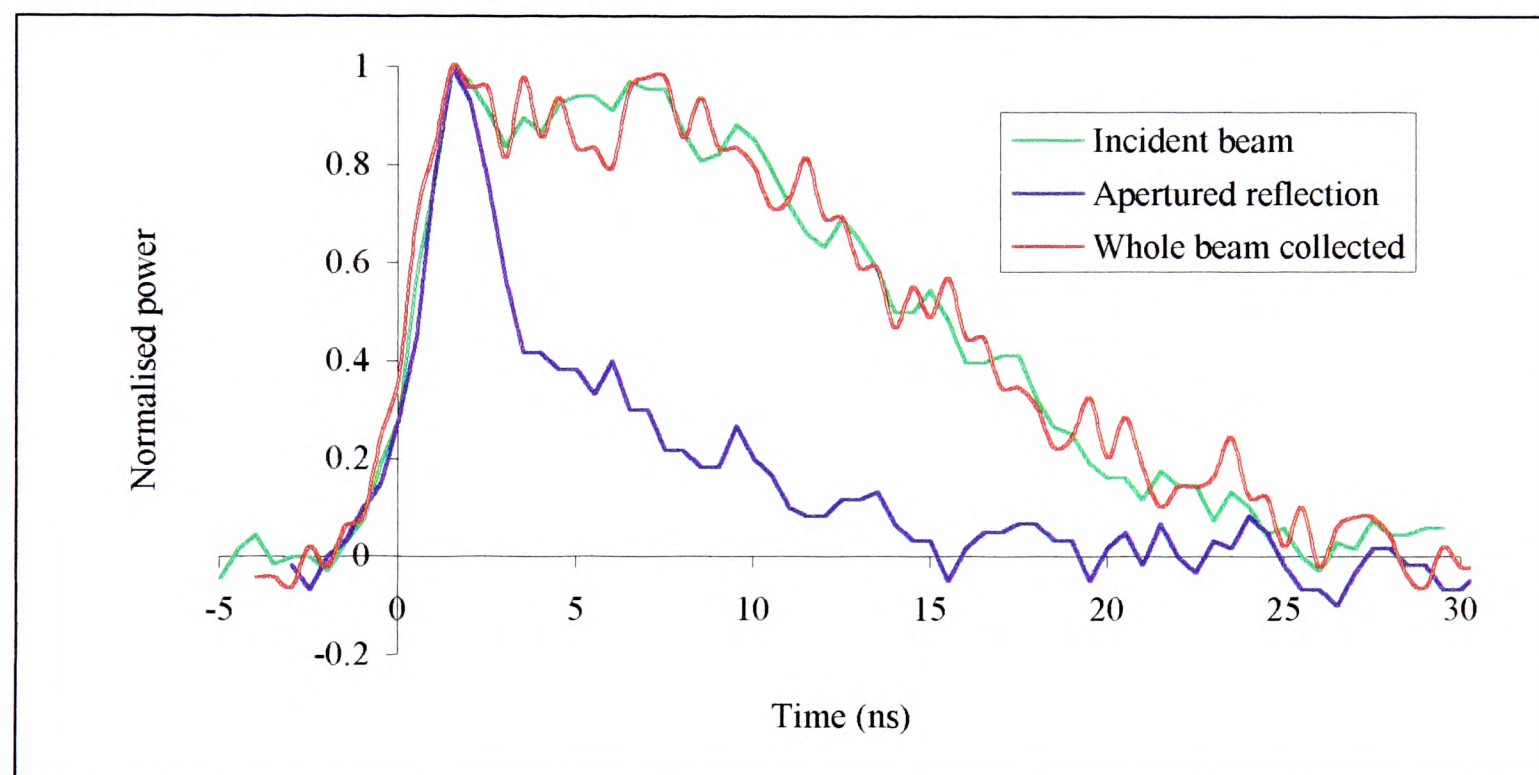


**Figure 4.7.** Temporal profiles of incident beam, and plasma-truncated reflections, according to how reflection collected. Reflections are for first shot onto a piece of copper target. Profiles have been normalised to their maximum power, and were not taken simultaneously. The relative timing is arbitrary.

A further conclusion from the experiments using copper targets was that the reflectivity (into the spatially-filtered detection system) fell sharply as more shots were fired on to a particular region of the target surface - by an order of magnitude over the first ten shots. This could either have been caused by crater formation, or the deposition of a (visible) black deposit of CuO on the target surface.



### 4.3.3 Experimental variations

Since pulse-shortening had been obtained, the technique was investigated further, and more carefully. Particular care was taken to ensure that the target was at the best focus of the lens, for all of the experiments conducted. Several variations of the experimental arrangement were investigated.

#### 4.3.3.1 Target materials

No further experiments were conducted using copper as a target material. Two other elements were used instead. The first of these, aluminium, was chosen because it has a higher reflectivity to the laser light when non-linear effects (*i.e.* plasma-formation) are absent, as was expected to be the case at the very start of the laser pulse. An aluminium foil target, of thickness 200  $\mu\text{m}$  was obtained. The surface was smooth, but not of mirror quality; marks produced in the rolling process were visible without magnification.

The other target material investigated was liquid mercury (Hg). This had the advantage of healing itself, and so did not need to be ‘wound-on’ as the solid targets had been. A cell containing a few cubic-centimetres of mercury was made and sealed (by fixing a 3 mm UV-transmitting flat, to the top of a glass bottle, using epoxy glue). A 45° mirror was used to steer the beam onto the (horizontal) mercury surface.

The mercury cell was not evacuated, and after several laser shots had been fired two different contaminants were observed floating on the surface. For a few millimetres around the focal region a specs of a black-brown powder were seen (possibly  $\text{Hg}_2\text{O}$ ). Surrounding this was a uniform layer of a fine white-grey powder (possibly  $\text{Hg}(\text{NO}_3)_2 \cdot \text{H}_2\text{O}$  [Lide 1992]). At the focus, however, the surface appeared clean. The brown-black powder could be dispersed into the bulk of the mercury by shaking it. The white-grey powder could also be dispersed in this way, causing much of it to stick to the glass walls of the cell.

#### 4.3.3.2 Optical arrangement

A more transmitting beamsplitter was used for the experiments with aluminium and mercury targets. This was in order to increase the intensity of light reaching the target, in the hope that this would give rise to faster breakdown. The new beamsplitter was an uncoated fused-silica optical flat. This had a reflectivity of 12% for light incident at 45°, giving rise to an energy of ~90 mJ incident on the target.

Another change to the optical arrangement was the use of a longer focal-length lens for focusing. This was an  $f=18$  cm biconvex lens, and was required (owing to geometrical constraints) for the mercury experiments. However, both this lens and the 6.8 cm lens were used for the aluminium experiments, and the results are compared in §4.3.4.

Finally, the observation aperture was moved further from the lens, to an optical path of ~2 m, to allow more spatial filtering of the reflected light. No wavelength discrimination was used, and so the experiment was sensitive to plasma emission in the spectral range 200 nm to 800 nm. However, no signals having a duration greater than that of the incident pulse were observed, and the light observed on a fluorescent (paper) screen at the detection position appeared exactly like KrF laser fluorescence. This suggests the profiles obtained were not contaminated by plasma emission. This is to be expected, since the specular reflection of the laser beam was being observed, and this will have been much more directional than the plasma emission.



4.3.3.3 Finding the focus

To ensure that results obtained were repeatable it was necessary to find the focus accurately. The focus was found first by reducing the energy incident on the target surface (using the NO<sub>2</sub> cell described in §5.3.1.1) until a plasma spark was just observed. Then the separation between the metal surface and the focusing lens was adjusted in order to produce a stronger plasma. Then the beam was attenuated further, and the process repeated until further adjustment could no longer give a stronger plasma.

This allowed the focus to be found repeatably, to within the divergence-limited depth-of-focus, calculated on the basis of expression (6.3), and the end-of-pulse divergences given in §4.3.5.1.

4.3.4 Experimental results

Qualitatively similar results were obtained from the aluminium and mercury targets, and the two focal-length focusing lenses. The results are summarised in table 4.1, and we shall discuss the qualitative behaviour observed.

The most striking feature of the experiments was the presence of spatial structure in the reflected beam, observed on a fluorescent (white paper) screen, 2 m from the focusing lens. The patterns observed varied, and in the case of mercury, the exact patterns were not repeatable from day to day. But in every case the patterns featured a dark central region, surrounded by a brighter region. This bright region took the form of four lobes, parallel horizontal lines, or a ring. In every case the pattern was wider than it was high, with heights varying over the range 10 mm to 15 mm, and widths of 40 mm to 60 mm. A schematic of the most intriguing pattern obtained, a structure of four lobes, which was found with the mercury target, is given in Fig. 4.8. The structural features were too far apart to be explained as the front-surface and back-surface reflections from the beamsplitter, which was not wedged.

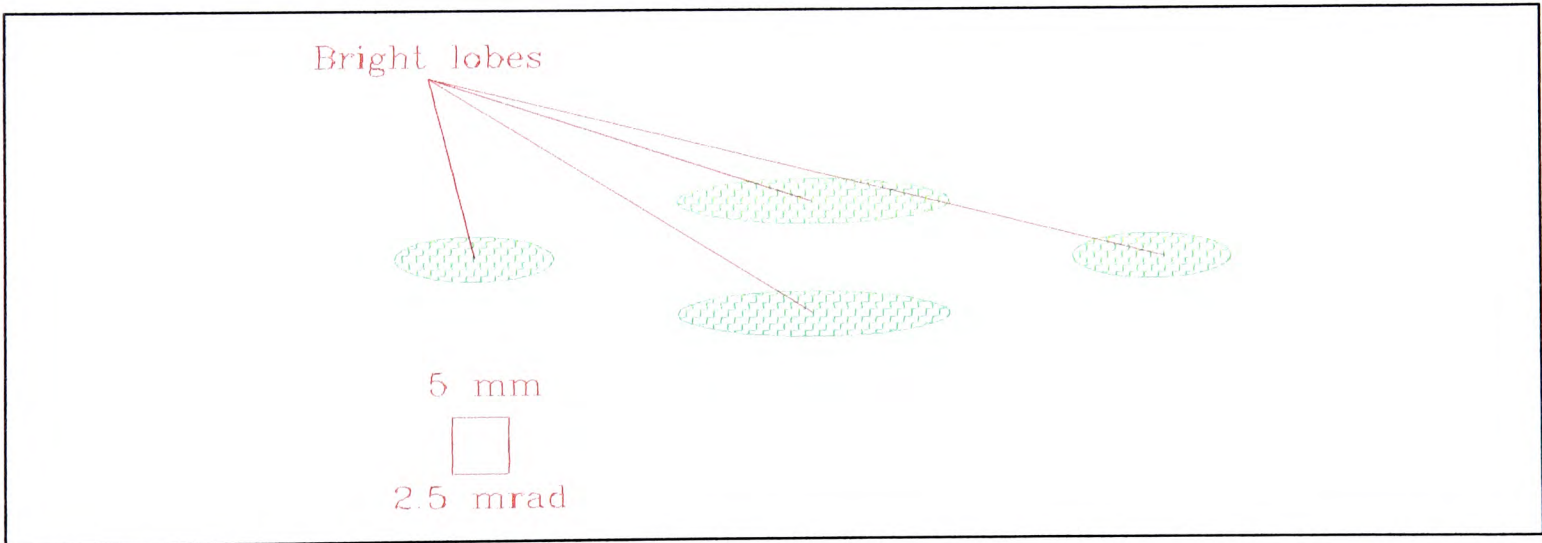


**Figure 4.8.** Schematic of four-lobe structure observed 2 m from focusing lens, obtained with a mercury target. Angle shown is subtended at lens.

The temporal profiles of the light in the dark and bright regions of the beam were compared, for the four-lobe structure illustrated in Fig. 4.8. The results obtained are shown in Fig. 4.9.



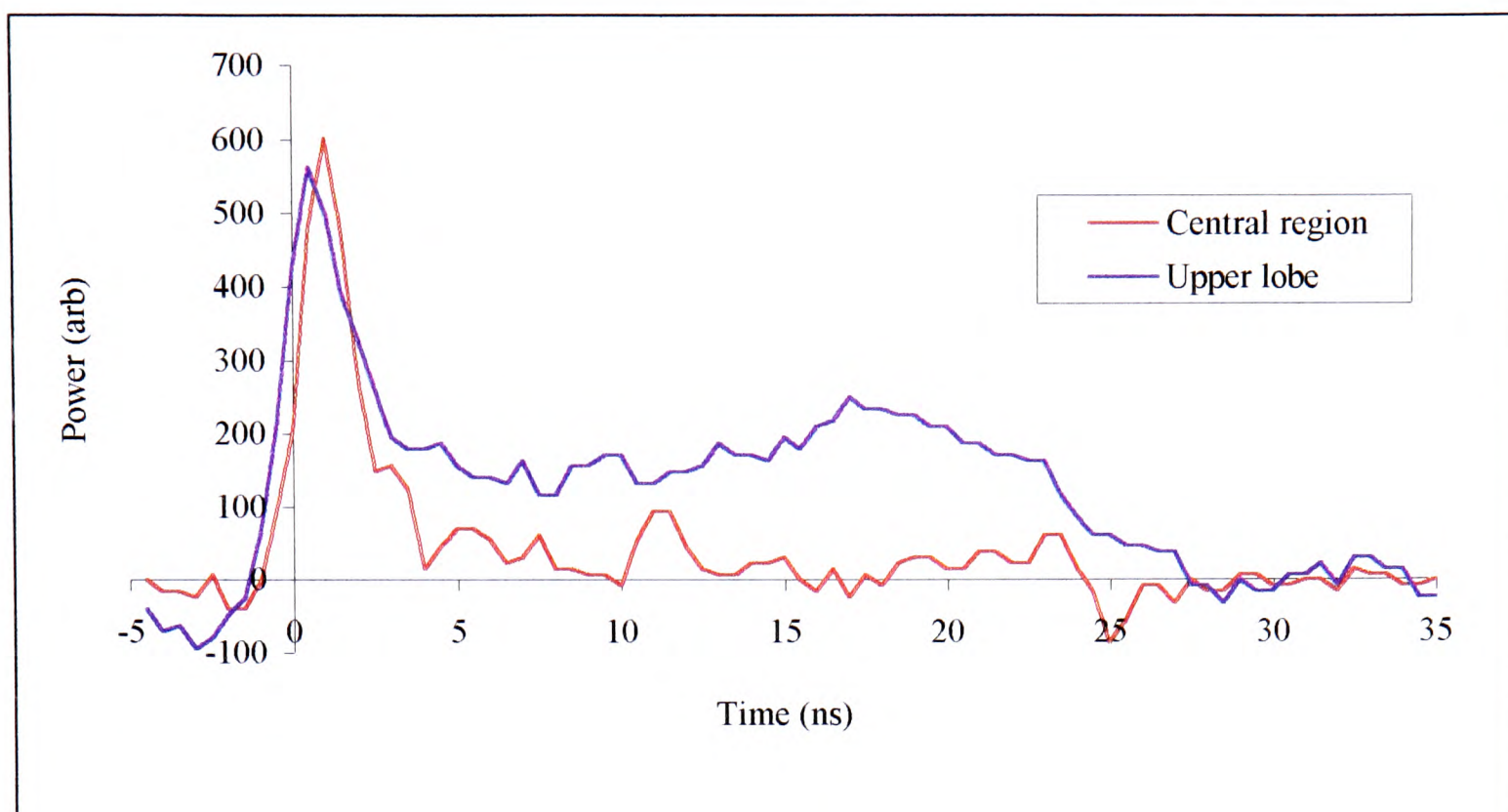


**Figure 4.9.** Temporal profiles for dark central region and upper lobe of plasma-truncated reflection from mercury target. Power scale is consistent between traces, but relative timing is arbitrary.

From Fig. 4.9 it is clear that the two detection positions are equivalent at the start of the pulse. Subsequently, however, little light is reflected into the dark region, whereas  $\sim 30\%$  of the peak power is reflected into the bright lobe - which is what makes it bright. Clearly, any pulse-tail is undesirable for application to short pulse generation, and so subsequent investigations were made with the detector in the centre of the central dark regions of the reflected beams. With the longer focal-length lens ( $f=18$  cm) no dark region could be observed on the first shot fired on to a particular piece of aluminium target. However, one did develop over subsequent shots, and this was used to position the detection aperture. With the detector positioned in the dark region, the temporal profiles obtained from the aluminium targets were qualitatively similar to that shown in Fig. 4.9 for the mercury target, *i.e.* they showed an initial short pulse.

No very sensitive investigation could be made of any pulse-tails for the light from the dark region of the beam. This was because electrical noise in the detection system limited the sensitivity of any such experiments to  $\sim 10\%$  of the peak power (see Fig. 4.9). The only scenario in which a tail much larger than  $10\%$  of the peak power was observed, was with the aluminium target and the  $6.7$  cm focal-length focusing lens. In this case a post-pulse of  $\sim 30\%$  of the peak was observed, lasting  $6$  ns after the initial pulse.

The aluminium target appeared to be much more reflective than the mercury one, and so this was quantified. A Star-Tech DUV 5/G pyroelectric detector was used to measure the time-integrated energy reflected into the detection aperture. Some of the lowest energies measured ( $500$  nJ) gave signals comparable with the electrical noise of the detection system, and care was taken to allow for this in the results presented here. The energies measured, and other salient experimental results are given in table 4.1.



	10% →90% rise (ns)	Initial pulse FWHM (ns)	Brightness (J sr <sup>-1</sup> )	Spatial structure of reflected beam
Al target; $f=18$ cm; 2.5 mrad sampled	1.3	2.1	8	Loop; 2 <sup>nd</sup> and later shots only
Al target; $f=6.8$ cm; 2.3 mrad sampled	0.85	1.8	3	Loop; 1 <sup>st</sup> and subsequent shots
Hg target; $f=18$ cm; 2.1 mrad sampled	1.3	2.1	0.4	Lobes, lines & loops, variously found on all shots

**Table 4.1.** Experimental variations for plasma-truncated reflection experiments, and mean results obtained. Angles given were subtended by detector at focusing lens. FWHM durations were measured in central (dark) region in each case, and for aluminium targets a fresh piece of sample was exposed each time.

From table 4.1 it is clear that the temporal properties of the reflected beam did not depend strongly on the target material. Termination of the reflection was earlier when the tighter focusing arrangement ( $f=6.8$  cm lens) was used. It is also clear that the aluminium target was an order of magnitude more reflective than the mercury one.

4.3.5 Discussion

No very probing investigation was made of the mechanism of the pulse-shortening. Furthermore, the physical processes involved are complicated by a sharp increase in focal intensity over the course of the pulse (§4.3.5.1). For these reasons, the discussion here will be brief, and will only seek to present explanations which are plausible, rather than to argue that there are no other possible explanations. We shall attempt to answer two questions: what causes the initial change in reflectivity, and what causes the spatial structure observed in the reflected beam?

4.3.5.1 Evolution of divergence

The divergence of the output reaching the focusing lens at the start of the pulse was 29 mrad x 15 mrad\*. This was determined by the 18 mm x 6 mm size of the gain region, and the aperture A1 of Fig. 4.6. However, by the end of the pulse, the divergence will have fallen. We may estimate the final divergence by considering the ‘unfolded’ cavity. This has a length of 6 m, determined by the 20 ns pulse-length. This suggests a divergence of 3 mrad x 1 mrad. The fall in divergence suggests the focal intensity rises by an order of magnitude during the course of the pulse.

4.3.5.2 Cause of initial truncation

We shall consider two possibilities for the initial pulse-truncation observed. The first is that the reflectivity falls sharply when a plasma is *formed*, 1 ns to 1.5 ns into the pulse. The second is that the plasma is formed earlier in the pulse, and the truncation occurs

\* All dimensions are given as horizontal x vertical.



when it has *expanded* sufficiently to give an underdense region. In this case the drop in reflectivity is caused by inverse bremsstrahlung absorption of the incident radiation in the underdense layer.

We shall consider whether the second explanation is plausible. In order to achieve significant absorption, the plasma must expand to a distance comparable with the inverse bremsstrahlung absorption length for the laser radiation (at the critical density). This distance is of order  $1\text{ }\mu\text{m}$  [Teubner *et al.* 1992]. If we assume that the plasma formed has a temperature of order 1 eV, this suggests a thermal ion velocity of a few microns per nanosecond (§7.6). This indicates that we should expect the plasma formed to have expanded to the skin depth within the first few nanoseconds after plasma formation. This phenomenon is of considerable importance in prepulsed LGP systems, as discussed in §8.4.5 and §9.2.5.

Evidence for the second explanation (*i.e.* plasma expansion) over the first (*i.e.* plasma creation) comes from estimating the focal intensity at the time in the pulse that truncation was observed. For the aluminium experiments, the intensity on target at the onset of pulse-truncation was  $8.5 \times 10^7\text{ W cm}^{-2}$  and  $1.9 \times 10^7\text{ W cm}^{-2}$  for the 6.8 cm and 18 cm focal-length focusing lenses respectively (assuming it is the leading edge of the pulse which is truncated). This factor of 4.5 difference in the intensity suggests that whatever causes the sudden drop in reflectivity is not associated with a sharp intensity threshold. Plasma-*formation* does have such a threshold, which suggests that plasma-*expansion* is the better explanation for the drop in reflectivity observed.

#### 4.3.5.3 Cause of spatial structure in reflected beam

We shall consider two plausible qualitative mechanisms for the generation of spatial structure in the reflected beam. The first explanation is that the absorption of the beam varies according to the angle of incidence of the beam, or because of spatial variations in the plasma generated (or both). The second explanation is that the shape of the critical surface changes during the course of the pulse. This will be relevant since most of the reflection takes place at the critical surface. It is worth noting that the critical surface is an idea rather than a particular set of ions or electrons, and so there is no limit on the speed at which it may move (although, of course, it cannot move beyond the edge of the plasma).

Both of these explanations are consistent with the experimental results. Consider the observation that, when using the longer focal-length focusing lens, more than one shot had to be fired\* on to a particular region of aluminium target before structure was observed. The difference in the target condition between the first and subsequent shots is that an ablation crater has formed, *i.e.* the reflector is a different shape. Furthermore, consider the observation that the shorter focal-length gave rise to structure on the first shot. This may be explained as due to the greater cone-angle associated with the shorter focal-length lens. This will allow the outer regions of the incident beam to ‘see around’ any local variations in the shape of the critical surface or underdense region.

Not only are these two explanations consistent with the experimental results, the processes involved are to be expected. This is because the drop in divergence during the pulse will lead the focusing to become tighter during the pulse. This can be expected to

---

\* Considerable care was taken to check this observation. Several attempts were made to observe structure in the reflected beams from the first shot, as the focal position was varied slowly.



cause a bulge in the critical surface, as well as increasing the extent of the underdense region in front of the centre of the plasma, compared to the edges of the plasma.

It must be pointed out, however, that it is hard to explain the observation that spatial filtering was required in order to achieve any pulse-shortening at all, for reflection from the copper target (§4.3.2). The experiment was not repeated for the aluminium or mercury targets, and so it is not possible to draw any firm conclusions from this observation, especially since the accuracy of the focusing for the experiments described in §4.3.2 was suspect, and may have been inconsistent between the profiles illustrated in Fig. 4.7.

#### 4.3.5.4 Comparison with previous reports in the literature

Much of this work is new. In particular, this author is not aware of any previous report of such spatial structure observed in the light reflected from an LGP, except that Alimpiev *et al.* [1993a, 1993b] reported, without comment, spatial structure in the light reflected by their TRUBS system.

The only report of a very similar technique applied to pulse-shortening has been made by Klopotek *et al.* [1987]. They report truncation of the specular reflections from kapton (polyimide) at  $\sim 60^\circ$  incidence. The experimental conditions were very similar to those used here (308 nm radiation, 120 mJ pulses from a plane-plane cavity laser, focused with  $f=20$  cm lens). Their results were also very similar to those reported here, *i.e.*  $\sim 2$  ns output pulses. They give very few experimental details, and no interpretation of their results, except that they believe a plasma is somehow responsible for the pulse-shortening.

Another plasma-truncation system has been reported by Tünnermann *et al.* [1990]. In this scheme a KrF (or XeCl) beam was focused on to a dye jet. The authors comment that they believe absorption by a plasma formed on the surface of the dye (rather than saturable absorption) to have been responsible for the pulse shortening they observed. They obtained KrF pulses of 1.5 ns duration by this technique.

Focusing excimer beams onto polymer targets has technological applications in materials processing; and there have been some experimental studies of the truncation of reflected radiation, under similar experimental conditions, with this in mind [Singleton *et al.* 1990, Ediger & Pettit 1992, Ediger *et al.* 1993]. These reports do not propose mechanisms for the pulse-shortening. We shall not delve into them in any detail, except to comment that two of them describe the diffuse reflectivity closely mimicking the specular reflectivity, for time-dependent measurement [Ediger & Pettit 1992], and time-integrated measurement [Ediger *et al.* 1993].

## 4.4 Plasma-truncated spatial filtering

### 4.4.1 Beam quality considerations

The plasma-truncated reflection technique described in the preceding sections provided short pulses, chopped from the start of a laser pulse. The start of the pulse corresponds to the greatest divergence radiation, however, and so a technique which held promise of producing low-divergence plasma-truncated radiation was investigated. Similar techniques, for different applications, have been reported by others. For example, Figueira *et al.* [1981] describe a similar arrangement used to eliminate back-reflections from a CO<sub>2</sub> laser system.



### 4.4.2 Experimental arrangement

The technique employed for the present work simply involved focusing a laser beam on to the surface of a piece of 200  $\mu\text{m}$  thick aluminium (as described in §4.3.3.1). The idea was that the plasma produced would ablate the aluminium, and after enough shots had been fired, a hole would be produced. Light passing through the hole could only be low divergence, since the hole would act as a spatial filter. Then a plasma formed around the edges of the hole would truncate the transmission.

A plano-convex, 9 cm focal-length lens was used to focus light on to the aluminium surface. The position of the focus was found, to within  $\sim 1.5$  mm, by the technique described in §4.3.3.3. The transmitted light was then recollimated with a further condensing lens.

With the full (100 mJ) beam energy incident on the aluminium surface, a strong plasma spark was produced, and about 45 shots were needed to make a hole in the aluminium. This figure rose to  $\sim 280$  shots when the aluminium was not correctly positioned at the beam focus, even though a plasma spark was formed every shot. The temporal properties of the transmitted pulses were measured, and some typical results are illustrated in Fig. 4.10. The results were interesting, but unhelpful for pulse-shortening.

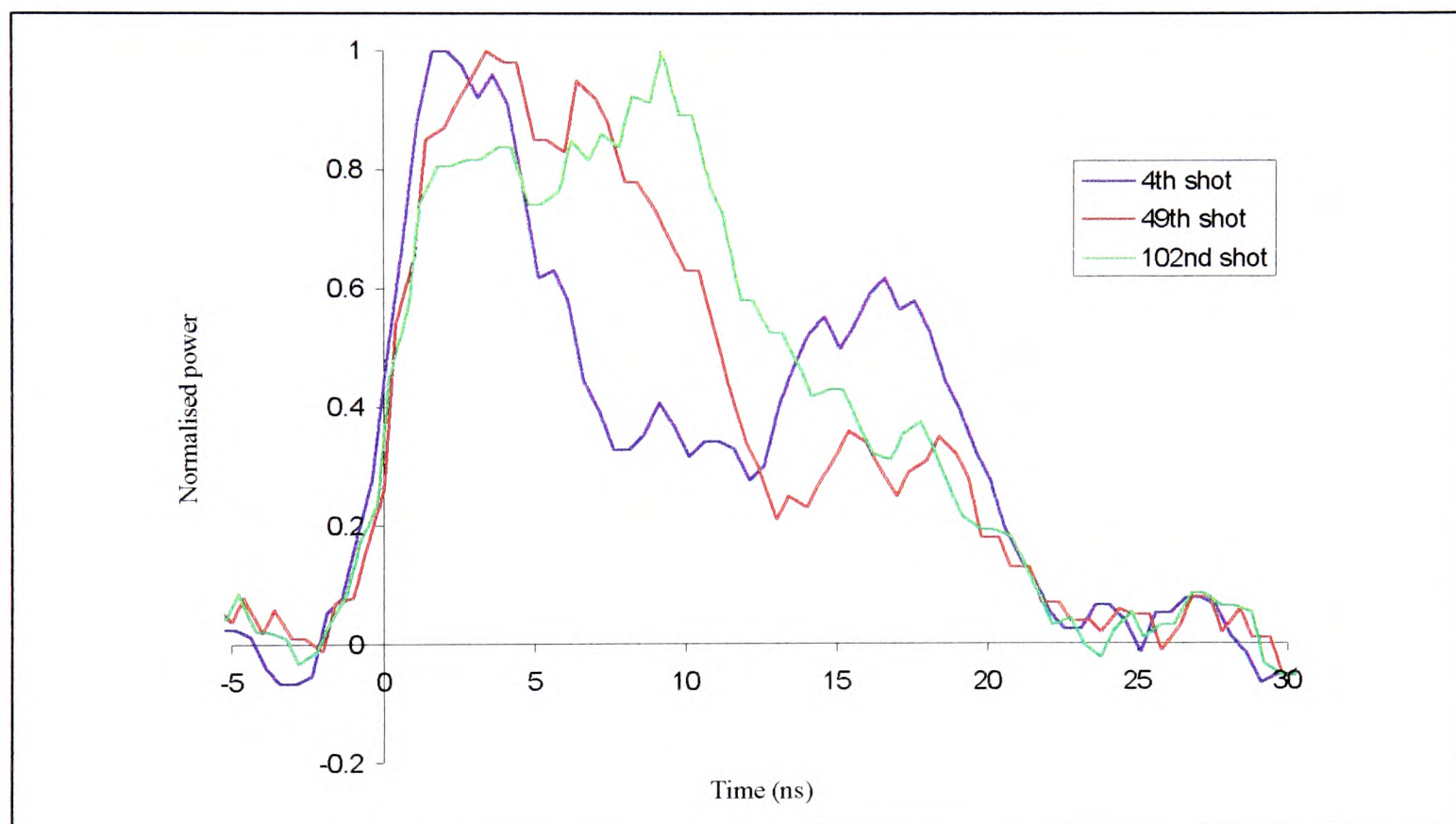


**Figure 4.10.** Temporal profiles of radiation transmitted by hole ablated in 200  $\mu\text{m}$  aluminium target, as a function of number of shots after breakthrough. Each profile has been normalised to give peak power of unity. The transmitted pulse-energies were 4 mJ, 17 mJ, and 34 mJ for the 4<sup>th</sup>, 49<sup>th</sup>, and 102<sup>nd</sup> shots respectively. The relative timing of the pulses shown is arbitrary.

Fig. 4.10 illustrates the behaviour observed. A double pulse structure was present in the first shots to be transmitted after breakthrough. This became less pronounced as more shots were fired, and was absent after  $\sim 100$  shots.

One modification to the technique was tested: the use of thinner foils. These had the advantage of giving a quicker breakthrough, and it was hoped that there might be some transmission in the laser shot which first punched through the foil, rather than all the transmission being in the following pulse.



The results were worse. A 20  $\mu\text{m}$  foil was first transmitting to the third shot incident on it. The transmitted pulse had a FWHM duration of 14 ns. An 8  $\mu\text{m}$  foil was first transmitting to the second shot incident on it. The transmitted pulse had an FWHM duration of 15 ns.

### 4.4.3 Discussion

We propose a mechanism for the results observed. With each shot fired on the thicker target, the hole was enlarged. For the first few shots the hole was sufficiently small that the plasma formed at its edges could expand into the transmission region, absorbing (or possibly scattering) the KrF radiation there. This gives rise to the decay in transmitted power, over a  $\sim 5$  ns timescale, observed for early shots through the thick target (Fig. 4.10). The transmitted power was then observed to recover. Two effects are relevant to this. Firstly, the reduction in beam divergence discussed in §4.3.5.1 will have caused more of the beam power to be incident on the hole. Secondly, expansion of the plasma may have reduced the absorption/scatter in the aperture.

The reason that the thinner targets gave poor results is that the holes created were, from the start, too large. For example, a single shot made a  $1720 \mu\text{m} \times 795 \mu\text{m}$  hole in the 8  $\mu\text{m}$  foil, whereas the hole in the 200  $\mu\text{m}$  foil was only  $650 \mu\text{m} \times 180 \mu\text{m}$  after more than 100 shots had been fired (after breakthrough). Most of the removal of the target material caused by LGPs is due to the shock wave, and occurs after the generating laser pulse has ended. This meant that the holes in the aluminium foils were created just after a pulse had ended. These holes were then too big to be of any use as spatial filters for the following pulse.

A way around this problem is to use foils so thin that they are entirely ablated during the laser pulse. Dhareshwar *et al.* [1991] have reported exactly such a technique, focusing on to 20 nm to 60 nm films of aluminium supported on glass slides, in order to truncate pulses from a Nd:glass infrared laser. A similar technique, for a slightly different application (as an optical shutter for light at a different wavelength to the main laser pulse), has also been reported by Ripin *et al.* [1977].

This technique was not investigated here. Although superficially attractive - Dhareshwar *et al.* [1991] observed sub-nanosecond pulses - there are some complications. Firstly, the spatial filtering effect would probably be less pronounced, since the technique is plasma-truncated transmission, rather than plasma-truncated spatial filtering. Secondly, transmission requires the plasma generated to become under-dense, which means the results obtained with infrared lasers cannot be expected to transfer directly to ultraviolet systems. Thirdly, a separate mechanism for truncation of the trailing edge of the pulse is needed [Dhareshwar *et al.* [1991]].

## 4.5 Conclusions about short pulses

In summary, pulse-shortening was observed from all of the plasma-truncation techniques investigated. The shortest pulses obtained were of duration 1.8 ns FWHM (plasma-truncated reflection from aluminium). These were slightly shorter than the shortest pulses obtained from the compact oscillator, having a FWHM duration of 2.0 ns.

For a given energy, pulses having a duration  $\sim 100$  ps are optimal for generating a plasma of the correct temperature to pump the Xe III laser (see discussion in §8.4.5 on the work of Yamakoshi *et al.* [1996] and Sher & Benerofe [1991]). Thus, even the



shortest pulses obtained here were of about an order of magnitude too long for optimal pumping of the Xe III system.

Xe III laser pulse durations reported in the literature have varied between 50 ps [Sher *et al.* 1987] and 600 ps [Kapteyn *et al.* 1986]. This suggests (assuming no storage in the Xe III gain medium) that any laser energy delivered to the target after a few hundred picoseconds from the onset of Xe III lasing would be wasted. However, this need not be disastrous, provided a sufficiently hot plasma can be generated. Indeed, several of the reports of Xe III lasing describe the use of pump-pulses which were longer than the Xe III output pulse [Kapteyn *et al.* 1986, Sher *et al.* 1987, Sher *et al.* 1991].

Provided the pumping-pulse duration is not too short (tens of picoseconds for 1064 nm pumping lasers [Yamakoshi *et al.* 1996, Sher & Benerofe 1991]), the most important factor in achieving a sufficient LGP temperature is the intensity on target. For a given focusing system (and provided the focusing is not limited by aberrations in this system), the focal intensity depends only on the power in the laser beam, and its divergence. Simple calculations (§6.6.1) indicated that the KrF laser system, arranged exactly as Fletcher [1993] had described, might be capable of giving the focal intensity required. The use of this laser system had the advantage of being experimentally straightforward - it had already been optimised by Fletcher [1993] and could easily be reassembled. Time was becoming a concern, and so no further attempts were made to achieve sub-nanosecond pulse-shortening. The choice, then, was between using the arrangement of oscillator and amplifier described by Fletcher [1993], or amplifying the short pulses which had been obtained, with a view to achieving a higher power-to-divergence ratio\*.

The arrangement used by Fletcher [1993] extracts energy from the laser medium continuously, over a total time of  $\sim 45$  ns. By amplifying a shorter pulse, it might be possible to extract a significant portion of the laser energy in a short time, thereby increasing the power in the beam. We may quantify this: the peak power available from the system as described by Fletcher [1993] was  $\sim 100$  MW. Saturation of the gain, followed by repumping, would cause sharpening of both the rise and fall of any amplified pulses. This is because, as we shall see, there is significant gain-recovery over the timescale of the pulse to be amplified. This effect would lead to lengthening of the FWHM duration of the pulses being amplified, to approximately the total duration of the incident pulse. This effect (a lengthening of the pulse FWHM duration, for amplification of pulses longer than the gain-recovery time) has been observed experimentally by Banic *et al.* [1980] and by Di Lazzaro *et al.* [1995].

This total duration was  $\sim 4$  ns for the shortest pulses obtained here. If all the 2.5 J extractable from the laser amplifier module could be extracted in a 4 ns pulse, the power in the amplified pulse would be 630 MW.

At first sight this factor of  $\sim 6$  in the laser power appears very attractive, but several factors conspire to make such an enhancement extremely difficult to realise. As we shall see in the following paragraphs, an enhancement factor of  $\sim 3$  is the most which might reasonably be expected, and even this would be at the expense of considerable experimental effort.

---

\* Let  $P$  be the laser power in a beam of divergence  $\theta$ . For a line focus the intensity scales as  $P/\theta$ , whereas for a spot focus the scaling is  $P/\theta^2$ .



#### 4.5.1.1 Arrangements for amplification of 4 ns pulses in KrF amplifier module

In this section we shall demonstrate that the factor of  $\sim 6$  improvement in beam power would be very difficult to realise, using only the KrF amplifier module available. In order to do this, we shall consider how such an enhancement might be achieved. Although the discussion here is not exhaustive, it will illustrate the considerable practical problems which would need to be overcome.

An excellent treatment of the relevant considerations for KrF-amplification of short pulses has been given by Shaw [1991]. Considerable use will be made of this work in the following paragraphs, without repeatedly referring to it. Some recent innovations have been reported by Szatmári [1994].

#### 4.5.1.2 Gain-recovery time and upper-state lifetime

A vital consideration for the amplification of short pulses is the storage time of the laser system. This is given by the upper-state lifetime of the  $\text{Kr}^+\text{F}^-$  excimer. The natural lifetime is  $\sim 6$  ns, but it is collisionally quenched. The resulting upper-state lifetime can be estimated from measurements of the gain-recovery time for a discharge-excited KrF laser, made by Taylor *et al.* [1988]. We shall first demonstrate that the gain-recovery time is the same as the upper-state lifetime. We assume that we may pass a short pulse through a KrF gain medium, and fully deplete the population inversion, at time  $t=0$ . This assumption is valid - Taylor *et al.* [1988] found they could fully depopulate the upper laser level by the passage of 1 ps pulses.

Next, we note that there is no lower level population in KrF lasers (which is why excimer lasers are so efficient), and so the inversion density is equal to the upper-state population,  $N$ . We assume a constant repumping rate,  $\Gamma$ , fuelled by energy transfer from the electrons in the discharge. There are two important considerations in this assumption. The first is that  $\Gamma$  is constant. Taylor *et al.* [1988] ensured that this was the case, by conducting their experiment at the time in the KrF gain-window corresponding to the peak of the fluorescence, where the pumping is temporally flat. Szatmári & Schäfer [1984] made similar measurements of gain recovery to those made by Taylor *et al.* [1988], but on the trailing edge of the gain. Consequently they measured a gain-recovery time about twice as long as that found by Taylor *et al.* [1988]. Differences between the discharge modules and gas mixtures used in them may also have been responsible for some of this difference.

The other consideration in our assumption of a constant  $\Gamma$  is that repopulation of the upper-state requires energy input from the discharge. In fact, this is not the case; some of the gain recovery is due to rotational relaxation into the upper laser level. This is fast (60-70 ps time-constant) but only accounts for a small fraction of the gain recovery. Different values have been measured for the fraction of the recovery which is fast. Taylor *et al.* [1988] measured a 10% fast recovery, whereas Szatmári [1994] reports a 25% fast recovery. The fast recovery is only relevant when one amplifies pulses shorter than the fast recovery time. In this case, the time delay required for rotational relaxation would limit the inversion density, and reduce the extraction efficiency. For amplification of  $\sim 100$  ps pulses, as would be ideal for the Xe III application, the fast gain-recovery would happen during the course of the pulse, and the repumping would indeed rely on energy input from the discharge.

Next, we assume that there is negligible ASE during the gain-recovery process. The justification for this is again that Taylor *et al.* [1988] ensured that this was the case (no



more than 5% gain depletion because of ASE). In this case the depopulation of the upper laser level is due to spontaneous decay and collisional quenching, giving a net lifetime,  $\tau$ . Thus, we may write

$$\frac{dN}{dt} = \Gamma - \frac{N}{\tau} \quad (4.2),$$

which has the solution

$$N = \Gamma \tau (1 - \exp(-t / \tau)) \quad (4.3).$$

In other words, the gain recovers exponentially from zero to  $\Gamma \tau$ , with time constant equal to the net upper-state lifetime,  $\tau$ . If we neglect the fast recovery component, the gain recovery found by Taylor *et al.* [1988] took the form of expression (4.3), having a time constant of 2.0 ns.

The KrF amplifier available for the system here operates at a higher total pressure (4 bar) than that investigated by Taylor *et al.* [1988] (2.5 bar), and Shaw [1991] has shown that the slow KrF gain recovery-time (*i.e.* the quenched upper-state lifetime) is pressure-dependent (for an electron-beam excited laser). Calculation of the exact pressure-dependence is complicated, since electron quenching may be a very important process, and evaluation of this requires a reasonably sophisticated model of the discharge. No attempt has been made to make such a model, but in the discussion which follows we shall assume a 1 ns upper-state lifetime.

Provided it exceeds the saturation intensity, a short ( $\ll$  storage time) pulse can extract all the energy which has been stored in the gain medium in the preceding storage time. However, for pulses longer than the storage time, the energy is extracted from the gain medium at almost exactly the rate at which it is pumped (assuming saturation is continuously present). But this is exactly what happens when the laser energy is extracted continuously. This means that if we are to obtain the sixfold enhancement in beam power, we must ensure the amplifier is always filled with light of sufficient intensity to saturate the gain. We must also find some way of compressing the energy extracted over the whole gain-window into our short pulse.

#### 4.5.1.3 Extraction techniques

One technique for making use of the whole gain time-window is to pass a single pulse repeatedly through the gain medium. The different passes are made at different angles, so that only the multiply-amplified beam reaches the target. The maximum intensity obtainable in this way is limited by nonsaturable absorption in the laser gas. Shaw [1991] quotes maximum intensities of  $10 \text{ MW cm}^{-2}$  to  $60 \text{ MW cm}^{-2}$  for typical KrF operating parameters. Assuming our best-case 630 MW extraction, the intensity would be  $\sim 80 \text{ MW cm}^{-2}$ . This suggests that nonsaturable absorption would limit the maximum energy which could be extracted by multipass amplification of a single pulse.

A way around this problem is to pass several time-multiplexed, and angle-multiplexed pulses through the gain medium. The reason this helps is that the light extracted in one pass is not retransmitted through the (absorbing) gain medium in the following pass. Once amplified, these pulses must be recombined, in both time and direction. The conventional technique for this is to make the pulses travelling at different angles travel different distances to a recombining mirror [Taylor & Goldhar 1983, Shaw 1991]. By careful alignment this can be arranged to make the pulses arrive at the same time, and subsequently travel along the same path.



So far, however, we have only considered the enhancement of the beam *power* which might be obtained by short-pulse amplification. This will only translate to an enhancement in *focal-intensity* over that which could be obtained from the system developed by Fletcher [1993], if its  $\sim 30 \mu\text{rad}$  divergence can be matched. Immediately this suggests an experimental difficulty - any angularly-multiplexed beams must be recombined with an accuracy of  $30 \mu\text{rad}$ . Although this might be possible, it would be extremely difficult for the  $\sim 5$  double-pass or  $\sim 10$  single-pass beams which would be required to achieve full energy extraction from the gain medium.

There are several ways around this alignment problem. One way is to use a Raman recombination system, and we shall return to this. Another way is to use a Sagnac interferometer arrangement for multiplexing [Szatmári & Simon 1993, Szatmári 1994]. This is an ingenious technique employing a ring cavity and counter-propagating beams which traverse the gain region at different times. When recombined, the beams are parallel, whatever the alignment of the cavity optics.

The problem with this technique, is how to generate, in the first place, low divergence light for amplification. To quantify this, we might expect to be able to generate pulses of divergence  $\sim 1 \text{ mrad}$  from the compact oscillator (by means of a suitable cavity [Yamada *et al.* 1988]), or by plasma-truncated reflection. This means the beams must be magnified by a factor of  $\sim 30$  in order to achieve an output divergence of  $30 \mu\text{rad}$ . We note that amplification is only efficient if the gain is saturated, and the beam fills the aperture of the gain medium. Thus, in order to achieve efficient energy extraction a three-pass amplification of the injected beam would probably be required. One of the many possible arrangements which could achieve this is illustrated in Fig. 4.11. The first pass would be used to achieve the saturation intensity in the beam. The second pass would be used to expand the beam both to fill the gain region, and to reduce the divergence. The magnification of 30 required corresponds to a reduction in intensity of  $\sim 900^*$ . A small-signal gain of  $e^7$  would be needed to make up for this. Such a small-signal gain should be exceeded by a 1 m KrF gain region [Fletcher 1993, Burrows *et al.* 1995]. Finally, the third pass is used for efficient energy extraction from the system.

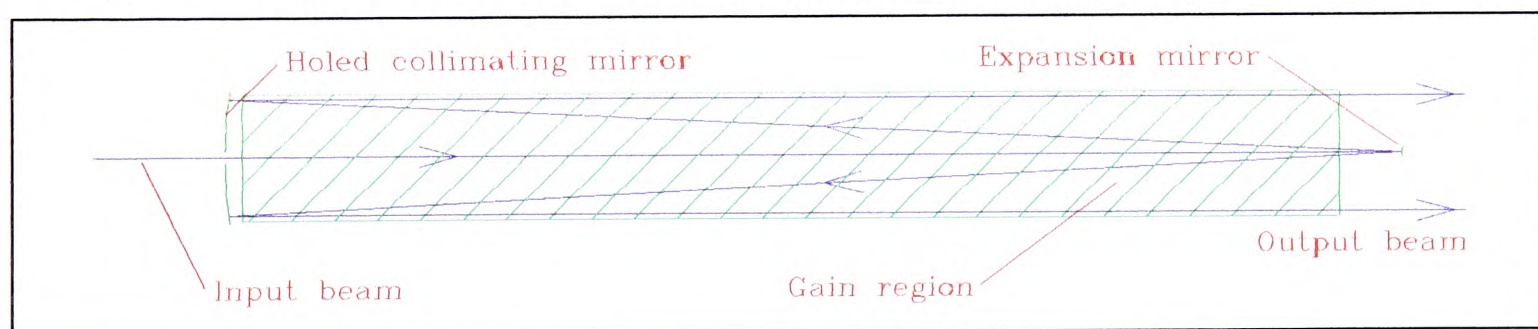


**Figure 4.11.** 3-pass geometry suitable for efficient extraction of low-divergence radiation from amplifier module. Aspect ratio of amplifier has been reduced for clarity.

The third-pass beam cannot be used efficiently as a seed beam for the angular multiplexing. The problem is the time taken to form such a multiplet. This is because a long beam-path is required to separate beams travelling at only slightly different angles. Large angular separations could be used to avoid this problem, but this would be at the expense of extraction efficiency, because such beams would miss most of the gain region (or would fill the gain region, but only part of the beam would be amplified).

\* For some line focusing geometries low divergence is only required in one direction. Thus, if cylindrical optics were used, the loss of intensity in the expansion stage could be  $\sim 30$  times less than this. This might eliminate the need for a first-pass.



Furthermore, it is not possible to multiplex the incident beam of a three-pass geometry, if a Sagnac interferometer arrangement is used. This is because the interferometer technique relies on the symmetry of the amplifier module for light travelling in opposite directions within it. These considerations mean that the Sagnac interferometer multiplexing arrangement described by Szatmári & Simon [1993] cannot be used for efficient extraction of low-divergence laser radiation.

As mentioned above, another beam recombination technique which does not need extremely precise alignment involves a Raman amplifier [Shaw *et al.* 1986]. Essentially, the KrF radiation is used to pump a very efficient (~60%) laser amplifier at the first Stokes frequency of a gaseous Raman medium. Neither the beam quality, nor the alignment of the KrF radiation is crucial, since all that is required is reasonably uniform pumping of a macroscopic volume. Furthermore, a backwards amplification arrangement allows the compression of energy from a long KrF pulse, into a much shorter counter-propagating Stokes (Raman) pulse [Burrows *et al.* 1995]. The theory behind the scheme is given by Murray *et al.* [1979].

Raman recombination adds considerably to the complexity of the system. This is especially true if, as here, low divergence, short-pulse output is required, since a low-divergence, short-duration seed beam is required for amplification in the Raman medium. For this reason the system was not investigated here.

#### 4.5.1.4 Implications for further work

In summary then, the compression of the output energy available from the KrF amplifier into a 4 ns pulse is far from straightforward. Furthermore, it is difficult to envisage a scheme which would allow this with an efficiency of more than about 50%. Thus, only a factor of ~3 power enhancement can be expected from such a scheme.

If, on the other hand, 100 ps pulses could be obtained, the situation would be very different. In particular, the geometry shown in Fig. 4.11 could be used\* to give a power enhancement of a factor of at least 5, without any multiplexing. This is because a 100 ps pulse can extract at least half the 100 mJ of energy stored in the amplifier during the storage time of ~1 ns. Any multiplexing could enhance this further.

The reason that only half the stored energy may be extracted efficiently is that the maximum fluence which can be extracted efficiently by a short pulse from KrF laser systems is limited by nonsaturable absorption to ~3 times the saturation fluence [Szatmári 1994, Divall *et al.* 1996]. The saturation fluence,  $E_{sat}$ , depends on the timescale of the pulse being amplified. This is because it depends on the gain cross-section, and very short pulses do not see all the available gain (since there is insufficient time for rotational relaxation to the upper laser level). For 100 ps pulses,

$$E_{sat} = \frac{E_{phot}}{\sigma} = 2 - 2.7 \text{ mJ cm}^{-2} \quad (4.4),$$

where  $E_{phot}$  is the laser photon energy, and  $\sigma$  the gain cross-section [Szatmári 1994]. This means the maximum pulse energy which could be expected from a single short pulse amplified in the module available, is ~50-70 mJ.

A short pumping pulse is desirable not only to *generate* Xe III emission at 109 nm, but also to allow the output to be *observed*. This is because any energy incident on the target

---

\* A different geometry, involving magnification outside the gain medium between the first and second passes, might be needed if ASE was found to limit the gain.



after the Xe III emission is complete will give rise to plasma emission, which will mask the Xe III laser output.

In the light of the considerations given in the last few sections, it was decided that further attempts at increasing the power of the KrF laser should concentrate on obtaining short ( $\sim 100$  ps) pulses, rather than amplifying the relatively long pulses (4 ns) which had been obtained. In the meantime, however, it appeared that the laser system, as used by Fletcher [1993] might be suitable for pumping the Xe III system, without modification. If this turned out not to be the case, further effort could be made on pulse-shortening. Thus, the next stage of the work was to reassemble the KrF laser system (described in chapter 5), and to assemble an Xe III laser system (chapter 6).

As it turned out, nanosecond pumping proved fruitless, and there was not sufficient time to undertake further pulse-shortening experiments. However, attempts were subsequently made to pump the Xe III laser using a picosecond KrF laser system (chapter 8). It is interesting to note that this picosecond system gave very similar performance to what might have been expected from the nanosecond system, had pulse shortening been successful. In particular, the energy of the pulses obtained from the picosecond system was 40 mJ, which is similar to the 50-70 mJ pulses which might be expected after short pulse amplification in the amplifier module available. In other words, the failure to achieve sub-nanosecond pulses did not ultimately limit the range of Xe III experiments available.



## 5. KrF laser technology

---

### 5.1 Existing KrF laser system

#### 5.1.1 Introduction

The evolution of the KrF laser system which was used here has been described in detail in two doctoral theses, by Cotton [1990] and Fletcher [1993]. It has also been the subject of a paper [Fletcher *et al.* 1994]. In this chapter, a brief summary of these works will be presented, as well as a description of the changes made to the system for this application. Then we shall consider two aspects of KrF laser technology which were investigated. These investigations were conducted partly for the main purpose of the project (Xe III laser pumping), and partly as important studies in themselves.

#### 5.1.2 Discharge laser modules

The laser system, as it was used in the experiments described in chapter 6, is illustrated in Fig. 5.1. In this section, however, we shall consider the system as it was described by Fletcher [1993]. Two discharge modules are used, a small master oscillator and a larger slave-amplifier. The reason for the use of two modules is to allow the use of injection-seeding of the amplifier (§5.1.4).

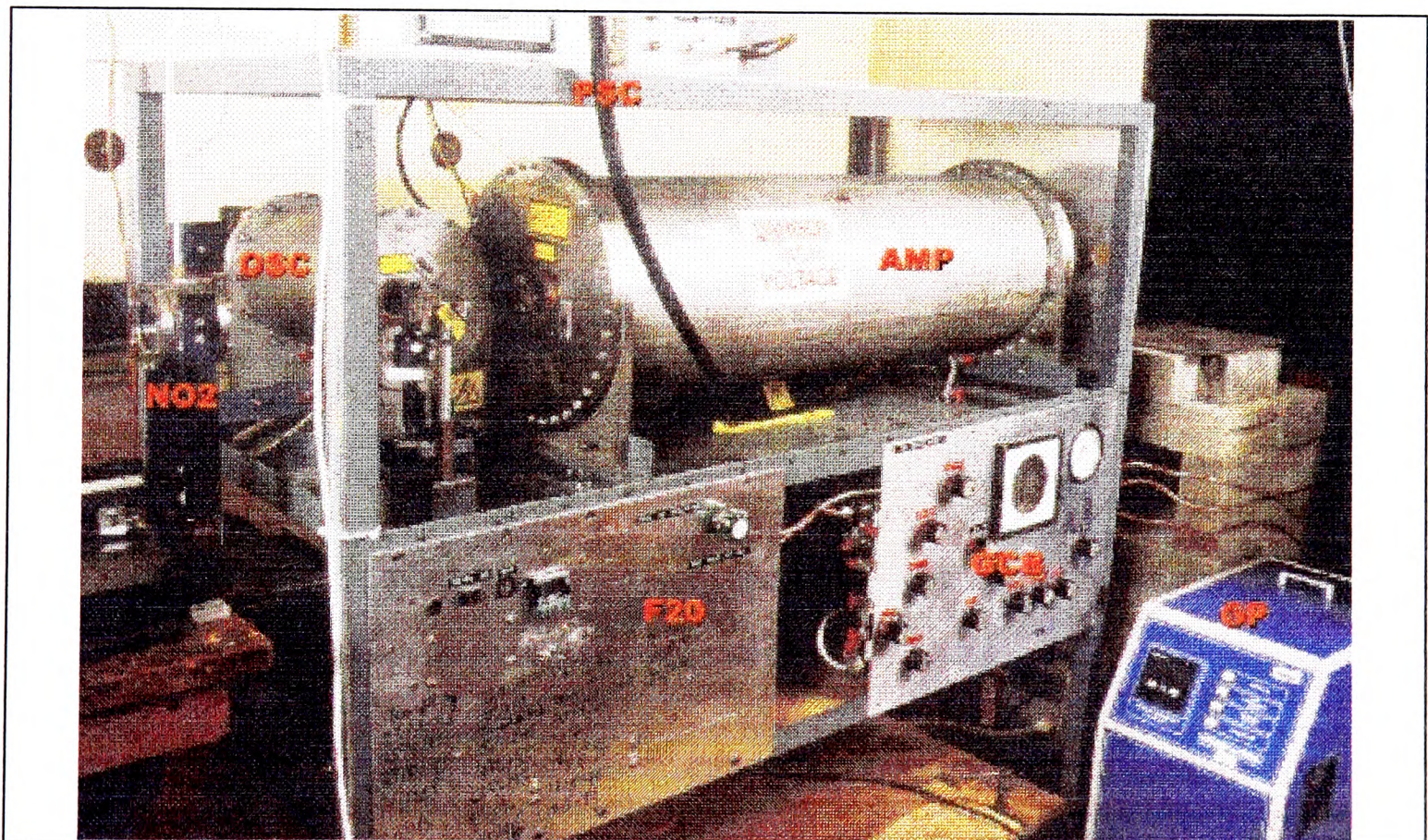


**Figure 5.1.** KrF laser system. Labels are: OSC, master oscillator; AMP, slave amplifier; NO<sub>2</sub>, NO<sub>2</sub> attenuation cell; F20, solid-state fluorine source; GCB, gas control board; GP, gas purifier; PSC, power-supply cable.



### 5.1.2.1 Master oscillator

Of the two discharge modules, the master oscillator is much the simpler, having a design very similar to that of the compact oscillator described in §3.2.1.1. A cross-section of the electrode structure is given in Fig. 5.2.

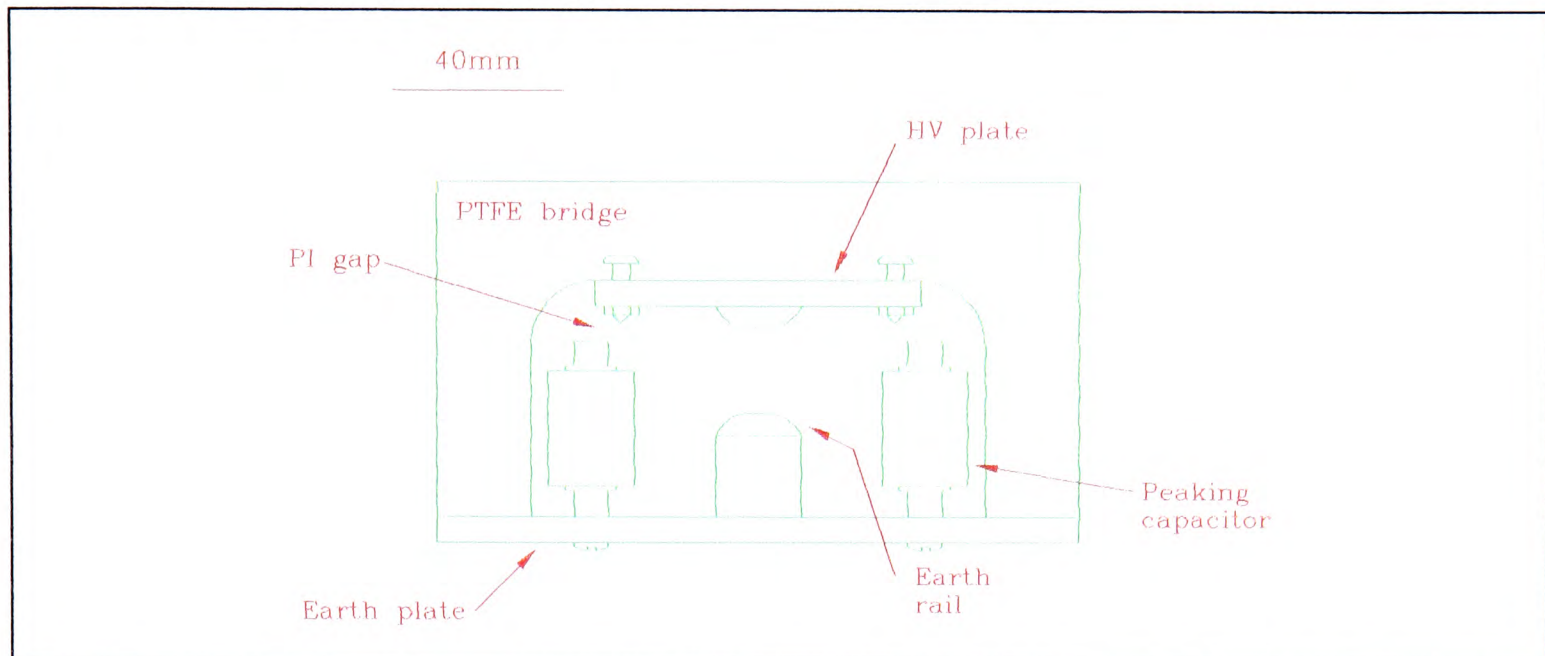


**Figure 5.2.** Cross section of electrode structure of master oscillator. PI gap: preionisation gap. Diagram is taken from Fletcher [1993].

Most of the development work on this was done by Cotton [1990]. The module had a gain volume of 7 mm x 19 mm x 225 mm. Fletcher [1993] obtained 120 mJ pulses from this module when it was used with a plane-plane cavity and the gas mixture which he had found to be optimal for the amplifier.

As in the compact oscillator described in §3.2.1.1, the preionisation gap is used to form a spark. This spark emits UV radiation, which ionises the laser gas before the main discharge. By having the spark gap in the main discharge loop, the problem of timing of the preionisation and main discharge is solved at a stroke. This near-universal feature of modern discharge-excited KrF lasers was invented (accidentally) by Kearsley [1980]. The technique provides a very simple way to enhance the uniformity of the discharge. The significance of this is discussed in §5.1.3.

### 5.1.2.2 Amplifier module

The larger amplifier module was an upgrade to a system designed and built by Cotton [1990]. Considerable optimisation of the electrode structure was conducted by Fletcher [1993]. The final arrangement he used is illustrated in Fig. 5.3.



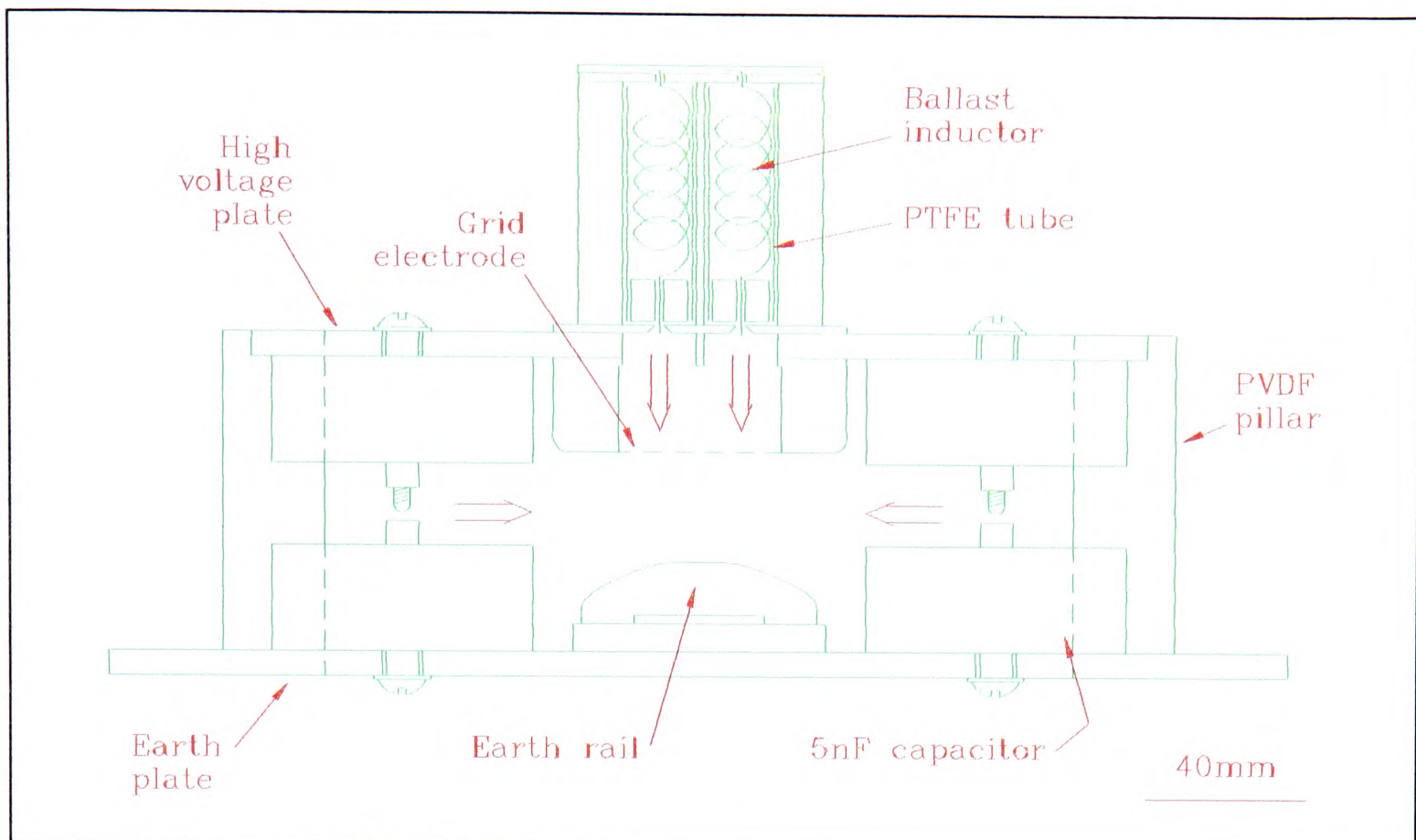


**Figure 5.3.** *Electrode structure of amplifier module, illustrating back and side preionisation. Large arrows indicate directions of preionisation radiation. Diagram is adapted from work of Fletcher [1993].*

The important features of the design are:

- The gain volume was 30 mm x 30 mm x 860 mm.
- The high-voltage electrode was semi-transparent. It was made by winding ~400 m of 125  $\mu\text{m}$  nickel wire around a support. The windings were separated by 453  $\mu\text{m}$ , leading to a geometrical transmission of 72%. The reason for this was to allow preionisation from behind the electrode (back-preionisation).
- Back-preionisation was obtained from sparks which formed between end-pins of the ballast inductors and the high-voltage plate. These sparks illuminated the gain volume, through the semi-transparent electrode. Ballast inductors were used in order to ensure that every single back-preionising spark actually formed (rather than all the current flowing through the first few sparks to form). The technique works because as soon as a spark is formed at a particular pin, and current starts to flow through it, a back-emf develops over the relevant inductor. This process takes place as the potential-difference across the electrode structure is rising, and the back-emf ensures that the potential across an inductor which has started to conduct is smaller than that over one which has not. This encourages breakdown at the other pins, and so breakdown occurs at all the back-preionisation gaps.
- Side preionisation was also used. This was provided by sparks between pairs of peaking capacitors. Further steps taken to ensure the discharge was uniform included iterative manual profiling of the earth-rail electrode.

### 5.1.2.3 Gas system

The oscillator and amplifier shared a common gas mixture. This was for the sake of experimental simplicity. The optimum gas mixture was determined empirically by Fletcher



[1993] to be 5.1 mbar of  $F_2$ , 120 mbar of  $Kr^*$ , and the balance He to a total pressure of 4 bar absolute. The criterion for this optimisation was maximum output energy of the amplifier, used with a plane-plane cavity. The maximum energy obtained after gas optimisation was 2.24 J.

An Oxford Lasers GP2000 cryogenic gas purifier was used, operating at 105 K. The function of this device is discussed in §5.3.2.3.

### 5.1.3 Electrical driver circuit

The electrical circuit used to power the two discharge modules is illustrated in Fig. 5.4. Both modules are triggered by a common spark gap. Once this has fired, the oscillator and amplifier circuits behave independently, until recharging begins (after the laser discharge has finished).

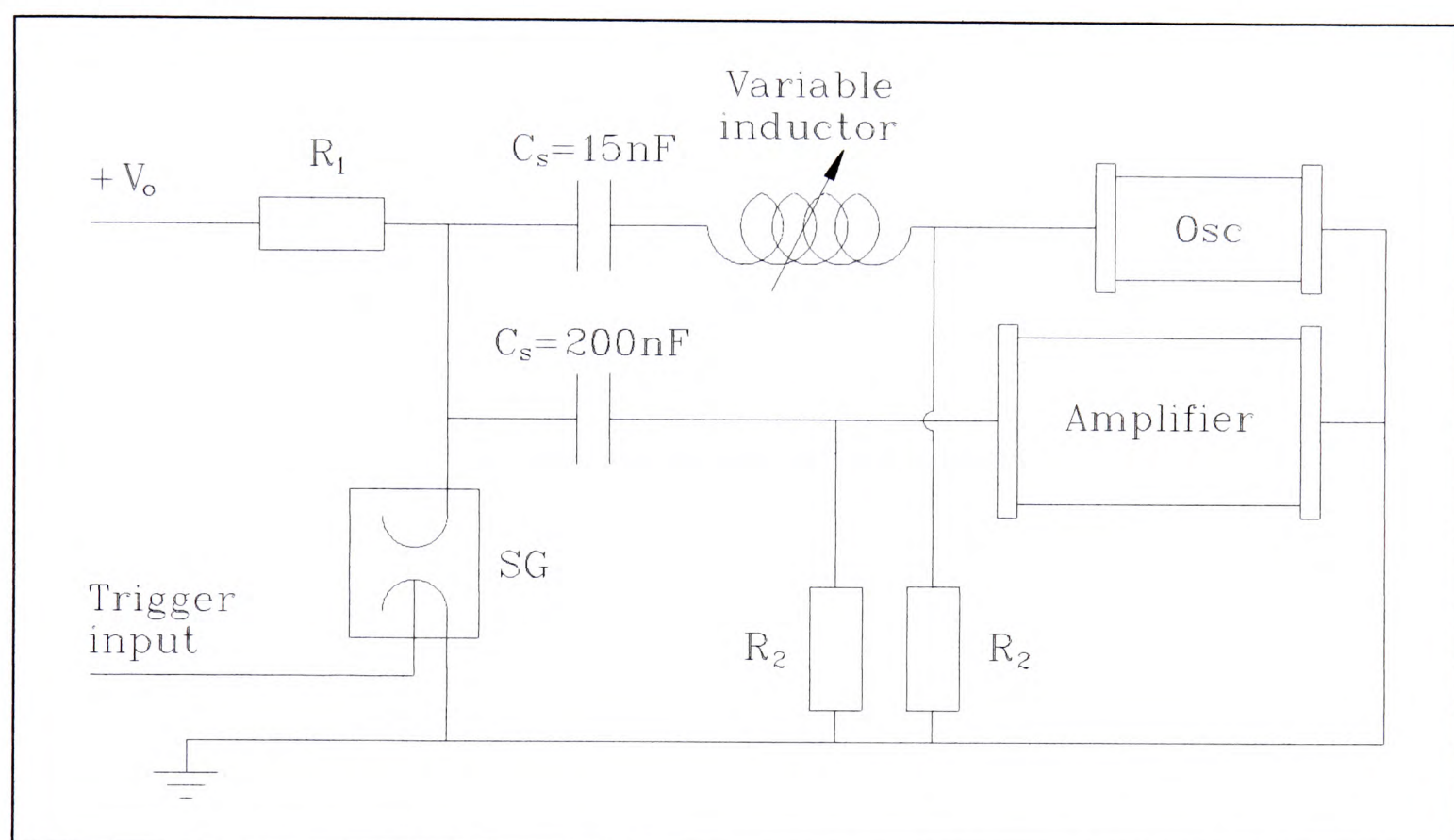


**Figure 5.4.** Electrical circuit using single spark-gap to trigger oscillator and amplifier discharge modules. Charging resistances are  $R_1=1\text{ M}\Omega$ ,  $R_2=27\text{ k}\Omega$ . Diagram is adapted from Fletcher [1993].

A variable inductor (consisting of turns of wire wound around a perspex post) was used in the oscillator circuit in order to control its timing. To see how this works, we consider in a little more detail the part of the electrical discharge circuit used to drive the oscillator. The circuit is illustrated in Fig. 5.5, and is functionally the same as that used to drive the compact oscillator described in §3.2.1.2.

\*These are not the same pressures as reported by Fletcher [1993], nor Fletcher *et al.* [1994]. This is because all gas-mix partial pressures in this thesis have been corrected for the inaccuracy of the pressure gauge, described in §5.3.2.1.



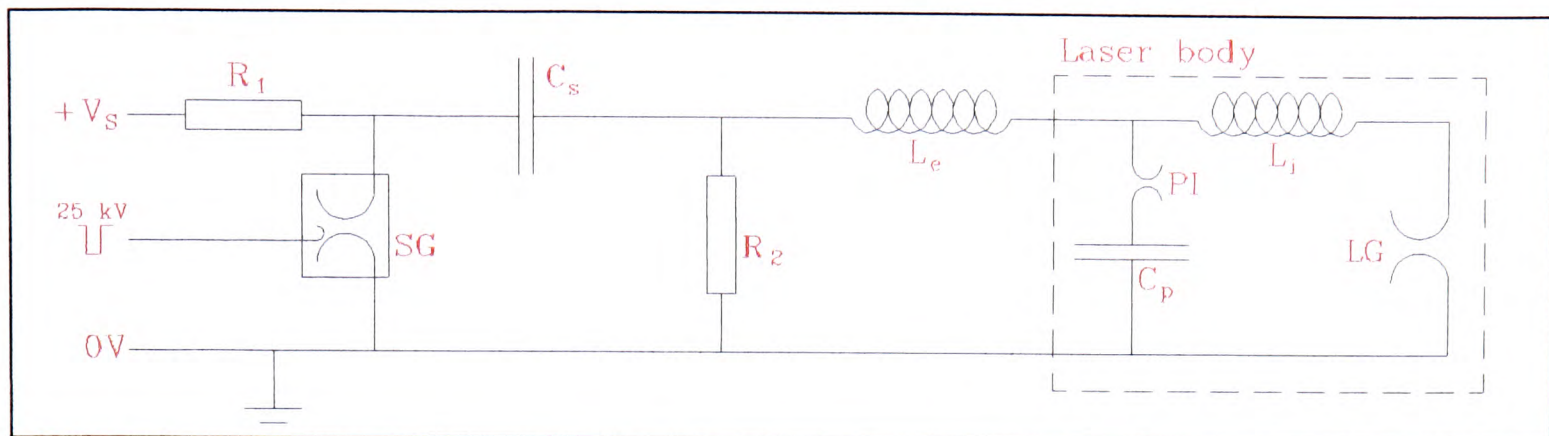


**Figure 5.5.** Schematic of circuit used to drive master oscillator. Abbreviations are: SG; spark gap, PI; preionisation spark gap, LG; laser gap. Charging resistances:  $R_1=1\text{ M}\Omega$ ,  $R_2=27\text{ k}\Omega$ .

The storage capacitor,  $C_s$ , of 15 nF is charged through resistors  $R_1$  (1 M $\Omega$ , inside DC power supply) and  $R_2$  (27 k $\Omega$ ).  $R_2$  is chosen to be much less than the resistance of the laser gap,  $LG$ , before breakdown, and much greater than its resistance after breakdown. Once charged, the left plate (on Fig. 5.5) of  $C_s$  reaches the supply potential  $V_s$ , limited to a maximum of +60 kV by the power supply. The spark gap,  $SG$ , contains a few atmospheres of air. The pressure is set according to the supply potential  $V_s$ , so that the spark gap is normally near breaking down. To fire the laser, a -25 kV trigger pulse from an induction coil is applied to a commercial spark plug within the spark gap. A spark is produced, and this initiates avalanche breakdown of the air in the gap.

The left plate of  $C_s$  then falls to earth potential, and the potential at the other plate follows, going from earth to  $-V_s$ . This potential appears over all of the preionisation spark gaps individually,  $PI$ , and they quickly break down. Once they have all broken down they may be considered as a single low resistance path to the aggregate peaking capacitance,  $C_p$ , which was 13 nF for the master oscillator.

The peaking capacitors are initially uncharged, and so charge transfer between the two capacitances begins. At this point the laser gap is slightly conducting, since it has been preionised, but it has sufficient resistance to ensure that most of the current from the storage capacitor flows into the peaking capacitor. This leads to a rising potential to appear over the laser gap, and when this reaches a critical value (depending on the gas mixture, preionisation, and electrode structure), avalanche breakdown occurs, and the discharge conducts efficiently. At this point the peaking capacitors discharge through the laser medium. This discharge loop is designed to have as low a stray inductance as possible. This is in order to achieve as much energy deposition into the gain medium as possible, before arcing occurs.

We are now in a position to see how the variable inductor can be used to control the timing of the discharge. The speed of the charge transfer from the storage to the peaking capacitors, and hence the potential rise over the laser gap, is limited by the total inductance of the external circuit,  $L_e$ . The variable inductor is used to add to this inductance, and so delay the discharge.

The amplifier discharge circuit works on the same principle, with the following differences:

- There is no extra inductance introduced externally to the laser, *i.e.*  $L_e$  is as small as possible.
- There are two sets of breaks in the charge-transfer circuit, which are used to provide the back and side preionisation.
- The total peaking capacitance is 65 nF, made from 52 individual capacitors, each of 5 nF capacitance, arranged into two rows of 13 series pairs each.



- The storage capacitance is 200 nF.

### 5.1.4 Injection seeded cavity

We now consider the optical cavity arrangement which Fletcher [1993] used to obtain low-divergence radiation from the KrF laser modules. The technique employs positive-branch unstable resonators with mirrors of uniform reflectivity across their apertures. It should be pointed out here that this is not the only way to achieve low-divergence output from short-pulse (*e.g.* excimer) lasers. In particular, the self-filtering unstable resonator uses a negative branch unstable resonator [Gobbi & Reali 1984, Nassisi & Primavera 1993], and mirrors of non-uniform reflectivity can be used to increase the mode volume of unstable resonators [Perrone *et al.* 1993].

Returning to the system developed by Fletcher [1993], both the amplifier and oscillator were equipped with a positive-branch unstable resonator. These were coupled together to produce injection seeding of the amplifier by the oscillator. We shall give a treatment of how the cavity arrangement works. This treatment will allow us to predict the important result for the Xe III application, which is the divergence of the output beam at the start of the pulse. A different treatment, which considers whether a diffraction-limited mode can be developed before the end of the laser pulse, may be found in Fletcher [1993] and Cotton [1990]. To see how a positive-branch (confocal) unstable resonator works, consider the single cavity shown in Fig. 5.6, which illustrates just such an arrangement.

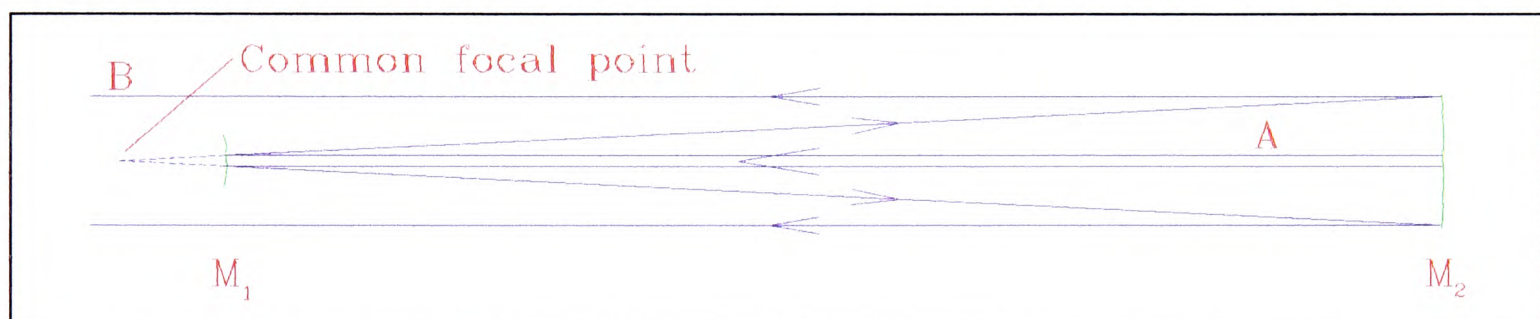


**Figure 5.6.** Confocal unstable cavity.

This shows two mirrors,  $M_1$ , and  $M_2$ , of (positive) focal-lengths  $f_1$ , and  $f_2$  respectively.  $M_1$  is a diverging mirror, whereas  $M_2$  is a converging mirror. The mirrors are arranged such that their foci are coincident. If we consider beam A, it is magnified to become beam B after one cavity round-trip. The magnification,  $M$ , is given by

$$M = \frac{f_2}{f_1} \quad (5.1).$$

In the process, the divergence of the beam falls by the magnification,  $M$  (until it becomes diffraction-limited). At the same time the beam intensity falls, and a fraction  $(1 - 1/M^2)$  of the beam escapes from the cavity. This loss must be (more than) compensated by amplification in the laser gain medium. This requirement restricts the maximum magnification which may be used.

After each round-trip, the remaining  $(1/M^2)$  fraction undergoes exactly the same process on the following round-trip. Thus, the magnification process can repeat indefinitely, while there is still sufficient gain in the laser medium. Furthermore, after sufficient round-trips a diffraction-limited output beam is obtained. The problem with simply using an unstable resonator with an excimer laser, however, is that there is not gain for long enough to give a diffraction-limited beam until the end of the laser pulse, if at all.



The solution to this problem is to use a master oscillator to seed a slave amplifier with low-divergence light. The two laser modules are timed so that the gain in the amplifier does not start until almost the end of the oscillator pulse, when the divergence of the oscillator beam is smallest. The practical arrangement used to achieve this is illustrated in Fig. 5.7.

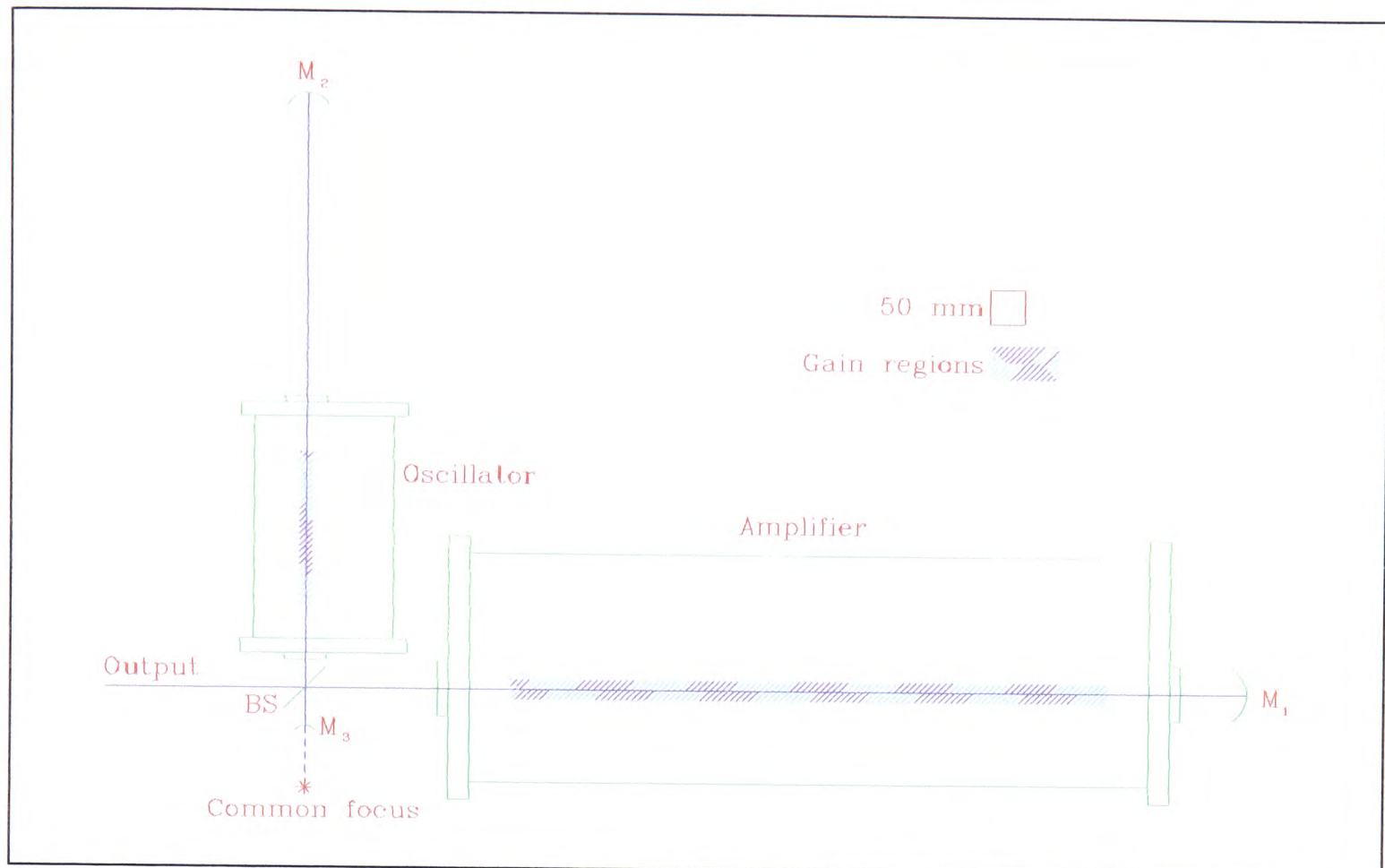


**Figure 5.7.** Coupled confocal cavity arrangement for injection seeding of amplifier. Positions, but not curvatures, of mirrors are to scale for experimental arrangement used for the work described here. BS: beamsplitter.

Both the oscillator and the amplifier are equipped with unstable resonator cavities, and these are coupled together by means of a 50% reflective spot on an AR coated beamsplitter. The spot size (projected onto the beam direction) is 3 mm x 3 mm. For the work described in this thesis the spot was positioned so that the injected beam exactly filled the aperture of the amplifier after a single pass. All the cavity mirrors have a common focal point, and this is known as a coupled-confocal-cavity injection-seeded system.

Fletcher [1993] investigated the influence on the beam divergence of the magnifications,  $M_o$ , and  $M_a$ , of the oscillator and amplifier respectively. The optics were arranged (for most of his experiments) such that the beam reflected by the beamsplitter into the amplifier (from the oscillator) filled the central 20 mm x 20 mm of the ~30 mm x 30 mm gain region. He also investigated the influence of the relative timing of the modules.

He measured the time-averaged beam-divergence by using a beam-profiling camera to image the far field intensity distribution of the system. This experiment was very similar to the one described in §7.2. He found the optimum arrangement was to use mirrors  $M_1$ ,  $M_2$ , and  $M_3$  (Fig 5.7) of focal-lengths 150 cm, 100 cm, and -9 cm respectively, with the amplifier firing 16.9 ns after the oscillator. He defined the divergence to be the FWHM



angle\* in the far field for which the intensity exceeded the peak intensity. For the arrangement described the divergence was 29  $\mu\text{rad}$ .

This optimum configuration was used for the experiments described in chapter 6. The only change made to the cavity was to adjust the relative position of the beamsplitter, so that the beam reflected into the amplifier just filled its full aperture after a single pass.

A crucial consideration for these experiments is the divergence at the start of the laser pulse. Fletcher [1993] neither directly measured nor modelled this. Here, however, we shall estimate it, following a technique described by Coutts [1995].

Coutts [1995] has shown that for copper vapour lasers, the output from an unstable resonator comes from the amplification and repeated magnification of a double-pass ASE seed beam. Excimer lasers show similar gain and pulse duration to copper vapour lasers, and so we shall assume that the treatment of Coutts [1995] is also applicable here. Owing to the relative timing of the oscillator and amplifier, the first ASE from the oscillator will have undergone two round-trips in the oscillator, followed by one in the amplifier, when the gain in the amplifier came on. We may define the geometric divergence,  $\theta_g$ , as the full range of ray exit angles from the system. Implicit in this is a geometrical optics treatment, which is valid until the divergence nears the diffraction limit. Coutts [1995] has shown that the geometric divergence of the KrF beam, after a total of two round-trips of the oscillator cavity, is given by

$$\theta_g = \frac{(M_o - 1)A}{M_o^2 d} \quad (5.2),$$

where  $A$  is the aperture of the gain medium, and  $d$  the mirror separation. This is then expanded in the amplifier, which causes the divergence to fall by a further factor  $M_a$ . This suggests a geometrical divergence in the beam first emitted from the amplifier is given by

$$\theta_g = \frac{(M_o - 1)A}{M_a M_o^2 d} = 104 \mu\text{rad} \times 40 \mu\text{rad} \quad (5.3),$$

for the 19 mm x 7 mm (horizontal x vertical) gain region in the oscillator. This is the full angular spread, however, and we might expect the FWHM to be about half this, *i.e.*  $\sim 50 \mu\text{rad} \times 20 \mu\text{rad}$ .

For the focusing system described in §6.6.1, it is only the vertical divergence which matters. The estimate of 20  $\mu\text{rad}$  is rather over-optimistic. The reason for this is that Fletcher [1993] found  $\sim 29 \mu\text{rad}$  to be the minimum time-averaged divergence which could be obtained from the laser, even when the aperture was filled with laser light, and higher magnification optics were used. This is about twice the diffraction limit, and suggests that the quality of the optics, or inhomogeneities in the gain medium were limiting the minimum divergence which could be obtained. Thus, a divergence of 29  $\mu\text{rad}$  is assumed for all the calculations which follow.

---

\* This was calculated from an 'FWHM area', and so includes a correction for any astigmatism in the divergence.



## 5.2 Modifications to the KrF laser system

### 5.2.1 Electrical changes

#### 5.2.1.1 *Simplified geometry for external driver circuit*

Several changes were made to the electrical design of the laser system when it was reassembled for the Xe III application. The first of these was to simplify the external charging circuit. The reason for this change was that the circuit had many conductors near to each other which had a 60 kV potential difference between them. Not only did this lead to occasional electrical breakdown external to the laser (“*flashover*”), it also necessitated the use of a very complex perspex structure to insulate the various conductors from each other. When this had to be replaced (owing to the failure of the spark gap which was an integral part of it), the electrical circuit was simplified.

This simplification will have had one undesirable side-effect; it will have increased the stray external inductance,  $L_e$ , of the amplifier driver circuit\*. This is undesirable for the following reason (amongst others): a higher inductance in this circuit slows the charge transfer to the peaking capacitors. This means that when avalanche breakdown occurs in the laser gap, the potential over the gap will be rising more slowly than it would otherwise have been. This tends to cause arcing. The reason for this is that inhomogeneities in the electrode will lead to some parts of the laser gap having a lower breakdown potential than the rest. These will break down first. Arcing occurs if too much current flows through one part of the discharge, causing heating of the gas. This increases the local  $E/N$  ratio of the discharge (by reducing  $N$ ), and this increases the local Townsend avalanche rate. This, in turn, leads to a higher current density, which leads to further heating, and so there is positive feedback into the process, and an arc develops. The halogen donor depletion instability (§1.2.1) is another mechanism for similar positive feedback.

Clearly, arcing is most likely in the region of the gap which breaks down first. If the voltage is rising sharply, however, the remainder of the laser gap will break down very soon after the first part to go. Thus, there is not a localised breakdown for long, and arcing is postponed until later in the discharge (it is almost impossible to avoid arcing completely).

A back-of-the-envelope calculation suggests that the extra inductance introduced by the change to the driver circuit was  $\sim 11$  nH. This should be compared to the total external inductance, which may be similarly estimated as at least 150 nH (predominantly associated with the storage capacitors). This  $\sim 7\%$  increase in inductance will have given rise to a  $\sim 3.5\%$  slower rise of the voltage over the laser gap (§3.2).

The change in the driver circuit will have changed the relative timing of the oscillator and amplifier. Thus, the inductance of the variable inductor had to be determined anew, in

---

\* It will also have increased the inductance of the oscillator driver circuit. However, the inductance of this is controlled by the variable inductor, and fixed by the timing requirement, so this does not matter.



order to ensure the oscillator fired 19 ns before the amplifier\*. This was achieved by fitting uncoupled plane-plane cavities to the oscillator and amplifier. The output from the two lasers was attenuated and steered onto a vacuum photodiode, with the optical path to the detector the same for both lasers. The temporal profiles obtained showed both the oscillator and amplifier pulses, with the timing varying according to the number of turns of the variable inductor in the charge-transfer circuit powering the master oscillator.

### 5.2.1.2 *Mechanised electrode winding*

From time to time one of the peaking capacitors in the amplifier module would fail, and have to be replaced. During one such replacement the wound electrode was accidentally broken, and had to be replaced. This involved the winding 400 m of nickel wire around a hollow electrode “substrate”, which was fixed to a lathe. Details of how the wound electrodes were then fixed into the laser system are given by Fletcher [1993].

During the winding process Fletcher [1993] had kept the wire under manual tension. However, this was found not to be an ideal technique - it was very difficult to maintain a constant tension in the wire. This was because the wire would break easily if too much tension was applied, whereas if there was too little tension, the windings would be loose and non-uniform. This led to something of a psychological battle as the winding process neared its end.

An innovation which eased the problem of the winding wire breaking, was the use of less pure (99%) nickel wire. This appeared to be less brittle than the wires which had previously been used (99.98% nickel), presumably because the less pure wires were softer. The more obvious solution to the problem - using thicker wire - was not suitable, since this had been found by Cotton [1990] to give a less uniform discharge.

The eventual solution to the problem of producing uniform windings was to make a mechanical tensioning system for the nickel wire. The device used is illustrated in Fig. 5.8. It was used by fixing it to the automatic feed of the winding lathe. The device employed a variable friction clutch (seen on the left of Fig. 5.8) to determine the tension in the wire. This was adjusted so that the wire just did not break when winding was started. A tension of  $\sim 4.4$  N was used, and a very uniform winding resulted.

---

\* In fact, a recent re-evaluation of the timing experiment suggests that the amplifier may have fired several ( $\sim 5$ ) nanoseconds too soon. Furthermore, there was  $\sim 1.5$  ns jitter in the timings. This means that the estimate of 29  $\mu$ rad for the beam divergence at the very start of the pulse, was not justified. This might not be detrimental for the Xe III application - a low intensity preheating plasma is preferable to a high-intensity one. However, as we shall see in §7.2, a quite different problem limited the divergence of the system for the experiments described in chapter 6, and thus the suspected timing mismatch will not have affected any of the experimental results presented in this thesis.



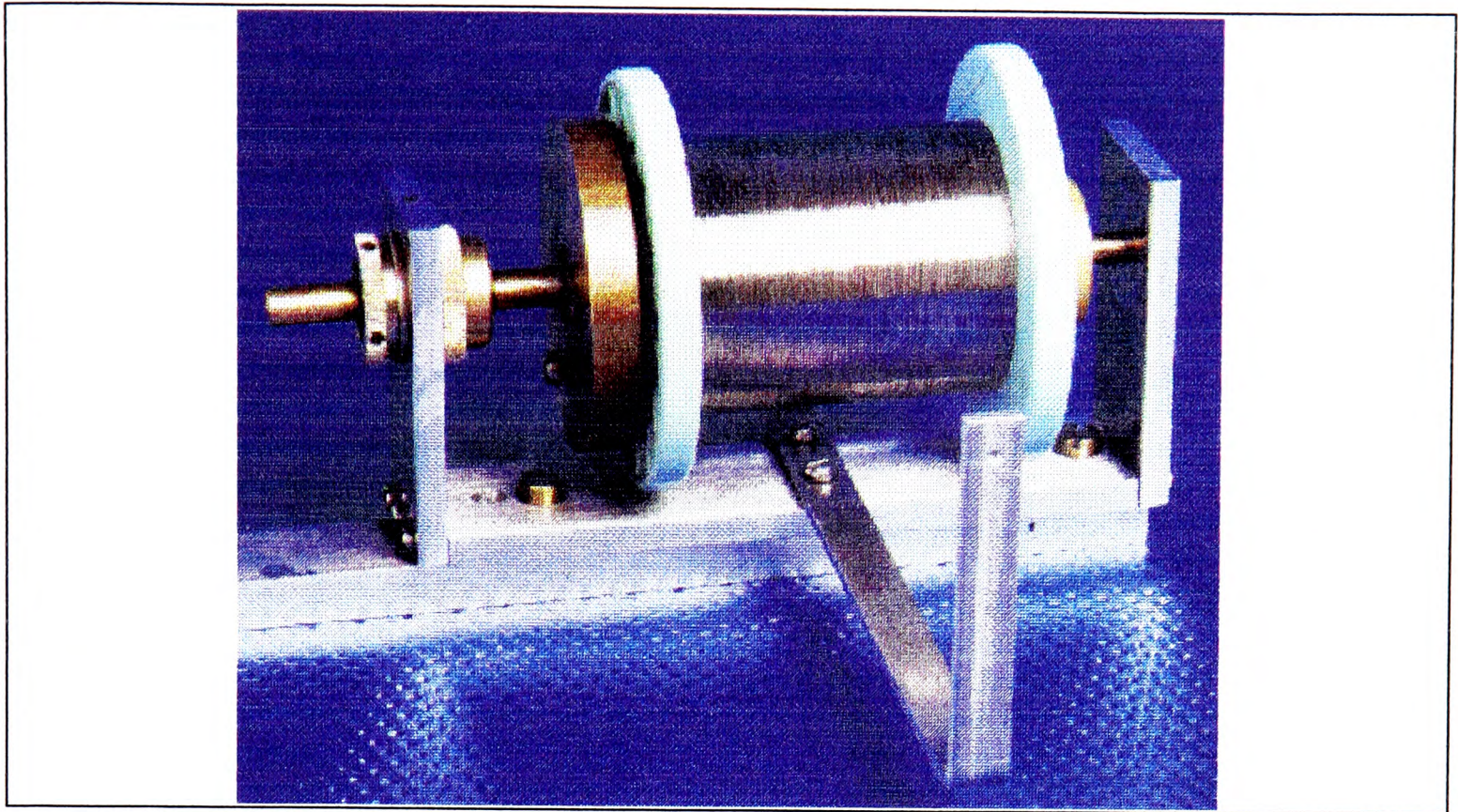


*Figure 5.8. Mechanical tensioning system used in the winding of mesh electrodes. System is shown holding a spool of wire for winding.*

## 5.2.2 Minor modifications

Maintenance and minor repairs to the KrF laser consumed a significant fraction of the experimental time devoted to the project. A home-built laser has the advantage of being easily repaired, but the disadvantage of being a prototype, and hence rather unreliable. For the sake of brevity, we will not go into the details of the repairs and minor modifications made, except to comment:

- Electrical noise caused severe problems, both to various pieces of electrical equipment used nearby, and to parts of the laser system itself (trigger unit and gas purifier).
- A safety dump switch was fitted to the 60 kV power supply. This ensured that when the power to the laser was switched off, the storage capacitor was rapidly discharged, reducing the risk of a possibly-fatal electric shock. A mechanical fault led this switch to close during normal operation, and this caused a small fire, owing to heating in the discharging resistor. In order to prevent a recurrence of this, the switch was interlocked in a more fail-safe manner, both mechanically and electrically, so that when it closed the power supply would switch itself off.

## 5.3 A safe solid-state fluorine source

### 5.3.1.1 Introduction

One of the practical difficulties in using a KrF laser is the handling of fluorine gas. This was underlined, when on one occasion during the project, there was a leak from part of the high-pressure fluorine supply system due to the failure of a seal. This led to water vapour from the air getting into part of gas delivery system, which in turn led to the formation of HF. This is highly corrosive, and several other seals in the system failed at the same time, presumably because of this.



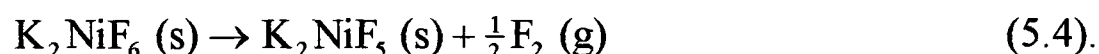
If a way could be found to supply fluorine without the need for a high pressure gas bottle, this would clearly be very desirable. Towards the end of the project\*, such a system became commercially available for the first time. This section describes experiments which were conducted in order to evaluate this novel solid-state fluorine source, for application to KrF laser systems.

### 5.3.1.2 The fluorine source

It was clear for many years that a solid state fluorine source for excimer lasers was a desirable goal. First, we shall describe how this has recently been achieved. This description is a summary of a private communication from McGrady [1995].

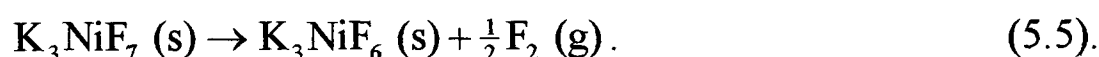
The key idea behind the system is that the oxidising power of fluorine can be exploited to prepare fluorides of a transition metal, M, in unusually high oxidation states. Generally, these are subject to extra stability in the form of complex ions derived from octahedral co-ordination of the metal by six small, electronegative fluoride ligands, with the formation of strong M-F bonds. The metal is found in a complex anion of the form  $\text{MF}_6^{n-}$  where  $n = 1-3$ . If a suitable redox reaction can be instigated, the oxidation state of the metal may be reduced, and elemental fluorine may be evolved. Thus, the compound containing the  $\text{MF}_6^{n-}$  may be used as a solid state source of fluorine.

Early studies [Klemm & Huss 1949] with an Ni(IV)→Ni(III) system focused on the compound  $\text{K}_2\text{NiF}_6$ , which decomposes when heated according to



This proved unrewarding - no significant amounts of fluorine gas were evolved below 500° C. The significance of this is that 500° C is approximately the maximum temperature which may be used with a nickel vessel before severe fluorine corrosion occurs.

The reason reaction (5.4) was not successful was that, although the entropy increase on the formation of  $\text{F}_2$  gas makes the reaction more favourable as the temperature is increased, the structure of the  $\text{K}_2\text{NiF}_6$  is not suitable. This is because all the fluorine in the complex is bound in  $\text{NiF}_6^{2-}$  ions and the Ni-F bonds are very strong. Asprey [1976a, 1976b] found a way around this problem, viz. the addition of KF to reaction (5.4). This gives



At a temperature of a few hundred degrees Celsius reaction (5.5) yields a partial pressure of up to a few hundred millibars of fluorine gas. The explanation proposed by Asprey [1976a] and McGrady [1995] for this improvement is that  $\text{K}_3\text{NiF}_7$  adopts a structure which may be formulated  $[\text{K}_2\text{NiF}_6] \cdot \text{KF}$ . This contains two types of anion,  $\text{NiF}_6^{2-}$  and  $\text{F}^-$ . The latter anion may be evolved as fluorine gas on heating, without the breaking of any strong covalent Ni-F bonds.

### 5.3.1.3 Installation of fluorine source

Reaction (5.5) is exploited in the fluorine source investigated here (Oxford Lasers Pure F20). The  $\text{K}_3\text{NiF}_7$  is contained in a high nickel alloy (Monel 400) vessel, surrounded by a thermostatically controlled heater. At room temperature the equilibrium pressure of

---

\* After the experiments described in chapter 6, but before those described in chapter 7.



fluorine is negligible. This makes the source intrinsically safe. When heated, the solid evolves fluorine, which is removed via valves in the vessel.

When exhausted, the source may be recharged. This requires heating the  $\text{K}_3\text{NiF}_6$  reaction product in the presence of excess fluorine gas. This process requires specialised gas handling equipment, and is undertaken by the manufacturers. The capacity of the source was quoted as  $\sim 14 \text{ dm}^3$  of fluorine at atmospheric pressure, sufficient for  $\sim 30$  fills of the KrF laser. At the time of writing it has provided 23 fills, and is not yet exhausted. The only maintenance recommended by the manufacturer is the occasional pumping on the source while it is heated to  $150^\circ \text{C}$ . This temperature is too cool for fluorine evolution, and so the process can remove contaminants from the system.

The source was plumbed into the gas system in its simplest possible configuration, replacing the gas cylinder which had previously been used to provide fluorine. A thermostatic temperature controller was installed, and the fluorine source was operated at approximately  $350^\circ \text{C}$ . Once this temperature was achieved (after a warm-up time of about fifteen minutes), the source evolved a pressure of  $\text{F}_2$  sufficient to fill to the working pressure the  $80 \text{ dm}^3$  volume of the laser in two minutes. Faster filling was possible if the source was heated a further few tens of degrees, or if  $\text{F}_2$  was allowed to evolve for a further few minutes after the working temperature had been reached, but before any gas was drawn from the source vessel.

## 5.3.2 Characterisation of the source

### 5.3.2.1 Pulse energy & gas lifetime

The first experiment conducted with the source was to measure the pulse energy and gas lifetime of the laser when it was filled with gas from the F20 source, compared with when fluorine from a conventional gas bottle was used. The laser was set up as described in the previous sections, and fired every 4.8 s for thirty minutes. It was then rested for 10 minutes, and the process repeated. The purpose of this intermittent operation was to show up, if present, any reversible decay in the pulse energy. Such decay might have been caused by, for example, heating effects, or incomplete replacement, between shots, of the laser gas in the gain region. No such decay was found.

The results initially obtained are shown in Fig. 5.9. Each point represents the mean energy of eight successive laser pulses, measured with a pyroelectric detector (Gentec ED 500). It seems from Fig. 5.9 that the pulse energy shows qualitatively different behaviour for gas from the two sources. In particular, an increasing pulse energy after a few hundred shots was found when fluorine from the F20 source was used. This initial rise was not present when the gas cylinder supplied the fluorine.



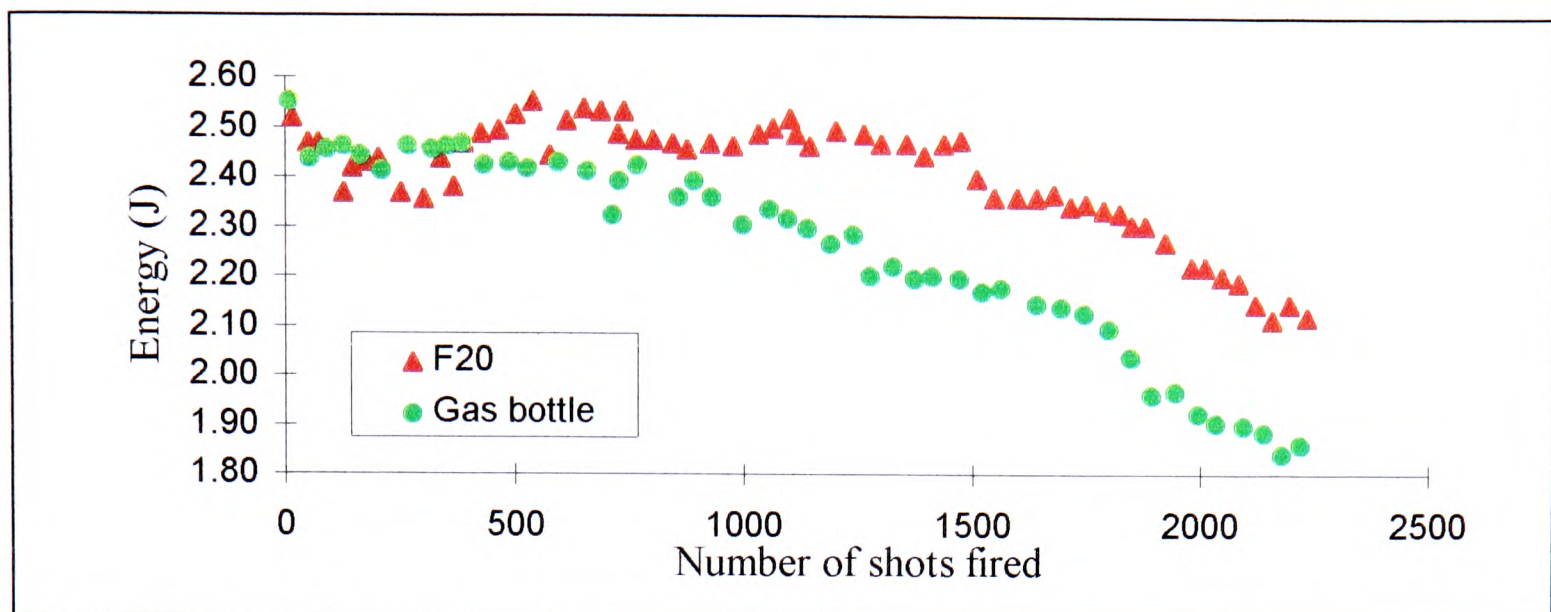


**Figure 5.9.** Energy obtained from KrF laser system, as function of number of shots fired, according to source of fluorine. Note vertical scale has suppressed zero.

For any given KrF laser system there is an optimum partial pressure of fluorine, which gives rise to the maximum laser pulse energy. The rise in pulse energy observed with the F20 gas fill could be explained if more than this optimum partial pressure of fluorine had been present. In this case, the rise in pulse energy corresponds to a fall in the partial pressure of fluorine present in the laser, as the fluorine reacts with exposed surfaces. The initial fall observed could be explained by the production of absorbing impurities in the laser gas. This is discussed further in §5.3.2.3.

Filling the laser with pure fluorine (as when using the F20 source) requires the measurement of a pressure twenty times smaller than when it is filled with a 5% mixture of fluorine in helium (as when using the gas cylinder). Thus, the mechanical gauge used when filling the laser to measure the pressure of fluorine, was used over different ranges for the two scenarios. The gauge was recalibrated, against a mercury manometer. A liquid nitrogen trap was used to preclude contamination of the laser system by mercury vapour.

The recalibration indicated that the gauge had been under-reading by 15% for the pressure range in which it was used for the supply of fluorine and helium mixture from the cylinder (leading to a partial pressure of 5.1 mbar of fluorine), but was accurate over the pressure range used for the pure fluorine gas fill (5.8 mbar partial pressure). In all cases the partial pressure of krypton was 122 mbar, and the remainder was helium to a total pressure of 4 bar absolute. All the laser-gas pressures given in this thesis have been corrected for the inaccuracy of this gauge.

The experiment described above was repeated, but this time with the same pressure of fluorine in both cases. The F<sub>2</sub> partial pressure used was 5.1 mbar, *i.e.* the pressure which had been found to be optimal by Fletcher [1993]. The results obtained are shown in Fig. 5.10.



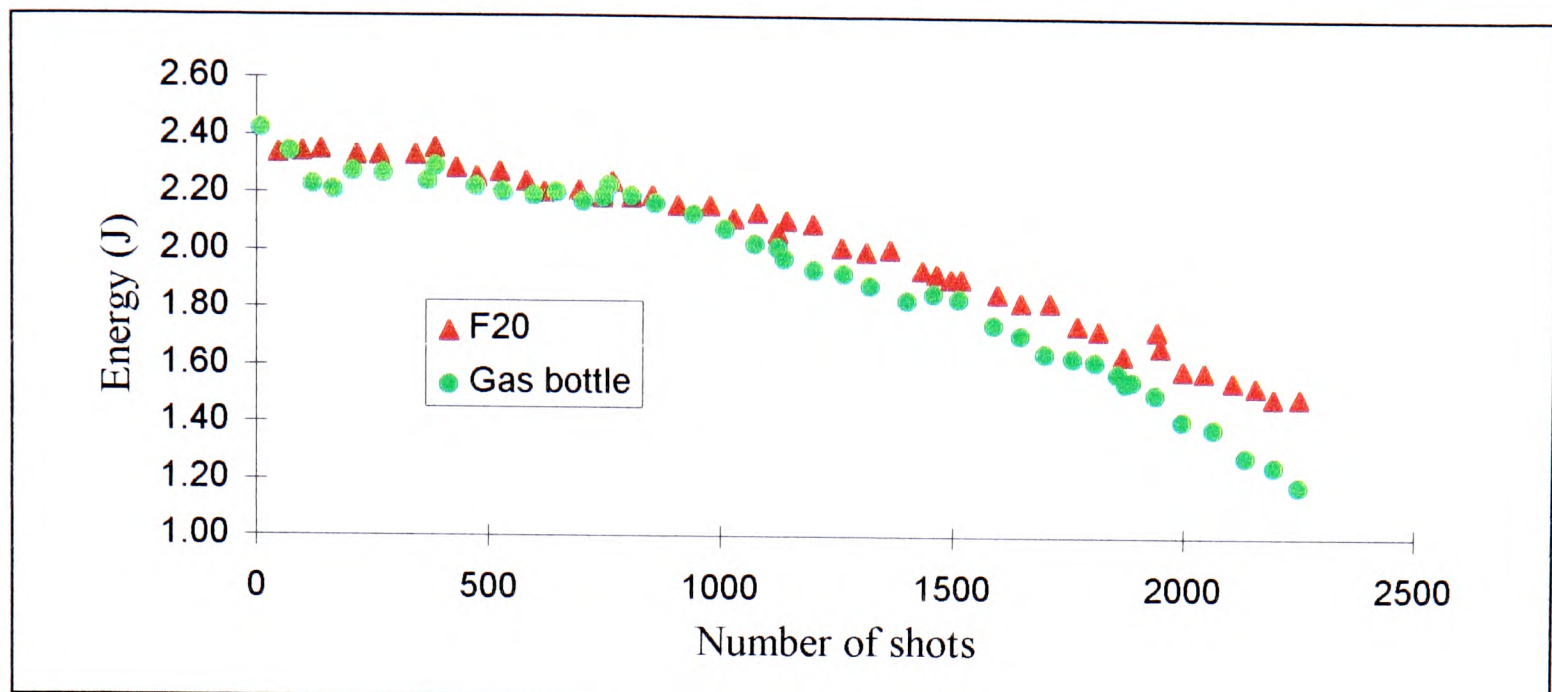


**Figure 5.10.** Repeat of experiment depicted in Fig. 5.9, with identical pressures of  $F_2$  in both cases. Graph shows energy obtained from KrF laser system, as function of number of shots fired, according to source of fluorine. Note vertical scale has suppressed zero.

There are several salient features of these sets of data, which we shall consider:

- The gas lifetime for  $F_2$  from both of the sources was found to be very similar when the initial pressures were the same (Fig. 5.10).
- The results obtained with the bottled gas fill in Figs. 5.9 and 5.10, are directly comparable. However, we can see that for the second set of data the pulse energies were initially  $\sim 9\%$  lower, and decayed faster.
- The highest energy pulses (2.55 J) were 14% more energetic than those obtained by Fletcher\*, from the same cavity. These pulses were obtained with the gas from the F20 source, and at a higher partial pressure than was used for the other experiments.
- 2.5 J pulses were obtained from the laser system when bottled  $F_2$  was used. This is 9% greater than those obtained by Fletcher, under nominally the same operating conditions.

### 5.3.2.2 Explanation of gas-lifetime results

We shall propose plausible explanations for the results observed. It is important to note that the data for Fig. 5.9 were obtained seven months before those illustrated in Fig. 5.10. Furthermore, the amplifier windows were uncoated for the later experiment, whereas they were AR coated (on the outside only) for the earlier experiment. Also, the beamsplitter used in the optical cavity for the second experiments was damaged, and so the optical feedback will have been less effective in this case. This explains the lower initial pulse energy found in the second experiment. The faster decay of the pulse energy is harder to explain, but may be because of a different chemical environment in the laser for the two sets of data. One possible cause of this is the backstreaming of the oil from the rotary pump used to pump the laser continuously when not in use. Another possibility is the presence of a slight leak in the laser envelope (allowing water vapour in during the pumping phase).

The fact that higher pulse energies than those found by Fletcher were obtained from the laser system when bottled  $F_2$  was used, may be explained by the new electrode winding scheme (§5.2.1) giving rise to a more uniform electrode. This is of paramount importance

\* Private communication, 1996



in excimer lasers [Cotton 1990, Fletcher 1993]. The reason is that uniform electrodes give a more even distribution of the electrical energy into the laser gas. This delays the onset of arcing, and in the current system, will have compensated for the higher inductance of the driver circuit (§5.2.1).

A more uniform electrode can also explain why still better results were obtained by using more  $F_2$  in the laser gas mix, although it should be pointed out that the following explanation is not the only possible interpretation of the experimental results. Consider the fall and then rise of the pulse energy observed with the F20-supplied  $F_2$  at 5.8 mbar (Fig. 5.9). A plausible explanation for this is the rapid generation of absorbing impurities (initial fall) followed by a reduction in fluorine concentration to the kinetically-optimum partial pressure (subsequent rise). If this is the case, then the optimum fluorine concentration is greater than the 5.1 mbar found by Fletcher [1993].

To see why this is so, suppose, for the sake of argument, that the optimum fluorine concentration is indeed 5.1 mbar. In this case, if we put too much fluorine into the initial gas mix, we would expect the pulse energy to rise as the fluorine reacted, until the partial pressure of fluorine was 5.1 mbar. However, when this was the case there would be more impurities in the gas mixture than would have been present if 5.1 mbar of fluorine had been added initially. Thus, although the pulse energy would peak when 5.1 mbar of fluorine remained, the peak energy would be lower than would be obtained from fresh a gas mixture containing 5.1 mbar of fluorine. In fact, we see that this is not the case (Fig. 5.9), which suggests that the optimum pressure of fluorine is greater than 5.1 mbar. Thus, when only 5.1 mbar of fluorine was used, the optimum pressure was never attained, whereas when more fluorine (5.8 mbar) was used, the optimum pressure was attained as the partial pressure of fluorine fell.

In other words, the optimum partial pressure of fluorine using the new electrode winding is greater than with the previous electrode winding. The reason that there is an optimum partial pressure of fluorine in a KrF laser is that there is a conflict between more fluorine giving rise to a greater inversion density, and it making the laser gas electrically hard (*i.e.* difficult to break down). The cause of this electrical property is that the gas is electronegative and “mops up” electrons in a discharge by the formation of negative ions, by reaction (1.12). This means that a high partial pressure of fluorine causes avalanche breakdown in the laser gap to be delayed. This leads to breakdown on a slower-rising part of the voltage pulse over the laser gap (as discussed in §5.2.1.1) and so it may cause discharge instability. However, a more uniform electrode profile can compensate for this, and this may explain why it appears that a greater partial pressure of fluorine is desirable with the new electrode winding.

### 5.3.2.3 Gas purity considerations

Another factor which is important in understanding the effect of introducing the solid-state fluorine source is the gas purity. The Oxford Lasers GP2000 gas purifier plays an important role in this. This contains a cold trap, which was operated at 105 K, and is used to condense impurities from the laser gas. The device also provides gas circulation around the laser system.

The only report in the literature of the use of a solid-state fluorine source with an excimer laser has been given by Baughan *et al.* [1994]. They found that gas from such a source was purer than its bottled equivalent. Indeed, this was the main claim of the first patent on the use of a solid-state fluorine source [Asprey 1976b]. In particular, Baughan *et al.* [1994] report significantly lower concentrations of HF,  $CO_2$ ,  $CF_4$ , and  $SiF_4$  in



fluorine gas obtained from an F20 source, compared to an He/F<sub>2</sub> mixture from a gas cylinder. Of these contaminants, only CF<sub>4</sub> is not solidified in the 105 K cold trap in the GP2000. Indeed, the removal of CF<sub>4</sub> is an unsolved technological problem in fluorine-based excimer lasers. Ito *et al.* [1996] have recently proposed a removal technique employing a cooled (-50 °C) activated charcoal filter. However, this requires the fluorine gas to be removed from the mixture beforehand, and so is only useful as a means of re-using expensive inert gases from one gas fill to the next.

Further CF<sub>4</sub> will have formed when the laser was fired; the necessary carbon being photolysed from the exposed organic materials in the laser gas envelope (especially the insulating coating around the peaking capacitors). Although CF<sub>4</sub> does not absorb significantly at the KrF laser wavelength, it can be expected to absorb the deep-UV preionising radiation very strongly. Thus, it can be expected to reduce the efficacy of the preionisation, and so reduce the output energy of the laser system.

There is no evidence in the experimental results presented here to show that the expected higher purity of the F20-supplied fluorine, gave rise to better performance of the laser. Although the results shown in Fig. 5.10 do show a longer gas-lifetime for the F20-supplied fluorine, it is not safe to infer that this is because of an enhanced purity. This is because of a ~4% random error in the measurement of the fluorine (and krypton) pressures for the bottled gas. Thus, the experiment would have to be repeated several times, before such an effect was shown conclusively. Furthermore, the most obvious effect that one would expect from the use of more pure fluorine, is a higher *initial* pulse energy, rather than a longer gas-lifetime. As can be seen in Fig. 5.10, no evidence for such an effect was observed.

It should be pointed out that the home-built laser used here is extremely far from the state-of-the-art in terms of its fluorine compatibility. For a more fluorine-compatible laser, one would expect the initial purity of the laser gas to have a greater effect on the laser performance, especially if cryogenic purification were not used. For example, Lou *et al.* [1990] have speculated that HF played a very important role in limiting the gas-lifetime of a particular KrF laser which did not employ cryogenic purification.

#### 5.3.2.4 Conclusions about pulse-energy

It is easy to devise further experiments which might have shed more light on the effects of gas-purity on the KrF laser system. Possibilities include IR or mass spectroscopy analysis of the laser gas mix as a function of time, or the operation of the laser system without cryogenic purification, not to mention repeating the experiments described here. However, these experiments would have been expensive in time and laser gas, and only of limited benefit to other workers in the field, because they would relate to the chemical conditions in this specific, and chemically fairly dirty laser system. A further consideration is the gas delivery system. For obvious safety reasons, bottled fluorine must be stored in a fume cupboard, or outside the laboratory building, and this inevitably requires long pipes for delivery to the laser system. Contamination of fluorine by reactions in this pipework must also be considered [Ito *et al.* 1996]. For a solid-state source, however, a much shorter delivery pipe may be used. For example, in the installation described here the length of the fluorine delivery pipe was reduced by a factor of five.

The important conclusion to be drawn from the work is that the energy output from the system was at least as good with gas from the F20 source as it was from the conventional bottled source. Of course, this comes as no surprise, but it does indicate, for example, that



there is not some impurity in bottled fluorine gas which makes (discharge-excited) KrF lasers work better.

Furthermore, the 2.55 J single-pulse energy obtained from the laser system makes it of world-class performance. Specifically, this laser system has achieved the highest single-pulse energy yet reported for a conventional-aperture UV-preionised discharge excited KrF laser. The next best such system was reported by Nodomi *et al.* [1991], who obtained 2.5 J pulses, from a laser aperture of 65 mm x 50 mm. This was significantly more complex than the laser system presented here, relying on three sets of capacitors, and a magnetic switch (saturable inductor) with a circulating silicone oil system for cooling and insulation.

A slightly higher energy, of 2.6 J, has been obtained from a UV preionised, discharge excited KrF laser with the aperture widened in one direction [Kovács & Szatmári 1994]. It gives 75 mm x ~10 mm\* beam profile, which restricts its use to short pulse off-axis amplification. It too, employs a much more complicated electric circuit than the laser system described in this work, using a thyratron, a spark gap, a magnetic switch, and an optically activated rail-gap switch.

#### 5.3.2.5 Temporal profiles

Some measurements of the temporal profiles of the laser pulses were made, according to the source of the laser gas. The whole beam was detected, using the detection system described in §3.2.1.3. No significant difference was observed. Fig. 5.11 shows typical temporal profiles obtained.

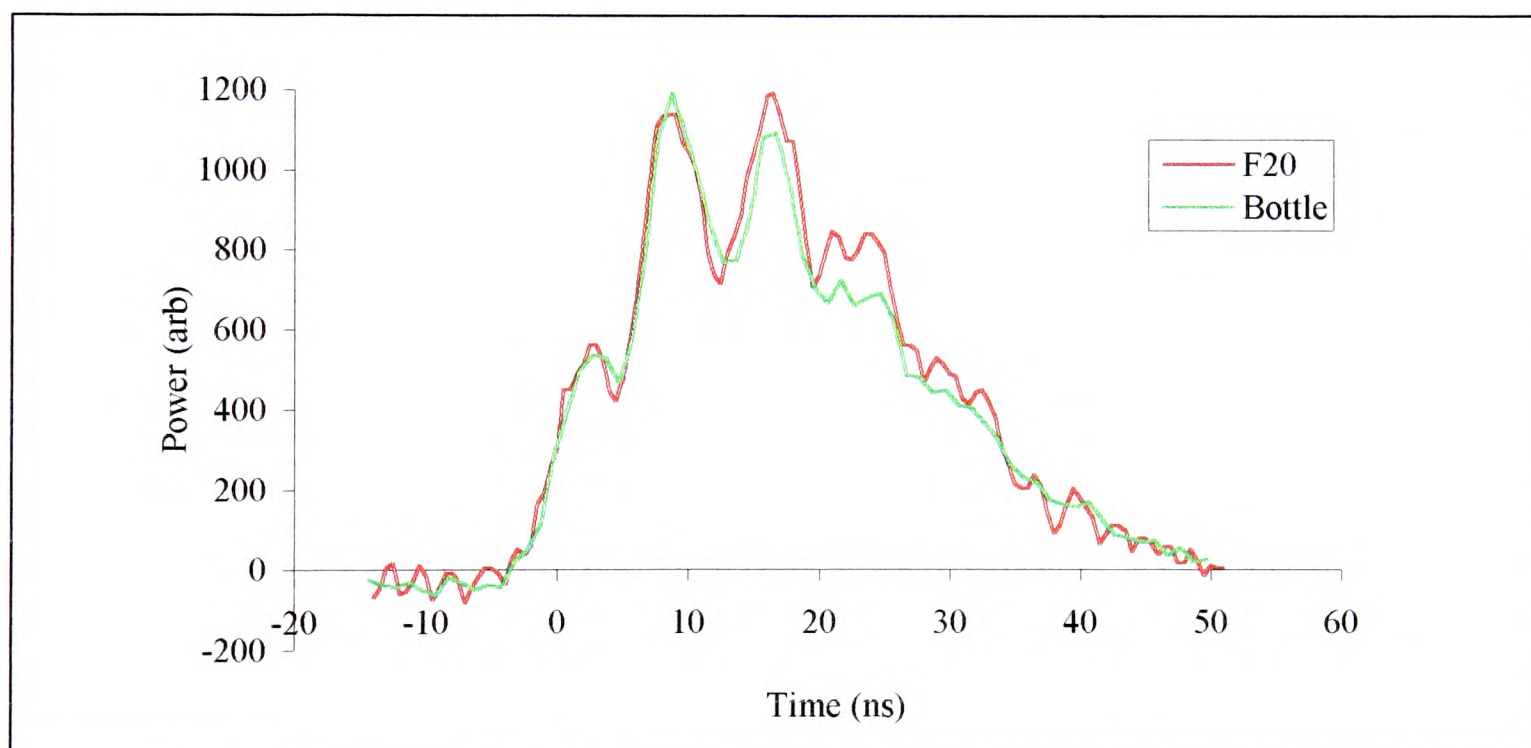


**Figure 5.11.** Temporal profile of KrF beam according to source of fluorine. In both cases 5.1 mbar of fluorine was used, and profiles were taken after laser had fired ~375 shots. Timing and powers are not consistent between the profiles. Note that the profiles were taken using a damaged beamsplitter, to couple the oscillator and amplifier. Thus, the rise is slower than the profile illustrated in Fig. 6.12, owing to less efficient seeding at the switch-on of amplifier gain.

An obvious feature of the profiles illustrated in Fig. 5.11 is the oscillation of the output power. The period of this oscillation is  $7.6 \pm 0.2$  ns, which does not correspond to the

---

\* Kovács & Szatmári [1994] do not give the shorter dimension. It has been estimated here from a diagram of their discharge module.



round-trip time of either the oscillator or the amplifier cavity (6.1 ns and 9.4 ns respectively). A possible explanation for this is LC ringing of the internal discharge loop in the amplifier module. A period of 7.6 ns is fairly typical for an excimer discharge loop [Kearsley 1980], and corresponds to an impedance of 0.02 nH, for the 65 nF peaking capacitance.

## 5.4 Nitrogen dioxide: a variable attenuator for KrF laser radiation

### 5.4.1 Introduction

An NO<sub>2</sub> gas absorption cell was used to attenuate the KrF beam, at various stages of the experiments described in this thesis. The use of such a cell (as a method for measuring the gain of rare-gas halide lasers) was first proposed by Armandillo *et al.* [1982]. By varying the pressure of gas in the cell, it was possible to vary the attenuation provided. This section describes novel work to calibrate and to investigate the limitations of the system. This work has also been reported in the *Journal of Measurement Science & Technology*, and this paper is annexed at the end of this thesis [Whybrew & Webb 1995].

The apparatus consisted of a silica windowed absorption cell, rotary gas pump, gas supply, and pressure gauge. The cell could be interconnected and isolated as necessary. The NO<sub>2</sub> (Air Products, 99.5%) was stored as a pressurised liquid, and vapour drawn off as required, into the absorption cell, which was then isolated from the gas supply. The stainless steel absorption cell had a path length of 5 cm, and a clear circular aperture of diameter 5 cm. The arrangement is illustrated schematically in Fig. 5.13, and can be seen in the photograph of Fig. 5.1.

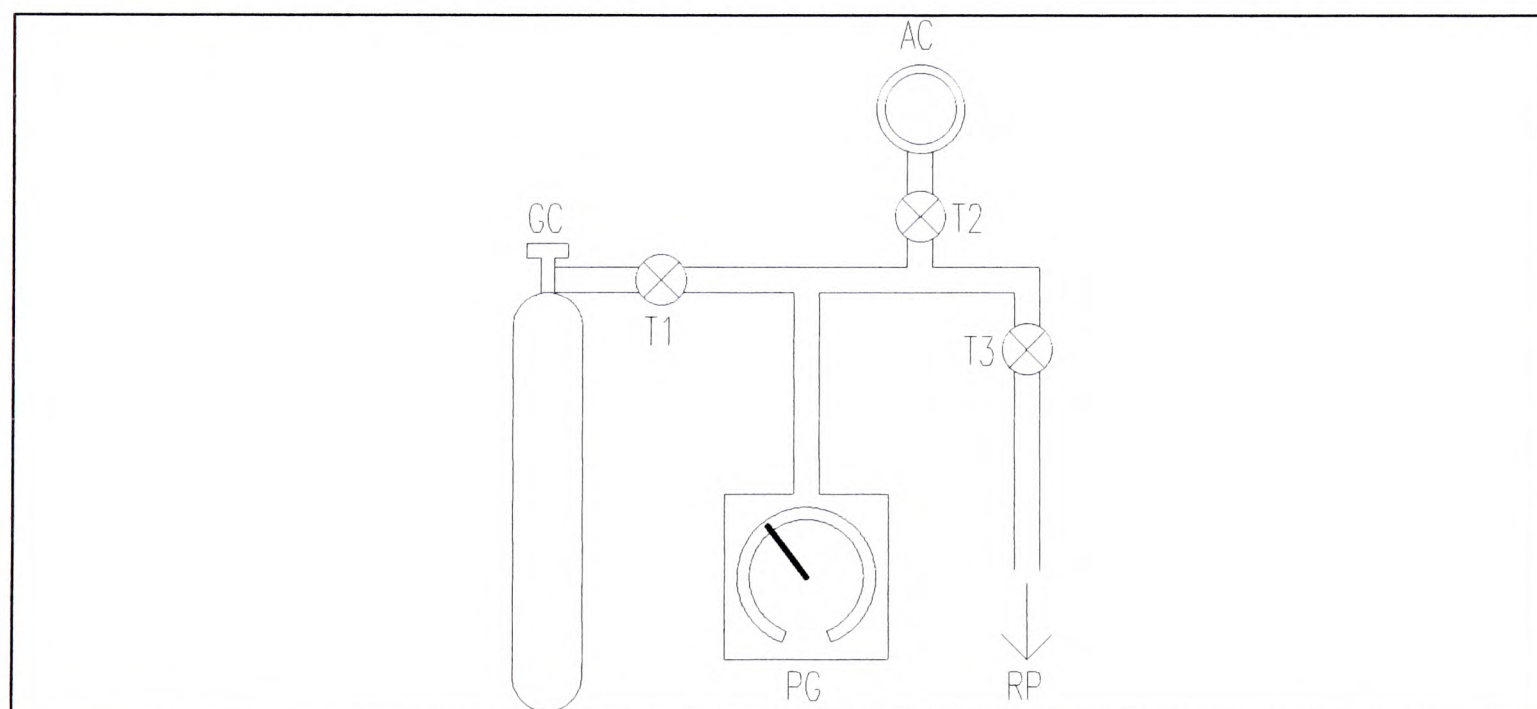


**Figure 5.13.** Schematic of gas system for NO<sub>2</sub> absorption cell. Abbreviations: GC, gas cylinder; T1, T2, T3, gas taps; PG, pressure gauge; AC, absorption cell; RP rotary pump.

### 5.4.2 Physical chemistry of the NO<sub>2</sub> ⇌ N<sub>2</sub>O<sub>4</sub> equilibrium

To model the absorption of the NO<sub>2</sub> cell we must consider the chemical equilibrium:





We define the partial pressure equilibrium constant\*,  $K_p$  according to

$$K_p = \frac{P_{\text{NO}_2}^2}{P_{\text{N}_2\text{O}_4}} \cdot \frac{1}{P^0} \quad (5.7)$$

where  $P_{\text{NO}_2}$  and  $P_{\text{N}_2\text{O}_4}$  are the partial pressures of  $\text{NO}_2$  and  $\text{N}_2\text{O}_4$  respectively, and  $P^0$  is one standard atmosphere, 101.32 kPa.  $K_p$  shows a strong temperature,  $T$ , dependence, which is found empirically to obey [Plekhothin 1970]

$$\lg(K_p) = -\frac{2692}{T} + 1.751\lg(T) + 4.83 \times 10^{-3} T - 7.144 \times 10^{-6} T^2 + 3.062 \quad (5.8).$$

Using (5.7) and (5.8) we may calculate the equilibrium composition of a mixture of  $\text{NO}_2$ , and  $\text{N}_2\text{O}_4$ , as a function of pressure,  $P$ . Three such composition curves are given in Fig. 5.14.

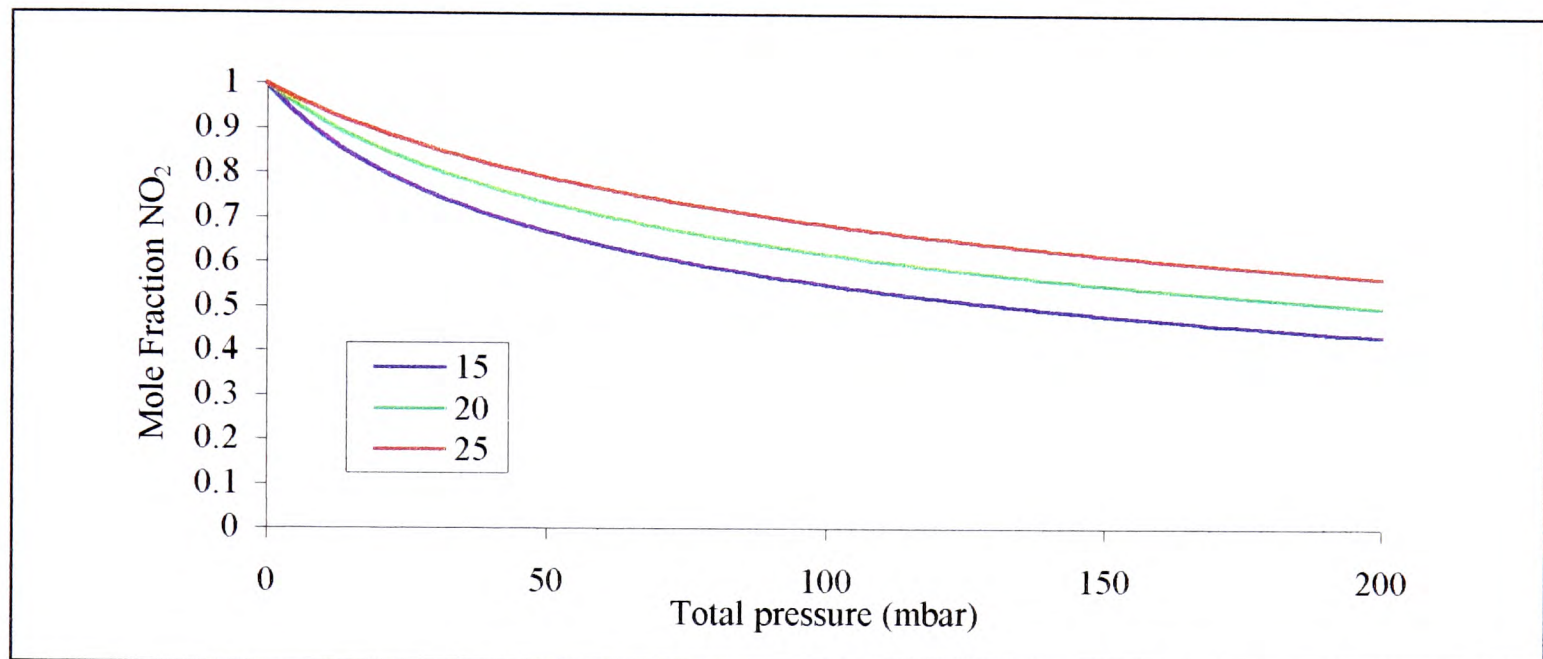


**Figure 5.14.** Calculated mole fractions of  $\text{NO}_2$  in an equilibrium mixture with  $\text{N}_2\text{O}_4$ , as a function of total pressure and temperature (in degrees Celsius).

$\text{NO}_2$  has an absorption cross-section for KrF radiation,  $\sigma_{\text{NO}_2}$ , about 16 times smaller than  $\sigma_{\text{N}_2\text{O}_4}$ , that of  $\text{N}_2\text{O}_4$  [Hall & Blacet 1952], and so we model the absorption coefficient,  $\alpha$ , as

$$\alpha = N_{\text{NO}_2} \sigma_{\text{NO}_2} + N_{\text{N}_2\text{O}_4} \sigma_{\text{N}_2\text{O}_4} \quad (5.9)$$

where  $N_{\text{NO}_2}$ , and  $N_{\text{N}_2\text{O}_4}$ , are the number densities of  $\text{NO}_2$  and  $\text{N}_2\text{O}_4$  respectively. Combining (5.7), (5.8), and (5.9), assuming ideal gas behaviour, we can find  $\alpha$ , as a function of temperature and total pressure

$$\alpha = \frac{1}{k_B T} \left[ P \sigma_{\text{N}_2\text{O}_4} + \frac{(\sigma_{\text{N}_2\text{O}_4} - \sigma_{\text{NO}_2}) (K'_P - \sqrt{K'^2_P + 4PK'_P})}{2} \right] \quad (5.10)$$

where

$$K'_P \equiv K_p \cdot P^0 \quad (5.11).$$

\*See, for example, Moore [1984].



Armandillo *et al.* [1982] give a different expression to expression (5.10), for the case of small total pressures,  $P$ . Their expression is dimensionally incorrect, however. The small pressure approximation of (5.10) is

$$\alpha = \left( \frac{\sigma_{NO_2}}{k_B T} \right) P + \left( \frac{\sigma_{N_2O_4} - \sigma_{NO_2}}{K'_P k_B T} \right) P^2 + O(P^3) \quad (5.12).$$

### 5.4.3 Absorption measurements

Expression (5.10) was tested by measuring the transmission of the  $NO_2$  cell as a function of the total pressure in it. The temperature of the cell was measured (determined by the ambient temperature in the room, measured with a total-immersion mercury-in-glass thermometer). Data were taken at two temperatures, namely 23.3 °C, and 25.4 °C. Light was provided by the KrF oscillator described in §5.1.2.1 with a plane-plane cavity, delivering about 75 mJ per pulse over a  $\sim 2 \text{ cm}^2$  area. The data were fitted to expression (5.10), allowing for the  $(81 \pm 2)\%$  transmission of the empty cell (due to fresnel losses at the window surfaces). The fits were optimised (using a spreadsheet) with  $\sigma_{NO_2}$  and  $\sigma_{N_2O_4}$  as free parameters. Table 5.1 gives the results obtained, and Fig. 5.15 a fit to one of the sets of data.

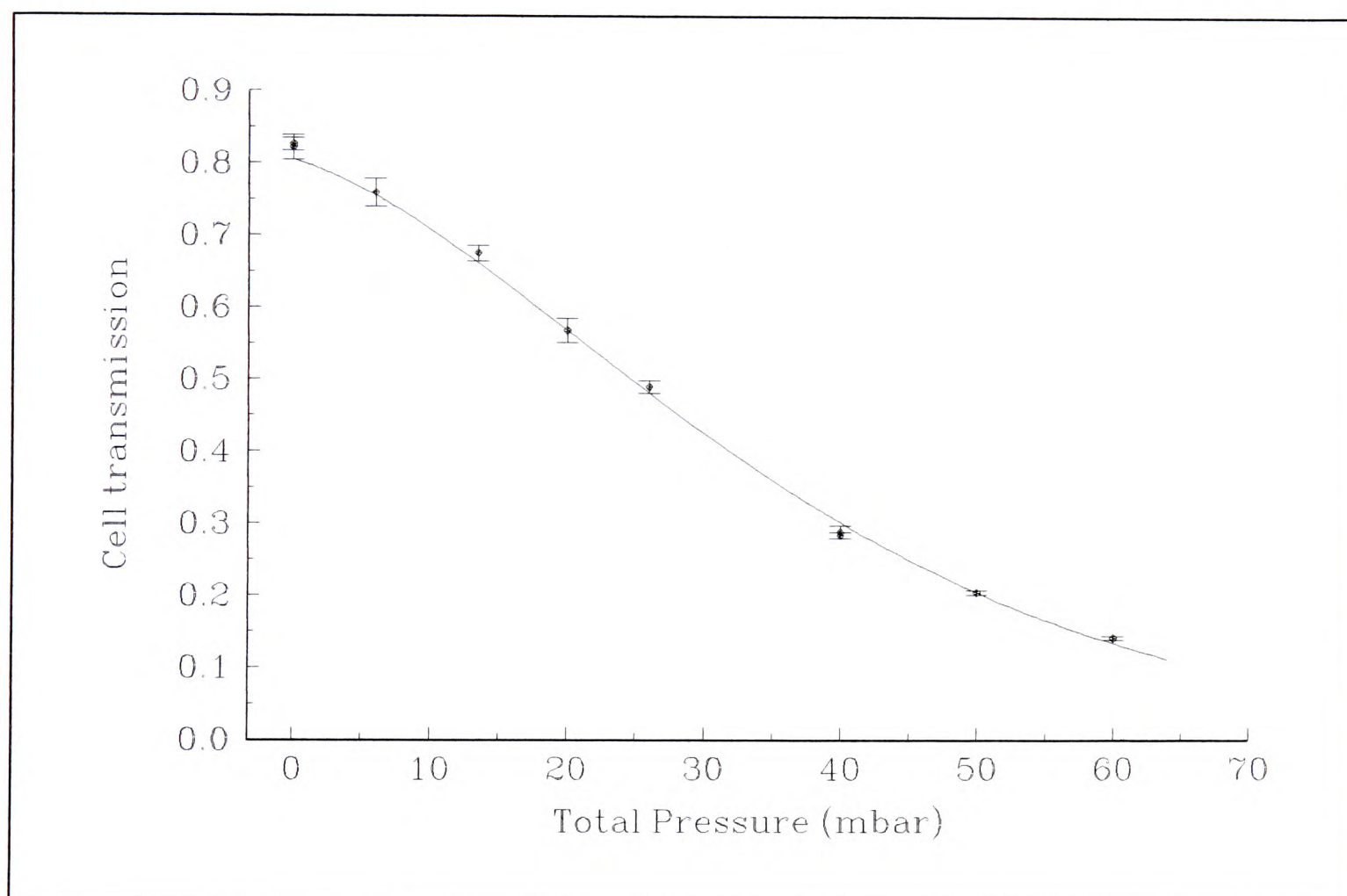


**Figure 5.15.** Transmission of  $NO_2$  cell as a function of total pressure, at 25.4 °C. Curve is based on cross-sections given in Table 5.1, and model of expression (5.10).

	This work	Hall & Blacet [1952]	Armandillo <i>et al.</i> [1982]
$\sigma_{NO_2} (10^{-24} \text{ m}^2)$	<b>6±1</b>	4-7	8.9
$\sigma_{N_2O_4} (10^{-24} \text{ m}^2)$	<b>87±5</b>	88.2	24

**Table 5.1.** Absorption cross-sections for 249 nm light of  $NO_2$  and  $N_2O_4$  found in this work and reported in the literature.



From these results it is clear that the model given here accurately predicts the cell transmission, and that the cross-sections measured agree closely with those measured by Hall & Blacet [1952]. The results disagree, however, with those of Armandillo *et al.* [1982]. There are two reasons for this. Firstly, Armandillo *et al.* [1982] assumed the absorption of the mixture of  $\text{NO}_2$  and  $\text{N}_2\text{O}_4$  to be entirely due to  $\text{NO}_2$  at total pressures up to 3 kPa. This assumption is false; for a total pressure of 3 kPa, and assuming a temperature of 298K, the higher absorption cross section of  $\text{N}_2\text{O}_4$  makes it responsible for 72% of the total absorption coefficient, despite forming only 15% of the equilibrium mixture. Secondly, Armandillo *et al.* [1982] assumed the gas mixture to be predominantly  $\text{N}_2\text{O}_4$  at pressures between 6 kPa and 29 kPa. This assumption is also false; for a total pressure of 6 kPa the mixture is only about a quarter  $\text{N}_2\text{O}_4$ . This caused them to underestimate the absorption cross section of  $\text{N}_2\text{O}_4$  by a factor of approximately four (the contribution to the total absorption from  $\text{NO}_2$  is small - about 20%).

The absorption model and fitted cross-sections were used to calculate the calibration curves given in Fig. 5.16.

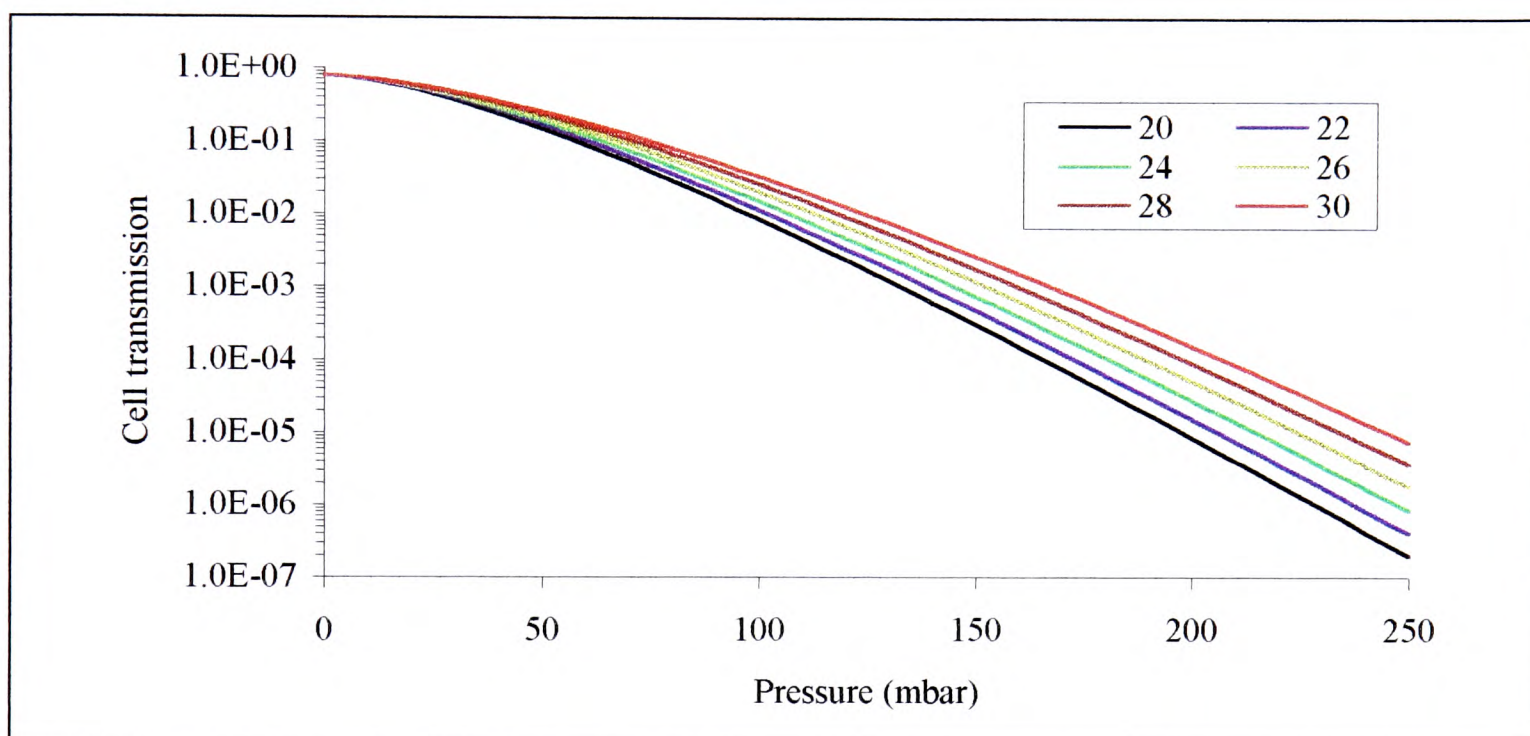


**Figure 5.16.** Calibration curves for  $\text{NO}_2$  cell transmission as a function of total pressure for six temperatures (shown in degrees Celsius).

It can be seen from Fig. 5.16 that the absorption cell can give many decades of attenuation. The ultimate limit on the attenuation which could be achieved is set by the vapour pressure of  $\text{NO}_2$ , which is about one atmosphere, at room temperature.

## 5.4.4 Photobleaching

### 5.4.4.1 Experimental observations

Fletcher [1993] found that the transmission of the  $\text{NO}_2$  cell rose with the number of laser pulses to which it was exposed. No evidence for this effect was found during the measurements described in §5.4.3. But, when the cell was subjected to the full pulse energy of the KrF amplifier, this effect was observed, as illustrated in Fig. 5.17. This shows a 40% rise in the cell transmission over 65 shots, followed by (partial) recovery over a timescale of tens of minutes.



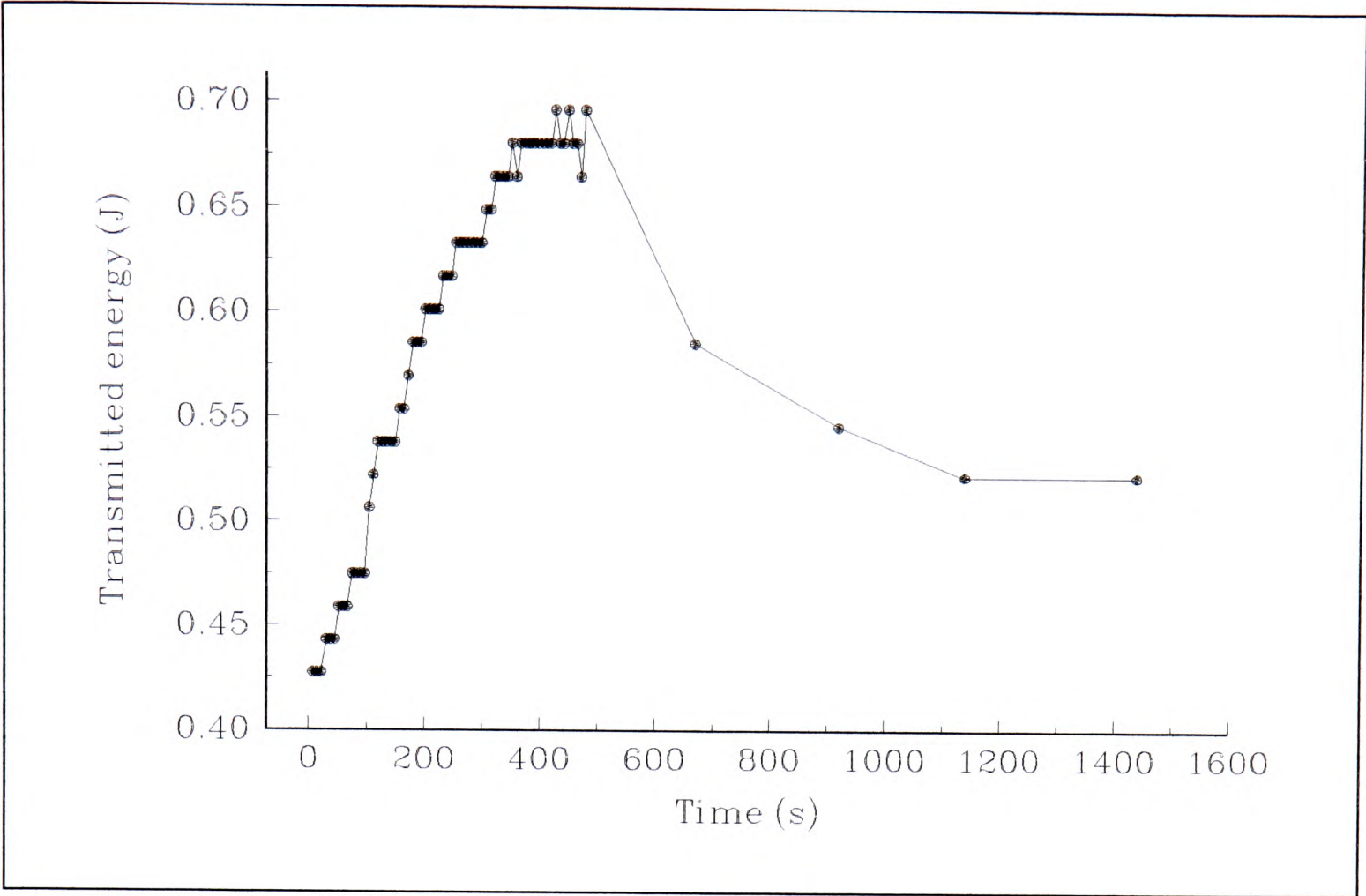


**Figure 5.17.** Photobleaching and recovery of  $\text{NO}_2$  cell transmission. Each data point represents an exposure of  $1.7 \text{ J}$  over an area of  $9 \text{ cm}^2$ . Initial total pressure of  $50 \text{ mbar}$ , at  $24.1^\circ \text{C}$ .

Clearly, this photobleaching effect makes the cell calibration invalid for high pulse energies, and so its severity was investigated. It was found to be less severe at both high and low pressures, and this is illustrated in Fig. 5.18.

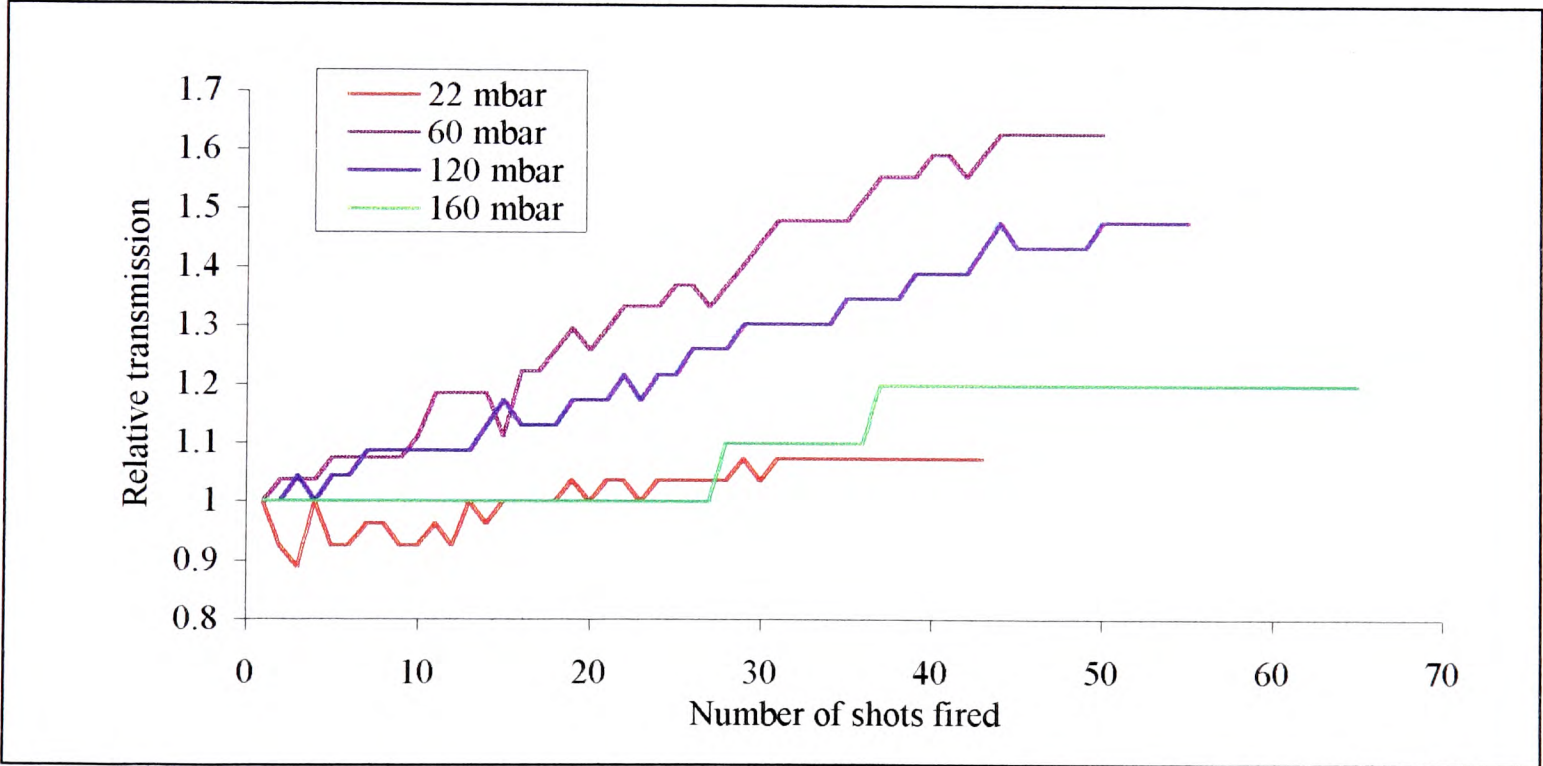


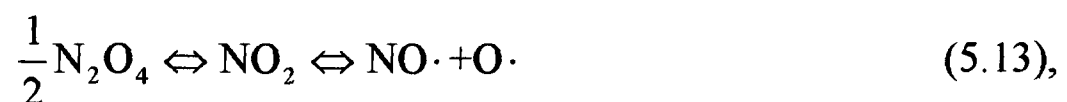
**Figure 5.18.** Transmission of  $\text{NO}_2$  cell as a function of time, normalised to first shot. The apparent quantisation is an artefact of the use of an oscilloscope to collect the data.

#### 5.4.4.2 Explanation for photobleaching

The photobleaching is presumably caused by photodissociation followed by slow recombination. For example,  $\text{NO}_2$  is known to photodissociate to give  $\text{NO}\cdot$  and  $\text{O}\cdot$  free



radicals with almost unit quantum efficiency, when irradiated with light of a wavelength below 313 nm [Calvert & Pitts 1966]. A full treatment of the possible processes is rather complicated, however, since many reactions must be considered. These include



as well as the generation and recombination of other photodissociation products of  $\text{N}_2\text{O}_4$ , reactions with the cell walls, and the heating effect of the absorption.

Other evidence of photodissociation was observed. Over the 65 shots causing the photobleaching shown in Fig. 5.17, the pressure of gas in the cell, which was isolated from the supply cylinder, rose from 50 mbar to 53 mbar. This had returned to 50 mbar after about 15 minutes. This suggests the presence of irreversible reactions, since in the same time the absorption did not recover to its initial magnitude.

The  $\text{NO}_2$  used for these experiments was stored as a pressurised liquid. When gas was required it was taken from the vapour in equilibrium with, and above, the liquid. The composition of the vapour in equilibrium with the liquid will not in general be the same as that of an equilibrium gas mix at a different pressure (as was used in the absorption cell). The process of reaching a new equilibrium composition could, in itself, cause changes in the transmission of the cell. This possibility was ruled out as a cause of the apparent photobleaching by measuring the pressure in, and transmittance of, the cell over half an hour, exposing it to laser radiation only four times in this period. Neither the pressure (49 mbar) nor the transmittance was found to change significantly. This suggests the equilibrium between  $\text{NO}_2$  and  $\text{N}_2\text{O}_4$  is reached quickly, and so non-equilibrium concentrations of  $\text{NO}_2$  to  $\text{N}_2\text{O}_4$  are unlikely to be the cause of the photobleaching and recovery.

No further investigation of the photobleaching was made, as the use of the  $\text{NO}_2$  cell was incidental to the main aims of the project. Instead, care was taken not to use the cell in such a way that photobleaching could cause errors (*i.e.* the gas was replenished often).

Finally, it is instructive to consider the photobleaching in the context of saturable absorption. Of the two gas species,  $\text{NO}_2$  and  $\text{N}_2\text{O}_4$ , it is  $\text{N}_2\text{O}_4$  which has the lower saturation/bleaching fluence. This is given by  $h\nu/\sigma_{\text{N}_2\text{O}_4}$ , and is  $\sim 1 \text{ J cm}^{-2}$ . This means the fluence used for the experiments described in §5.4.3 is  $\sim 30$  times too low to cause saturation/bleaching of the  $\text{N}_2\text{O}_4$  absorption. This means that the populations of the gas species in the mixture did not change appreciably during the laser pulses used in §5.4.3. Indeed, if this were not the case expression (5.10) would be inaccurate. However, for the photobleaching experiments, a fluence five times greater was used. Furthermore, the larger pulse energy means that the dilution of the exposed gas by the unexposed gas will have been less effective at causing the absorption to recover between shots. Then, since the absorption recovery is slow, the fluence may be effectively increased by firing more laser shots. Thus, the absorption can be made to saturate - and this was exactly the photobleaching effect observed.

## 5.5 Summary

In this chapter we have:

- Detailed a KrF laser system which was expected to generate a beam of  $29 \mu\text{rad}$  divergence, throughout the entire duration of its output pulse.



- Indicated how the laser system developed by Fletcher [1993] was made safer (fluorine source and electrical dump switch).
- Indicated how two changes to the laser system gave rise to pulses of 14% higher energy than had ever been obtained from the system previously. This gave the laser almost the highest single-pulse energy yet reported for a discharge-excited UV-preionised KrF laser. The relevant changes were a new electrode winding technique, coupled with the use of a slightly more fluorine-rich laser gas mixture.
- Reported the successful use of a novel source of fluorine for excimer laser systems. This is the first report of this to be found outside conference proceedings, and a paper on the subject is under preparation.
- Successfully modelled the absorption of an NO<sub>2</sub> absorption cell, and used this model to calculate the absorption cross-sections of the two gas species present, and in the process have cleared up a disagreement in the literature about these quantities.



# 6. A first attempt at the Xe III laser

---

## 6.1 Introduction

This chapter describes an attempt at pumping the Xe III laser, using the KrF laser arrangement described in the preceding chapter. We start with a discussion of focusing techniques, suitable for generating an intense line focus. We then consider a specific experimental arrangement, and its alignment in particular. Then a technique is described for detecting 67 eV to 100 eV photons, suitable for pumping the Xe III system. Finally, experimental results are presented.

## 6.2 Focusing geometries

### 6.2.1 Introduction

Even at its peak power of  $\sim 100$  MW, the KrF laser to be used here is of almost an order of magnitude lower power than the lowest power pumping lasers previously used to achieve lasing on the Xe III system. These were 930 MW [Yin *et al.* 1987], 940 MW [Sher & Benerofe 1991], and 1 GW [Sher *et al.* 1991]. In order to produce a LGP sufficiently hot to produce the 67 eV to 100 eV pumping photons, a threshold focal intensity must be achieved. The requirement on the laser beam power required for this may be relaxed if tight focusing can be achieved. The shorter wavelength of the proposed KrF system over the infrared lasers used for all previous demonstrations of Xe III lasing makes tighter focusing likely to be possible. Indeed, the low pump-power Xe III systems listed above all employed focal lines of width  $\geq 100$   $\mu\text{m}$ , which leaves plenty of scope for improvement. Thus, it was decided to use tighter focusing to make up for the lower KrF beam power. It must be pointed out that there is a limit on the extent to which tight focusing can help in LGP formation. This is discussed in §7.6.

### 6.2.2 Focal intensity required

The lowest focal intensity ever used to produce an LGP suitable for Xe III pumping was  $3 \times 10^{10} \text{ W cm}^{-2}$  [Sher *et al.* 1991]. This was reported to give an Xe III gain coefficient of  $1.6 \text{ cm}^{-1}$ . This intensity was taken as a goal for the focusing system. A 3 cm gain length was chosen. This was somewhat arbitrary, being the shortest gain length ever reported for a successful Xe III laser system [Yin *et al.* 1987]. With a  $1.6 \text{ cm}^{-1}$  gain, this suggests a single-pass small-signal-gain of  $e^{4.8} = 120$ . With the mirror described in §8.4.1, we might expect to increase this to  $\sim 850$ .

In considering how to achieve a focused intensity of  $3 \times 10^{10} \text{ W cm}^{-2}$ , we must know the dimensions of our focus, and the power of the KrF pumping laser during the first few nanoseconds of its pulse, since it is only during this time that the Xe III laser can show any gain. The leading edge of the laser output was measured, and a typical pulse obtained is shown in Fig. 6.1.



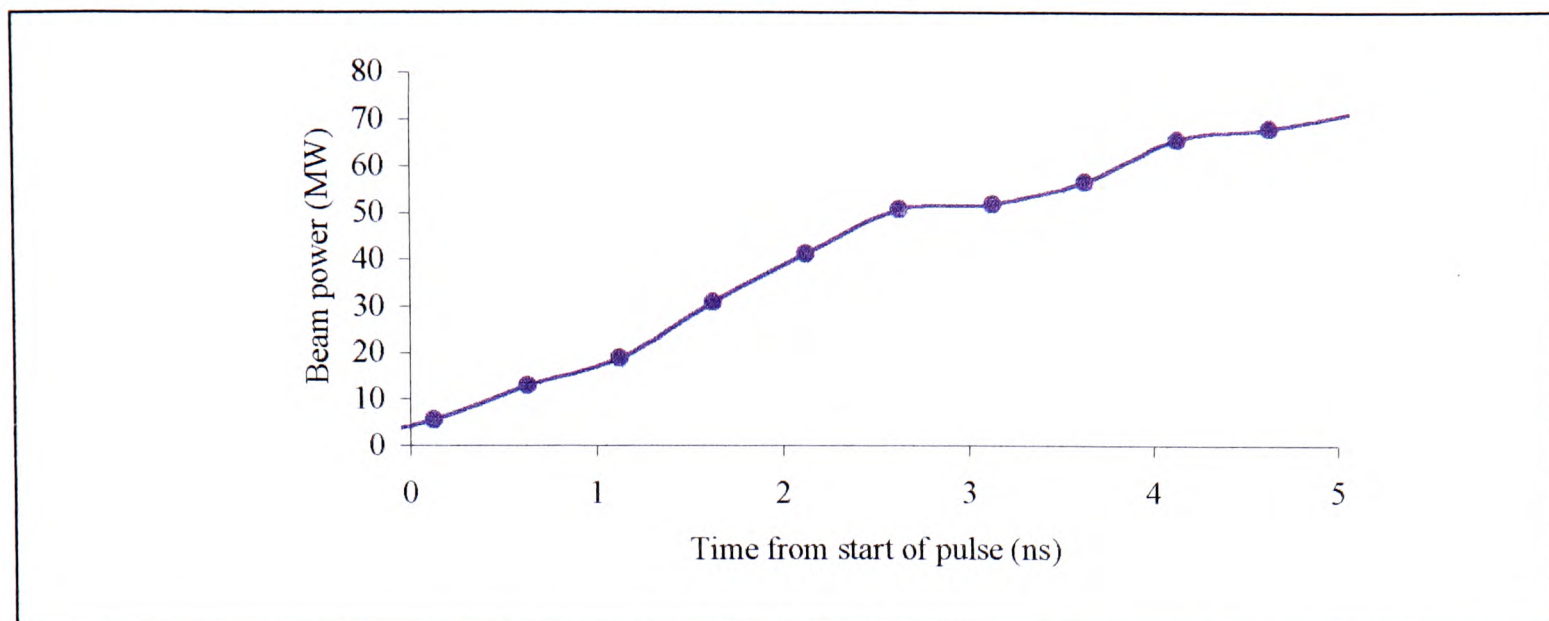


**Figure 6.1.** Leading edge of a KrF laser pulse. Apparent non-zero power at zero time is (mainly) because of electrical noise.

The  $\sim 5$  ns risetime of the laser system is comparable to the upper-state lifetime of the Xe III system. Furthermore, reported Xe III laser pulse durations are typically of only a few hundred picoseconds. The problem is to estimate at what point on the leading edge of the KrF pulse these few hundred picoseconds of Xe III emission might be observed. This is a complicated problem - the plasma temperature will change during the rise, and Xe III lasing can only occur when there is significant emission in the 67 eV to 100 eV spectral region.

The work of Sher & Benerofe [1991] sheds some light on the problem. They found significant enhancement of Xe III laser output when they used a low-energy prepulse up to 2.3 ns before the main 80 ps, 1064 nm pulse used to produce their pumping LGP. Even more dramatic enhancement caused by prepulsing (for 1.6 ns delays only) has been reported more recently by Yamakoshi *et al.* [1996]. The reason for this is discussed in §8.4.5. Briefly, the explanation is that the plasma expands to a size comparable with the inverse-bremsstrahlung absorption length for the exciting radiation in the time between the two pulses. This expansion allows more efficient absorption of the main pulse. The rate of expansion and skin depth depend on the experimental conditions. However, it is not wildly optimistic to expect that a timescale of  $\sim 2$  ns might apply here too, before the plasma becomes very absorbing. For want of a better approximation, we shall assume this is the case. However, as we shall see in §7.6, hydrodynamic expansion of the plasma may mean that any SXR emission must be produced somewhat earlier in the laser pulse. If this is the case (and it is hard to model so we cannot be sure), it would probably be impossible to generate a plasma sufficiently hot to pump the Xe III laser system, using the laser pulse available, without modification.

Returning to our consideration of the focal intensity, we see from Fig. 6.1 that a power of  $\sim 50$  MW is available  $\sim 2$  ns into the KrF laser pulse. If we are to focus this to  $3 \times 10^{10} \text{ W cm}^{-2}$  along a line 30 mm long, a focal width of  $5.5 \mu\text{m}$  is needed. The beam divergence was taken to be  $\sim 30 \mu\text{rad}$ , suggesting a system with a focal-length of  $\sim 170$  mm was required.



## 6.3 Normal incidence focusing geometries

In this section we shall consider focusing geometries suitable for generating a line-focus, at normal (or near-normal) incidence on target. This is in contrast to the pumping geometries required for travelling-wave excitation, which are discussed briefly in §6.3.5.

A design goal is that our focusing system should give a tight focus. How tight the focus can be depends on the pulse length of the laser generating the plasma, for reasons discussed in §7.6. For the moment, however, we will set aside consideration of the desirability of a tight focus, and consider only how we might make one. A further design goal is that the focusing scheme should be easy to realise, and not require very elaborate optics. As will be shown, a spherical mirror used at oblique incidence meets these criteria. Before considering this, however, we shall review some of the alternatives.

### 6.3.1 Random phase plates

Danson *et al.* [1990] and Desselberger *et al.* [1992] have described the use of random phase plates to produce a line focus. This is a simple holographic technique, by which rectangular regions (all of the same size) on a plate are randomly assigned a phase retardation of either zero or  $\pi$  to transmission of light of a particular wavelength. If this plate is placed before a converging lens its Fraunhofer diffraction pattern is found in the focal plane of the lens. This pattern has an aspect ratio associated with it equal to the reciprocal of the aspect ratio of the rectangular random-phase regions.

The technique is not suitable for the application here because of the demands it would make on the imaging system. This would require a focal-length of 170 mm (or less) and give near diffraction-limited performance over the whole 30 mm length of the line focus in the image plane.

### 6.3.2 Control of KrF beam-divergence

Lisi\* has suggested an ingenious technique for achieving high-quality line-foci. Although unsuitable here, we shall consider it because it has not been suggested elsewhere, and might be of use in other line-focusing schemes. The technique is to use cylindrical optics in an unstable KrF resonator. This could be arranged to give rise to an astigmatic beam, having near diffraction-limited divergence in one direction only. Focusing with a spherical (or aspheric) optic would then give rise to a line focus. This is because there would be tight focusing only in the low-divergence direction.

Simple consideration of the scheme indicates that the  $\sim 10^4$  aspect ratio of the line focus required makes it unsuitable here. The aspect ratio of the line focus generated would be equal to the ratio of the divergences in the astigmatic beam. If the divergence in one direction was 29  $\mu$ rad (the lowest which Fletcher [1993] obtained), then the divergence in the other direction would need to be  $\sim 0.3$  rad. This is clearly impractical.

An obvious modification to the technique is to introduce some geometrical spreading into a beam, by means of a weak cylindrical lens, and then focus with a spherical optic. However, Ross *et al.* [1987] have commented that they have had problems with such techniques, due to off-axis aberrations in the lens, and field curvature. Both of these problems would also limit the divergence-based technique.

---

\* Private communication, 1996.



### 6.3.3 Cylindrical lenses & mirrors

The obvious choice for production of a line focus is a cylindrical lens or mirror. However, Ross *et al.* [1987] have commented that conventional cylindrical optical designs (*i.e.* involving cylindrical mirrors and lenses) have been found not to be suitable for achieving line foci having widths of a few microns, coupled with lengths of more than 10 mm. In the next few paragraphs we shall see why this is the case, and we will discuss solutions to the problem.

Our approach will be to consider the limits imposed by geometrical optics on focusing systems. It should be pointed out that the requirement of a focusing system with minimal geometrical aberrations is a necessary, but not a sufficient requirement for high-quality focusing. Thus, the treatment given here will indicate what schemes certainly will not work (*i.e.* ones with severe geometrical aberration). However, this treatment will not show which schemes certainly will work; a more sophisticated, wave-optics treatment is needed for this.

#### 6.3.3.1 Cylindrical lenses

First, we consider the use of a cylindrical lens. The factor limiting the quality of the focus (when used at normal incidence) is the cylindrical equivalent of spherical aberration. Spherical aberration is the property of a lens having different focal-lengths for light striking it different distances from its centre. A line focus is produced along the optical axis. The equivalent for cylindrical lenses is a plane focus, rather than the line required. To quantify the severity of the problem, we consider the longitudinal extent of the focal region. This is known as the longitudinal spherical aberration. For a thin, plano-convex lens of focal-length,  $f$ , used at an aperture,  $A$ , the primary\* longitudinal spherical aberration,  $S$ , of the focus is given by Curry [1953] as

$$S = \frac{1}{4} \frac{A^2}{f} \left( \frac{2 - 2n^2 + n^3}{2n(n-1)^2} \right) \approx \frac{0.28A^2}{f} \quad (6.1),$$

where  $n$  is the refractive index of the lens, and the expression has been calculated for  $n=1.51$ , the refractive index of fused silica at the KrF wavelength. Clearly, the same result holds for the aberration to be found in a plano-convex cylindrical lens.

In spherical lenses the aberration can be reduced slightly (~10%) by *bending* the lens; that is changing the radii of its surfaces, without changing its paraxial focal-length. This is less desirable for cylindrical lenses, since it makes them much more expensive, requiring two curved faces rather than one, and provides only a limited performance improvement.

In order to quantify the aberration which will seriously degrade the quality of the focus, we shall derive a result which is used in many places throughout this thesis. This is an estimate of the depth-of-focus of a focusing system, where the quality of the focus is limited by the divergence of the beam being focused. The geometry assumed near the focus is illustrated in Fig. 6.2.

---

\* In the paraxial approximation of geometrical optics, we make the assumption that  $\sin \theta = \theta$  in raytracing calculations. If the next term in the expansion is included, *i.e.* we assume  $\sin \theta = \theta - \theta^3/6$ , we find the five Siedel, or primary, aberrations of optical systems.



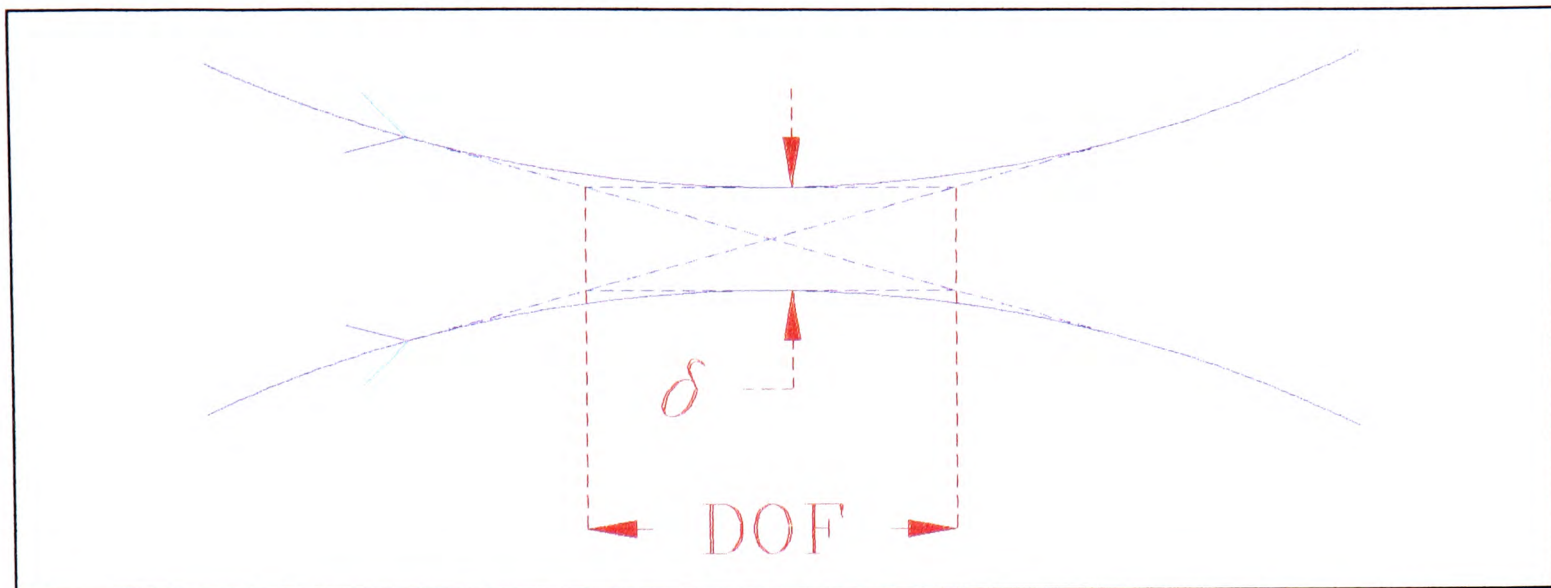


**Figure 6.2.** Geometry used to estimate depth-of-focus.

We consider a beam of divergence  $\theta_a$ , focused by a focusing system having an aperture  $A$ , and focal-length  $f$ . The divergence-limited width of the focal line,  $\delta$ , is given by

$$\delta = f \cdot \theta_a \quad (6.2).$$

We may estimate the depth-of-focus,  $DOF$ , as the distance over which geometrical optics predicts a focal width narrower than the divergence-limited width. This is illustrated in Fig. 6.2, and is given by

$$DOF = \frac{2f^2\theta_a}{A} \quad (6.3).$$

We are now in a position to compare the smearing of the focus owing to spherical aberration, with the unavoidable smearing owing to the divergence of the incident beam. We may be confident that geometrical aberration will degrade the focusing system if the longitudinal spherical aberration,  $S$ , is greater than or equal to the divergence-limited depth-of-focus,  $DOF^*$ . For the KrF beam considered here, the divergence,  $\theta_a$ , is  $29 \mu\text{rad}$ ; and the beam size,  $A$ , is 30 mm. Thus, we find that 50 cm is the shortest focal-length of a single plano-convex cylindrical lens which may be used without introducing severe geometrical aberrations. The option of compressing the beam in order to reduce aberrations is considered in §6.3.3.3.

For circularly symmetric lenses the way around this problem is to use a aspheric surfaces. For cylindrical lenses, however, technology lets us down; it is not currently possible to make a cylindrical lens of arbitrary section. A possible way around the problem would be to design an optimised system using several cylindrical lenses. This would be a complicated and expensive solution, and would be at the cost of introducing some random wavefront distortion to the system, since it is difficult to make accurate cylindrical surfaces.

---

\* We are using a geometrical optics treatment, and this is only valid if it predicts a focal spot size larger than  $\sim \lambda / NA$ , where  $NA$  is the numerical aperture of the imaging system [Levi 1968]. The numerical aperture here is  $\sim A/2f$ . It is easily shown that the criterion given above for geometrical aberrations to degrade the quality of the focus, is approximately the same as the criterion given for geometrical optics to be a valid approximation.



### 6.3.3.2 Cylindrical mirror

An obvious choice of focusing optic, apart from a cylindrical lens, is a cylindrical mirror. A paraboloid is the optimum form of a mirror to focus a collimated laser beam to a point. Similarly, for a line focus, the section of the ideal mirror is also parabolic. Unfortunately, such surfaces cannot be made to optical quality, and we are forced to make do with circular sections.

To treat aberrations in a mirror-based focusing system, we use an analogous treatment to that used for the lens in the previous section. It is easily shown that the primary spherical aberration,  $S$ , of a mirror of focal-length,  $f$  (equal to half its radius-of-curvature), used at aperture,  $A$ , is given by

$$S = \frac{A^2}{32f} \approx \frac{0.031A^2}{f} \quad (6.4).$$

Comparison of expressions (6.1) and (6.4) shows that a mirror exhibits much less spherical aberration than a lens. For this reason, only mirrors will be considered in the discussion which follows. Applying the same criterion as before, we find the minimum focal-length of mirror which may be used here is 24 cm.

### 6.3.3.3 Reducing beam size to reduce aberrations

From expression (6.4) it is clear that the spherical aberration scales with the square of the aperture of the focusing system. Thus, it might seem attractive to reduce the aperture, in order to reduce aberrations. The drawback of the technique is that the divergence scales with the reciprocal of the aperture, *i.e.* reducing the beam size increases its divergence. Overall there is a slight net advantage in reducing the aperture. It is easily shown that if we apply the criterion used above to calculate the minimum acceptable focal-length of focusing mirror, then the intensity we may expect on target scales as  $A^{-(1/3)}$ .

A limit to the extent of such aperture-reduction is the point at which laser damage to the mirror would become a problem. Taking a damage threshold of  $2 \text{ J cm}^{-2}$ , and with 2.5 J pulses, the illuminated area on the mirror must be no less than  $1.25 \text{ cm}^2$ . For a 30 mm long focus, this corresponds to a beam width of no less than 4 mm.

This would allow a 17 mm focal-length mirror to be used. Assuming there were no aberrations, this would give rise to a focal line  $3.6 \text{ }\mu\text{m}$  wide. Although this might seem very attractive, there are several practical problems with the scheme (aside from the possible undesirability of such a tight focus). These include:

- Debris - having the target so near the focusing mirror would give rise to serious problems with debris from the plasma being deposited on the focusing mirror.
- Alignment - the use of a mirror requires the target to shadow the incident beam, since the mirror cannot be tilted (this is equivalent to using it at a larger aperture). This means, for example, that the microscope slide alignment technique described in §6.6.9.2 would not be feasible. Furthermore, the target would have to be a wire, rather than a ribbon, in order to prevent severe geometrical losses caused by shadowing of the incident beam. Because of the curvature of a wire, alignment of a line focus along a wire is much more difficult than alignment along a flat ribbon.
- Beam compression - one-dimensional compression of the KrF beam would be required. This could be achieved either by an aberration-correction cylindrical telescope, or by two or three anamorphic prisms (one prism could not give the required compression



without disastrous reflection losses). Both these arrangements add to the complexity of the scheme, and would introduce some phase distortion to the beam.

### 6.3.4 Off-axis spherical mirrors

As we have seen in the preceding sections, cylindrical mirrors and lenses are not ideal for the generation of long, tight line foci. The problem has been treated theoretically by Ross & Hodgson [1985], and solutions tested experimentally by Ross *et al.* [1987]. In these works, several methods for generating diffraction-limited line foci have been proposed. Here we shall concentrate on two of them, which use only standard optical components. In both cases, the technique takes advantage of the spherical aberration found in off-axis focusing geometries.

#### 6.3.4.1 Mirror & lens scheme

The first scheme we consider employs a spherical lens, and a spherical mirror. A line focus is generated on the line joining the centre of curvature of the mirror with the focus of the lens. This line focus suffers no geometrical aberrations, and is perfectly straight, whatever the alignment of the mirror and lens. A discussion of why this is so is given in §6.3.4.2. An example of how such an arrangement might be applied here is illustrated in Fig. 6.3. This shows an arrangement which was designed using only optics which were already available or were stock items available from one of the major optics suppliers.

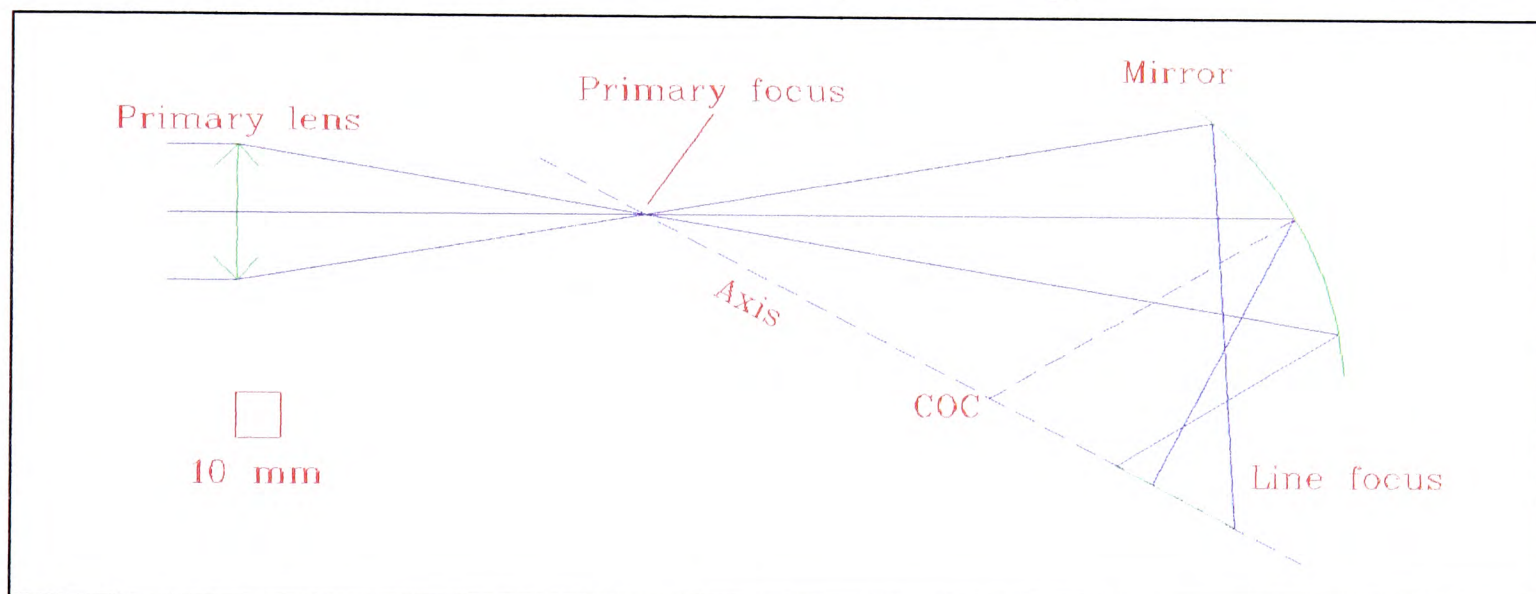


**Figure 6.3.** An arrangement of spherical mirror and lens giving rise to a diffraction-limited 3 cm line focus, employing scheme proposed by Ross *et al.* [1987]. COC is centre-of-curvature of mirror.

#### 6.3.4.2 Single mirror scheme

The primary lens of the mirror and lens scheme is not essential. A single spherical mirror, used off-axis, is equivalent, but with the primary focus at infinity. This gives rise to a line focus on the line including the centre of curvature of the mirror, and parallel to the direction of the incident beam. Again, the line is perfectly straight, and free from geometrical aberration. The geometry is illustrated in Fig. 6.4, for 45° incidence on the mirror (as used in all the experiments described in this thesis).



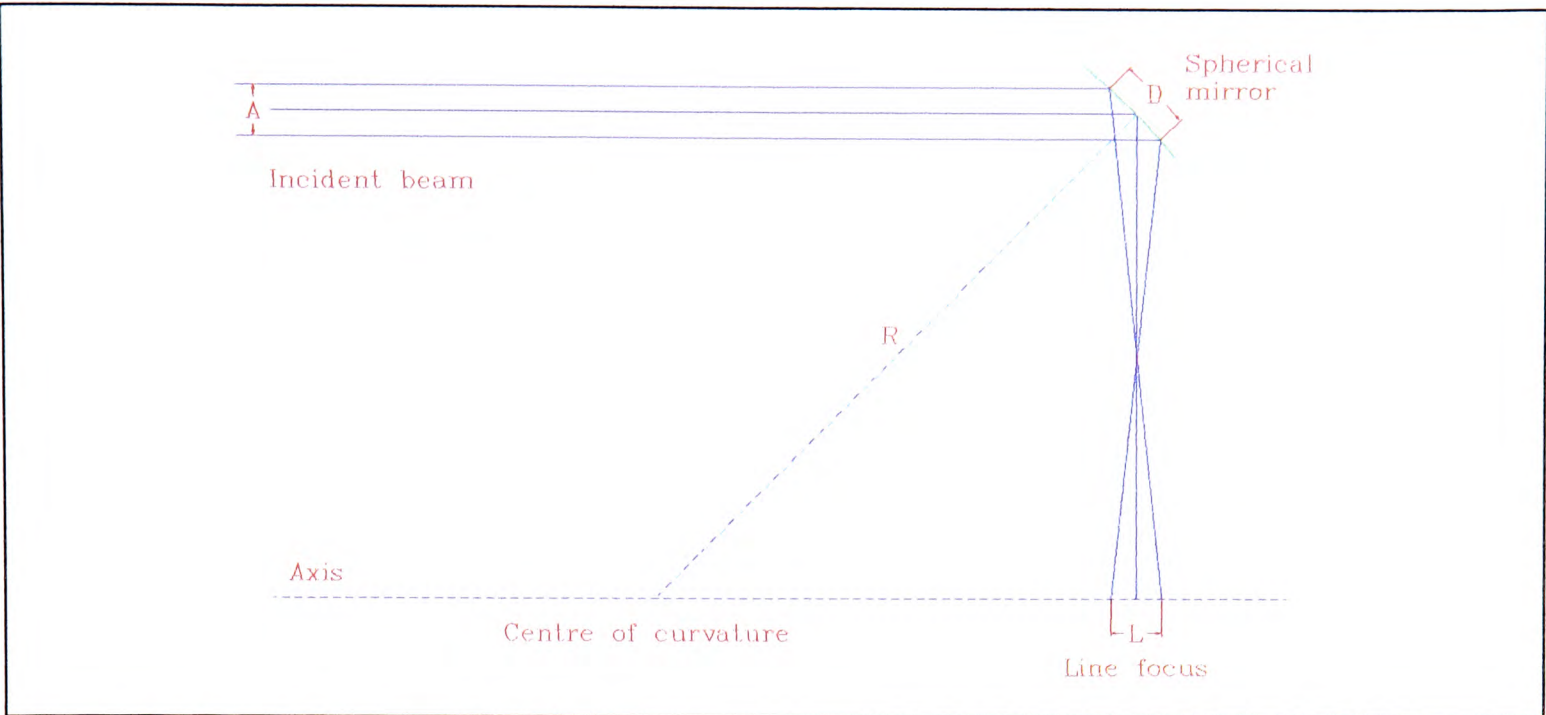


**Figure 6.4.** Single off-axis mirror line focus geometry. To scale for experiments described in this chapter.

We consider why there is no geometrical aberration associated with the scheme. Fig. 6.4 depicts an axis which is parallel to the direction of incidence, and contains the centre of curvature of the mirror. It is easily shown that in the plane of Fig. 6.4 all the incident rays pass through a section of this axis of length,  $L=A$  (for  $45^\circ$  incidence, and small  $D/R$ ). Now consider rotating the plane of interest about the axis. The rotated plane samples a new set of rays from the incident beam, and these rays are parallel to the plane. Also, the section of the mirror is unchanged, since the axis of rotation includes its centre of curvature. Furthermore, the mirror normals all lie in the new plane of incidence (since they are radii), and so all the rays pass through the same portion of the axis of rotation. Thus, the geometrical focus is a perfectly thin, straight line.

From this treatment, it is clear that the locus of points in the incident beam which are mapped to a particular point on the line focus, is an arc centred on the focal line. This is illustrated in Fig. 6.5.

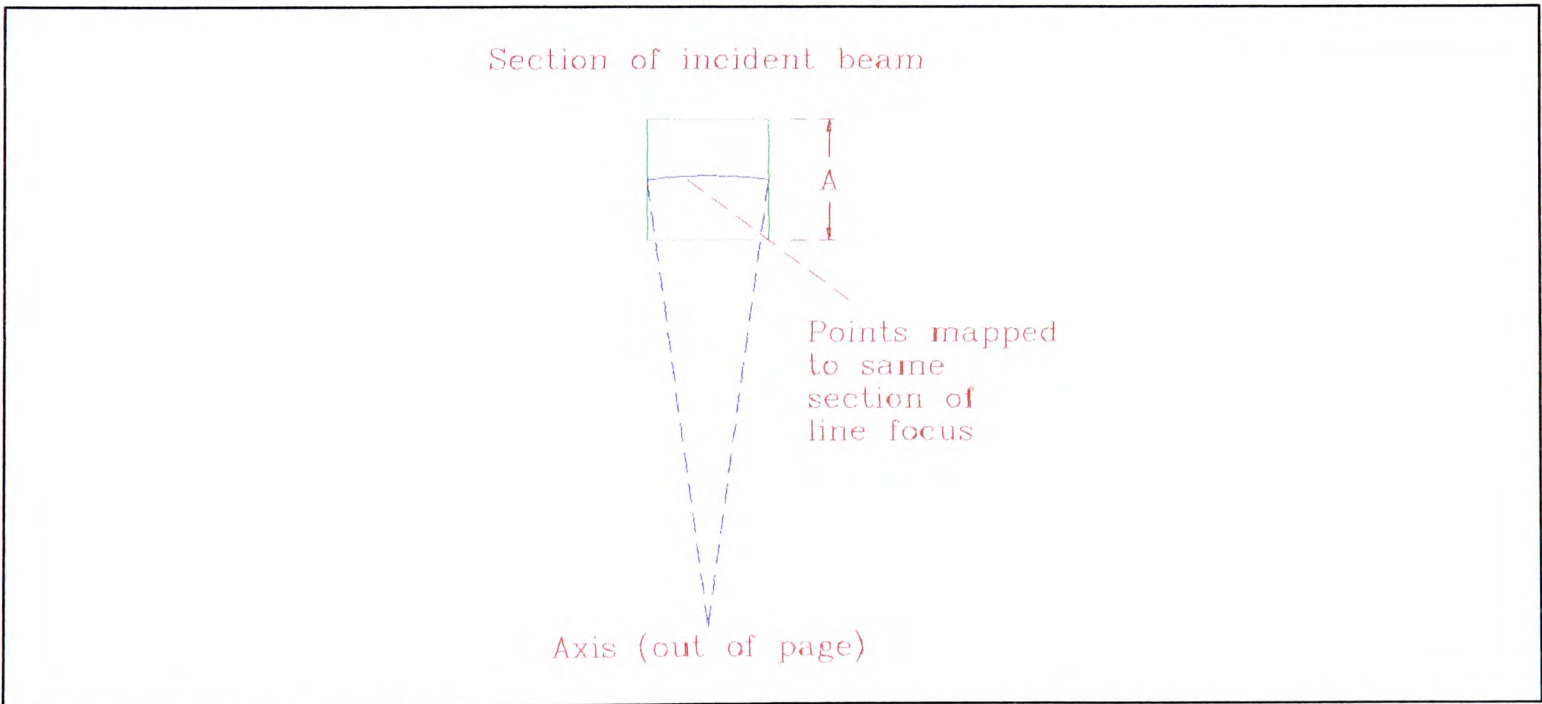


**Figure 6.5.** Section of incident beam showing locus of points mapped to a single position of the line focus.

The beauty of the technique is that tight focusing does not introduce any geometrical aberration. The limit on the scaling of the technique to very tight focusing is an



increasingly uneven distribution of energy along the line focus. This is illustrated by the unequal separation of the rays incident on the line focus, shown in Fig. 6.6.

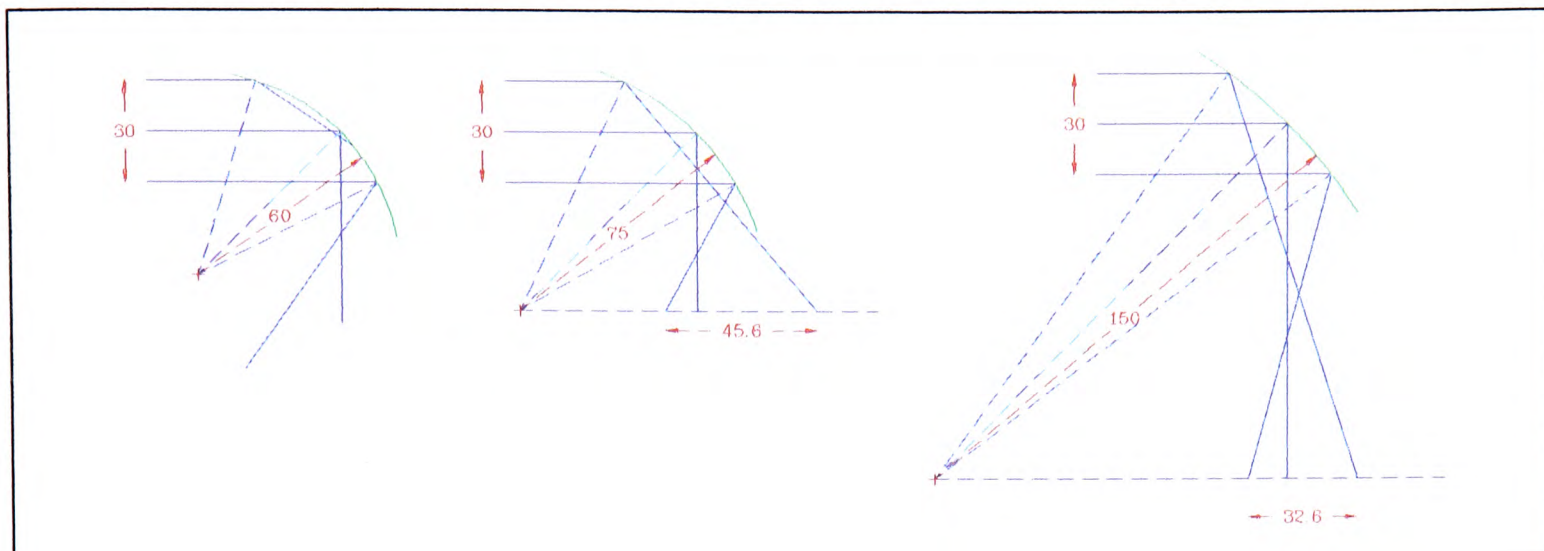


**Figure 6.6.** Several off-axis mirror line focusing geometries, illustrating how energy distribution along line becomes skewed as tighter focusing is used. Diagrams are to scale, and dimensions are in millimetres.

For a mirror having radius-of-curvature,  $R$ , the effective focal-length of the system is given by  $R/\sqrt{2}$ . This gives rise to a focal-line of width  $R\theta_d/\sqrt{2}$ , where  $\theta_d$  is the laser beam divergence. If we take the 150 mm radius-of-curvature arrangement illustrated in Fig. 6.6 as the most uneven distribution we are prepared to accept, then the off-axis mirror focusing technique is scaleable to focal-line widths of  $3.1\ \mu\text{m}$ . This is narrower than the best line which can be produced by a mirror, and dispenses with the requirement for beam compression. Furthermore, since the focusing optic required is spherical, it is easily available, cheap, and can be made to a very high optical quality.

### 6.3.5 Travelling-wave geometry

#### 6.3.5.1 Cylindrical mirror systems

The travelling-wave geometry first reported by Sher *et al.* [1987] has several advantages for pumping of the Xe III system. One of these is that it allows a line plasma to be divided into spots and hence distributed along a line much longer than the total aggregate length of plasma. This is illustrated in Fig. 6.7, for a cylindrical mirror focusing geometry. A cylindrical mirror introduces less aberration than an equivalent cylindrical lens for the travelling-wave geometry [Sher *et al.* 1991, Clement *et al.* 1994], and so this is what we shall consider here.

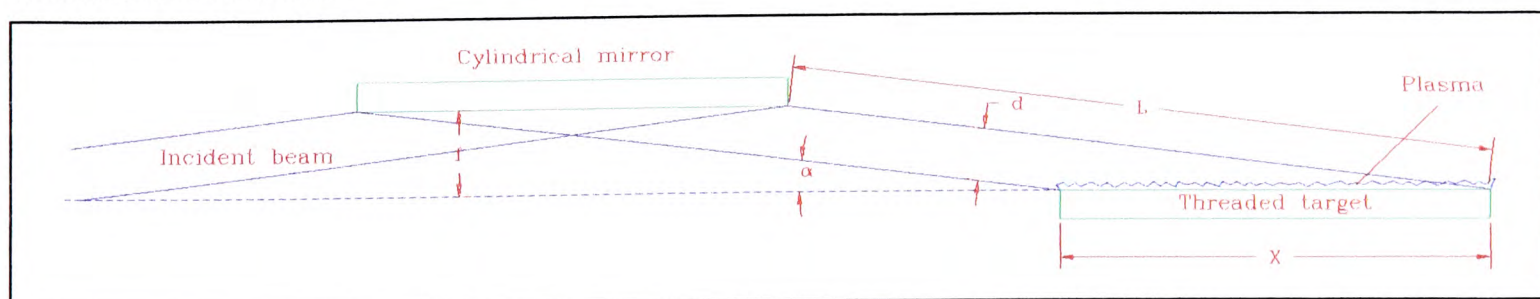


**Figure 6.7.** Schematic of travelling wave geometry, illustrating various relevant parameters.

Referring to Fig. 6.7, the total aggregate length of all the microscopic plasma spots is  $d$ . These spots are distributed along a longer length,  $X$ . The length  $X$  is related to  $d$  by



$$X = \frac{d}{\sin \alpha} \quad (6.5).$$

Thus, it might appear that the travelling-wave geometry might be used to extend the length of the Xe III gain region, without spreading the generating laser beam any more thinly. Equivalently, for a given total excited length,  $X$ , it might appear to be possible to use more intense plasma spots, by compressing the beam to a width,  $d$ , before focusing at an oblique angle. Although this is the case, it is not quite so simple as it appears at first sight, and the reason is that the focal line gets wider as the target is moved away from the mirror. Quantifying this, the width of the line (perpendicular to the plane of Fig. 6.7) is given by  $L\theta_d$ . This gives a total aggregate area of plasma,  $A_F$ , given by

$$A_F = d \cdot L \cdot \theta_d \quad (6.6).$$

But the geometric aberrations introduced by the mirror are determined by its focal-length,  $f$ , and are unaffected by the oblique incidence\*. This introduces the restriction on  $L$  (for the tightest possible focusing) that

$$L = \frac{f_{\min}}{\sin \alpha} \quad (6.7),$$

where  $f_{\min}$  is the shortest focal-length mirror acceptable. The wider the focal line is, due to the beam divergence, the shorter the focal-length of the mirror which may be used before its aberrations widen the line further. Thus, the value of  $f_{\min}$  depends on  $L$ , and hence  $\alpha$ . It is easily shown that applying the same criterion as before, we have

$$f_{\min} = f_o M^{-1/3} \quad (6.8)$$

where  $M = 1/\sin \alpha$ , and  $f_o$  is the shortest focal-length acceptable for normal incidence. Combining these expressions, we find

$$A_F = X \cdot f_o \theta_d M^{-1/3} \quad (6.9).$$

Since  $f_o$  and  $\theta_d$  are fixed, this means that the total area of plasma depends on the *total* length of the gain region ( $X$ ), rather than the aggregate length of the plasma spots ( $d$ ). However, the factor of  $M^{-1/3}$  means that there is a slight advantage to using a travelling wave geometry, in terms of the focal intensity, for a given total target length. To quantify this, for the most oblique incidence system used in an Xe III system to date,  $M$  was 8.2. This corresponds to a doubling of the focal intensity over what could be achieved at normal incidence. It also provides another advantage, discussed in §7.6. The technique was not used for the first attempt at pumping the Xe III system, mainly for reasons of experimental simplicity.

#### 6.3.5.2 Off-axis spherical mirror systems

Although it is possible to devise a travelling-wave system using the off-axis mirror focusing arrangements described in §6.3.4ff, it is not an advantage. The problem is illustrated in Fig. 6.8.

---

\* Consider that the directions of rays resolved perpendicular to the mirror are unchanged by oblique incidence.



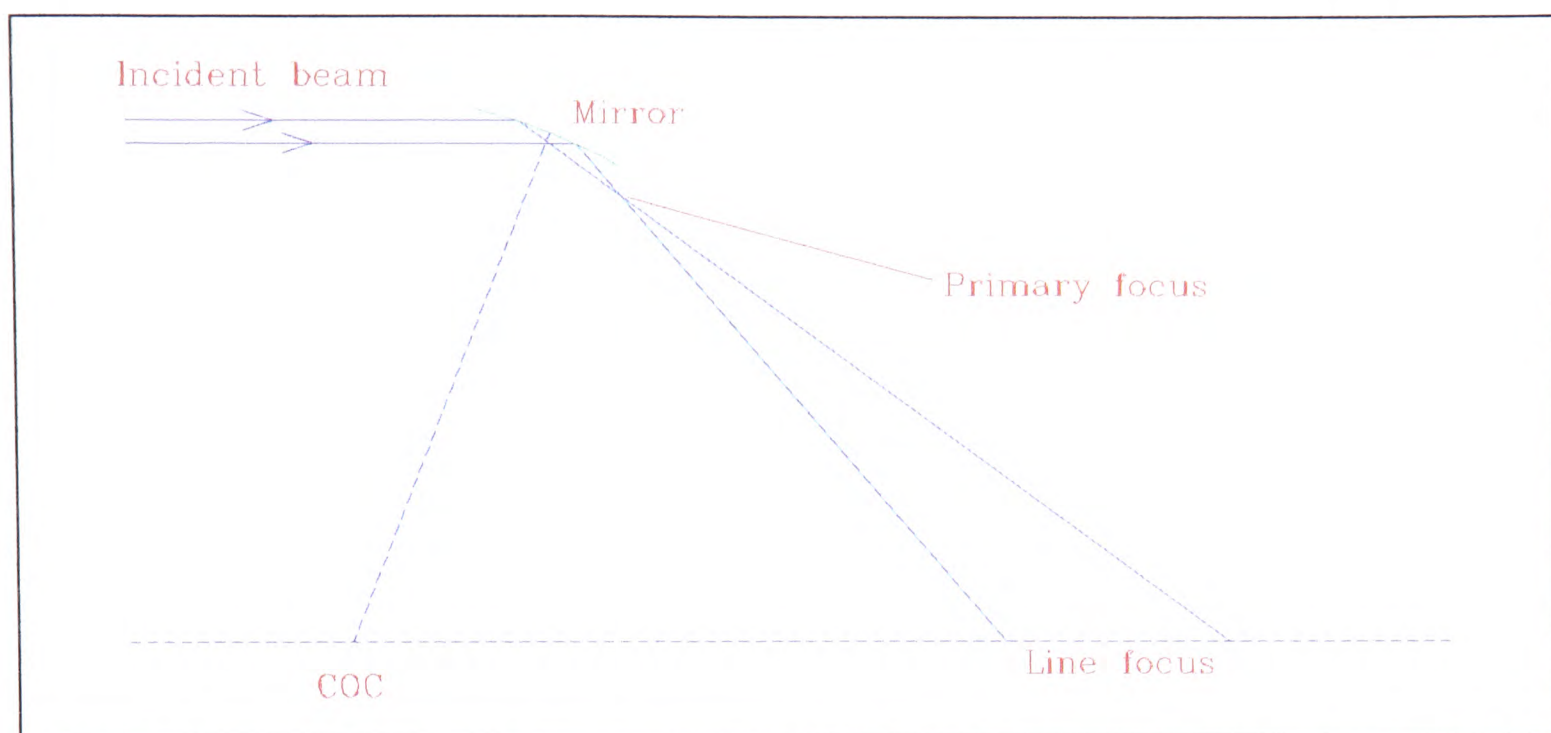


**Figure 6.8.** Travelling-wave geometry applied to off-axis spherical mirror focusing geometry. COC is centre-of-curvature of focusing mirror.

The presence of the primary focus near the mirror means that the beam has spread significantly by the time it reaches the line focus. The more oblique the incidence on the focal line, the greater the spreading. Although we will not go into the numerical details here, it is easily shown that oblique incidence is not beneficial (in terms of on-target intensity) to the off-axis spherical mirror line-focusing technique. The same problem also leads to the same conclusion for the mirror and lens focusing scheme (Fig. 6.3).

## 6.4 Conclusions

In summary, the off-axis mirror technique for generating a line-focus is simple, cheap, and very attractive. It provides straight, diffraction-limited focal lines, and the technique is scalable down to focal line-widths of  $\sim 3.1 \mu\text{m}$ . This focusing technique was employed for all the line-focus experiments described in this thesis. It was used with a (nominally) 406 mm radius-of-curvature mirror in experiments described in this chapter and chapter 8, and with a 152 mm radius-of-curvature mirror in experiments described in §7.5.

## 6.5 Focusing through a window

Before detailing the experimental investigation of the focusing system, we shall discuss a final consideration for focusing; the use of a window. This is major experimental simplification, since it allows the focusing optic to be outside the low-pressure Xe III gain region. Obviously, this makes alignment much easier. We shall calculate how thick a window must be in order for it to introduce severe geometrical aberration to the focal line.

Consider the rays shown in Fig. 6.9. A pair of rays incident at angle  $\theta$  do not meet where they would have done in the absence of the window. The meeting point is offset by some distance  $x$ . The amount of offset is a function of the incident angle,  $\theta$ , and the thickness,  $t$ , of the window.



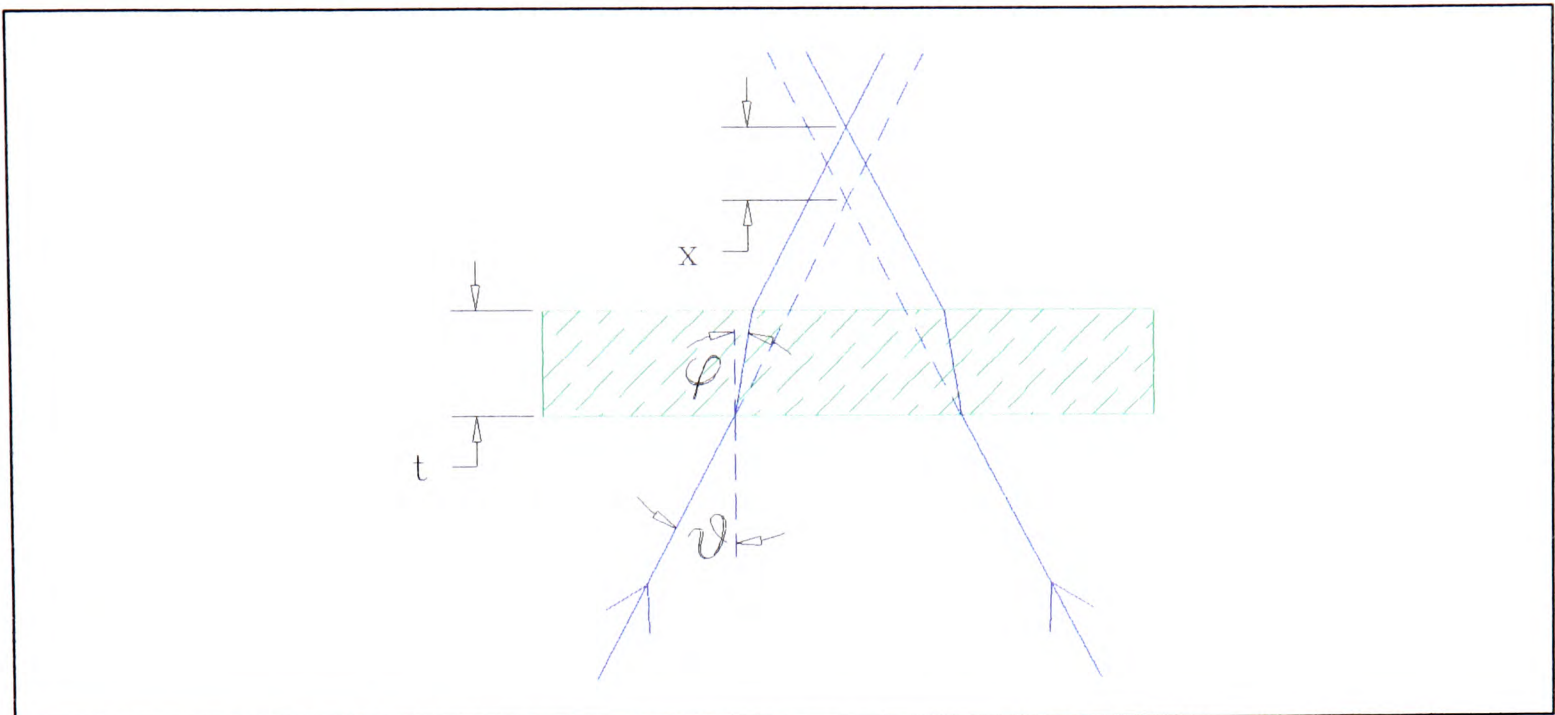


**Figure 6.9.** Geometry of focusing through a window.

The offset may be calculated by simple geometry and Snell's Law as

$$x = t \left( 1 - \frac{\tan \varphi}{\tan \theta} \right) \quad (6.10),$$

where  $\varphi$  is the angle of refraction of the light. In the limit of small angles of incidence this gives an offset

$$x_0 = t \left( 1 - \frac{1}{n} \right) \quad (6.11),$$

where  $n$  is the refractive index of the window. We calculate the distance,  $x'$ , of the focal point for light incident at angle  $\theta$  from the focus for near-normal rays, given as

$$x' = x - x_0 \quad (6.12).$$

This will introduce a serious geometrical aberration if the longitudinal smearing,  $x'$ , of the focus is comparable to the depth of focus, given by expression (6.3).

Clearly, the maximum angle of incidence,  $\theta_{\max}$ , on a window is related to the focal-length of the system and the beam size. The exact relationship depends on the focusing geometry. The relationship may be written as

$$\theta_{\max} = \arctan \left( \frac{A}{2f'} \right) \quad (6.13),$$

where  $f'$  is an effective focal-length. For a lens  $f' = f$ , but for an off-axis mirror the situation is a little more complicated because the system is astigmatic, and there are two focal-lengths. This is illustrated in Fig. 6.10. In order to be sure the focal smearing effect is not severe the shorter focal-length must be taken as the relevant one. In this case  $f' \approx f/2$ .



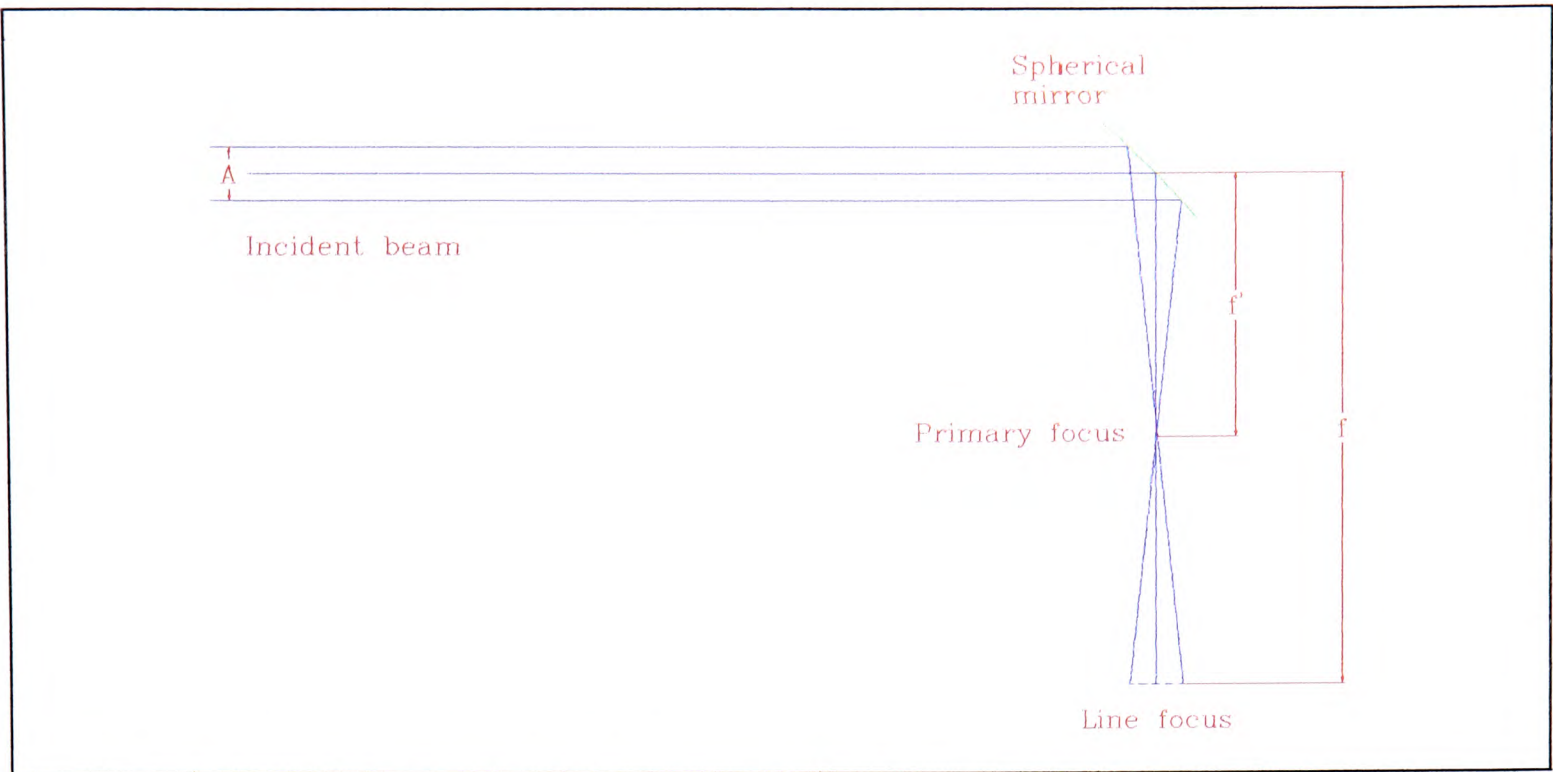


**Figure 6.10.** Two focal-lengths found in off-axis mirror line focus geometry.

We may use this to calculate a maximum permissible window thickness for a focusing system of a given focal-length, and aperture size. We take the beam size to be 30 mm, and assume a fused silica window. Combining (6.3), (6.12), and (6.13), and requiring the smear to be no more than a quarter of the depth of focus, we obtain the data shown in Fig. 6.11.

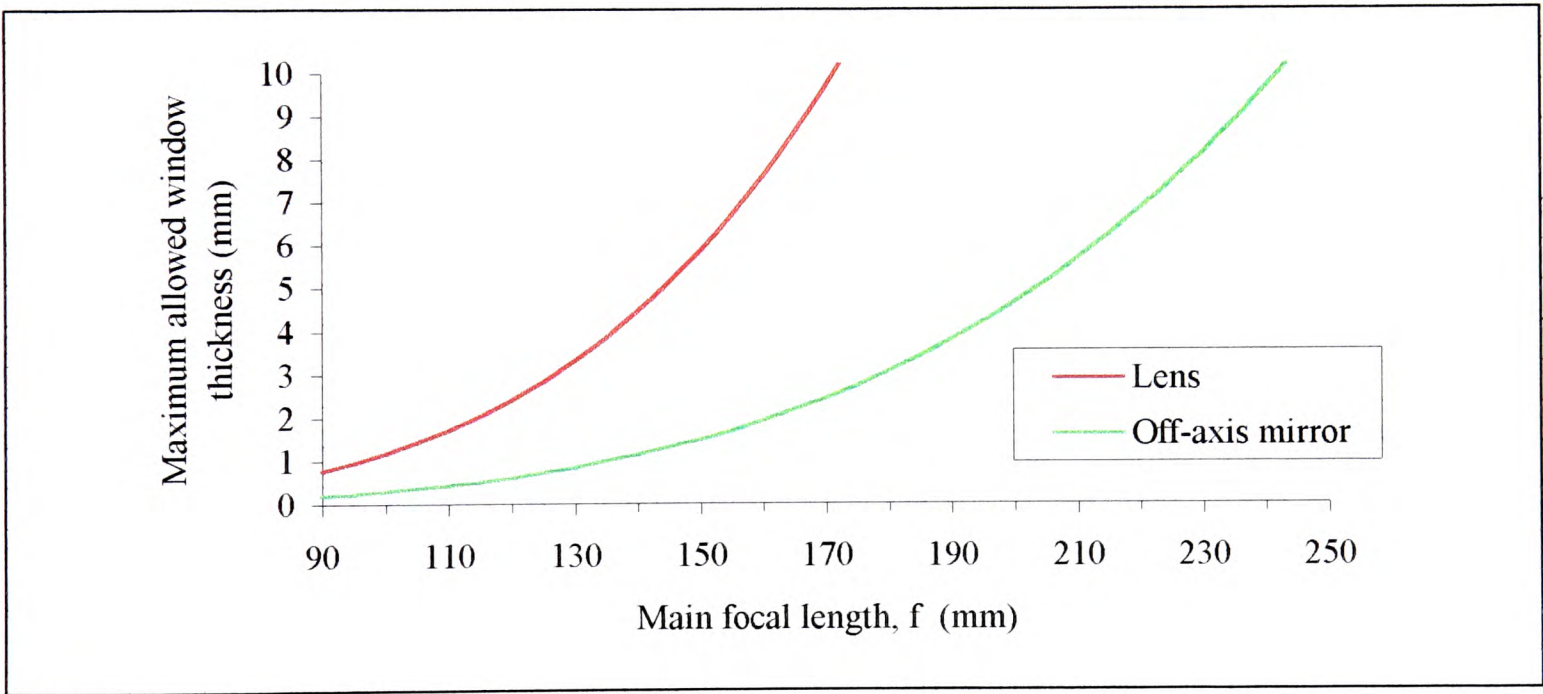


**Figure 6.11.** Maximum permissible thickness of flat, fused silica window, for a 30 mm beam, as a function of focal-length of focusing system.

For the experiments described in this chapter, and in chapter 8, a spherical mirror having an effective focal-length  $f=287$  mm was used in conjunction with a 6 mm window. From the results illustrated in Fig. 6.11 it can be seen that this will not have introduced severe geometrical aberrations into the focusing system. This was verified empirically (§8.2.2.4). The results of Fig. 6.11 also indicate that the focusing scheme



described in §7.5, for which  $f = 108$  mm, cannot be used with a window\*, owing to geometrical aberration.

## 6.6 Experimental arrangement

### 6.6.1 Focusing system

The first attempt made to generate a line focus employed the off-axis mirror arrangement described in §6.3.4.2. A spherical mirror of nominal radius-of-curvature 406 mm was obtained. Used at  $45^\circ$ , this gives rise to a line focus 287 mm from the mirror. It may be seen from the discussion above that an equally narrow focus could be obtained from a cylindrical mirror. The spherical optic was chosen rather than a cylindrical mirror, mainly for reasons of cost.

Assuming the focal line width is limited only by the divergence of the laser, we can expect this to be  $8.6 \mu\text{m}$ , corresponding to an intensity of  $2 \times 10^{10} \text{ W cm}^{-2}$ , following the calculation method described in §6.2.2. This is 30% lower than the lowest intensity which has been reported previously for pumping the Xe III laser [Sher *et al.* 1991]. However, all previous demonstrations of the Xe III laser system have used 1064 nm lasers for plasma generation. It was hoped that the higher conversion efficiency associated with the shorter wavelength (248 nm) laser employed here might allow lower intensities to be used.

Furthermore, the use of a long focal-length optic is experimentally desirable for several reasons: it gives a large depth-of-focus which makes it easy to align; it gives a uniform energy distribution along the focal line; and it allows the use of a window without introducing severe geometrical aberrations (§6.5). In addition, the off-axis mirror technique is scaleable to shorter focal-lengths, without the introduction of aberrations (see §6.3.4.2). This means the experimental tricks devised for the use of this rather long focal-length mirror could be applied to any future system, using a faster focusing optic. Another important consideration is the plasma-expansion considered in §7.6. This suggests that for the rather slow-rising laser pulse to be used, there might well be no advantage to using a tighter focusing arrangement.

The experiments described in this chapter were unsuccessful - no SXR's were observed. It turned out that this had rather a mundane cause (described in §7.2). The experiment is reported here, however, because it turned out to be of great relevance to work on pumping the Xe III system with a picosecond KrF laser system. The experiments with picosecond pumping, which are described in chapter 8, used the same target chamber, and many of the same experimental techniques. Furthermore, an extension of this work to a shorter focal-length focusing geometry is described in §7.5.

### 6.6.2 Target chamber

A target chamber was commissioned and constructed for these experiments. This was designed to be as small as reasonably possible, so as to reduce the volume of (expensive) xenon gas needed. An extension tube was employed to allow the entrance window to be placed well away from the line focus, while not increasing the overall volume of the target chamber significantly. The main advantage of having the window far from the focus is the

---

\* In order to hold off atmospheric pressure, with the clear aperture required, the thinnest window which may be used is  $\sim 1$  mm.



reduction of debris deposition on the window. The target chamber is illustrated in Fig. 6.12.

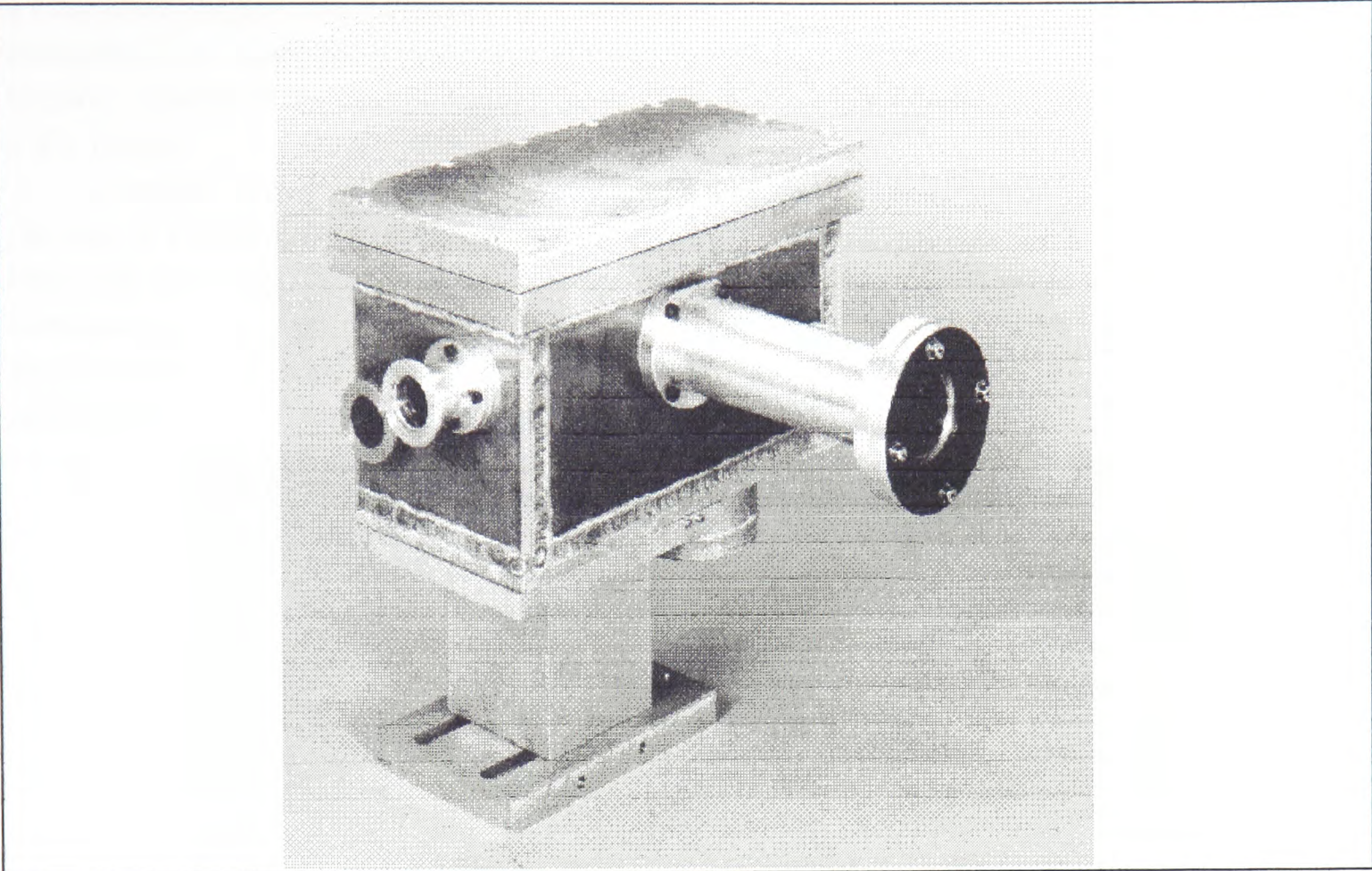


Figure 6.12. Target chamber commissioned for Xe III experiments.

### 6.6.3 Target winder

An experimental arrangement was needed to allow a fresh piece of target to be exposed to the laser beam, without letting air into the system. To this end a target winder was designed and constructed. A schematic of the design is given in Fig. 6.13.

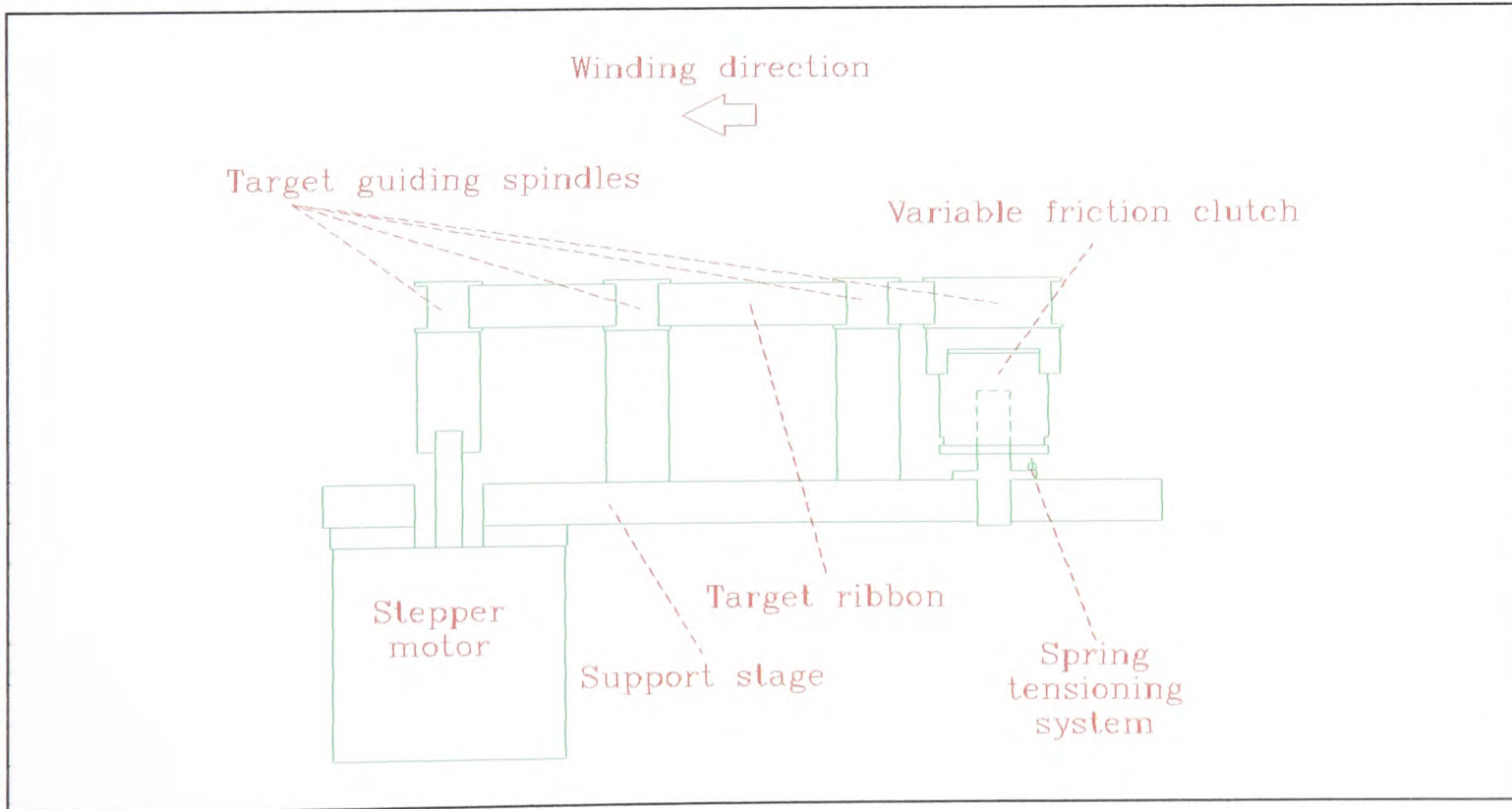
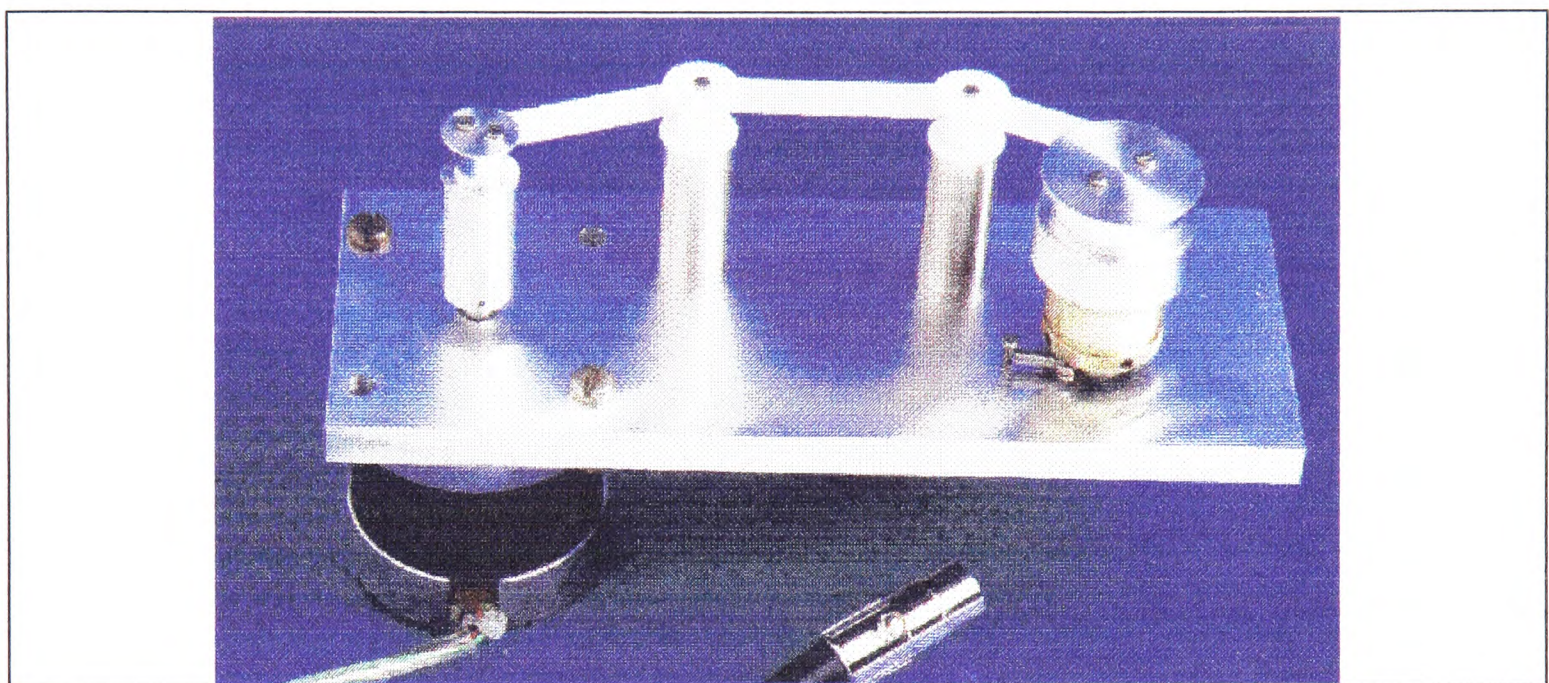


Figure 6.13. Schematic side elevation of target winder used in target chamber. Seen from rear, i.e. looking towards the laser beam.



A stepper motor was used to wind the target. It was kept under tension by means of a spring mounted variable-friction clutch. This allowed the target to be wound on as long as a (variable) torque was exceeded (*i.e.* when the motor was turning). If this torque was not exceeded (*i.e.* when the motor was stationary), the spring mounting kept the target under tension. Power to the stepper motor was provided via electrical feed-throughs mounted in a KF flange.

The target winder underwent several modifications as experiments progressed, to allow the use of a different sized target ribbon (§6.6.4), and the addition of a mirror for 109 nm light (§8.4.1). Fig. 6.14 is a photograph of it which was taken in its earliest (and most immaculate) incarnation. Soon after this photograph was taken (and before the experiments reported here) the support stage was blackened to reduce spurious reflections.



**Figure 6.14.** Photograph of target winder in its earliest incarnation.

### 6.6.4 Alignment

The target chamber and incident laser beam were arranged as shown in Fig. 6.15. A laser energy of 1.9 J was incident on the target chamber. Initially, the system was crudely aligned to give a bright breakdown spark on 10 mm wide strips of 100  $\mu\text{m}$  thick tantalum foil in air.



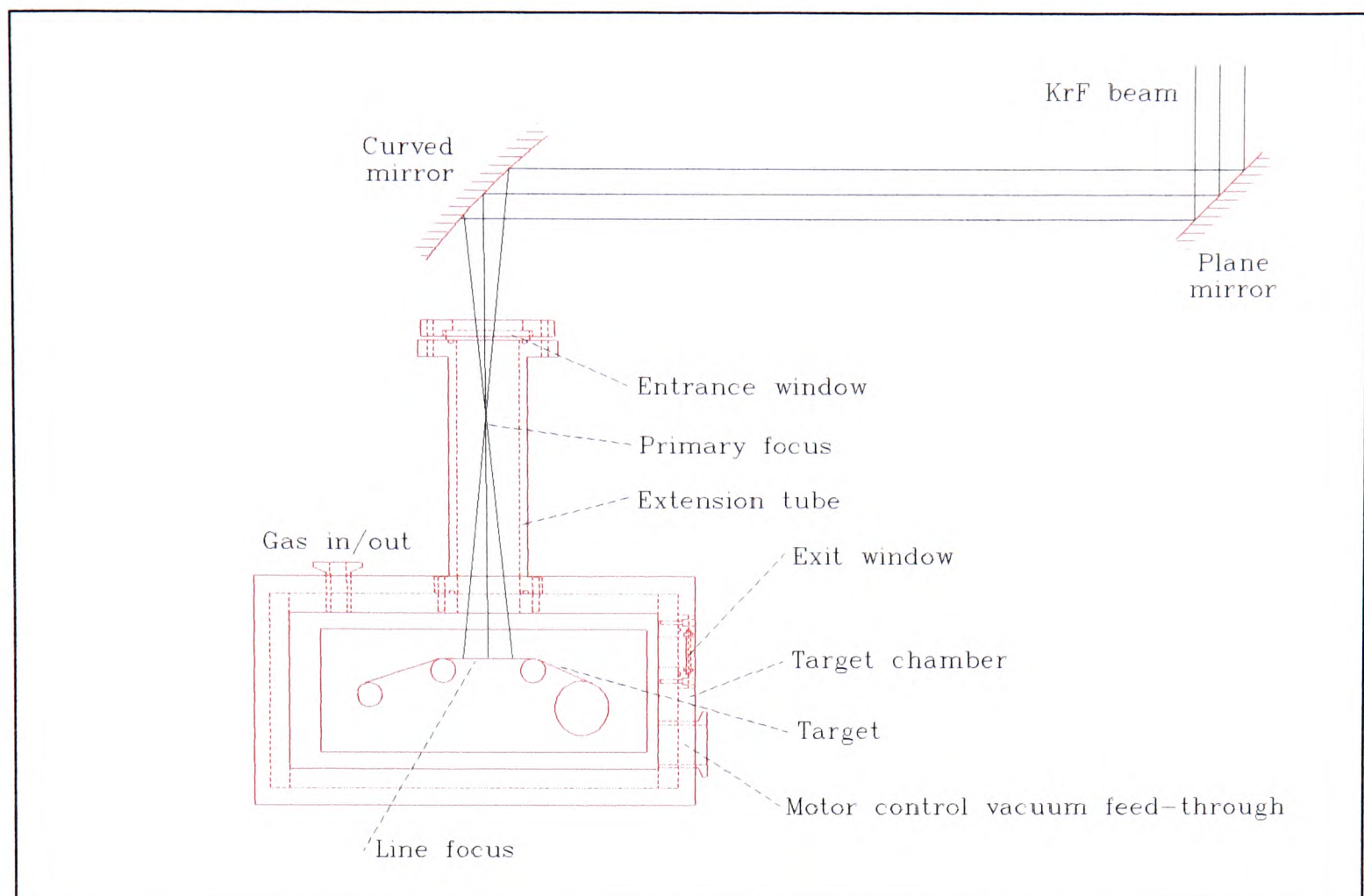


**Figure 6.15.** Schematic of line focus experiments.

It soon became clear that the 100  $\mu\text{m}$  tantalum foil target was too stiff, and tended to crease. For this reason, it was replaced by 25  $\mu\text{m}$  thick tantalum ribbon, of width 1 mm. Such ribbon was used in all subsequent experiments. Then work began on the alignment of the focusing system, to ensure the line focus coincided with the surface of the target.

### 6.6.5 Overview

The precision of the alignment required depends on the size of the focal-region. Applying expression (6.3) we find the depth-of-focus, DOF, to be

$$DOF = \frac{2f^2\theta_d}{A} = \frac{R^2\theta_d}{A} \quad (6.14),$$

where  $A$  is the width of the incident beam (30 mm) here.

For the focusing mirror used in these experiments,  $R$  was 406 mm, suggesting a depth-of-focus of 150  $\mu\text{m}$ . Clearly, it was essential to ensure the target surface was in the focus region, and all the degrees of freedom of translation and rotation of the target were considered. First, we consider the rotational degrees of freedom, pitch, roll, and yaw\*. These are defined in Fig. 6.16.

---

\* It may be helpful to consider the target as the wings of an aeroplane with the laser incident along its body.



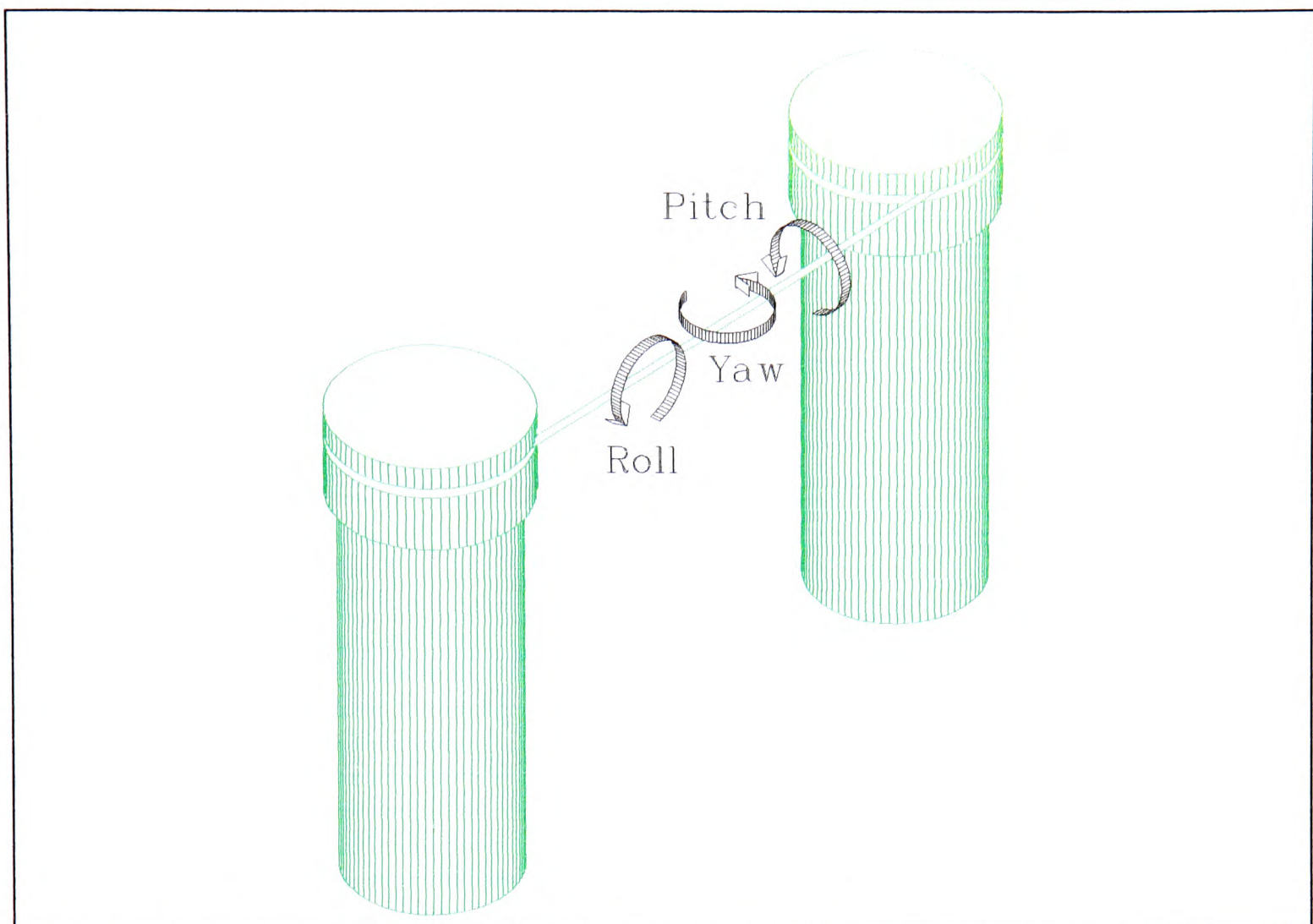


**Figure 6.16.** Target tape, showing the directions of pitch, yaw and roll.

## 6.6.6 Yaw

### 6.6.6.1 Overview of yaw alignment

The yaw of the target was critical; if incorrect, some of the target would be outside the focal volume. The accuracy required, in order not to tilt any of the 30 mm line out of the 150  $\mu\text{m}$  depth-of-focus, is simply the ratio of these lengths, *i.e.* 5 mrad. Considerable care had to be taken to achieve this accuracy.

The key to the process was to use an optical rail to define the direction along which the KrF beam was incident on the focusing mirror, and then to ensure the target was parallel to this direction. Once a HeNe beam had been aligned along the optical rail, a pentaprism was used to steer it through exactly  $90^\circ$  (see §6.6.6.2), and the optical rail on which the target chamber was mounted was rotated, to ensure that the reflection of this beam from the target was along the line of incidence. The shadow of a plumb line was used to determine whether the incident and reflected HeNe beams were in the same vertical plane. This is shown schematically in Fig. 6.17.



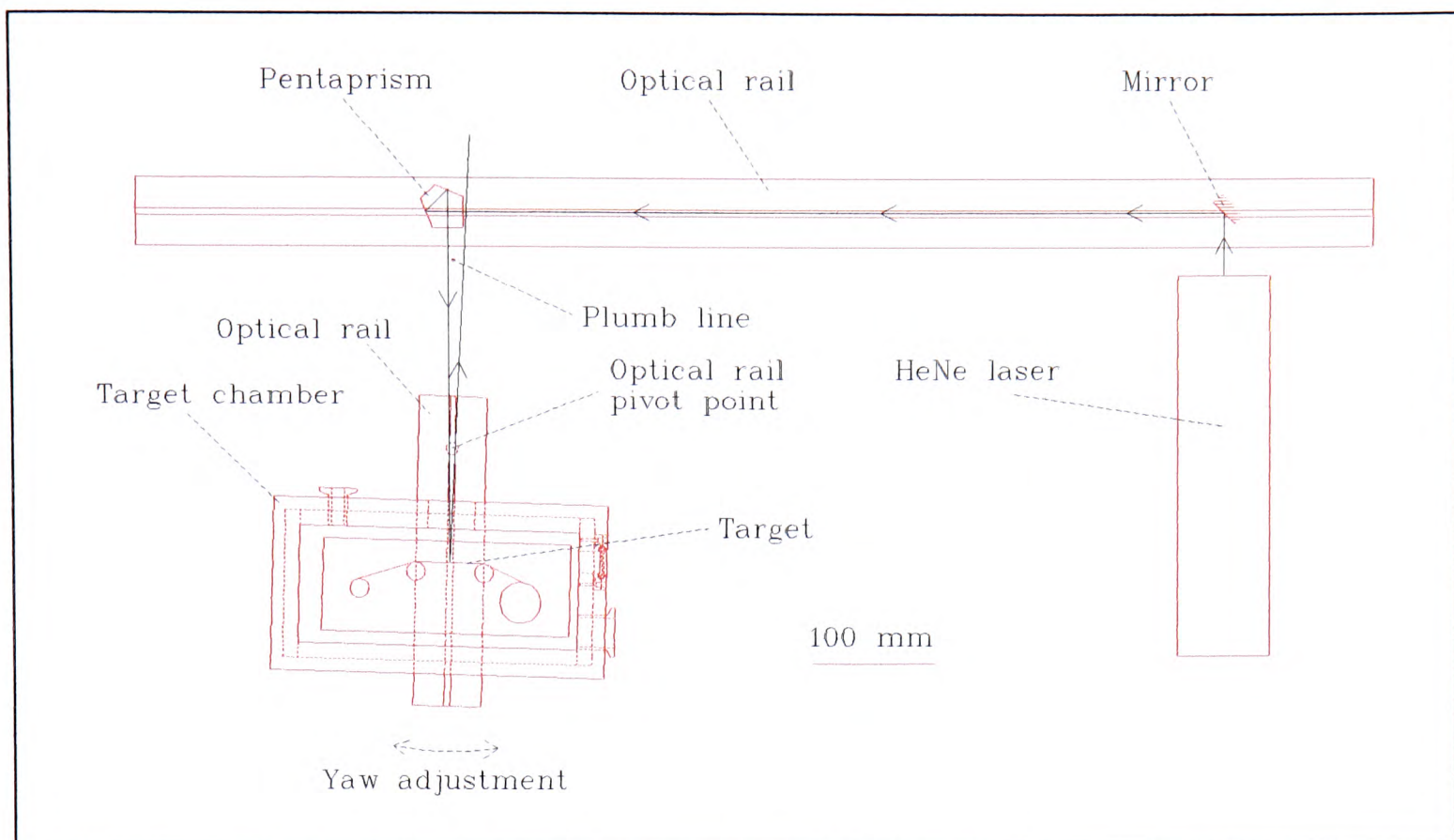


**Figure 6.17.** Schematic plan of pentaprism technique for yaw adjustment. For clarity the system is shown slightly misaligned. Diagram is to scale.

This technique ensured the target was parallel to the optical rail. The final stage of the yaw alignment was to ensure the KrF beam was parallel to the optical rail. For this, a target was rigidly mounted to a jockey on the optical rail. The target consisted of a pair of crossed wires obscuring a ribbon of thermal paper. The alignment of the KrF beam was adjusted with the plane mirror (see Fig. 6.15) until the burn pattern (and in particular the shadow of the  $45^\circ$  reflective spot beamsplitter used to couple the KrF oscillator and amplifier) on the thermal paper was in the same position relative to the crossed wires, regardless of its position along the optical rail.

#### 6.6.6.2 How a pentaprism works

In this section we shall consider how a pentaprism works, since it is essential to the alignment technique, and must be used with a little care. The pentaprism has entrance and exit faces forming a right angle; the other two faces at which there are reflections form an angle of  $45^\circ$  to each other. This will rotate a horizontal beam through a right angle in the horizontal plane of incidence, almost regardless of the alignment of the pentaprism. This is not immediately obvious, and we consider here why this is so.



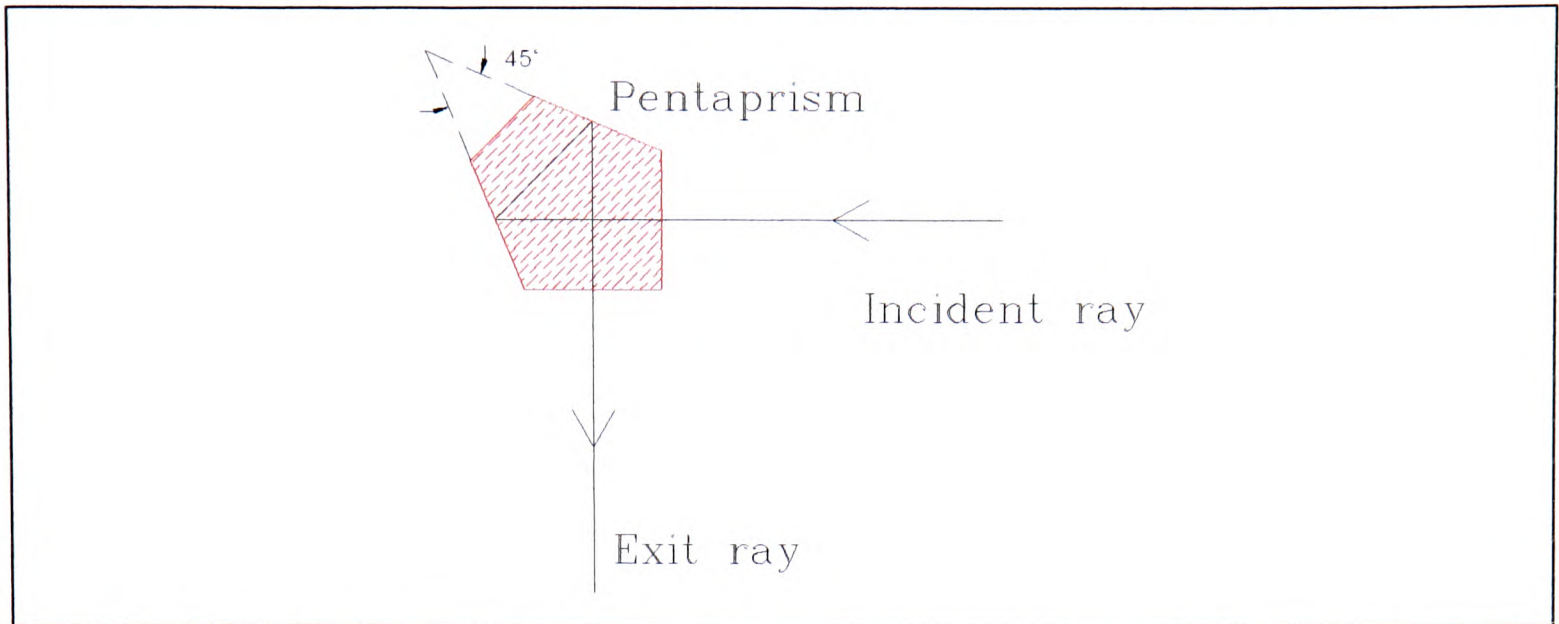


**Figure 6.18.** Horizontal section, showing a pentaprism steering an incident beam through  $90^\circ$ .

Consider the horizontal section shown in Fig. 6.18. This shows how a horizontal beam incident normally on the pentaprism is deviated through a right angle by it. We must consider how any misalignment of the pentaprism affects this deviation. First we note that we may translate the pentaprism in any way without affecting the angular deviation.

Next we consider rotations. The vital property of the pentaprism is that two of the faces are angled at  $45^\circ$  to each other. It is easily shown that such an arrangement will deviate a beam through a right angle, regardless of any rotation of the prism about a vertical axis. However, it is possible to misalign the prism by rotating it about horizontal axes.

For the alignment of the line focus target, it is only the beam deviation projected onto a horizontal plane that is relevant (and it must be exactly  $90^\circ$ ). To calculate how a misalignment of the prism can affect this angle, we consider how the horizontal section of the pentaprism (as illustrated in Fig. 6.18) varies with the orientation of the pentaprism. In particular, we are interested in how the apparent angle between the  $45^\circ$  faces varies.

We use the normal to the top face to define the orientation of the pentaprism. We define its angle from the vertical as  $\theta$ , and its azimuthal orientation\* as  $\phi$ . In this case, it may be shown that the apparent angle,  $\xi$ , between the  $45^\circ$  faces, is given by

$$\xi = \frac{\pi}{4} + \left( \frac{\cos 2\phi + \sin 2\phi}{4} \right) \theta^2 + O(\theta^4) \quad (0.15),$$

where all angles are in radians and  $\theta$  is small. This indicates that a slight misorientation of the pentaprism gives rise to only a second-order error in the apparent angle between the  $45^\circ$  faces. An equivalent calculation for the perpendicular entrance and exit faces also yields only a second-order dependence on  $\theta$ .

These results indicate that a small misalignment of pentaprism *can* alter the beam deviation angle (projected onto a horizontal plane), but that the deviation is second order in the misalignment angle. By looking at the reflection of the HeNe beam in the entrance face of the pentaprism, it was possible to minimise the misalignment angle to the extent that it will have contributed a negligible error to the yaw alignment.

---

\* For the results presented here the zero of azimuthal orientation is taken as corresponding to a direction perpendicular to one of the  $45^\circ$  faces.



### 6.6.6.3 Geometrical spreading of KrF beam

Any geometrical spreading (whether converging or diverging) of the KrF beam will give rise to yaw error. We shall save a detailed discussion of this until §8.2.2.2. Briefly, any such spreading gives rise to a virtual focus, and makes the focusing system equivalent to the mirror and lens geometry described in §6.3.4.1. For the results presented here, no spreading was measurable (on the burn patterns used to align to KrF beam with the optical rail). This corresponds to any virtual focus being at least 144 m from the focusing mirror (cf. §8.2.2.2, for which this distance is  $\sim 10$  m). This lack of geometrical spreading is to be expected, since the cavity arrangement is designed to give a parallel beam. The accuracy with which the cavity mirrors were positioned (and with which their focal-lengths were known) is consistent with this 144 m limit on the geometrical spreading.

The effect of a virtual focus 144 m from the mirror would be to give a 2.1 mrad yaw error, and we take this as an upper limit for the error due to geometrical spreading.

### 6.6.6.4 Overall yaw accuracy

Table 6.1. shows the various contributions to the inaccuracy of the yaw alignment. The parallelism of the pentaprism faces is not known; an estimate of 1 mrad was chosen\* as this is the most coarse pentaprism tolerance offered by the manufacturer *Melles-Griot*. The overall random error of alignment was estimated as 2.8 mrad, easily below the 5 mrad ceiling (§6.6.6.1). A 2.8 mrad yaw of the target out of the focal region would halve the effective depth-of-focus to about 70  $\mu\text{m}$ . However, it is not entirely undesirable - it would give rise to a distance of 225  $\mu\text{m}$  over which half the target would be in focus. Although this situation would be disastrous for Xe III output, it would only halve any SXR signal observed.

Cause of error	Contribution to yaw error (mrad)
Alignment of HeNe with optical rail	0.9
Alignment of target perpendicular to HeNe beam	1.1
Parallelism of pentaprism faces	1
Alignment of KrF beam with optical rail	0.4
Geometrical spreading of beam	2.1
<b>Total (statistical)</b>	<b>2.8</b>

*Table 6.1. Upper limits on contributions to inaccuracy of yaw alignment.*

## 6.6.7 Pitch

The pitch of the target is not very important to the quality of plasma produced; but if the KrF radiation were incident too obliquely (more than about  $10^\circ$ , say), one would expect detrimental effects, as some of the KrF radiation reflected from the overdense region of the plasma would be reflected out of the plasma, and would not be able to heat it.

---

\* This may have been a dangerous assumption - really it should have been checked experimentally.



The pitch was measured by looking at the vertical deviation of the HeNe beam reflected from the target ribbon, during the yaw alignment (see Fig. 6.17). Severe pitch angles (up to  $\sim 30^\circ$ ) were observed, and these were investigated. The pitch angle was found to change as the target ribbon was wound on.

Several modifications were tried in order to correct this. The PTFE spindles over which the target slipped were replaced by stainless steel ones, in case the sharp edges of the target were cutting into the softer PTFE supports. The slipping torque of the variable friction clutch used to tension the ribbon was varied. Neither of these changes produced a significant improvement.

Finally, the problem was solved by machining a groove on the spool supporting the unexposed target, and winding the unexposed target into it. This ensured the height of the target (from the support stage) did not vary along its length - such a height variation had been causing twists in the target and hence the severe pitch angles observed.

After this process, the pitch angle still varied as the target was wound on, but did not exceed  $3^\circ$ , and this was considered acceptable.

### 6.6.8 Roll

The roll of the target makes no difference to the quality of the plasma produced, but must be adjusted simply to ensure that all the whole length of the line focus is on the target. To this end, one of three posts holding the target winder support stage off the floor of the target chamber took the form of a stiff spring, with its length adjustable by a screw running down its centre. This allowed the roll to be adjusted to ensure the target was horizontal.

### 6.6.9 Depth

Once the rotational degrees of freedom of the target had been set, there remained the problem of ensuring that the line focus was on the target surface. The target chamber was mounted on an optical rail and a translation stage to allow both coarse and fine adjustments of its position.

#### 6.6.9.1 *Crude geometric estimation*

Fig. 6.19 shows a geometric technique used to find the position of the focus. The KrF beam was attenuated, and focused near the target. This gave a burn pattern with a shadow in the centre of a thermal paper target held on the back wall of the target chamber (and so a constant distance from the target). As the target is moved in and out of the focus, there is variation in both the total width,  $w$ , of the burn pattern and the shadow of the target (width  $s$ ).



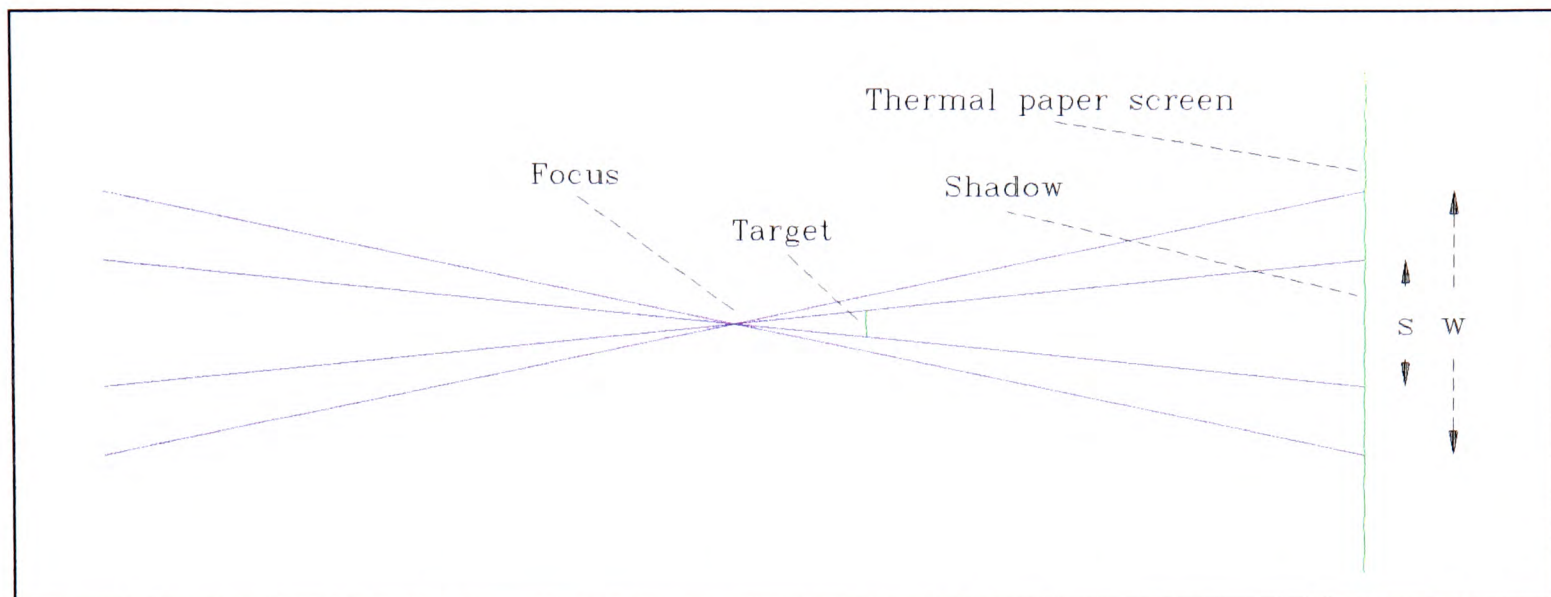


**Figure 6.19.** Geometrical technique used to find location of line focus. Section of beam and target.

It is easily shown that, provided the distance between the target and the screen remains fixed, the ratio  $\pm(s/w)$  varies linearly with the distance of the target from the focus (with the sign different on opposite sides of the focus). This allowed a crude (1.5 mm) estimate of the position of the focus.

#### 6.6.9.2 Line etching

Solving an unrelated technological problem provided an estimate of the focus position much more accurately than the geometrical technique. The problem was to scribe 2 cm x 25  $\mu\text{m}$  lines on glass microscope slides, for use in an optical spectroscopy experiment. A glass slide of known thickness was rested against the target and the laser focused on to it. A line could be marked in a single shot. Extra cracks, perpendicular to the line, were seen when the full beam energy was used. To prevent this, the beam was attenuated (by the  $\text{NO}_2$  cell) by a factor of 3, corresponding to an energy of 20  $\text{mJ mm}^{-1}$  in the line focus.

The width of the lines marked on the glass was measured by inspection with an optical microscope. The position of the target was varied, and the widths plotted against position, for the focusing region in which the width was determined geometrically. In this way, it was possible to find the position of the focus to an accuracy of 50  $\mu\text{m}$ .

## 6.7 Detection of soft x-rays

The first (and, it turned out, only) experiment to be conducted with this system was to see whether any SXR of photon-energy greater than 67 eV could be produced by the plasma. It is photons of energy 67 eV to 100 eV\* which are of particular interest for pumping the Xe III system. A detector sensitive to these SXRs, but not to visible light, or scattered KrF radiation was needed.

\* Although photons of energy greater than 100 eV can be used, their use is inefficient. Thus, in this work we shall concentrate only on the generation of 67 eV to 100 eV photons.



## 6.8 Sodium salicylate as a scintillator

Various techniques can be used for SXR detection, and these are discussed briefly in §6.9. The technique chosen, however, was to use a scintillator, in which incident photons cause (multiple) ionisation, and the resulting electron-hole recombination generates visible photons. These photons were detected with a Thorn-EMI type 9783B photomultiplier tube (PMT). The use of a PMT makes the system very sensitive, since it can be used to give several orders of magnitude of gain.

Sodium salicylate,  $C_6H_4(OH).COONa$ , is well established as a scintillator for SXR detection, giving a quantum conversion efficiency of  $\sim 5$  in the 67-100 eV range [Husk *et al.* 1992]. Although other scintillators may give a higher conversion efficiency [Regan *et al.* 1994, Kumar & Datta 1979], sodium salicylate has been the most extensively characterised, and so was chosen for this application.

## 6.9 Other SXR detectors

There are other detectors suitable for the 67 eV to 100 eV spectral region. Some of these were considered for this application but not used. We review them briefly below:

### 6.9.1.1 Photographic film

Suitable photographic film can be used to detect SXRs, but has the disadvantage over sodium salicylate of needing to be wound on (or only used for a single experiment), then developed, and then having a nonlinear relationship between exposure and the extent of chemical changes in the emulsion [Henke *et al.* 1984].

### 6.9.1.2 Photoelectric effect based detectors

Several detectors take advantage of the photoelectric effect to detect SXR radiation. The simplest of these, is the vacuum photodiode (VPD); a current of photoelectrons is measured when photons are incident on a photocathode.

All solids are strongly absorbing to light in the range 67-100 eV, and so only very thin (and hence fragile) windows are available. For this reason VPDs without windows have been developed for SXR detection. Canfield & Swanson [1987] report detection over the range 10 eV to 248 eV using aluminium photocathodes, thickened with an oxide layer. VPDs operate at unit gain (electrons out per photoelectron). Because of this lack of sensitivity, and for reasons of cost and complexity, windowless VPDs were not used for this application.

The problem of low gain can be avoided by using a windowless PMT. But this is more complex and more expensive than using a scintillator to sensitise a windowed PMT, the approach adopted here.

Another common tool for x-ray detection is the micro-channel plate (MCP). This is a two dimensional array of micro-channels. These contain devices similar to photomultipliers, but which provide optical rather than electrical output; photoelectrons emitted from a photocathode are amplified in each channel, and then hit a scintillator, producing visible light. They are used for imaging, but as this was not needed for this application they had no advantage over using a scintillator, and would have been a great deal more expensive.



### 6.9.1.3 Silicon PIN photodiodes

Finally, we consider solid-state photodiode detectors. These devices consist of very pure silicon which has been doped, to give a p-type and an n-type conduction region, separated by an undoped (intrinsic conduction) region. For maximum sensitivity, the resulting p-i-n (PIN) diode is reverse biased, and only allows a current to flow when electron-hole pairs are created (by incident x-rays) in the undoped region.

A PIN diode was used for the detection of SXR photons for the experiments described in §8.3 and in chapter 9. Such a diode was not used for the experiments described in this chapter since none was immediately available, and since it would have a lower sensitivity than the PMT system. This was confirmed by the experiments described in §8.3.

## 6.10 SXR filters

Sodium salicylate is useful as a scintillator over a very wide spectral range, and a filter was needed to eliminate visible, UV, and VUV light, leaving only 67-100 eV SXRs. Some suitable substrates were available, consisting of 2 mm squares of 125 nm thick  $\text{Si}_3\text{N}_4$  overcoated with 25 nm of  $\text{SiO}_2$ . The theoretical bulk transmission of these is shown in Fig. 6.20.

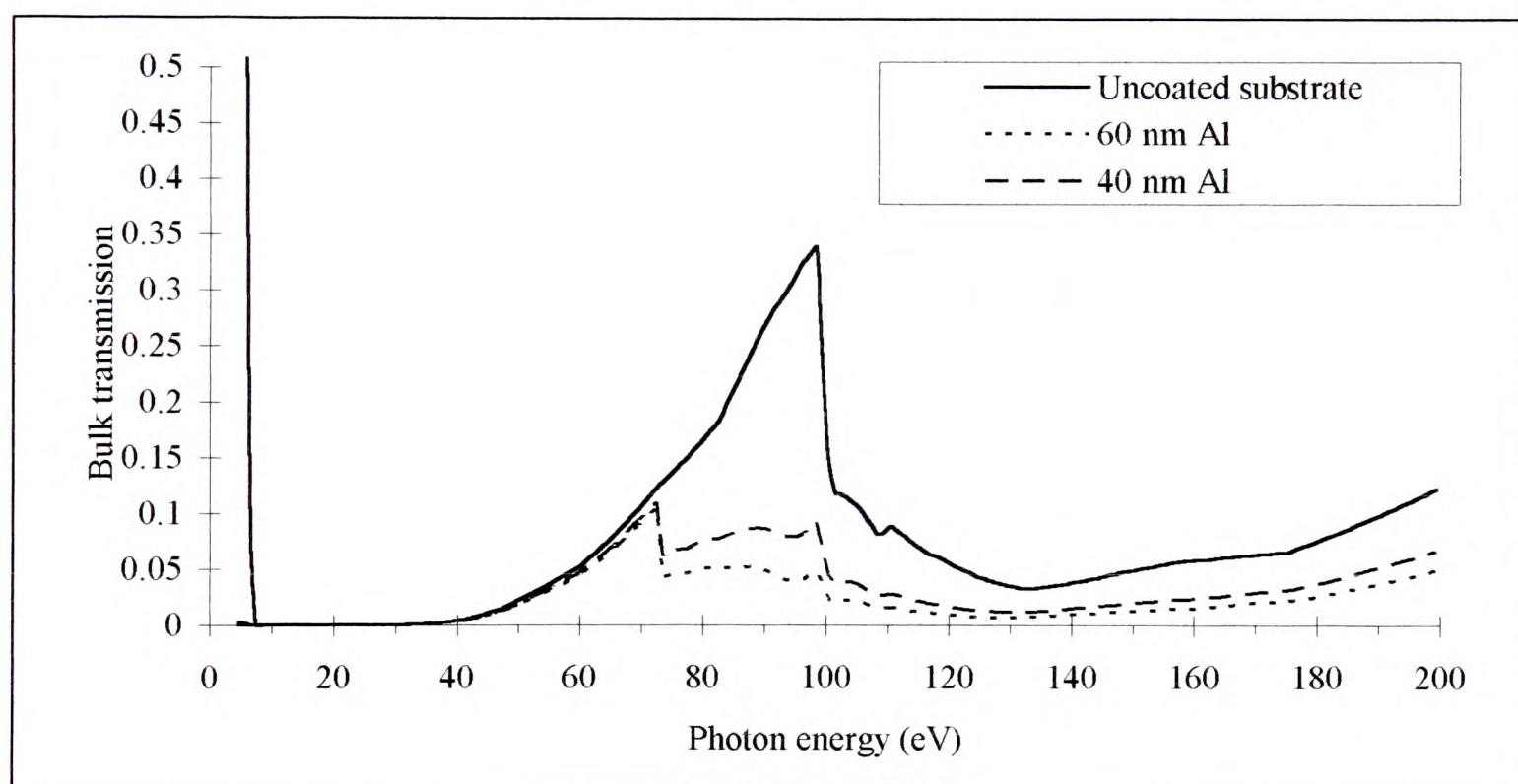


**Figure 6.20.** Theoretical bulk transmission (i.e. losses due to absorption only) of uncoated substrate, and the same overcoated with 40 nm and 60 nm of Al. Calculated from data given by Cotton [1990] and Palik [1985].

It is clear from Fig. 6.20 that the substrates were transmitting in the UV and visible spectral regions. In particular, for KrF laser photons (5 eV) the bulk transmission predicted is about 90%. Since sodium salicylate is sensitive to this light (and transmitting to visible light), a filter overcoating material was needed to block UV and visible light, but pass the soft X-rays. Aluminium was found to be an ideal candidate.

Filters of two different designs were made, ones with 40 nm, and ones with 60 nm of Al, and the calculated bulk transmissions for these are shown in Fig. 6.20. All the experiments described here used the 60 nm design, after initial experiments with the 40 nm filters suggested they were not rejecting sufficient visible and UV light. With this 60 nm



design, the bulk transmission of the filter was 0.012% at the KrF laser photon energy, but between 7.8% and 1.6% over the 67 eV to 100 eV spectral region of interest. The actual transmission of the filter for the KrF laser photon energy will have been even less than the 0.012% bulk transmission, owing to reflection at the aluminium surface. This reflectivity is typically ~90% over the UV and visible spectrum [Koller 1965], and so the filter transmission is ~0.0012% at the KrF laser wavelength. The reflectivity to SXR is negligible, however, partly because of the presence of a 2-5 nm thick layer of aluminium oxide on the surface [Palik 1985]. This means the visible/UV transmission is three orders of magnitude lower than the transmission in the SXR spectral region of interest.

The use of aluminium coated silicon nitride as a filter to remove UV from LGPs for a different (SXR contact microscopy) application has been reported by Stead *et al.* [1990].

## 6.11 Manufacture and use of scintillators

### 6.11.1 Spray coating technique

An investigation was made of how to make sodium salicylate scintillators. Husk *et al.* [1992] used four different techniques for this; grains of sodium salicylate were glued to glass substrates with water glass (sodium silicate), or solutions of sodium salicylate in acetone, water or methanol were sprayed directly on to substrates.

Some 99.9% pure sodium salicylate was obtained\*, and various techniques were investigated for producing uniform coatings of it. The use of hot or cold substrates, the spraying or painting of solutions of different concentrations of sodium salicylate in methanol, and the use of smooth or roughened substrates were all investigated.

The best technique found was to sandblast a microscope slide, clean it, and heat it to ~80 °C. The hot slide was sprayed with a room-temperature saturated solution of sodium salicylate in methanol. Four coats were needed to produce a coating of mean thickness ~2 mg cm<sup>-2</sup>. This thickness was chosen because Husk *et al.* [1992] have commented that it approximately maximises the fluorescence†. This coating technique is very similar to that used by Samson & Haddad [1974].

The coatings showed little variation in thickness over the ~20 cm<sup>2</sup> area of the microscope slides used; this was assessed by observing the fluorescence of the scintillator under a mercury lamp. No features larger than about 200 µm were visible.

After laying down the coatings they were held at 80 °C for 10 minutes to drive off any excess solvent. The temperature was chosen to be below the dissociation temperature of between 100 °C and 150 °C reported by Husk *et al.* [1991].

## 6.12 Quantum efficiency of sodium salicylate

The efficiency of sodium salicylate has been measured over various photon energy ranges by various authors. Husk *et al.* [1992] have reviewed measurements over the range 5-400 eV, and give their own measurements for absolute efficiency over the range

---

\* Sodium salicylate, ANALAR, Obtained from Merck Ltd., of Poole.

† In fact, based on an absorption spectrum given in the same work, rather thinner coatings would probably have worked equally well, as long as they could be made to cover the whole substrate area.



70-400 eV. Significant discrepancies between authors are found, for the range 5-70 eV, only some of which can be ascribed to effects such as fatigue and experimental error. This is discussed in greater depth in §9.3.1.2.

For the 67-100 eV range the quantum efficiency has been found to rise linearly from 400% to 600% [Husk *et al.* 1992]. For UV light, e.g. for 4.9 eV photons (253.7 nm, almost the KrF laser wavelength) Kumar & Datta [1979] report 37% quantum efficiency. They comment, however, that other authors have found values spanning the range 25% to 99%.

Fortunately, we do not need a precise calibration. The salient point is that the energy efficiency for SXR is at least four times that for UV light. This means the signal (SXR) to noise (longer wavelength components) ratio of the SXR detection experiments is enhanced by the energy response of the scintillator.

## 6.13 Experiments to detect SXRs

### 6.13.1 Experimental arrangement

A mount was constructed for the scintillator and filter, and this is shown in Fig. 6.21. This allowed the region between the filter and scintillator to be evacuated, without letting light in around the edges of the filter. The filter was fixed to the mount by means of 10  $\mu\text{m}$  thick aluminium foil, which in turn was held to the mount and filter by PVC adhesive tape. The whole arrangement was fixed to the wall of the target chamber by the same foil/PVC tape technique. Light from the scintillator escaped from the target chamber through a glass window, where it was detected by the PMT.

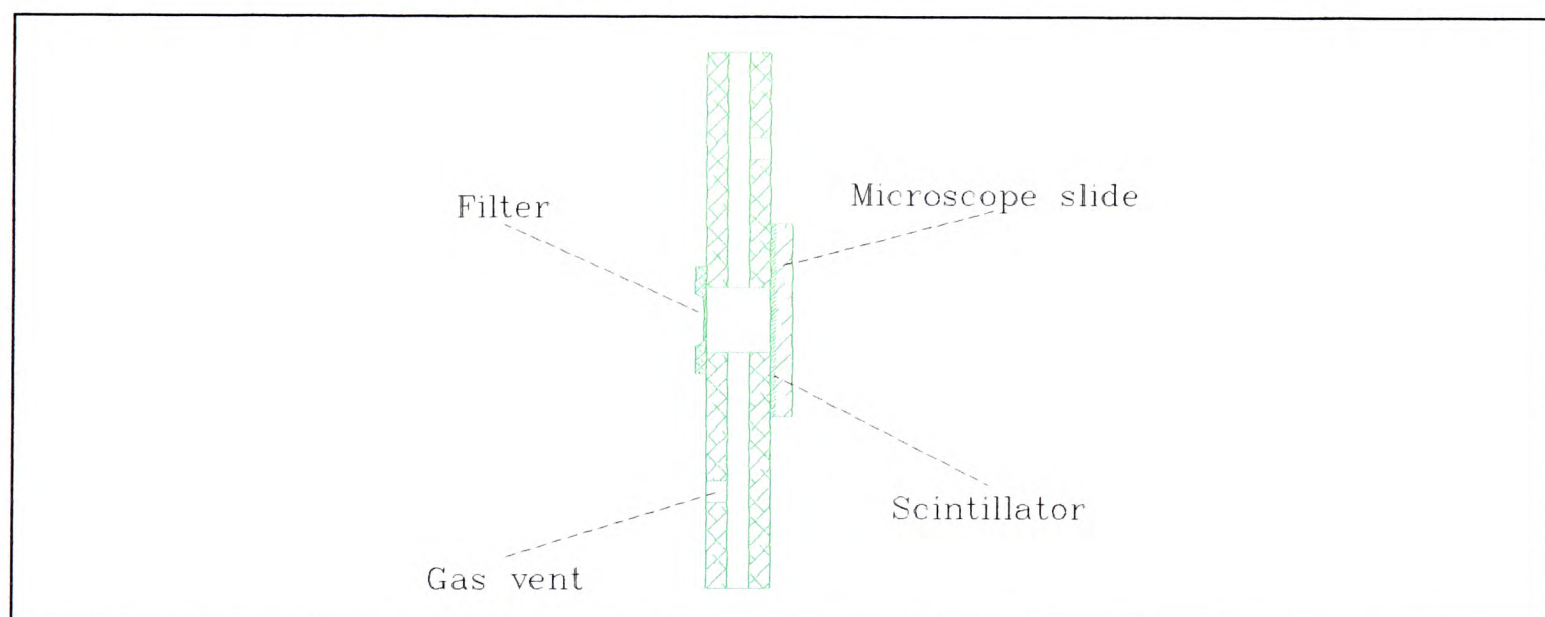


**Figure 6.21.** Section of mount for filter and scintillator, allowing for evacuation of the space between them, without admitting extraneous light. All surfaces were blackened.

The experimental arrangement is shown in Fig. 6.22. The x-ray detection system was placed 7 mrad ( $0.4^\circ$ ) in front of the line defined by the target ribbon. This was primarily for convenience - there was a window in the target chamber there to allow the exit of any 109 nm radiation. Furthermore, this is the direction in which the (droplet) debris emission is least. Unfortunately, it is also the direction in which x-ray emission is least.



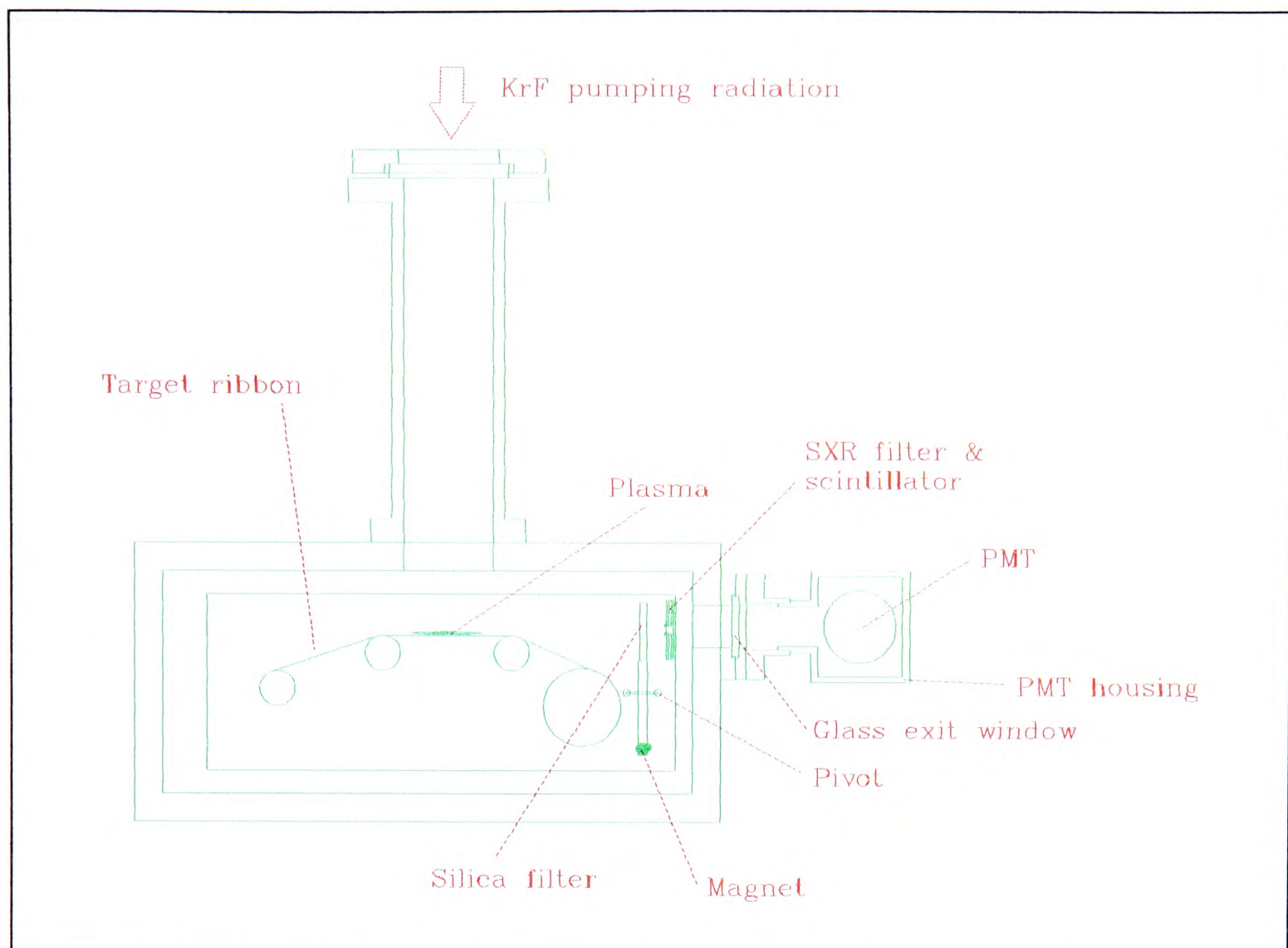


**Figure 6.22.** Schematic of arrangement used to detect soft x-rays from line focus.

A 6 mm thick fused silica filter was mounted on a magnetically-activated pivot. This allowed the filter to be moved into and out of the line of SXR detection, simply by placing a magnet on top of the sealed (and evacuated) target chamber\*. The rise and fall of the pivot arm could be felt by touching the target chamber as the magnet was moved. This check was made each time the filter was moved into or out of the beam.

The purpose of the filter was to distinguish between an SXR signal, and one caused by visible/UV scatter. The filter will have totally blocked SXRs, but allowed visible/UV light to pass, down to the  $\sim 180$  nm transmission cut-off wavelength of fused silica. The aim of the experiment was to find a signal which disappeared when the silica window was in the beam.

## 6.14 Results

No SXRs were detected. Experiments which were subsequently conducted, and are reported in chapter 7, indicated that the laser beam quality was much poorer than had been assumed in the calculations of §6.6.1, and the system could not have been expected to show a significant x-ray conversion efficiency. For this reason, we shall not go into

---

\* The presence of a magnetic field bends the trajectories of electrons in a PMT. This reduces the gain. For these experiments, the magnet was positioned  $\sim 10$  cm from the PMT. The effect this had on the gain was measured, by looking at changes to a constant optical signal, when the magnet was moved in and out of position. For the gains used here, the reduction in sensitivity was less than 4%, and has been ignored.



sufficient detail of the experimental conditions to present this as a definitive negative result. However, the following points are worth noting:

- An optical signal was observed - it disappeared when the laser was fired but the beam was blocked. It was not an SXR signal, however, because it remained when the fused silica filter was in place.
- The sensitivity of the experiment could be estimated from the size of the noise signal. We shall not describe this calculation in detail here; it is based on almost identical\* assumptions to those used in a similar calculation given in §8.5.2. For the 2.1 J KrF energy on target, the upper limit on the conversion efficiency into the spectral region of detection, was 0.2%. This is extremely poor for an LGP (see, for example, Powers & Shields [1994]).
- Scintillators were stored in a dessicator when not in use, and none was older than 14 days old. These were precautions against contamination by atmospheric moisture. Such contamination has been reported by Allison *et al.* [1964a], who also found that storage in a dessicator gave rise to constant yield for 10 eV photons, over a period of seven months.
- Radiation damage to sodium salicylate has been reported by Husk *et al.* [1991 & 1992]. A simple, worst-case estimate suggested that if very high conversion efficiencies were present here, this could have caused the yield of the scintillator to fall by 50% over a few tens of laser shots. No such fall was observed over the course of the experiment. Thus, we may empirically rule out the possibility of radiation damage to the sodium salicylate being responsible for the absence of an SXR signal.
- At the time of the experiments it was not possible to rule out (rotary) vacuum pump oil, or the lubrication oil from the stepper motor as having been responsible for the absence of an SXR signal. This could have contaminated the surface of the scintillator [Kumar & Datta 1979], or, as a vapour, could have absorbed any SXRs produced. One experiment to investigate this was conducted. Weighing of a scintillator exposed to the vacuum system for 20 days suggested it was absorbing rotary pump oil, at a rate of  $0.8 \mu\text{g cm}^{-2}$  per day. No scintillator was exposed to the vacuum system for more than 28 hours before use, and this suggests an absorption of SXRs due to deposited oil of less than 5%†.

## 6.15 Repercussions

Since no signal had been observed it was important to be confident that had there been significant SXR production, it would have been observed. This could only be proved convincingly by observing an SXR signal, and this is described in §7.3.4.1. The negative result of this experiment also led to several other repercussions, which are described in the following chapters.

---

\* For the calculation here the differences are: different position and size of detector, 5% transmittance, mean scintillator quantum efficiency of 4, 70 eV photon-energy.

† This calculation assumes the *mass* attenuation coefficients of the pump-oil to be the same as that of the simplest hydrocarbon, methane. Values for these coefficients were taken from Lide [1992].



# 7. Experimental repercussions: beam cleaning and spot foci

---

## 7.1 Introduction

There were several repercussions of the failure of the attempt described in chapter 6 to generate any x-rays. These repercussions are described in this chapter. Although presented sequentially, they were actually carried out in parallel.

The KrF beam quality was measured, and SXR emission was observed from a spot-focus LGP. In the process, some investigations of a novel SXR detection technique were undertaken. Attempts were made to use these SXRs to generate 109 nm fluorescence from Xe III.

## 7.2 Beam quality

Some of the etch patterns generated by the line focus on microscope slides were wider than had been expected. In particular, for the focusing experiment described in §6.6.9.1, the narrowest lines observed were 30  $\mu\text{m}$  across. This compares badly with the  $\sim 9 \mu\text{m}$  width expected from a 29  $\mu\text{rad}$  divergence beam focused over a distance of 290 mm. At the time this was attributed to nonlinearity in the response of the slide to the incident energy, because narrower lines (18  $\mu\text{m}$ ) had been observed when a little more attenuation was used. However, there was a double-line structure within these narrower lines.

The cause of these observations was suspected to be poor KrF laser beam quality, and so this was investigated. The experimental arrangement used is illustrated in Fig. 7.1. An  $f=2.5$  m focal-length spherical mirror was used to produce a far-field image of the beam. This was sufficiently large to be mapped by a 15.6  $\mu\text{m}$  resolution beam-profiling video camera (Exitech Profile 256). In order to avoid aberrations, the mirror was used at exactly normal incidence. This required the presence of the flat beamsplitter shown in Fig. 7.1. A filter was used (near the focus, so as to minimise aberrations) to eliminate visible light, but pass the KrF beam. The  $\text{NO}_2$  cell described in §5.3.1.1 was used to attenuate the beam to prevent optical damage to the camera. The camera was placed outside the screened laser-room, to protect it from damage from electrical noise when the laser was fired.



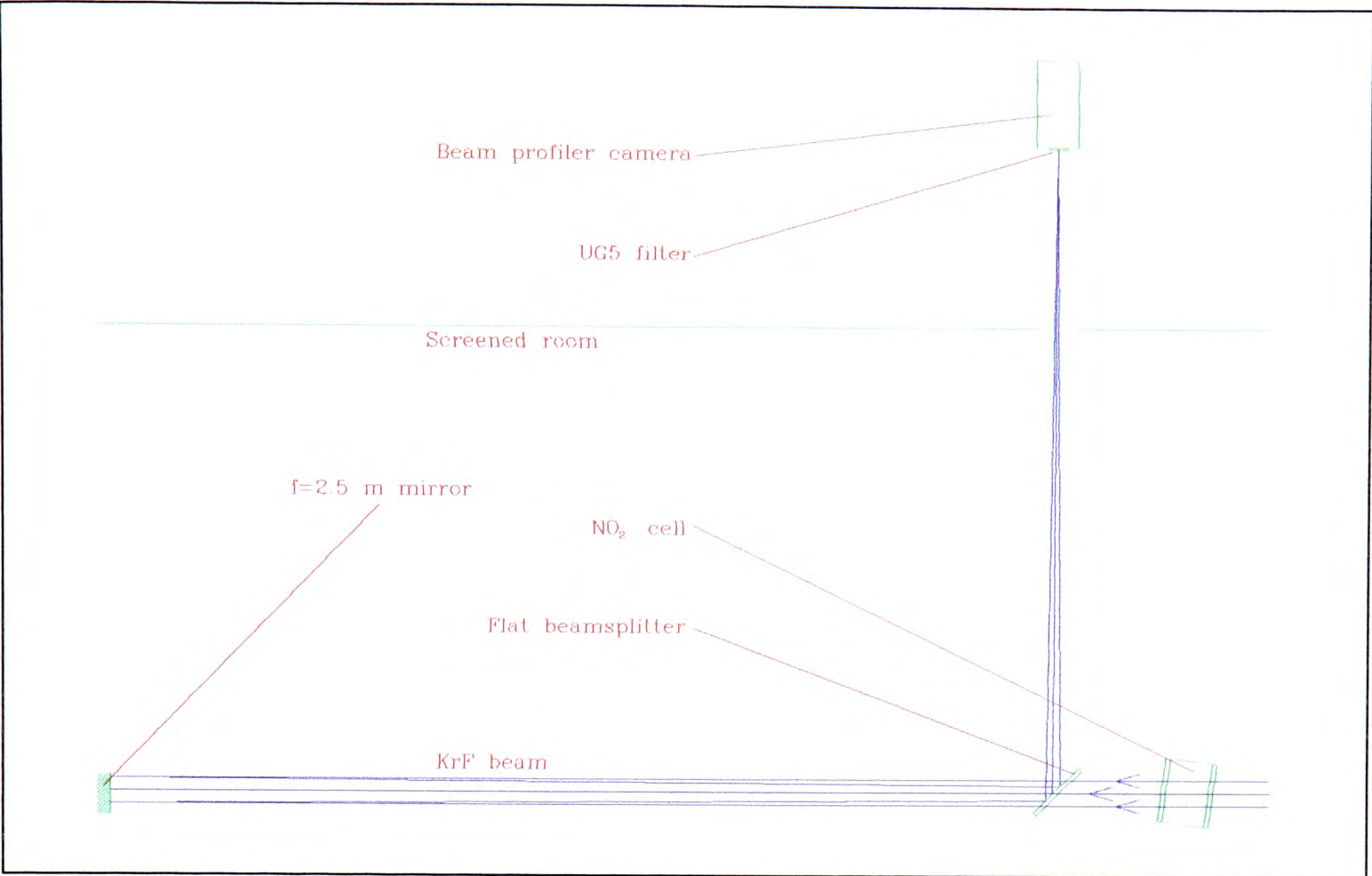


**Figure 7.1.** Experimental arrangement used for beam divergence measurements. To scale.

The camera has an integration time of 20  $\mu$ s, and so gives no indication of the time evolution of the divergence. Furthermore, the spot focus produced is so intense that the experiment is completely insensitive to high-divergence light. Even if it contains a significant portion of the beam energy, this could appear as a pedestal too weak to detect in the far field intensity distribution. A way around these problems has been reported by Coutts *et al.* [1993] and Coutts [1994], applied to similar high-gain, unstable-cavity, nanosecond-pulse lasers, namely copper vapour lasers.

Despite the drawbacks of the experimental arrangement, the results were illuminating. A double peak dominated the far field pattern. This is illustrated in Fig. 7.2.

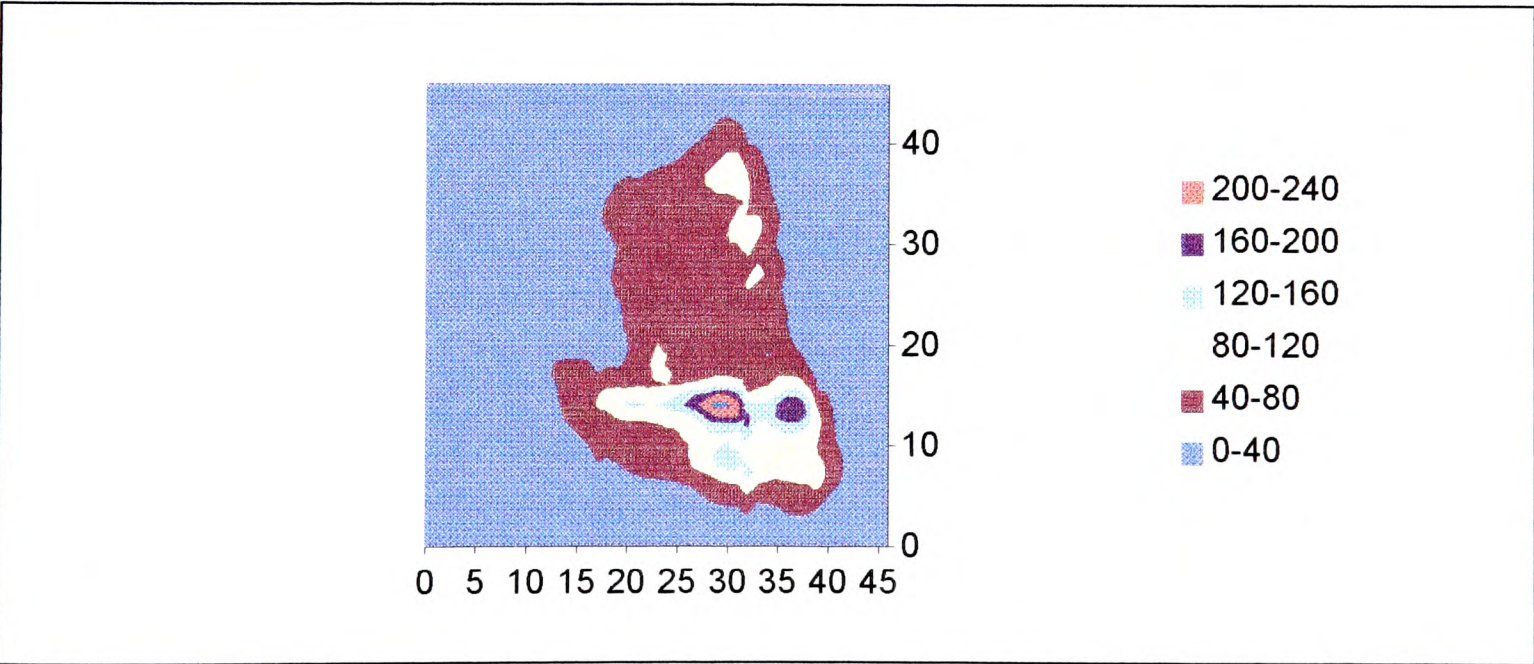


**Figure 7.2.** Contour map of far field pattern of KrF beam. Axes are labelled in pixels, which are separated by 15.6  $\mu$ m, which corresponds to an angular separation of 6.24 mrad. To emphasise the double-beam structure, the profile presented here was taken with the camera a few millimetres in front of the best focus. At the best focus there was the same double-peak structure, but it was slightly harder to resolve.



Ideally, the intensity profile observed should be a two-dimensional  $\text{sinc}^2$  function [Fletcher 1993]. The extra structure (double peak) observed, corresponds to a high divergence beam. This is shown in Fig. 7.3, from which it is clear that a significant fraction of the beam energy was contained in an angular region 100-250  $\mu\text{rad}$  across. This should be compared to results obtained by Fletcher [1993], who found the FWHM of the intensity profiles to be 30  $\mu\text{rad}^*$  across, when a smaller (2 cm x 2 cm) beam aperture was used. This corresponds to approximately twice the diffraction limit.

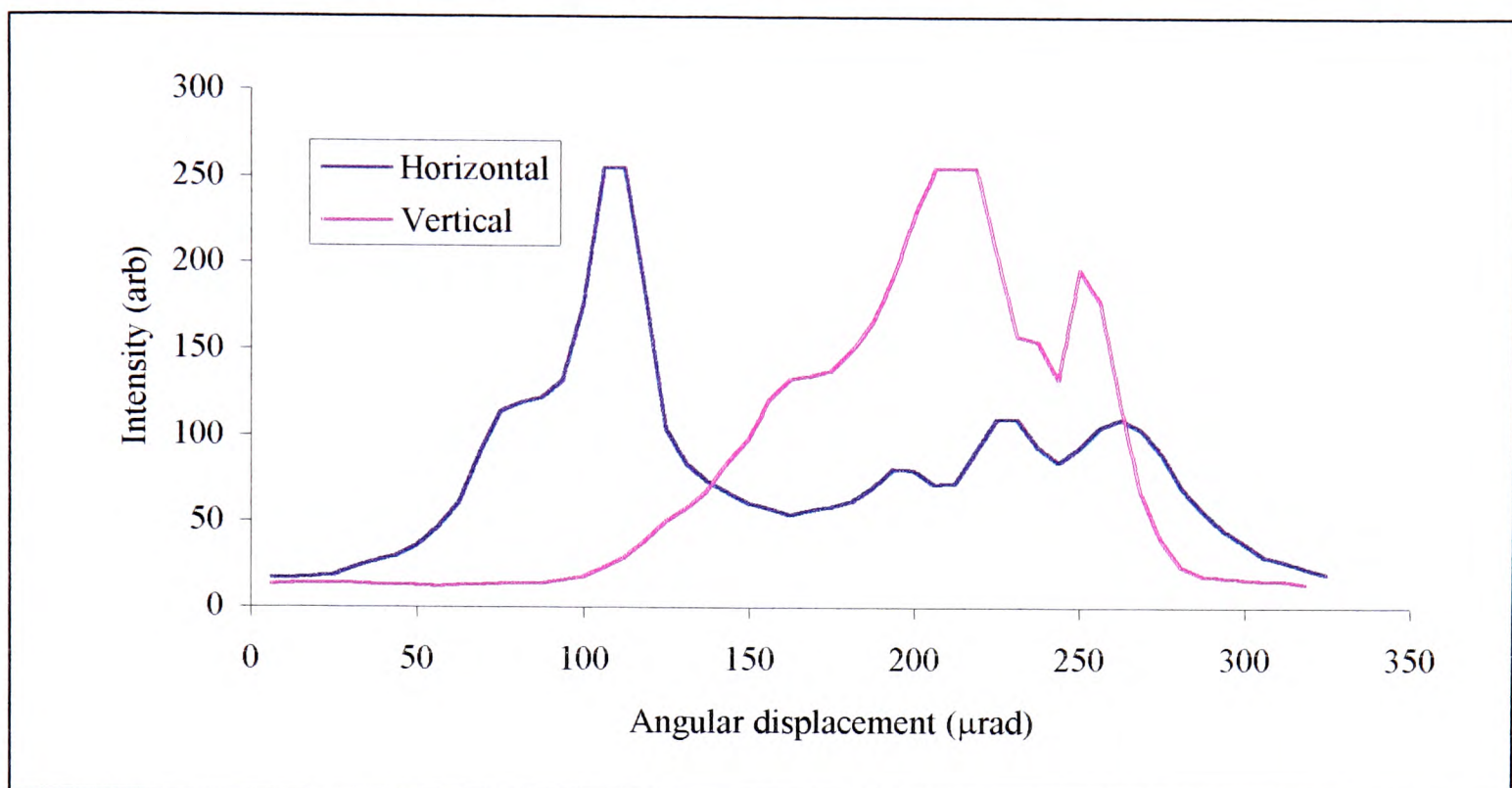


**Figure 7.3.** Horizontal and vertical sections through peak of intensity profile obtained at optimum focus of KrF beam.

Clearly, something was seriously amiss, and the quality of the optics in use was investigated. The exact technique for doing this depended which part of the system was being tested, but the idea was the same in each case<sup>†</sup>. A circular HeNe beam was expanded to fill the aperture of the optic in question, and the transmitted or reflected beam (as appropriate) was then brought to a focus. The focusing was done by either the optic itself, or by the use of a long focal-length lens. The focus was examined (by eye) for signs of being anything other than a perfect circle. Any distortion of the focus was a sign of phase distortions being introduced to the beam.

The problem was quickly traced to the (nominally  $\lambda/10$ ) beamsplitter used to couple light from the oscillator to the amplifier. When this was inspected under a sodium lamp on an optical flat, it was clear that one side had been polished to give two distinct, equally-sized, regions. Although these were both flat, they were not coplanar. These two regions were responsible for the two beams observed in the far-field intensity distribution.

The beamsplitter was replaced by a flat one, and the far-field pattern measured again. In this case no double peak structure was observed. The intensity profiles obtained had FWHM angular widths of  $25 \pm 4$   $\mu\text{rad}$  horizontally, and  $31 \pm 4$   $\mu\text{rad}$  vertically. This shows clearly that the faulty beamsplitter had been responsible for the poor beam quality observed.

\* This figure is based on a “FWHM area”, and thus any astigmatism is averaged.

† The author is indebted to Dr. David Coutts for suggesting the technique.



## 7.3 Soft x-rays from a plasma spot

### 7.3.1 Introduction

With no x-rays observed in the experiments described in §6.14, there was some doubt as to whether the filter/scintillator/PMT system would have detected any x-rays had they been present. In order to investigate this, a spot-focus experiment was conducted. Fletcher [1993] had used the same laser system with a spot-focus to produce x-rays in the 280 eV - 530 eV spectral region, and so it was envisaged that there would be no difficulty in obtaining the 67 eV photons required to test the detection system.

### 7.3.2 Filter breakage

The experimental arrangement used was very similar to that used in the search for SXR from a line focus, and is shown in Fig. 7.4. A 96 mm focal-length aspheric\* lens was used to bring the beam to a spot focus. Detection of SXRs was (initially) attempted using exactly the same system as described in §6.13.1.

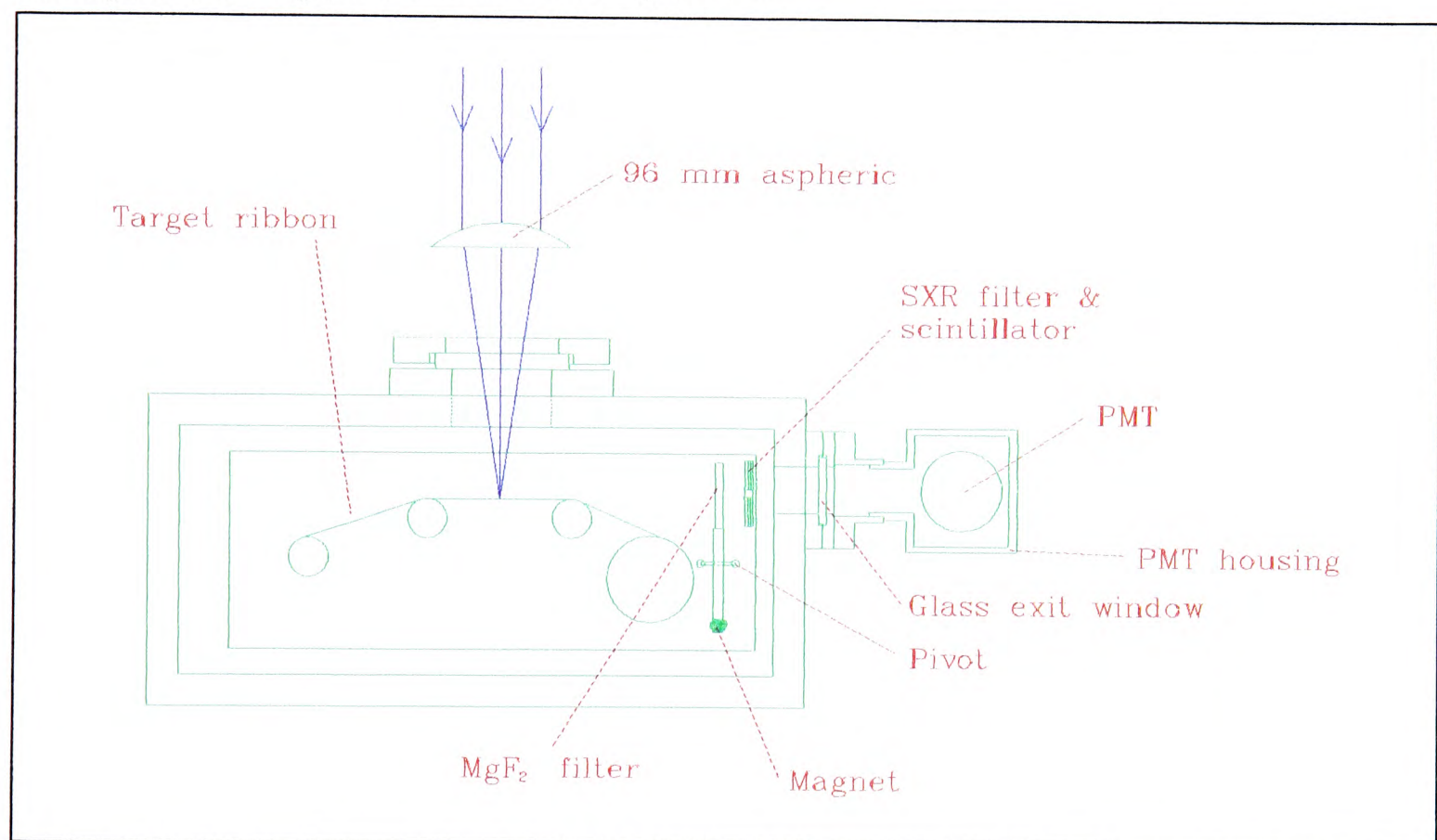


**Figure 7.4.** Schematic of experimental arrangement used to look for SXRs from a spot plasma.

The position of the focus was found using the geometrical technique described in §6.6.9.1 for the line focus†. When the experiment was performed, however, it was found

\* The presence of the 6 mm entrance window will have eliminated the advantage of using an aspheric lens over a plano-convex lens, in terms of the quality of the focus it could produce.

† This was an expensive mistake. The process involves moving the lens towards and away from the target, and at one of these positions the reflection from the entrance window reached its focus within the lens, and drilled it. Fortunately, the damage was not so severe as to ruin the lens. Care was taken not to repeat the mistake in the VUV plasma source experiment described in chapter 9.



that the thin  $\text{Si}_3\text{N}_4/\text{SiO}_2/\text{Al}$  filter shattered on its first exposure to x-rays from the laser plasma (*i.e.* as soon as the laser was fired without the  $\text{MgF}_2$  filter obscuring the  $\text{Si}_3\text{N}_4/\text{SiO}_2/\text{Al}$  filter). Debris from the plasma seems the most likely explanation for this.

In order to reduce the debris, the KrF pulse energy was reduced, by attenuating the beam with the  $\text{NO}_2$  cell. Even with only 20 mJ on target, the filter still broke on the first shot.

Some evidence was found for x-ray production; the signals obtained from the PMT were greater on the first shot for which the  $\text{MgF}_2$  filter was absent. However, this could conceivably have been caused by visible light after the filter had broken. As well as this, the experiment was going to be slow, and hard to repeat, if a new filter was needed for each laser shot. Instead, attempts were made to strengthen the filter.

### 7.3.3 Direct coating of Sodium Salicylate

#### 7.3.3.1 Theory

A very attractive solution to the problem was to coat the filter layers directly on to the sodium salicylate scintillator. This would have several advantages over using a separate filter. It would be much stronger; it would not require an elaborate light-tight but gas-permeable mounting (as described in §6.13.1); and the coating might protect the sodium salicylate from attack by atmospheric moisture (§6.14). Furthermore, by tailoring the coating to different spectral regions, the technique held promise of providing a new class of easy-to-use, highly sensitive, and wavelength-selective x-ray detectors.

If direct coating is to be used, it is important to consider surface effects. If such effects are part of the scintillation mechanism, the quantum efficiency may be modified by the presence of a surface coating. The model given by Husk *et al.* [1992] for the quantum efficiency of sodium salicylate indicates that surface effects can be relevant. This is due to non-radiative surface recombination of charge carriers created by incident photons [Benitez *et al.* 1991]. However, for the spectral region considered here (67 eV to 100 eV), surface effects are negligible. This is because the diffusion length of the charge carriers (25 nm) is smaller than the absorption length of the incident photons (50 nm to 100 nm), and so most of the charge carriers created do not reach the surface [Husk *et al.* 1992].

Photons of lower energies, however, are absorbed nearer the surface. This means that surface effects could be relevant if the direct coating technique were extended to other spectral regions.

#### 7.3.3.2 First attempt

A new recipe for the SXR filter was devised to allow coating of the sodium salicylate with the coating plant available. The coating comprised 60 nm of aluminium to reject visible light, and 170 nm of  $\text{SiO}$  to reduce VUV light of photon-energy less than the 67 eV



excitation threshold for Xe III. The transmission predicted\* is illustrated in Fig. 7.5 [Palik 1985].

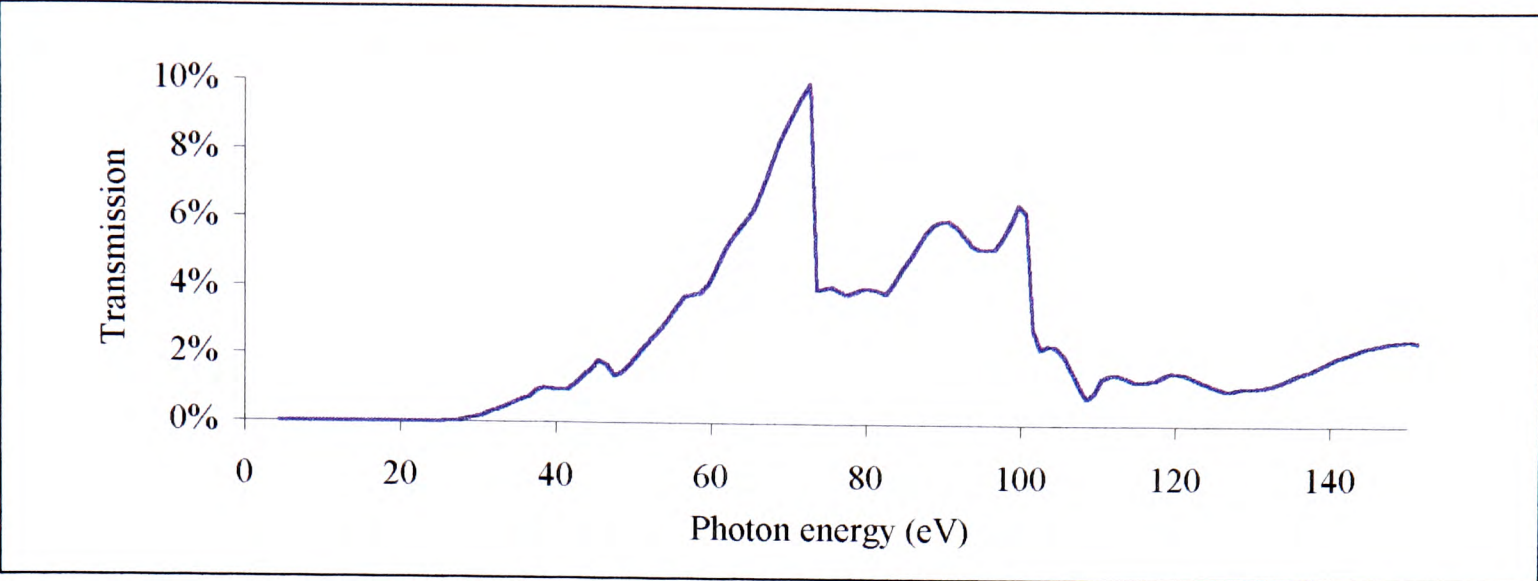


**Figure 7.5.** Transmission of 60 nm of Al on 170 nm SiO [Palik 1985].

This coating was deposited on a scintillator which was deposited on a sandblasted microscope slide, according to the technique described in §6.11.1. This experiment was not successful: the sodium salicylate surface was too rough to allow the coating to cover it all. As a result of this, the coated scintillators were not opaque to visible light. This is illustrated in Fig. 7.6, which shows such a sample, viewed in transmitted white light. A black cross under the target is clearly visible in transmission through the filter.

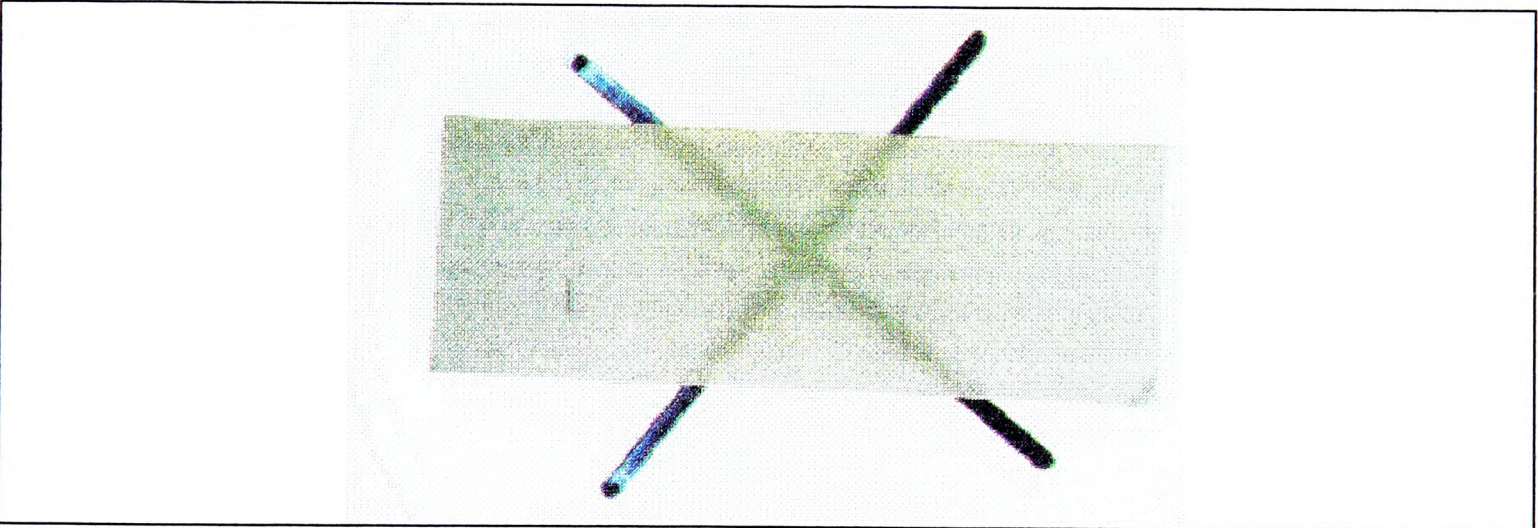


**Figure 7.6.** Aluminium and SiO coated scintillator viewed in transmission. Black cross beneath sample is visible through it.

### 7.3.3.3 Spin coating

The difficulty of making smooth sodium salicylate coatings has been reported by others [Husk *et al.* 1992]. For this application a novel technique was attempted, namely spin coating. Glass microscope slides, of thickness 1.1 mm, were used as substrates. They were

---

\* The absorption cross section for photon energies < 25 eV is based on experimental data collated by Palik [1985]. For the higher energy region the cross sections of SiO<sub>2</sub> and Si reported by Palik [1985] have been combined in the relevant linear combination for SiO. This is valid provided the chemical environment of the elements does not influence their SXR absorption properties, which is a reasonable approximation. To illustrate this, the measured and deduced absorption cross-sections for 25 eV photons differ by only 25%.



cut into 20 mm by 30 mm rectangles, and cleaned ultrasonically in methanol before use to remove dust particles which might act as crystal nucleation sites. The cleaned substrates were mounted on a vacuum chuck and solutions of various concentrations of sodium salicylate in water or methanol were dropped on to them. They were then given a pre-spin to spread the drops, and a faster main spin to evaporate the solvent. The experimental parameters were varied, and the resulting coatings examined with the naked eye, and under an optical microscope. Although the investigation was not systematic, the experimental results supported the following conclusions.

- Coatings of thicknesses comparable to those which had been used before\* ( $2 \text{ mg cm}^{-2}$ ) could only be obtained by using the most concentrated solution which could be made. This was a saturated solution of sodium salicylate in water, and was  $\sim 6.4 \text{ mole dm}^{-3}$ . This was  $\sim 7$  times more concentrated than a saturated solution in methanol. This is because water is the more polar solvent, and the solute is ionic.
- Coating thicknesses of up to  $\sim 1 \text{ mg cm}^{-2}$  could be obtained in this way, from a single coat. Applying extra coats increased the thickness of the sodium salicylate, but not the surface quality.
- Heating the substrates to  $80^\circ \text{C}$  before coating gave streakier coatings than were obtained from room-temperature substrates. This was assumed to be caused by crystallisation of sodium salicylate during the pre-spin, or very early in the main spin.
- Two distinct microstructures were observed. The first contained fine (sub-micron) crystals, and was very rough. Macroscopically, this took the form of opaque white blotches. The second microstructure was much smoother, and was macroscopically fairly transparent and slightly shiny. Under the microscope this second structure appeared to consist of randomly oriented crystals (possibly embedded in a solid matrix), of width  $\sim 2 \text{ }\mu\text{m}$ , and length  $\sim 15 \text{ }\mu\text{m}$ .
- The speed and duration of the pre-spin and main spin were varied, in order to produce samples with as much of the second type of microstructure as possible. The results were fairly insensitive to the exact parameters used. A typical recipe which produced good results was a 7 s pre-spin at  $34 \text{ revs s}^{-1}$ , followed by a long ( $\sim 1$  minute) spin at 40 to  $78 \text{ revs s}^{-1}$ .

#### 7.3.3.4 Characterisation of spun coatings

In this way, samples were obtained with the smoother microstructure covering  $\geq 98\%$  of their surface. Some of these were coated, with 170 nm of SiO and 60 nm of aluminium (as described in §7.3.3.2). The resulting samples looked considerably better than those which had been obtained by the spray coating of sandblasted microscope slides. In particular, the aluminium layer had a definite shine, which had been absent previously. Nevertheless, the samples still transmitted some visible light. One, of sodium salicylate thickness  $0.6 \text{ mg cm}^{-2}$ , was characterised using the VUV source described in chapter 9.

For this experiment, the coated scintillator was used instead of the uncoated scintillator, which had been used for VUV detection. The sizes of the signals obtained in

---

\* The production of thin coatings was not investigated, for fear that these coatings could have been too thin to absorb all the incident x-rays. This may have been a mistake - there was some evidence that smoother coatings could be produced in this way, using saturated sodium salicylate in methanol. See [Husk *et al.* 1992] and the discussion in §9.3.1.3 for more details on the thickness of sodium salicylate required.



the two cases were compared, in order to establish the effect of the coating. The results are shown in Fig. 7.7.

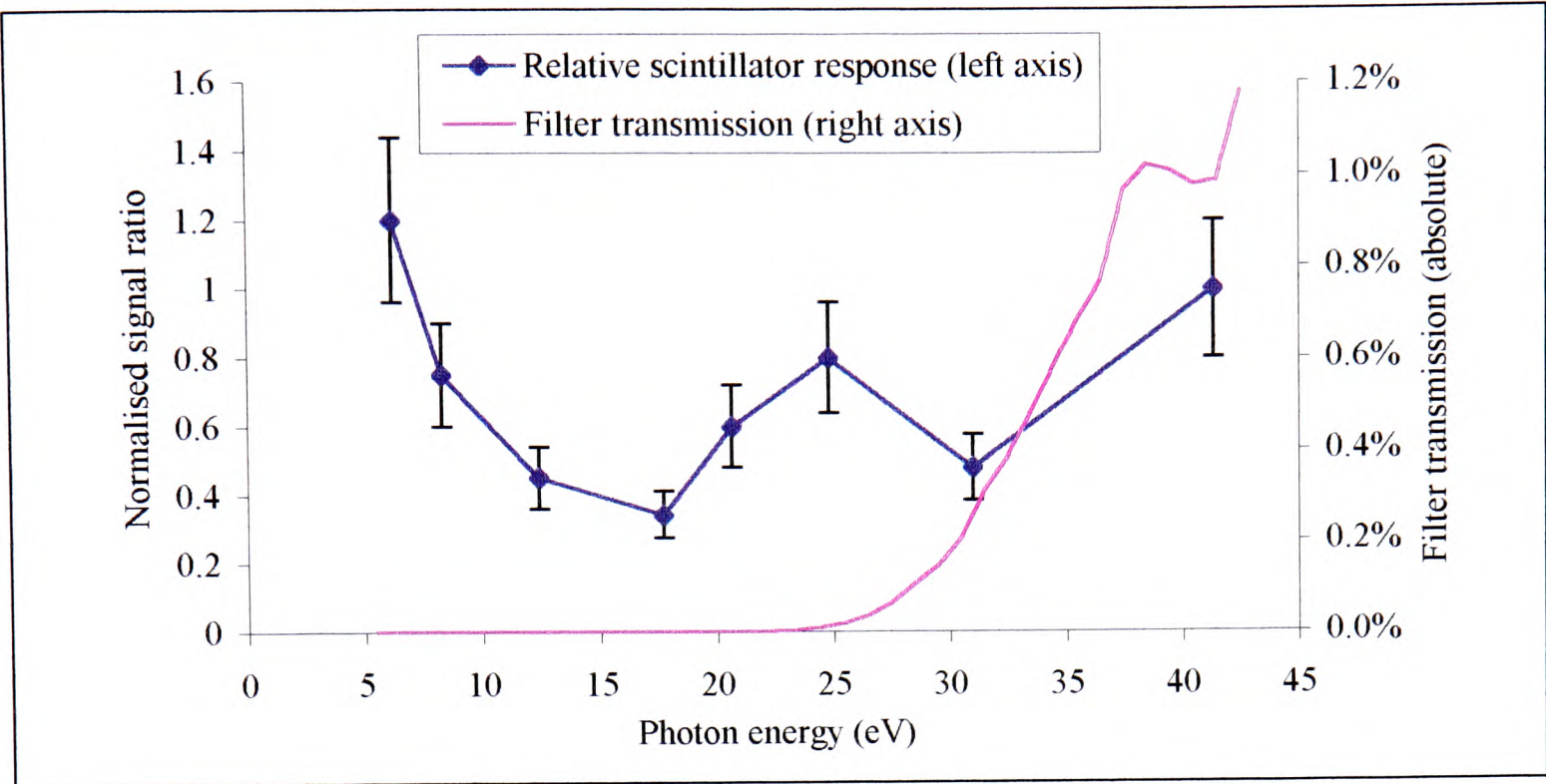


**Figure 7.7.** Response of coated scintillator, relative to uncoated scintillator, normalised to ratio at 41 eV. Also shown is transmission of filter layers, as calculated in §7.3.3.2.

From Fig. 7.7. it is clear that there is no wavelength selectivity in the coated filter response. This means that the signal is dominated by the light which passes through voids in the filter layers, rather than the light which is transmitted through these layers. This indicates that even the spun coatings were not sufficiently smooth to allow direct coating of filter layers. The direct coating of scintillators was not investigated further.

### 7.3.4 Use of helium to reduce debris

The next, and successful, approach taken to solving the problem of smashed filters was to stop the debris before it hit the filter. Debris from LGPs can be divided into two types: atomic debris, and droplets [Richardson *et al.* 1993]. As the name suggests, atomic debris comprises atoms and ions ablated from the target. Droplet debris comes from the (much larger) region of the target which is melted by the intense shock wave driven into the target by the LGP. The shock wave reflects from the rear surface of the target, and ejects the melt from the front of the target when it arrives back there. There is little one can do to reduce droplet debris\*, but atomic debris may be stopped even by a very low pressure of gas.

Since the soft x-rays were to be observed travelling almost parallel to the target, the debris which had smashed the filters in previous experiments will have been mostly atomic in origin. Atomic debris may be stopped by low pressures (fractions of a millibar) of buffer

\* One can, however, reduce its main damaging effect, which is the coating of the focusing optic with the target material. The LGP x-ray plasma source referred to in §8.1.2 does this in three ways. Firstly, it operates in circulating helium at atmospheric pressure which stops the droplets hitting the focusing lens. Secondly, the droplet emission back towards the lens is reduced by using a thin target with space behind it, so that melt comes out of the back of the target. Thirdly, the laser is incident at 45° to the target normal, so the reflected shock wave ejects debris perpendicular to the incident laser beam.



gas. For example, Ginter & McIlrath [1988] have reported a reduction of more than an order of magnitude in debris deposited by an LGP, owing to the presence of a 2 cm mbar pressure-length product of He. Using another LGP system, Richardson *et al.* [1993] also found an order of magnitude reduction in debris, using only a 0.7 cm mbar pressure-length product of He.

The mechanism for the debris reduction is subtle since neutral-neutral collisions cannot transfer sufficient momentum from the debris to the buffer gas. Instead, it is believed that radiation from the LGP photoionises the surrounding helium gas, and there is a build-up of  $\text{He}^+$  and  $\text{He}^{2+}$  ions in front of the ions expanding from the LGP. This “snowplough effect” allows collisionless transfer of momentum from the debris to the buffer gas [Ginter & McIlrath 1988].

For the experimental arrangement here, the 15 cm path length suggests a pressure of  $\sim 0.1$  mbar of He should give significant debris reduction. The maximum pressure of He which may be used is determined by its transmission to the soft x-rays generated, but 0.5 mbar gives more than 80% transmission in the 67 eV to 100 eV region of interest [Thomas 1989]. This is illustrated in Fig. 7.8.

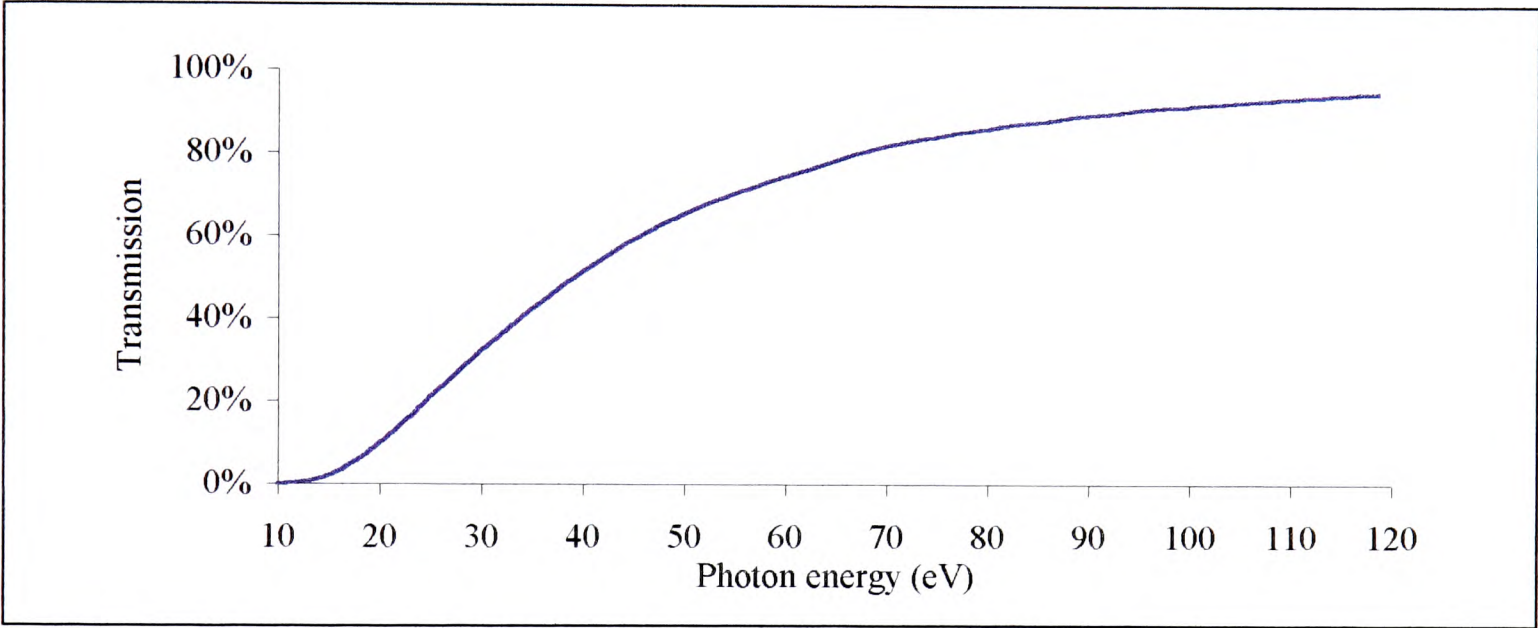


**Figure 7.8.** Transmission of 15 cm of 0.5 mbar He [Thomas 1989].

Taking advantage of this, the target chamber was filled with 0.5 mbar of He, and a filter and scintillator arrangement, with a magnetically movable  $\text{MgF}_2$  filter, as described in §6.13.1, was used for x-ray detection. The filter (as in §6.13.1) was a 2 mm square of 125 nm thick  $\text{Si}_3\text{N}_4$  overcoated with 25 nm of  $\text{SiO}_2$  and 60 nm of aluminium. The filter and scintillator were mounted  $\sim 150$  mm from the plasma, 55 mrad ( $3.1^\circ$ ) from the axis defined by the target surface.

The presence of the helium buffer allowed 9 laser shots to be fired before the filter broke. This improvement on the lifetime of one shot which had been observed in the absence of a buffer gas was sufficient to allow useful data to be collected.

7.3.4.1 Results

The laser focus was found by the target shadow ratio technique described in §6.6.9.1. The  $\text{NO}_2$  cell described in §5.3.1.1 was used to provide variable attenuation of the beam. This allowed the investigation of a range of intensities on target spanning three orders of magnitude. The ambient temperature was measured to allow the  $\text{NO}_2$  cell attenuation to be calculated.



An x-ray signal was observed, *i.e.* a signal which disappeared when the  $\text{MgF}_2$  filter was placed in front of the x-ray detector. The noise in the experiment was the signal measured when  $\text{MgF}_2$  filter was present. A signal-to-noise ratio of 280 was observed for the strongest plasma emission. This demonstrates clearly that the filter/scintillator/PMT technique for detecting soft x-rays did work. A measurement of the focal spot size was made in order to measure how the conversion efficiency of the LGP varied with the focal spot intensity.

First attempts at this were made by laser-etching glass microscope slides and PET sheets of known thickness. The position of the lens was corrected for this thickness. Attenuation was necessary to prevent severe damage to the sample outside the focal region due to thermal or acoustic effects. This attenuation was provided by the  $\text{NO}_2$  cell and was varied between  $2 \times 10^4$  and  $10^9$ . These limits were chosen to give a fluence on target comparable to those used for industrial applications in the etching of these materials. These are of order  $2 \text{ J cm}^{-2}$  for PET, and about ten times more for glass\*. The number of shots fired on to each target was varied between 1 and 20. This technique was not successful. No compromise could be found between too much fluence (damaging the sample), and too little (not leaving any mark at all).

Rather than attempt a more painstaking ablation study, a scanning knife edge technique was adopted instead. A knife edge (flat to within  $10 \mu\text{m}$ ) was brought up to the target ribbon so it was just touching it. The ribbon was then removed and an energy detector (Gentec ED100 pyroelectric detector) placed behind the knife edge. The knife edge was then scanned and the amount of energy reaching the detector measured as a function of position.

The formation of a plasma at the focus would have distorted the results of this experiment. In order to avoid this, attenuation of  $10^4$  was provided by the  $\text{NO}_2$  cell. The attenuation required was determined by the detector used, which was chosen to be as sensitive as possible, in order to reduce the peak focal intensity. No plasma spark could be observed by eye on the knife edge, even with the laboratory lights off. Both horizontal and vertical scans were made, and checks were made to ensure the focal widths measured did not vary within the precision ( $\sim 200 \mu\text{m}$ ) with which the knife edge could be positioned next to the target surface. This was not found to cause any error; the focal spot size was determined by severe coma and astigmatism in the focus, due to the lens having been used somewhat off-axis.

The spot size was taken as 1.5 times the distance of knife-scan containing half the beam energy (*i.e.* between the 25% and 75% transmission points), and was found to be  $100 \mu\text{m}$  (horizontally)  $\times$   $160 \mu\text{m}$  (vertically). The FWHM duration of 22.6 ns was used to calculate the mean beam power on target. Using all these data, the relative conversion efficiency as a function of focal intensity could be calculated, and the results obtained are shown in Fig. 7.9.

---

\* Based on data given in a brochure for laser machining services provided by Exitech Ltd., Long Hanborough, UK.



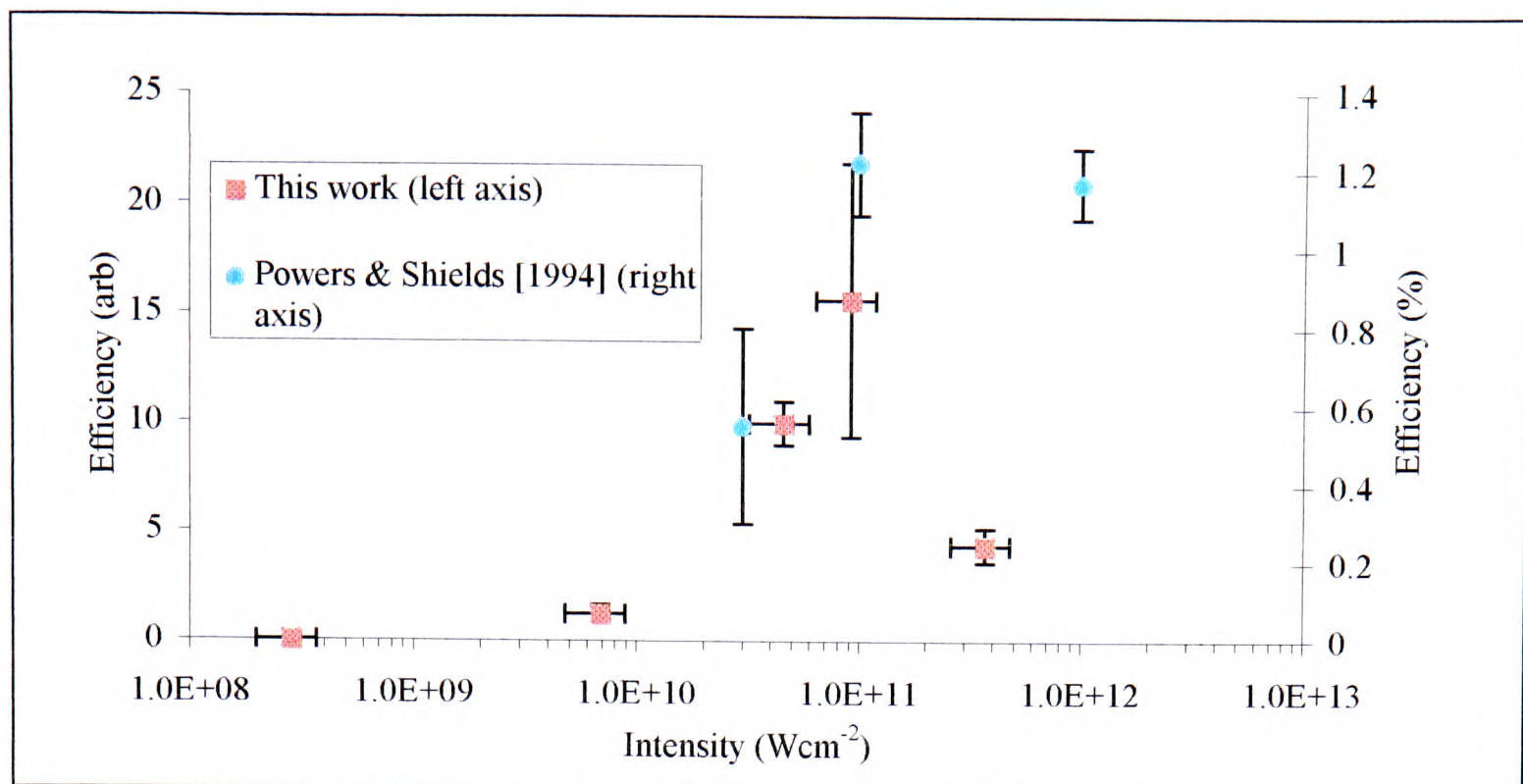


**Figure 7.9.** Conversion efficiency into soft x-rays as a function of focal spot intensity.

It is instructive to compare these results with efficiencies measured under similar circumstances by Powers & Shields [1994]. Some representative data from this work is also illustrated in Fig. 7.9. They used 5 ns duration XeCl (308 nm) laser pulses, focused to a spot on a copper ( $Z=29$ ) target. They detected x-rays in a spectral region centred on 92.5 eV, with a 6.5 eV FWHM bandwidth. They comment that they found the efficiencies to be independent of pulse duration (up to 25 ns at which it started to fall), focal spot size, and laser pulse energy (for a given intensity). They also comment that they obtained similar results for targets of tin ( $Z=50$ ) and gold ( $Z=79$ , which is similar to tantalum, for which  $Z=73$ ).

It is clear from Fig. 7.9 that the results obtained here are similar to those obtained by Powers & Shields [1994], except at the highest intensity of  $3.7 \times 10^{11} \text{ W cm}^{-2}$ , for which the efficiency deduced here seems anomalously low. Assuming the effect is real (it is only based on a single data point), the most likely explanation for it lies in the higher plasma temperature which will be produced at this intensity. This will have two effects. Firstly, the emission will be shifted to higher photon energies (at least at the start of the laser pulse). Powers & Shields [1994] detected 89-96 eV photons, whereas in this work lower energy photons were detected (40-100 eV). Secondly, the hydrodynamic expansion will be faster. This is discussed further in §7.6, but comparison with the experiments reported by Spitzer *et al.* [1996] suggests that this could be expected to reduce the time-averaged conversion efficiency for the pumping conditions used here.

Although this shift to higher energy emission will be partially responsible for the apparent reduction in conversion efficiency, the angular distribution of the emission is also relevant. This is because the detection angle used here, of  $\sim 0^\circ$  to the target surface, makes the experiment very sensitive to changes in the angular distribution of the radiation. The distribution depends on the shape of the emitting region, which in turn depends on the rates of plasma expansion and emission. Both of these increase with increasing plasma temperature. Without further information on these parameters, no more can be deduced about the apparent loss of conversion efficiency at high intensities.



## 7.4 Search for 109 nm fluorescence pumped by spot-plasma emission

Once it was known that suitable x-rays for generating the Xe III upper laser level could be observed, attempts were made to see whether this could be used to generate 109 nm fluorescence from Xe III. The experimental arrangement is shown in Fig. 7.10.

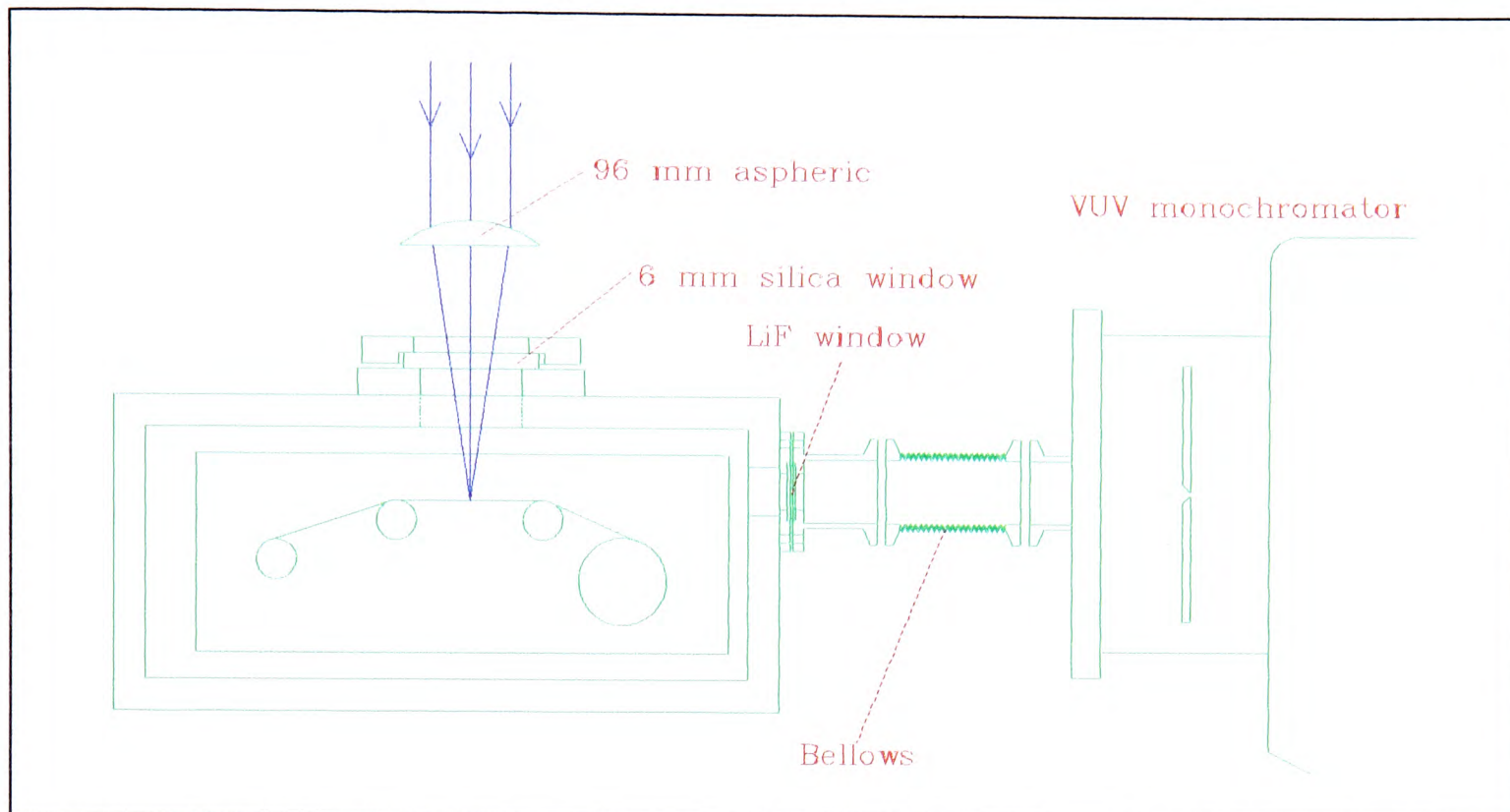


**Figure 7.10.** Schematic of experimental arrangement used to look for fluorescence at 109 nm from xenon pumped by a spot plasma.

The target was set back a few millimetres from the observation axis of the monochromator. This was in order to ensure that light from the plasma entered the monochromator.

### 7.4.1 VUV monochromator

The VUV monochromator was a 20 cm, f/4.5 CGA/McPherson model 234. It contained a single optical element, namely an iridium-coated, aberration-corrected holographic-ruled grating with 1200 lines/mm. A Thorn-EMI type 9426 PMT was used to detect VUV radiation exiting the monochromator. The properties of this PMT are described in more detail in §9.3.1.6. The PMT has an  $\text{MgF}_2$  entrance window, which has its transmission cut-off at  $\sim 115$  nm, and so was unsuitable for detection of 109 nm radiation. In order to give sensitivity at this wavelength, a sodium salicylate scintillator was placed behind the exit slit of the monochromator. This scintillator was made to exactly the same recipe as those used in the detection of SXRs.

The monochromator and PMT had been obtained for earlier investigations of VUV lasers in the Clarendon Laboratory, and could be controlled by computer. Automated spectra could be taken, with the computer sending trigger pulses to fire the laser, and reading the signal detected by the PMT. To avoid electrical noise problems, the computer was sited outside the laser laboratory (a Faraday cage), and the laser was fired with all its covers on. Even so, the noise was sufficiently severe that the computer could reliably be crashed by firing the laser. Ferrite coils and aluminium foil screening were applied liberally



to the mains leads and connector cables, and obvious earth loops were eliminated. This prevented the computer from crashing, allowing the next most susceptible part of the control system, the trigger unit, to fail. This would typically last about ten laser shots, and so both computer-controlled and manually-obtained spectra are reported here.

The monochromator wavelength selection was calibrated using a mercury lamp and a deuterium lamp. First of all, spectral lines from the mercury lamp were used to calibrate the system in the range 253.7 nm to 407.9 nm. The output from the deuterium lamp (which had an  $\text{MgF}_2$  window) was then observed in this wavelength region, in second order. This allowed the exact wavelengths of several peaks of the deuterium lamp spectrum to be measured. Care was taken to repeat all  $\text{D}_2$  spectra to check there were no wavelength shifts caused by the warming of the lamp.

The  $\text{D}_2$  spectrum was then taken in first order, and this allowed the monochromator to be calibrated down to the 121.54 nm Lyman- $\alpha$  spectral line. This calibration was extrapolated down to the shortest wavelengths reported here (100 nm). The overall accuracy obtained was 0.05 nm, which was the precision of the manual scale provided on the monochromator.

## 7.4.2 Experimental results

Spectra of the output were taken with various pressures of xenon and various KrF pulse energies. The 105 nm transmission cut-off of the LiF window was visible in the spectra obtained, but typical signals at 110 nm were only 2 or 3 times larger than those obtained with the monochromator set to 100 nm. The signal at the short wavelength was optical rather than electrical, since it was absent when the laser was fired but no plasma was generated (because the beam was blocked). The spectra presented here (Fig. 7.10) have had the 100 nm signal subtracted.

No strong signal at the Xe III wavelength (108.9 nm) was observed over the background plasma emission, even at the highest wavelength resolution available on the monochromator, estimated\* as 0.15 nm. The only hint of fluorescence at 109 nm was found when the KrF beam was attenuated to 160 mJ on target, and a slight emission peak was observed. This is illustrated in Fig. 7.10, in which the data are normalised to the signal at 108 nm, since the two sets of data were taken with different geometrical couplings between the target chamber and monochromator (because the apparatus was dismantled and reassembled between the two experiments reported). Thus, the quantity plotted against wavelength,  $\lambda$ , in Fig. 7.10 is

---

\* This assumes the resolution is limited by the linear dispersion of the monochromator, used with the narrowest slits (35  $\mu\text{m}$ ) which gave a measurable optical signal. The number of slits illuminated is assumed not to limit the resolution, on account of a large ( $>500 \mu\text{m}$ ) source. The source size depends on the wavelength, but for 109 nm fluorescence the excited xenon is the source, and this is a reasonable estimate. For other wavelengths, the plasma is the source and may be smaller, depending on how much the plasma has expanded, while still emitting in the VUV spectral region. If the plasma source is small, the wavelength resolution will be coarser ( $\sim 1 \text{ nm}$ ). This would mean the emission spectrum of the plasma would be smeared on exit from the monochromator, but any Xe III fluorescence would not be, which is the ideal situation for a good signal-to-noise ratio.



$$\frac{E'_\lambda}{E'_{108}} \quad (7.1),$$

where

$$E'_x = E_x - E_{100} \quad (7.2),$$

and  $E_x$  is the signal observed with the monochromator set to a wavelength of  $x$  nanometres.

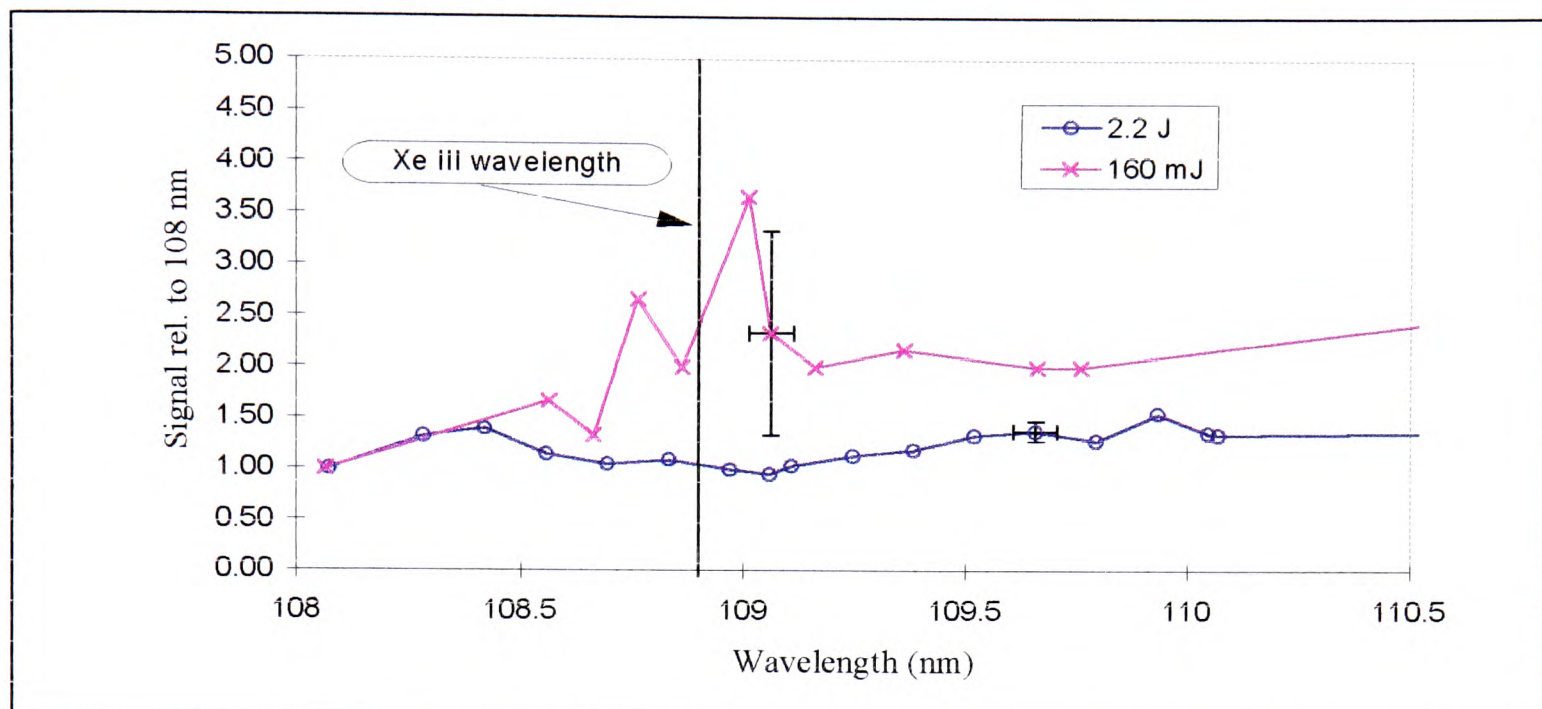


**Figure 7.11.** Emission spectrum observed from xenon excited by LFPs of different energies. For 2.2 J exposures, target intensity is  $\approx 8 \times 10^{11} \text{ W cm}^{-2}$  and xenon pressure was 10.8 mbar. For 160 mJ exposures, target intensity is  $5 \times 10^{10} \text{ W cm}^{-2}$  and xenon pressure was 8 mbar. Sample error bars shown, including wavelength calibration error of  $\pm 0.05 \text{ nm}$ .

As can be seen from Fig. 7.10, the evidence for 109 nm emission with the beam attenuated is far from overwhelming. There are several ways in which the experiment could be made more sensitive to 109 nm fluorescence. These include: introducing time-discrimination to the detection (but see below), putting a mirror (see §8.4.1) behind the plasma spot to take advantage of any gain available, and shadowing the direct emission from the plasma (see §8.4.3). No such attempts were made for two reasons. Firstly, it was not expected to be of use to the main goal of achieving lasing at 109 nm. Secondly, the odds are stacked against the observation of 109 nm emission, pumped by a spot plasma, because of the long KrF pulse length. This means that the plasma emits radiation for much longer than the Xe III. Indeed, the long lifetime of the lower Xe III will cause it to absorb direct plasma emission at 109 nm, and this may even reduce the signal observed at this wavelength. The problem cannot be avoided simply by time-gating the existing detection system for the emission, because sodium salicylate is not sufficiently fast, with a decay time of  $\sim 10 \text{ ns}$  [Tóth *et al.* 1993].

The experiment had served its main goal, however, which was to bring the VUV monochromator into service, with an intense VUV source (the spot plasma), so that it could be used in any further attempts to observe 109 nm lasing.



## 7.5 Tighter line focusing arrangement

The data presented in Fig. 7.9, (especially those due to Powers & Shields [1994] for which hydrodynamic expansion did not influence the conversion efficiency), indicate that a focal intensity higher than the  $2 \times 10^{10} \text{ W cm}^{-2}$  assumed in §6.6.1, would be needed for efficient pumping of the Xe III laser system. At first sight, this suggests that a tighter focusing arrangement should be used. The apparatus needed to test such a geometry was assembled. The experimental arrangement is shown schematically in Fig. 7.11.

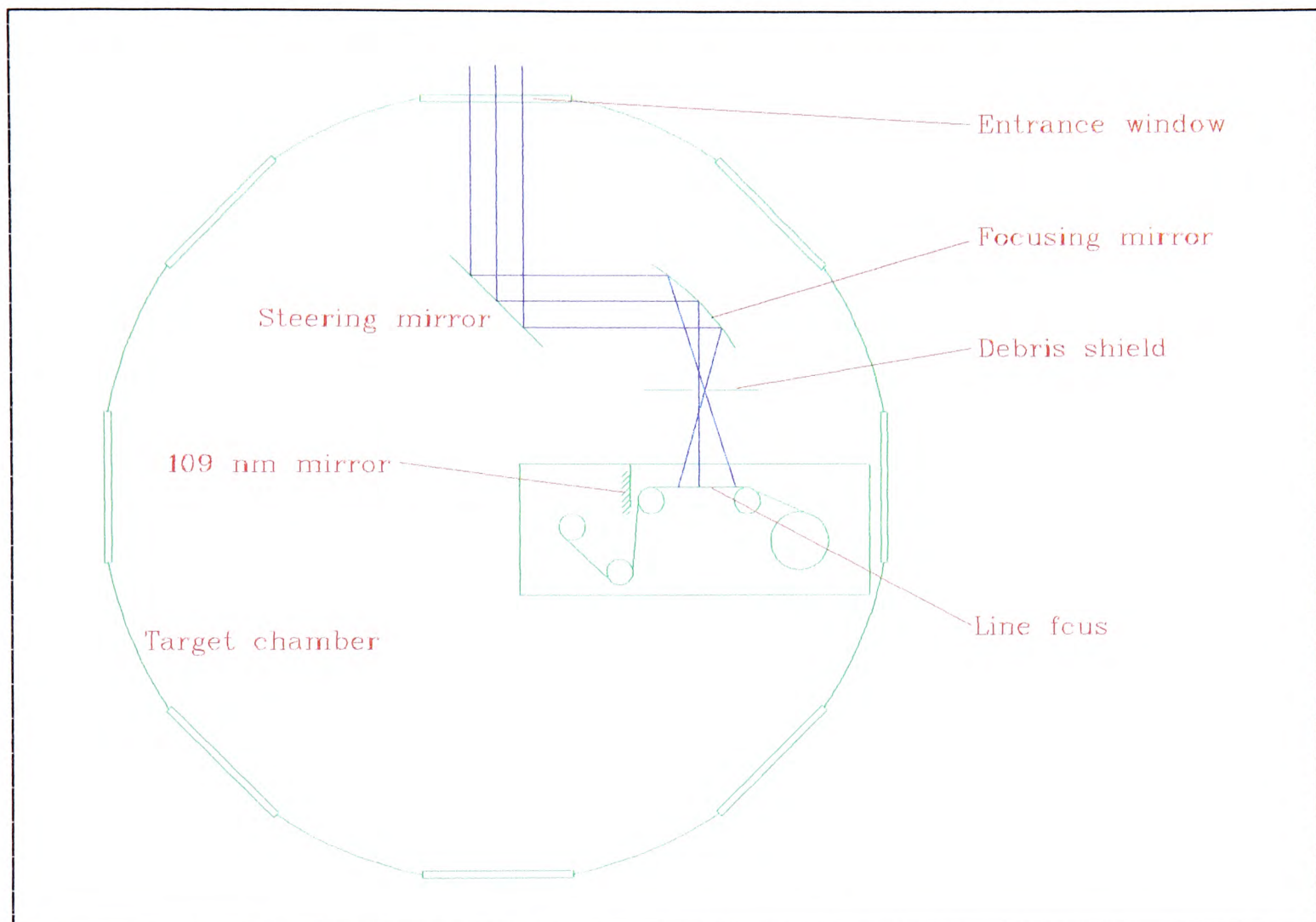


**Figure 7.11.** Experimental geometry used for tighter line focusing. Gas, mechanical, electrical and optical feed-throughs have been omitted for simplicity.

The following are important features of the experimental arrangement.

- An off-axis spherical mirror was used, as in the experiments described in the previous chapter, except that its radius of curvature was 152 mm, giving an effective focal-length of 108 mm. This could be expected to give a divergence-limited line of width  $3.1 \mu\text{m}$ . This would correspond to a mean focal intensity of  $5 \times 10^{10} \text{ W cm}^{-2}$ , after about 2 ns from the start of the pulse. The non-uniformity of the energy deposition along the line (§6.3.4.2) means that intensities both greater and lower than this would be generated at different positions along the line.
- As discussed in §6.5, the use of a mirror of this effective focal-length precludes focusing through a window. For this reason, the whole arrangement was placed in a larger target chamber (of volume  $70 \text{ dm}^3$ ), which had been developed in the Clarendon Laboratory, by others, and for an unrelated experiment.
- Mechanical feed-throughs were used to allow adjustment of the optics from outside the vacuum.



- The very short focal-length of the focusing mirror will have given rise to a depth-of-focus of only  $20\text{ }\mu\text{m}$ . Thus, considerable care was needed for the yaw alignment.

A photograph of the experimental arrangement is given in Fig. 7.12.

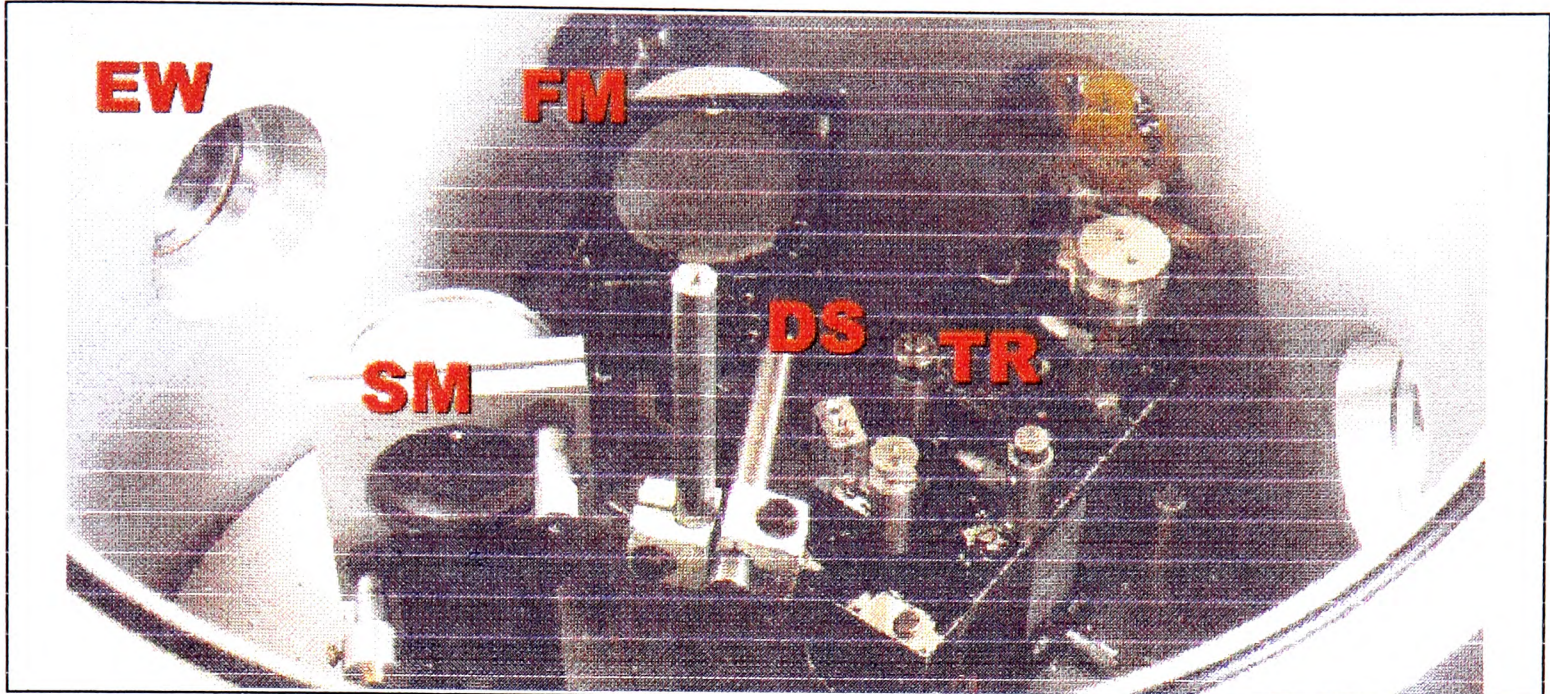


**Figure 7.12.** Experimental arrangement for tight focusing. Labels are: EW, entrance window; SM, steering mirror (plane); FM, focusing mirror; DS, debris shield; TR, target reel.

At the time this experiment was assembled (in the final few months of the project), experimental work using the picosecond laser system described in the following two chapters was also under way. This picosecond-pumping work was given priority, and there was not sufficient time to test the new focusing geometry before this thesis had to be written. Nevertheless, the following preliminary conclusions were made.

- From inspection of etch patterns on microscope slides, it was clear that a narrow focus could be obtained. The width of the line observed depended on the degree of attenuation, but the narrowest features observed were  $\sim 2.5\text{ }\mu\text{m}$  wide. A photograph of a tightly-focused region is given in Fig. 7.13. for which there was insufficient attenuation to prevent extra damage to the microscope slide, and the central line was  $\sim 5\text{ }\mu\text{m}$  wide.
- Even with a catalytic pump-oil remover in the pumping line, a liquid nitrogen trap was needed to prevent deposition of rotary pump oil on optical surfaces exposed to the incident laser beam.
- As expected, the alignment technique described in §6.6.4 was not sufficiently precise to adjust the yaw of the target with the sub-milliradian precision required.
- Instead, a different technique was developed. This involved measuring how the position of the most intense part of the line focus moved along the focus, as measured on a microscope slide. There was insufficient time to perfect the technique, when preliminary results showed that there was some large scale ( $>10\text{ }\mu\text{m}$ ) structure in the patterns recorded on the microscope slides, as well as finer lines.
- The next stage of the experiment would have been an investigation of the time-evolution of the KrF beam divergence. This was needed partly on account of the doubt about the relative timing of the oscillator and amplifier (§5.2.1.1), and partly because the *initial* divergence of the beam is a very important experimental parameter, and could not be measured by the technique described in §7.2.



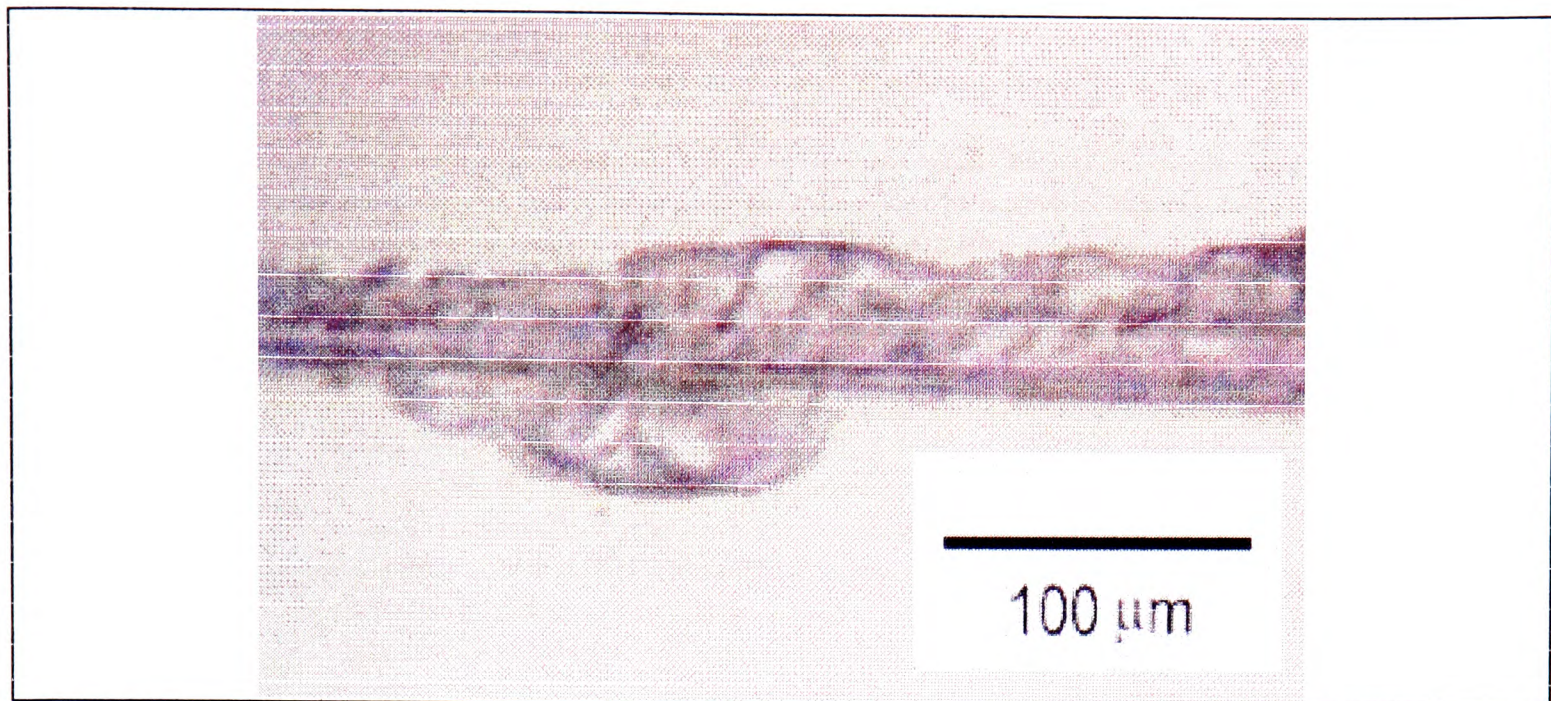


**Figure 7.13.** Etch pattern obtained on microscope slide using tighter focusing arrangement. Extensive extra damage is visible around focal line, which is  $\sim 5 \mu\text{m}$  wide. Line fluence was  $80 \text{ mJ cm}^{-1}$ . Area fluence was  $170 \text{ J cm}^{-2}$ , assuming  $5 \mu\text{m}$  line.

## 7.6 Effect of spot size on conversion efficiency

Although it was unfortunate that there was not sufficient time to test the new geometry, it is unlikely to have worked much better than the system it was replacing. The problem is that, if used with the relatively slowly rising laser pulse available, hydrodynamic expansion of the plasma would cause so much cooling that there would be very limited advantage in using a tighter focusing arrangement. The issue has been investigated both experimentally and theoretically, for spot plasmas, by Spitzer *et al.* [1993], Cerjan [1993], Kauffman *et al.* [1993], and Spitzer *et al.* [1996]. Of these reports, the two most relevant to our application here are due to Spitzer *et al.* [1993], and Spitzer *et al.* [1996]. They measured the conversion efficiency of LGPs into both broadband and narrowband spectral regions centred at 97 eV, for 7.5 ns duration 1064 nm and 532 nm radiation, focused to  $10^9$  to  $10^{13} \text{ W cm}^{-2}$ , and for various targets. They found that for a given intensity on target, the conversion efficiency increased as the spot size was increased. On a gold target ( $Z=79$ ), the effect was found to saturate at a focal spot diameter of  $\sim 150 \mu\text{m}$  for 7.5 ns pulses of 532 nm radiation [Spitzer *et al.* 1993]. The observations can be explained by considering the expansion of a spot plasma.

Early in the laser pulse, the plasma expands cylindrically (from the circular laser spot). Once the plasma has expanded a distance comparable to the diameter of the plasma spot, the planar (rather than spot-like) nature of the laser focus is lost. Thus, the expansion becomes spherical rather than cylindrical. Thus, the volume of the underdense region expands more rapidly, with an associated cooling effect. To quantify this, the effect becomes evident if

$$d \leq c_e \tau_p \quad (7.3),$$

where  $c_e$  is the expansion velocity,  $d$  is the spot diameter, and  $\tau_p$  is the laser pulse duration [Max 1982].

A crude order-of-magnitude thermodynamic estimate of the ion velocity is given by Yamakoshi *et al.* [1996]



$$c_e \approx \sqrt{\frac{k_B T_e}{M_i}} \quad (7.4).$$

This gives a speed of  $3.6 \mu\text{m ns}^{-1}$  for a 25 eV plasma.

A more accurate estimate for the speed of the expansion is the local speed of sound [Max 1982]

$$c_e = \sqrt{\frac{Z k_B T_e}{M_i}} = 300 \left[ \left( \frac{Z}{A} \right)^{\frac{1}{2}} \left( \frac{k_B T_e}{1 \text{ keV}} \right)^{\frac{1}{2}} \right] \mu\text{m ns}^{-1} \quad (7.5),$$

where  $Z$  is the ionic charge (not the atomic number of the target material),  $M_i$  is the ion mass,  $A$  is the atomic mass (in atomic mass units\*), and  $T_e$  is the electron temperature. The extra factor of  $\sqrt{Z}$  in expression (7.5) compared with expression (7.4) suggests an expansion velocity two or three times greater than the  $3.6 \mu\text{m ns}^{-1}$  obtained from the thermodynamic estimate, *i.e.* a speed of up to  $\sim 10 \mu\text{m ns}^{-1}$ .

For LGPs produced by 532 nm radiation, and emitting strongly at 92 eV, somewhat higher estimates of  $\sim 20 \mu\text{m ns}^{-1}$  are needed to explain the experimental results [Kauffman *et al.* 1993], and are predicted by computer hydrodynamic models [Cerjan 1993]. This speed would be an overestimate for the 248 nm LGPs proposed here. This is on account of the shorter wavelength, and the sub-optimal ( $< 10^{11} \text{ W cm}^{-2}$ ) focused intensity, both of which give rise to a cooler plasma.

Furthermore, for a line focus, the hydrodynamic cooling will be less severe than for a spot focus. To illustrate this: for a constant expansion velocity, in the long-timescale regime, the total plasma volume scales with the cube of the expansion time for a hemi-spherical plasma. On the other hand, for a hemi-cylindrical line plasma, the volume scales with only with the square of the expansion time.

It is difficult to predict the exact severity of the cooling effect for the systems modelled here, on account of the line geometry, and the slow rise ( $\sim 5 \text{ ns}$ ) of the laser pulse. This slow rise means that the intensity required to generate SXR efficiently cannot be achieved until a couple of nanoseconds into the pulse (§6.2.2). Thus, it should be clear from the discussion above that there may well be very little advantage in using a line focus tighter than  $\sim 10 \mu\text{m}$  for the current application.

Of course, the only sure way to establish this is to do the experiment, and this was part of the motivation for the tighter focusing experiment described above. Also, by defocusing, a broader line focus could be achieved, which would be equivalent to repeating the experiment described in chapter 6. Thus, the tighter focusing experiment would have served a valid purpose, and could have yielded some interesting physics (*e.g.* by taking pinhole camera images of the plasma through an aluminium filter), even though it still might not have generated sufficient SXRs to pump the Xe III laser efficiently.

In fact, a better approach to achieving a higher focused intensity would probably have been to apply the travelling wave geometry with a cylindrical mirror, using a 3 cm total target length. The reason for this is that it would have provided a similar microscopic intensity on target, but divided the plasma into larger spots.

Efficient SXR generation could be made more likely by sharpening the risetime of the laser pulse, in order to suppress the hydrodynamic expansion of the plasma before the focal intensity was sufficient to generate the required SXRs. This would require the use of

---

\* 1 atomic mass unit is  $1.66 \times 10^{-27} \text{ kg}$



an optical switch in the output beam. Clearly, the switch would need to have very high transmission when “open”, since there is no further amplification of the beam to compensate for any losses. Another requirement is that the switch be initially “closed”. Of the switching schemes discussed in chapters 3 and 4, the only ones with the potential for both high transmission, and being initially closed, are:

- **electro-optic switching** - the main problem with this would be how to avoid damage to the optical components (this requires a large clear aperture), while at the same time minimising the capacitance of the switch (which requires a small clear aperture); and
- **ozone as a saturable absorber** - the main problem with this would be how to achieve saturation of the absorber on the leading edge of the pulse, without causing damage to the cell windows. A radiation-induced opacity cell could be used to mitigate the problem.

## 7.7 Conclusions

With the benefit of hindsight, the attempts at pumping the Xe III laser system described in this, and the previous chapter, may have been ill-advised. The reason for this is that the laser intensity on target would probably not have been enough to generate a sufficiently hot plasma. For example, the work of Wellegehausen *et al.* [1989] indicates that a plasma temperature of only 10.5 eV is created by focusing nanosecond duration UV radiation onto high Z targets at  $2 \times 10^{10} \text{ W cm}^{-2}$ . These were the approximate conditions aimed for in the work described in chapter 6. From Fig. 2.6, it is clear that this plasma emission temperature would give rise to a much lower inversion density and a much higher electron density than is optimal.

However, even if a sufficiently hot plasma could be achieved, the Xe III laser would still be operating far from optimally. To illustrate this, if we assume an Xe III gain lifetime of 500 ps, the useful energy in the KrF laser pulse on its leading edge cannot reasonably be assumed to be more than about 10-20 mJ. This should be compared with the lowest energy which has ever been used to saturate the Xe III laser, which is 140 mJ [Yamakoshi *et al.* 1996]. Although the higher conversion efficiency of UV LGPs, compensates for this somewhat, the laser power available on the leading edge of the KrF laser used here is only about 20 MW, compared to 4 GW for the system used by Yamakoshi *et al.* [1996]. This makes it much more difficult to generate a sufficiently hot plasma, over a sufficiently long target length, in order to achieve saturation, which is required for efficient energy extraction from the 109 nm laser.

As well as this, ~2.5 J of useless laser energy follows the 10 mJ of useful energy in the laser pulse, which will give rise to plasma emission at the laser wavelength. This will mask any laser output, as well as inevitably reducing the overall efficiency of the system by a factor of 125-250. Furthermore, this extra laser energy would give rise to debris.

Thus, although it might have been possible to show gain on the Xe III transition, the use of the leading edge of the KrF laser pulse for pumping the Xe III laser would be very unlikely to allow efficient energy extraction. Further effort would be best spent on further pulse-shortening experiments with the KrF laser. An equally good approach would be the application of an already existing, faster laser system, and this is described in chapter 8.



## 7.8 Summary

The discussion and experiments described in this chapter allowed the following conclusions to be drawn.

- The KrF laser beam quality was so poor for the experiments described in chapter 6, that their failure was inevitable.
- The SXR detection technique (filter/scintillator/PMT) was valid - SXRs were detected when known to be present.
- An intensity of as close to  $10^{11} \text{ W cm}^{-2}$  as possible would be desirable in the generation of SXRs to pump the Xe III laser.
- A tighter line focus than that used for the experiments described in chapter 6 could be generated.
- Even so, there is reason to believe that hydrodynamic expansion of the plasma could mean that there was little advantage to tighter focusing. Using the same laser pulse in the travelling wave geometry, could mitigate the effect of this expansion.
- The use of the unsharpened laser pulse is unlikely to give very effective pumping of the Xe III laser system, however, and should not be investigated further.
- Further work should concentrate on pulse shortening of the nanosecond KrF laser, or the use of a higher power laser to pump the Xe III laser system.



# 8. Picosecond pumping

## 8.1 Introduction

### 8.1.1 Rationale

The main thrust of the work reported in this thesis was to pump the Xe III laser with a nanosecond duration KrF laser. During the later stages of this work an opportunity arose to use an altogether different laser for pumping. This was a KrF laser capable of generating 40 mJ pulses of 7 ps duration. The idea of using this laser was extremely attractive, for several reasons. Firstly, the peak power was fifty times that of the nanosecond laser system, while the divergence was only three times worse, suggesting an increase of more than order of magnitude in the focal intensity available for any given focusing geometry. Secondly, the short KrF pulses would produce a short burst of SXR's, and the problems of electron quenching and self-termination of the Xe III laser would be eased.

The main problem envisaged was the comparatively low energy of the pumping pulse. To put this in context, the lowest energy pumping laser ever used to achieve saturated output from the Xe III laser is 140 mJ of 1064 nm radiation [Yamakoshi *et al.* 1996]. However, we expect KrF laser-generated plasmas to be several times more efficient than their infrared counterparts, and so the low pulse energy was not seen as disastrous. Indeed, (anticipating the discussion to follow) we note that the parameters of the pumping scheme which was used with the picosecond KrF laser, bear a close resemblance to those used by Sher & Benerofe [1991], who observed a gain of  $1.7 \text{ cm}^{-1}$  at 109 nm (but not saturation). A comparison of the two schemes is given in table 8.1.

	Sher & Benerofe [1991]	This work
Pumping wavelength (nm)	1064	248
Pump pulse duration (ps)	80 (with prepulse 1.6 ns earlier)	7
Pump pulse energy (mJ)	75	40
Geometry	Travelling wave	Normal incidence
Total gain length (mm)	42	30-60 (depending on effectiveness of mirror)
Focal intensity ( $\text{W cm}^{-2}$ )	$1.7 \times 10^{11}$	$6.7 \times 10^{11}$
Target material	Au (Z=79)	Ta (Z=73)

**Table 8.1.** Comparison of parameters of 109 nm laser system used in this work and reported by Sher & Benerofe [1991].

As can be seen from table 8.1, the two systems are very similar, with the KrF system having the edge on gain length and focal intensity. This suggested it should have been possible to observe significant gain (if not saturation) at 109 nm, using the picosecond pumping system.



### 8.1.2 Picosecond laser system

The KrF laser system used for this work (situated at the Rutherford Appleton Laboratory\*) was developed and operated by others†. It has been described elsewhere [Turcu *et al.* 1993], and is normally used for the generation of a debris-free plasma source of 1 keV x-rays. We shall summarise its configuration for 1 keV generation, and then comment on the modifications made to allow its use in this work.

Briefly, there are three stages to the pulse generation. Firstly, low energy short pulses at the KrF wavelength are generated. Secondly, these are multiplexed to give two angularly-separated pulse trains of eight pulses each. Finally, these are amplified in two KrF amplifiers.

Generation of the short pulses begins with frequency-doubled pulses from a modelocked Nd:YAG laser, which are used to pump a 746 nm dye laser. The cavity length of the dye laser is adjusted to make the cavity round-trip time equal to the pulse separation of the Nd:YAG pumping pulses. This means that no sooner has the gain in the dye been switched on by the arrival of a pumping pulse, it is quenched by the return of the previous pulse. This is known as synchronous pumping. Pulses lasting 7 ps and of energy 250 pJ are obtained in this way. Three dye amplifiers are used to boost the energy of these to 300  $\mu$ J. These dye amplifiers are pumped by an XeF laser, operating at up to 100 Hz. It is the maximum repetition rate of this XeF laser (and of the two KrF amplification lasers), which limits the maximum repetition rate of the system as a whole. After this amplification the dye laser pulses are frequency-tripled to the KrF laser wavelength, giving 10  $\mu$ J pulses. The frequency-tripling is achieved by frequency-doubling, followed by mixing the frequency-doubled radiation with the 746 nm fundamental.

The beams are multiplexed by an arrangement of beamsplitters to give 16 equal pulses, separated by 2 ns each. The pulses are formed in two chains (of eight pulses each), separated in angle by 1.4 mrad. Finally, two commercial KrF laser modules are used to amplify first one chain, and then the other. The individual output pulses in the resulting chains are of energy up to  $\sim$ 10 mJ and duration 7 ps. The beam divergence was quoted as 100  $\mu$ rad both horizontally and vertically, with some geometrical spreading, as discussed in §8.2.2.2.

The only modification to this arrangement for the experiments described here, was the selective blocking of elements of the pulse stacker, to give, variously: single pulses, double pulses, and a single train of eight pulses.

## 8.2 Experimental arrangement

### 8.2.1 Line focus geometry

Sher's travelling wave system [Sher *et al.* 1987] is the obvious choice of pumping geometry for a picosecond pumping laser. The advantages of this arrangement are discussed in §2.2.2. It is worth noting that all of them apply to the pumping laser proposed here. That is, it is beneficial to have the pumping travelling with the Xe III laser pulse, since the x-ray pulse emitted will be short. Furthermore, the very high power

---

\* Run by the Council for the Central Laboratory of the Research Councils. Address: Chilton, Didcot, Oxfordshire, OX11 0QX.

† Edmond Turcu, Ric Allott, and Nicola Lisi.



( $\sim 3$  GW) of the laser system removes the need for very tight focusing in order to achieve the focal intensities required ( $\sim 10^{11}$  W cm $^{-2}$ , but see §8.5) for efficient production of the pumping x-rays. This is important, since very tight focusing is not possible for the travelling wave geometry, as discussed in §6.3.5ff.

However, the travelling wave geometry was not used for the experiments described here. There were two main reasons for this. The first was pressure of time; it would not have been possible to have assembled the necessary optics and target chamber, in the few weeks available for experimental preparation. Furthermore, only one week of experimental time was available for the experiment, which would not have been long enough to devise the tricks which are bound to be needed in order to align, characterise, and use the travelling wave geometry.

The second reason for not using the travelling wave geometry was to allow a more direct comparison of the experimental results with those obtained from the nanosecond KrF laser system used for the other experiments presented in this thesis.

The travelling wave geometry acts to maximise the total gain-length product of the Xe III laser system. The more usual means to this end in lasers is by the use of mirrors. The unidirectional nature of the travelling wave geometry makes mirrors of very little benefit to such systems. For the work described here, however, a mirror could almost double the total gain-length product; and one was used to offset some of the disadvantages of using a normal incidence geometry. This is described in §8.4.1.

The off-axis spherical mirror geometry was used for this experiment; all the optics and target chamber were already assembled and tested, and an alignment technique had been devised (§6.6.4).

## 8.2.2 Alignment

The focusing geometry used is shown in Fig. 8.1. As in §6.6.4ff we shall consider separately the three rotational degrees of freedom of the target (see Fig. 6.16).

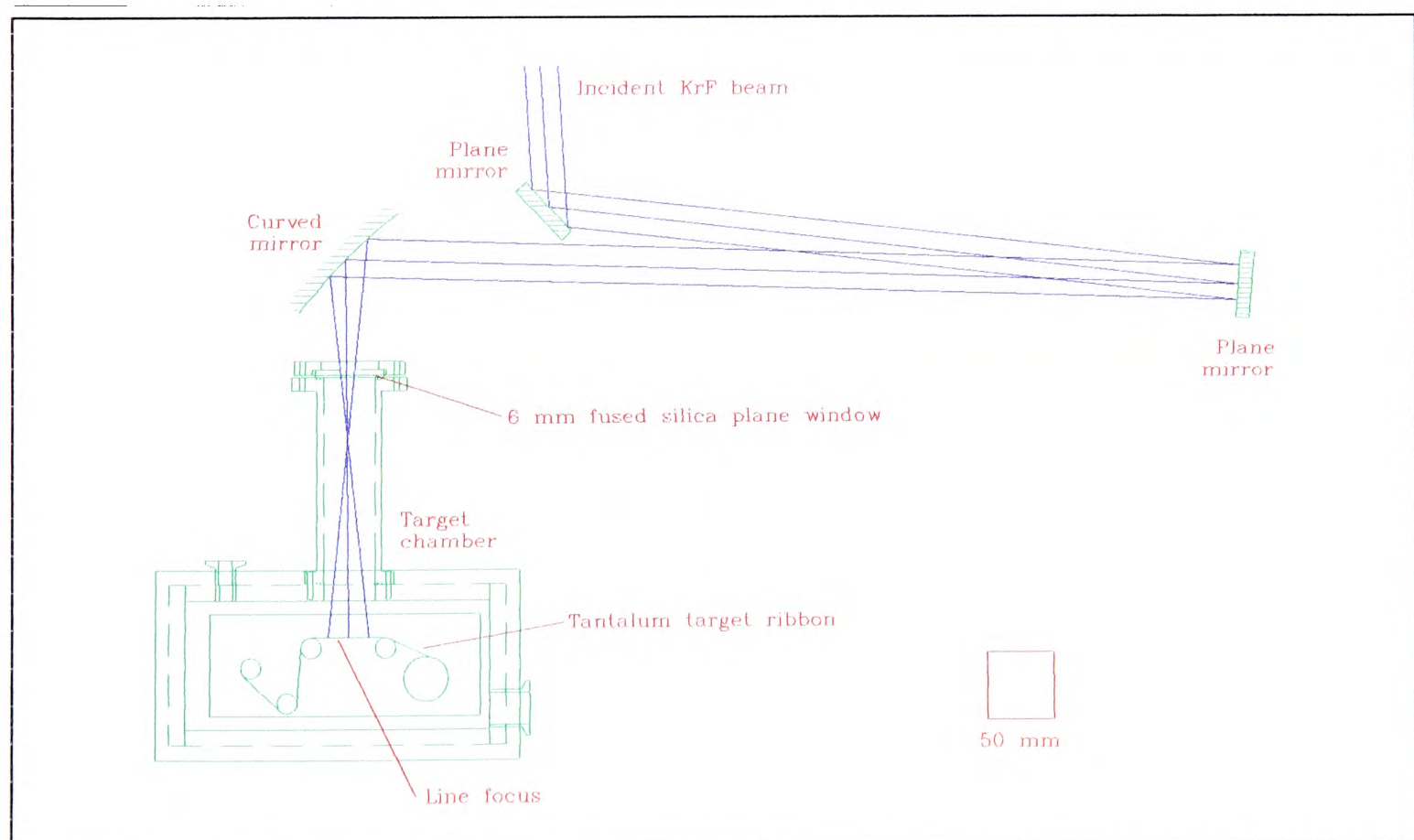


**Figure 8.1.** Focusing geometry used for experiments described in this chapter (to scale). The use of two plane mirrors for beam steering was dictated by physical constraints in the laser laboratory.



### 8.2.2.1 Roll

The roll alignment required the target to be made horizontal, and the line focus made parallel to it. This was achieved by looking at the shadows cast by the target reels on a screen, when illuminated by light from a 300  $\mu\text{m}$  pinhole. This pinhole diameter was chosen to provide the sharpest possible shadows on the observation screen - had it been much smaller diffraction would have caused blurring, whereas if had it been much bigger geometrical effects would have caused blurring. The technique is illustrated in Fig. 8.2.

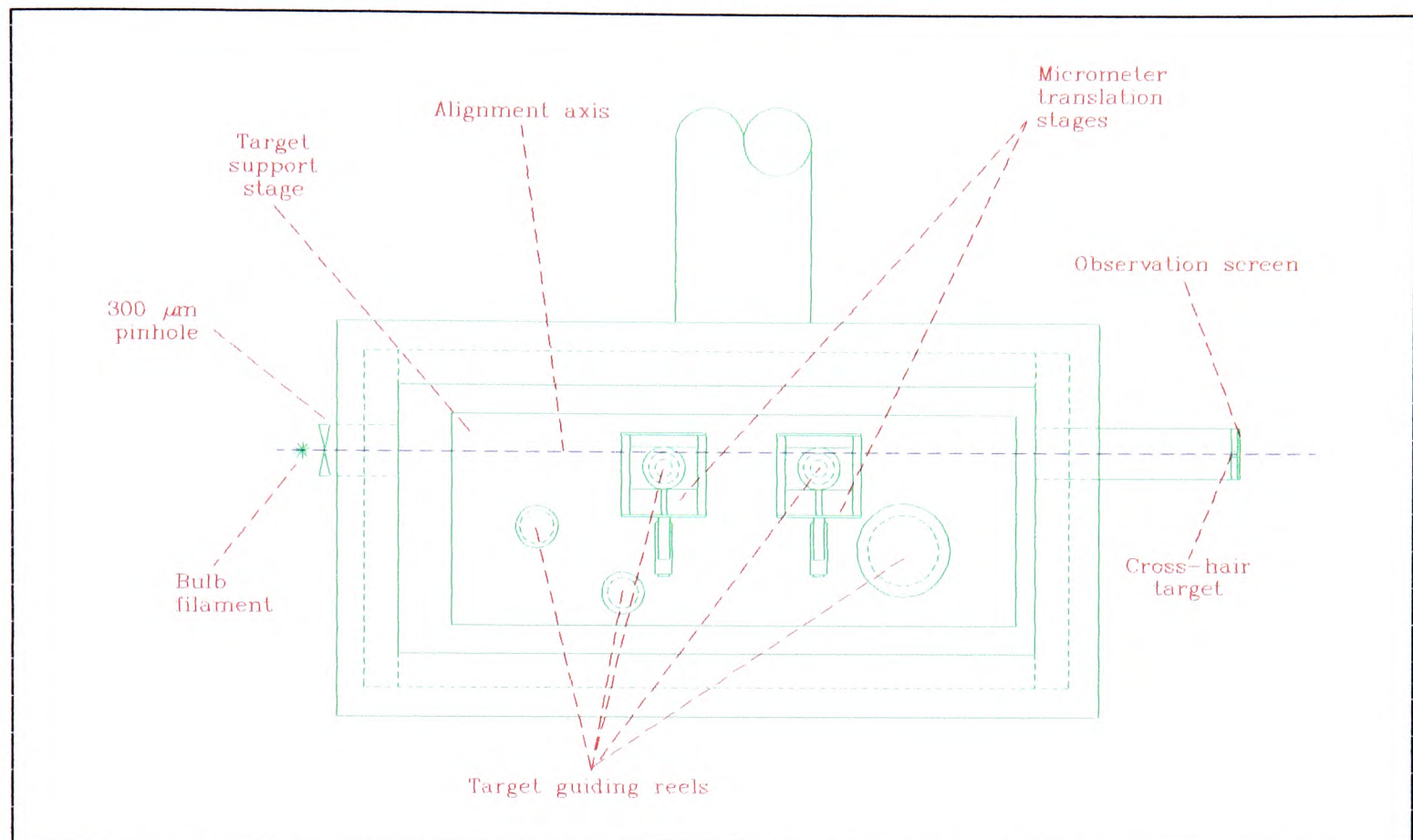


**Figure 8.2.** Schematic of alignment technique used to align target reels. Plan view of target chamber.

The target ribbon sat in grooves in the target guiding reels. Grooves in the two reels on the alignment axis were used for the alignment.

The target support stage was fixed at three points on adjustable spring mountings. These were adjusted until the centres of the grooves were both level with the alignment axis. The line focus could be made horizontal simply by ensuring the KrF beam was travelling horizontally before it hit the curved focusing mirror. This gave rise to a horizontal line focus, independent of the alignment of the mirror\*. Once this was achieved the laser was used to make line plasmas on the target ribbon. The roll of the whole target chamber was then adjusted by setting the tilt of the plinth to which it was clamped, in order to make the line plasmas parallel to the target ribbon. This gave a roll alignment accurate to within about 100  $\mu\text{m}$  over the 30 mm length of the line focus.

\* In fact this is not quite true. The geometrical divergence of the KrF beam used here means there is a slight change in the roll of the line focus, according to the relative heights of the centre of curvature of the focusing mirror and the geometrical focus of the incident KrF beam. The correction is tiny, and for the system here it represents a deviation from horizontal of no more than 10  $\mu\text{m}$  over the length of the line focus.



### 8.2.2.2 Yaw

The focusing mirror used in these experiments was the same as that used in the experiments described in chapter 6, having a nominal radius of curvature of 406 mm. The laser divergence was quoted as  $100\ \mu\text{rad}$ , and the KrF beam height was 14 mm before focusing. Expression (6.14) indicates this will give rise to a depth of focus of 1.2 mm. This means that for the whole length of the focal line to be in focus on the target its yaw must be correct to within 40 mrad.

First, the target ribbon was aligned with the target chamber axis. This was done using the pinhole and screen technique depicted in Fig. 8.2. In this way it was possible to ensure the target ribbon was pointing at the cross-hair target to within  $\sim 15\ \mu\text{m}$ . The target reels were then set back  $375\ \mu\text{m}$  from the alignment axis. This was to allow for the  $25\ \mu\text{m}$  thickness of the target ribbon, then to set the target surface  $350\ \mu\text{m}$  behind the alignment axis. This is because the maximum Xe III gain is found at about this distance from the laser plasma (see §8.4.3). This should have ensured any 109 nm emission was incident on the entrance slit of the monochromator used to look for laser radiation (but see §8.4.3).

After this, a technique very similar to that described in §6.6.4ff was used to align the KrF beam with the target ribbon. First, a HeNe beam was aligned along the KrF beam, and then a pentaprism was used to divert it through exactly  $90^\circ$  on to the target ribbon. The target chamber was mounted on an optical rail, which was rotated until the HeNe beam reflected by the target ribbon was in the same vertical plane as the incident beam. The total error in this process was less than 2 mrad.

Finally, another correction was needed. This was because the KrF beam was geometrically diverging. This means it behaved as though it was coming from a point behind the focusing mirror. This situation is identical to the method of producing a line focus with a mirror and lens proposed by Ross & Hodgson [1985] and described in §6.3.4.1. The line focus is on the line joining the centre of curvature of the mirror to the geometrical focus of the KrF beam. Although this is illustrated, to scale, in Fig. 8.1, the correction is barely discernible, and so an exaggerated version is illustrated in Fig. 8.3.

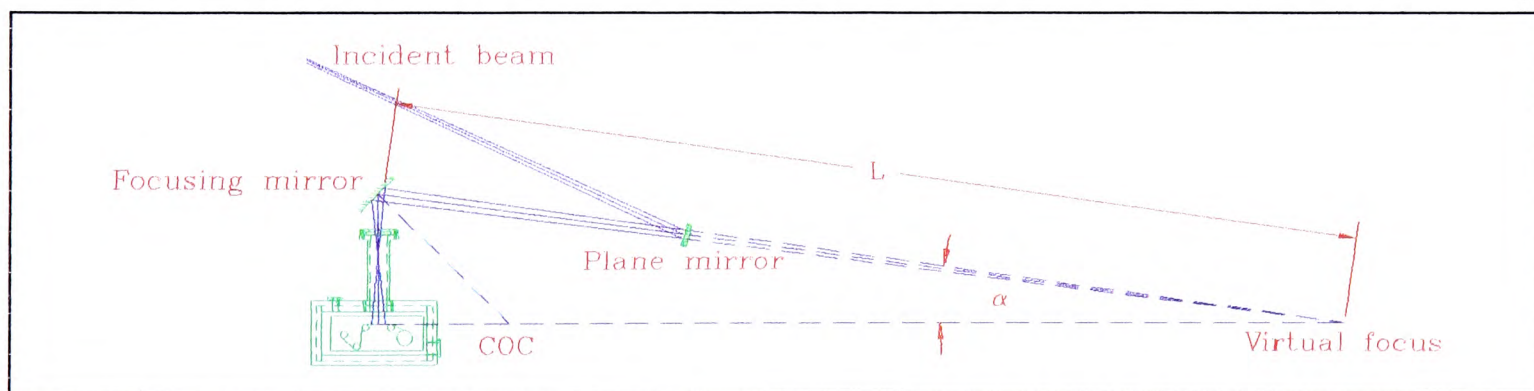


**Figure 8.3.** Correction to beam alignment needed to ensure correct yaw of focus on target ribbon. Size of correction needed is exaggerated fivefold for clarity. COC is centre of curvature of focusing mirror.

From Fig. 8.3 it is clear that the beam incident on the focusing mirror should not be parallel to the target, but tilted through an angle,  $\alpha$ , if the line focus is to be parallel with the target. Calculation of  $\alpha$  involves knowing  $L$ , the distance between the virtual focus of the incident beam, and the focusing mirror. This was calculated as  $10.5 \pm 0.4\ \text{m}$  by measuring the geometrical spreading of the beam, by exposing thermally sensitive (fax) paper to the beam at different distances along it. The fax paper was held against a plate which was attached to an optical rail, to ensure that the angle of incidence of the beam on the paper was constant.



The deviation of the beam through angle  $\alpha$  (which was\* 28 mrad) was achieved by tilting the plane mirror shown in Fig. 8.3 through an angle  $\alpha/2$ , which was measured by using a calibrated mount for the mirror.

### 8.2.2.3 Pitch

The pitch of the target was not critical (see §6.6.7), and was estimated (by inspection of the HeNe beam reflected by the target during the yaw alignment) as no more than  $3^\circ$ .

### 8.2.2.4 Depth

Finally, it was necessary to adjust the separation of the focusing mirror and the target ribbon, to place the line focus on the target. The target chamber was mounted on a rail, and moved manually towards and away from the focusing mirror, while the laser was firing. The focus could be found, repeatably to within 1 mm, by looking at the brightness of the plasma formed in air, and by listening for a characteristic ‘crack’ sound, only found at the focus. Once the focus had been found in this way the target chamber was fixed to its mounting rail. All further adjustments were made by translating the focusing mirror, which was mounted on a micrometer translation stage. References in this chapter to translation of the mirror relate to translating it perpendicular to the line focus.

Both the position† and quality of the focus were assessed by exposing glass microscope slides to the laser, and inspecting under a microscope the etch lines produced. Individual slides were suspended by a piece of cotton thread and gently rested against the target ribbon, to ensure the surface of the slide was exactly parallel to the surface of the target. The thread was used since it could transmit only a negligible torque from the support to the microscope slide.

Initial experiments showed some care was needed in interpreting the results. In particular, for a single-shot exposure some of the lines observed were only  $2.5\ \mu\text{m}$  wide, *i.e.* half the diffraction-limited width. Non-linearity in the response of the slide to incident radiation intensity seems the most likely explanation for this. By firing 25 laser shots on to the slide, more straightforward results were observed. A series of photographs of the etch lines produced at different mirror-target separations, allowed the focus to be found to within  $\sim 200\ \mu\text{m}$ . Two such photographs are reproduced in Fig. 8.4.

The position of the focus was obvious, because it corresponded to a narrow etch line, surrounded by extra damage ‘blobs’, presumably caused by acoustic or thermal effects. One of these is visible as feature B of Fig. 8.4 (a). These ‘blobs’ were much less pronounced away from the focus. Furthermore, it was found that a single laser shot could only produce visible etch lines on the slides over a  $\sim 600\ \mu\text{m}$  range of focal positions. The

---

\* In fact, a calculation error led to a correction of 33 mrad being applied. The 5 mrad systematic error introduced in this way should not have been detrimental to the focus quality, since this is small compared with the 40 mrad error required to preclude the production of a divergence-limited focus along the whole length of the line focus. This assertion was confirmed by inspection of the glass slides used to find the focal depth (§8.2.2.4).

† In fact, this experiment was not performed until after the scintillator-based soft x-ray detection experiments. The focal depth was varied sufficiently in these experiments to ensure that the correct focal position was sampled; and so the exact position of the focus, determined by the etching of glass slides, was not needed.



focal position at which these lines were strongest (thickest), corresponded to the position of the focus deduced from the 25-shot exposures.

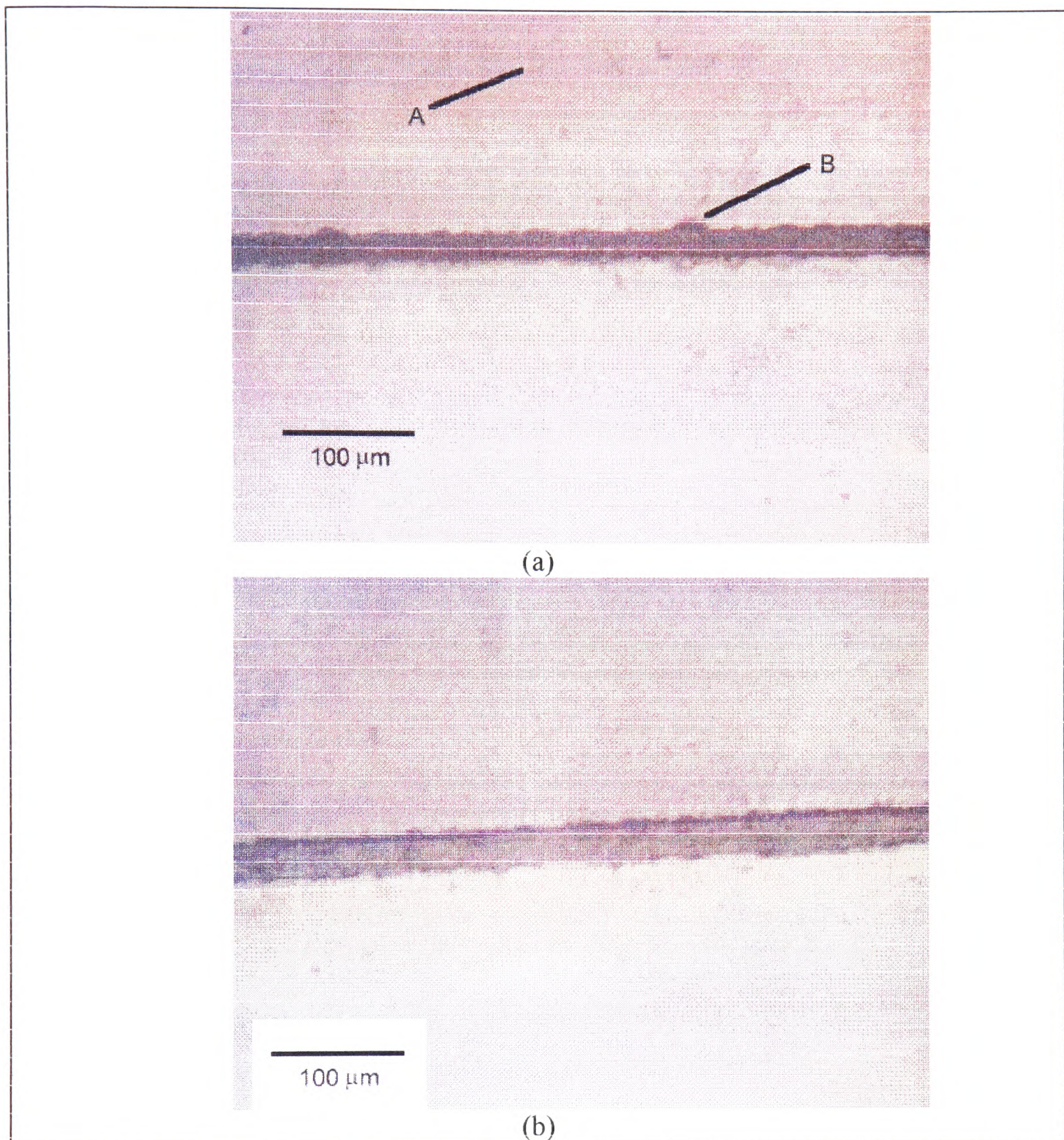


**Figure 8.4.** Central sections of lines etched on glass microscope slides by 25 laser shots, (a) within 100  $\mu\text{m}$  of focus, and (b) with line focus 700  $\mu\text{m}$  in front of slide. Colour contrast has been enhanced by observing in green transmitted light. See text for explanation of features A and B.

From Fig. 8.4 (a), it is clear that the focal line produced was  $\sim 25 \mu\text{m}$  wide. This suggests a divergence of the KrF laser of  $85 \mu\text{rad}$ , in good agreement with the nominal  $100 \mu\text{rad}$  divergence quoted by the laser operators. The width of the etch line did not vary along its length, which indicates that the yaw alignment was correct.

An unexpected feature was observed in the etch patterns taken within a few hundred microns of the focus. This was a very weak extra line focus  $125 \mu\text{m}$  from the main focal line. Easily spotted by eye under an optical microscope, this was just visible in the photographs taken, as feature A of Fig. 8.4. The extra line corresponds to an extra KrF beam with a vertical angular offset of  $0.4 \text{ mrad}$ . This was assumed to be caused by a



reflection from a back surface of a slightly wedged optic, somewhere in the laser system. The second beam was clearly much less intense than the first; 25 laser shots did not produce an etch line as clear as that produced by a single shot from the main beam. For this reason, the cause of this extra line was not investigated further, and nor was it eliminated.

### 8.3 Search for soft x-rays

The first stage in the production of a 109 nm Xe III laser is the production of soft x-rays in range of the 67 eV to 100 eV. The first experiments with the system concentrated on looking for these. Initially, a filter and scintillator arrangement was used for detection. The filter (as described in §6.13) was a 2 mm square of 125 nm thick  $\text{Si}_3\text{N}_4$  overcoated with 25 nm of  $\text{SiO}_2$  and 60 nm of aluminium. The filter was mounted in front of a sodium salicylate scintillator, and scintillation detected by a Thorn-EMI type 9783B photomultiplier.

A 3 mm thick  $\text{MgF}_2$  filter was mounted on a magnetically-activated pivot, so that it could be moved in and out of the beam path by placing a magnet on top of the target chamber. By touching the target chamber it was possible to feel the rise and fall of the magnetic mount. This check was made every time the magnet was put in place or removed, and on no occasion did the system fail. The purpose of the  $\text{MgF}_2$  filter, as in §6.13.1, was to eliminate any soft x-ray signal - the absorption length for 67 eV to 100 eV radiation in  $\text{MgF}_2$  is much less than a micron [Thomas 1989] - while leaving as much of the VUV and visible signal as possible.

The filter and scintillator were mounted  $\sim 60$  mrad ( $3.3^\circ$ ) in front of the axis defined by the line focus. 35 mJ single KrF pulses were focused on to the target. No soft x-ray signal was observed (i.e. signal which disappeared when the  $\text{MgF}_2$  filter obscured the detector).

Adjusting the focal depth was no help. The finite ( $10^{-5}$ , see §6.10) transmission of the Al filter to KrF laser radiation was suspected\* as being the cause of a significant background signal, masking any x-ray signal. In order to eliminate this possibility a much thicker aluminium filter was used. This was 1  $\mu\text{m}$  thick; self-supporting; and contained no pinholes visible to the naked eye. The calculated bulk transmission of this is shown in Fig. 8.5 [Thomas 1989].

---

\* In fact, this was not the main cause of background signal. It was instead a leaky light-seal around the coupling of the PMT used to detect visible photons produced by the scintillator. The problem was eliminated (by shrouding the coupling with black card) in the 1  $\mu\text{m}$  aluminium filter experiments which followed.



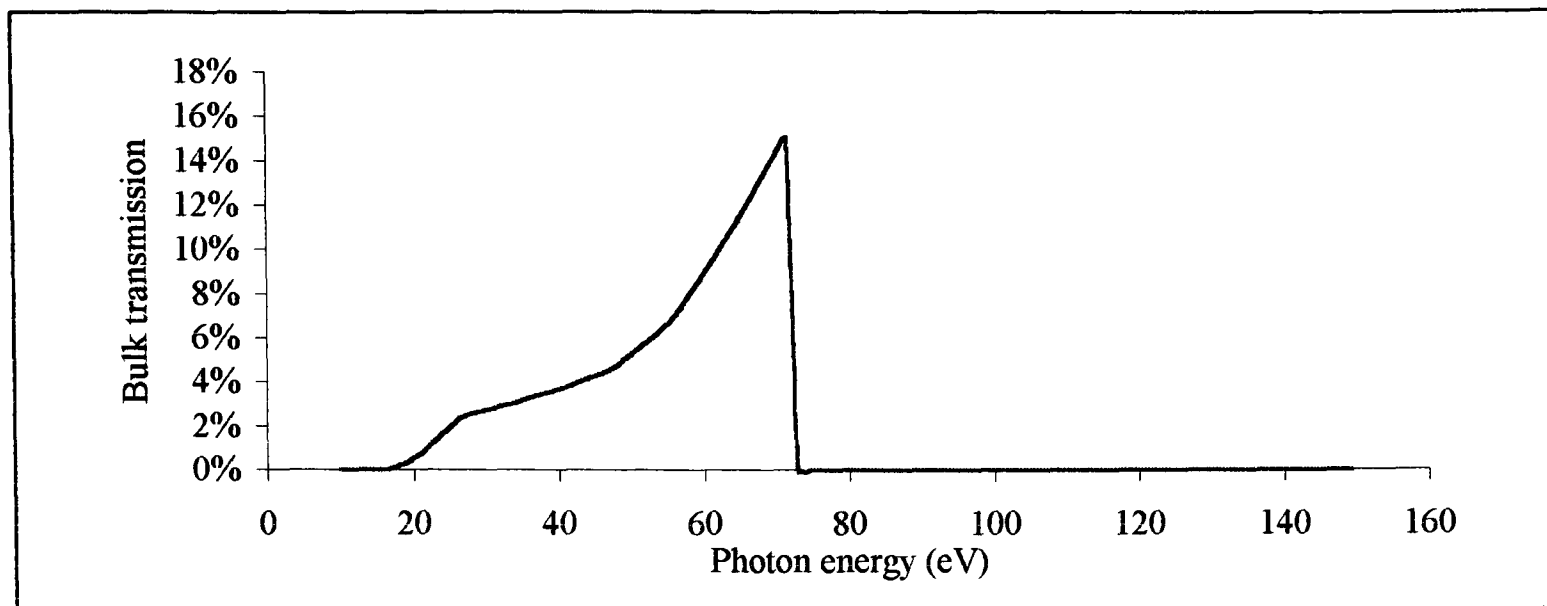


**Figure 8.5.** Bulk transmission of 1  $\mu\text{m}$  of aluminium [Thomas 1989].

From Fig. 8.5 it is clear that this filter passes x-rays of lower energy (18 eV to 71 eV) than are required to pump the Xe III laser (67 eV to 100 eV). Nevertheless, it is a useful diagnostic, since the production of useful SXR will be accompanied by the production of lower energy photons.

The filter, which was fixed to a metal washer, was mounted in place of the Al/Si<sub>3</sub>N<sub>4</sub>/SiO<sub>2</sub> filter on the same mount (Fig. 6.21). In this case the detection aperture was limited by the 3 mm diameter of the central hole in the mount. The detector was mounted  $\sim 33$  mrad in front of the axis defined by the line focus. Again, the MgF<sub>2</sub> filter was used to distinguish between visible/UV/VUV and SXR signals. A fresh piece of scintillator surface was exposed, in case the initial surface had been damaged by the previous experiment.

Again, no SXRs were detected, including when the focus position was varied, both by moving the focusing mirror and the whole target chamber. An optical signal was measured, however, which is not surprising since the gain of the photomultiplier was increased until a signal was observed; but this did not disappear when the MgF<sub>2</sub> filter was obscuring the detector.

The source of this background optical signal was investigated. It could be eliminated by preventing the picosecond KrF pulses from entering the final KrF amplifier, but keeping the entire laser system firing (and hence generating all the same electrical noise and optical scatter). With the picosecond seed pulses blocked, only ASE from the final amplifier was incident on the target, and no plasma was created. This indicates the signal was due to the presence of the plasma.

The signal cannot have been due to photons of energy less than 18 eV (in particular scattered pumping laser photons) getting through the filter - its transmission at 248 nm is of order  $10^{-66}$ . It must have been due to photons of energy less than the 11 eV transmission cut-off of MgF<sub>2</sub>, since the presence of MgF<sub>2</sub> did not eliminate the signal. These photons must have leaked around the sides of the filter, or possibly through invisible pinholes in it. The system was operated in air and selected parts of the filter and its mount were carefully obscured with black paper. This indicated that the air vent was not to blame (blocking it did not reduce the signal); but that light reaching the detector was passing through the filter itself or getting in around its immediate edges. The filter was fixed (around its edges) to the mount with clear double-sided adhesive tape, with  $\sim 10$   $\mu\text{m}$  aluminium foil stuck to the exposed side. Fluorescence within the thickness of this tape seems the most likely culprit. The size of this background signal relative to any likely x-ray signal is considered in §8.5.2.



At the end of the experiments described in this chapter, another attempt was made to detect SXR, using a different detector. This was a calibrated photodiode, (IRD model AXUV-100, as used also in experiments described in §9.3.3), having a quantum efficiency ranging from 2 to 15 over the aluminium transmission window. A fresh 1  $\mu\text{m}$  aluminium filter was used, in case there had been any deposition of debris or pump oil on the original filter. In this case, the filter was mounted  $\sim 3$  mrad in front of the axis defined by the target, with the 5 mm diameter active area of the diode 60 mm behind it.

In this case, no signal at all was observed, even when the diode was given a 9V reverse bias, which increases its sensitivity approximately tenfold. In order to check the diode was working, the aluminium filter was removed and a glass slide used in its place to absorb scattered KrF radiation which might have been sufficiently intense to damage the diode. The system was operated in air, and the diode registered a signal owing to visible light from the laser plasma.

## 8.4 Search for 109 nm emission

### 8.4.1 Experimental arrangement

Despite the dearth of SXRs detected, attempts were made to observe the Xe III 109 nm laser system. The experimental arrangement is shown in Fig. 8.6.

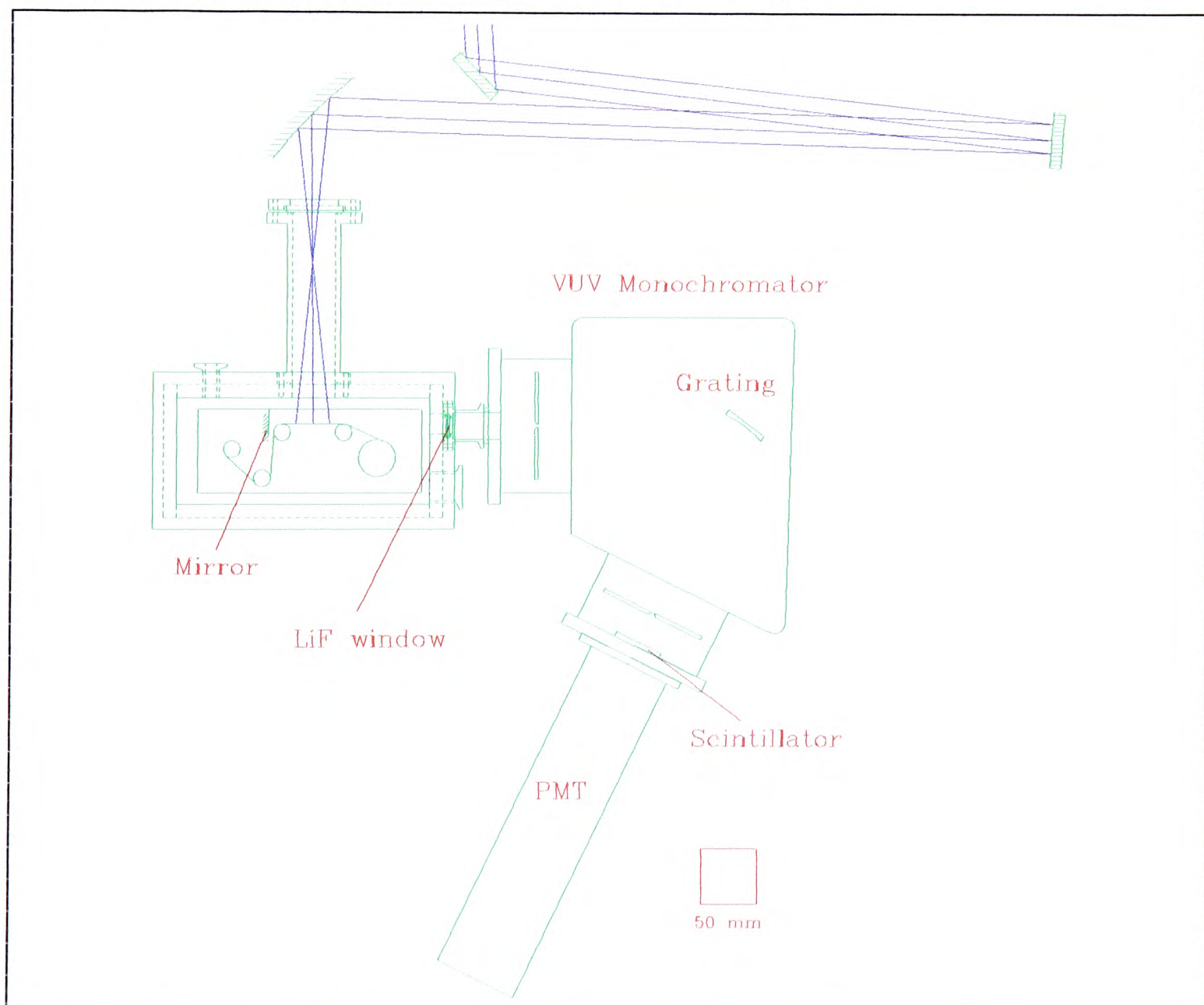


**Figure 8.6.** Geometry used to detect 109 nm laser light.



An  $f/4.5$  VUV monochromator (Acton Research Corporation model VM 502), sodium salicylate scintillator, and Thorn-EMI type 9426 photomultiplier, were used to detect any 109 nm laser radiation generated. The arrangement was identical to the one used for the experiments described in chapter 9, and is described in detail in §9.3.

A mirror was used to increase the effective total gain-length product for 109 nm Xe III laser radiation. It was an Acton Research Corporation 1000-1D-FLP mirror, of aluminium overcoated with a thin layer of  $\text{MgF}_2$ , optimised for reflectivity around 100 nm. The specified reflectivity at 109 nm was 50%-60%. Although this was not tested for the particular mirror used here, its reflectivity down to 120 nm had been measured by the manufacturers, and exceeded its specification.

The mirror can be expected approximately to double the total gain-length product of the system, provided the gain is sufficient to counteract its 40%-50% loss over a short distance of gain region. A further consideration is the duration of the population inversion, compared to the 300 ps round-trip time of the system. This is comparable with experimentally observed pulse durations (for similar pumping energy line fluences) [Clement *et al.* 1994]. This might limit the improvement in output provided by the mirror.

The 20 mm diameter, 2 mm thick, LiF window was obtained from Crystran\* and was selected by the manufacturer for high VUV transmittance (measured at 121.6 nm). The transmittance of the window to 109 nm radiation is discussed further in §8.5.1.

### 8.4.2 A first attempt

The mirror was aligned along the target tape, using the reflection from the back of the reflective surface of the mirror of a HeNe beam. This was accurate to within about 7 mrad.

The target chamber was filled with xenon to a pressure of 18.5 mbar (14 torr). Both the entrance and exit slits of the monochromator were opened to 250  $\mu\text{m}$ , giving rise to a 1 nm passband. The signals from the PMT were compared with the monochromator set to 108.9 nm (the Xe III laser wavelength) and 111.9 nm. There was no peak at the laser wavelength. Several modifications were tested:

- An attempt was made to increase the wavelength discrimination of the monochromator, in case the problem was that the laser emission was masked by continuum emission from the plasma. The monochromator entrance and exit slits were closed their full extent, to 5  $\mu\text{m}$ . The linear dispersion (4 nm/mm) of the monochromator suggests a 0.02 nm passband, but this overestimates the resolution because only a finite number of grating lines will have been illuminated. Diffraction at the entrance slit would ensure that at least 500 grating lines were illuminated, corresponding to a wavelength resolution<sup>†</sup> of better than 0.2 nm. This reduced the optical signal, and so the gain of the PMT had to be increased. Unfortunately, optical signals were swamped by electrical noise from the lasers firing (i.e. there was no clear difference in signal obtained when the KrF beam was blocked), and this technique was abandoned.

---

\* Crystran Ltd., Poole, UK

† The fundamental limit on the wavelength resolution,  $\delta\lambda$ , of a diffraction grating depends on the number of lines illuminated,  $N$ ; the diffraction order; and the wavelength,  $\lambda$ , in question. For first order observation as used here, the relationship is

$$\frac{\lambda}{\delta\lambda} = N.$$



- 250  $\mu\text{m}$  slits were used for subsequent measurements since they gave an easily-measurable optical signal. Furthermore, the resulting 1 nm wavelength discrimination is almost the best possible. This is a trade-off between wide slits illuminating many grating lines, and narrow slits giving a small passband due to the linear dispersion of the monochromator. The focusing mirror was translated in case the focusing was not optimal. This did not give rise to any increase in signal at 108.9 nm.
- The source of the signals observed was investigated. Using the calibration of the detection system (scintillator & PMT) discussed in §9.3ff, the size of the signal corresponded to  $9 \times 10^4$  photons leaving the monochromator exit slit, assuming they were of wavelength 108.9 nm. The signal disappeared when the KrF beam was blocked, or when the picosecond seed pulses were blocked from entering the final KrF amplifier. It was unaffected by putting a black cloth over the PMT, covering all the light-tight seals which could have been leaky. Clearly, then, the production of a plasma was necessary to observe the signals.
- The monochromator was set to 50 nm, well below the 105 nm cut-off wavelength of the LiF window. A similarly-sized signal was observed. This cannot have been caused by 50 nm photons. Nor can it have been caused by second or higher diffraction orders of longer wavelength radiation, since this appears at *longer* wavelengths than its correct wavelength. The signal varied approximately linearly with the width of the exit slit, as it was reduced below the width of the incident slit. This indicates the light causing the signal must have passed through the exit slit. All this evidence points to the signal being caused by scatter of light coming from the plasma (either its own emission or scatter of the KrF pumping radiation). This light could have been scattered by the grating itself, or by the monochromator walls, or by the grating mounting.
- Finally, an attempt was made to use a train of eight 7 ps KrF pulses. These were of mean individual energy 12.5 mJ, and separated by 2 ns. The reasons for this are discussed in §8.4.5.2. The xenon gas was changed, and a pressure of 15.5 mbar (11.8 torr) used. This did not provide any signal at 108.9 nm which was not also present at 50 nm.

### 8.4.3 Plasma shadowing

With light from the laser plasma established as the main source of noise in the experiment, an experimental geometry was devised to reduce the severity of the effect. This is shown in Fig. 8.7.



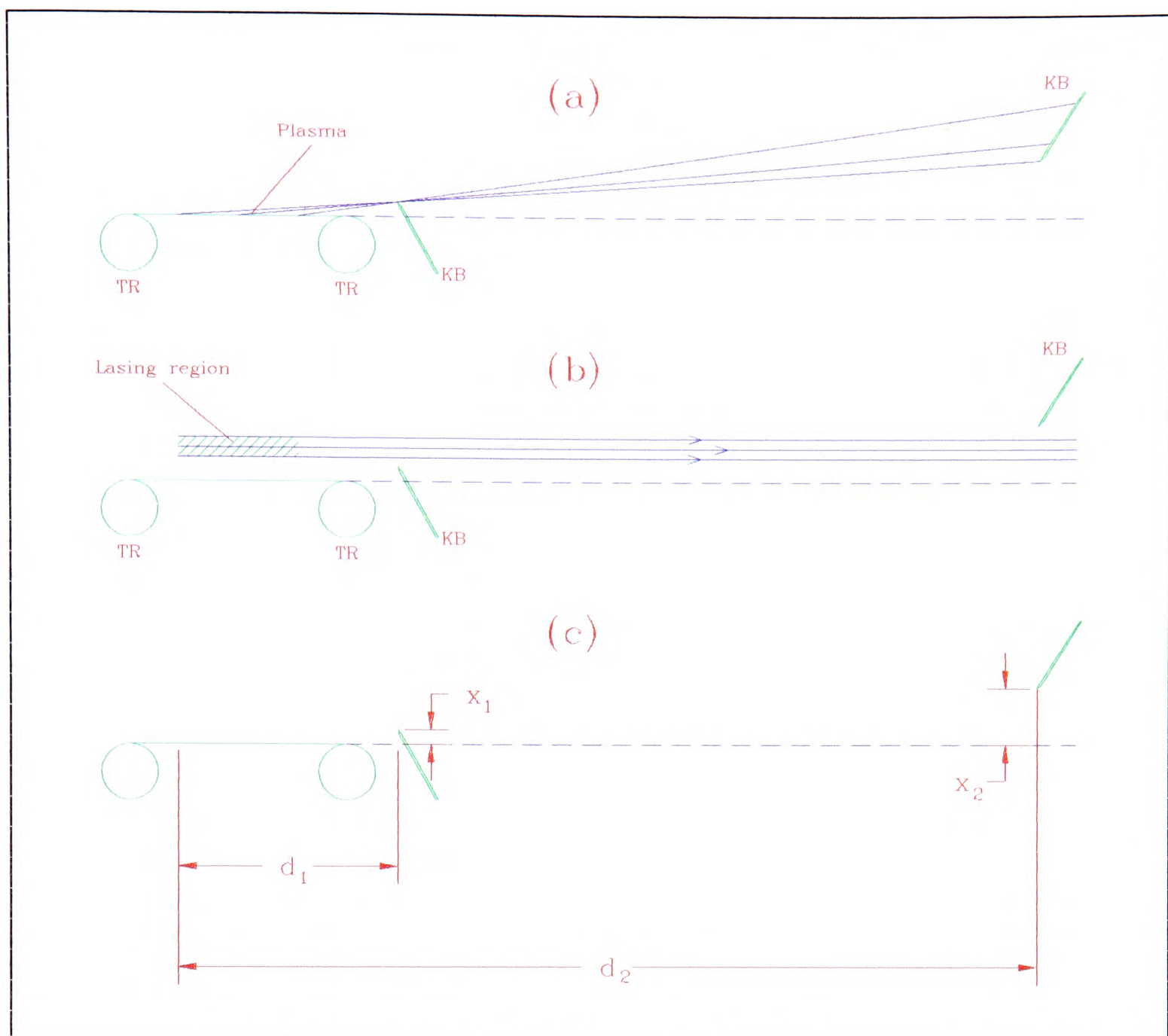


**Figure 8.7.** Double knife edge geometry used to shadow detector from direct plasma emission and scatter. Symbols are: TR; target reel, KB; knife blade. In (a) we see light from the plasma being blocked, whereas in (b) light from the lasing region is not obscured by the knife blades, and (c) shows the geometry. The offset of the lasing region has been exaggerated for clarity.

The technique takes advantage of the fact that the lasing region is offset from the plasma. For the knife edges to just shadow the plasma it is clear that we require

$$\frac{x_2}{x_1} = \frac{d_2}{d_1} \quad (8.1).$$

For the application here, the ratio  $d_2 / d_1$  was 3.6, and  $x_1$  was set to  $150 \mu\text{m}$ . This means light from the region between  $150 \mu\text{m}$  and  $530 \mu\text{m}$  from the plasma was not obscured\* by the double knife edge arrangement. This choice was dictated by measurements of Sher *et al.* [1991], Clement *et al.* [1994], and Kubodera *et al.* [1995] of the distance between the

\* We have only considered light travelling parallel to the axis defined by the line focus. It is easily seen from Fig. 8.7 that not all the light travelling obliquely from the lasing region passes the second knife edge. The severity of the effect depends on the exact distribution of gain in the lasing medium, but in any case it can cause no more than half the oblique light to be blocked. This is because any light travelling down (and to the right) of the plane of Fig. 8.7 can pass the second knife edge.



LGP and the axis of maximum 109 nm gain. These measurements were made with similar pumping laser energy line densities to that used here (30, 9, and 16 mJ cm<sup>-1</sup> respectively at 1.06 μm, compared to ~12 mJ cm<sup>-1</sup> at 248 nm used here). In each case, the distance of the region of maximum gain was found to be between 200 μm and 400 μm from the LGP target.

#### 8.4.4 A second attempt

Since the first attempt at observing 109 nm laser action had been unsuccessful, tremendous care was taken with the second attempt to ensure that if any laser action was possible with this pumping arrangement, it would be observed. To this end several aspects of the experimental technique were sharpened.

##### 8.4.4.1 109 nm mirror alignment

The alignment of the 109 nm mirror was improved. A HeNe beam was aligned exactly along the axis defined by the pinhole and target screen of Fig. 8.2. Moving neither the cross-hair target nor the pinhole, this axis was then used to realign the target reels according to the technique described in §8.2.2.2. Once this was done the target reels were set back 175 μm (*i.e.* the target surface was set back 150 μm) from the axis, and the first knife edge aligned with it. Finally the 109 nm mirror was put in place, and its normal was aligned along the target ribbon to within 0.7 mrad.

This means the main error in the alignment of the mirror along the gain region was in the roll alignment of the line plasma on the target. This was good to within ~3 mrad, or 100 μm over the length of the line focus (§8.2.2.1). This accuracy is sufficient to ensure the mirror will have reflected any 109 nm radiation back into the gain region.

##### 8.4.4.2 LiF diffuser

A diffusing LiF screen was placed ~10 mm in front of the entrance slit of the monochromator. This was to ensure that any 109 nm radiation produced did not simply miss the monochromator entrance slit. Although the pinhole and cross-hair alignment technique described in §8.2.2.2 should have been sufficiently precise to prevent this, it relied on Klein Flange vacuum fittings being perfectly perpendicular. Since they were used between massive, independently-supported objects (target chamber and monochromator), and included an easily compressible o-ring, it would be foolish to assume the flange faces were perfectly perpendicular.

The diffusing screen was made by taking a 2 mm thick LiF window and roughening both sides with increasingly fine grades\* of clean and dry abrasive paper. In common with all VUV grade LiF, the material was soft, and very easily scratched in this way. Finally any particles of silicon carbide which had become detached from the abrasive paper were removed with an optical blower spray (100% chlorodifluoromethane).

##### 8.4.4.3 Double knife-edge plasma shadowing

The double knife edge technique described in §8.4.3 was used. The first knife edge was fixed, as described in §8.4.4.1. The second knife edge was mounted so that it could be rotated in and out of the beam, from outside the vacuum. With the blade not impinging on

---

\* The finest grade used was English Abrasives Silicon Carbide paper, 166.



the beam at all, the KrF wavelength signal observed at the exit slit of the monochromator was five times more than when the blade was totally blocking the direct plasma emission. The KrF wavelength was used because the bulk of the signal measured at this wavelength will have been direct scatter of the laser radiation, and this must happen over the picosecond timescale of the pumping radiation. The plasma expansion will be negligible in this time, and this means the arrangement was optimised to shadow emission from the target surface, and not some region in front of it. This might not have been the case had a different wavelength (or visual observation of the plasma) been used to determine the position of the second knife edge.

The reason for this rather modest fivefold improvement is that the knife edge will have blocked direct scatter of KrF radiation from the plasma, but not emission from the plasma once it had expanded into the unshadowed region. Furthermore, even with the second knife edge out of the beam, the first knife edge will still have caused some shadowing of the plasma. Multiple reflections are also a possible cause, although the inner surfaces of the target chamber and beam pipes were blackened to reduce this effect.

The correct position of the knife edge was determined by setting it to its most closed position, and then slowly opening it until the signal observed at the KrF wavelength began to rise sharply. At this point the knife will have been just shadowing the whole direct plasma emission. After all the experiments described here this adjustment was checked, by continuing to rotate the blade, and checking there was an *immediate* sharp rise in the signal observed at the KrF wavelength. Such an immediate rise was found, and so we may be confident the second knife edge was not shadowing the expected 109 nm gain region.

#### 8.4.4.4 *Experimental results: still no 109 nm action*

With these changes made, the resulting experimental arrangement is shown schematically in Fig. 8.8, and a photograph of it is shown in Fig. 8.9.



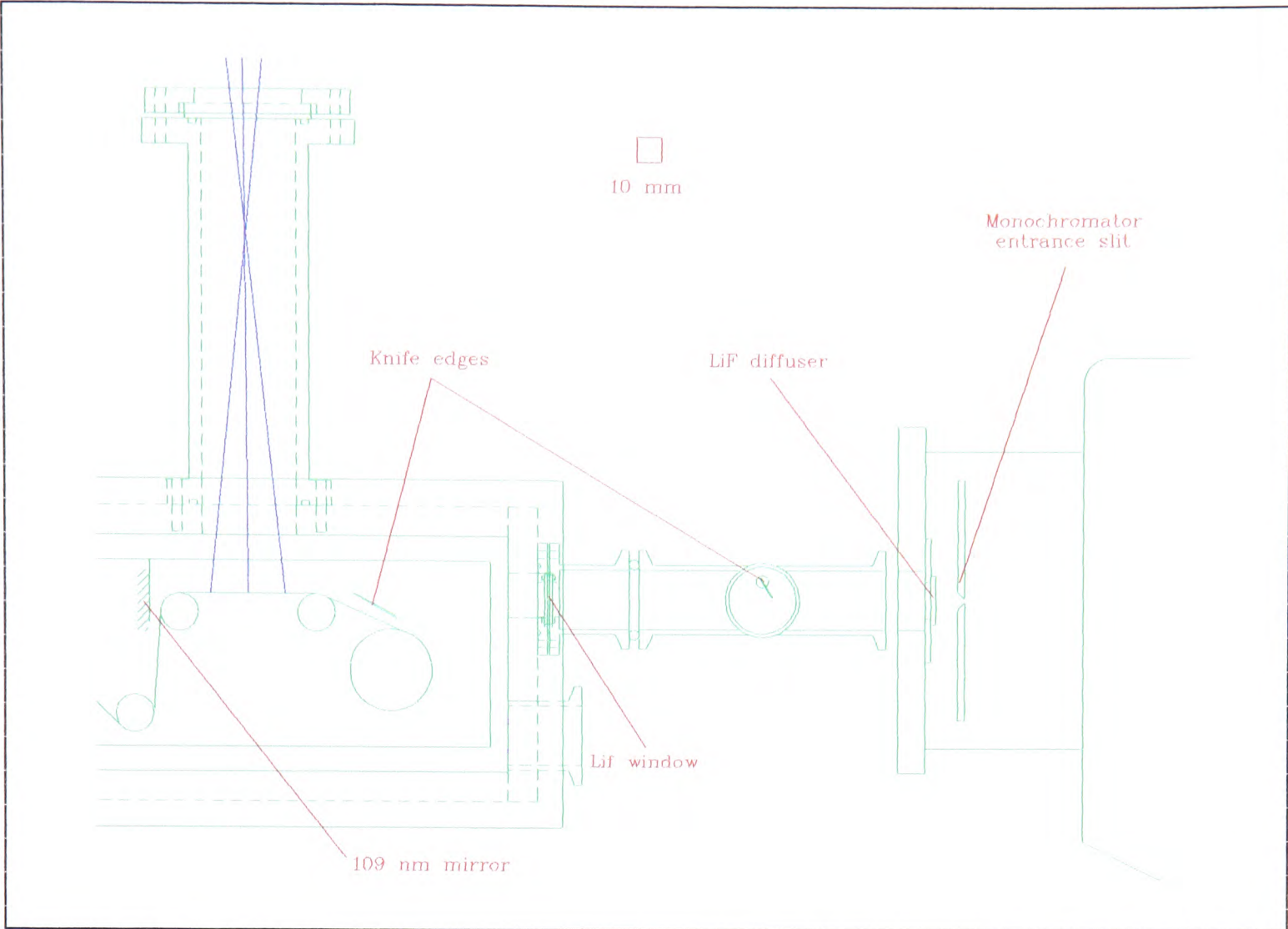


**Figure 8.8.** Schematic of experimental arrangement using plasma shadowing and diffusing screen.

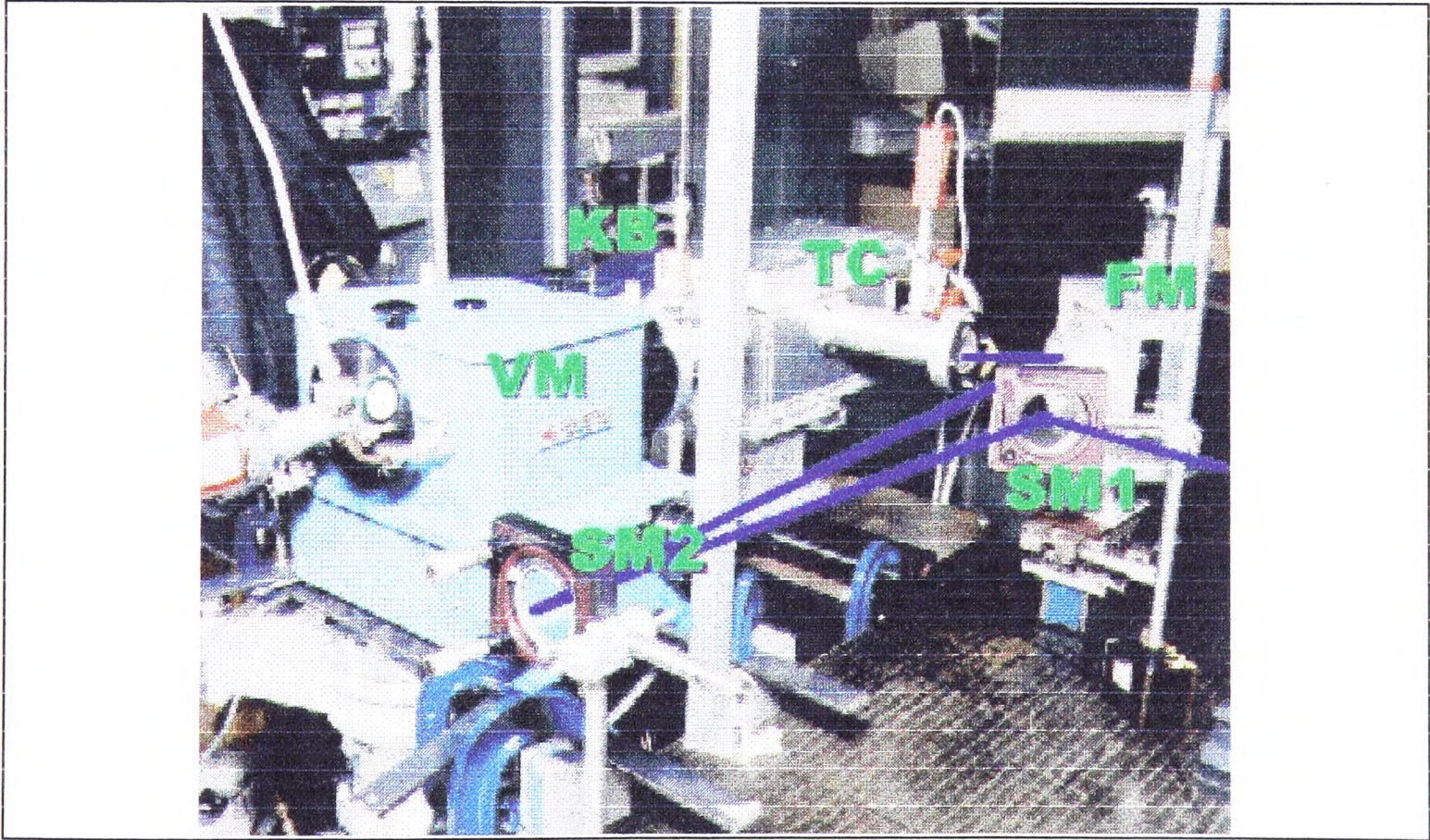


**Figure 8.9.** Experimental apparatus used for 109 nm lasing experiment, with plasma shadowing. Blue line indicates beam path. Abbreviations are: SM1, SM2, steering mirrors; FM, focusing mirror; TC, target chamber; KB, knife blade adjuster; VM, vacuum-ultraviolet monochromator.

These improvements to the detection system were still insufficient to observe laser action. 40 mJ single KrF pulses were used. A fresh piece of target was exposed for each



new gas pressure or focal position tried, even though no systematic decay of signal was observed with the number of pulses fired on to a particular piece of target (for the results reported here). Xenon pressures were tried of 7.3, 14.3, 26, 39.4, and 49 mbar (5.5, 10.9, 22, 29.9, and 37.2 torr respectively). With 26 mbar of xenon the focusing mirror was translated  $\pm 275 \mu\text{m}$  from the optimum focus, determined by the microscope slide technique. In all cases an optical signal was observed (*i.e.* one which disappeared when the KrF laser beam was blocked with all the laser modules still firing). But this signal was identical with the monochromator set to 108.9 nm and 90 nm, and so must be attributed to scatter of longer wavelength radiation.

### 8.4.5 Preheating

A lack of pumping x-rays was suspected as the cause of the lack of 109 nm laser action. The problem may have been that the 7 ps KrF laser pulses were too short to allow efficient plasma emission. Such an effect, in relation to the 109 nm Xe III laser, has been reported by Yamakoshi *et al.* [1996]. They compared the output of an Xe III laser system when 1064 nm laser pulses of duration 300 ps, 32 ps, and 1.4 ps, were used to generate a pumping plasma on a mercury target. For a given pump laser fluence on target, they found that the 109 nm output fell “*precipitously*” (40 fold) when the pump pulse duration was reduced from 300 ps to 32 ps. Since the target fluence was held constant, this drop in output was despite a 9 fold increase in the laser intensity on the target. When the pulse duration was reduced further, to 1.4 ps, no lasing action was obtained from their Xe III system.

All was not lost, however, because Yamakoshi *et al.* [1996] found they could surpass the performance obtained with 300 ps pumping, using 32 ps pump pulses, provided they applied a 300 ps duration laser prepulse to the mercury target. Applying prepulses to their shortest (1.2 ps) pumping pulses allowed them to observe 109 nm lasing, although it was typically of 2 to 10 times lower energy than was achieved from prepulsed 32 ps pumping, for a comparable fluence on target.

Yamakoshi *et al.* [1996] did not vary the prepulse delay (1.3 ns), nor the fraction of the main pulse energy (20%). They chose these parameters because they had been found to be approximately optimal in previous work by Sher & Benerofe [1991]. Sher & Benerofe [1991] had investigated the effect of prepulses on x-ray conversion efficiency and Xe III laser output, for 1064 nm pulses of duration 170 ps, 70 ps, and 20 ps. We concentrate on their data for 20 ps pulses\*, since these are likely to be most relevant to the 7 ps pulses used here.

Sher & Benerofe [1991] used prepulses of 20 ps duration and varied the energy fraction and delay. For x-ray production in the spectral region 120 eV to 285 eV, from a 100  $\mu\text{m}$  circular spot plasma, they found prepulse delays between 1 ns and 2.4 ns (the longest delay their experiment allowed) to give equal, and optimum, yields. The optimum energy for the prepulse was typically 10% of the main pulse energy. The enhancement in x-ray conversion efficiency produced by a prepulse was greatest for low ( $4 \times 10^{11} \text{ W cm}^{-2}$ ) focal intensities, for which it was a factor of 10.

As discussed in §8.1.1, they also pumped a 4.2 cm travelling-wave geometry 109 nm Xe III laser, using 75 mJ, 80 ps pulses, focused to  $1.7 \times 10^{11} \text{ W cm}^{-2}$ . They observed a 26

---

\* The actual duration of these pulses varied between 20 ps and 26 ps.



fold increase in the output energy when prepulses\* were used. This was accompanied by a factor of 2.4 improvement in the soft x-ray (90 eV to 285 eV) yield. The small signal gain of their laser system was unchanged (at  $1.7 \text{ cm}^{-1}$ ) by the presence of the prepulse. They interpreted this to indicate that the mechanism for the improvement in the 109 nm output was the pumping of a greater volume of xenon, rather than the changing of the spectrum of the emitted radiation.

The generally accepted mechanism for the improvement of plasma conversion efficiencies in the presence of prepulses, is increased inverse bremsstrahlung absorption of the incident radiation in the preformed plasma [Sher & Benerofe 1991, Teubner *et al.* 1992]. Ideally, the prepulse plasma should just have time (before the main pulse arrives) to expand to a size comparable to the skin depth for the laser pumping radiation [Teubner *et al.* 1992]. Since the expansion rate and skin depth are both functions of laser wavelength and intensity, the optimum prepulse arrangement for KrF laser pumping of the Xe III laser system must be found experimentally, and several different regimes were investigated.

#### 8.4.5.1 Double pulses

Little time was available for pulse shape sculpting, and so the variations tried were limited to what could be achieved easily with the existing laser system optics. One such modification was to reintroduce the pulse stacker described in §8.1.2, but with all but one of its mirrors obscured. This gave rise to two 7 ps pulses, each of mean energy  $\sim 40 \text{ mJ}$ , and separated by 2 ns. There was considerable shot-to-shot variation, but the first pulse typically contained 80% of the energy of the second pulse.

A xenon pressure of 16 mbar (12.1 torr) was used, and the focusing mirror translated through a distance of  $\pm 1 \text{ mm}$ , from the optimum focus (as determined by the microscope slide technique described in §8.2.2.4) in steps of 200 and 300  $\mu\text{m}$ . A fresh piece of target was used for each exposure. Again, no signal was found with the monochromator set to 108.9 nm which was not also present at 90 nm.

#### 8.4.5.2 Pulse trains

Another modification tested was the use of a whole train of eight pulses from the pulse stacker. This provided pulses of mean energy 11 mJ each, separated by 2 ns, with the first pulse typically having about 50% of the energy of the second. The later pulses are unlikely to have been any use, since any Xe III population inversion should have been destroyed by then.

The same xenon pressure, of 16 mbar (12.1 torr) was used, and again the focusing mirror was translated through a distance of  $\pm 1 \text{ mm}$ , from the optimum focus in steps of 200 and 300  $\mu\text{m}$ . Once again, no signal was found with the monochromator set to 108.9 nm which was not also present at 90 nm.

#### 8.4.5.3 Picosecond prepulse

The final modification tested involved using the KrF laser in single pulse mode. A prepulse was separated from the main pulse, after the final KrF amplification, simply by taking the front and back reflections from a thick, unwedged, mirror. The front surface was uncoated

---

\* Compared to the main pulses, these prepulses were of the same duration, carried 20% of the energy, were focused into an area twice as wide, and arrived 1.6 ns earlier.



(~5% reflectivity at  $45^\circ$ ), while the back surface had a high-reflectivity coating on it. A normal incidence mirror would have been ideal, but none could be found in the few hours which remained for the experiment. Instead a  $45^\circ$  system was used, with the optic in the place of the  $45^\circ$  mirror illustrated in Fig. 8.1. A HeNe alignment laser was used to ensure the reflection from the back surface of the optic was in the same direction as that from the  $45^\circ$  high reflector had been, to within  $0.4 \text{ mrad}^*$ . The arrangement is illustrated schematically in Fig. 8.10.

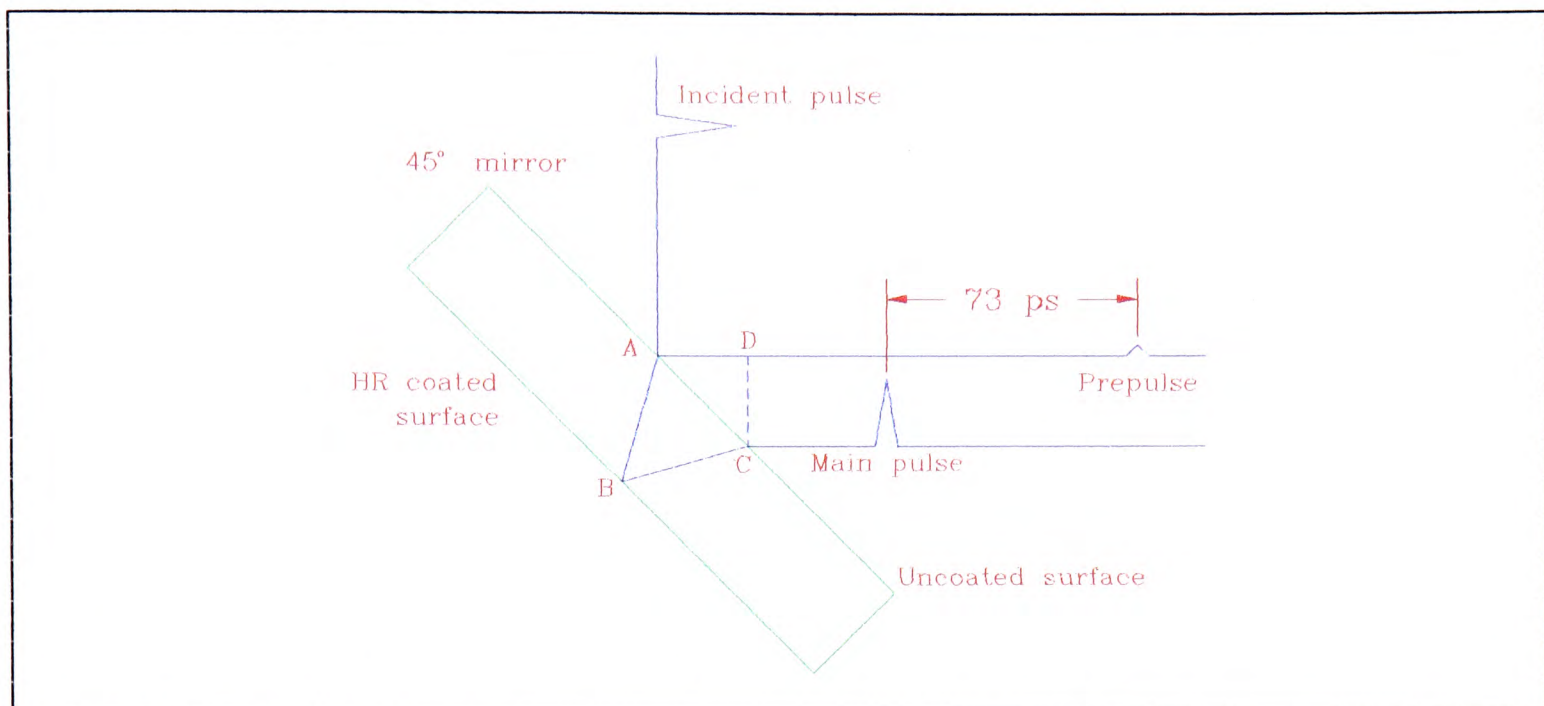


**Figure 8.10.** Schematic of arrangement used to achieve prepulses 73 ps before main pulse.

The delay (73 ps) introduced is found from the difference in optical path lengths ABC and AD of Fig. 8.10. The 11 mm lateral translation of the main beam introduced by the arrangement, will have had two effects. Firstly, it will have reduced, by 11 mm, the length of the line focus over which the main pulse and prepulse overlapped. Thus, there will only have been overlap of the two beams over the 19 mm of the line focus nearest to the 109 nm mirror<sup>†</sup>. Secondly, it will have moved the focus of the prepulse  $310 \mu\text{m}$  away from the focusing mirror<sup>‡</sup>. Since this is still well within the 1.2 mm depth of focus, this was not considered a problem.

With 16.5 mbar (12.9 torr) of xenon in the target chamber, the focal position was varied  $\pm 1.1 \text{ mm}$  in steps of 200 and  $300 \mu\text{m}$  from the optimum focus of the main pulse. Then, with the focusing mirror set to put the line foci of the prepulse and main pulse on opposite sides of the target ribbon, xenon pressures of 7.3, 17, and 26 mbar (5.5, 12.9 ,

\* This is important, since an error in this direction would give rise to a shift in the distance of the line focus from the focusing mirror. This  $0.4 \text{ mrad}$  accuracy limits such a shift to  $120 \mu\text{m}$ , significantly less than the 1.2 mm depth of focus.

† Furthermore, vignetting of the prepulse beam by the mount of the  $45^\circ$  mirror as the beam passed on its way to the focusing mirror meant the 11 mm of prepulse beam which did not overlap the main beam did not enter the target chamber.

‡ To see why: consider that it displaces the virtual focus of the prepulse beam 11 mm towards the focusing mirror. The centre of curvature of the mirror is clearly unmoved by the change. The line focus is on the line joining the centre of curvature of the mirror to the geometrical focus of the KrF beam, and this produces a “lever effect” on the position of the line focus, so that the shift is both smaller than and in the opposite direction to the 11 mm shift.



and 22.0 torr) were tried. In all cases no signal could be observed with the monochromator set to 109 nm which could not also be observed with it set to 90 nm.

## 8.5 Discussion

In summary then, neither SXR nor 109 nm lasing were observed. We shall consider the sensitivity of the experiments conducted, determined from the size of the noise signals observed. From these we shall find upper limits on the SXR and 109 nm conversion efficiencies.

### 8.5.1 Vacuum quality

Both SXR and 109 nm detection require the partial pressure of air in the system to be less than about 0.1 mbar. This ensures better than 80% transmission over the 150 mm path length to the detector/window, for SXR detection, and better than 90% transmission at the 109 nm Xe III laser wavelength.

During the SXR detection experiments, pressures between  $10^{-3}$  mbar and  $10^{-1}$  mbar were achieved, with the pumping (by a rotary pump) applied continuously during the experiments.

For the 109 nm detection experiments, the target chamber had to be filled with gas and then sealed. Measurement of the leak rate when the chamber was evacuated and sealed indicated that about two hours were available in which to make measurements (*i.e.* before the pressure rose to 0.1 mbar). All the experiments reported here were taken within this time.

One further precaution was taken for the Xe III experiments; the chamber was flushed with a few millibar of xenon before readings were taken. This was pumped out before the main gas fill was made. This was to remove any contamination due to backstreaming of rotary pump oil, and to ensure that xenon was the predominant gas leaking from any trapped volumes in the vacuum system.

We may conclude that contamination of the vacuum and gas systems was not responsible for the lack of SXRs and laser action.

### 8.5.2 Upper limit on SXR conversion efficiency

We may estimate an upper limit on the x-ray conversion efficiency observed (in the absence of a prepulse). We make the following assumptions:

- We assume a cosine distribution of radiation emitted into  $2\pi$  sr. This corresponds to an emitter with area with area but no thickness. Allowing for this and the solid angle of detection, we estimate that a fraction  $1.7 \times 10^{-6}$  of the radiation emitted by the plasma reaches the aluminium filter. We assume 8% transmission for the filter, over the entire range of detection.
- We estimate a mean quantum efficiency of 2 of the sodium salicylate scintillator for the 18 eV to 71 eV spectral region transmitted by the Al filter [Husk *et al.* 1992].
- In considering how much of the fluorescence of the sodium salicylate escapes the microscope slide on which it was deposited, and then reaches the PMT, we apply the model described in §9.3.1.1 to the geometry used here. For simplicity we neglect the reflection at the filter of fluorescence from the scintillator. This indicates that 0.3% of the fluorescence reaches the PMT.



- The manufacturer's data indicates the PMT has a photocathode quantum efficiency of 20% for the 410 nm fluorescence from the scintillator, and that the PMT gave a gain\* of  $10^5$  for the 300 V potential applied.
- Due to serious shot-to-shot variations observed in the signal, we assume a signal-to-noise ratio of unity would be the minimum required to detect an SXR signal.

These assumptions indicate that no more than 4400 photons were incident on the PMT photocathode, corresponding to  $9 \times 10^6$  photons incident on the filter. This suggests no more than  $5 \times 10^{12}$  of 18 eV to 71 eV photons were emitted in total. Taking a mean energy of 50 eV, this corresponds to 40  $\mu$ J. This sets an upper limit of 0.1% on the conversion efficiency of KrF radiation into the 18 eV to 71 eV energy range.

For comparison, a 25 eV blackbody emits 34% of its energy into this spectral region. Thus, if we assume 25 eV blackbody plasma emission spectrum, the total conversion efficiency (KrF  $\rightarrow$  all photon energies) of the plasma is only 0.3%. This is very poor for a LGP. For example a 33% total conversion efficiency was deduced for 5 ns XeCl laser pulses in §2.3.9.

There are significant uncertainties in the calculation, notably in the angular distribution of the emission (which is very relevant for the glancing angle of detection), and the PMT gain. Even so, it seems very unlikely that the plasma was emitting efficiently in the SXR region needed to pump the Xe III laser. Unfortunately there was not time to look for SXR emission from the prepulsed plasmas, and these may have been significantly more efficient.

### 8.5.3 LiF windows

We shall also estimate the maximum 109 nm emission which could have been present. The transmission of the LiF window and diffusing screen are the vital to this calculation. Great care must be taken in the use of LiF, since it is hygroscopic, and its transmission at wavelengths shorter than 160 nm falls on exposure to moisture in the laboratory air [Patterson & Vaughan 1963]. Care was taken to minimise the exposure to the laboratory air of the LiF windows, and they were stored in a dessicator when not in use.

The 2 mm LiF window used for the second set of 109 nm experiments (*i.e.* the one used with the LiF diffuser and plasma shadowing) had been used for other experiments†, and there had been concern after these that its transmittance at 109 nm was poor. For this reason its transmittance had been measured (before any of the experiments described in this chapter were undertaken). This measurement was made using the laser plasma VUV source described in chapter 9. The window was placed between the exit slit of the VUV monochromator and the scintillator used to detect VUV emission. By comparing the spectrum obtained in this way, with the spectrum obtained in the absence of the LiF window, its (relative‡) transmittance spectrum could be deduced. The spectrum showed a

---

\* See §9.3.1.6 for a definition of PMT gain and photocathode quantum efficiency.

† It was used in looking for 109 nm fluorescence from Xe excited by a SXR from a spot plasma, produced with the nanosecond KrF laser. These experiments are described in §7.5ff.

‡ An extra aperture was introduced in front of the window to prevent leakage of light around the edges of the window. This means that the absolute transmittance could not be deduced without making guesses about the effect this had on the detection geometry. However, the reduction in throughput at 200 nm appeared approximately commensurate with the size of the aperture.



sharp transmission cut-off at 105 nm, as expected, and also indicated that the transmission at 109 nm was ~50% of that 200 nm. This is in agreement, within the experimental errors, with the transmittance spectrum for an almost identical (2.09 mm) thickness of LiF, reported by Heath & Sacher [1966]. For this reason the window was assumed to be as transmitting as it is currently possible to make 2 mm of LiF at 109 nm (30%-40%), and was used for the 109 nm pumping experiments.

The sharp reader will have spotted the flaw in this experiment, as did Johnson *et al.* [1951]. The problem is that if there is any (109 nm-excited) fluorescence in the LiF (or on a surface layer), this will appear as spurious transmittance when the window is placed at the *exit* slit of a monochromator, provided the detector used is also sensitive to the fluorescence.

In order to investigate the problem the transmission of the LiF window (and diffuser) was measured, with the window placed before the *entrance* slit of a monochromator. A deuterium lamp with an MgF<sub>2</sub> window was used as the light source\*. Care was taken to repeat spectra to ensure there was no change in the intensities recorded, possibly owing to the lamp warming up. The transmissions measured here are accurate to better than 10% of the value reported (except where stated).

The transmission cut-off of MgF<sub>2</sub> limited the shortest wavelength at which the spectrum could be taken to 114 nm. Nevertheless, the results obtained were illuminating, and are shown in Fig. 8.11.

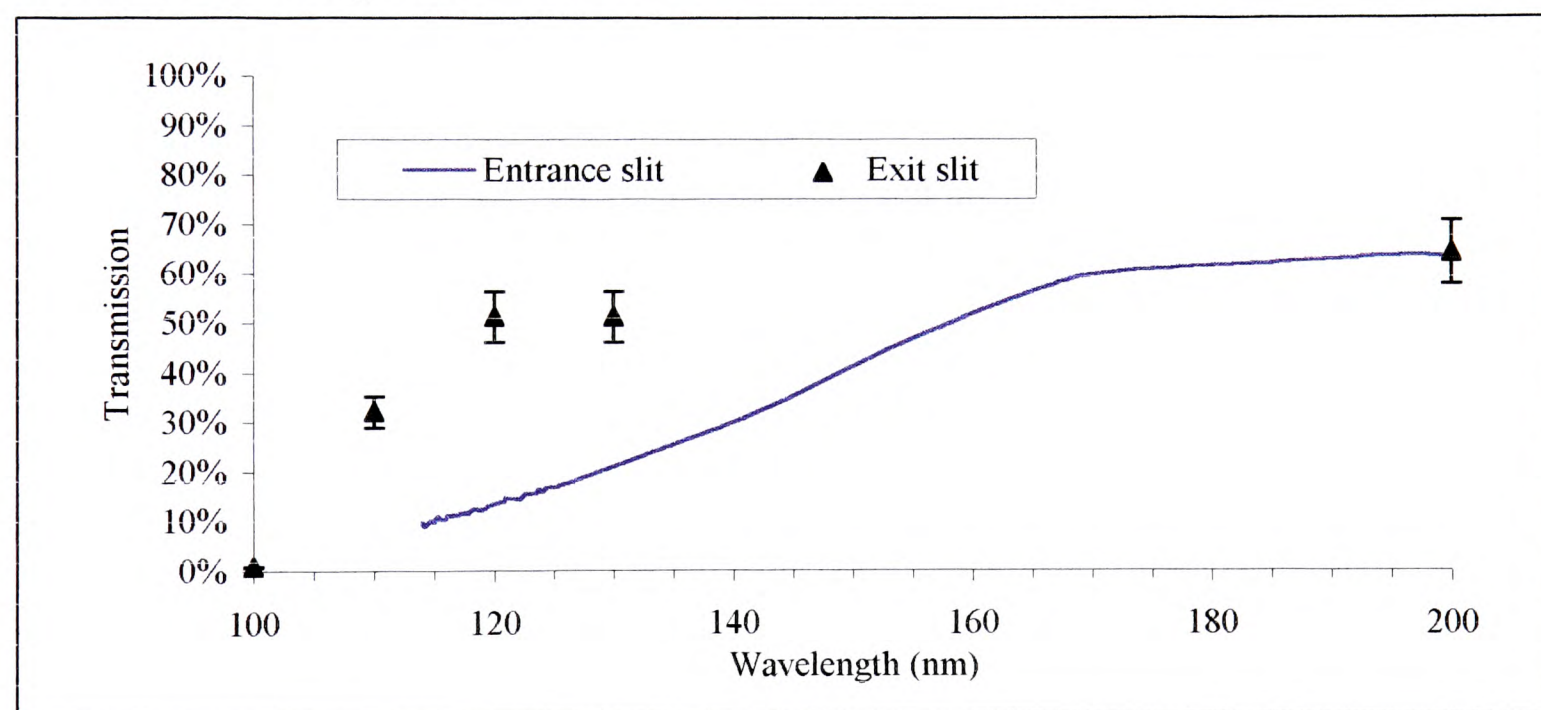


**Figure 8.11.** Apparent transmission of 2 mm LiF window according to whether measured at monochromator entrance or exit slit.

From Fig. 8.11 it is clear the LiF window had considerably less transmittance at 109 nm than had been thought. The reason for this could either be bulk fluorescence, or the deposition of a layer of oil† on the window, probably exacerbated by the presence of

\* The very sharp reader will have spotted that there may also be a flaw in this experiment, since a broadband source could give fluorescence at the wavelength at which the transmission was being measured. Since we are interested in the short-wavelength behaviour of the LiF this is unlikely to cause a problem. For the best measurements of transmission two monochromators are needed.

† This could have been either rotary pump oil, or lubrication oil from the stepper motor used to wind the target.



UV emission from the plasma. We can distinguish between the two possibilities by considering the transmittance of a fresh LiF window. This was measured, and is illustrated in Fig. 8.12, which also shows the transmission of a 2.09 mm LiF window reported by Heath & Sacher [1966].

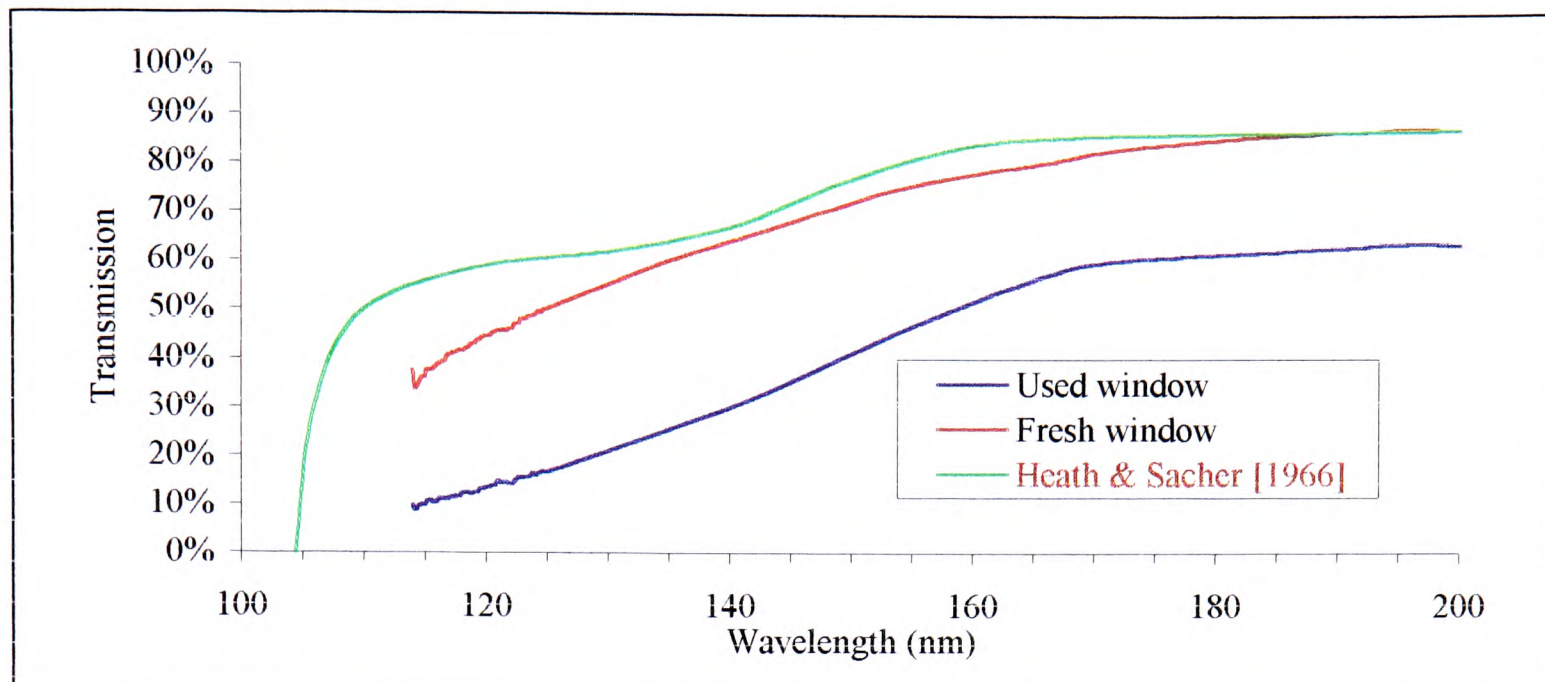


**Figure 8.12.** Transmission of various LiF windows. Transmittance of used window and fresh window were both measured at entrance slit of monochromator. Data due to Heath & Sacher [1966] relate to 2.09 mm LiF window, measured at exit slit of monochromator, and appear (from inspection of the data reported) to have a random error of ~5% of the value plotted above.

From Fig. 8.12 it is clear that the transmission of the LiF window used was several times less than that of a fresh window, suggesting contamination of the window. Although the fresh sample investigated here may be of a different purity to that investigated by Heath & Sacher [1966], it is interesting to note that they report a higher transmittance at short wavelengths than was observed here. This suggests that they also may have incorrectly interpreted fluorescence as transmittance\*.

In order to estimate the sensitivity of the 109 nm detection system, we must also know the transmittance of the diffusing screen. The measurement is complicated by any wavelength-dependent effects in the diffusivity. The spectrum of the light reaching the exit slit of the monochromator was measured both with and without the diffuser in front of the entrance slit. The ratio of these measurements gave an “apparent transmission spectrum”. For these measurements the diffuser was placed 95 mm from the entrance slit (which was 100  $\mu\text{m}$  wide).

For want of a better alternative we shall make the following assumptions:

- The diffusivity of the screen is independent of wavelength. The diffusivity was estimated by observing a red HeNe beam transmitted by the sample. This was diffused approximately evenly into a cone of full angle  $30^\circ$ .

\* Indeed, this is a recurring problem in reports of LiF transmittance. For example Patterson & Vaughan [1963] report transmission of 70% at 109 nm, and do not indicate whether the window (of a thickness which they only describe as between 1.25 mm and 2.0 mm) was at the entrance or exit of their monochromator. Laufer *et al.* [1965] have also reported LiF transmittance, measured at the exit slit of a monochromator, but they comment that their sample “was sufficiently far from the detector to preclude fluorescence”, although they give no details to justify this.



- The bulk transmittance of the diffuser at 200 nm is the same as that measured for the fresh sample. This allows us to scale the “apparent transmittance spectrum”, and the result obtained in this way is shown in Fig. 8.13.

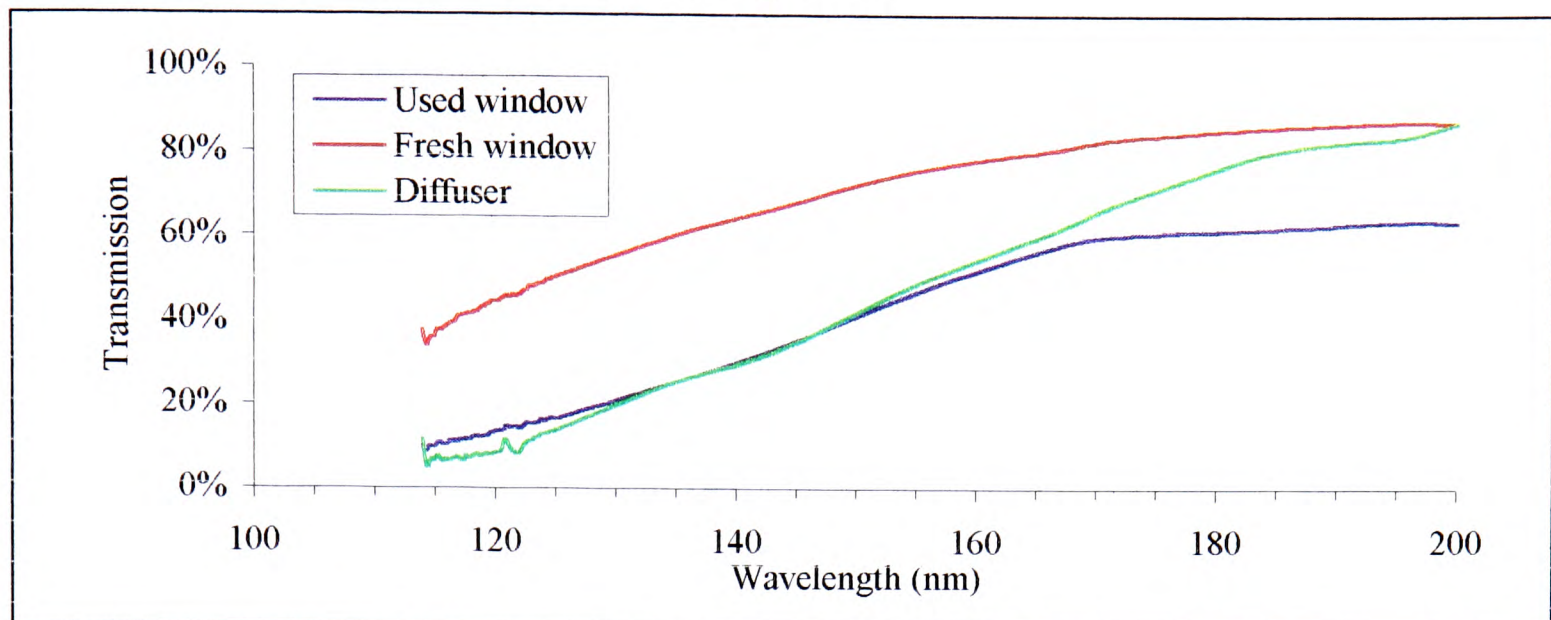


**Figure 8.13.** Scaled transmittance of LiF diffuser. Used window and fresh window transmittances are also shown, for comparison. Small signal levels obtained in the measurement of the transmission of the diffuser mean that the error for these measurements is up to ~20% of the values reported.

The result is not altogether satisfactory - the roughening of both surfaces of the diffuser should have removed any surface contamination, yet the scaled transmittance falls well below that of the fresh window at short wavelengths. This suggests the presence of either bulk contamination, surface contamination during the roughening process, or stronger diffusivity at shorter wavelengths. It is fiendishly complicated to distinguish between these options, and so we shall not attempt it. Instead we shall note that the calculation of the effect of the diffusing screen may introduce an order of magnitude error into the calculation of the sensitivity of the 109 nm detection.

#### 8.5.4 Upper limit on laser pulse energy

We are now in a position to estimate an upper limit on the energy of any 109 nm radiation obtained during this experiment. We extrapolate the data of Figs. 8.11 and 8.13, to estimate a 5% bulk transmittance for both the diffuser and the LiF window. Geometrical calculations indicate that the beam spreading due to the diffuser reduces the intensity of light reaching the exit slit by factors of ~20 in each of the horizontal and vertical directions. We also assume 40% reflection efficiency of the VUV monochromator (manufacturer's data). The results obtained in this way are summarised in table 8.2.

Also included in table 8.2 are equivalent estimates for the first attempt to find 109 nm emission, as described in §8.4.2. Slightly different assumptions were required for this calculation. These were 30% transmission of the LiF window\*, and the 250  $\mu\text{m}$  monochromator entrance slit seeing 14% of the beam energy. This assumption is based on

---

\* The window used for this experiment was subsequently turned into the diffuser for the following experiment. The window was fresh at the start of the experiments described at the beginning of this chapter. There is a possibility of some contamination due to oil-film deposition, but it is not expected to be nearly as severe as that suspected for the window used for the following experiment (which had been exposed to more VUV in a dirtier vacuum before it was used).



a 200  $\mu\text{m}$  diameter beam, spreading by a factor of nine due to divergence before reaching the monochromator entrance slit. The factor of nine comes from the entrance slit being a distance from the gain region equal to nine times its length.

Form of pumping	Individual pulse energy (mJ)	Number of photons at exit slit	Upper limit on 109 nm laser energy (pJ)	KrF→Xe III conversion efficiency upper limit
<i>Plasma shadowing &amp; diffuser present</i>				
Single pulse	40	170	150	$4 \times 10^{-9}$
2 pulses	40	270	240	$10^{-8}$
8 pulses	11	480	410	$4 \times 10^{-8}$
73 ps prepulse	38	100	90	$2 \times 10^{-9}$
<i>No plasma shadowing or diffuser - single LiF window</i>				
Single pulse	40	$9 \times 10^4$	8	$2 \times 10^{-10}$
8 pulses	13	$1.3 \times 10^5$	12	$10^{-9}$

**Table 8.2.** Upper limits on 109 nm laser energy and overall conversion efficiencies. For multiple-pulse laser shots, conversion efficiency is based on energy in a single pulse, rather than a single laser shot.

From table 8.2 it is clear that the first experiment was actually more sensitive than the second, since it gave rise to lower values of the upper limits for the conversion efficiency. The reasons for this are the low transmission of the LiF window, and the fact that the diffuser scatters ‘noise’ light into the monochromator entrance slit.

Efficiencies for the 109 nm Xe III laser (when saturated) have been reported by several authors [Sher *et al.* 1987, Sher *et al.* 1991, Clement *et al.* 1994, Kubodera *et al.* 1995, Dennis *et al.* 1995] and vary between  $10^{-7}$  [Yamakoshi *et al.* 1993] and  $6 \times 10^{-6}$  [Sher *et al.* 1987]. This means we may also conclude from table 8.2 that the 109 nm detection experiments were sufficiently sensitive to have detected 109 nm lasing if it were saturated or near-saturated.

### 8.5.5 Conclusions

The upper limits on SXR and 109 nm conversion efficiencies found in §8.5.2 and §8.5.4, allow us to draw the following conclusions:

- With single pulse pumping the x-ray conversion efficiency was extremely poor - at least two orders of magnitude worse than might be expected with efficient excitation. The intensity on target was  $6.7 \times 10^{11} \text{ W cm}^{-2}$ , which has been found by others (see table 2.1 for references) to be easily sufficient to generate the required SXRs, when longer duration pump pulses have been used. This suggests that the lack of prepulsing may have been responsible for the low conversion efficiency observed.
- It is not possible to deduce from the 109 nm data whether prepulsing had any effect on the soft x-ray conversion efficiency. It is possible to deduce, however, that any effect it did have, was not sufficient to make the system operate efficiently (*i.e.* to saturate the 109 nm emission).
- It is possible that there was some (unsaturated) gain at 109 nm, and that the experiments which were used to detect it were not sensitive enough to find it. For example, the 109 nm detection sensitivity of the 2 pulse pumping experiment was 0.24 nJ. Several authors have reported gain on the 109 nm transition with comparable



output energies [Sher *et al.* 1987, Sher *et al.* 1991, Clement *et al.* 1994, Dennis *et al.* 1995]. However, in each of these cases this has been at the limit of their detection sensitivity.

In summary then we have two clear negative results: the x-ray conversion efficiency is low in the absence of a prepulse, and the presence of all of the prepulsing regimes attempted here was insufficient to allow anything approaching saturated pumping of the Xe III laser.

### 8.5.6 Suggestions for further work

Further work on picosecond KrF pumping of the Xe III 109 nm laser system should start with a study of the effect of prepulsing on the plasma conversion efficiency. The regimes tested here did not allow sufficient variation of the prepulse energy splitting ratio, nor the time delay. For the 2 pulse and 8 pulse experiments, the first pulse will almost certainly have contained too much energy for efficient prepulsing, and may well have been harmful to the 109 nm lasing, by producing a high electron density in the xenon, before the second pulse arrived to give SXR and so pump the Xe III laser. This conclusion is supported by the experimental results of Sher & Benerofe [1991], who found that *“it was possible to increase the prepulse energy so much that the 109-nm output of the main pulse was actually reduced”*.

For the 73 ps prepulse experiment the splitting ratio will have been much closer to optimal, but the delay may not have been optimal (not to mention the problem that only two thirds of the length of the plasma was prepulsed).

The glancing angle of observation used for the SXR experiments described here both reduces their sensitivity, and makes them very sensitive to the angular distribution of the emission. Further studies should be made much nearer normal observation, using a buffer gas to eliminate debris if necessary. Once an SXR signal is found it can be optimised, and then the system used to pump the Xe III laser, whether in the travelling wave geometry or the normal incidence geometry used here.

The sensitivity of detection of 109 nm radiation could be improved upon in several ways - apart from the obvious expedient of not using a fluorescent LiF window! The diffusing screen should be eliminated, but the plasma shadowing retained. Use of photographic film at the exit aperture of the monochromator would also enhance the sensitivity, by simultaneously averaging out the shot-to-shot variation for the 109 nm laser wavelength and background plasma emission.

Only time-integrated measurements were made here, and the use of time-resolved measurements of the monochromator output might also enhance the sensitivity. This would be by allowing discrimination against long-timescale direct plasma emission. This is particularly relevant where plasma shadowing is present, because in this case the direct plasma emission does not reach the detector unless the plasma has expanded into the unshadowed region - a process which will take tens of nanoseconds.



## 9. Photons for biologists: a laser-plasma source for the VUV

---

The work described in this chapter was undertaken at the Rutherford Appleton Laboratory, in conjunction with Ric Allott, Nicola Lisi, & Edmond Turcu. The impetus for the investigation of the source came from them. My involvement was in the provision of a calibrated detection system (described in §9.3), and as a collaborator in the experimental design, the execution, and the interpretation of results. This chapter does not detail all the experiments conducted on the source, but concentrates on aspects into which I had a significant input. Results of significant experiments at which I was not present when the data were collected are indicated thus: ★.

### 9.1 Introduction

This chapter describes experiments conducted at the Rutherford Appleton Laboratory, to develop a tunable VUV/XUV\* source for applications. The pumping source was the picosecond KrF laser system described in §8.1.2 (this was also used for the experiments to pump the Xe III laser described in chapter 8). This laser had been developed in order to provide a high repetition rate (up to 100 Hz) laser plasma source of 1 keV photons [Turcu *et al.* 1993]. As such, it is currently the brightest laboratory-sized 1 keV photon source in the world, with a mean power of 1 W delivered to  $2\pi$  steradians [Allott *et al.* 1995].

The idea was to extend its operation into the VUV/XUV, and particularly the wavelength range 200 nm down to 30 nm (6 eV to 41 eV). This was in response to demand from users of the laser facility. For example, photochemists require such sources to allow single-photon ionisation of large organic molecules without the photofragmentation associated with multi-photon ionisation. Another application is in cancer research, for which a source of  $\sim 10$  eV photons is useful to study the repair mechanisms of DNA in cells. Indeed, during the course of the experiments described in this chapter, the source was developed sufficiently to allow it to be used for experiments in both photochemistry and DNA-damage.

It is difficult to make meaningful comparisons between VUV sources, since the criteria on which the source is judged depend upon the application. For example, it may be either the average power or the peak power of a pulsed source which is important; perfectly continuous tunability into a very narrow wavelength region may be essential, or a peaky line-emission spectrum may be acceptable, or desirable.

Synchrotrons are the best established sources of incoherent, but broadly tunable radiation in the VUV (and beyond). Typically, LGP sources of such radiation have a greater peak brightness but lower average brightness than synchrotrons [O'Sullivan *et al.* 1994]. However, the great advantages of a plasma source over a synchrotron are that the former is simpler, smaller, cheaper, and only has modest vacuum requirements.

---

\* Many different definitions of the vacuum ultraviolet (VUV) and extreme ultraviolet (XUV) are found in the literature. In this work the term VUV is used to mean the spectral region from 105 nm to 190 nm, and the term XUV is used for light of wavelength shorter than 105 nm.



Another technology capable of generating tunable VUV radiation is nonlinear frequency conversion. Such schemes can be operated with laser systems of a scale comparable to that of the one used here. Wellegehausen *et al.* [1996] have recently reported a frequency mixing scheme, employing short-pulse, laboratory-scale (200 fs) lasers capable of generating tunable radiation in the spectral region of 30 nm to 85 nm. Of prime interest to the users of such systems is the absolute number of photons which can be delivered to a target. Unfortunately, Wellegehausen *et al.* [1996] have not reported such measurements. One of the main aims of the experiment described in this chapter was to establish absolute photon numbers.

### 9.1.1 Picosecond KrF laser system

The KrF laser system used for this work is exactly the same as that used in the attempts at picosecond pumping of the Xe III 109 nm laser. This is described in §8.1.2. The only difference between the configuration used for the work described in chapter 8 and the configuration used for the work described in this chapter is that for this work the whole pulse stacker was used. This gave rise to two consecutive trains of eight pulses of 10 mJ mean energy, with duration 7 ps, separated by 2 ns.

## 9.2 Investigations of the source

### 9.2.1 Experimental arrangement

The experimental arrangement used is shown in Fig. 9.1. An aspheric lens of focal-length 95 mm was used to focus the KrF beam on to a target ribbon. This ribbon was wound on between laser shots. As indicated in Fig. 9.1, the lens was mounted to form a vacuum seal. A plasma was formed at the focus, and emission from it was observed normal to the target, and at 45° to the incident KrF laser radiation.

An Acton Research Corporation model VM 502 f/4.5 VUV monochromator was used to determine the wavelength spectrum of the emission, as well as to provide light of the required central wavelength and bandwidth for applications. The monochromator grating was blazed for use in first order, and no investigation of the influence of higher diffraction orders was made. If any higher orders were present they will have caused an overestimate of the output at long wavelengths.

Two detection systems were used, a scintillator and photomultiplier (as shown in Fig. 9.1), and a calibrated photodiode. These are described in §9.3ff. Unless otherwise indicated, all data given here are based on the former system.



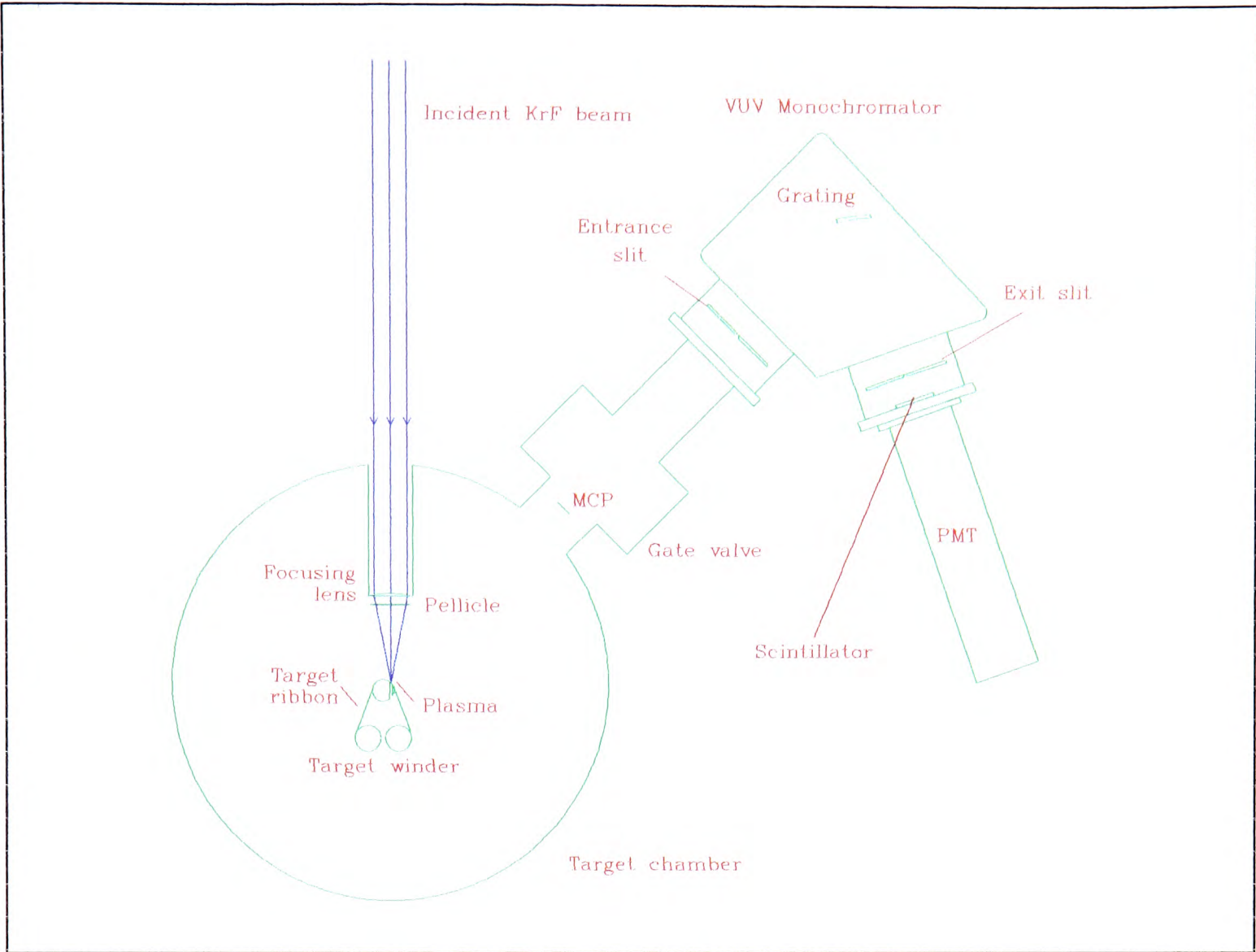


**Figure 9.1.** Schematic of experimental arrangement for LGP VUV source. Gas and electrical feed-throughs, and observation windows have been omitted for clarity. Microchannel plate (MCP) was not installed for the first experiments described here.

A photograph of the experimental arrangement is given in Fig. 9.2.

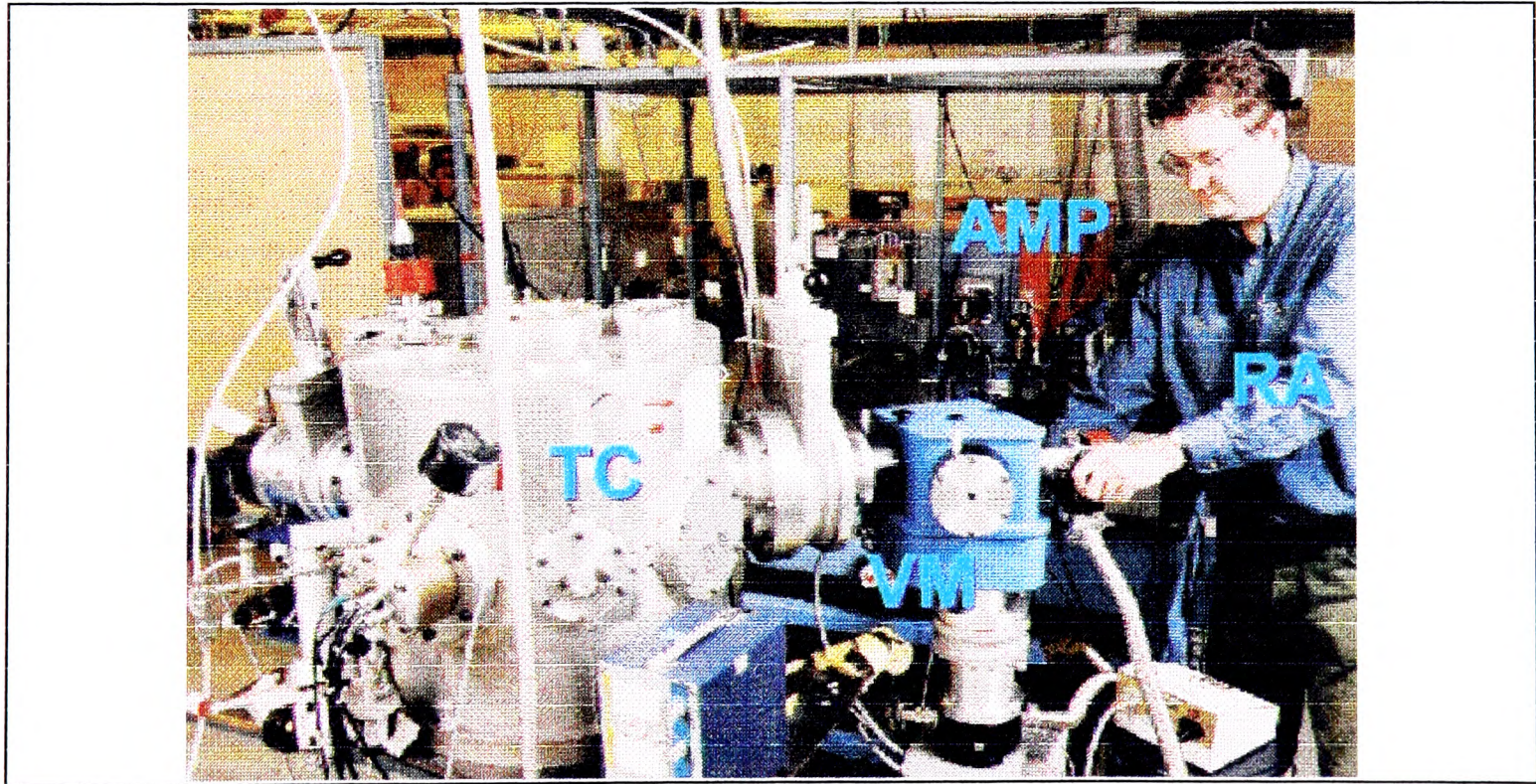


**Figure 9.2.** Laser-plasma VUV source. Labels are: AMP, final KrF amplifier; RA, Dr. Ric. Allott (co-investigator); TC, target chamber; VM, vacuum-ultraviolet monochromator. Arrangement is as illustrated in Fig. 9.1, except that the PMT is not fitted.



### 9.2.1.1 Pellicle

A 450  $\mu\text{m}$  fused silica pellicle (Hoya plate) was placed in front of the lens to protect it from debris from the plasma. Careful thought was given to the positioning of this pellicle: it was mounted sufficiently near ( $\sim 5\text{ mm}$ ) to the lens to ensure that the portion of the beam reflected in it was not brought to a focus within the lens, which would have damaged it. It was also tilted to prevent back-reflections into the laser system.

The pellicle will have introduced spherical aberration to the beam, and so smeared the smallest focal spot size which could be obtained. According to the analysis given in §6.5 the geometrical aberration so introduced should be negligible compared to the divergence. This was investigated empirically by measuring the x-ray emission of the laser plasma with a copper target, both with and without the pellicle in place. The emission was measured with an x-ray diode, placed in the target chamber, equipped with a 10  $\mu\text{m}$  Be filter, making it sensitive to  $\sim 0.9\text{--}1.3\text{ keV}$  photons. For convenience (since it did not require the production of a high quality vacuum), the experiments were conducted in atmospheric pressure He, which transmits 80-90% of these photons over the  $\sim 200\text{ mm}$  path length to the detector used [Thomas 1989].

In each case, the target was moved perpendicular to the lens until the maximum x-ray signal was obtained. The x-ray signal was found to fall  $(24 \pm 11)\%$  in the presence of the pellicle. This is not significantly different from the expected 8% energy loss due to Fresnel reflections at the pellicle surfaces. Since introduction of the pellicle does not smear the focus enough to reduce significantly the plasma emission efficiency for  $0.9\text{--}1.3\text{ keV}$  photons, it should have a negligible effect for VUV photons. This assertion is confirmed in §9.2.5.

A coating of debris was just visible on the pellicle after a few thousand shots had been fired. After about 20 000 shots had been fired on to a copper target, the pellicle was coated with a highly reflective film (estimated by eye as 10% transmitting). In all cases the coating could be removed, and the previous performance obtained from the system, by cleaning the pellicle with a mildly abrasive suspension of tin oxide in methanol.

### 9.2.1.2 Vacuum quality

Separate turbomolecular pumps were used to evacuate the monochromator and target chamber, which could be isolated both optically and physically by means of a gate valve. The residual air pressures (measured by a Penning ionisation gauge) in the target chamber did not exceed  $1.3 \times 10^{-3}\text{ mbar}$  for most of the experiments presented here. This gives a maximum absorption due to air of 5% over the 520 mm path length from the plasma to the entrance slit of the monochromator, over the wavelength range 30 nm to 250 nm [Calvert & Pitts 1966, Thomas 1989]. It will be indicated where higher residual air pressures were present.

In the monochromator the residual air pressure did not exceed  $7 \times 10^{-5}\text{ mbar}$ ; a pressure sufficiently low to prevent damage to the reflective coating of the grating by the deposition of ions or radicals formed by photolysis of oxygen or nitrogen. This differential pumping arrangement was made possible by the constriction of gas flow at the entrance slit of the monochromator.



### 9.2.2 Possible harmonic generation

A spectrum was taken of the radiation obtainable from a copper target. The entrance and exit slits of the monochromator were both opened to 1 mm, corresponding to 4 nm passband (varying no more than  $\pm 5\%$  over the range of wavelengths for which data are given here). The spectrum of the plasma emission obtained is shown in Fig. 9.3.

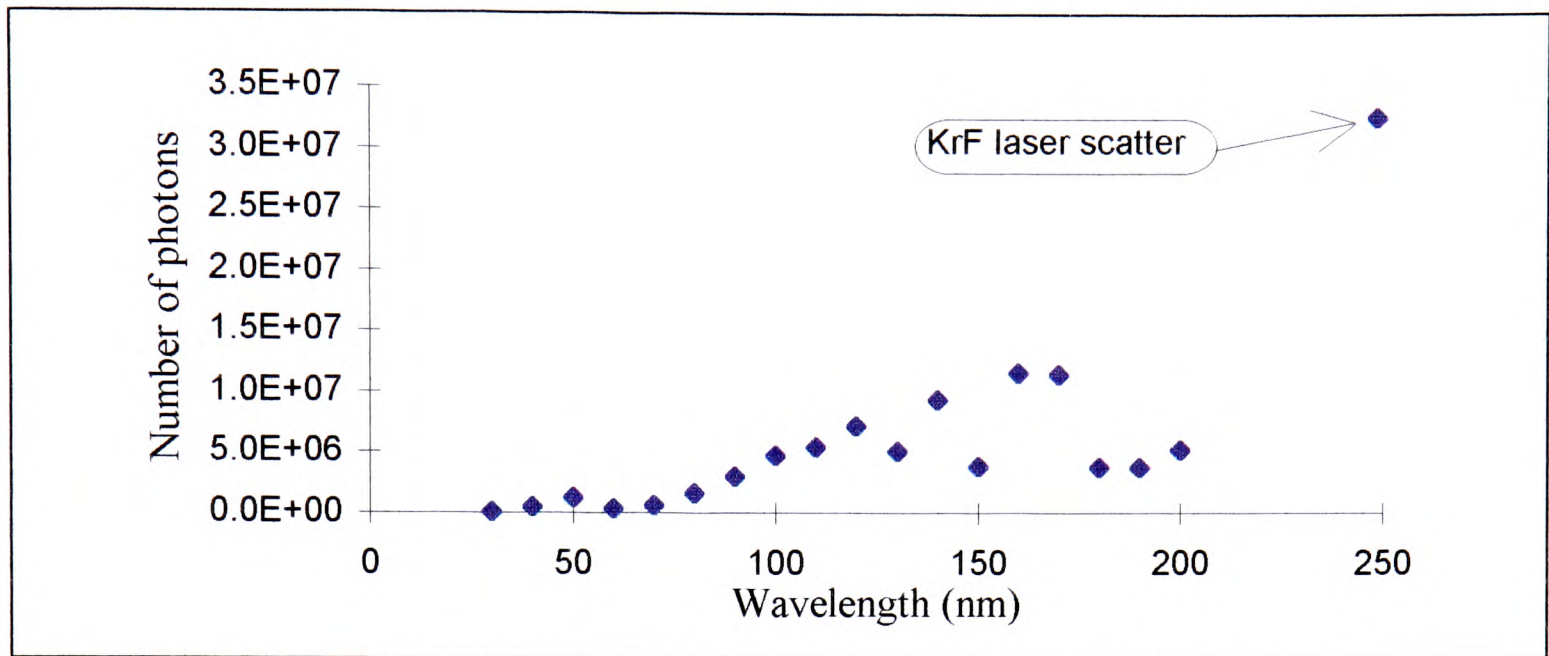


**Figure 9.3.** Mean number of photons arriving at monochromator exit slit, in 4 nm bandwidth. See text for further details of experimental conditions.

The peak observed at 50 nm was immediately interesting, since this corresponds to the 49.7 nm wavelength of the fifth harmonic of KrF laser radiation. Odd and even harmonics may be generated by laser plasmas [Norreys *et al.* 1996], and the possibility of this was investigated by looking at the spectrum around the wavelengths of the 5<sup>th</sup>, 6<sup>th</sup>, and 7<sup>th</sup> harmonics. For this the monochromator entrance and exit slits were closed down to 250  $\mu\text{m}$ , corresponding to a 1 nm passband. The results of this investigation are shown in Fig. 9.4.

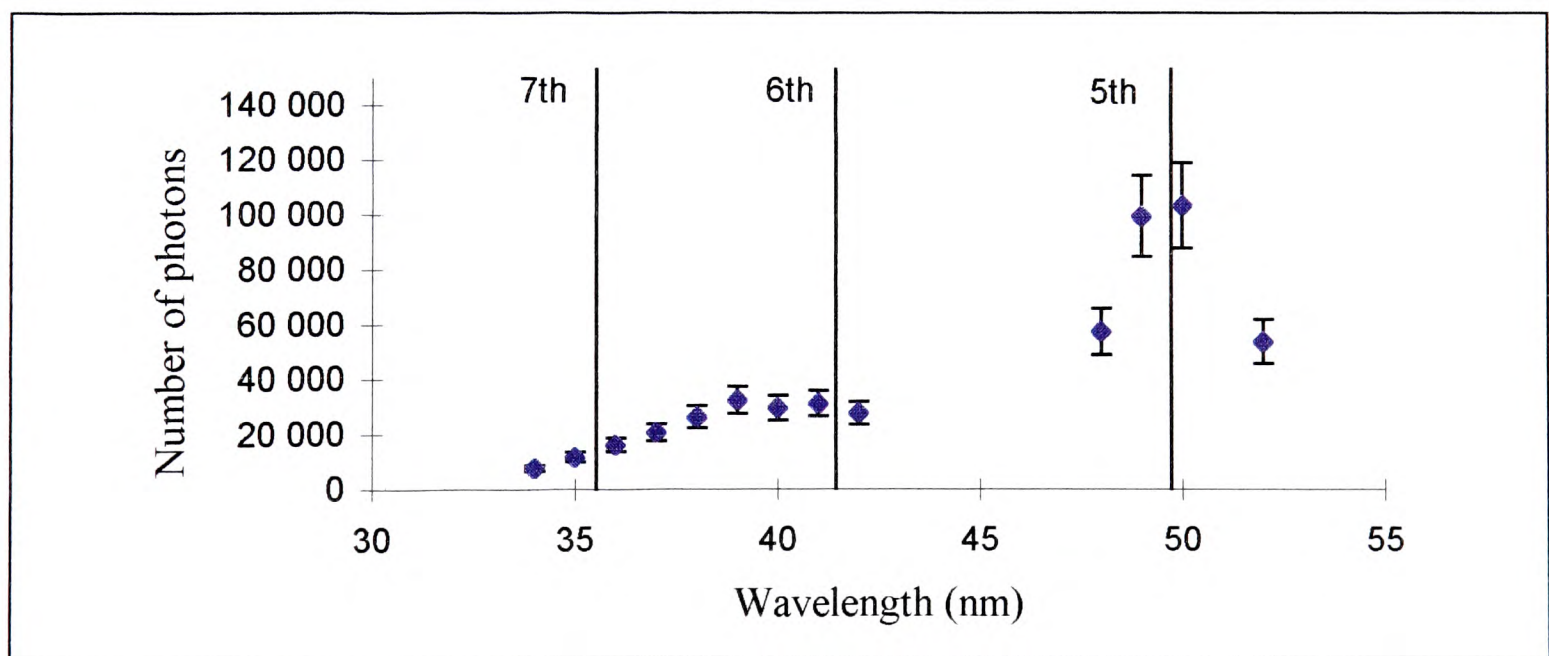


**Figure 9.4.** Detailed spectrum around 5<sup>th</sup>, 6<sup>th</sup>, and 7<sup>th</sup> harmonics of KrF laser radiation. Vertical lines indicate wavelengths of these harmonics. Data was taken at wavelengths separated by 1 nm, and so the whole spectral region around the possible harmonics was sampled.

From this it is clear that there is negligible 6<sup>th</sup> and 7<sup>th</sup> harmonic generation, and this suggests that the peak at 50 nm is due to line emission rather than harmonic generation.



The presence of strong line emission in the spectrum was confirmed when the exit slit of the monochromator was replaced by a photographic plate\*. This is not an ideal experiment, because the monochromator grating is not designed for this imaging arrangement, and geometrical aberrations will be present. What was clear from the spectra, however, was that lines in the output were present.

### 9.2.3 Microchannel plate focusing

The next stage of the investigation was to couple more efficiently the light from the LGP into the monochromator. Since light of wavelengths below 105 nm was required, refractive optics could not be used. Instead, a microchannel plate (MCP) was used. An MCP is an array of parallel channels, which are conventionally used as independent electron multipliers. By putting a photocathode on the front surface, and an electron scintillator on the rear surface, they may be used for x-ray imaging; incident x-rays give rise to photoelectrons, which are amplified along each individual channel, and cause fluorescence at the rear scintillator. If the front and rear screens are absent, however, they may be used as x-ray or VUV focusing optics.

Two types are commonly available, having either square or circular channel sections. Circular-channel arrays are easier to make than square channel ones, but less efficient as focusing optics [Chapman *et al.* 1993], and were not investigated for this application. Instead, square-channel MCPs were used. A comprehensive model of their efficiency as x-ray focusing optics is given by Chapman & Nugent [1991].

MCPs work in a similar way to cube-corner reflectors. The key feature is that a ray is reflected from two perpendicular surfaces. The component of the direction of travel of the ray *perpendicular* to both surfaces is reversed. On the other hand, the direction of travel is unchanged in the direction *parallel* to both surfaces. This can be used to achieve 1:1 imaging, as illustrated in Fig. 9.5.

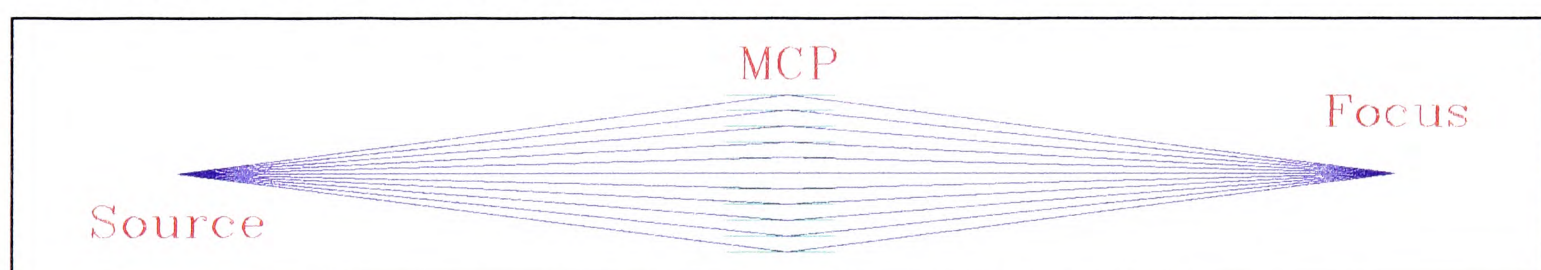


**Figure 9.5.** Schematic of macroscopic focusing by a micro-channel plate (MCP). For simplicity reflection from only one surface is shown.

For the application here, two square-channel MCPs were investigated. Both were made from (unreduced) SiO<sub>2</sub>, and had 8 μm wide channels separated by 12 μm. This means 44% of the area was open. Macroscopically, they both were plane and square, of side 20 mm. They differed in their channel aspect ratios, which were 30:1 and 60:1, i.e. channel lengths of 240 μm and 480 μm respectively.

The MCP being investigated was mounted half way between the plasma and monochromator slit (to within ~2 mm). This provided an extra advantage: the MCP shielded the monochromator grating against debris from the plasma. This was desirable because it is all but impossible to clean either MCPs or gratings, but MCPs are cheaper.

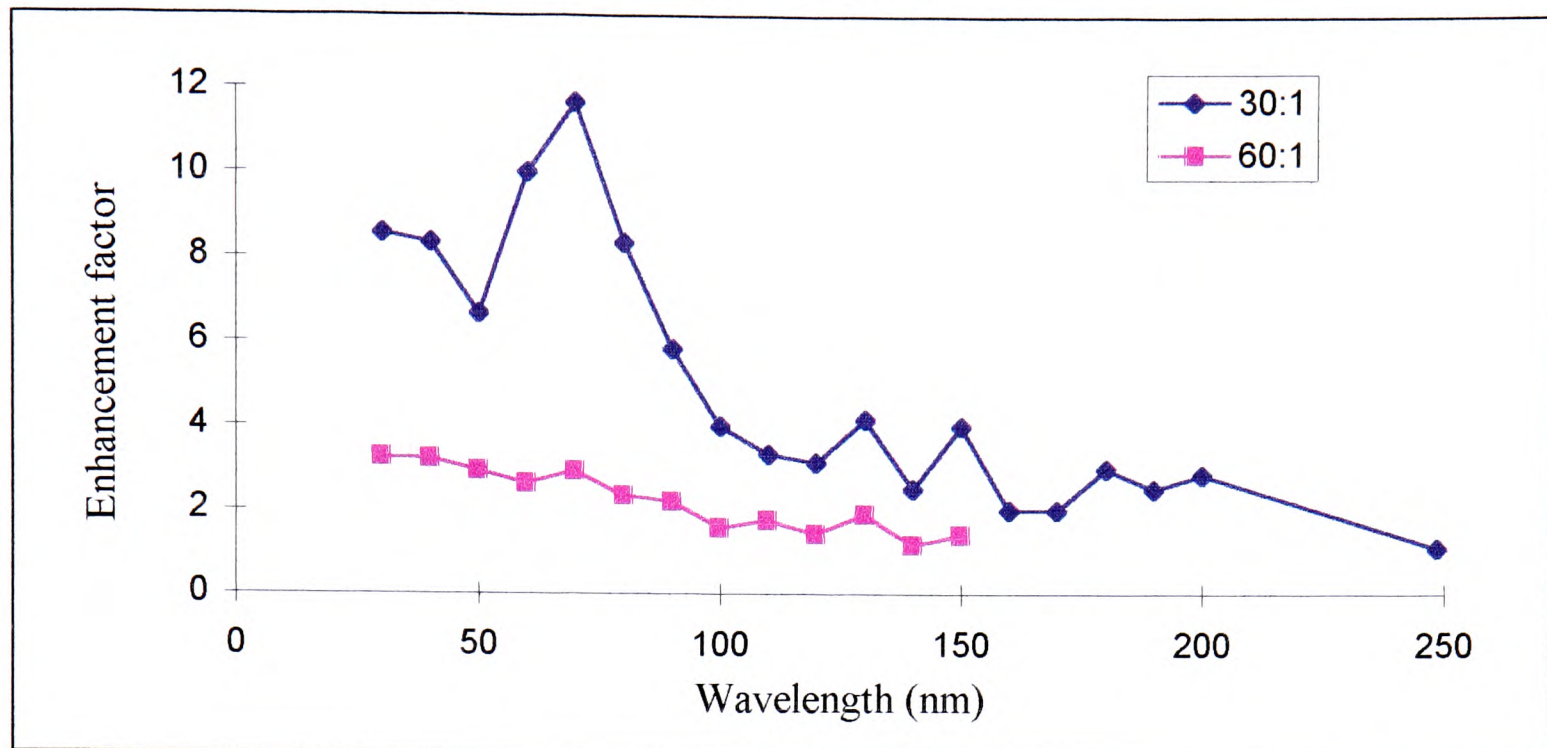
The MCP mount was equipped with two electric motors, allowing two tilt-adjustment screws to be adjusted from outside the target chamber. This was essential in order to

---

\* This experiment was conducted with the MCP focusing optic installed.



ensure that the focused spot was accurately positioned on the entrance slit of the monochromator. The tilt was adjusted while the laser was firing in order to maximise the signal obtained at the monochromator exit slit. Dramatic enhancement of the photon throughput was observed. This is illustrated in Fig. 9.6\*.



★**Figure 9.6.** Enhancement of number of photons detected at monochromator exit slit due to use of MCP focusing, for the two different MCPs investigated.

There are two striking features of this behaviour. Firstly, the 30:1 plate is much more efficient than the 60:1 plate. Consideration of rays from the plasma indicates why this is the case. Denoting the channel aperture size as  $d$  ( $8\ \mu\text{m}$ ), and the channel length as  $l$ , then the approximate acceptance angle† of the MCP is given by  $(d/l)$ . This corresponds to the 30:1 MCP being able to accept light over almost its whole aperture. The 60:1 MCP, however, has a collection area about four times smaller, and thus we see, that in the short wavelength (ray optics) limit, the 30:1 MCP is  $\sim 3$  times more efficient than the 60:1 MCP.

The second striking feature of the results presented in Fig. 9.6 is that both the MCPs are more effective at shorter wavelengths than they are at longer wavelengths. This is because of diffraction. Consider light of the KrF laser wavelength, incident on a square aperture of side  $8\ \mu\text{m}$ . Diffraction gives rise to an angular spread  $(\lambda/d)$  of  $31\ \text{mrad}$ . This should be compared to the angle subtended by the exit aperture of one of the channels in the MCP, at the entrance to the channel. For the 30:1 MCP this angle is  $33\ \text{mrad}$ , and for the 60:1 MCP it is  $17\ \text{mrad}$ . This means that the behaviour of either of the MCPs for light of the KrF wavelength is dominated by diffraction. Thus, each incident KrF ray is so smeared by diffraction in the micro-channel that it fills the whole of the channel, and so the ray-focusing effect is absent. From Fig. 9.6 it is clear that the efficiency cut-off for the 30:1 MCP is at a wavelength of  $\sim 100\ \text{nm}$ . This corresponds to a diffraction angle  $(\lambda/d)$  of  $13\ \text{mrad}$ , which is 2.6 times less than the  $33\ \text{mrad}$  angular extent of each microchannel.

\* For the 60:1 aspect ratio MCP data the residual air pressure in the target chamber, at  $3 \times 10^{-3}\ \text{mbar}$ , was higher than it was for the other data presented here. However, this will have given rise to a reduction of no more than 7% in the VUV signal observed, and no correction has been made for this.

† For an MCP the acceptance angle is not sharply defined, as it is for an optical fibre, and thus we cannot calculate an exact acceptance angle.

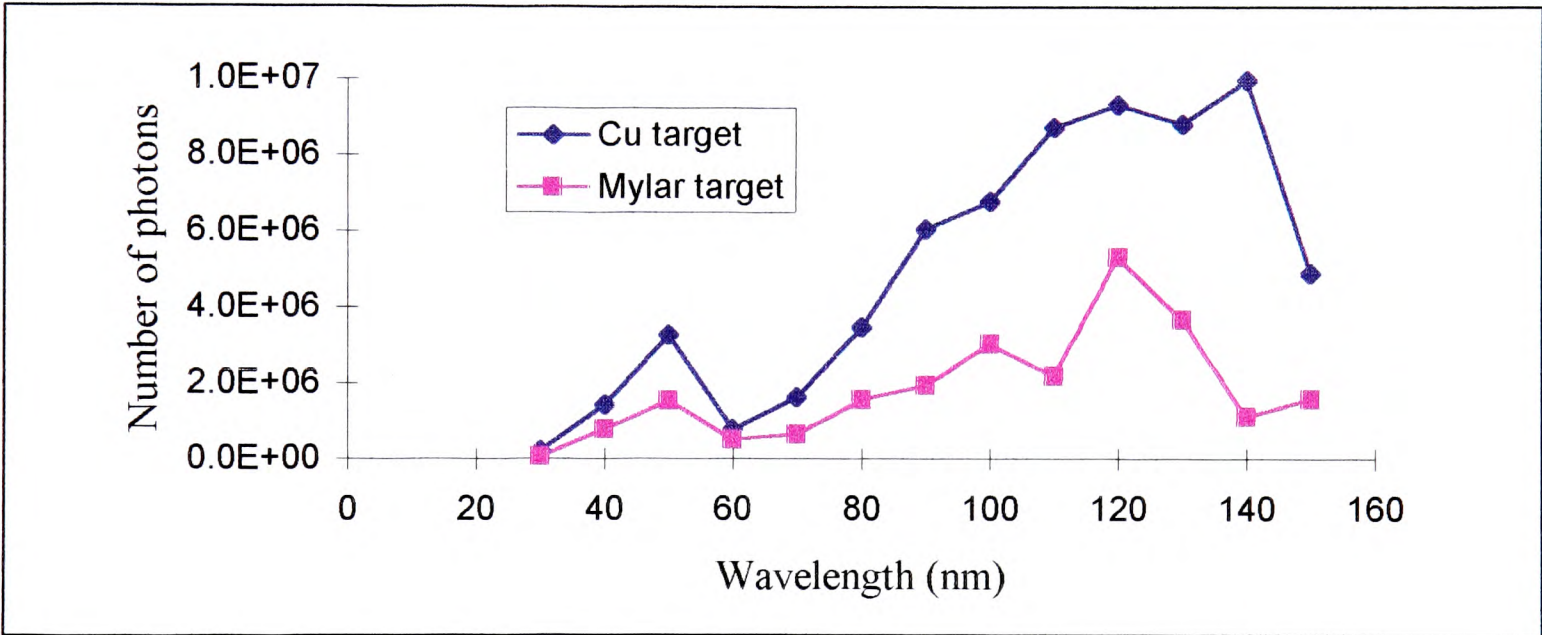


The enhancement spectrum of the 30:1 MCP has a peak at 70 nm and a trough at 50 nm. These wavelengths correspond to a trough and peak respectively in the spectrum of the laser plasma (see Fig. 9.3). If this is real, it may be explained in the following way. The intense emission at 50 nm is line-emission from the expanding (and cooling) plasma, whereas the emission around 70 nm is continuum emission which peaks while the laser plasma is hot, and hence small. Thus, the source of the radiation is smaller for the 70 nm emission, and this allows tighter focusing by the MCP. This is because the size of the focus produced by an MCP cannot be smaller than whichever is the larger of the channel width and the source size.

It is clear from Fig. 9.6 that use of the 30:1 aspect ratio MCP gave a considerable improvement to the output of the laser system. For this reason it was used for all further experiments (unless otherwise stated).

9.2.4 Target material

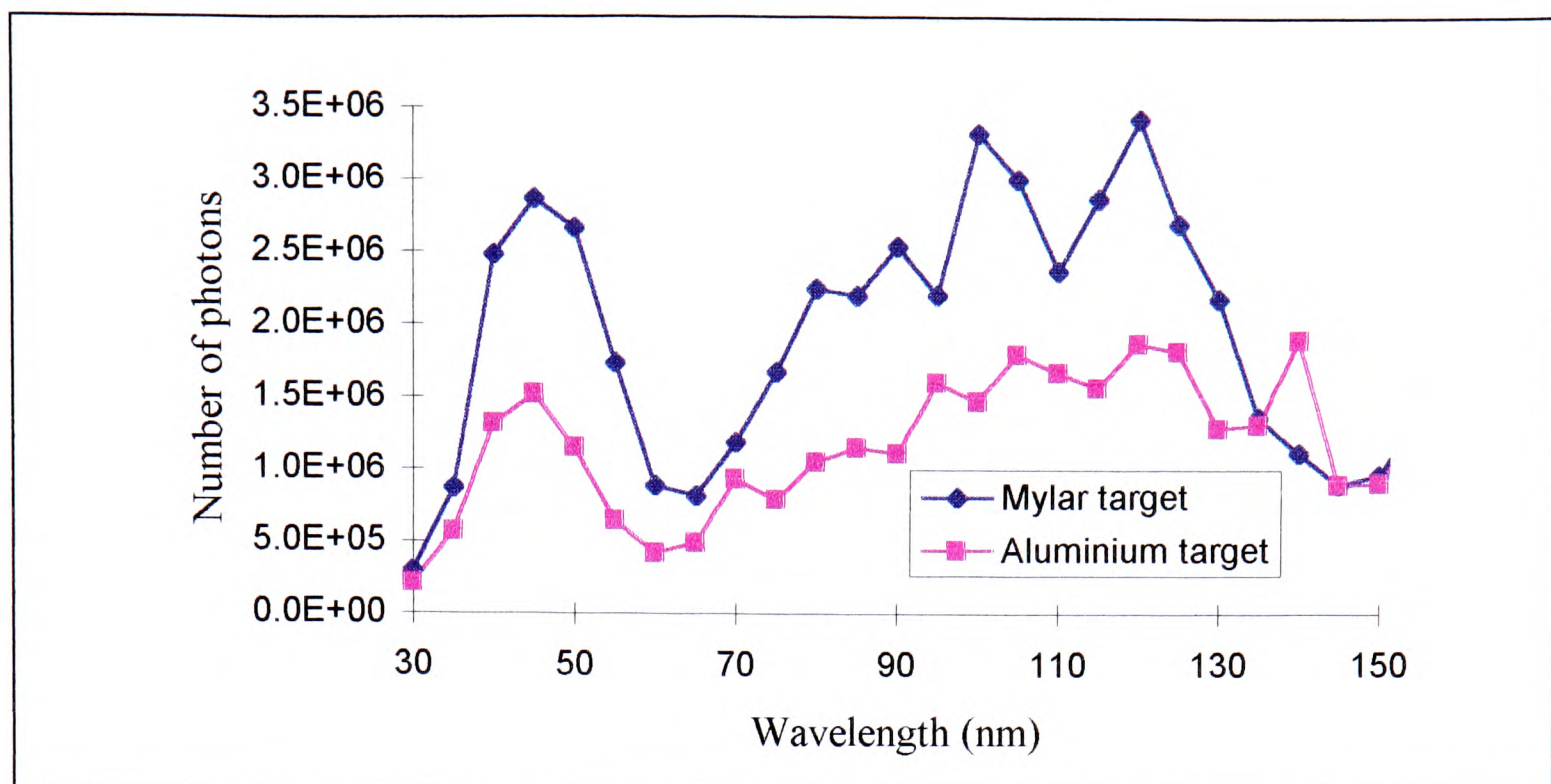
The effect of the target material on the output spectrum was investigated. A mylar (polyethylene terephthalate - predominantly CH) target, in the form of the non-magnetic side of a magnetic audio cassette tape, was substituted for the copper target used for previous experiments, and the spectra measured. The results obtained are shown in Fig. 9.7.



★**Figure 9.7.** Comparison of copper and mylar as target materials. Graph shows number of photons at exit slit of monochromator per laser shot into a 4 nm bandwidth. 60:1 aspect ratio MCP was used to couple light into monochromator; this is not the optimal coupling optic. Boxcar averaging was used to obtain mean signal. Lines between points are a guide to the eye.

From this it is clear that copper gives a significantly better performance than mylar as a target material, over the 30 nm to 150 nm range investigated. Towards the end of the experiment, when the VUV diode described in §9.3.3 was in service as a detector, a comparison was made of aluminium and mylar as target materials. In this case the 30:1 MCP was used to couple light into the monochromator. The results obtained are shown in Fig. 9.8.





★**Figure 9.8.** Comparison of mylar and aluminium as target materials. Graph shows number of photons per laser shot observed at exit slit of monochromator, for 4 nm passband, measured with the diode described in §9.3.3. Lines between points are a guide to the eye.

From Fig. 9.8 it is clear that aluminium is even less suitable than mylar as a target material. The targets investigated, in order of increasing atomic number, were mylar ( $Z=1$  & 6), aluminium ( $Z=13$ ), and then copper ( $Z=29$ ). On the other hand, the order of emission efficiencies was aluminium (worst), then mylar, then copper (best). It is worth mentioning that this does not follow the trend of high- $Z$  LGP targets giving high conversion efficiency (§2.3.7.2). This illustrates that other effects are important - notably the availability of electronic transitions at the wavelengths of interest in the various ion species present. The dramatic enhancement in conversion efficiency by the use of a copper target suggests that other cheap elements, such as iron ( $Z=26$ ), zinc ( $Z=30$ ), or tin ( $Z=50$ ), should be investigated as targets. Other elements which might be interesting (but very expensive) as targets are the rare-earth metals. These have been shown to give truly line-free continuum plasma emission over parts of the spectral region which were considered here [Carroll *et al.* 1980]. For the region below 200 nm samarium ( $Z=62$ ) has been found to be particularly suitable [Carroll *et al.* 1983], although it is about a hundred times more expensive than copper.

### 9.2.5 Defocusing

The picosecond KrF laser used for these experiments (see §9.1.1) was developed in order to produce focal intensities of the order of  $10^{15} \text{ W cm}^{-2}$ , in order to produce 1 keV x-ray photons. For a VUV plasma source, however, the photon energies to be obtained are two orders of magnitude lower. If we assume a plasma temperature,  $T_{\text{plas}}$ , scaling with laser intensity,  $I$ , according to

$$T_{\text{plas}} \propto I^{\frac{4}{9}} \quad (9.1)$$

[Hube *et al.* 1988, Wood *et al.* 1986], then we might expect four orders of magnitude less intensity at the focus to produce significant VUV emission. This was investigated by defocusing the laser, and measuring the plasma emission spectrum. The focus was found for this experiment, as it was for all the other experiments presented here, by moving the



target towards and away from the lens in order to maximise the 1 keV x-ray plasma emission. This was measured with the target chamber evacuated, but otherwise as described in §9.2.1.1. The optimum focus corresponds to a 10  $\mu\text{m}$  spot size.

Then the target was moved towards the lens first by 1 mm, and then by 4.7 mm. These offsets are sufficient to ensure that the spot size may be calculated geometrically, without a requirement for extreme accuracy in knowing the position of the focus. The direction of motion was towards the target, rather than away from it, in order to eliminate any complications due to the presence of a focus in front of the target. For the 4.7 mm defocusing it was found necessary to readjust the tilt of the MCP to ensure that the plasma emission was optimally coupled into the monochromator entrance slit. The spectra obtained are shown in Fig. 9.9.

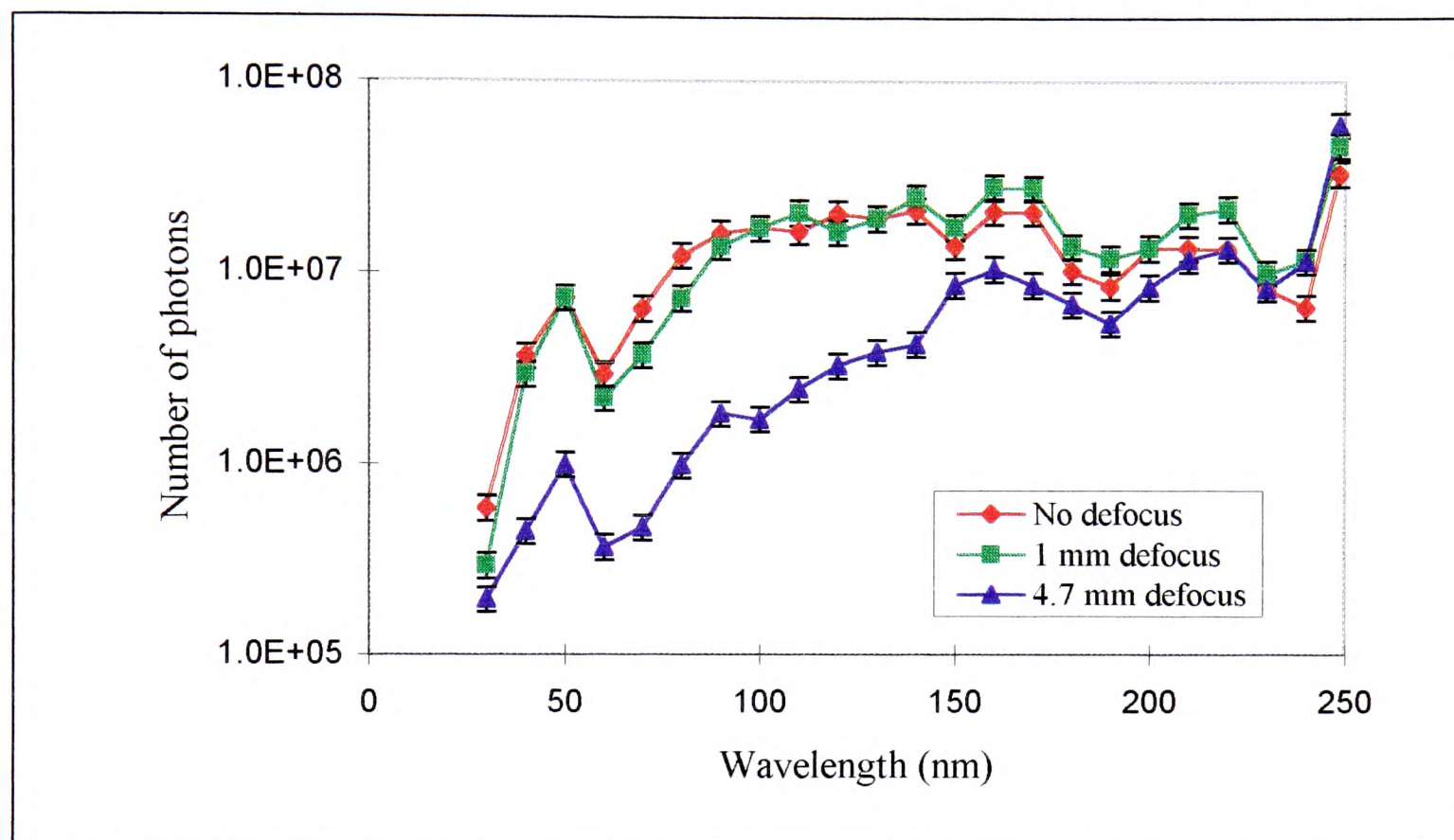


**Figure 9.9.** Effect of defocus on number of photons reaching exit slit of monochromator. Intensities in the focal spot are  $1.1 \times 10^{15} \text{ W cm}^{-2}$  with no defocus,  $1.2 \times 10^{12} \text{ W cm}^{-2}$  with 1 mm defocus, and  $5.4 \times 10^{10} \text{ W cm}^{-2}$  with 4.7 mm defocus. Note the scale is logarithmic. Lines between points are a guide to the eye.

Several conclusions may be drawn from Fig. 9.9. By comparing the spectra obtained with no defocus ( $1.1 \times 10^{15} \text{ W cm}^{-2}$ ) and with 1 mm defocus ( $1.2 \times 10^{12} \text{ W cm}^{-2}$ ), it is clear that for wavelengths below about 90 nm the higher intensity focus gives rise to between 30% and 100% more plasma emission\*. For wavelengths above about 150 nm however, the defocused arrangement gives 30% to 80% more output. This may be explained by considering that the plasma formed when the KrF beam is tightly focused is much hotter than in the defocused case, and this gives rise to short wavelength emission, at the expense of the long wavelength emission.

\* It should be noted that tiring of the laser gas mixture meant the single pulse energies were not the same for all the measurements presented here. For the defocused spectrum, trains of mean pulse energy 8.8 mJ were used, whereas for both the defocused spectra they were 28% less energetic, at 6.3 mJ. This affects the relative efficiencies of the focusing regimes, but nevertheless the higher intensity focus is still a significantly more efficient emitter at short wavelengths.



Despite these differences, however, it is striking how little difference there is between the two plasma emission spectra, considering one was produced by a focus which was one thousand times less intense than the other. Similar observations have been noted by other workers using similar sources [Carroll *et al.* 1983]. The insensitivity of the output to the focusing conditions provides approximate support for the assertion made above, that a focal intensity much lower than the maximum obtainable from the laser system, could still give rise to significant VUV emission.

But this is not the end of the story - the intense focus is known to generate 1 keV x-rays, and presumably emits over the whole energy spectrum between this energy and the highest energy (40 eV) photons detected here. This means that a considerable fraction of the total plasma emission is not detected here. For the 1 mm defocused plasma this will be much less the case. This suggests that the more intense focus gives rise to a higher total plasma emission efficiency.

A further pointer to this conclusion is found in considering the signal observed at the laser wavelength, which is predominantly scatter of the incident radiation. This is 45% greater in the case of the 1 mm defocus plasma than in the zero defocus case. This trend is continued in the 4.7 mm defocus case. This indicates that the incident radiation is coupled into the plasma more efficiently at the higher plasma intensities.

Thus, we may explain the similarity between the output spectra as being the result of comparing an efficient but too hot plasma, and a less efficient but cooler plasma. This suggests that there may be some intermediate focal intensity which could provide greater emission into a given wavelength region of interest, if a cooler but not much less efficient plasma could be created. This was not investigated during the experiments described here, but could be fruitful avenue for further investigation.

Another effect which we must consider is the interaction between the plasmas generated by successive pulses in the 16 pulse train. In particular, each pulse will act as a prepulse for its successor. A pertinent experimental study has been reported by Teubner *et al.* [1992]. They investigated the emission in the spectral region 3 nm to 17 nm (413 eV to 73 eV), from Cu and Al plasmas generated by 25 mJ, 0.5 ps KrF laser pulses, focused to  $5 \times 10^{15} \text{ W cm}^{-2}$ . As in this work, they found copper to give much stronger emission than aluminium. They also found that when they applied even a very weak (0.5%) prepulse 150 ps before the main pulse, the emission was enhanced several times. The enhancement was greatest at short wavelengths, suggesting that the prepulse gave rise to a hotter plasma than would otherwise have been obtained.

Teubner *et al.* [1992] give a simple explanation of the effects of varying both the prepulse delay and magnitude, based on the (temperature-dependent) expansion of the preplasma. The key to the argument is that the prepulse is most effective if the preplasma just expands (before the main pulse arrives) to the inverse-bremsstrahlung absorption length ( $\sim 1 \mu\text{m}$ ) corresponding to the critical electron density. Then the main pulse is absorbed entirely within the plasma (rather than any reaching the solid target surface), and this gives rise to efficient coupling of radiation into the plasma. If the plasma is allowed to expand too much (650 ps delay for the Teubner *et al.* [1992] experiments), the enhancement is reduced, because the electron density becomes subcritical everywhere within the preplasma, and the main pulse sees the target surface.

The experimental arrangement used in the present work, in the zero-defocus case, is very similar to that used by Teubner *et al.* [1992], from which we may deduce that the 2 ns delay between the pulses is too long to give an effective preheat. When the system is defocused, however, we expect plasmas two orders of magnitude cooler, and so the plasma expansion will be an order of magnitude slower. In this case, a pulse separation of



order 2 ns may be ideal, and this may have influenced the spectrum observed for the defocused experiments.

The effect of varying the pulse separation was not investigated. The range of separations available without a drop in the total energy of a pulse-train is restricted by the gain window and repumping time of the KrF laser amplifiers. Even so, adjustments of this separation, combined with defocusing, could enhance the VUV emission.

Next, we consider the 4.7 mm defocus experiment. Some care is needed in interpreting these results, since the focal spot is rather large at 2.2 mm (horizontally)  $\times$  0.7 mm (vertically), allowing for the oblique ( $45^\circ$ ) incidence on the target. We must consider the effect this will have on the focusing efficiency of the MCP. The MCP cannot focus to a spot smaller than the source, i.e. 2.2 mm wide. On the other hand, the monochromator entrance slit was only 1 mm wide, and so at least half the energy focused by the MCP will have been lost, since it will not have passed through the slit. A further complication associated with use of the 2.2 mm wide focal spot is that successive laser shots will have overlapped on the target. Although both of these features will affect the total emission reaching the monochromator exit slit, neither of them is wavelength-dependent.

The only thing which would give rise to wavelength dependent effects would be light from the plasma hitting the walls of the MCP channels at different angles. This is because the finite-angle reflectivity is a function of wavelength. However, the spot size of 2.2 mm is still much smaller than the MCP width of 20 mm. This means that the changes are small in the distribution of angles of incidence of rays from the plasma on the channel walls, owing to the finite source size. Furthermore, grazing incidence reflectivities for smooth absorbing media are only slowly varying functions of angle of incidence [Chapman *et al.* 1991], and so any slight differences in this distribution cannot have drastic effects on the MCP throughput.

Thus, for the 4.7 mm defocus experiment, the large source size will give rise to a reduction in the signal observed, but this will be largely independent of wavelength. This means that comparisons are still valid of the shape of the spectrum obtained with that from the optimally focused plasma.

In this case it is evident from Fig. 9.9 that the plasma emission from the 4.7 mm defocus experiment is strongly shifted towards longer wavelengths, in comparison to less defocused plasmas. Clearly, this corresponds to a cooler plasma.

### 9.2.6 A whiff of neon

Debris was found to be a limitation on the source, as described in §9.2.1.1. The idea of operating the system in the presence of a low pressure of neon was investigated. Neon was chosen because, being a noble gas, it cannot form deposits on the monochromator grating, and it has a high photon energy transmission cut-off.

The results were startling. Even with 70 torr of neon in the target chamber, the signal observed at a wavelength of 45 nm was comparable to that obtained with no neon in the target chamber. The first ionisation energy of neon is 21.6 eV, corresponding to a photon wavelength of 57 nm. Thus, photoionisation means that the transmission of neon to light at 45 nm is negligible [Thomas 1989]. Thus, the signal observed with the monochromator set to 45 nm cannot have been caused by photons of this wavelength. The signal was only observed when the laser was incident on the target (*i.e.* it was optical in origin).

There are several possible explanations for this observation. One is that the signal at short wavelengths was entirely due to scatter of light of other wavelengths from the grating in the monochromator. However, this conclusion is not supported by the



observations that the MCPs were more effective at focusing for short wavelengths, and that defocusing caused a reduction in the short-wavelength signal. There is further evidence that the signal observed when the monochromator was set to short wavelengths was not an artefact. This had been found in an experiment conducted before the MCP was added to the system. In this experiment, a fused silica plate was placed in the beam path between the plasma and the monochromator. As expected, this caused the signal at 100 nm to disappear (fall by at least two orders of magnitude), on account of absorption in the plate.

Other possible explanations for the effects observed with neon are that  $\sim 600$  eV to 1 keV x-rays generated by the plasma, which are transmitted (a few percent) by the relevant length and pressure of neon [Thomas 1989], are scattered or give rise to fluorescence in the neon in the monochromator. With neon in the target chamber, a halo was visible around the plasma spot, and this suggests that there may have been such a fluorescence effect. Unfortunately there was insufficient time for further investigation of this.

## 9.3 Photon detectors

In this section we consider the absolute calibration of the systems used to detect radiation output from the system. Two systems were used, a sodium salicylate scintillator in conjunction with a photomultiplier, and a less-sensitive, but better-calibrated XUV photodiode.

### 9.3.1 Sodium salicylate & photomultiplier

The use of sodium salicylate as a scintillator for detecting soft x-ray photons is described in §6.8. When x-rays strike (solid) sodium salicylate they generate photoelectrons which recombine radiatively, giving a blue fluorescence. This may be detected with a windowed photomultiplier. The technique was chosen for this application partly for convenience - a photomultiplier and scintillators were already available as a result of the work described in other chapters of this thesis, and partly because it can be very sensitive, since the photomultiplier can be used at a gain of up to  $10^7$ . A further advantage was that it is possible to calibrate the detection, to establish an absolute number of photons available for applications; and this process is described here.

#### 9.3.1.1 Geometrical collection efficiency

Scintillators were prepared according to the recipe given in §6.11.1. They were mounted in the geometry shown in Fig. 9.10. First, we estimate the geometrical collection efficiency of the system.



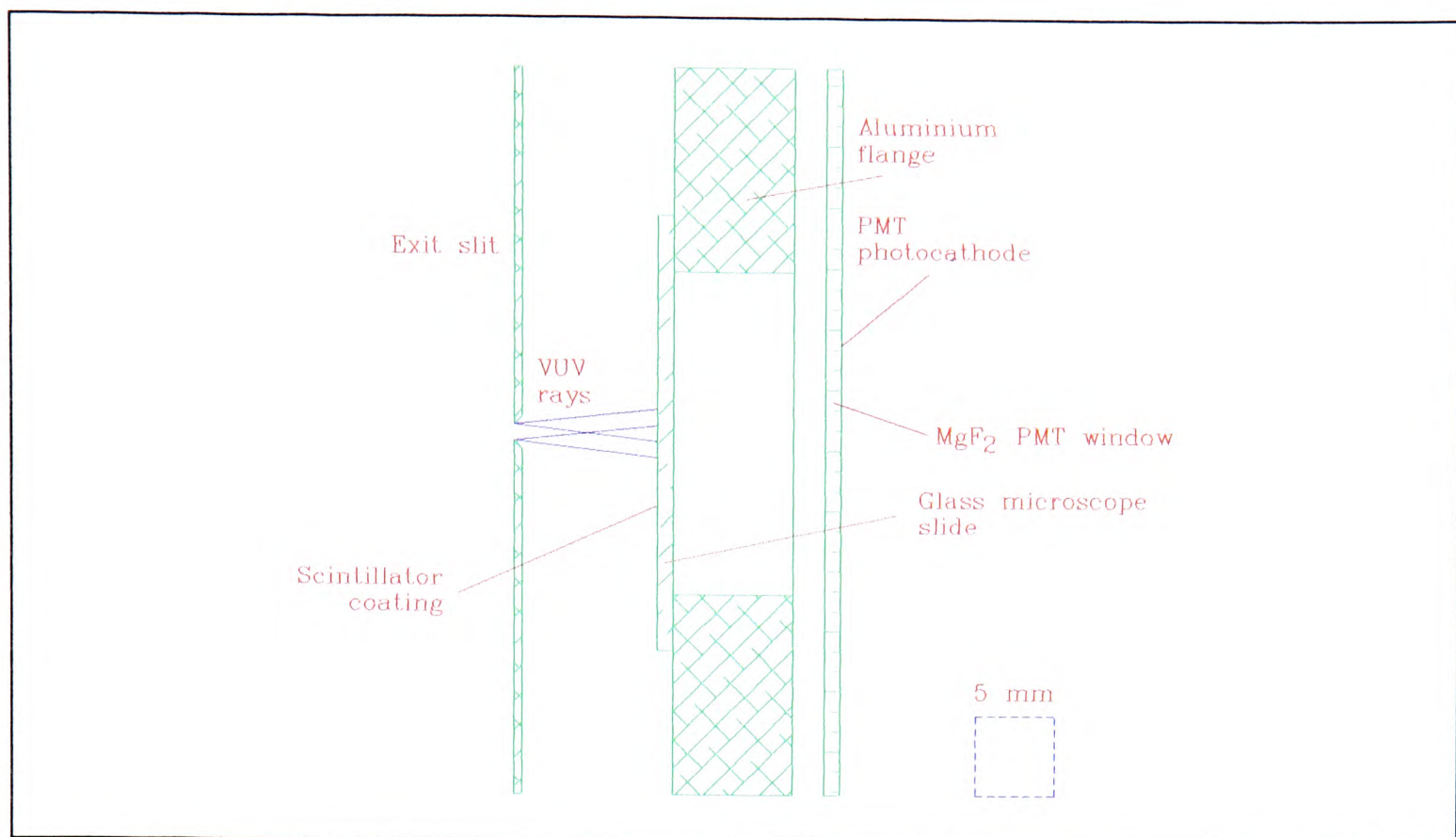


**Figure 9.10.** Geometry in which scintillator was used. Diagram is to scale, including exit angle of VUV rays from  $f/4.5$  monochromator. View is section in horizontal plane. All parts except slit have circular symmetry about central axis. Slit was 5 mm long in direction perpendicular to diagram.

It is clear from Fig. 9.10 that all the VUV photons leaving the exit slit strike the scintillator. Of those emitted by the scintillator, half will be emitted back towards the slit, and half towards the PMT photocathode. As described in §6.11.1, the surface on to which the scintillator was deposited was roughened, and we assume that this gives rise to an isotropic angular distribution of photons within the microscope slide, up to a maximum angle of  $45^\circ$  to the normal. This corresponds (approximately) to assuming that the optical contact between the scintillator and the substrate is poor, and that the sandblasting process gives microscopic facets of isotropic angular distribution up to  $45^\circ$ .

On exit from the slide, these photons are refracted or suffer total internal reflection, depending on their angle of incidence. Assuming unpolarised light, and allowing for the Fresnel reflectivity of the glass-vacuum interface for the two polarisations separately, we may deduce a transmittance of 78%.

We assume that 50% of the light which suffers total internal reflection is scattered at the scintillator surface (completely re-randomising its polarisation and direction in the process) back towards the exit face of the microscope slide. Allowing for multiple reflections, this suggests that 88% of the photons initially emitted towards detector do subsequently escape the microscope slide in this direction.

The geometrical arrangement (Fig. 9.10) means that about a third of these photons strike the shiny walls of the aluminium flange, and we assume an 80% reflectivity for this. The photons then hit the  $\text{MgF}_2$  window of the photomultiplier. In general, they do not strike at normal incidence, and we must allow for the extra reflection losses this introduces. The light escaping from the microscope slide is polarised, and this polarisation is included in this calculation. This suggests a 10% reflection loss (including the effect of the finite aluminium reflectivity) above that expected for normal incidence illumination, for which the PMT is calibrated.

Combining these factors we estimate a net geometrical efficiency,  $\gamma_{\text{geo}}$ , of 38%. This comprises 50% emission towards the PMT (less 4% Fresnel loss on entry to the



scintillator substrate), of which 88% escapes the microscope slide, and then a 10% reflection loss at the aluminium walls of the flange, and due to oblique incidence on the PMT entrance window.

9.3.1.2 Spectral response of sodium salicylate

Sodium salicylate is a very widely studied scintillator. Unfortunately, experimental investigations of it have found differing results. It is not possible to isolate the causes of these disagreements in every case. For example, the geometry of the collection systems used in these experiments are rarely described in sufficient detail for the assumptions made about collection efficiencies to be analysed. This means the calibration of the sodium salicylate used here is somewhat arbitrary, and can only be trusted to within a factor of 2-3.

A recent review is given by Husk *et al.* [1992] who have modelled the material and summarise measurements over the range 5-400 eV. For the application here, an absolute calibration was needed for the range 30 nm to 248 nm (41 eV to 5 eV). No single measurement has been reported covering the whole of this range, and so an amalgamation of several sources was used. The quantum efficiency,  $\gamma_{\text{scint}}(\lambda)$ , as a function of wavelength,  $\lambda$ , assumed is shown in Fig. 9.11.

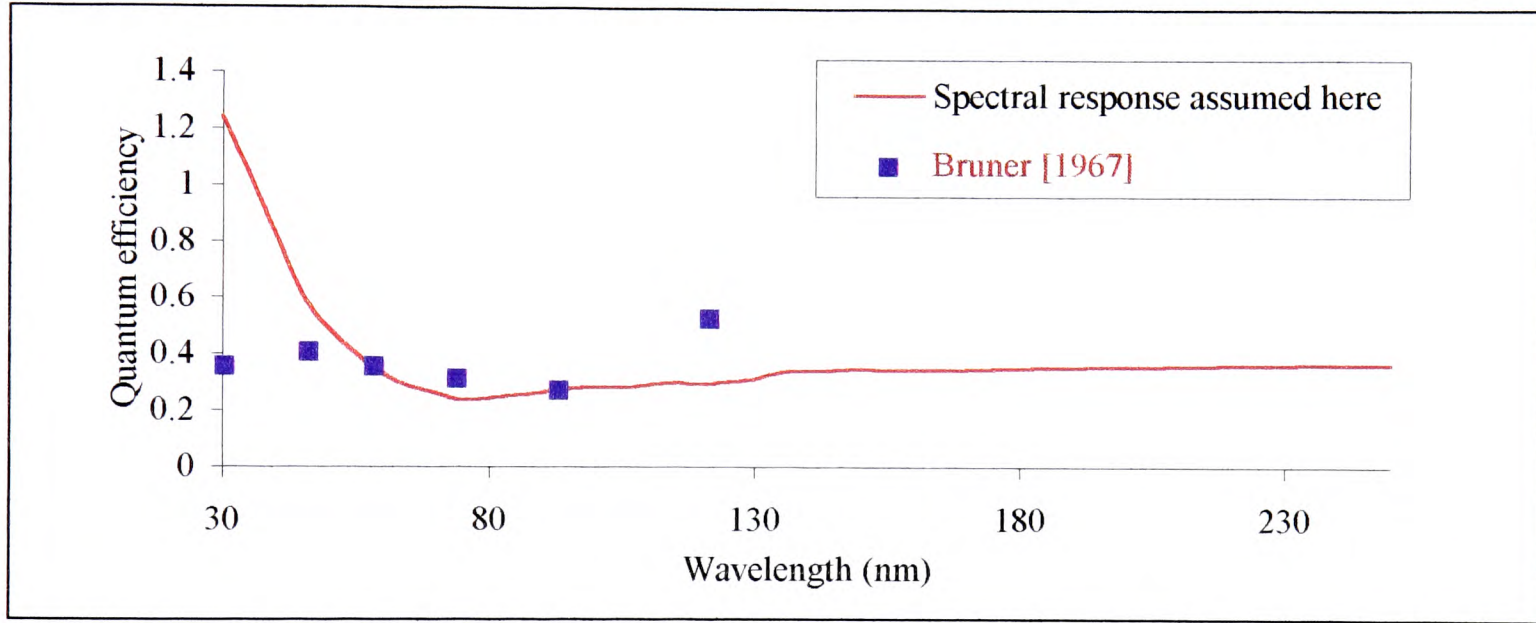


**Figure 9.11.** Quantum efficiency spectrum for sodium salicylate assumed here. Also shown are experimental data due to Bruner [1967], which have been reduced by 15% to allow for self-absorption of the fluorescence, as described in §9.3.1.3.

For wavelengths shorter than 94 nm, the theoretical predictions of Husk *et al.* [1992] were used for absolute quantum efficiencies. These may be compared to efficiencies measured at some specific spectral lines by Bruner [1967], which are also shown in Fig. 9.11. It is clear that there is reasonable agreement in the range 46 nm to 93 nm, but at 30.4 nm there is a factor of 3 of disagreement. It is not possible to rule out radiation damage (§9.3.1.5) to the samples measured as the cause of the apparent underestimate of this efficiency made by Bruner [1967] - some damage was found during his experiments. We return to this low wavelength disagreement in §9.3.3.

For the range 94 nm to 160 nm relative quantum efficiencies obtained by Knapp & Smith [1964] were used. These were converted to absolute efficiencies by scaling them to agree with the absolute efficiency predicted by Husk *et al.* [1992] at 94 nm. The prediction for 121.6 nm obtained in this way is a factor of 2 lower than that of Bruner [1967], whose estimate of this quantum efficiency incorporates a correction for damage to



the sample. It is difficult to find the cause of the discrepancy; the question of the thickness of the samples measured is discussed in §9.3.1.3.

An absolute measurement of 37% for the quantum efficiency at the 253.7 nm mercury line has been reported by Kumar & Datta [1979]. They comment that other authors have reported efficiencies ranging up to 99% [Allison *et al.* 1964b] at the same wavelength. There is no straightforward way of choosing whom to believe, and this underlines the observation that the calibration given here is somewhat arbitrary.

The 253.7 nm result of Kumar & Datta [1979] was used as a final point in the calibration. Efficiencies in the range from 160 nm (where the efficiency was modelled as 35%) to this point were linearly interpolated. This disagrees with the relative quantum efficiency measurements of Johnson *et al.* [1951], who report a 20% drop over this region of the spectrum. This may be explained by the thickness of the samples they measured, and need not concern us. This is discussed in §9.3.1.3.

### 9.3.1.3 Absolute quantum efficiency vs. number of photons collected

The discussion so far has concentrated on the absolute quantum efficiency of the scintillator. This may be defined as ratio of the number of fluorescence photons emitted in an element of volume of the scintillator, to the number of VUV photons absorbed in the same region. This is always greater than the experimentally deduced ratio of the total number of fluorescence photons leaving the scintillator to the number of VUV photons incident on it. The two reasons for this difference are incomplete absorption of VUV photons by the sample, and self-absorption of the fluorescence.

Incomplete absorption of the incident radiation can be due to surface reflection or insufficient thickness of scintillator. Surface reflection need not concern us; it will be a constant effect in all the experimental studies of the scintillator, and is included in the model of Husk *et al.* [1992]. Insufficient thickness of the sample is more of a problem. Husk *et al.* [1992] give the absorption spectrum of sodium salicylate. The scintillators used for the experiments described here were of coating density  $2.2 \text{ mg cm}^{-2}$ . This thickness was found by Kumar & Datta [1979] to give approximately the most fluorescence for 253.7 nm excitation. It is optimal because it corresponds to complete absorption of the incident photons. Since this wavelength is near the minimum absorption of the spectrum given by Husk *et al.* [1992], we may deduce that the coatings used for the experiments reported here were sufficiently thick to absorb all the photons incident on them.

The same cannot be said, however, for the scintillators used in the work of Johnson *et al.* [1951]. They measured relative efficiencies of sodium salicylate over the range 90 nm to 225 nm. Although they do not state their sample thickness, it is possible to estimate it, based on how they prepared their samples (from a drop of a saturated solution of sodium salicylate in ethanol). Such an estimate\* suggests a coating thickness of order  $0.05 \text{ mg cm}^{-2}$ . This will not have been sufficient to absorb all the incident photons at the longer wavelength end of their spectral range, and for this reason their results were not used for this application.

The relative efficiency data of Knapp & Smith [1964] which were used for the range 94 nm to 160 nm, were obtained from samples of described as "on the order of  $10^{17}$

---

\* Estimate assumes 2 mm diameter spherical drop used to coat an area of  $10 \text{ cm}^2$ . Solution concentration was taken to be the  $1 \text{ mole dm}^{-3}$  maximum solubility of sodium salicylate in methanol (see §7.3.3.3).



$\text{mol/cm}^2$ ". This suggests a coating density of the order of  $0.03 \text{ mg cm}^{-2}$ , or a thickness of  $\sim 50 \text{ nm}$  (taking a density of  $1.8 \text{ g cm}^{-3}$  for sodium salicylate [Husk *et al.* 1992]). This is comparable with the absorption length of the radiation over some of the spectral range for which it was used [Husk *et al.* 1992]. If the thickness of the scintillator was insufficient to absorb the incident radiation completely, a minimum response at  $150 \text{ nm}$  would have been observed, corresponding to a minimum in the absorption spectrum. No such feature was present, and so we assume the sample measured to have been sufficiently thick to have absorbed all the radiation incident on it.

Finally, we consider the self-absorption of the emitted fluorescence. For a  $2.6 \text{ mg cm}^{-2}$  coating, self absorption of 18% was measured by Bruner [1969]. This is consistent with a result of  $\sim 14\%$  obtainable by interpolating to zero thickness the high-thickness efficiency measurements of Kumar & Datta [1979]. This interpolation is then compared with the actual efficiency found for a  $\sim 2 \text{ mg cm}^{-2}$  thickness, and the difference of 14% ascribed to self-absorption of the fluorescence.

Firstly, we note that this is a fairly small effect. Secondly, for a given sample thickness, it is independent of the wavelength of the exciting radiation. Thus, it is of no relevance to the relative quantum efficiencies due to Knapp & Smith [1964], which were used over the spectral range  $94 \text{ nm}$  to  $160 \text{ nm}$ . Kumar & Datta [1979], whose data was used for the calibration at  $253.7 \text{ nm}$ , do not allow for self absorption in their calculation of quantum efficiency, which was of a  $2 \text{ mg cm}^{-2}$  scintillator. This means that in using their data we do not need to allow for it either, since their calculation was based on the measurement of the amount of fluorescence escaping the back surface of a scintillator, as were the measurements described here.

It is interesting to note that the model described by Husk *et al.* [1992], and used here for the wavelength range  $30 \text{ nm}$  to  $94 \text{ nm}$ , does not explicitly include the effect of self absorption. Despite this, it agrees very well with their experimental measurements for  $1.8 \text{ mg cm}^{-2}$  scintillators (taken over the spectral region from  $3 \text{ nm}$  to  $18 \text{ nm}$ ). Since the effect is small, we shall not concern ourselves with speculation about the causes or implications of this.

Thus, we assume that the calibration curve shown in Fig. 9.11 includes the effect of self-absorption. Bruner [1967] went to great lengths to eliminate the effect of self-absorption from his results. To allow these to be compared with the efficiencies assumed for this work, his efficiencies have been reduced by 15% before being plotted in Fig. 9.11.

#### 9.3.1.4 Total internal reflection

However, our troubles do not end once the fluorescence has escaped the scintillator. We must consider the effect of total internal reflection (as discussed in §9.3.1.1) on the efficiency calibration experiments summarised in the previous section. All of these experiments employed sodium salicylate films deposited on smooth glass substrates.

Only one set of authors [Allison *et al.* 1964b] considered the effect of total internal reflection. They assert correctly that if the scintillator makes poor optical contact with the substrate, the effect will be absent, because the substrate will simply behave as a parallel plate inserted between the fluorescent source and detector. They also assert that the insertion of such a plate does not affect the angular distribution of the fluorescence observed. This is false; the Fresnel reflectivity of the surfaces will cause loss for high angles of incidence (about 10% for  $60^\circ$  incidence, for example). They then go on to cite experimental evidence to support their false assertion. This is an *exact* (within 1%) cosine



dependence of fluorescence with angle of detection behind the substrate. This casts some doubt on their result.

We shall, however, accept their main conclusion, that the optical contact in their samples was poor, especially since they observed many voids in their coatings when they inspected them under a microscope. Further, we shall assume that this was the case for all the measurements used for the calibration described in §9.3.1.2 [Knapp & Smith 1964, Kumar & Datta 1979]. This is on the grounds that they all used similar spray coating techniques for making their scintillators. In this case, the effect of reflection losses in the substrate was small, and we ignore it.

### 9.3.1.5 Radiation damage

Many workers have reported a deterioration in the fluorescence efficiency of sodium salicylate. This may arise either from radiation damage or chemical attack due to the storage environment. This is considered in more detail in §6.14.

Husk *et al.* [1991 & 1992] have described radiation damage to sodium salicylate. They found the yield decayed as  $\exp(-\delta D)$  where  $\delta$  is an energy dependent damage coefficient, and  $D$  is the total dose (expressed in photons per unit area).  $\delta$  increases sharply with photon energy. For 40 eV photons, the most energetic used here,  $\delta$  is  $1.4 \times 10^{15} \text{ cm}^2 \text{ photon}^{-1}$  [Husk *et al.* 1991]. For the collection geometry used here (Fig. 9.10) this suggests a dose of  $6 \times 10^{14}$  photons is needed to observe a  $1/e$  reduction in quantum efficiency due to radiation damage. This corresponds to more than 10 days of continuous exposure for the 5 Hz laser repetition rate at which the measurements presented here were taken. This is about two orders of magnitude more than the total radiation exposure given. Thus, radiation damage to the scintillator may confidently be ruled out.

The possibility of damage to the scintillator due to its storage environment was also ruled out. A scintillator used for the first two weeks of the experiment, which had been made some six months earlier, and stored for four months in a monochromator with a less clean vacuum system than used here, was replaced by one made twelve days earlier, which had been stored in a dessicator. No increase in photon output was observed after the change was made.

### 9.3.1.6 Photomultiplier efficiency and gain

The photomultiplier (PMT) used was a Thorn-EMI 9426, with a bialkali photocathode coated on to the rear of an  $\text{MgF}_2$  entrance window. This gives rise to sensitivity in the spectral region from 115 nm ( $\text{MgF}_2$  cut-off) to 630 nm (photocathode cut-off). Sodium salicylate fluoresces over a 70 nm FWHM wavelength region, centred at 410 nm [Kumar & Datta 1979]. For this spectral region, a calibration from the PMT manufacturer indicated a 22% wavelength-integrated quantum efficiency,  $\gamma_{\text{PMT}}$ , (i.e. ratio of the number of photoelectrons reaching the first dynode of the PMT to the number of photons incident on the entrance window).

The gain,  $G(V_{\text{PMT}})$ , of a photomultiplier is the ratio of the charge delivered to a detection system after amplification, to the number of photoelectrons reaching the first dynode. Provided the currents drawn are not too great, this is a function only of the potential,  $V_{\text{PMT}}$ , applied to the dynode chain. The gain of the *particular* photomultiplier used here had been calibrated by the manufacturer for two applied potentials (1380 V and



1560 V) and this calibration was extended to the lower potentials used here, simply by comparing signals obtained as the applied potential was varied.

If too large a peak current is drawn from a PMT it ceases to respond linearly to increases in the optical signal it is measuring. This is caused by the build-up of a space charge in the final amplification stage. The PMT was operated with a potential of 910 V, equally divided between each of the 14 BeCu dynodes. The manufacturer's data indicated that this arrangement would respond linearly (no more than 5% deviation from linearity) at output currents of no more than  $\sim 30$  mA. The greatest peak output current generated in any of the measurements reported here was estimated as 30 mA. This estimate is based on a measurement of the duration of the current pulse emitted from the PMT. This measurement was made by connecting the PMT to a fast oscilloscope, and was found to be no less than 40 ns FWHM. From this we deduce that the photomultiplier output was not (severely) saturated for the measurements presented here.

#### 9.3.1.7 Electrical detection circuit

There are two ways of measuring the output of a PMT, when, as here, it is used for measurements of the number of photons in a pulse (as opposed to a photon counting application). One may either measure the output current directly, using a sufficiently fast detection system (e.g. a  $50\ \Omega$  input impedance, fast oscilloscope), or the current may be integrated by making it charge a capacitor. This causes a voltage to be developed across the capacitor, and this is measured. The latter approach was used for the measurements presented here. The capacitor charged consisted of the internal capacitance of the PMT ( $<12$  pF, and neglected), the capacitance of the voltage detector (an oscilloscope of 28 pF input capacitance), and the coaxial cable used to connect the PMT to the oscilloscope, combining to give a capacitance,  $C$ . The cable capacitance dominated, at  $101\text{ pF m}^{-1}$  for the 1 m to 4 m cables used for these measurements. This was confirmed simply by measuring the same signal with different cable lengths.

### 9.3.2 Overall detection efficiency

Summarising the results of the preceding sections, the number of photons,  $N_{phot}$ , at the exit slit of the monochromator was derived from the potential,  $V_{sig}$ , measured on an oscilloscope, according to the relationship

$$N_{phot} = \frac{V_{sig} C}{G(V_{PMT}) \gamma_{PMT} \gamma_{geo} \gamma_{scint}(\lambda) q_e} \quad (9.2),$$

where  $q_e$  is the elementary charge.

### 9.3.3 Calibrated diode

Another detection system was also employed for some experiments. This was an absolutely-calibrated photodiode (IRD model AXUV-100). Unfortunately, problems with the laser, and with debris, meant that no two *directly* comparable spectra were taken where the only difference between them was the detection system used. However, two spectra were taken for which the only differences between them were the detection system and the KrF laser power. These two spectra are illustrated in Fig. 9.12, with the photon numbers obtained from the photodiode system doubled to allow for the KrF power being



half what it was for the spectrum obtained using the scintillator and photomultiplier detection system.

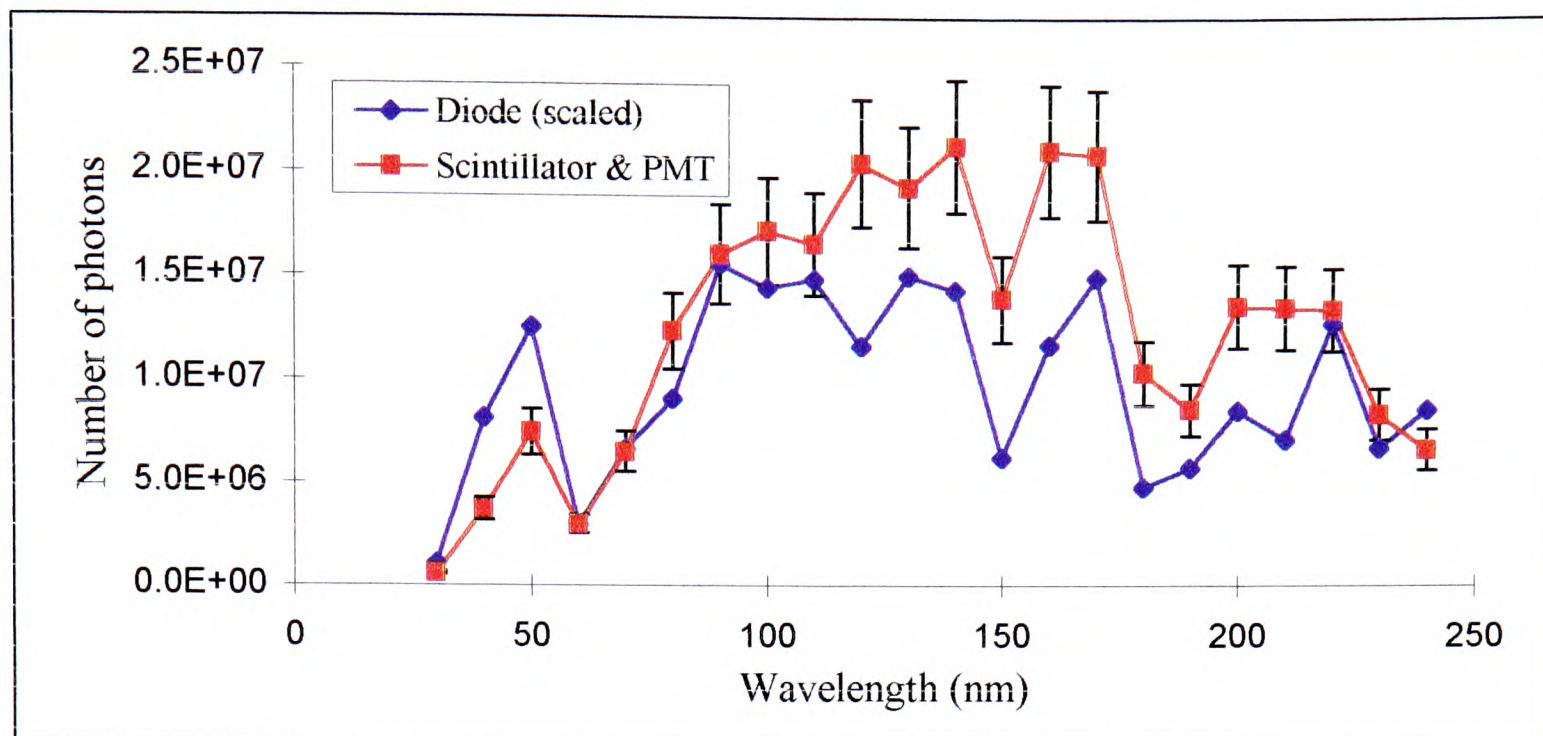


Figure 9.12. Spectrum obtained at exit slit of monochromator from copper target into 4 nm bandwidth, as a function of detection system. Lines between points are a guide to the eye.

From Fig. 9.12 is clear that the two detection systems agreed to within a factor of  $\sim 2$ . Considering the uncertainties in the calibration, especially the sodium salicylate response and the PMT gain, this agreement is remarkably good. Furthermore, the apparent under-reading of the scintillator and PMT system at short wavelengths suggests that the quantum efficiency may have been over-estimated in this region. This lends credence to the quantum-efficiency results of Bruner [1967] over those of Husk *et al.* [1992] (see §9.3.1.2).

## 9.4 Conclusions

In this chapter we have described the successful operation and characterisation of a laser-plasma source of 30 nm to 250 nm radiation. The following conclusions were drawn.

- Copper, mylar, and aluminium were investigated as target materials. Copper gave much the best emission over the whole spectral region of interest.
- Microchannel-plate focusing of the emitted radiation gave about a tenfold improvement in the energy per shot which could be delivered on target, at the short wavelength end of the spectral region of interest. A 30:1 aspect ratio MCP performed better than a 60:1 MCP, at all wavelengths, on account of geometrical collection-efficiency effects.
- A reduction of the focal intensity by almost three orders of magnitude, from  $1.1 \times 10^{15} \text{ W cm}^{-2}$  to  $1.2 \times 10^{12} \text{ W cm}^{-2}$  made remarkably little difference to the emission efficiency. The effect of the change was approximately to halve the efficiency at the short wavelength end of the spectral region of interest, and to increase the efficiency by about a half at the long wavelength end. However, a further reduction in focal intensity, to  $5.4 \times 10^{10} \text{ W cm}^{-2}$ , led to significant cooling of the plasma.
- The production of debris, leading to coating of optics, was found to be a problem over the course of a DNA damage experiment. Debris production could not be mitigated by introducing neon to the laser-plasma chamber, since this was found to lead to spurious radiation reaching the output of the system.



- Two calibrated detection systems were used, which agreed to within a factor of two. This allows us to be confident of the key result of this study. This is that in the spectral region 30 nm to 250 nm, for a 4 nm bandwidth, a dose of  $\sim 10^6$  to  $\sim 10^7$  photons per shot (depending on the wavelength required) could be delivered to a target.



# 10. Conclusion

---

## 10.1 Discussion and suggestions for further work

### 10.1.1 Nanosecond pumping of the Xe III laser

Unfortunately, lack of time meant that nanosecond pumping of the Xe III laser system was not fully tested. However, as discussed in §7.5, it is unlikely that sufficient intensity could have been achieved on target to allow efficient conversion of KrF radiation into soft x-rays. Tighter focusing, which was under investigation, might have helped, but hydrodynamic expansion could have made this an unproductive approach.

It was shown in §7.3.4.1 that a plasma capable of generating photons of the required energy could be generated by using a spot plasma. Thus, breaking the line into spot foci could have been an effective alternative to using a line focus. This could be achieved by the travelling-wave pumping technique [Sher *et al.* 1987]. If fewer (up to ~10) spots were needed, a single spherical lens with several beams incident at different angles (or by means of several lenses), could achieve a similar effect. The optimum number of microscopic spots depends on the quenching processes in the Xe III system. This is because the ideal spot separation is about equal to the distance between a plasma spot and its associated region of maximum gain in the xenon gas. Since the quenching processes have not yet been well characterised, the optimum number and spacing of the spots would have to be determined empirically.

However, as discussed in §7.7, even if a sufficiently hot plasma could be created using the leading edge of the nanosecond laser pulse, it could not be used to give efficient energy extraction from the Xe III laser system. Although sharpening of the pulse risetime would improve this situation, the experimental effort required would probably be better expended on generating sub-nanosecond pulses for amplification. This would also remove the problem of most of the KrF pulse being useless and serving only to damage the optics, generate debris, and produce plasma emission which would mask any laser emission.

### 10.1.2 Pulse-shortening

Of the all-excimer pulse shortening techniques reviewed in chapters 3 and 4, the most promising scheme which was not investigated for the work described in this thesis is the use of electro-optic chopping of a laser pulse [Curry *et al.* 1989]. The TRUBS technique also merits more systematic investigation [Alimpiev *et al.* 1993b].

### 10.1.3 Picosecond pumping of the Xe III laser

Recommendations for future work on picosecond pumping of the Xe III laser system are given in §8.5.6. Of these, the most important is a thorough investigation of the use of pre-pulses in order to improve the plasma conversion efficiency. If this were successful, the next major enhancement of the system should be the application of the travelling-wave geometry.

In fact, some further experimental investigations of pumping the Xe III system have been made very recently (a few weeks before the completion of this thesis), by Lisi,



Turcu, and Allott at the Rutherford Appleton Laboratory. They used the equipment developed for the work described in this thesis, combined with exactly the same laser system as that described in chapter 8. These extra experiments differed from those described in chapter 8 in the following ways:

- A 20 cm focal-length cylindrical lens was used to achieve a 3 cm long line focus, using full KrF pulse trains produced by the laser system.
- Any 109 nm emission was passed through a filter of 300 nm of indium. This has a transmission window in the wavelength region 80 nm to 120 nm. The filter was coated on LiF, giving a narrower net transmission window in the region 105 nm to 120 nm.
- The detection system was a photographic plate placed 16 cm from the plasma, and beyond the indium filter.
- The 109 nm mirror was not used.

Initial results were very promising - a black spot was observed on the developed photographic plate when a plasma was created with xenon in the target chamber, but not when it was evacuated. The blackened spots were of area  $\sim 2 \text{ mm}^2$ , and became smaller and darker as the xenon pressure was increased. However, a subsequent careful examination of the filter showed it contained a  $\sim 5 \text{ }\mu\text{m}$  pinhole, approximately in line with the laser plasma. Back-of-the-envelope calculations suggested that this hole would let through approximately the correct amount of scattered light from the LGP to produce the blackening observed. Thus, an explanation which could not be ruled out is that the black spots observed on the photographic plates were simply pinhole-camera images of the plasma. Sadly, this explanation was confirmed when the same blackening was observed when the system was operated with air, rather than xenon, in the target chamber.

#### 10.1.4 Laser-plasma VUV/XUV source

The VUV/XUV source has already proved its worth for applications - independent workers from other disciplines have used it. An upgrade to the system is planned. This will involve moving the plasma to the entrance slit of the monochromator. Provided that the obvious problems with debris can be overcome, this should increase the energy available at the exit slit. A simple calculation, based on the geometry of the collection system, suggests that this improvement should be by a factor of  $\sim 600$ .

#### 10.1.5 Ultraviolet laser technology

There are a few aspects of excimer laser technology which could easily be addressed in extensions of the work presented here. One such extension is the use of other rare-gas halide excimer laser systems in the simple, high-pulse energy laser module described in chapter 5. It would also be very interesting to investigate the use of the solid-state fluorine source with a molecular fluorine laser. In previous work in the Clarendon Laboratory other workers have found that the presence of a greater concentration than normal of impurities in a commercially-supplied fluorine gas bottle was sufficient to prevent lasing in a molecular fluorine laser. Thus, a significant enhancement of the output energy of such a laser might be possible by the use of an intrinsically purer source of fluorine (in the form of the solid-state fluorine source described in §5.3).



## 10.2 Summary

Finally, having considered what might be achieved in the future, we summarise what has already been achieved in the many areas investigated during the work described in this thesis.

Several subjects have been *reviewed* in this thesis, including:

- short wavelength lasers;
- Xe III lasers;
- all-excimer techniques for generating short pulses of KrF laser radiation, and how they may then be amplified; and
- the generation of tight line foci.

The following experimental work was carried out by the author.

- **The use of a compact oscillator.** This produced KrF laser pulses of FWHM duration 2 ns.
- **The use of TRUBS to achieve pulse shortening.** The shortest pulses obtained were of FWHM duration 5.1 ns. This is many times longer than the 200 ps pulses reported by Alimpiev *et al.* [1993b]. The reason for the poor performance of the system investigated here is suspected to be that the focal intensity rose too slowly at the surface of the TRUBS medium.
- **Plasma-truncated reflection from aluminium and mercury targets.** Aluminium was found to be more reflective. Tight focusing generated the shortest pulses, of 1.8 ns FWHM duration. Spatial structure was observed in the reflected beams, and an explanation proposed.
- **Plasma-truncated spatial filtering.** This technique was investigated and found to be unsuitable for generating low-divergence short pulses. This was because of recovery of the transmission of the spatial filter at late times in the transmitted laser pulse.
- **A mechanical technique for winding KrF laser electrodes.** This gave a more uniform discharge, and allowed a more fluorine-rich mixture to be used in the laser. This led to a single-pulse energy of 2.55 J, some 14% more than had been obtained previously from the same laser system. This single-pulse energy is the greatest ever reported for a conventional-aperture, UV-preionised, discharge-excited KrF laser.
- **The installation and characterisation of a safe, novel solid-state fluorine source.** This gave a gas lifetime and single pulse energy at least as good as that obtained when bottled fluorine was used. The temporal pulse-shape of the output was unchanged.
- **The characterisation of NO<sub>2</sub> as a variable attenuator for KrF laser radiation.** A model of the absorption was devised and found to fit the experimental data, and absorption cross-sections for NO<sub>2</sub> and N<sub>2</sub>O<sub>4</sub> were deduced. A disagreement between these cross-sections and those deduced by Armandillo *et al.* [1982] was explained. Photobleaching of NO<sub>2</sub> was also investigated.
- **Attempts at pumping the Xe III laser using nanosecond-duration KrF pulses.** A very low conversion efficiency into soft-x-rays was deduced. The beam quality of the KrF laser was measured and found to have been very poor. This will have made inevitable the low conversion efficiency.



- **The investigation of coated scintillators as a simple, novel detection system for x-rays.** This involved the spin-coating of sodium salicylate. The coatings were not sufficiently smooth to allow effective coating.
- **The detection of soft-rays from a spot-focus.** This proved the validity of the SXR detection system used in the nanosecond-pumping experiments. However, no convincing evidence of 109 nm fluorescence from Xe III ions was found, when xenon was introduced to the target chamber.
- **The use of a very tight line focusing arrangement for nanosecond pumping of the Xe III laser.** Preliminary experiments showed that the focusing technique could generate 2.5  $\mu\text{m}$  wide line foci, but other priorities meant there was insufficient time to complete the experiment.
- **Attempts at picosecond pumping of the Xe III laser system.** Vigorous attempts at using picosecond KrF pulses to pump the Xe III system did not yield any lasing action. The reason for this was suspected to be a low conversion efficiency into soft-x-rays, and preliminary attempts were made to use preformed plasmas in order to improve this.
- **The production and characterisation of a plasma source of VUV/XUV.** Various target materials, focal spot sizes, and focusing optics were compared. The source was found to be capable of delivering to a target  $10^6$  to  $10^7$  photons per shot over a wavelength range of 30 nm to 200 nm into a 4 nm bandwidth. A scintillator-based detection system was developed and calibrated absolutely to within a factor of  $\sim 2$ .



# References

---

- Alcock et al. 1987** A J Alcock, I J Miller & O L Bourne. *Generation of 50ps 308nm pulses by truncated stimulated Brillouin scattering*. Opt. Comms. **62**, 2, pp 127-129. (1987)
- Alimpiev et al. 1993a** S S Alimpiev, S K Vartapetov, I A Vesolovskii, S V Likhanskii, & A Z Obidin. *Shortening the pulses of KrF and ArF lasers during near-surface breakdown on a liquid*. Quantum Electron. **23**, 3, pp 198-200. (1993)
- Alimpiev et al. 1993b** S S Alimpiev, S K Vartapetov, I A Veselovsky, S V Likhansky, & A Z Obidin. *Pulse shortening of KrF and ArF lasers in a process of optical breakdown on a liquid surface*. Opt. Comms. **96**, pp 71-74. (1993)
- Allison et al. 1964a** R Allison, J Burns, & A J Tuzzolino. *Stability of Fluorescence of Sodium Salicylate*. J. Opt. Soc. Am. **54**, 11, pp 1381-1382. (1964)
- Allison et al. 1964b** R Allison, J Burns, & A J Tuzzolino. *Absolute Fluorescent Efficiency of Sodium Salicylate*. J. Opt. Soc. Am. **54**, 6, pp 747-751. (1964)
- Allott et al. 1995** R Allott, E Turcu, & K Ledingham. *Spectral characterisation of a laser plasma source in the vacuum-ultraviolet*. Private Communication. (1995)
- Anderson 1989** H L Anderson (Ed.). *A Physicist's Desk Reference*. AIP, New York. 2nd Ed. (1989)
- Andreev & Ryzhov 1992** A D Andreev, & V V Ryzhov. *Atomic-field bremsstrahlung of multicharged ions as a pump source for a short-wavelength Auger laser*. Kvantovaya Elektronika **19**, 1, pp 29-31. (1992)
- Armandillo et al. 1982** E Armandillo, A J Kearsley, & C E Webb. *A simple technique for measuring the gain of RGH lasers*. J. Phy. E: Sci. Instrum. **15**, pp 177-179. (1982)
- Asprey 1976a** L B Asprey. *The Preparation of Very Pure Fluorine Gas*. J. Fluor. Chem. **7**, pp 359-361 (1976).
- Asprey 1976b** L B Asprey. *Method of preparing pure fluorine gas*. US Patent 3,989,808 (1976)
- Badziak & Jablonski 1993** J Badziak, & S Jablonski. *Generation of picosecond pulses by fast periodic Q-switching in KrF excimer laser with saturable absorber*. Optics Communications **103**, pp 277-284. (1993)



- Badziak et al. 1992** J Badziak, A Dubicki & J Piotrowski. *On the possibility of picosecond pulses in an excimer laser by fast periodic Q-switching*. Opt. Comms. **91**, pp 147-154. (1992)
- Bakos 1990** J S Bakos. *Laser Plasmas '89*. Prog. Quantum Electr. **14**, pp 251-288 (1990).
- Banic et al. 1980** J Banic, T Efthimiopoulos, & B P Stoicheff. *Gain and saturation intensity measurements of a mode-locked KrF oscillator-amplifier*. Appl. Phys. Lett. **37**, 8, pp 686-688. (1980)
- Barr et al. 1987** J R M Barr, N J Everall, C J Hooker, I N Ross, M J Shaw & W T Toner. *High energy amplification of picosecond pulses at 248nm*. Opt. Comms. **66**, 2,3, pp 127-132. (1988)
- Barty et al. 1988** C P J Barty, D A King, G Y Yin, K H Hahn, J E Field, J F Young, & S E Harris. *12.8-eV Laser in Neutral Cesium*. Phys. Rev. Lett. **61**, 19, pp 2201-2204. (1988)
- Barty et al. 1991** C P J Barty, G Y Yin, J E Field, S J Benerofe, J F Young, & S E Harris. *Photo-electron and photoionization pumping of XUV lasers by laser produced plasmas*. Inst. Phys. Conf. Ser. **116**, pp 21-28. (1991)
- Barty et al. 1992** C P J Barty, G Y Yin, J E Field, D A King, K H Hahn, J F Young & S E Harris. *Studies of a 96.9-nm laser in neutral cesium*. Phys. Rev. A **46**, 7, pp 4286-4296. (1992)
- Bashkin & Stoner 1975** S Bashkin & J O Stoner. *Atomic Energy Levels and Grotian Diagrams I*. North-Holland Publishing Company, Amsterdam. (1975)
- Basov et al. 1970** N G Basov, V A Danilychev, Yu. M. Popov, & D D Khodevich. *Laser operating in the vacuum ultraviolet region of the spectrum by excitation of liquid xenon with an electron beam*. JETP Lett. **12**, pp 329-331. (1970)
- Basu et al. 1993** S Basu, P L Hagelstein, J G Goodberlet, M H Muendel, & S Kaushik. *Amplification in Ni-Like Nb at 204.2 Å Pumped by a Table-Top Laser*. Appl. Phys. B **57**, pp 303-307. (1993)
- Bates et al. 1962** D R Bates, A E Kingston & R W P McWirtter. *Recombination between electrons and ions I. Optically thin plasmas*. Proc. Royal Soc. London **267 A**, pp 297-312. (1962)
- Baughan et al. 1994** A K Baughan, A H Ferguson, A J Kearsley, & G S McGrady. *Improvements in excimer laser performance and safety*. CLEO digest, pp CTuK100. (1994)



- Benerofe et al. 1991** S J Benerofe, G-Y Yin, C P J Barty, J F Young, & S E Harris. *116-nm H<sub>2</sub> Laser Pumped by a Traveling-Wave Photoionization Electron Source*. Phys. Rev. Lett. **66**, 24, pp 3136-3139. (1991)
- Benitez et al. 1991** E L Benitez, D E Husk, S E Schnatterly, & C Tarrio. *A surface recombination model applied to large features in inorganic phosphor efficiency measurements in the soft x-ray region*. J. Appl. Phys. **70**, 6, pp 3256-3260. (1991)
- Berkowitz 1979** J Berkowitz. *Photoabsorption, Photoionization, and Photoelectron Spectroscopy*. Academic Press, New York. (1979)
- Bigio & Thomas 1986** I J Bigio & S J Thomas. *Effective saturable absorber for KrF lasers*. Appl. Phys. Lett. **49**, 16, pp 989-991. (1986)
- Bijkerk 1993** F Bijkerk. *Laser plasma soft x-ray sources, application in microlithography*. Doctoral thesis, Vrije Universiteit, Amsterdam (1993)
- Boehly et al. 1990** T Boehly, M Russotto, R S Craxton, R Epstein, B Yakobi, L B Da Silva, J Nilsen, E A Chandler, D J Fields, B J MacGowan, D L Matthews, J H Schofield, & G Shimkaveg. *Demonstration of a narrow-divergence x-ray laser in neonlike titanium*. Phys. Rev. A **42**, 11, pp 6962-6965 (1990)
- Bokor et al. 1982** J Bokor, R R Freeman, & W E Cooke. *Autoionization-Pumped Laser*. Phys. Rev. Lett. **48**, 18, pp 1242-1245. (1982)
- Bourne & Alcock 1984** O L Bourne, & A J Alcock. *Subnanosecond-pulse generation at 308nm and 450nm by truncated stimulated Brillouin scattering*. Opt. Lett. **9**, 9, pp 411-413. (1984)
- Bridges et al. 1986** J M Bridges, C L Cromer, & T J McIlrath. *Investigation of a laser-produced plasma VUV light source*. Appl. Opt. **25**, 13, pp 2208-2214. (1986)
- Broughton & Fedosejevs 1992** J N Broughton & R Fedosejevs. *Efficient keV x-ray generation from 50 mJ KrF laser plasmas*. Appl. Phys. Lett. **60**, 15, pp 1818-1820. (1992)
- Bruner 1969** E C Bruner Jr., *Absolute Quantum Efficiency of Sodium Salicylate for Excitation by Extreme Ultraviolet*. J. Opt. Soc. Am. **59**, 2, pp 204-211 (1969)
- Bucksbaum et al. 1982** P H Bucksbaum, J Boker, R H Storz & J C White. *Amplification of ultrashort pulses in krypton fluoride at 248nm*. Opt. Lett. **7**, 9, pp 399-401. (1982)



- Burnett et al. 1989** N H Burnett, & P B Corkum. *Cold-plasma production for recombination extreme-ultraviolet lasers by optical-field-induced ionization*. J. Opt. Soc. Am. B **6**, 6, pp 1195-1199. (1989)
- Burrows et al. 1995** M D Burrows, F Bormann, & P Anderson. *Tunable, sub-nanosecond KrF-Raman laser in the ultraviolet*. Appl. Phys. B **61**, pp 451-459. (1995)
- Calvert & Pitts 1966** J G Calvert & J N Pitts Jr., *Photochemistry*. Wiley, New York (1966).
- Canfield & Swanson 1987** L R Canfield & N Swanson. *Far ultraviolet detector standards*. J. of Research of Nat. Bureau of Standards **92**, 2, pp 97-112. (1987)
- Caro & Wang 1986** R G Caro, J C Wang. *Population distributions in Li vapor excited by a photoionization electron source*. Phys. Rev. A. **33**, 4, pp 2563-2574. (1986)
- Caro et al. 1983** R G Caro, & J C Wang, R W Falcone, J F Young & S E Harris. *Soft x-ray pumping of metastable levels of Li<sup>+</sup>*. Appl. Phys. Lett. **42**, 1, pp 9-11. (1983)
- Carroll et al. 1980** P K Carroll, E T Kennedy, & G O Sullivan. *Laser-produced continua for absorption spectroscopy in the VUV and XUV*. Appl. Opt. **19**, 9, pp 1454-1462. (1980)
- Carroll et al. 1983** P K Carroll, E T Kennedy, & G O'Sullivan. *Table-Top EUV Continuum Light Source*. IEEE J. Q.-E. **19**, 12, pp 1807-1811. (1983)
- Cashmore 1995** J Cashmore. *VUV Laser Oscillation in Optically Pumped LaF<sub>3</sub>:Nd<sup>3+</sup>*. D.Phil. Thesis, Oxford (1995).
- Cerjan 1993** C Cerjan. *X-ray plasma source design simulations*. Appl. Opt. **32**, 34, pp 6911-6913 (1993).
- Chaker et al. 1988** M Chaker, H Pépin, V Bateau, B Lafontaine, I Toubhans, R Fabbro & B Faral. *Laser plasma x-ray sources for microlithography*. J. Appl. Phys. **63**, 3, pp 892-899. (1988)
- Chapman & Nugent 1991** H N Chapman & K A Nugent. *X-ray focusing using square channel-capillary arrays*. Rev. Sci. Instrum. E **62**, 6, pp 1542-1561. (1991)
- Chapman et al. 1993** H N Chapman, K A Nugent, & S W Wilkins. *X-ray focusing using cylindrical capillary arrays. I. Theory*. Appl. Opt. **32**, 31, pp 6316-6340. (1993)



- Chenais-Popovics *et al.* 1987** C Chenais-Popovics, R Corbett, C J Hooker, M H ey, G P Kiehn, C L S Lewis, G J Pert, C Regan, S J Rose, S Sadaat, R Smith, T Tomie, & O Willi. *Laser Amplification at 18.2 nm in Recombining Plasma from a Laser-Irradiated Carbon Fiber*. Phys. Rev. Lett. **59**, 19, pp 2161-2164 (1987)
- Chiao *et al.* 1964** R Y Chiao, C H Townes, & B P Stoicheff. *Stimulated Brillouin Scattering and coherent generation of intense hypersonic waves*. Phys. Rev. Lett. **12**, 21, pp 592-595. (1964)
- Christensen *et al.* 1976** C P Christensen, L W Braverman, W H Steier, & C Wittig. *Active mode locking of the XeF laser*. Appl. Phys. Lett. **29**, 7, pp 424-425. (1976)
- Clement *et al.* 1994** T S Clement, C. Tóth, J Wu, & J F Young. *A Reasonably Practical XUV Laser for Applications*. IEEE J. Quantum. Electron. **30**, 9, 2136-2140 (1994).
- Cotton 1990** R A Cotton. *Pulsed UV gas lasers and their applications*. D. Phil. Thesis. Clarendon Laboratory. (1990)
- Coutts & Webb 1986** J Coutts, & C E Webb. *Stability of transverse self-sustained discharge-excited long-pulse XeCl lasers*. J. Appl. Phys. **59**, 3, pp 704-710. (1986)
- Coutts 1994** D W Coutts. *Influence of off-axis unstable resonator alignment on copper vapour laser output divergence*. Opt. Comms. **113**, pp 283-291 (1994)
- Coutts 1995** D W Coutts. *Time Resolved Beam Divergence from a Copper Vapor Laser with Unstable Resonator*. IEEE J. Q-E, **31**, 2, pp340-342. (1995)
- Coutts *et al.* 1993** D W Coutts, D J W Brown, & J A Piper. *Measurements of the divergence evolution of a copper-vapor laser output by using a cylindrical imaging technique*. Applied Optics **32**, 12, pp 2058-2061. (1993)
- Curry 1953** C Curry. *Geometrical Optics*. Richard Clay & Co., Bungay, Suffolk. (1953)
- Curry *et al.* 1989** J J Curry, S T Feng, & J Goldhar. *Generation of KrF laser pulses on a picosecond time scale using electro-optic modulation*. Opt. Lett. **14**, 15, pp 782-784. (1989)
- Damzen & Hutchinson 1983** M J Damzen & M H R Hutchinson. *High-efficiency laser-pulse compression by stimulated Brillouin scattering*. Opt. Lett. **8**, 6, pp 313-315. (1983)



- Danson et al. 1990** C Danson, R Bann, J Excley, D Pepler, I Ross, & I Watson. *The generation of line foci using random phase plates*. IOP Conf. Series (Colloquium on X-Ray lasers, York), **116**, pp 81-84. (1990)
- Davis 1987** G M Davis. *Application of phase conjugate imaging to excimer laser lithography*. D. Phil. thesis, Clarendon Laboratory, Oxford, 1987.
- Davis et al. 1988** G M Davis, M C Gower, F O'Neill, & I C E Turcu. *Plasma x-ray source for lithography generated by a 30 J, 30 ns KrF laser*. Appl. Phys. Lett. **53**, 17, pp 1583-1585. (1988)
- Dennis et al. 1995** T Dennis, H M Duiker, J Wu, Cs Tóth, & J F Young. *Comparison of Laser-Produced Plasma Target Materials for Pumping the 109-nm Xe<sup>2+</sup> Auger Laser*. IEEE J. Sel. Top. Q.-E. **1**, 3, pp 867-871. (1995)
- Derzhavin & Noreav 1991** S I Derzhavin & D A Noreav. *UV generation in ArII, NeII pumped by the soft X-Ray radiation of Laser Plasma*. Radiation Effects and Defects in Solids **123**, pp 743-751. (1991)
- Desselberger et al. 1992** M Desselberger, L Gizzi, V Barrow, J Edwards, F Khattak, S Viana, O Willi, & C N Danson. *High-aspect-ratio line focus and plasma production using a random phase plate*. Appl. Opt. **31**, 19, pp 3759-3766. (1992)
- Dhareshwar et al. 1991** L J Dhareshwar, P A Naik, & D D Bhawalkar. *A plasma shutter to generate a synchronised subnanosecond pulse for optical probing of laser-produced plasmas*. Rev. Sci. Instrum. **62**, 2, pp 369-375. (1991)
- Di Lazzaro et al. 1995** P Di Lazzaro, F Flora, A Gerardino, & T Letardi. *The self-injected XeCl excimer laser*. Appl. Phys. B. **61**, pp 619-628. (1995)
- Divall et al. 1996** E J Divall, C B Edwards, G J Hirst, C J Hooker, A K Kidd, J M D Lister, R Mathumo, I N Ross, M J Shaw, W T Toner, A P Visser, & B E Wyborn. *Titania - a  $10^{20}$  W cm<sup>-2</sup> ultraviolet laser*. J. Mod. Opt. **43**, 5, pp 1025-1033. (1996)
- Duguay & Rentzepis 1967** M A Duguay & P M Rentzepis. *Some Approaches to Vacuum UV and X-Ray Lasers*. Appl. Phys. Lett. **10**, 12, pp 350-352. (1967)
- Durnin 1987** J Durnin. *Exact solutions for nondiffracting beams I. The scalar theory*. J. Opt. Soc. Am. A **4**, 4, pp 651-654 (1987)
- Eden et al. 1978** J G Eden, R W Waynant, S K Searles & R Burnham. *New quenching rates applicable to the KrF laser*. Appl. Phys. Lett. **32**, 11, pp 733-735. (1978)



- Eder et al. 1992** D C Eder, P Amendt, & S C Wilks. *Optical-field-ionized plasma x-ray lasers*. Phys. Rev. A **45**, 9, pp 6761-6772. (1992)
- Ediger & Pettit 1992** M N Ediger, & G H Pettit. *Time-resolved reflectivity of ArF laser-irradiated polyimide*. J Appl. Phys. **71**, 7, pp 3510-3514. (1992)
- Ediger et al. 1993** M N Ediger, G H Pettit, & R Sauerbrey. *Diffuse reflectivity measurements of polyimide during argon fluoride excimer laser ablation*. J. Appl. Phys. **74**, 11, pp 6982-6984. (1993)
- Edwards et al. 1979** C B Edwards, M H R Hutchinson, D J Bradley, & M D Hutchinson. *Repetitive vacuum ultraviolet xenon excimer laser*. Rev. Sci. Instrum. **50**, 10, pp 1201-1207. (1979)
- Efthimiopoulos et al. 1979** T Efthimiopoulos, J Banic, & B P Stoicheff. *Passive mode-locking of a KrF excimer laser*. Can. J. Phys. **57**, pp 1437-1438. (1979)
- Efthimiopoulos et al. 1989** T Efthimiopoulos, B P Stoicheff, & R I Thompson. *Efficient population inversion in excimer states by supersonic expansion of discharge plasmas*. Opt. Lett. **14**, 12, pp 624-626. (1989)
- Einstein 1917** A Einstein. *Zur Quantentheorie der Strahlung. (On the quantum theory of radiation)*. Physikalische Zeitschrift **18**, pp 121-128 (1917).
- Ellis 1984** H Ellis (Ed.). *Nuffield Advanced Science Book of Data*. Longman, Harlow, Essex. Revised Edition (1984).
- Endoh et al. 1989** A Endoh, M Watanabe, N Sakukura, & S Watanabe. *Multiterawatt subpicosecond KrF laser*. Opt. Lett. **14**, 7, pp 353-355. (1989)
- Ewing & Brau 1975** J J Ewing & C A Brau. *Laser action on the  $^2\Sigma^+_{1/2} \rightarrow ^2\Sigma^+_{1/2}$  bands of KrF and XeCl*. Appl. Phys. Lett. **27**, 6, pp 350-352. (1975)
- Fabbro et al. 1985** R Fabbro, C Max, & E Fabre. *Planar laser-driven ablation: Effect of inhibited electron thermal conduction*. Phys. Fluids **28**, 5, pp 1463-1481. (1985)
- Falcone & Kapteyn 1988** R W Falcone & H C Kapteyn. *Photopumped Short Wavelength Lasers*. Nucl. Instr. & Meth. Phys. Res. **B31**, pp 321-323. (1988)
- Figueira et al. 1981** J F Figueira, S J Czuchlewski, C R Phipps Jr. & S J Thomas. *Plasma-breakdown retropulse isolators for the infrared*. Appl. Opt. **20**, 5, pp 838-841. (1981)
- Filippo & Perrone 1992** A A Filippo & M R Perrone. *Shortening of free-running XeCl laser pulses by stimulated Brillouin scattering*. J. Mod. Opt. **39**, 9, pp 1829-1836. (1992)



- Filippo & Perrone 1993** A A Filippo, & M R Perrone. *Stimulated Brillouin Scattering in SF<sub>6</sub> with a Free-Running XeCl Laser as Pump*. Appl. Phys. B **57**, pp 103-107. (1993)
- Fletcher 1993** J H Fletcher. *Soft x-ray contact microscopy using laser generated plasma sources*. D. Phil. Thesis. Clarendon Laboratory. (1993)
- Fletcher et al. 1994** J H Fletcher, R A Cotton, C E Webb, & A J Andrews. *Design and performance of a simple 2 joule KrF laser*. Meas. Sci. Technol. **5**, pp 255-259. (1994)
- Ford et al. 1986** J E Ford, J Meyer, & H Houtman. *Measurement of electrical characteristics and electron density in a fast discharge pumped XeCl excimer laser*. Appl. Phys. Lett. **48**, 24, pp 1639-1641. (1986)
- Gigosos et al. 1994** M A Gigosos, S Mar, C Pérez, & I de la Rosa. *Experimental Stark widths and shifts and transition probabilities of several Xe II lines*. Phys. Rev. E **49**, 2, pp 1575-1585. (1994)
- Ginter & McIlrath 1988** M L Ginter, & T J McIlrath. *Debris and VUV emission from a laser-produced plasma operated at 150 Hz, using a krypton fluoride laser*. Appl. Opt. **27**, 5, pp 885-889. (1988)
- Glenzer & Kunze 1994** S Glenzer, & H J Kunze. *Amplification of extreme-ultraviolet radiation in a gas-liner pinch plasma*. Phys. Rev. E. **49**, 2, pp 1586-1593. (1994)
- Gobbi & Reali 1984** P G Gobbi, & G C Reali. *A novel unstable resonator configuration with a self filtering aperture*. Optics Communications **52**, 3, pp 195-198. (1984)
- Golub et al. 1991** I Golub, T R Gosnall, & A J Taylor. *Suppression of amplified spontaneous emission in a subpicosecond KrF amplifier laser system using acridine dye*. Opt. Comms. **85**, 5 & 6, pp 299-302. (1991)
- Gower & Caro 1982** M C Gower, & R G Caro. *KrF laser with a phase-conjugate Brillouin mirror*. Opt. Lett. **7**, 4, pp 162-164. (1982)
- Gower 1982** M C Gower. *KrF laser amplifier with phase conjugate Brillouin retroreflectors*. Opt. Lett. **7**, 9, pp 423-425. (1982)
- Gower et al. 1982** M C Gower, S Rolt, & C E Webb. *Direct measurement of photoabsorption cross-sections: application to UV laser photolysis of OCSe and Se<sub>2</sub> + CO*. J. Phys. D.: Appl. Phys. **15**, pp 27-34. (1982)
- Green & Webb 1975** J M Green, & C E Webb. *Second-kind collisions of electrons with excited Cd<sup>+</sup>, Ca<sup>+</sup>, Ga<sup>+</sup>, Tl<sup>+</sup>, and Pb<sup>+</sup> ions*. J. Phys. B. **8**, 9, pp 1484-1500. (1975)



- Hall & Blacet 1952** T C Hall, Jr., & F E Blacet. *Separation of the Absorption Spectra of NO<sub>2</sub> and N<sub>2</sub>O<sub>4</sub> in the Range of 2400-5000 Å*. J. Chem. Phys. **20**, 11, pp 1745-1748. (1952)
- Hara et al. 1989** T Hara, K Ando, N Kusakabe, H Yashiro, & Y Aoyagi. *Soft X-Ray Lasing in an Al Plasma Produced by a 6 J Laser*. Jap. J. Appl. Phys. **28**, 6, pp L1010-1012. (1989)
- Harris & Caro 1986** S E Harris, & R G Caro. *Shake-up as a mechanism for vacuum-ultraviolet lasers*. Opt. Lett. **11**, 1, pp 10-11. (1986)
- Harris et al. 1984** S E Harris, D J Walker, R G Caro, A J Mendelsohn, & R D Cowan. *Quasi-metastable quartet levels in alkaline atoms and ions*. Opt. Lett. **9**, pp 168-170. (1984)
- Hasted 1972** J B Hasted. *Physics of Atomic Collisions*. Butterworth, London, 2nd. Ed. (1972).
- Haxell et al. 1993** A M Haxell, S M Hooker, & C E Webb. *Observation of vacuum ultraviolet laser oscillation in nitric oxide*. Appl. Opt. **32**, 12, pp 2062-2065. (1993)
- Hay & Dunning 1977** P J Hay, & T H Dunning, Jr. *The electronic states of KrF*. J. Chem. Phys. **66**, 3, pp 1306-1316. (1977)
- Heard 1963** H G Heard. *Ultra-violet Gas Laser at Room Temperature*. Nature, **4907**, p 667 (1963)
- Heath & Sacher 1966** D F Heath, & P A Sacher. *Effects of a Simulated High-Energy Space Environment on the Ultraviolet Transmittance of Optical Materials between 1050 Å and 3000 Å*. Appl. Opt. **5**, 6, pp 937-943. (1966)
- Henke et al. 1984** B L Henke, F G Fujiwara, M A Tester, C H Dittmore, & M A Palmer. *Low-energy x-ray response of photographic films. II. Experimental characterisation*. J. Opt. Soc. Am. **1**, 6, pp 828-849. (1984)
- Hercher 1967** M Hercher. *An Analysis of Saturable Absorbers*. Appl. Opt. **6**, 5, pp 947-954. (1967)
- Hilbig & Wallenstein 1983** R Hilbig, & R Wallenstein. *Tunable VUV Radiation Generated by Two-Photon Resonant Frequency Mixing in Xenon*. IEEE J. Q.-E. **19**, 2, pp 194-201. (1983)
- Hirst et al. 1987** G J Hirst, V Rivano, & C E Webb. *Spatially resolved gain measurements in a discharge-pumped KrF laser amplifier*. J. Appl. Phys. **61**, 7, pp 2438-2444. (1987)



- Hodgson & Dreyfus 1972** R T Hodgson, & R W Dreyfus. *Vacuum-uv Laser Action Observed in H<sub>2</sub> Werner Bands: 1161-1240 Å*. Phys. Rev. Lett. **28**, 9, pp 536-539. (1972)
- Hodgson 1970** R T Hodgson. *Vacuum-ultraviolet laser action observed in the Lyman bands of molecular hydrogen*. Phys. Rev. Lett. **25**, 8, pp 494-497 (1970)
- Hon 1980** D T Hon. *Pulse compression by stimulated Brillouin scattering*. Opt. Lett. **5**, 12, pp 516-518. (1980)
- Hooker & Webb 1994** S M Hooker, & C E Webb. *Progress in vacuum ultraviolet lasers*. Prog. Quan. Electr. **18**, pp 227-274. (1994)
- Hooker et al. 1992a** S M Hooker, A M Haxell, & C E Webb. *Influence of Cavity Configuration on the Pulse Energy of a High-Pressure Molecular Fluorine Laser*. Appl. Phys. B. **55**, pp 54-59. (1992)
- Hooker et al. 1992b** S M Hooker, A M Haxell, & C E Webb. *Observation of New Laser Transitions and Saturation Effects in Optically Pumped NO*. Appl. Phys. B. **54**, pp 119-125. (1992)
- Hube et al. 1988a** M Hube, R Brinkman, H Welloing, R Beigang, & B Welleghausen. *A Cadmium Photoionization Laser Pumped by Laser Induced Plasma Radiation from a Multi Foci Device*. Appl. Phys. B **45**, pp 197-201. (1988)
- Hube et al. 1988b** M Hube, M Kumkar, M Dieckmann, R Beigang & B Welleghausen. *Potassium photoionization laser produced by innershell ionization of excited potassium*. Opt. Comms. **66**, 2,3, pp 107-110. (1988)
- Hughes 1980** T P Hughes. *An introduction to the absorption of laser light in plasmas*. Proc. 20<sup>th</sup> Scottish Universities Summer School in Physics 1979 "Laser-Plasma Interactions" R A Cairns & J J Sanderson (Eds.) pp 1-90, Edinburgh University Physics Dept. (1980).
- Huo et al. 1985** Y S Huo, A J Alcock & O L Bourne. *A Time-Resolved Study of Sub-Nanosecond Pulse Generation by the Combined Effects of Stimulated Brillouin Scattering and Laser-Induced Breakdown*. Appl. Phys. B **38**, pp 125-129. (1985)
- Husk et al. 1991** D E Husk, C Tarrio, E L Benitez, & S E Schnatterly. *Observation of second-order kinetic damage in sodium salicylate due to soft-x-rays*. Appl. Phys. Lett. **59**, 16, pp 2052-2054. (1991)
- Husk et al. 1992** D E Husk, C Tarrio, E L Benitez, & S E Schnatterly. *Absolute photoluminescent efficiency and photon damage of sodium salicylate in the soft-x-ray region*. J. Opt. Soc. Am. B **9**, 1, pp 152-156. (1992)



- Hutchinson 1987** I H Hutchinson. *Principles of plasma diagnostics*. Cambridge University Press. (1987)
- Ilcisin et al. 1994** K J Ilcisin, F Aumayr, J L Schwob, & S Suckewer. *Demonstration of resonant fluorescence in Mo VII induced by Mo XII for possible lasing near 600 Å*. J. Opt. Soc. Am. B. **11**, 8, pp 1436-1444. (1994)
- Ito et al. 1996** S Ito, T Saito, & A Tada. *A new gas purifier for ArF excimer lasers*. Rev. Sci. Instrum. **67**, 3, pp 658-661. (1996)
- Jaroszynski & King 1983** D A Jaroszynski, T A King. *Subnanosecond pulse generation of 193 nm radiation by pulse slicing*. J. Phys. E: Sci. Instrum. **16**, pp 862-865. (1983)
- Johnson et al. 1951** F S Johnson, K Watanabe, & R Tousey. *Fluorescent Sensitized Photomultipliers for Heterochromatic Photometry in the Ultraviolet*. J. Opt. Soc. Am. **41**, 10, pp 702-708. (1951)
- Kaplan & Gibson 1986** R D Kaplan & R B Gibson. *Metal halide saturable absorbers at 248 nm*. Appl. Phys. Lett. **49**, 5, pp 251-252. (1986)
- Kapteyn & Falcone 1988** H C Kapteyn & R W Falcone. *Auger-pumped short wavelength lasers in xenon and krypton*. Phys. Rev. A **37**, 6, pp 2033-2038. (1988)
- Kapteyn 1989** H C Kapteyn. *Photoionization-Pumped Short-Wavelength Lasers*. Ph.D. Thesis, University of California, Berkeley, USA. (1989)
- Kapteyn 1992** H C Kapteyn. *Photoionization-pumped x-ray lasers using ultrashort-pulse excitation*. Appl. Opt. **31**, 24, pp 4931-4939 (1992)
- Kapteyn et al. 1986a** H C Kapteyn, R W Lee & R W Falcone. *Observation of a Short-Wavelength Laser Pumped by Auger Decay*. Phys. Rev. Lett. **57**, 23, pp 2939-2942. (1986)
- Kapteyn et al. 1986b** H C Kapteyn, M M Murnane, R W Falcone, G Kolbe, & R W Lee. *Measurements on a Proposed Short Wavelength Laser System in Xenon III*. Proc. SPIE **688**, pp 54-60. (1986)
- Kapteyn et al. 1987** H C Kapteyn, M M Murnane & R W Falcone. *Time-resolved measurements of short wavelength fluorescence from x-ray-excited ions*. Opt. Lett. **12**, 9, pp 663-665. (1987)
- Kapteyn et al. 1992** H C Kapteyn, L B de la Silva, & R W Falcone. *Short-Wavelength Lasers*. Proc. IEEE **80**, 3, pp 342-347. (1992)
- Kaschke et al. 1988** M Kaschke, N P Ernsting, & F. P. Schäfer. *Rubrene, a saturable absorber for 308 nm*. Opt. Comms. **66**, 4, pp 211-215. (1988)



- Kato et al. 1990** Y Kato, E Miura, T Tachi, H Shiraga, H Nishimura, H Daido, M Yamanaka, T Jitsuno, M Takagi, P R Herman, H Takabe, S Nakai, C Yamanaka, M H Key, G J Tallents, S J Rose, & P T Rumsby. *Observation of Gain at 54.2 Å on Balmer-Alpha Transition of Hydrogenic Sodium*. Appl. Phys. B **50**, pp 247-256. (1990)
- Kauffman et al. 1993** L Kauffman, D W Phillion, & R C Spitzer. *X-ray production ~13 nm from laser-produced plasmas for projection x-ray lithography applications*. Appl. Opt. **32**, 34, pp 6897-6900. (1993)
- Keane et al. 1989** C J Keane, N M Ceglio, B J MacGowan, D L Matthews, D G Nilson, J E Trebes & D A Whelan. *Soft x-ray laser source development and applications experiments at Lawrence Livermore National Laboratory*. J. Phys. B: Mol. Opt. Phys. **22**, pp 3343-3362. (1989)
- Kearsley 1980** A J Kearsley. *Gas laser efficiency*. D. Phil. Thesis, Clarendon Laboratory, Oxford, (1980).
- Kearsley et al. 1979** A J Kearsley, A J Andrews, & C E Webb. *A novel pre-ionization technique for discharge excited rare gas halide lasers*. Opt. Comms. **31**, 2, pp 181-184. (1979)
- Key 1985** M H Key. *Laboratory production of X-ray lasers*. Nature, **316**, pp 314-319 (1985).
- Kim et al. 1989** D Kim, C H Skinner, G Umesh & S Suckewer. *Gain measurements at 18.22 nm in C VI generated by a Nd:glass laser*. Opt. Lett. **14**, 13, pp 665-667. (1989)
- Klemm & Huss 1949** W Klemm & E Huss. Zeitung Anorg. Chem. **258**, p 221 (1949)
- Klopotek et al. 1987** P Klopotek, B Burghardt, & W Muckenheim. *Short pulses from excimer lasers*. J. Phys. E.: Sci. Instrum. **20**, pp 1269-1270. (1987)
- Knapp & Smith 1964** R A Knapp, & A M Smith. *Fatigue Effects in the Luminescent Yield of Sodium Salicylate*. Appl. Opt. **3**, 5, pp 637-639. (1964)
- Kodama et al. 1986** R Kodama, K Okada, N Ikeda, M Mineo, K A Tanaka, T Mochizuki, & C Yamanaka. *Soft x-ray emission from  $\omega_0$ ,  $2\omega_0$ , and  $4\omega_0$  laser-produced plasmas*. J. Appl. Phys. **59**, 9, pp 3050-3052. (1986)
- Koller 1965** L R Koller. *Ultraviolet radiation*. Wiley, New York. 2nd Ed. (1965)
- Konjević & Pittman 1986** N Konjević & T L Pittman. *Stark broadening of spectral lines of homologous, doubly-ionized inert gases*. J. Quant. Spectrosc. Radiat. Transfer **37**, 3, pp 311-318. (1987)



- Kovács & Szatmári 1994** G Kovács, & S Szatmári. *KrF gain module for short-pulse off-axis amplification*. Meas. Sci. Technol. **5**, pp 127-137. (1994)
- Kubodera et al. 1992** S Kubodera, P J Wisoff, & R Sauerbrey. *Spectroscopy and kinetics of ionic alkali halide excimers excited by a laser-produced plasma*. J. Opt. Soc. Am. B **9**, 1, pp 10-21. (1992)
- Kubodera et al. 1995** S Kubodera, K Midorikawa, M Obara, H Tashiro, & K Toyoda. *Numerical Modeling of the Xe Auger Laser Kinetics*. IEEE J. Q-E **31**, 8, pp 1543-1547. (1995)
- Kuizenga et al. 1973** D J Kuizenga, D W Phillion, T Lund, & A E Siegman. *Simultaneous Q-switching and mode-locking in the cw Nd:YAG laser*. Opt. Comms. **9**, 3, pp 221-226. (1973)
- Kumar & Datta 1979** V Kumar, & A K Datta. *Vacuum ultraviolet scintillators: sodium salicylate and p-terphenyl*. App. Opt. **18**, 9, pp 1414-1417. (1979)
- Kurnit & Thomas 1989** N A Kurnit & S C Thomas. *Application of a Phase-Conjugate Brillouin Mirror to Generation of High-Quality Variable-Duration KrF Pulses*. IEEE J. Quant.-Elect. **25**, 3, pp 421-429. (1989)
- Kurosawa et al. 1991** K Kurosawa, Y Takigawa, W Sasaki, M Okuda, E Fujiwara, K Yoshida, & Y Kato. *High-Power Operation of an Argon Excimer Laser with a MgF<sub>2</sub> and SiC Cavity*. IEEE J. Q.-E. **27**, 1, pp 71-76. (1991)
- Lacy et al. 1989** R A Lacy, A C Nilsson, R L Byer, W T Silfvast, O R Wood II, & S Svanberg. *Photoionization-pumped gain at 185 nm in a laser-ablated indium plasma*. J. Opt. Soc. Am. B. **6**, 6, pp 1209-1216. (1989)
- Laufer et al. 1965** A H Laufer, J A Pirog, & J R Nesby. *Effect of Temperature on the Vacuum Ultraviolet Transmittance of Lithium Fluoride, Calcium Fluoride, Barium Fluoride, and Sapphire*. J. Opt. Soc. Am. **55**, 1, pp 64-66. (1965)
- Laycock & Webster 1992** L C Laycock & S C Webster. *Bessel Beams: Their generation and application*. GEC J. Research **10**, 1, pp 36-51 (1992)
- Laycock & Whybrew 1990** L C Laycock & A Whybrew. *Bessel Beams*. Report DORL 109, GEC-Marconi Hirst Research Centre, Wembley (1990).
- Lee et al. 1987** T N Lee, E A McLean, & R C Elton. *Soft X-Ray Lasing in Neonlike Germanium and Copper Plasmas*. Phys. Rev. Lett. **59**, 11, pp 1185-1188. (1987)
- Lemoff et al. 1994** B E Lemoff, C P J Barty, & S E Harris. *Femtosecond-pulse-driven, electron-excited XUV lasers in eight-times-ionized noble gases*. Opt. Lett. **19**, 8, pp 569-571. (1994)



- Lemoff et al. 1995** B E Lemoff, G Y Yin, C L Gordon III, C P J Barty, & S E Harris. *Demonstration of a 10-Hz Femtosecond-Pulse-Driven XUV Laser at 41.8 nm in Xe IX*. Phys. Rev. Lett. **74**, 9, pp 1574-1577. (1995)
- Lemoff et al. 1996** B E Lemoff, G Y Yin, C L Gordon III, C P J Barty, & S E Harris. *Femtosecond-pulse-driven 10-Hz 41.8-nm laser in Xe IX*. J. Opt. Soc. Am. B **13**, 1, pp 180-184. (1996)
- Lide 1992** D R Lide (Ed.). *CRC Handbook of Chemistry and Physics*. CRC Press, Boca Raton. 73rd edition (1992).
- Lister et al. 1994** J M D Lister, E J Divall, S W Downes, C B Edwards, G J Hirst, C J Hooker, M H Key, I N Ross, M J Shaw, & W T Toner. *Sprite. A very high brightness, ultraviolet laser system*. J. Mod. Opt. **41**, 6, pp 1203-1215. (1994)
- Lou et al. 1990** Q Lou, T Yagi, K Igarashi, & H Saito. *The effects of F<sub>2</sub> concentration on discharge pumped KrF laser characteristics*. J. Appl. Phys. **68**, 6, pp 2572-2576. (1990)
- Luches et al. 1989** A Luches, V Nassisi, & M R Perrone. *Experimental characterization of a self-filtering unstable resonator applied to a short pulse XeCl laser*. Appl. Opt. **28**, 11, pp 2047-2051. (1989)
- Ludewigt et al. 1987** K Ludewigt, W Pfingsten, C Mohlmann, & B Wellegehausen. *High-power vacuum-ultraviolet anti-Stokes Raman laser with atomic selenium*. Opt. Lett. **12**, 1, pp 39-41. (1987)
- Luk et al. 1989** T S Luk, A McPherson, G Gibson, K Boyer, & C K Rhodes. *Ultrahigh-intensity KrF\* laser system*. Opt. Lett. **14**, 20, pp 1113-1115. (1989)
- Lundberg et al. 1984** H Lundberg, J J Macklin, W T Silfvast, & O R Wood II. *High-gain soft-x-ray-pumped photoionization laser in zinc vapor*. Appl. Phys. Lett. **45**, 4, pp 335-337. (1984)
- MacGowan et al. 1987** B J MacGowan, S Maxon, P L Hagelstein, C J Keane, R A London, D L Matthews, M D Rosen, J H Scofield, & D A Whelan. *Demonstration of Soft-X-Ray Amplification in Nickel-like Ions*. Phys. Rev. Lett. **59**, 19, pp 2157-2160. (1987)
- MacGowan et al. 1992** B J MacGowan, L B Da Silva, D J Fields, C J Keane, J A Koch, R A London, D L Matthews, S Maxon, S Mrowka, A L Osterheld, J H Schofield, G Shimkaveg, J E Trebes, & R S Walling. *Short wavelength x-ray laser research at the Lawrence Livermore National Laboratory*. Phys. Fluids B, **4**, 7, pp 2326-2337 (1992)
- Maiman 1960** T H Maiman. *Stimulated Optical Radiation in Ruby*. Nature, **4736**, pp 493-494 (1960)



- Matthews & Rosen 1988** D L Matthews, & M D Rosen. *Soft-X-Ray Lasers*. Scientific American. December 1988, pp 60-65. (1988)
- Matthews et al. 1985** D L Matthews, P L Hagelstein, M D Rosen, M J Eckart, N M Ceglio, A U Hazi, H Medeck, B J MacGowan, J E Trebes, B L Whitten, E M Campbell, C W Hatcher, A M Hawryluk, R L Kauffman, L D Pleasance, G Rambach, J H Schofield, G Stone, & T A Weaver. *Demonstration of a Soft X-Ray Amplifier*. Phys. Rev. Lett. **54**, 2, pp 110-113 (1985)
- Max 1982** C E Max. *Physics of the coronal plasma in laser fusion targets*. Les Houches, Session XXXIV, 1980 - Interaction Laser-Plasma/Laser-Plasma Interaction, R Balian & J C Adam (Eds.), p 304, North Holland Publishing Co. (1982).
- McGrady 1995** G S McGrady. *Nickel Fluorides as reversible F<sub>2</sub> sources*. Private communication, 1995.
- McGuire 1975** E J McGuire. *Soft-X-Ray Amplified Spontaneous Emission via the Auger Effect*. Phys. Rev. Lett. **35**, 13, pp 844-848. (1975)
- McIntyre et al. 1987** I A McIntyre, K Boyer & C K Rhodes. *Shortening of KrF\* laser pulses using stimulated Brillouin scattering*. Opt. Lett. **12**, 11, pp 909-911. (1987)
- Mendelsohn & Harris 1985** A J Mendelsohn & S E Harris. *Proposal for an extreme-ultraviolet selective autoionization laser in Zn III*. Opt. Lett. **10**, 3, pp 128-130. (1985)
- Michette 1993** A G Michette. *Plasma X-Ray Sources*. In "X-Ray Science & Technology", A G Michette & C J Buckley (Eds.) Institute of Physics Publishing, Bristol, (1993)
- Milchberg et al. 1996** H M Milchberg, T R Clark, C G Durfee III, T M Antonsen, & P Mora. *Development and applications of a plasma waveguide for intense laser pulses*. Phys. Plasmas **3**, 5, pp 2149-2155. (1996)
- Miyazaki et al. 1991** K Miyazaki, T Fukatsu, I Yamashita, T Hasama, K Yamada & T Sato. *Output and Picosecond Amplification Characteristics of an Efficient and High-Power Discharge Excimer Laser*. Appl. Phys. B **52**, pp 1-7. (1991)
- Moore 1984** W J Moore. *Basic Physical Chemistry*. Prentice/Hall, London (1984)
- Morsell et al. 1992** A L Morsell, M Powers & H Shields. *Plasma soft x-ray source generated by 4-ns excimer laser pulses*. Appl. Phys. Lett. **60**, 4, pp 425-427. (1992)



- Murnane et al. 1991** M M Murnane, H C Kapteyn, M D Rosen, & R W Falcone. *Ultrafast X-ray Pulses from Laser-produced Plasmas*. Science, February 1991, pp 531-536. (1991)
- Murray et al. 1979** J R Murray, J Goldhar, D Eimerl, & A Szöke. *Raman Pulse Compression of Excimer Lasers for Application to Laser Fusion*. IEEE J. Quantum-Electron. pp 342-368. (1979)
- Nagata et al. 1993** Y Nagata, K Midorikawa, S Kubodera, M Obara, H Tashiro, & K Toyoda. *Soft-X-Ray Amplification of the Lyman- $\alpha$  Transition by Optical-Field-induced Ionization*. Phys. Rev. Lett. **71**, 23, pp 3774-3777. (1993)
- Nassisi & Pecoraro 1993** V Nassisi, & A Pecoraro. *Stimulated Brillouin and Raman Scattering for the Generation of Short Excimer Laser Pulses*. IEEE J. Quantum Electron. **29**, 9, pp 2547-2552. (1993)
- Nassisi & Primavera 1993** V Nassisi, & M Primavera. *Experimental characterization of a folded self-filtering unstable resonator applied to an excimer laser*. Opt. Comms. **102**, pp 452-456. (1993)
- Nilsen 1992** J Nilsen. *Resonantly photo-pumped Li-like x-ray lasers*. Appl. Opt. **31**, 24, pp 4957-4961 (1992).
- Nilsen et al. 1992** J Nilsen, J H Scofield, & E A Chandler. *Reinvestigating the early resonantly photopumped x-ray laser schemes*. Appl. Opt. **31**, 24, pp 4950-4956. (1992)
- Nishioka et al. 1989** H Nishioka, H Kuranishi, & H Takuma. *UV saturable absorber for short pulse KrF laser systems*. Opt. Lett. **14**, 13, pp 692-694. (1989)
- Nodomi et al. 1991** R Nodomi, Y Oeda, K Sajiki, S Nakajima, M Watanabe, & S Watanabe. *High Repetition Rate, Wide-Aperture KrF Lasers for Subpicosecond Amplification*. IEEE J. Q-E **27**, 3, pp 441-447. (1991)
- Norreys et al. 1996** P A Norreys, M Zepf, S Moustazis, A P Fewes, P Lee, M Bakarezos, C N Danson, A Dyson, P Gibbon, P Loukakos, D Neely, F N Walsh, J S Wark, & A E Dangor. *Efficient Extreme UV Harmonics Generated from Picosecond Laser Pulse Interactions with Solid Targets*. Phys. Rev. Lett. **76**, 11, pp 1832-1835. (1996)
- O'Neill 1988** F O'Neill. *Laser-plasma XUV sources*. Proc. Scottish Universities Summer School in Physics, **35**, "Laser plasma interactions 4", M B Hooper (Ed.) (1989)



- O'Sullivan et al. 1994** G O'Sullivan, P K Carroll, J Conway, P Dunne, R Faulkner, T McCormack, C McGuinness, P van Kampen, & B Weinmann. *Extreme ultraviolet continuum emission from laser-generated plasmas and applications to spectroscopy*. Opt. Eng. **33**, 12, pp 3993-3998. (1994)
- Pacala & Laudenslager 1980** T J Pacala, & J B Laudenslager. *High-energy subnanosecond pulse amplification in XeCl*. Appl. Phys. Lett. **37**, 4, pp 366-368. (1980)
- Pakula 1991** R A Pakula. *Radiation-pumped C VI lasing scheme*. J. Opt. Soc. Am. B **8**, 3, pp 639-645 (1991)
- Palik et al. 1985** E D Palik (Ed) *Handbook of optical constants of solids*. Acad. Press (1985).
- Patterson & Vaughan 1963** D A Patterson, & W H Vaughan. *Influence of Crystal Surface on the Optical Transmission of Lithium Fluoride in the Vacuum-Ultraviolet Spectrum*. J. Opt. Soc. Am. **53**, 7, pp 851-855. (1963)
- Pepper 1982** D M Pepper. *Nonlinear optical phase conjugation*. Opt. Eng. **21**, 2, pp158-183 (1982).
- Perrone et al. 1993** M R Perrone, A Piegari & S Scaglione. *On the Super-Gaussian Unstable Resonators for High-Gain Short-Pulse Laser Media*. IEEE J. Q.-E. **29**, 5, pp 1423-1427. (1993)
- Persson et al. 1988** W Persson, C-G Wahlström, G Bertuccelli, H O Di Rocco, J G Reyna Almandos, & M Gallardo. *Spectrum of Doubly Ionized Xenon (Xe III)*. Physica Scripta **38**, pp 347-369. (1988)
- Popil et al. 1987** R Popil, P D Gupta, R Fedosejevs, & A A Offenberger. *Measurement of KrF-laser-plasma x-ray radiation from targets with various atomic numbers*. Phys. Rev. A **35**, 9, pp 3874-3882. (1987)
- Powers & Shields 1994** M F Powers, & H Shields. *Excimer laser technology for Soft X-ray generation*. Proc. SPIE Conf. Visible and UV lasers. **2115**, pp 62-68. (1994)
- Präg et al. 1996** A R Präg, A Glinz, J E Balmer, Y Li, & E E Fill. *Prepulse dependence of J=0-1 lasing at 32.6 nm in neon-like titanium*. Appl. Phys. B **63**, pp 113-116. (1996)
- Preston et al. 1996** S G Preston, A Sanpera, M Zepf, W J Blyth, C G Smith, J S Wark, M H Key, K Burnett, M Nakai, D Neely, & A A Offenberger. *High-order harmonics of 248.6-nm KrF laser from helium and neon ions*. Phys. Rev. A **53**, 1, pp 31-34. (1996)



- Purić et al. 1991** J Purić, S Djeniže, J Labat, A Srećković, & M Platiša. *Stark Broadening Regularities within Successive Ionization Stages in Krypton and Xenon*. Contrib. Plas. Phys. **31**, 1, pp 63-69. (1991)
- Rácz et al. 1992** B Rácz, A Patócs, G Szabó, Zs Bor & F Ignácz. *Direct Generation of Sub-Nanosecond Pulses in a High-Pressure Miniature Excimer Laser*. Appl. Phys. B **54**, pp 513-515. (1992)
- Regan et al. 1994** S P Regan, L K Huang, M J May, H W Moos, D Stutman, S Kovnovich, & M Finkenthal. *Measured conversion efficiencies of P45, paraterphenyl, tetraphenyl butadiene, and sodium salicylate phosphors in the soft-x-ray wavelength range*. Appl. Opt. **33**, 16, pp 3595-3599 (1994)
- Reksten et al. 1981** G Reksten, T Varghese, & W Margulis. *Active mode locking of a XeCl laser*. Appl. Phys. Lett. **39**, 2, pp 129-131. (1981)
- Richardson et al. 1993** M Richardson, W T Silfvast, H A Bender, A Hanzo, V P Yanovsky, F Jin, & J Thorpe. *Characterization and control of laser plasma flux parameters for soft-x-ray projection lithography*. Appl. Opt. **32**, 34, pp 6901-6910. (1993)
- Ripin et al. 1977** B H Ripin, U Feldman, & G A Doschek. *Picosecond optical gate*. Rev. Sci. Instrum. **48**, 7, pp 935-937. (1977)
- Rocca 1996** J Rocca. *Researchers Close the Gap in the Hunt for Soft X-ray Lasers*. Photonics Spectra, July 1996, pp 102-108
- Rocca et al. 1988** J J Rocca, D C Beethe, & M C Marconi. *Proposal for soft-x-ray and XUV lasers in capillary discharges*. Opt. Lett. **13**, 7, pp 565-567. (1988)
- Rocca et al. 1993a** J J Rocca, O D Cortázar, F G Tomasel, & B T Szapiro. *Efficient generation of highly ionized calcium and titanium plasma columns for collisionally excited soft-x-ray lasers in a fast capillary discharge*. Phys. Rev. E. **48**, 4, pp 2378-2381. (1993)
- Rocca et al. 1993b** J J Rocca, M C Marconi, & F G Tomasel. *Study of the Soft X-Ray Emission from Carbon Ions in a Capillary Discharge*. IEEE J. Q.-E. **29**, 1, pp 182-191. (1993)
- Rocca et al. 1993c** J J Rocca, O D Cortazar, B Szapiro, K Floyd, & F G Tomasel. *Fast-discharge excitation of hot capillary plasmas for soft-x-ray amplifiers*. Phys. Rev. E **47**, 2, pp 1299-1304. (1993)
- Rocca et al. 1995** J J Rocca, M C Marconi, J L A Chilla, D P Clark, F G Tomasel, & V N Shlyaptsev. *Discharge-Driven 46.9-nm Amplifier with Gain-Length Approaching Saturation*. IEEE J. Sel. Top. Q-E **1**, 3, pp 945-948. (1995)



- Rosen et al. 1985** M D Rosen, P L Hagelstein, D L Matthews, E M Campbell, A U Hazi, B L Whitten, B MacGowan, R E Turner, R W Lee, G Charatis, G E Bush, C L Shepard, & P D Rockett. *Exploding-Foil technique for Achieving a Soft X-Ray Laser*. Phys. Rev. Lett. **54**, 2, pp 106-109. (1985)
- Ross & Hodgson 1985** I N Ross, E M Hodgson. *Some optical designs for the generation of high quality line foci*. J. Phys. E: Sci. Instrum. **18**, 2, pp 169-173. (1985)
- Ross et al. 1987** I N Ross, J Boon, R Corbett, A Damerell, P Gottfeldt, C Hooker, M H Key, G Kiehn, C Lewis, & O Willi. *Design and performance of a new line focus geometry for x-ray laser experiments*. Appl. Opt. **26**, 9, pp 1584-1588. (1987)
- Samson & Haddad 1974** J A R Samson & G N Haddad. *Fluorescent efficiency of sodium salicylate between 116 and 600 Å*. J. Opt. Soc. Am. **64**, 10, pp 1346-1347. (1974)
- Schawlow & Townes 1958** A L Schawlow, C H Townes. *Infrared and Optical Masers*. Phys. Rev. **112**, 6, pp 1940-1949. (1958)
- Schulz-von der Gathen 1990** V Schulz-von der Gathen, T Bornemann, V Kornas, & F Dobelev. *VUV Generation by High-Order CARS*. IEEE J. Q.-E. **26**, 4, pp 739-743. (1990)
- Schwarzenbach et al. 1986** A P Schwarzenbach, T S Luk, I A McIntyre, U Johann, A McPherson, K Boyer, & C K Rhodes. *Subpicosecond KrF\* excimer-laser source*. Opt. Lett. **11**, 8, pp 499-501. (1986)
- Searles & Hart** S K Searles & G A Hart. *Stimulated emission at 281.8 nm from XeBr*. Appl. Phys. Lett. **27**, 4, pp 243-245. (1975)
- Sharp et al. 1992** T E Sharp, M J Byrd, & J F Young. *Practical XUV laser for applications research*. CLEO, OSA Technical Digest Series **12**, CTuH1. (1992)
- Shaw 1991** M J Shaw. *Prospects for high-power KrF lasers*. Las. & Part. Beams **9**, 2, pp 309-328 (1991)
- Shaw et al. 1986** M J Shaw, J P Partanen, Y Owadano, I N Ross, E Hodgson, C B Edwards, F O'Neill. *High-power forwards Raman amplifiers employing low-pressure gases in light guides. II. Experiments*. J. Opt. Soc. Am. B **3**, 10, pp 1466-1475. (1986)
- Shay et al. 1988** T M Shay, R C Sze, M Maloney, & J F Figueira. *120-ps duration pulses by active mode locking on an XeCl laser*. J. Appl. Phys. **64**, 7, pp 3578-3760. (1988)



- Sher & Benerofe 1991** M H Sher & S J Benerofe. *Prepulsing of laser-produced plasmas for more efficient pumping of extreme-ultraviolet lasers*. J. Opt. Soc. Am. **8**, 12, pp2437-2441 (1991).
- Sher et al. 1987** M H Sher, J J Macklin, J F Young & S E Harris. *Saturation of the Xe II 109-nm laser using travelling-wave laser-produced-plasma excitation*. Opt. Lett. **12**, 11, pp 891-893. (1987)
- Sher et al. 1991** M H Sher, S J Benerofe, J E Young & S E Harris. *2-Hz 109-nm mirrorless laser*. J. Opt. Soc. Am. B **8**, 1, pp 114-116. (1991)
- Shin et al. 1994** H-J Shin, D-E Kim, & T-N Lee. *Soft x-ray amplification in a capillary discharge*. Phys. Rev. E. **50**, 2, pp 1376-1382. (1994)
- Sigel 1989** R Sigel. *X rays from Laser Produced Plasmas*. Proc. SPIE, **1140**, pp 6-12 (1989).
- Sigel et al. 1990** R Sigel, K Eidmann, F Lavarenne, & R F Schmalz. *Conversion of laser light into soft x rays. Part I: Dimensional analysis*. Phys. Fluids B **2**, 1, pp 199-207. (1990)
- Silfvast & Wood 1989** W T Silfvast, O R Wood II. *Simple efficient travelling-wave excitation of short-wavelength lasers using a conical pumping geometry*. Opt. Lett. **14**, 1, pp 18-20. (1989)
- Silfvast 1982** W T Silfvast. *Inner Shell Photoionization Laser in Cd Vapor Produced by Black Body Laser-Plasma Source*. Private Communication 1995, originally written in 1982.
- Silfvast et al. 1983** W T Silfvast, J J Macklin, & O R Wood II. *High-gain inner-shell photoionization laser in Cd vapor pumped by soft-x-ray radiation from a laser-produced plasma source*. Opt. Lett. **8**, 11, pp 551-553. (1983)
- Singleton et al. 1990** D L Singleton, G Paraskevopoulos, & R S Taylor. *Dynamics of Excimer Laser Ablation of Polyimide Determined by Time-Resolved Reflectivity*. Appl. Phys. B. **50**, pp 227-230. (1990)
- Skinner et al. 1990** C H Skinner, D Kim, D Voorhees, & S Suckewer. *Development of small-scale soft-x-ray lasers: aspects of data interpretation*. J. Opt. Soc. Am. B **7**, 10, pp 2042-2047. (1990)
- Slatkline et al. 1982** M Slatkline, I J Bigio, B J Feldman, & R A Fisher. *Efficient phase conjugation of an ultraviolet XeF laser beam by stimulated Brillouin scattering*. Opt. Lett. **7**, 3, pp 108-110. (1982)
- Spitzer et al. 1993** R C Spitzer, R L Kauffman, T Orzechowski, D W Phillion, & C Cerjan. *Soft x-ray production from laser produced plasmas for lithography applications*. J. Vac. Sci. Technol. B **11**, 6, pp 2986-2989. (1993)



- Spitzer et al. 1996** R C Spitzer, T J Orzechowski, D W Phillion, R L Kauffman, & C Cerjan. *Conversion efficiencies from laser-produced plasmas in the extreme ultraviolet regime*. J. Appl. Phys. **79**, 5, pp 2251-2258. (1996)
- Stead et al. 1990** A D Stead, T W Ford, J A Catchside, C P Hills, & A Ridgeley. *Soft X-Ray Contact Microscopy of Biological Specimens: Aluminium-Coated Silicon Nitride Windows as XUV Filters*. J. X-Ray Sci. & Tech. **2**, pp 172-179. (1990)
- Steyer et al. 1990** M Steyer, F P Schäfer, S Szatmári, & G Kühnle. *Feasibility of a Laboratory X-Ray Laser Pumped by Ultrashort UV Laser Pulses*. Appl. Phys. B, **50**, pp 265-273. (1990)
- Suckewer & Fishman (1980)** S Suckewer, & H Fishman. *Conditions for soft x-ray lasing action in a confined plasma column*. J Appl. Phys. **51**, 4, pp 1922-1931. (1980)
- Suckewer et al. 1985** S Suckewer, C H Skinner, H Milchberg, C Keane, & D Voorhees. *Amplification of Stimulated Soft-X-Ray Emission in a Confined Plasma Column*. Phys. Rev. Lett. **55**, 17, pp 1753-1756. (1985)
- Suckewer et al. 1990** S Suckewer, & C H Skinner. *Soft X-ray Lasers and Their Applications*. Science **247**, pp 1553-1557. (1990)
- Szatmári & Schäfer 1984** S Szatmári, & F P Schäfer. *Picosecond Gain Dynamics of KrF*. Appl. Phys. B **33**, pp 219-233. (1984)
- Szatmári & Schäfer 1988** S Szatmári, & F P Schäfer. *Simplified laser system for the generation of 60ps pulses at 248 nm*. Opt. Comms. **68**, 3, pp 196-202. (1988)
- Szatmári & Simon 1993** S Szatmári, & P Simon. *Interferometric multiplexing scheme for excimer amplifiers*. Opt. Comms. **98**, pp 181-192. (1993)
- Szatmári 1994** S Szatmári. *High-Brightness Ultraviolet Excimer Lasers*. Appl. Phys. B. **58**, pp 211-223. (1994)
- Szatmári et al. 1987** S Szatmári, F P Schäfer, E Müller-horsche, & W Muckenheim. *Hybrid dye-excimer laser system for the generation of 80 fs, 900GW pulses at 248nm*. Opt. Comms. **63**, 3, pp 305-309. (1987)
- Takahashi et al. 1984** A Takahashi, M Maeda, & Y Noda. *Short Pulse Generation and Compression in XeCl lasers*. IEEE J. Q.-E. **20**, 10, pp 1196-1201. (1984)
- Tambay & Thareja 1993** R Tambay, & R J Thareja. *Laser produced plasma: A pumping source for cadmium photo-ionization laser*. Pramana J. Phys. **41**, 3, pp 257-269. (1993)



- Taylor & Goldhar 1983** M W Taylor, & J Goldhar. *Pulse compression by pulse-stacking in a KrF amplifier*. Appl. Opt. **22**, 9, pp 1288-1292. (1983)
- Taylor & Mihailov 1985** R S Taylor & S Mihailov. *Excited Singlet-State Absorption in Laser Dyes at the XeCl Wavelength*. Appl. Phys. B **38**, pp 131-137. (1985)
- Taylor et al. 1988** A J Taylor, R B Gibson, & J P Roberts. *Picosecond gain dynamics in KrF amplifiers*. Appl. Phys. Lett. **52**, 10, pp 773-775. (1988)
- Teubner et al. 1992** U Teubner, G Kühnle, & F P Schäfer. *Detailed Study of the effect of a Short Prepulse on Soft X-Ray Spectra Generated by a High-Intensity KrF\* Laser Pulse*. Appl. Phys. B **54**, pp 493-499. (1992)
- Thomas et al. 1989** M Thomas, J Davis, C Jacobsen, & R C C Perera. *Optical Constants Grapher*. A computer program presented to SRI 1989, Berkeley, CA, August 7-11 (1989).\*
- Tóth et al. 1993** Cs Tóth, J F Young, & R Sauerbrey. *Optical gain in the ionic excimer  $Cs^{2+}F^-$  excited by soft x rays from a laser-produced plasma*. Opt. Lett. **18**, 24, pp 2120-2122. (1993)
- Toubhans et al. 1989** I Toubhans, R Fabbro, J C Gauthier, M Chaker, & H Pepin. *X-Ray conversion efficiency in laser-produced plasmas. Application to X-ray lithography*. Proc. SPIE **1140**, pp 358-364. (1989)
- Tsakiris 1996** G Tsakiris. *X-ray sources strive for the water window*. Physics World, June 1996, pp 22-23.
- Tünnermann et al. 1990** A Tünnermann, K Wrede, & B Wellegehausen. *Generation of High Peak Power Excimer Laser Radiation by Pulse Shortening*. Appl. Phys. B. **50**, pp 361-364. (1990)
- Tünnermann et al. 1991** A Tünnermann, H Eichman, A Maetzing, M Hube & B Wellinghausen. *Investigations of a new inner-shell photoionisation laser at 165nm in the mercury ion*. J. Opt. Soc. Am. B **8**, 10, pp 2042-2046. (1991)
- Turcu et al. 1993** I C E Turcu, I N Ross, P Trenda, C W Wharton, R A Meldrum, H Daido, M S Schulz, P Fluck, A G Michette, A P Juna, J R Maldonado, H Shields, G J Tallents, L Dwivedi, J Krishnan, D L Stevens, T J Jenner, D Batani, & H Goodson. *Picosecond excimer laser-plasma X-ray source*. Proc. SPIE, **2015**, pp 243-259 (1993)
- Verdeyen 1981** J T Verdeyen. *Laser Electronics*. Prentice Hall, London, 2<sup>nd</sup> edition (1981).

---

\* Contact R C C Perera at LBL, Centre for X-ray Optics 4-200, Berkeley, Ca 94703; email: rupert@lbl.bitnet for details.



- Villeneuve et al. 1991** D M Villeneuve, G D Enright, H A Baldis, & J -C Kieffer. *Novel laser line focus geometry applied to X-ray lasers*. Opt. Comms. **81**, 1&2, pp 54-58. (1991)
- Wada et al. 1992** S Wada, A Kasai, & H Tashiro. *Efficient generation of higher-order anti-Stokes VUV radiation by steep reise pumping*. Opt. Lett. **17**, 2, pp 97-98. (1992)
- Wagner et al. 1996** T Wagner, E Eberl, K Frank, W Hartmann, D H H Hoffmann, & R Tkotz. *XUV Amplification in a Recombining z-Pinch Plasma*. Phys. Rev. Lett. **76**, 17, pp 3124-3127. (1996)
- Walker et al. 1986** D J Walker, R G Caro & S E Harris. *Proposal for an extreme-ultraviolet Auger laser at 63.8nm in Cs III*. J. Opt. Soc. Am. B **3**, 11, pp 1515-1518. (1986)
- Walker et al. 1987** D J Walker, C P J Barty, G Y Yin, J F Young & S E Harris. *Observation of super Coster-Kronig-pumped gain in Zn III*. Opt. Lett. **12**, 11, pp 894-896. (1987)
- Wallmeier & Zacharias 1988** H Wallmeier, & H Zacharias. *Continuously Tunable VUV Radiation (129-210 nm) by Anti-Stokes Raman Scattering in Cooled H<sub>2</sub>*. Appl. Phys. B. **45**, pp 263-272. (1988)
- Wang et al. 1995** Q Wang, C Zhou, & Z Ma. *VUV spectra from the krypton-fluoride ionic excimer*. Appl. Phys. B **61**, pp 301-304. (1995)
- Watanabe et al. 1983** M Watanabe, S Watanabe, & A Endoh. *Generation of a 300-psec pulse by direct mode locking of a long-pulse XeCl laser*. Opt. Lett. **8**, 12, pp 638-640. (1983)
- Waynant 1972** R W Waynant. *Observations of Gain by Stimulated Emission in the Werner Band of Molecular Hydrogen*. Phys. Rev. Lett. **28**, 9, pp 533-535 (1972)
- Waynant et al. 1970** R W Waynant, J D Shipman Jr., R C Elton, & A W Ali. *Vacuum ultraviolet laser emission from molecular hydrogen*. Appl. Phys. Lett. **17**, 9, pp 383-384. (1970)
- Webb 1983** C E Webb. *Discharge excited rare gas halide lasers*. Quantum Electronic and Electro-Optics (P L Knight, Ed.), Wiley (1983).
- Weigold & Piper 1990** A M Weigold, & J A Piper. *Proposal for a magnesium photoionization laser at 24.7 nm*. Opt. Lett. **15**, 21, pp 1209-1211. (1990)
- Weigold 1991** A M Weigold. *Model investigation of a Soft X-ray Photoionisation Laser*. Aust. J. Phys. **44**, pp 217-276 (1991)



- Weigold et al. 1993** A M Wiegold, A V Rode, & J A Piper. *Traveling-wave excitation of the Ar II shake-up laser at 476.5 nm*. J. Opt. Soc. Am. B **10**, 8, pp 1470-1474. (1993)
- Wellegehausen et al. 1989** B Wellegehausen, M Hube, & F. Jin. *Investigations on Laser Plasma Soft X-Ray Sources Generated with Low Energy Laser Systems*. Appl. Phys. B. **49**, pp 173-178. (1989)
- Wellegehausen et al. 1996** B Wellegehausen, H Welling, C Momma, M Feuerhake, K Mossavi, & H Eichmann. *Generation of short-pulse VUV and XUV radiation*. Opt. Quantum. Elect. **28**, pp 267-281. (1996)
- White & Henderson 1983** J C White, & D Henderson. *Anti-Stokes Raman laser emission at 149 nm in atomic bromine*. Opt. Lett. **8**, 10, pp 520-522. (1983)
- Whybrew & Webb 1995** A Whybrew, & C E Webb. *Nitrogen dioxide: a variable attenuator for KrF laser radiation*. Meas. Sci. Technol. **6**, pp 432-434. (1995)
- Wisoff et al. 1984** P J K Wisoff, J F Young. *Active Mode Locking of a Microwave-Pumped XeCl Laser*. IEEE J. Q-E **20**, 3, pp 195-197. (1984)
- Wood & Silfvast 1982** O R Wood II, W. T. Silfvast. *Electron density and energy output limits of plasma-recombination lasers*. Appl. Phys. Lett. **41**, 2, pp 121-123. (1982)
- Wood et al. 1986** O R Wood II, W T Silfvast, J J Macklin & P J Maloney. *Comparison of extreme-ultraviolet flux from 1.06- and 10.6  $\mu$ m laser-produced plasma sources for pumping photoionization lasers*. Opt. Lett. **11**, 4, pp 198-200. (1986)
- Xia & Ballik 1993** Z M Xia, & E A Ballik. *Investigations of a compact short-pulse discharge-excited XeCl laser*. Opt. Comms. **98**, pp 172-180. (1993)
- Yamada et al. 1988** K Yamada, K Miyazaki, T Hasama, & T Sato. *1-ns High-Power High-Repetitive Excimer Laser Oscillator*. IEEE J. Q.-E. **24**, 2, pp 177-182. (1988)
- Yamakoshi et al. 1993** H Yamakoshi, C T Chin, S Jaimungal, P R Herman, F W Budnik, G Kulcsar, L Zhao, & R S Marjoribanks. *Extreme-ultraviolet laser photo-pumped by a self-healing Hg target*. "Applications of laser plasma radiation". Proc. SPIE **2017**, pp 227-231. (1993)
- Yamakoshi et al. 1996** H Yamakoshi, P R Herman, M P Le Flohic, B Xiao, L Zhao, G Kulcsar, F W Budnik, & R S Majoribanks. *Picosecond pumping of extreme-ultraviolet lasers using preformed laser plasmas*. J. Opt. Soc. Am. B **13**, 2, pp 436-442. (1996)
- Yin et al. 1987** G -Y Yin, C P J Barty, D A King, D J Walker, S E Harris & J F Young. *Low-energy pumping of a 108.9 nm xenon Auger laser*. Opt. Lett. **12**, 5, pp 331-333. (1987)



- Yoshida *et al.***  
**1994** H Yoshida, K Nakamura, H Nimomiya, & S Horiguchi. *Experimental study of excimer formation kinetics in a discharge-pumped KrF excimer laser*. Opt. Communs. **105**, 1,2, pp 133-141. (1994)
- Zel'dovich *et al.***  
**1972** B Ya Zel'Dovich, V I Popovichev, V V Ragul'skii, & F S Faizullov. *Connection between the wave fronts of the reflected and exciting light in stimulated Mandel'shtam-Brillouin scattering*. JETP Lett. **15**, pp 109-113. (1972)



## DESIGN NOTE

# Nitrogen dioxide: a variable attenuator for KrF laser radiation

Adam Whybrew and Colin E Webb

University of Oxford, Department of Physics, Clarendon Laboratory, Parks Road, Oxford OX1 3PU, UK

Received 23 November 1994, in final form 9 January 1995, accepted for publication 16 January 1995

**Abstract.** Nitrogen dioxide ( $\text{NO}_2$ ) in gaseous equilibrium with dinitrogen tetroxide ( $\text{N}_2\text{O}_4$ ) is investigated as a variable attenuator for KrF excimer laser radiation (at 249 nm). A model for the physical chemistry of the equilibrium mixture is given and used to predict its absorption coefficient. Experimental data are presented, which confirm the model, and absorption cross sections of  $6 \times 10^{-24} \text{ m}^2$  for  $\text{NO}_2$  and  $87 \times 10^{-24} \text{ m}^2$  for  $\text{N}_2\text{O}_4$  are deduced. Photobleaching of the gas was observed when it was exposed to high (1.7 J) pulse energies. This effect was found to be most severe at total absorbing gas pressures of approximately 5 kPa, for which there was a 60% increase in transmission after exposure to 60 laser pulses, with recovery over tens of minutes. The possibility of the  $\text{NO}_2$  and  $\text{N}_2\text{O}_4$  concentrations taking a significant time to equilibrate in a fresh gas sample was investigated, and not found to cause a measurable change in the gas absorption.

## 1. Introduction

Optical attenuation is often vital to prevent saturation or damage in optical detectors when measuring the temporal and spatial properties of KrF laser pulses. A nitrogen dioxide ( $\text{NO}_2$ ) gas cell provides a continuously variable and calculable attenuation. The use of such an absorber for KrF laser radiation, as a means of measuring the gain of a laser system, has been reported by Armandillo *et al* (1982). Here we extend this work to give a full model of the physical chemistry of the system, and consider some of its limitations.

## 2. The model of the equilibrium between $\text{NO}_2$ and $\text{N}_2\text{O}_4$

Armandillo *et al* (1982) observed that the behaviour of  $\text{NO}_2$  as an absorber for 249 nm KrF radiation is determined by the chemical equilibrium between  $\text{NO}_2$  and dinitrogen tetroxide ( $\text{N}_2\text{O}_4$ ). The relevant equilibrium constant,  $K_P$  is defined as

$$K_P = \frac{P_{\text{NO}_2}^2}{P_{\text{N}_2\text{O}_4}} \frac{1}{P^0} \quad (1)$$

where  $P_{\text{NO}_2}$  and  $P_{\text{N}_2\text{O}_4}$  are the partial pressures of  $\text{NO}_2$  and  $\text{N}_2\text{O}_4$ , respectively, and  $P^0$  is one standard atmosphere, 101.32 kPa. The equilibrium constant,  $K_P$ ,

shows a strong dependence on the temperature,  $T$ , and is found empirically (Plekhothin 1970) to obey

$$\log_{10}(K_P) = -\frac{2692}{T} + 1.75 \log_{10}(T) + 4.83 \times 10^{-3}T - 7.144 \times 10^{-6}T^2 + 3.062 \quad (2)$$

where  $T$  is measured in kelvins.

The total pressure,  $P$ , is the sum of the partial pressures of  $\text{NO}_2$  and  $\text{N}_2\text{O}_4$ . In the limit of low total pressures, only  $\text{NO}_2$  is present in an equilibrium mix of the gases. In contrast, for a temperature of 293 K and total pressure of 16 kPa (the greatest pressure used in this work), we find that expressions (1) and (2) indicate that the mixture is 40%  $\text{N}_2\text{O}_4$ , and so the effect of both forms must be included in the absorption model.

The absorption coefficient,  $\alpha$ , of the equilibrium mixture is

$$\alpha = N_{\text{NO}_2}\sigma_{\text{NO}_2} + N_{\text{N}_2\text{O}_4}\sigma_{\text{N}_2\text{O}_4} \quad (3)$$

where  $N_{\text{NO}_2}$  and  $N_{\text{N}_2\text{O}_4}$  are the number densities and  $\sigma_{\text{NO}_2}$  and  $\sigma_{\text{N}_2\text{O}_4}$  the absorption cross sections of  $\text{NO}_2$  and  $\text{N}_2\text{O}_4$ , respectively. Combining expression (3) with expression (1), and assuming ideal gas behaviour, we find  $\alpha$  as a function of  $T$  and  $P$ :

$$\alpha = \frac{1}{k_B T} (P\sigma_{\text{N}_2\text{O}_4} + \frac{1}{2}(\sigma_{\text{N}_2\text{O}_4} - \sigma_{\text{NO}_2})[K'_P - (K'^2_P + 4PK'_P)^{1/2}]) \quad (4)$$

where  $K'_P \equiv K_P P^0$ .



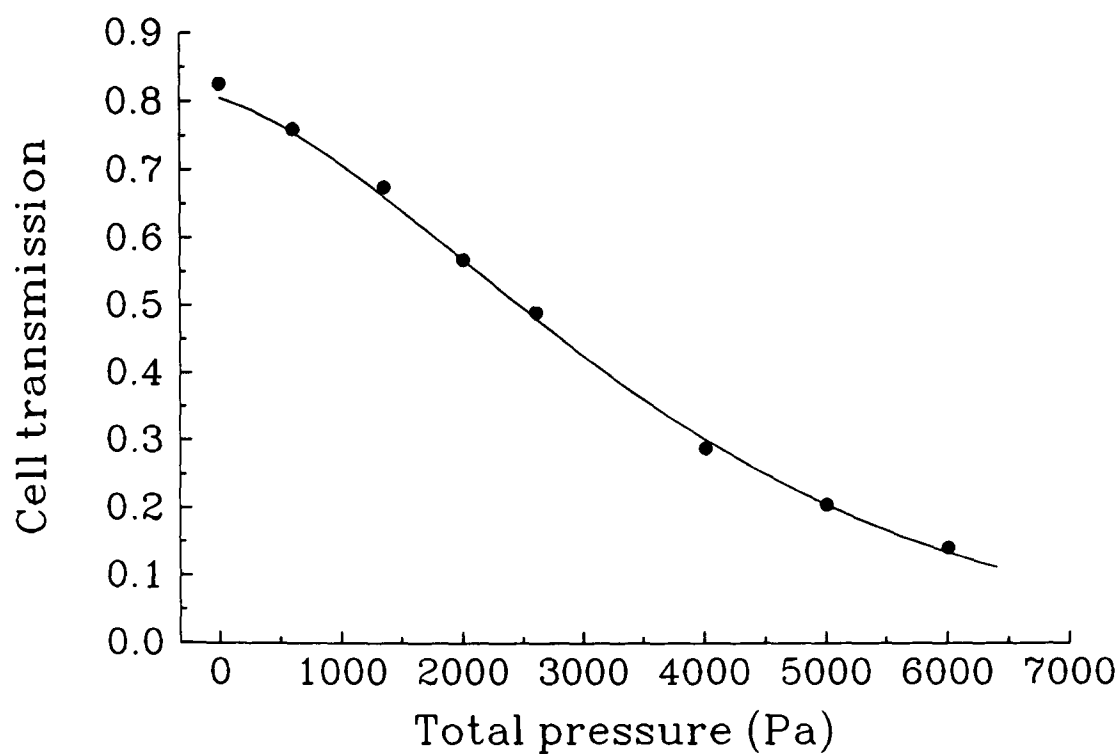


**Figure 1.** Data points show observed transmission of absorption cell as a function of total absorbing gas pressure, at 25.4 °C. The curve is a fit to these data based on expression (4), using the cross sections given in table 1.

3. Experimental observations

Expression (4) was tested using apparatus consisting of a silica-windowed absorption cell, rotary gas pump, gas supply and pressure gauge. The cell could be interconnected and isolated as necessary. The NO<sub>2</sub> (Air Products, 99.5%) was stored as a pressurized liquid, and vapour drawn off as required into the absorption cell, which was then isolated from the gas supply. The stainless steel absorption cell had a path length of 6 cm and a clear circular aperture of diameter 5 cm. Measurements were made of the transmission of the cell to 75 mJ pulses of KrF radiation, over an area of 2 cm<sup>2</sup>.

The ambient temperature in the room was measured, and absorption data were taken at two temperatures (23.3 and 25.4 °C). With  $\sigma_{\text{NO}_2}$  and  $\sigma_{\text{N}_2\text{O}_4}$  as free parameters, the data were fitted to expression (4), correcting for the Fresnel losses at the window surfaces. Figure 1 shows a fit of expression (1) to one of the sets of data points, and table 1 shows the cross sections obtained.

From these, it is clear that the model given here accurately predicts the cell transmission, and that the cross sections measured agree closely with those measured by Hall and Blacet (1952). They disagree, however, with those of Armandillo *et al* (1982). There are two reasons for this. Firstly, Armandillo *et al* (1982) assumed the absorption of the mixture of NO<sub>2</sub> and N<sub>2</sub>O<sub>4</sub> to be entirely due to NO<sub>2</sub> at total pressures up to 3 kPa. This assumption is false; for a total pressure of 3 kPa, and assuming a temperature of 298 K, the higher absorption cross section of N<sub>2</sub>O<sub>4</sub> makes it responsible for 72% of the total absorption coefficient, despite its forming only 15% of the equilibrium mixture. Secondly, Armandillo *et al* (1982) assumed the gas mixture to be predominantly N<sub>2</sub>O<sub>4</sub> at pressures in the range 6–29 kPa. This assumption is also false; for a total pressure of 6 kPa

**Table 1.** Absorption cross sections for 249 nm light of NO<sub>2</sub> and N<sub>2</sub>O<sub>4</sub> found in this work and reported in the literature.

	$\sigma_{\text{NO}_2}(10^{-24} \text{ m}^2)$	$\sigma_{\text{N}_2\text{O}_4}(10^{-24} \text{ m}^2)$
This work	$6 \pm 1$	$87 \pm 5$
Hall and Blacet (1952)	4–7	$88.2 \pm 0.7$
Armandillo <i>et al</i> (1982)	8.9	24

the mixture is only about a quarter N<sub>2</sub>O<sub>4</sub>. This caused them to underestimate the absorption cross section of N<sub>2</sub>O<sub>4</sub> by a factor of approximately four (the contribution to the total absorption from NO<sub>2</sub> is small, about 20%).

4. Photobleaching

In similar experiments with the same apparatus, Fletcher (1993) found the apparent transmission of the gas to rise with the number of laser pulses to which it was exposed. This was not observed during the measurements described in section 3, which employed 75 mJ pulses, but was found when the cell was subjected to KrF pulses of energy 1.7 J (over an area of 9 cm<sup>2</sup>). For example, with a total gas pressure of 5 kPa, the cell transmission rose by 60% after it had been exposed to 60 such laser pulses at 7.5 s intervals. When the cell was no longer exposed to the laser radiation (except for five pulses to measure the instantaneous transmission), the absorption recovered. After 3 min the transmission had returned to 140% of that of the fresh gas, and after 30 min this ratio had recovered to 120%. The 0.1 K change in the ambient temperature over the same time is too small to explain the effect.

The photobleaching was found to be less severe at both high and low pressures; after the cell had been



exposed to 30 laser pulses the transmission of the cell rose only 4% for a total gas pressure of 2 kPa and 10% for a total pressure of 16 kPa, but 40% for a 5 kPa total pressure.

Possible causes of the effect include the photodissociation of gas molecules and slow recombination (Calvert and Pitts 1966) of  $\text{NO}_2$  to  $\text{N}_2\text{O}_4$ , and of  $\text{NO}^\cdot$  and  $\text{O}^\cdot$  radicals to  $\text{NO}_2$ , reactions with the cell walls of any of the gas species present and the heating effect of the absorption. These mechanisms are all consistent with the observation that the photobleaching caused less severe changes in the cell transmission at both low and high gas pressures.

The composition of the vapour in equilibrium with the liquid in the  $\text{NO}_2$  reservoir will not have been the same as that of the gas in the absorption cell. This is because gas in these two places will have been at different pressures. The transmission of the cell could have changed as the gas composition in the cell equilibrated. This possibility was ruled out by measuring the total pressure in the cell, and its transmittance, over 30 min, exposing it to laser radiation only four times. Neither the total pressure (5 kPa), nor the transmittance were found to change significantly.

## 5. Conclusion

No attempt was made to pinpoint the causes of the photobleaching; for  $\text{NO}_2$  to be a useful tool it must be used in a regime in which this effect is minimized. Anyone using  $\text{NO}_2$  as a calibrated absorber should therefore check that photobleaching is not occurring, simply by observing whether the transmission of the

absorption cell rises with its exposure to laser energy. A circulating gas system could be used to avoid the problem.

The range of cell transmittances observed varied from 82% (Fresnel losses only) with no gas in the absorption cell, to a transmission of about  $2 \times 10^{-4}$  with a total gas pressure of 16 kPa, although the lowest transmission used for the calibration experiments was only 7.4%. The minimum transmittance observed was determined simply by the availability of laser energy detectors; many orders of magnitude more attenuation could be achieved by using a longer path length, or a gas pressure greater than 16 kPa (although the vapour pressure of the mixture defines a maximum possible pressure of about 100 kPa at room temperature).

Provided that photobleaching is absent and the gas temperature is known, we have shown that  $\text{NO}_2$  provides a simple, cheap, calibrated and continuously variable attenuator for KrF laser radiation.

## References

- Armandillo E, Kearsley A J and Webb C E 1982 A simple technique for measuring the gain of RGH lasers *J. Phys. E: Sci. Instrum.* **15** 177–9
- Calvert J G and Pitts J N Jr 1966 *Photochemistry* (New York: Wiley)
- Fletcher J H 1993 Soft x-ray contact microscopy using laser generated plasma sources *D Phil Thesis* Oxford University (Bodleian Library)
- Hall T C Jr and Blacet F E 1952 Separation of the absorption spectra of  $\text{NO}_2$  and  $\text{N}_2\text{O}_4$  in the range of 2400–5000 Å *J. Chem. Phys.* **20** 1745–8
- Plekhotkin V F 1970 Second virial coefficients of nitrogen oxides *Russ. J. Phys. Chem.* **44** 1156–7



